7th edition

Copernicus Marine Service

COPERNICUS

OCEAN STATE REPORT

7th edition of the Copernicus Ocean State Report | 2023

PROGRAMME OF THE EUROPEAN UNION

Copernicus Europe's eyes on Earth

Implemented by MERCATOR OCEAN INTERNATIONAL

Copernicus Publications The Innovative Open Access Publisher

STATE OF THE PLANET

About the Copernicus Ocean State Report

As part of the Copernicus Marine Service, the annual Copernicus Ocean State Report (OSR) launched in 2015 is the key tool of its ocean reporting framework. The OSR reports on the state, variability, and ongoing changes in the marine environment of the global ocean and the European regional seas over the past decades up to close to real time. Using observation-based (remote sensing, in situ) and ocean reanalysis data, the OSR provides a comprehensive 4-dimensional (latitude, longitude, depth, and time) analysis of the Blue, Green, and White Ocean. The OSR is intended to act as a reference, providing a unique ocean monitoring dashboard for the scientific community and for policy makers and others with decision making responsibilities.

Copernicus Marine Service

PROGRAMME OF THE EUROPEAN UNION

Copernicus Europe's eyes on Earth

Implemented by MERCATOR OCEAN INTERNATIONAL

STATE OF THE PLANET

About State of the Planet

State of the Planet (SP) is a journal dedicated to the publication of scientific synthesis reports and assessments on all subjects of the Earth and environmental sciences. In a rapidly changing world, expert-based assessments of academic findings curated for a wider audience to support decision making, science communication, education, and funder mandates are becoming more and more widespread. Such reports are extensive science community efforts offering timely, state-of-the-art insight into a specific field of the Earth sciences. State of the Planet is open to any reporting and assessment initiative by (inter-) governmental agencies, environmental services, learned societies or associations of researchers that aim to publish on a regular basis.

Copernicus Publications
The Innovative Open Access Publisher

publications@copernicus.org
http://publications.copernicus.org

This document was produced with funding by the European Union. Views and opinions expressed are however those of the author(s) only and the European Commission cannot be held responsible for any use which may be made of the information contained therein.

Cover photo by Ivan Bandura on Unsplash

von Schuckmann, K., Moreira, L., Le Traon, P.-Y., Grégoire, M., Marcos, M., Staneva, J., Brasseur, P., Garric, G., Lionello, P., Karstensen, J., and Neukermans, G. (Eds.): 7th edition of the Copernicus Ocean State Report (OSR7), Copernicus Publications, State Planet, 1-osr7, https://doi.org/10.5194/sp-1-osr7, 2023.

Editorial

The Copernicus Ocean State Report (OSR) gathers an ensemble of peer-review publications that analyse the state, variability, and trend of the physics and biogeochemistry of the ocean and sea ice (respectively the blue, green, and white ocean). Contributions to the OSR are short, cover the global ocean and European regional seas, and target a wide audience made up of the scientific community, policy makers, industries, and the general public. They are based on an in-depth analysis of Copernicus Marine products (and others) constituting model reanalysis and satellite and in situ data available over several decades back in time up to 1 year before the publication of the OSR. Copernicus Marine products are regularly updated with the best available information and produced according to a coordinated and high-quality control protocol. All products and their documentation are openly available from https://marine.copernicus.eu/. This guarantees an assessment based on consistent and well-documented datasets. The Copernicus OSR is produced annually, and its preparation is coordinated by the OSR team at Mercator Ocean International.

This 7th issue of the Copernicus OSR gathers 14 peer review papers covering the European regional seas (9) and the global ocean (5) with contributions on the blue (10) and green (4). The main findings of OSR7 are summarized in Figures 1 and 2 and here below according to the topic they addressed: 1) identification and impact of extreme/unusual events (5), 2) identification of long-term trends (5), 3) new methodology/indicators for ocean monitoring (2), and 4) analysis of ocean variability (2). A detailed description can be found in von Schuckmann et al. (2023).

Extreme/Unusual events

Peal et al. (2023) show that marine heatwaves have become more frequent and more extended globally, whereas marine cold spells became less frequent over 1982 to 2021, except in the Southern Ocean, where the reverse is observed. Mayer et al. (2023) show a record-low biennial reduction in oceanic heat exchange across the Greenland–Scotland Ridge around the year 2018. This reduction amounted to 4%–9% of the usual heat exchange with respect to the reference period 1993–2020. Mourre et al. (2023) show that an intense and long-lasting storm in the Balearic Islands resulted in important modifications of the physical conditions of the region with intense upwelling, a reversal of the regional current system, and extreme cold surface temperatures. Renshaw et al. (2023) highlight unusual coccolithophore blooms in summer 2021 in Scottish waters and explain their occurrence due to unusual weather conditions. Gramcianinov et al. (2023) highlight that extreme wave events have impacted the eastern coast of South America and offshore regions and have created coastal hazards in the São Paulo area.

eISSN 2752-0706

Long-term trend

De Pascual-Collar et al. (2023) detect a long-term warming trend in waters below 150m in the Iberia–Biscay–Ireland region over 1993–2021. Aydogdu et al. (2023) show that the salinity in the upper 300m of the Mediterranean Sea has increased in the last 3 decades, with a basin average trend in the range from 0.0020 to 0.0110 psu per year depending on the product considered, with higher values in the eastern basin. Raudsepp et al. (2023) presented an overall decrease in ocean freshwater content in the Baltic Sea over the last 2 decades, with distinct regional patterns. Di Biagio et al. (2023) identify a potential regime shift that happened over 1999–2021 in the regional circulation of the southern Adriatic Sea, with potential implications for the ventilation of the Ionian–Adriatic. Xi et al. (2023) find that the mean status, trends, and phenology of phytoplankton functional types in the Atlantic Ocean do not change significantly over 2002–2021, except for prokaryotes, which slightly decline. The study highlights an abrupt increase in diatoms during the years 2018 and 2019 in the North Atlantic.

Monitoring

Lorente et al. (2023) propose a new indicator for the monitoring of coastal upwelling intensity tested in two pilot areas (i.e. the north-western Iberian Peninsula and the Bay of Biscay) in view of its application at larger scales (the coastal global ocean). Loisel et al. (2023) propose a new algorithm for the monitoring of suspended materials' composition (organic and inorganic) from space. The algorithm is tested in the English Channel and the southern North Sea, with the perspective of being extended to the global coastal ocean.

Ocean variability

Baker et al. (2023) investigate the variability of the South Atlantic meridional overturing circulation and the meridional heat transport, focusing on the period from 2013 to 2017. The study shows that the South Atlantic transport variability is still uncertain and recommends improved monitoring and modelling. Oikonomou et al. (2023) explore wave energy resources at the basin scale, along with the dominant wave regime. Results suggest that although the basin is characterized by low energy potential and large energy flux variability, it could serve as a deployment zone for low-power devices due to low peak period variability and high site accessibility levels.

The editors

Marilaure Grégoire, Pierre Brasseur, Gilles Garric, Johannes Karstensen, Piero Lionello, Marta Marcos, Griet Neukermans, and Joanna Staneva.

State Planet, 1-osr7, 1, 2023
https://doi.org/10.5194/sp-1-osr7-1-2023

Introduction to the 7th edition of the Copernicus Ocean State Report (OSR7)

Karina von Schuckmann, Lorena Moreira, and Pierre-Yves Le Traon

Mercator Ocean International, Toulouse, France

Correspondence: Karina von Schuckmann (karina.von.schuckmann@mercator-ocean.fr)

Published: 27 September 2023

Changes in the state of the ocean affect the well-being of the planet, its ecosystems, and human societies (IPCC, 2019). The ocean is home to a vast array of plant and animal species, many of which are still undiscovered (Census of Marine Life, 2010), and it is hence critical in supporting global biodiversity and sustaining complex ecosystems (Pörtner et al., 2021; IPCC, 2022). The ocean supports various industries, such as fishing, shipping, tourism, and renewable and non-renewable resources, and provides job opportunities, income, and economic growth (OECD, 2016; European Commission, 2022). The ocean plays a vital role in regulating Earth's climate. It acts as a massive heat sink, absorbing and storing vast amounts of surplus heat accumulated in the Earth system from human activities (von Schuckmann et al., 2023). It absorbs significant quantities of anthropogenic carbon through physical and biological processes, helping to mitigate climate change by reducing the greenhouse gas concentration in the atmosphere (Friedlingstein et al., 2022; Crisp et al., 2022). The ocean is intricately affected by climate change. Rising sea levels, warming, deoxygenation and acidification of the ocean, changing currents, and loss of sea ice and biodiversity all pose significant risks to coastal communities, infrastructure, economies, and vulnerable ecosystems (IPCC, 2021, 2022). In addition, overexploitation and ocean pollution, including plastic waste and chemical contaminants, can harm both marine life and human health, posing risks through the food chain and direct exposure (e.g., Landrigan et al., 2020; Lamb et al., 2018). The degradation of the ocean and increased pressure on its functioning and services can lead to economic losses, unemployment, and reduced opportunities for sustainable development (OECD, 2016). Protecting and preserving the ocean is essential for ensuring a sustainable future, maintaining biodiversity, regulating climate, supporting economies, and safeguarding human health and well-being (IPCC, 2019; Pörtner et al., 2021). Monitoring and reporting on any change in the state of the ocean can help to achieve this goal, while at the same time it allows developing timely strategies for adaptation measures as well as to raise awareness, inform decision-making, encourage action to protect and conserve the ocean, and hence transition towards sustainable ocean stewardship (e.g., von Schuckmann et al., 2020; Blunden and Boyer, 2022; IOC-UNESCO, 2022). Most recently, on 19 June 2023, the Treaty of the High Seas was adopted by consensus and standing ovation during the United Nations meeting in New York. This treaty, also known as BBNJ (Biodiversity Beyond National Jurisdiction), is key to protecting the ocean, promoting equity and fairness, tackling environmental degradation, fighting climate change, and preventing biodiversity loss in the high seas (An historic achievement: Treaty of the High Seas is adopted, 2023).

Regular reporting on the state, variability, and change of the ocean provides state-of-the-art science-driven findings to various stakeholders, including policymakers, scientists, industries, and the general public. Ocean reporting involves several components as part of a so-called added value chain (von Schuckmann et al., 2020). Firstly, data collection from different methods including satellite observations (e.g., sea level, sea surface temperature (SST), sea surface salinity (SSS), ocean color, waves) and in situ measurements – autonomous, moored, and taken during research expeditions – are paramount for building data products from the global to regional scale (IOC, 2019). Reprocessed data are also used to feed ocean reanalyses that combine them with numerical models through data assimilation schemes (Decade Collaborative Centre for Ocean Prediction, DCC-OP, 2023). All these different products build the baseline of the Copernicus Marine Service and include information about ocean physics (blue ocean; e.g., temperature, salinity, currents, waves), biogeochemistry and biodiversity (green ocean; e.g., chlorophyll

Published by Copernicus Publications.

a, ocean pH), and sea ice parameters (white ocean; e.g., sea ice concentration, extent, or thickness), which are all relevant to understanding and reporting on the ocean state (Le Traon et al., 2019). Combined with scientific expertise, they provide the fundamental ingredients for the development of ocean monitoring indicators that are fit for purpose for ocean reporting. At this higher level of the added value chain, the tools then help identify trends, patterns, and changes in the ocean environment triggered by climate change and other human-made pressures, climate variability, and ocean processes.

This 7th edition of the Copernicus Ocean State Report covers a wide range of topics tackling variations, trends, and new tools for socioeconomic applications for Europe and on a global scale. The studies are built on the suite of Copernicus Marine products and are complemented with other products from the global community.

1 The ocean in Europe

During summer 2021, two unusual coccolithophore blooms were observed in Scottish waters, one in the Clyde Sea and the other by the east coast of the Shetland Islands. These blooms have attracted lot of public attention because they turned the sea a turquoise color (BBC News, 2023). The OSR7 is taking a close look at these events back-boned by the use of reanalysis and satellite data to examine the environment that led to these blooms. Unusual weather conditions were a contributory factor in both cases, leading to high concentrations of nutrients in summer as cold temperatures restricted the regular spring bloom of diatoms in this area. These factors provide ideal conditions for coccolithophores to flourish as temperatures and sunlight increase (see Renshaw et al. in OSR7 Chap. 4). Widespread routine monitoring of nutrient levels and phytoplankton components could greatly help in understanding future blooms.

The OSR7 explored dissolved oxygen variations in the Mediterranean Sea, more precisely in the southern Adriatic Sea, over the period 1999–2021, which is an essential undertaking to further enhance our understanding of marine ecosystem functioning and for assessing the marine environmental status (see Di Biagio et al. in OSR7 Chap. 3). The results, derived from a regional ocean reanalysis system, highlight the critical role of heat fluxes, ocean currents, and biological production in driving dissolved oxygen variations in this area. A potential regime shift in the regional circulation was identified. It can have substantial implications for the ventilation of the Ionian–Adriatic Ocean region and hence for marine organisms, and it needs to be further analyzed in future studies.

Ocean warming is one of the major indicators of monitoring the state and evolution of climate change (von Schuckmann et al., 2016). The OSR7 is tackling this indicator aiming to regionalize capacities for reporting on ocean warming (see de Pascual-Collar et al. in OSR7 Chap. 2), while developing a multi-product approach based on data from observations and ocean reanalysis systems for the Iberia–Biscay–Ireland region. Over the period 1993–2021, the results reveal that the upper near-surface layer of the ocean (0–150 m) is dominated by natural variations at the interannual to decadal scale and that the long-term ocean warming trend is emerging in the intermediate to deep-ocean layers (> 150 m) in this region. This trend amounts to about 50 % of the global ocean warming trend and is strongly affected by interannual- to decadal-scale variations. Moreover, the study could elevate the major players of these changes that are linked to the Sub-Arctic Intermediate Water and Mediterranean Outflow Water variations, leveraging the role of major characteristics of the ocean in redistributing heat and hence triggering regional variations of ocean warming remotely, i.e., from the Mediterranean Sea and the North Atlantic Ocean.

In OSR7, a new scientific method has been developed for monitoring coastal upwelling, a process which is a major communicator between offshore waters and coastal ecosystems (see Lorente et al. in OSR7 Chap. 2). Any change in coastal upwelling can have implications for, for example, water quality, fisheries, and aquaculture production in coastal areas (Sydeman et al., 2014). The method incorporates information on ocean currents, wind, sea level pressure, and sea surface temperature, and it has been developed based on various data products ranging from direct coastal observations provided by a high-frequency radar (HFR), buoy measurements, and ocean reanalysis. Two pilot areas have been chosen, i.e., the northwestern Iberian Peninsula and the Bay of Biscay. This new indicator, the so-called coastal upwelling index, has been scientifically tested in OSR7, and its proof of concept revealed that this new method can be used for direct upwelling monitoring over any coastal area of the global ocean.

The OSR7 has also analyzed the interference of extreme events with ocean processes, like the coastal upwelling of the Balearic Islands (see Mourre et al. in OSR7 Chap. 4), and has demonstrated the implications of long-lasting storms of record strength on the ocean and coasts. In November 2021, an intense and long-lasting storm named "Blas" hit the area of the Balearic Islands, which resulted in intense upwelling along the northwestern coasts of the islands of Mallorca and Ibiza, as well as a reversal of the regional current system. These record implications have in turn resulted in extreme cold coastal surface temperatures up to 6 °C colder than usual. This study demonstrates the benefits of operational oceanography for the characterization of extreme events through the provision of time series of high-resolution modeling results in coastal areas.

Change in ocean salinity can have important implications for ocean density and ocean currents, the water cycle, and ocean biodiversity. The OSR7 has tackled an important indicator based on ocean salinity in the Mediterranean Sea during the last decades using Copernicus Marine reanalysis and ob-

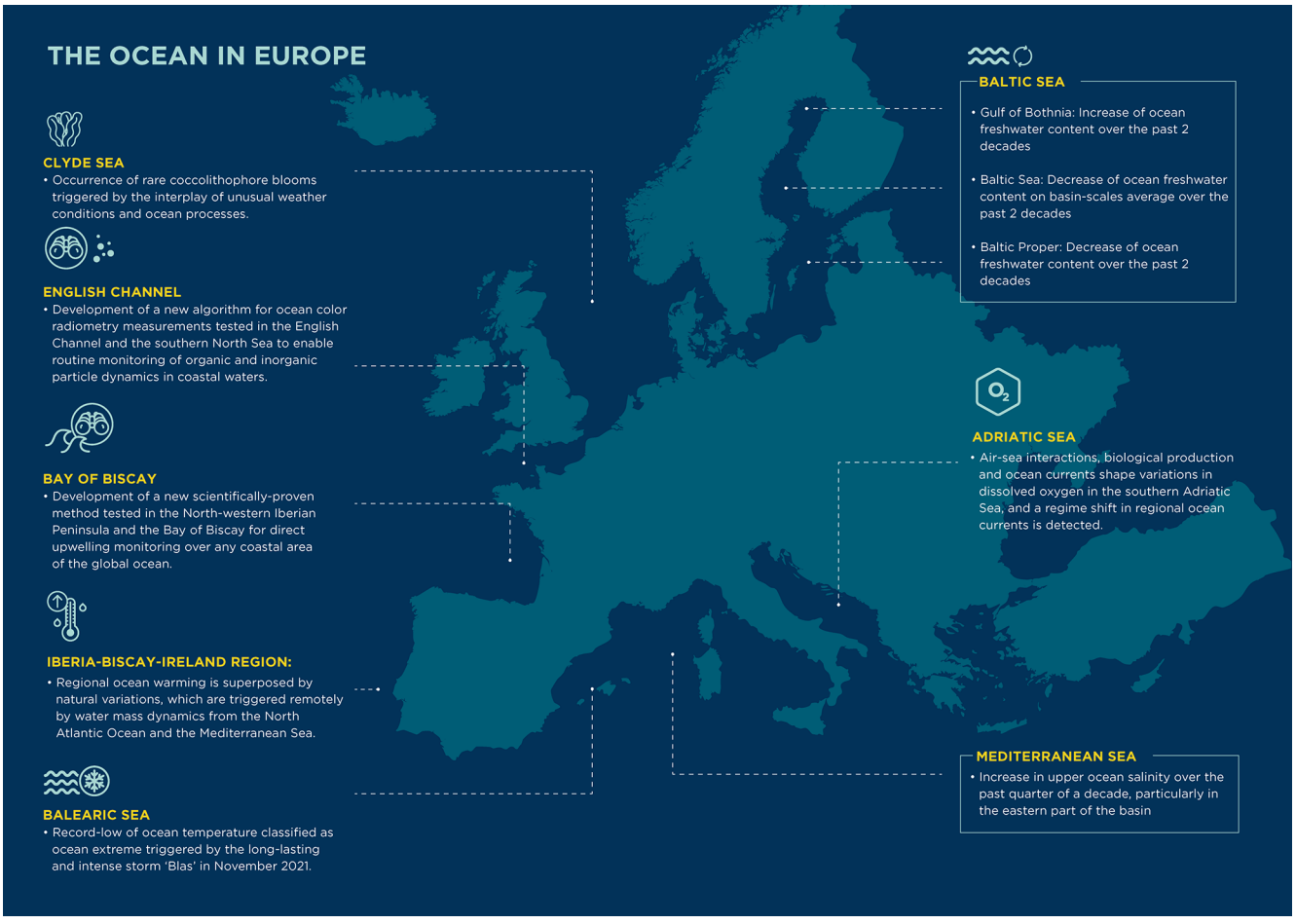

Figure 1. Overview of major outcomes for the European regional seas in the 7th edition of the Copernicus Ocean State Report.

servation products (see Aydogdu et al. in OSR7 Chap. 2). The results show that, overall, salinity has increased in the upper (< 300 m) Mediterranean Sea at particularly strong rates in the eastern basin. A similar analysis has been performed for the Baltic Sea area (see Raudsepp et al. in OSR7 Chap. 2). Particularly, freshwater content has been calculated from the Copernicus Marine regional reanalysis, which allows monitoring the specific hydro-physical conditions of each subbasin of the Baltic Sea. Results show that the total freshwater content in the Baltic Sea shows a steady decrease on average over the past 2 decades. However, at the regional scale, changes in freshwater content are not spatially uniform and are affected in the Baltic Sea by different processes, such as changes in ocean circulation, precipitation, river runoff, and sea ice formation. For example, the Gulf of Bothnia shows a freshwater content increase, and the freshwater content in the Baltic proper decreased over the past 2 decades.

Monitoring coastal waters is of uppermost importance to provide insight into changes in these complex and highly variable environments. In OSR7, a new algorithm has been developed to estimate the organic and inorganic particulate fraction of suspended material needed to monitor particle dynamics and biogeochemical cycles in coastal waters (see Loisel et al. in OSR7 Chap. 3). This new algorithm is based on a neural network approach and has been applied as a test bed to satellite observations from ocean color radiometry in the English Channel and the southern North Sea. The scientific evaluations as done in OSR7 have shown that this algorithm can be directly applied to all ocean color radiometry measurements, which enables routine monitoring of particulate composition over the global coastal ocean.

2 The ocean around the globe

Climate change is causing extreme climate events to become more frequent and more severe (Seneviratne et al., 2021). Marine heatwaves and marine cold spells are prolonged; discrete periods of anomalously high or low ocean temperatures have wide-ranging impacts from dramatic shifts in biodiversity to changes in fishery yields. In OSR7, global sea surface temperature measurements have been used to study the intensity and frequency of marine heatwaves and marine cold

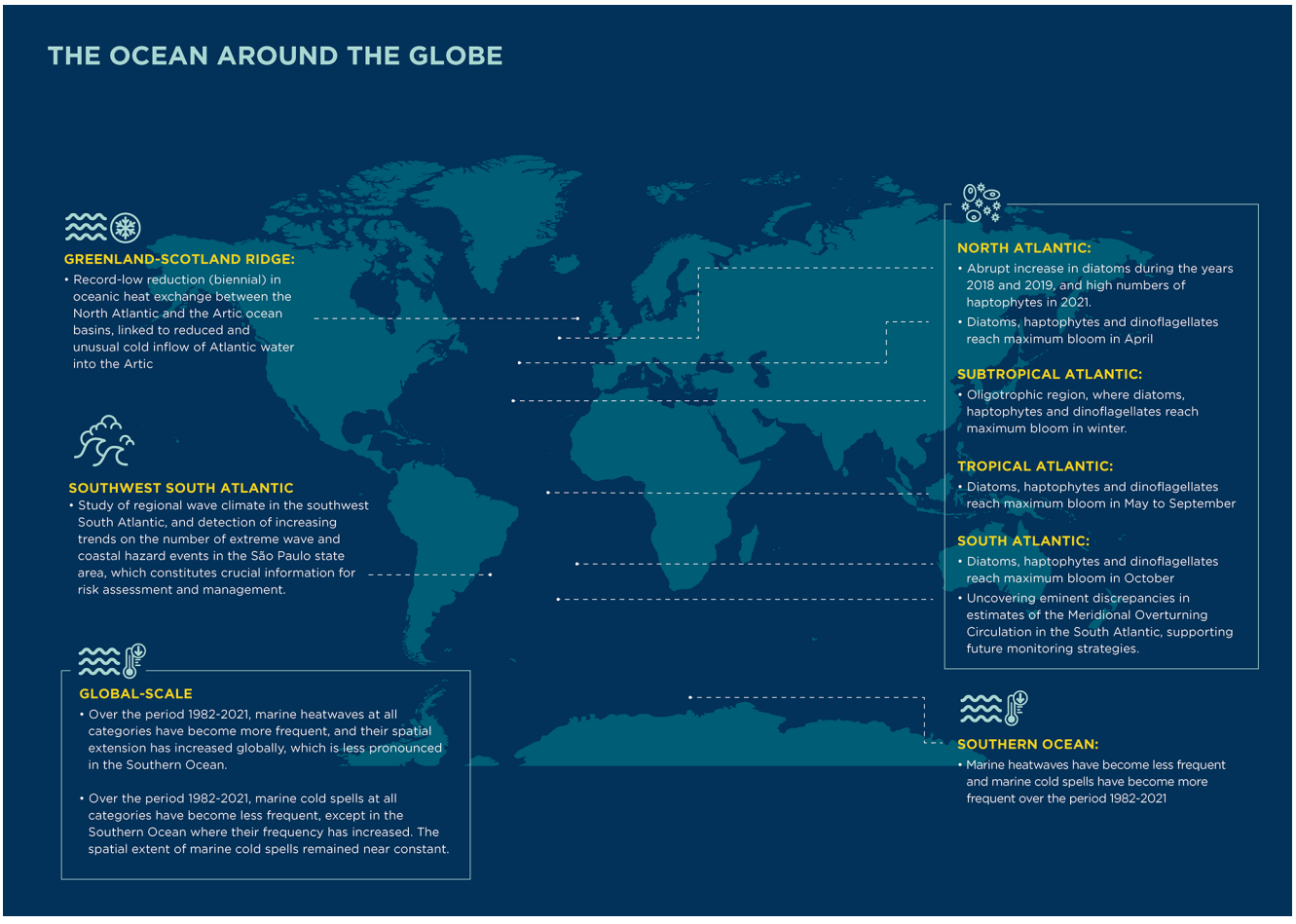

Figure 2. Overview of major outcomes for the global ocean in the 7th edition of the Copernicus Ocean State Report.

spells over several decades from 1982 to 2021 across different categories from moderate (category 1) to extreme (category 4). The findings show that in large areas of the ocean it can be said with 99 % confidence that marine heatwaves have become more frequent globally, whereas marine cold spells have become less frequent (see Peal et al. in OSR7 Chap. 2). An exception is the Southern Ocean where marine heatwaves are becoming slightly less frequent and marine cold spells are becoming more frequent. The most extreme events in categories 3 and 4 follow this trend, but at a lower rate. This evolution for marine heatwaves is accompanied by an even faster trend with respect to their spatial extension, whereas the spatial extent of marine cold spells remained nearly constant.

Extreme events can induce major hazards along coastlines. The OSR7 has investigated extreme events and coastal hazards in the southwestern South Atlantic over the past quarter of a decade, which hosts the most economically important harbors in South America, high oil and gas production demands, and rich biodiversity (see Gramcianinov et al. in OSR7 Chap. 3). Particularly, Copernicus Marine reanalysis and near-real-time data have been used to investigate extreme wave indicators impacting offshore regions and the coasts in this area and have provided a comprehensive overview of the regional wave climate across timescales and space scales. In addition, national monitoring and warning system data in the São Paulo state area have been combined with Copernicus Marine data, and these results reveal that the increasing number of coastal hazards in this area are strongly linked to the increasing number of extreme wave events from the coast to adjacent offshore regions.

The Southern Ocean region is a major player triggering changes in the global ocean circulation (Lee et al., 2023), and the OSR7 has addressed inter-basin transports in this region (see Baker et al. in OSR7 Chap. 2). To allow for reliable monitoring of changes in the regional circulation in this sensitive area for global climate, the accuracy and feasibility of the available ocean products must be analyzed. The analysis in this issue of the ocean state report has investigated the variability of the South Atlantic meridional overturning circulation and the meridional heat transport focusing on the period from 2013 to 2017, i.e., when direct observations in

this region are available. The findings have manifested a surprising discrepancy in seasonal to multi-annual circulation change between the observations and model results. This prevents a reliable estimate of how the meridional overturning circulation and heat transport are changing at the latitude that connects the Atlantic Ocean to the Southern Ocean. The mean and variation of real-world South Atlantic transports and the amplitude of their fluctuations are uncertain. This in turn provides fundamental guidance for future strategies as well as investments in urgently needed sustained monitoring and improved modeling in this important area of the ocean for global climate.

Given its crucial importance, circulation variations linked to the meridional overturning circulation have also been analyzed in the North Atlantic in OSR7 (see Mayer et al. in OSR7 Chap. 4). Particularly, focus had been set on the oceanic exchange across the Greenland–Scotland Ridge, which not only links to the meridional overturning circulation, but is also shaping Arctic climate. The results of this study have uncovered a record-low biennial reduction in oceanic heat exchange across the Greenland–Scotland Ridge around the year 2018. This reduction, amounting to 4 %–9 % of the usual heat exchange with respect to the reference period 1993–2020, occurred because of a reduction in the inflow of water from the Atlantic into the Arctic area through the Faroe–Shetland branch, which was exacerbated by the unusually cold temperatures of Atlantic Water arriving at the Greenland–Scotland Ridge. These low temperatures have been triggered by a stronger North Atlantic subpolar gyre varying naturally at interannual to decadal timescales.

Ocean phytoplankton prevails in the upper part of the ocean, where sunlight penetrates the water, and constitutes the base of the marine food web fueling fisheries and regulating key biogeochemical processes (Xi et al., 2021). There are different classes of phytoplankton – so-called phytoplankton functional types – which include haptophytes, prokaryotes, dinoflagellate, and diatoms. OSR7 investigated the mean status, trends, phenology, and most recent anomalies in the Atlantic Ocean (see Xi et al. in OSR7 Chap. 2). Their phenology ranges with different climate zones, reaching seasonal maximum blooms (Fig. 1). The results also reveal that most phytoplankton functional types remained stable over the period 2002–2021, except for prokaryotes, which slightly declined over this period. The study also uncovered, for example, an abrupt increase in diatoms during the years 2018 and 2019 in the northern part of the basin.

Disclaimer. Please note that this article has undergone editorial review only.

References

An historic achievement: Treaty of the High Seas is adopted: https://oceans-and-fisheries.ec.europa.eu/news/historic-achievement-treaty-high-seas-adopted-2023-06-19_en, last access: 20 June 2023.

BBC News: Marine algae turned Scotland's water bright blue, BBC News, https://www.bbc.com/news/uk-scotland-57720790, last access: 12 June 2023.

Blunden, J. and Boyer, T.: State of the Climate in 2021, B. Am. Meteorol. Soc., 103, S1–S465, https://doi.org/10.1175/2022BAMSStateoftheClimate.1, 2022.

Census of Marine Life: First Census of Marine Life 2010: Highlights of a Decade of Discovery, edited by: Ausubel, J. H., Crist, D. T., and Waggoner, P. E., Census of Marine Life, ISBN 978-1-4507-3102-7, 2010.

Crisp, D., Dolman, H., Tanhua, T., McKinley, G. A., Hauck, J., Bastos, A., Sitch, S., Eggleston, S., and Aich, V.: How Well Do We Understand the Land-Ocean-Atmosphere Carbon Cycle?, Rev. Geophys., 60, e2021RG000736, https://doi.org/10.1029/2021RG000736, 2022.

Decade Collaborative Centre for Ocean Prediction (DCC-OP): https://oceandecade.org/actions/decade-collaborative-centre-for-ocean-prediction-dcc-op/, last access: 12 June 2023.

European Commission: The EU blue economy report 2022, Publications Office of the European Union, Luxembourg, https://doi.org/10.2771/793264, 2022.

Friedlingstein, P., O'Sullivan, M., Jones, M. W., Andrew, R. M., Gregor, L., Hauck, J., Le Quéré, C., Luijkx, I. T., Olsen, A., Peters, G. P., Peters, W., Pongratz, J., Schwingshackl, C., Sitch, S., Canadell, J. G., Ciais, P., Jackson, R. B., Alin, S. R., Alkama, R., Arneth, A., Arora, V. K., Bates, N. R., Becker, M., Bellouin, N., Bittig, H. C., Bopp, L., Chevallier, F., Chini, L. P., Cronin, M., Evans, W., Falk, S., Feely, R. A., Gasser, T., Gehlen, M., Gkritzalis, T., Gloege, L., Grassi, G., Gruber, N., Gürses, Ö., Harris, I., Hefner, M., Houghton, R. A., Hurtt, G. C., Iida, Y., Ilyina, T., Jain, A. K., Jersild, A., Kadono, K., Kato, E., Kennedy, D., Klein Goldewijk, K., Knauer, J., Korsbakken, J. I., Landschützer, P., Lefèvre, N., Lindsay, K., Liu, J., Liu, Z., Marland, G., Mayot, N., McGrath, M. J., Metzl, N., Monacci, N. M., Munro, D. R., Nakaoka, S.-I., Niwa, Y., O'Brien, K., Ono, T., Palmer, P. I., Pan, N., Pierrot, D., Pocock, K., Poulter, B., Resplandy, L., Robertson, E., Rödenbeck, C., Rodriguez, C., Rosan, T. M., Schwinger, J., Séférian, R., Shutler, J. D., Skjelvan, I., Steinhoff, T., Sun, Q., Sutton, A. J., Sweeney, C., Takao, S., Tanhua, T., Tans, P. P., Tian, X., Tian, H., Tilbrook, B., Tsujino, H., Tubiello, F., van der Werf, G. R., Walker, A. P., Wanninkhof, R., Whitehead, C., Willstrand Wranne, A., Wright, R., Yuan, W., Yue, C., Yue, X., Zaehle, S., Zeng, J., and Zheng, B.: Global Carbon Budget 2022, Earth Syst. Sci. Data, 14, 4811–4900, https://doi.org/10.5194/essd-14-4811-2022, 2022.

IOC: The Global Ocean Observing System 2030 Strategy, IOC, Paris, IOC Brochure 2019-5, IOC/BRO/2019/5 rev.2, GOOS Report No. 239, 2019.

IOC-UNESCO: State of the Ocean Report, pilot edition, Paris, IOC-UNESCO, IOC Technical Series, 172, 2022.

IPCC: IPCC Special Report on the Ocean and Cryosphere in a Changing Climate, edited by: Pörtner, H.-O., Roberts, D.

C., Masson-Delmotte, V., Zhai, P., Tignor, M., Poloczanska, E., Mintenbeck, K., Alegría, A., Nicolai, M., Okem, A., Petzold, J., Rama, B., and Weyer, N. M., Cambridge University Press, Cambridge, UK and New York, NY, USA, 755 pp., https://doi.org/10.1017/9781009157964, 2019.

IPCC: Climate Change 2021: The Physical Science Basis. Contribution of Working Group I to the Sixth Assessment Report of the Intergovernmental Panel on Climate Change, edited by: Masson-Delmotte, V., Zhai, P., Pirani, A., Connors, S. L., Péan, C., Berger, S., Caud, N., Chen, Y., Goldfarb, L., Gomis, M. I., Huang, M., Leitzell, K., Lonnoy, E., Matthews, J. B. R., Maycock, T. K., Waterfield, T., Yelekçi, O., Yu, R., and Zhou, B., Cambridge University Press, Cambridge, United Kingdom and New York, NY, USA, 2391 pp., https://doi.org/10.1017/9781009157896, 2021.

IPCC: Climate Change 2022: Impacts, Adaptation and Vulnerability. Contribution of Working Group II to the Sixth Assessment Report of the Intergovernmental Panel on Climate Change, edited by: Pörtner, H.-O., Roberts, D. C., Tignor, M., Poloczanska, E. S., Mintenbeck, K., Alegría, A., Craig, M., Langsdorf, S., Löschke, S., Möller, V., Okem, A., and Rama, B., Cambridge University Press, Cambridge, UK and New York, NY, USA, 3056 pp., https://doi.org/10.1017/9781009325844, 2022.

Lamb, J. B., Willis, B. L., Fiorenza, E. A., Couch, C. S., Howard, R., Rader, D. N., True, J. D., Kelly, L. A., Ahmad, A., Jompa, J., and Harvell, C. D.: Plastic waste associated with disease on coral reefs, Science, 359, 460–462, https://doi.org/10.1126/science.aar3320, 2018.

Landrigan, P. J., Stegeman, J. J., Fleming, L. E., Allemand, D., Anderson, D. M., Backer, L. C., Brucker-Davis, F., Chevalier, N., Corra, L., Czerucka, D., Bottein, M. Y. D., Demeneix, B., Depledge, M., Deheyn, D. D., Dorman, C. J., Fénichel, P., Fisher, S., Gaill, F., Galgani, F., Gaze, W. H., Giuliano, L., Grandjean, P., Hahn, M. E., Hamdoun, A., Hess, P., Judson, B., Laborde, A., McGlade, J., Mu, J., Mustapha, A., Neira, M., Noble, R. T., Pedrotti, M. L., Reddy, C., Rocklöv, J., Scharler, U. M., Shanmugam, H., Taghian, G., Van De Water, J. A. J. M., Vezzulli, L., Weihe, P., Zeka, A., Raps, H., and Rampal, P.: Human Health and Ocean Pollution, Ann. Glob. Health, 86, 1–64, https://doi.org/10.5334/AOGH.2831, 2020.

Lee, S.-K., Lumpkin, R., Gomez, F., Yeager, S., Lopez, H., Takglis, F., Dong, S., Aguiar, W., Kim, D., and Baringer, M.: Human-induced changes in the global meridional overturning circulation are emerging from the Southern Ocean, Commun. Earth Environ., 4, 69, https://doi.org/10.1038/s43247-023-00727-3, 2023.

Le Traon, P. Y., Reppucci, A., Alvarez-Fanjul, E., Aouf, L., Behrens, A., Belmonte, M., Bentamy, A., Bertino, L., Brando, V. E., Brandt Kreiner, M., Benkiran, M., Carval, T., Ciliberti, S. A., Claustre, H., Clementi, E., Coppini, G., Cossarini, G., De Alfonso Alonso-Muñoyerro, M., Delamarche, A., Dibarboure, G., Dinessen, F., Drevillon, M., Drillet, Y., Faugere, Y., Fernandez, V., Fleming, A., Garcia-Hermosa, M. I., Garcia Sotillo, M., Garric, G., Gasparin, F., Giordan, C., Gehlen, M. Gregoire, M. L., Guinehut, S., Hamon, M., Harris, C., Hernandez, F., Hinkler, J. B., Hoyer, J., Karvonens, J., Kay, S., King, R., Lavergne, T., Lemiuex-Dudon, B., Lima, L., Mao, C., Martin, M. J., Masina, S., Melet, A., Nardelli, B. B., Nolan, G., Pascual, A., Pistoia, J., Palazov, A., Piolle, J. F., Pujol, M. I., Pequignet, A. C., Peneva, E., Perez Gomez, B., Peiti de la Velleon, L., Pinardi, N., Pisano, A., Pouliquen, S., Reid, R., Remy, E., Santoleri, R., Siddorn, J., She, J., Staneva, J., Stoffelen, A., Tonani, M., Vandenbulcke, L., von Schuckmann, K., Volpe, G., Wettre, C., and Zacharioudaki, A.: From Observation to Information and Users: The Copernicus Marine Service Perspective, Front. Mar. Sci., 6, https://doi.org/10.3389/fmars.2019.00234, 2019.

Mohrholz, V.: Major Baltic inflow statistics – Revised, Front. Mar. Sci., 5, 385391, https://doi.org/10.3389/FMARS.2018.00384, 2018.

OECD: The Ocean Economy in 2030, OECD Publishing, Paris, https://doi.org/10.1787/9789264251724-EN, 2016.

Pörtner, H.-O., Scholes, R. J., Agard, J., Archer, E., Arneth, A., Bai, X., Barnes, D., Burrows, M., Chan, L., Cheung, W. L., Diamond, S., Donatti, C., Duarte, C., Eisenhauer, N., Foden, W., Gasalla, M. A., Handa, C., Hickler, T., Hoegh-Guldberg, O., Ichii, K., Jacob, U., Insarov, G., Kiessling, W., Leadley, P., Leemans, R., Levin, L., Lim, M., Maharaj, S., Managi, S., Marquet, P. A., McElwee, P., Midgley, G., Oberdorff, T., Obura, D., Osman Elasha, B., Pandit, R., Pascual, U., Pires, A. P. F., Popp, A., Reyes-García, V., Sankaran, M., Settele, J., Shin, Y.-J., Sintayehu, D. W., Smith, P., Steiner, N., Strassburg, B., Sukumar, R., Trisos, C., Val, A. L., Wu, J., Aldrian, E., Parmesan, C., Pichs-Madruga, R., Roberts, D. C., Rogers, A. D., Díaz, S., Fischer, M., Hashimoto, S., Lavorel, S., Wu, N., and Ngo, H.: Scientific outcome of the IPBES-IPCC co-sponsored workshop on biodiversity and climate change, IPBES secretariat, Bonn, Germany, https://doi.org/10.5281/zenodo.4659158, 2021.

Seneviratne, S. I., Zhang, X., Adnan, M., Badi, W., Dereczynski, C., Di Luca, A., Ghosh, S., Iskandar, I., Kossin, J., Lewis, S., Otto, F., Pinto, I., Satoh, M., Vicente-Serrano, S. M., Wehner, M., and Zhou, B.: Weather and Climate Extreme Events in a Changing Climate, Climate Change 2021: The Physical Science Basis. Contribution of Working Group I to the Sixth Assessment Report of the Intergovernmental Panel on Climate Change, 1513–1766, https://doi.org/10.1017/9781009157896.013, 2021.

Sydeman, W. J., García-Reyes, M., Schoeman, D. S., Rykaczewski, R. R., Thompson, S. A., Black, B. A., and Bograd, S. J.: Climate change and wind intensification in coastal upwelling ecosystems, Science, 345, 77–80, https://doi.org/10.1126/science.1251635, 2014.

von Schuckmann, K., Palmer, M. D., Trenberth, K. E., Cazenave, A., Chambers, D., Champollion, N., Hansen, J., Josey, S. A., Loeb, N., Mathieu, P. P., Meyssignac, B., and Wild, M.: An imperative to monitor Earth's energy imbalance, Nat. Clim. Change, 6, 138–144, https://doi.org/10.1038/nclimate2876, 2016.

von Schuckmann, K., Cheng, L., Palmer, M. D., Hansen, J., Tassone, C., Aich, V., Adusumilli, S., Beltrami, H., Boyer, T., Cuesta-Valero, F. J., Desbruyères, D., Domingues, C., García-García, A., Gentine, P., Gilson, J., Gorfer, M., Haimberger, L., Ishii, M., Johnson, G. C., Killick, R., King, B. A., Kirchengast, G., Kolodziejczyk, N., Lyman, J., Marzeion, B., Mayer, M., Monier, M., Monselesan, D. P., Purkey, S., Roemmich, D., Schweiger, A., Seneviratne, S. I., Shepherd, A., Slater, D. A., Steiner, A. K., Straneo, F., Timmermans, M.-L., and Wijffels, S. E.: Heat stored in the Earth system: where does the energy go?, Earth Syst. Sci. Data, 12, 2013–2041, https://doi.org/10.5194/essd-12-2013-2020, 2020.

von Schuckmann, K., Minière, A., Gues, F., Cuesta-Valero, F. J., Kirchengast, G., Adusumilli, S., Straneo, F., Ablain, M., Allan, R. P., Barker, P. M., Beltrami, H., Blazquez, A., Boyer, T., Cheng, L., Church, J., Desbruyeres, D., Dolman, H., Domingues, C. M., García-García, A., Giglio, D., Gilson, J. E., Gorfer, M., Haimberger, L., Hakuba, M. Z., Hendricks, S., Hosoda, S., Johnson, G. C., Killick, R., King, B., Kolodziejczyk, N., Korosov, A., Krinner, G., Kuusela, M., Landerer, F. W., Langer, M., Lavergne, T., Lawrence, I., Li, Y., Lyman, J., Marti, F., Marzeion, B., Mayer, M., MacDougall, A. H., McDougall, T., Monselesan, D. P., Nitzbon, J., Otosaka, I., Peng, J., Purkey, S., Roemmich, D., Sato, K., Sato, K., Savita, A., Schweiger, A., Shepherd, A., Seneviratne, S. I., Simons, L., Slater, D. A., Slater, T., Steiner, A. K., Suga, T., Szekely, T., Thiery, W., Timmermans, M.-L., Vanderkelen, I., Wjiffels, S. E., Wu, T., and Zemp, M.: Heat stored in the Earth system 1960–2020: where does the energy go?, Earth Syst. Sci. Data, 15, 1675–1709, https://doi.org/10.5194/essd-15-1675-2023, 2023.

Xi, H., Losa, S. N., Mangin, A., Garnesson, P., Bretagnon, M., Demaria, J., Soppa, M. A., Hembise Fanton d'Andon, O., and Bracher, A.: Global Chlorophyll a Concentrations of Phytoplankton Functional Types With Detailed Uncertainty Assessment Using Multisensor Ocean Color and Sea Surface Temperature Satellite Products, J. Geophys. Res.-Oceans, 126, e2020JC017127, https://doi.org/10.1029/2020JC017127, 2021.

State Planet, 1-osr7, 2, 2023
https://doi.org/10.5194/sp-1-osr7-2-2023

Evaluation of operational ocean forecasting systems from the perspective of the users and the experts

Stefania A. Ciliberti[1], Enrique Alvarez Fanjul[2], Jay Pearlman[3], Kirsten Wilmer-Becker[4], Pierre Bahurel[2], Fabrice Ardhuin[5], Alain Arnaud[2], Mike Bell[4], Segolene Berthou[4], Laurent Bertino[6], Arthur Capet[7], Eric Chassignet[8], Stefano Ciavatta[2], Mauro Cirano[9], Emanuela Clementi[10], Gianpiero Cossarini[11], Gianpaolo Coro[12], Stuart Corney[13], Fraser Davidson[14], Marie Drevillon[2], Yann Drillet[2], Renaud Dussurget[2], Ghada El Serafy[15], Katja Fennel[16], Marcos Garcia Sotillo[1], Patrick Heimbach[17,18], Fabrice Hernandez[19], Patrick Hogan[20], Ibrahim Hoteit[21], Sudheer Joseph[22], Simon Josey[23], Pierre-Yves Le Traon[2], Simone Libralato[11], Marco Mancini[24], Pascal Matte[25], Angelique Melet[2], Yasumasa Miyazawa[26], Andrew M. Moore[27], Antonio Novellino[28], Andrew Porter[29], Heather Regan[6], Laia Romero[30], Andreas Schiller[31,32], John Siddorn[33], Joanna Staneva[34], Cecile Thomas-Courcoux[2], Marina Tonani[2], Jose Maria Garcia-Valdecasas[1], Jennifer Veitch[35], Karina von Schuckmann[2], Liying Wan[36], John Wilkin[37], and Romane Zufic[2]

[1]Nologin Oceanic Weather Systems, Madrid, Spain
[2]Mercator Ocean International, Toulouse, France
[3]Institute of Electrical and Electronics Engineers, Paris, France
[4]Met Office, Exeter, United Kingdom
[5]Laboratoire d'Océanographie Physique et Spatiale (LOPS), IFREMER, Brest, France
[6]Nansen Environmental and Remote Sensing Center, Bergen, Norway
[7]Operational Directorate Natural Environment (OD Nature), Royal Belgian Institute of Natural Sciences (RBINS), Brussels, Belgium
[8]Department of Earth, Ocean and Atmospheric Science, Center for Ocean–Atmospheric Prediction Studies, Florida State University, Tallahassee, FL, USA
[9]Department of Meteorology, Institute of Geosciences, Universidade Federal do Rio de Janeiro, Rio de Janeiro, Brazil
[10]Ocean Modeling and Data Assimilation Division, Fondazione Centro Euro-Mediterraneo sui Cambiamenti Climatici (CMCC), Bologna, Italy
[11]National Institute of Oceanography and Applied Geophysics – OGS, Trieste, Italy
[12]Istituto di Scienza e Tecnologie dell'Informazione "Alessandro Faedo", Centro Nazionale delle Ricerche (CNR), Pisa, Italy
[13]Institute for Marine and Antarctic Studies, Oceans and Cryosphere, University of Tasmania, Hobart, TAS, Australia
[14]Oceanography Department, Fisheries and Oceans Canada, North Atlantic Fisheries Center, St. John's, NL, Canada
[15]Unit of Marine and Coastal Systems, Deltares, Delft, Netherlands
[16]Department of Oceanography, Faculty of Science, Dalhousie University, Halifax, NS, Canada
[17]Oden Institute for Computational Engineering and Sciences, The University of Texas at Austin, Austin, TX, USA
[18]Jackson School of Geosciences, The University of Texas at Austin, Austin, TX, USA
[19]Institut de Recherche Pour le Développement (IRD), Marseille, France
[20]NOAA, National Centers for Environment Information, Stennis Space Center, Hancock County, Missisipi, USA
[21]Physical Sciences and Engineering Division, King Abdullah University of Science and Technology (KAUST), Thuwal, Saudi Arabia

Published by Copernicus Publications.

[22]Indian National Centre for Ocean Information Services (INCOIS), Pragathi Nagar, Nizampet, Hyderabad, Telangana 500090, India
[23]Marine Systems Modelling, National Oceanography Center, Southampton, UK
[24]Advanced Scientific Computing Division, Fondazione Centro Euro-Mediterraneo sui Cambiamenti Climatici (CMCC), Lecce, Italy
[25]Meteorological Research Division, Environment and Climate Change Canada, Québec, QC, Canada
[26]Application Laboratory, Japan Agency for Marine–Earth Science and Technology, Yokohama, Kanagawa, Japan
[27]Physical & Biological Sciences Division, Ocean Sciences Department Institute of Marine Sciences, Institute of Marine Sciences, University of California Santa Cruz, Santa Cruz, California, USA
[28]ETT – People and Technology, Genoa, Italy
[29]Science and Technology Facilities Council, Daresbury Laboratory, Hartree Centre, Daresbury, UK
[30]Lobelia Earth, Barcelona, Spain
[31]CSIRO Environment, Castray Esplanade, Hobart, Tasmania, Australia
[32]Institute for Marine and Antarctic Studies, University of Tasmania, Hobart, Australia
[33]Data, Science and Technology, National Oceanography Centre, Southampton, UK
[34]Institute for Coastal Systems, Helmholtz Centre Hereon Geesthacht, Geesthacht, Germany
[35]Egagasini Node, South African Environmental Observation Network (SAEON), Cape Town, South Africa
[36]National Marine Environmental Forecasting Center Beijing, China
[37]Department of Marine and Coastal Sciences, Rutgers, The State University of New Jersey, New Brunswick, NJ, USA

Correspondence: Enrique Alvarez Fanjul (ealvarez@mercator-ocean.fr)

Published: 27 September 2023

1 Introduction

The Intergovernmental Oceanographic Commission (IOC) has an Ocean Decade Implementation Plan (UNESCO-IOC, 2021) that states seven outcomes required for the ocean we want, with the fourth outcome being "A predicted ocean where society understands and can respond to changing ocean conditions." To facilitate the achievement of this goal, the IOC has endorsed Mercator Ocean International to implement the Decade Collaborative Center (DCC) for OceanPrediction (https://www.mercator-ocean.eu/oceanprediction/, last access: 21 August 2023), which is a cross-cutting structure that will work to develop global-scale collaboration between Decade Actions related to ocean prediction.

To have a predicted ocean, the OceanPrediction DCC understands that is critical to co-design ocean forecasting architecture that will permit different services to deliver as one and that could take advantage of the concept of digital twinning (European Union, 2022). This architecture will be designed to overcome the present-day limitations of our systems in terms of interoperability and tools sharing. This will translate into a new scenario for ocean forecasting, where more robust systems will be easier to implement thanks to a common set of agreed tools, standards, and best practices. This new architecture will serve as inspiration for the development targets of the different decadal actions related to ocean forecasting, such as ForeSea (https://oceanpredict.org/un-decade-of-ocean-science/foresea/, last access: 21 August 2023), DITTO (https://ditto-oceandecade.org/, last access: 21 August 2023), CoastPredict (https://www.coastpredict.org/, last access: 21 August 2023), Global Environment Monitoring System for the Ocean and Coasts (GEMS Ocean (https://www.unep.org/explore-topics/oceans-seas/what-we-do/ocean-and-coastal-observations, last access: 21 August 2023)), Ocean Best Practices (https://www.oceanbestpractices.org/, last access: 21 August 2023), and others.

To develop this architecture, the OceanPrediction DCC has implemented the Ocean Forecasting Co-Design Team (OFCT), which is composed of 43 international experts on all of the different aspects of the ocean forecasting value chain. The first task of this group is to analyze the present status of ocean forecasting at a global level, in order to properly identify the existing gaps before moving into the design phase.

One of the first steps in this process has been to explore the degree of satisfaction of both users and experts with respect to the existing ocean forecasting systems. This has been done by launching a series of surveys among the members of the OFCT and another one among the users of the forecasting services. This paper describes the findings derived from the analysis of these surveys. Section 2 introduces the surveys, while Sect. 3 presents the results. Section 4 establishes a discussion and identifies some conclusions as part of the outlook for future exploitation.

2 Methodology

This work is based on the analysis of a series of surveys. Polls have been designed to champion specific categories – namely, experts and end-users – in order to provide a score for each type of application (e.g., from ports, coastal engineering and disaster risk reduction to ecosystem health) and for each type of Essential Ocean Variable (EOV) used (The Expert Team on Operational Ocean Forecasting System, 2022; e.g., a reference list of the key EOVs per ocean universe in blue, green, and white has been provided), focusing on some specific Operational Ocean Forecasting Systems (OOFS) which have properties that are related to their availability and quality (including the timeliness, reliability, and accessibility).

A first set of two surveys (named diagnosis and applications) has been designed for the experts participating in the OFCT, with the main purpose being obtaining a highly skilled subjective view on the availability and quality of today's OOFS at different spatial scales, ranging from global to coastal.

The diagnosis poll focuses on addressing the evaluation of a nowcast and a short-/middle-term forecast (up to 10 d) to solve a proposed list of EOVs such as currents, sea level, or groups of EOVs that are generically related to ice, waves, biochemistry, and biological variables. The question to be answered was as follows: "Qualify, based on your knowledge and experience, from 1 (not satisfied) to 10 (extremely satisfied), our ability to provide a solution at each spatial scale (global, regional and coastal)." The evaluation is driven by four main OOFS properties, namely existence, quality, accessibility, and timeliness, that are defined as follows: existence refers to the availability of sufficient OOFS at the required scale; quality certifies that delivered product/service consistently functions well and provides useful results; accessibility, as defined by Information Technology Infrastructure Library (ITIL, 2023), is considered to be the process of granting the right to use a service; and timeliness refers to the expected time needed to access a product/service. Timeliness can be measured as the time between when information is expected and when it is readily available for use.

The applications poll complements the diagnosis one by gathering the experts' indications on which EOV is useful for serving a specific proposed list of applications that spans from coastal management, ports, energy, navigation, and marine and ecosystem health to disaster risk reduction and aquaculture.

A third poll has been designed for end-users of ocean forecasting services. The objective is to explore the satisfaction level perception with respect to what today's OOFS offer. The survey has been disseminated through several channels, including the OceanPrediction DCC community, Ocean Predict (https://oceanpredict.org/, last access: 25 August 2023), Global Ocean Observing System (GOOS), and others. As with the diagnosis poll, the end-users' survey focuses on a specific list of EOVs (e.g., currents, sea level, temperature, salinity, waves, ice variables, and biochemical and biological variables) analyzed according to specific OOFS properties (e.g., quality, reliability, timeliness, accessibility, and usability).

Note that the questions on the polls for users and experts are not the same. For example, we consider that the differentiation between OOFS spatial scales does not make sense to the users. The methodology employed, based on polls, does not pretend to be mathematically precise, but it is providing significant results on the perception on the status of OOFS, both from the perspective of users and developers, making it therefore a valuable reference for the identification of gaps that will be carried out by the OFCT during a second step.

3 Results

3.1 Experts survey: analysis of the results

All of the 43 OFCT experts have been invited to complete the diagnosis poll. An analysis of the provided rating values per EOV is given in Fig. 1.

For analyses, based on the scale of 1–10, the ratings were grouped into very satisfied (8–10), satisfied (6 to 8), moderately satisfied (4 to 6), unsatisfied (2–4), and very unsatisfied (0–2). The analysis reveals that experts are satisfied about the performances of blue and white ocean variables at global and regional scales (rates from 6.5 to 8, except for quality, with respect to currents and ice, which has a mean rating of 5.3). For the same variable, at coastal scale the degree of satisfaction is only moderate, with mean rates spanning from about 4.5 to 5.7. Wave forecasting is particularly well located on the rating scale, as mean rates above 7.0 are given for all OOFS properties, with maximum value of 7.9 for timeliness at global scale. When considering the coastal scale, the rates are above 6.0.

Considering green ocean variables, the values in Fig. 1 are clearly lower (from slightly satisfied to not satisfied at all), indicating a poor level of appreciation for biogeochemical solutions and a very poor one for systems dealing with biological forecasts (quality values around 2.6).

The analyzed results reveal also that standard deviation from the mean is particularly higher if the EOVs are evaluated per each OOFS type at the coastal scale (values higher than 2.0), reflecting that the experts provided a wide range of ratings with respect to the OOFS capabilities. The only exception is given by waves, whose quality has been positively evaluated (mean rates about 7.0 with a standard deviation of 1.1).

The applications poll results are summarized in Fig. 2, which shows the aggregation of the answers given by experts from a global to coastal scale, mapping the need for specific EOVs to serve a target application. From a qualitative point of view, the panels show that a wide range of EOVs are requested and that the demand increases with the resolu-

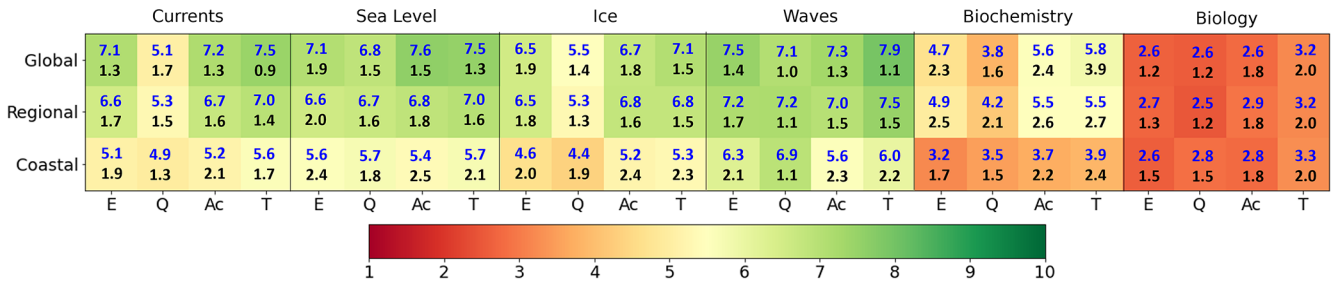

Figure 1. The experts' average rates (in blue) and standard deviations (in black) per OOFS property (E is for existence, Q is for quality, Ac is for accessibility, and T is for timeliness), considering a proposed list of EOVs (e.g., currents, sea level, ice, waves, biochemistry, and biology) at a given scale (e.g., global, regional, and coastal). The color scale corresponds to mean values.

tion and proximity to the coast. There is quite a consensus as green ocean variables are considered to be very important for applications like fisheries, aquaculture, and water quality (Fig. 2b–c). It is in fact quite striking that at a coastal scale almost all EOVs or families of EOVs are used for almost the vast majority of applications, demonstrating the relevance and the need for high-resolution ocean forecasting services.

3.2 End-user survey: analysis of the results

A total of 164 responses were received from end-users working on all continents and have been evaluated; 70 % of them belong to public institutions, while 25.6 % are from private companies. These percentages are close to the ones corresponding to end-users downloading data from the Copernicus Marine Data Store (Le Traon et al., 2019). Figure 3 gives a comprehensive overview of end-user feedback by showing the absolute number of detected uses of EOVs in the different applications. Currents and sea level variables are the most demanded variables for applications related to coastal management and disaster risk reduction (entries higher than 10 for each considered application), and temperature has major impact on applications that refer to fisheries, aquaculture, ecological and biological uses (entries at around 10 for each application and up to 15 for the fisheries one), together with biochemical and biological variables (entries lower than 10). Almost all of the proposed applications gain direct benefits from the waves products. Lower entries are found for ice variables, mainly supporting navigation applications, and for salinity.

As done with the expert survey, a map providing an evaluation of OOFS properties with respect to a subset of EOV is shown in Fig. 4, which displays the mean values and the associated standard deviation. It shows a general and positive level of perception of the overall OOFS capacity for providing products – as demonstrated by mean rates that are generally above 7 for timeliness, accessibility, and usability. Figure 4 reveals that, in contrast with the experts' opinion, biogeochemical and biological variables are well appreciated, with score values ranging from 6 to 8. It is interesting to note that the temperature score is around 6.5, despite currents having an average score between 7.5 and 8. Waves variables are also well positioned, with an average score above 7.5. Looking at all quality values, mean scores span from 6.5 to 7, with standard deviations lower than 2.0. This analysis confirms that more than 90 % of the end-users are satisfied with today's OOFS products.

4 Discussion and conclusions

Maybe the most unexpected and surprising result of this exercise is the large difference existing in the perception between users and experts. While users are always quite satisfied with the systems, experts are generally more critical, especially regarding those services related to the green ocean. These different perceptions are probably due to several factors. Experts are considering the quality by validating with observations, a process that can be more severe than the users' perception, which is based on application experience. On top of that, and probably more importantly, an approximate indication of the value of an EOV could be more than sufficient to allow the satisfactory practical use of a system. For example, a port pilot could be satisfied by knowing if wave heights will or will not be over a given threshold, but they are not affected if the waves have one value or another over that threshold because operations will be canceled independent of how much the variable is exceeding the threshold. On top of that, the experts know where to look to find the problems in the systems, and they do so by scrutinizing all variables, oceanographic situations, and geographical regions of the domain of the system, while the end-users commonly have a perspective limited into one particular aspect of the service. When the range of processes and results under scrutiny is larger, it is to be expected that more mishaps can be found.

To the trained eye, the evaluation of the experts is not surprising. It clearly shows that wave and sea level forecasting systems are quite mature and that more effort must be made with respect to the green ocean, probably at all points of the value chain, from observations to downstream services. Also, the progressive degradation of the system's performance as we come closer to the coast is obvious. This is most likely

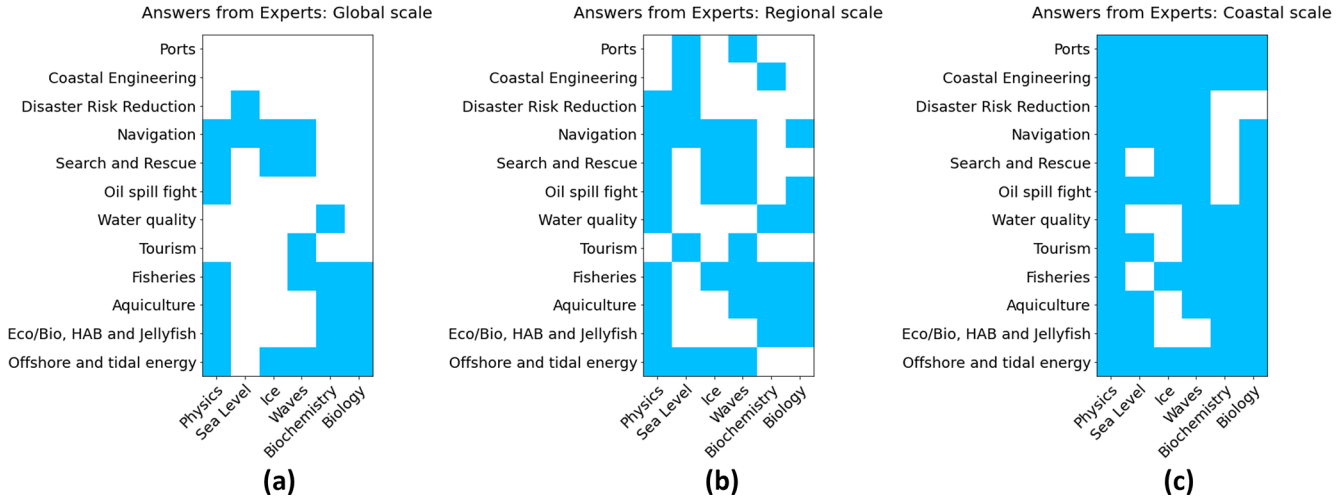

Figure 2. Schematic overview of survey outcomes related to the needs of different EOVs (x axis) for each application area (y axis) at **(a)** global, **(b)** regional, and **(c)** coastal scales.

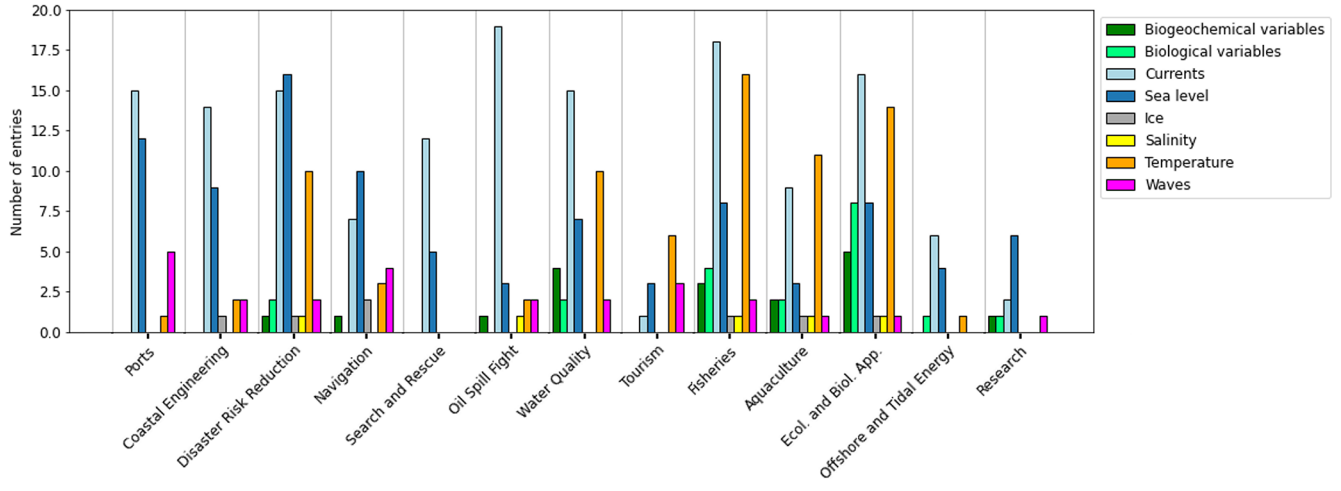

Figure 3. Histogram of the survey outcomes related to end-users' answers, considering different EOVs (colors) being employed at each application area (x axis).

due to several factors that can be present on some occasions, such as the lack of an appropriate resolution, poor atmospheric forcing at that scale, the lack of river data, and the complexity and importance of the nonlinear effect and interactions between EOVs near the coast. Take, for example, a sea level that has a striking low mean quality value of only 5.7 at the coast. The degradation could be due to lack of coupling with waves near the coast or to poor bathymetry. The importance of this skill's degradation is reinforced with the analysis of the results from the applications survey, which demonstrates that it is precisely near the coast where ocean forecasting EOVs are more widely used.

It is also not surprising that in most cases, the lowest value for the experts is associated with quality and not with existence, timeliness, or accessibility. This demonstrates the relative maturity of the operational chains and the need to improve in all the aspects related to the prediction engines, including the acquisition of new data to be assimilated.

Nevertheless, there are some aspects that would require further investigation. It is striking that, when not satisfied, the experts tend to evaluate all aspects of the system in a negative way at the same time. There is no evident reason why biogeochemical or biological models behave so poorly in technical aspects such as timeliness. Maybe the difficulty in obtaining good, accurate solutions is biasing the criteria of the experts when evaluating these on more purely technical aspects. This fact will be further investigated in the future. Another potentially biased result is the qualification on the existence of systems. Both users and experts are replying based on their experience and, obviously, the geographical

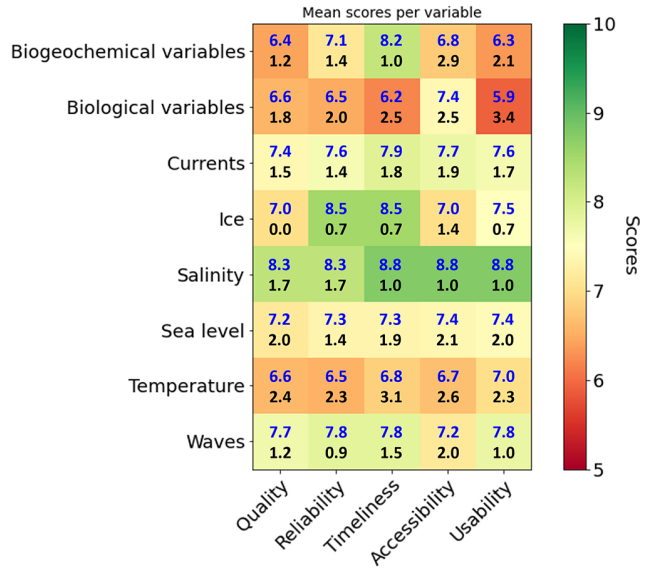

Figure 4. Mean values (in blue) and standard deviations (in black) of the end-users' evaluation of the Operational Ocean Forecasting Services (OOFS; e.g., quality, reliability, timeliness, accessibility, and usability), when considering a proposed list of EOVs (e.g., biogeochemical and biological variables, currents, ice, salinity, sea level, temperature, and waves). The color scale corresponds to the mean values. See the text for more details on the scoring.

areas where they are developing or using systems, including at least the system(s) that they deal with. This situation can be different in another regions, unbeknownst to the participants. OceanPrediction DCC is developing a global map of existing OOFS that will illuminate this question.

In summary, during the last 3 decades, the evolution and improvement of ocean forecasting services has been dramatic, and this exercise has proven that the existing systems are useful and accurate in the opinion of the users. Nevertheless, the experts have clearly stated that further improvements are required, mainly when approaching the coast and for the systems dealing with the green ocean. The Ocean Decade Implementation Plan is giving us a framework to further develop the systems, and this is the objective of OceanPrediction DCC and its associated decadal actions, such as ForeSea, Ocean Best Practices, DITTO, CoastPredict, GEMS Ocean, and others. To measure the success of these initiatives, it could be interesting to repeat this exercise by the end of the decade.

Code and data availability. The authors will make the software code and data available upon request to the corresponding author.

Author contributions. SAC and EAF developed the methodology and led the investigation. EAF supervised the work, which was conceptualized with PB. SAC curated the data and worked on the visualization of the main results. The original draft of this work was prepared by EAF and SAC; then JP and KWB reviewed it. All co-authors kindly participated in the surveys.

Competing interests. At least one of the (co-)authors is a member of the editorial board of *State of the Planet*. The peer-review process was guided by an independent editor, and the authors also have no other competing interests to declare.

Disclaimer. Please note that this article has undergone editorial review only.

Publisher's note: Copernicus Publications remains neutral with regard to jurisdictional claims in published maps and institutional affiliations.

References

European Union: European Commission, Directorate – General for Research and Innovation, The digital twin ocean: an interactive replica of the ocean for better decision-making, Publications Office of the European Union, 2022, https://data.europa.eu/doi/10.2777/343496 (last access: 21 August 2023), 2022.

ITIL (The Information Technology Infrastructure Library): The Information Technology Infrastructure Library (ITIL), https://www.itlibrary.org/, last access 7 July 2023.

Le Traon, P. Y., Reppucci, A., Alvarez-Fanjul, E., Aouf, L., Behrens, A., Belmonte, M., Bentamy, A., Bertino, L., Brando, V. E., Brandt Kreiner, M., Benkiran, M., Carval, T., Ciliberti, S. A., Claustre, H., Clementi, E., Coppini, G., Cossarini, G., De Alfonso Alonso-Muñoyerro, M., Delamarche, A., Dibarboure, G., Dinessen, F., Drevillon, M., Drillet, Y., Faugere, Y., Fernandez, V., Fleming, A., Garcia-Hermosa, M. I., Garcia Sotillo, M., Garric, G., Gasparin, F., Giordan, C., Gehlen, M. Gregoire, M. L., Guinehut, S., Hamon, M., Harris, C., Hernandez, F., Hinkler, J. B., Hoyer, J., Karvonens, J., Kay, S., King, R., Lavergne, T., Lemiuex-Dudon, B., Lima, L., Mao, C., Martin, M. J., Masina, S., Melet, A., Nardelli, B. B., Nolan, G., Pascual, A., Pistoia, J., Palazov, A., Piolle, J. F., Pujol, M. I., Pequignet, A. C., Peneva, E., Perez Gomez, B., Peiti de la Velleon, L., Pinardi, N., Pisano, A., Pouliquen, S., Reid, R., Remy, E., Santoleri, R., Siddorn, J., She, J., Staneva, J., Stoffelen, A., Tonani, M., Vandenbulcke, L., von Schuckmann, K., Volpe, G., Wettre, C., and Zacharioudaki, A.: From Observation to Information and Users: The Copernicus Marine Service Perspective, Front. Mar. Sci., 6, 234, https://doi.org/10.3389/fmars.2019.00234, 2019.

The Expert Team on Operational Ocean Forecasting Systems: Implementing Operational Ocean Monitoring and Forecasting Systems. Editors: Enrique Alvarez Fanjul, Stefania Ciliberti, Pierre Bahurel, IOC-UNESCO, GOOS-275, https://doi.org/10.48670/ETOOFS, 2022.

UNESCO-IOC: The United Nations Decade of Ocean Science for Sustainable Development (2021–2030) Implementation plan – Summary, Paris, UNESCO (IOC Ocean Decade Series, 19), https://unesdoc.unesco.org/ark:/48223/pf0000376780 (last access: 21 August 2023), 2021.

State Planet, 1-osr7, 3, 2023
https://doi.org/10.5194/sp-1-osr7-3-2023

Comparing global trends in marine cold spells and marine heatwaves using reprocessed satellite data

Robert Peal, Mark Worsfold, and Simon Good

Met Office, FitzRoy Road, Exeter, Devon, EX1 3PB, UK

Correspondence: Mark Worsfold (mark.worsfold@metoffice.gov.uk)

Received: 28 July 2022 – Discussion started: 10 October 2022
Revised: 25 January 2023 – Accepted: 27 January 2023 – Published: 27 September 2023

Abstract. Climate change is causing extreme climate events to become more frequent and more severe. Marine heatwaves (MHWs) and marine cold spells (MCSs) are prolonged, discrete periods of anomalously high or low ocean temperatures with wide-ranging impacts from dramatic shifts in biodiversity to changes in fishery yields. Previous research has found that MHWs are increasing in frequency and intensity, but MCSs remain less well understood.

We used sea surface temperature (SST) data to compare the global observed MCS and MHW intensities and trends in their frequency over the period 1982–2021. These events were also assigned a category from I (moderate) to IV (extreme). Our findings show that in large areas of the ocean it can be said with 99 % confidence that MCSs have become less frequent and MHWs have become more frequent. In those regions, the occurrence of MCSs has typically reduced by one event every 5 years, while there is one extra MHW every 5 to 10 years. However, parts of the Southern Ocean go against these trends with MHWs becoming slightly less frequent and MCSs becoming more frequent.

The trend of increasing numbers of MHWs and decreasing numbers of MCSs is mostly due to increases (and decreases) in category I and II events. Category III and IV MHWs are less common than the milder events, and a trend analysis demonstrated that across most of the ocean they are occurring at a slightly increased rate. However, the spatial extent of the ocean affected by these events is increasing at a faster rate. The occurrences of category III and IV MCSs are infrequent, and a trend analysis also found that their rates of occurrence, as well as the spatial extent of the ocean affected, remain near constant.

Many of our results are in agreement with previous studies; what is significant about this study is the fact that it uses a different, higher-resolution input SST dataset. The similarity of the results between the different research efforts strengthens the argument that these events are not just a feature of their input dataset.

1 Introduction

There is now overwhelming evidence that climate change will increase the frequency and intensity of extreme climate events such as marine heatwaves (MHWs) (IPCC, 2021; Frölicher et al., 2018; Oliver, 2019), which are defined as "prolonged discrete anomalously warm water events" (Hobday et al., 2016) and have attracted a growing amount of interest in recent years. These events often have dramatic and sometimes devastating impacts on local ecology including shifting local biodiversity (Wernberg et al., 2013, 2016; Frölicher and Laufkötter, 2018) and triggering coral bleaching events (NOAA, 2015). They also have a range of socio-economic impacts (Smith et al., 2021) such as altering fishery yields (Mills et al., 2013; Smale et al., 2019; Cheung et al., 2021). Marine cold spells (MCSs), which are defined equivalently to MHWs as a "discrete, prolonged anomalously cold water event at a particular location" (Schlegel et al., 2021), remain less well understood, but a growing body of research suggests that low-SST (sea surface temperature) events can also have significant impacts on ecology including coral reef destruction (Lirman et al., 2011) and have links to extreme climate events on land (Duchez et al., 2016). Previous re-

Published by Copernicus Publications.

Table 1. Data used for report.

Product ref. no.	Product ID and type	Data access	Documentation
1	SST_GLO_SST_L4_REP_OBSERVATIONS_010_011; satellite observations	EU Copernicus Marine Service Product (2022)	Quality Information Document (QUID): Worsfold et al. (2022a) Product User Manual (PUM): Worsfold et al. (2022b)

search into MCSs has focussed on certain regions including investigating drivers of shallow-water events in some coastal regions (Schlegel et al., 2017) and effects of MCSs on fisheries in the North Sea (Wakelin et al., 2021).

The field of MHW and MCS research moves rapidly, but two research papers in particular are very relevant to this investigation. Both papers used the Optimum Interpolation Sea Surface Temperature (OISST) climate dataset produced by the National Oceanic and Atmospheric Administration (NOAA) and the same detection method (Sect. 2) over the period 1982–2020.

Schlegel et al. (2021) provided a comprehensive review of previous studies into MCSs and the possible causes of MCSs, which were found to be often driven by anomalous winds, although other drivers were also identified. The trends in MCSs were also investigated for different MCS categories. Wang et al. (2022) calculated and compared the trends in MHWs and MCSs but did not delve into event categories.

This investigation has some parallels with the first two, but it is the first to use the higher-resolution Operational Sea Surface Temperature and Ice Analysis (OSTIA) climate SST dataset (Table 1) produced for the Copernicus Marine Environment Monitoring Service (CMEMS), and it can therefore provide an independent assessment of the occurrence of MHWs and MCSs.

2 Methods

2.1 Input SST dataset used

Most previous MHW–MCS investigations have used the 0.25° resolution NOAA OISST climate SST (version 2.1) dataset (for example Schlegel et al., 2021, and Wang et al., 2022), which represents the SST at 0.5 m depth (Huang et al., 2020). This is often called a SST depth product, which will increase during the day due to solar heating and cool at night (termed a diurnal cycle).

This investigation used the 0.05° resolution CMEMS OSTIA climate dataset for the period 1982–2021 (Table 1). OSTIA is formed from nighttime SSTs, and daytime SSTs whenever windy conditions mean that it can be assumed that the diurnal cycle is not affecting the daytime temperature (Good et al., 2020). Therefore, it represents the foundation SST, which can be defined as the temperature from which the growth and decay of the diurnal heating develops each day (GHRSST, 2022).

OSTIA uses the NEMOVAR variational data assimilation scheme (Mogensen et al., 2009) to combine satellite and in situ data with a background field that is based on the previous day's analysis (Good et al., 2020). In areas of the ocean where there are no observations, if the sea ice concentration is greater than 50 %, the SSTs will eventually relax to −1.8 °C and elsewhere to a 1985–2007 climatology.

As a result of RAM memory overflow issues encountered by the R programming language (unfortunately a fundamental limitation of this language) when processing the full-resolution data, the OSTIA dataset was linearly regridded to 0.25° resolution for the purpose of this investigation.

2.2 Definition and detection of marine heatwaves and marine cold spells

Fundamentally an MHW is detected whenever the SSTs exceed a threshold value, but this threshold has a variety of interpretations depending on the investigation requirements. One of the simpler definitions is to use a chosen percentile (usually 99th) as a threshold SST value calculated from a chosen climatology period (Darmaraki et al., 2019; Frölicher et al., 2018; Laufkötter et al., 2020). For this study we are using the Hobday definition of a heatwave (Hobday et al., 2016, 2018; Schlegel et al., 2021; Wang et al., 2022), which has gained wide acceptance in the MHW–MCS research community. To detect an MCS, consider that each pixel of the dataset has the following mathematical elements:

A. a time series of SST values (thin black line in Fig. 1a and b)

B. the daily climatology using the period January 1982–December 2011 as the baseline (smooth, thicker black line in Fig. 1a and b)

C. the 10th percentile of the climatology data B, taken from an 11 d rolling window centred on each day (solid green line in Fig. 1a and b), which is the threshold used to determine if there is an MCS

D. the difference between the 10th percentile C and the climatology B.

A pixel is considered to have an MCS wherever the SST value A is below the 10th percentile threshold value C for at least 5 d. If there is a gap of less than 2 d between an MCS, they are considered to be one event.

Furthermore, the difference value D then allows this MCS to then be categorized. A heatwave is considered category I (moderate) when the SST value A is less than the sum of the climatology value B and the difference value D (i.e. where $A <= B + D$) (below solid green line in Fig. 1a and b). A category II (strong) MCS would be where $A <= B + 2D$ and so on for severe and extreme events (dashed green lines in Fig. 1a and b).

MHWs are defined equivalently as a period of at least 5 d where the SST value is above the 90th percentile of the SST data from an 11 d rolling window centred on each day.

Using the Hobday definition, events can be described by the following characteristics:

- Duration is the number of consecutive days where the SST exceeded the 90th percentile value for MHWs or was below the 10th percentile value for MCSs.
- Maximum intensity is the maximum difference between the SST and the climatology value during the event (MHWs have positive intensity, and MCSs have negative intensity).
- Category describes the severity of an event by assigning a category to the maximum intensity value relative to the local climatology.

All these MHW and MCS characteristics are calculated for each individual grid cell separately; the neighbouring cells are not considered.

The MHWs and MCSs and their characteristics were calculated from the SST dataset using the heatwaveR package (Schlegel and Smit, 2018; Hobday et al., 2016). An important consideration is that areas with persistently high SSTs do not necessarily suffer as many heatwaves. While this may seem counter-intuitive at first, consider that MHWs are defined relative to the climatology. Therefore, an area with historically high average SST values will present less opportunity for recent SSTs to exceed that high climatology threshold. This characteristic is valuable since researchers are often most interested in areas with significant deviations from historical temperatures.

3 Results and discussions

3.1 Using the Hobday MCS framework to describe anomalous low-SST events

To highlight the consequences of cold spells and how the Hobday category framework (Hobday et al., 2016, 2018) can help describe the severity of MCSs, two case studies of known cold-water events were selected and investigated.

The first case study illustrates the effect of MCSs on marine ecosystems (Fig. 1a). An investigation by Abram et al. (2003) linked the coral reef death off Sumatra in October 1997 to the combination of Indonesian wildfires exacerbated by El Niño and anomalously low SST caused by the Indian Ocean Dipole (IOD) which caused increased upwelling of cold, nutrient-rich water in the region. Such upwelling events are associated with increased biological activity, which can lead to large algal blooms (often called "red tides") (Genin et al., 1995). These events can limit oxygen supplies to coral reefs but usually pose only a minor threat as the biological activity is usually iron limited (Johnson et al., 2001). However, in October 1997 the ash cloud from the Indonesian forest fires dumped large quantities of iron on the ocean, causing one of the largest red tides the region had ever seen, leading to mass asphyxiation of the coral (Abram et al., 2003).

This event was examined using the Hobday framework, and Fig. 1a shows that the anomalous SST in the region may be classified as a category IV MCS with a duration of around 100 d peaking in early November.

Extreme low-SST events have also been linked to significant global weather events, which is illustrated by the second case study (Fig. 1b). Duchez et al. (2016) showed that the 2015 European summer continental heatwave, 1 of the top 10 hottest in the last 65 years, as well as several other severe European summer heatwaves, were preceded by anomalously cold SSTs in the North Atlantic, but establishing causality (if any) is the subject of further research.

The inset in Fig. 1b shows that a category III MCS prevailed over much of the region in 2015, with some areas classified as a category IV. Further time series analysis of a pixel within a category IV region shows an MCS with a duration of around 69 d peaking in late March.

In these examples, the Hobday category framework has been used to describe the severity of marine SST anomalies that have been linked with significant environmental and ecological events. Use of this framework may help researchers to better communicate the severity of both low- and high-SST anomalies with public and local officials, allowing the area to prepare for the effects of marine temperature extremes.

3.2 A global perspective of MHW and MCS distribution and strength

The average maximum intensity of events and the average number of yearly events for both MHWs and MCSs were calculated over the global domain for the period 1982–2021 to produce a map of the distribution of such events (Fig. 2). Figure 2a and b show that the mean maximum intensity of both types of events at most locations in the global ocean was 1 to 2 °C and between 2 and 4 °C in the Niño 3 region of the eastern Pacific (defined as 5° N–5° S, 90–150° W) (Trenberth, 1997). Moreover, other regions with higher-intensity

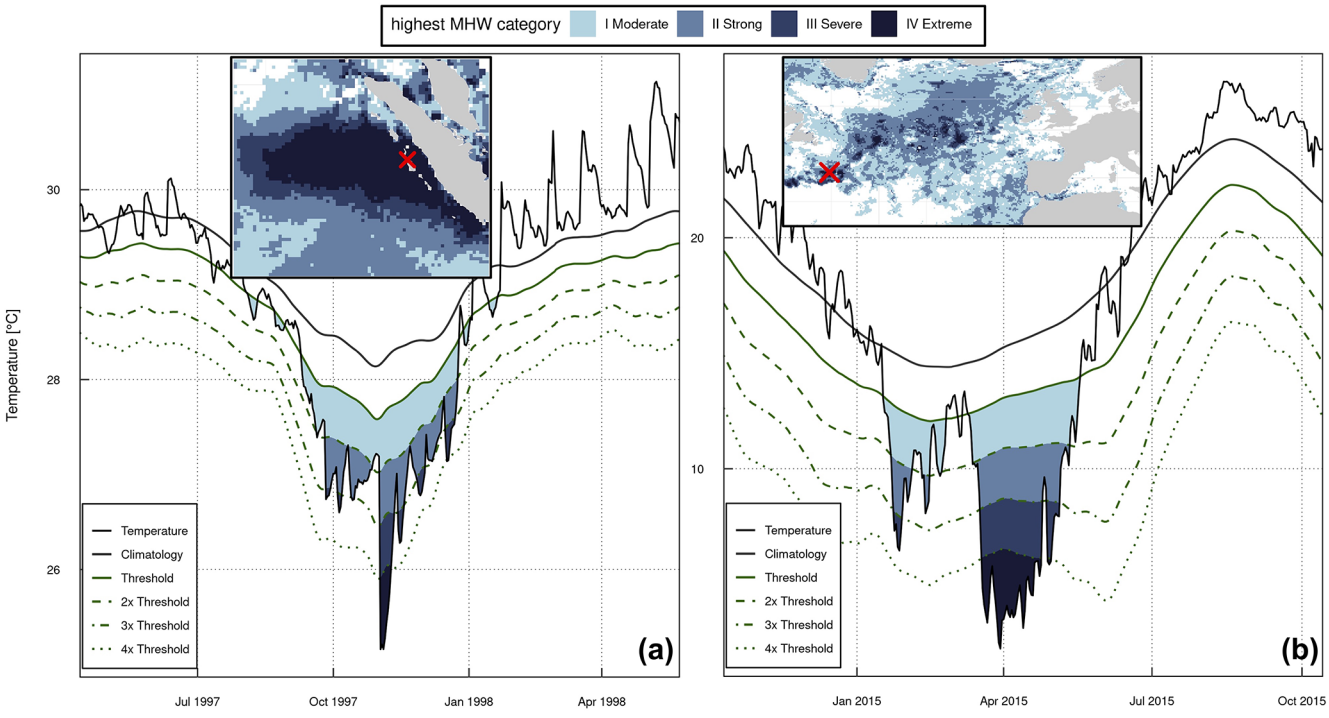

Figure 1. Significant MCSs. **(a)** Sumatra 1997. Main figure: SST values and MCS threshold during late 1997 at lat 0.875, long 98.625. Inset: highest MCS category detected across the region during 1997 (the red cross denotes the location where the time series data were extracted). **(b)** North Atlantic 2015. Main figure: SST values and MCS threshold during early 2015 at lat 41.125, long −50.375. Inset: highest MCS category detected across the region during 2015 (the red cross denotes the location where the time series data were extracted).

MHWs (sometimes exceeding 6 °C) also experienced MCSs of similar intensity. These regions of high-intensity MHWs–MCSs were also located in areas in which western boundary currents (WBCs) are found (NW Atlantic – Gulf Stream, SW Atlantic – Brazil Current, South Africa – Agulhas Current, Japan – Kuroshio Current; Le Traon and Morrow, 2001). WBCs are found at the western edges of ocean gyres and transport warmer waters towards the poles (Holbrook et al., 2019).

The average number of heatwaves per year was calculated for each pixel of the dataset and plotted. Examining Fig. 2c and d it can be seen that in most locations, MHWs were slightly more common than MCSs, with between one to three events detected per year compared to one to two MCS per year.

However, MHWs were rare in the Niño 3 region, occurring no more than once per year, while MCSs occurred between two and three times per year in the same region.

Regions with a higher frequency of MCSs tended to coincide with regions where they were more intense. The north-west Atlantic, south-west Atlantic, region off South Africa, and north-west Pacific off Japan all had up to three MCSs per year.

Schlegel et al. (2021) carried out a similar investigation into MCS count and intensity for the period 1982–2020, and Oliver et al. (2018) also did the same for MHWs for the 1982–2016 period. As mentioned earlier, Wang et al. (2022) compared the trends in MCSs and MHWs (using similar but different metrics). An important point to reiterate is that these previous studies had used the NOAA OISST dataset.

Despite the differences between investigations, it is remarkable that the spatial distribution of the values in Fig. 2 are very similar to the results from the previous investigations.

3.3 An exploration of linear trends in MHW and MCS events for each category

In order to determine whether there was a change in the number of MHWs and MCSs per year, a linear trend was calculated for each pixel of the global dataset and plotted (Fig. 3). Further plots were also generated for each event category, and contours were added wherever the trend exceeded a 99 % confidence level.

Figure 3a shows that occurrences of MCSs in much of the Atlantic, Indian, and western Pacific oceans are decreasing at a rate of up to one event every 5 years and that these decreases exceed the 99 % confidence interval for most of the region. Figure 3c shows a large decrease in category I (moderate) events at a rate of almost one event every 5 years at the locations which exceed the 99 % confidence value. A smaller but still significant decrease in category II (strong) events of

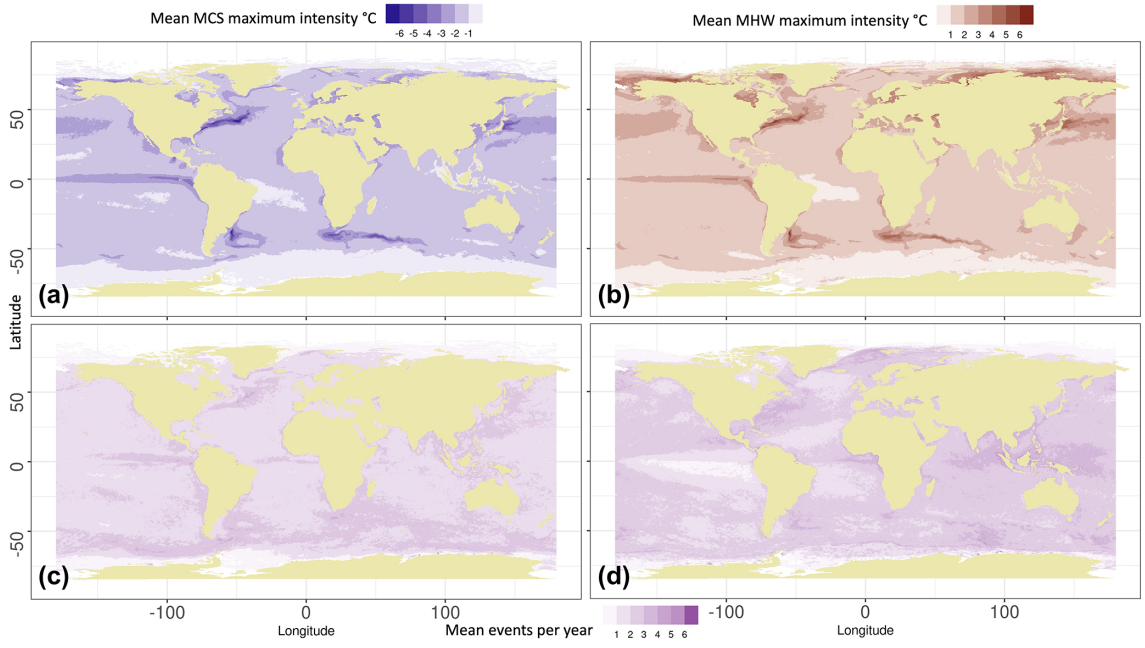

Figure 2. Comparison of global MHW and MCS mean maximum intensity and frequency of occurrence during the period 1982–2021, calculated from product 2.1.1. **(a)** Mean MCS maximum intensity and **(c)** average number of MCSs per year at each grid point. **(b)** Mean MHW maximum intensity and **(d)** average number of MHWs per year at each grid point.

about one event every 20 years was also observed (Fig. 3e). Figure 3g and i show that category III and IV events are continuing to occur at a roughly constant rate. Therefore, the overall decrease in MCS is largely due to decreases in the numbers of category I and II events.

Figure 3b shows that MHWs in the central Atlantic, Indian, and western Pacific oceans are increasing by one event every 5 to 10 years, and this trend is significant to the 99 % confidence level in much of the region. Figure 3d and f show that this is largely due to increases in category I and II MHWs of up to one event per 10 years in much of the region. Figure 3h and j show that the trends in category III and IV MHWs are close to zero.

It is also notable that the southern Pacific Ocean (in particular, east of South America) goes against the general trends. Figure 3a shows that MCSs are becoming more frequent in the southern Pacific Ocean by one event every 10–20 years, which is largely due to increases in category II events (Fig. 3e). Meanwhile MHWs are also becoming less frequent in this region by one event every 10–20 years (Fig. 3b), which is largely due to decreases in category I events (Fig. 3d).

Interestingly, the increasing number of MCSs (for all categories) in the Southern Ocean was also observed by Schlegel et al. (2021), although their research did not determine whether events of a specific category were responsible for this behaviour.

Oliver (2019) determined that rising average SSTs were the main driver of trends in MHWs, which was also confirmed by Wang et al. (2022), who also determined that rising SSTs were responsible for trends in MCSs. In addition, climate change research has also found that, while SSTs are increasing on average, the southern Antarctic Ocean has cooled slightly (Auger et al., 2021; Rye et al., 2020; Armour et al., 2016). The observed spatial patterns in our results for MHWs and MCSs fits into a wider picture of the ocean's behaviour changing as a consequence of climate change.

3.4 Changes in the affected ocean area over time

To investigate whether there are any changes in how much of the ocean is affected by MHWs and MCSs, each pixel was examined to determine the most severe event that had occurred in each year. This information was used to produce a time series for the fraction of the ocean area affected by an event (Fig. 4).

Figure 4 (left) shows that MCSs are now occurring in less of the ocean than historically. The amount of ocean where the highest MCS categories detected were category I and II has decreased from 41.8 % in 1982 to 25.3 % in 2021 and from 27.8 % in 1982 to 13.2 % in 2021 respectively, while the amount of ocean without any MCSs at all has increased from 26 % to 56.6 % in 2021. In contrast, category III and IV MCSs have been detected at a near constant ∼ 1 %–3 % of the ocean. This suggests that even in a warming world, extreme MCSs have so far remained consistently rare.

The investigation by Schlegel et al. (2021) also found that category III and IV events remained steady and that the area

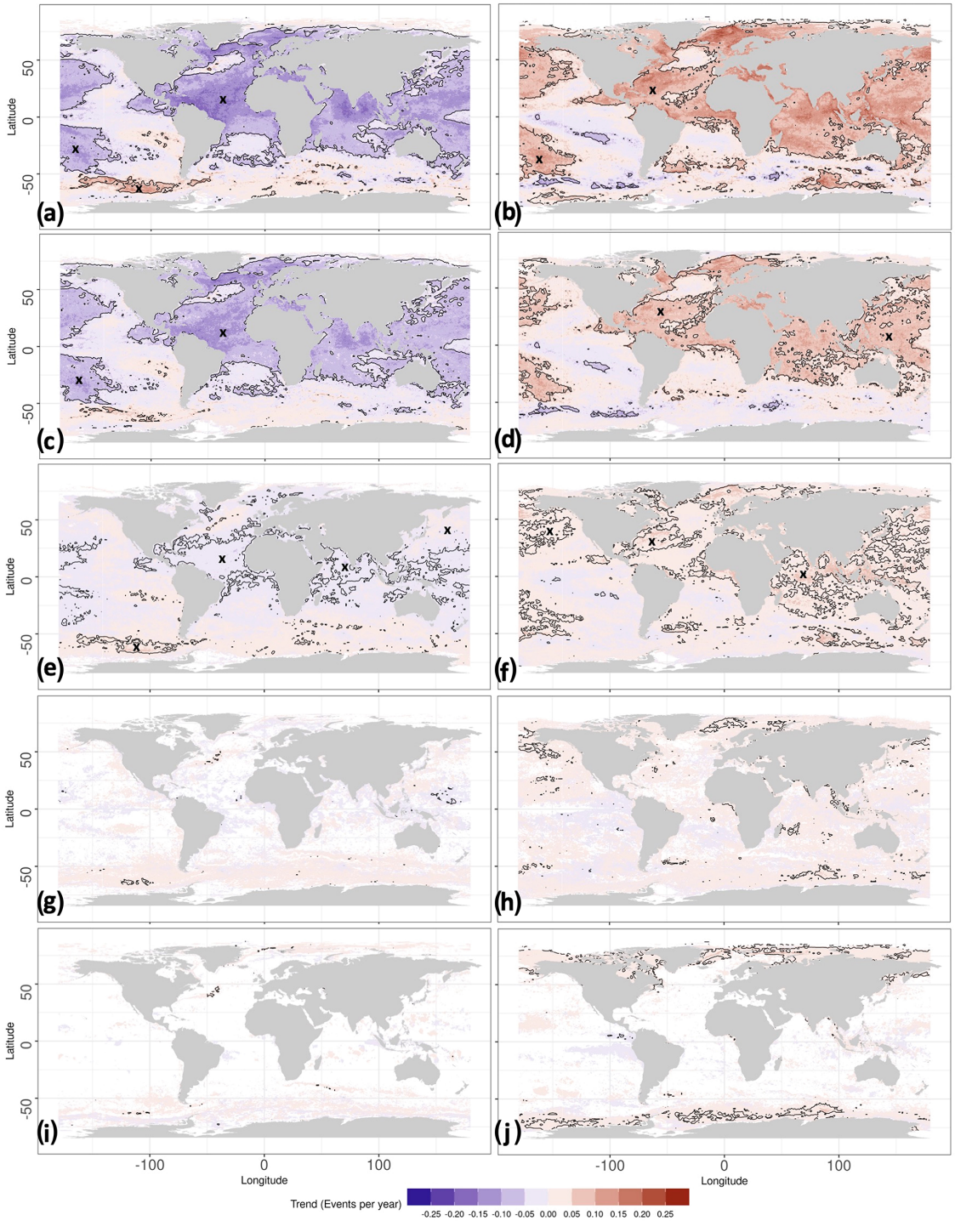

Figure 3. Trends in the number of MCS and MHW events per year for **(a)** all MCSs, **(b)** all MHWs **(c, e, g, i)**, category I–IV MCSs **(d, f, h, j)**, and category I–IV MHWs. The year of an event has been defined as the year of peak intensity. Linear trends were calculated using a least-squares fit, and the contour line bounds the region where the trends exceed the 99 % confidence level of a two-tailed *t* test compared to a constant rate of occurrence. The X markers indicate the inside of the contour to aid interpretation. Areas with no shading are where no events were detected.

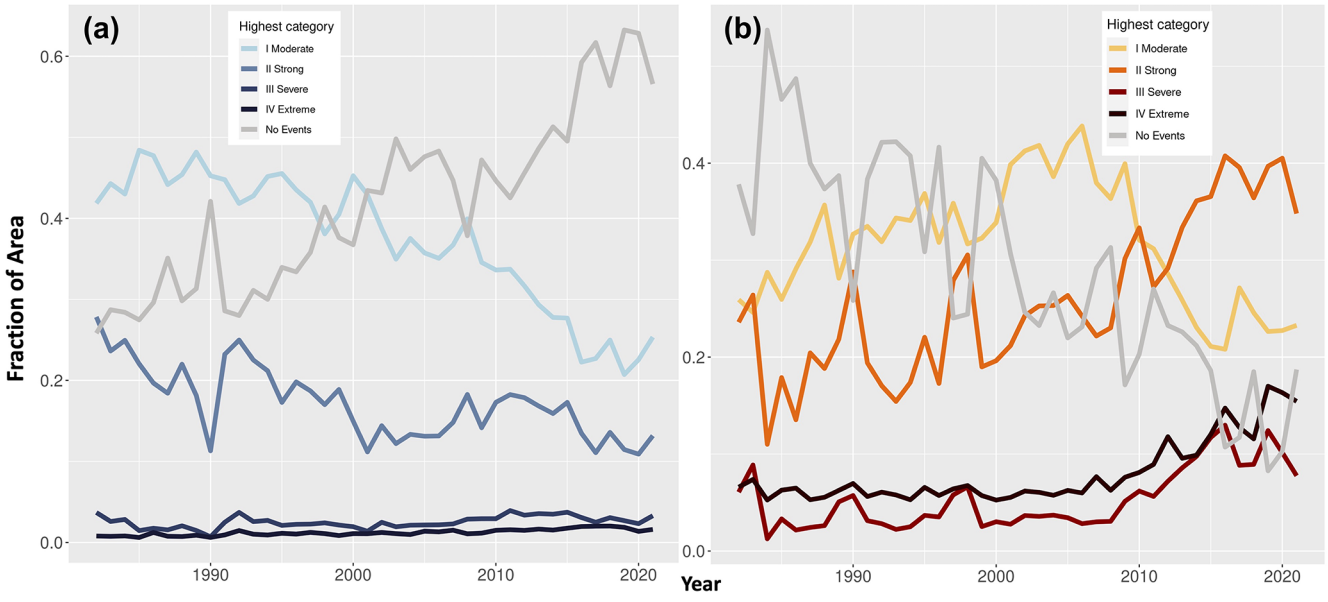

Figure 4. The fraction of the area of the ocean where the highest **(a)** MCS and **(b)** MHW category detected was I, II, III, IV, or no events being detected. The year of an event is defined as the year of the peak intensity.

of the ocean which experienced an MCS had decreased (61 % in 1982 to 25 % in 2020). However, their investigation differed in that they determined that this was mainly due to a decrease in category II–IV events.

Figure 4 (right) demonstrates that the area of ocean with no MHWs has seen a steady decline throughout the time period from 37.8 % in 1982 to 18.7 % in 2021, indicating that MHWs are occurring at more locations in the ocean. Breaking down the results by category, it can be observed that category I events were initially the most common; the area dominated by these events increased from 25.9 % to 43.8 % between 1982 and 2006 before decreasing sharply to just 23.3 % in 2021. In the same period, the area of ocean where II was the highest MHW category increased from 23.6 % to 34.8 % in 2021, overtaking category I as the most common category. The amount of ocean where the highest category was III or IV initially remained at around 3 % and 6 % respectively until 2008, after which there was a sharp increase in both categories to 7.7 % for category III and 15.4 % for category IV in 2021. The spatial increase in these categories is especially a cause for concern since these types of events tend to have more dramatic impacts compared to lower-category events (Hobday et al., 2018).

It is also interesting to note that the same investigation by Hobday et al. (2018) also produced a graph displaying a similar behaviour (a reduction in "no events" and category I MHWs and an increase in other categories).

4 Conclusions

In this study, we have compared global MHWs and MCSs in the period 1982–2021. We have revealed that the mean peak intensity of MHWs and MCSs at most locations was 1 to 2 °C and the mean peak intensity was highest (up to 6 °C for both kinds of event) in regions where western boundary currents dominate. We have also shown that in much of the ocean, MCSs have become less frequent by around one event every 5 years, while there is one extra MHW event every 5 to 10 years. Most of the changes are due to increases in category II–IV MHWs and decreases in category I and II MCSs. However, events in parts of the Southern Ocean go against these trends with MHWs becoming slightly less frequent and MCSs becoming more frequent. Category III and IV MHWs remain less common than the less severe events, and at individual locations they are occurring at a slightly increased rate over time. However, these events are becoming more widespread. Category III and IV MCSs are rare but are continuing to occur at near-constant rates in much of the ocean.

The average global frequency and maximum intensity (Fig. 2) and the trend analysis for all categories of events (Fig. 3a and b) had a similar spatial distribution to the MCS results obtained by Schlegel et al. (2021) and Wang et al. (2022) as well as the MHW results obtained by Oliver et al. (2018). The temporal changes in the ocean area affected (Fig. 4) were also similar to the results from investigations carried out by Schlegel et al. (2021) and Hobday et al. (2018).

The mechanisms that drive these trends in MHWs and MCSs are still under investigation, and further research would provide valuable insight into the changing nature of

MHWs and MCSs. Future research also should focus on improving understanding of how MCSs form and their impact on ocean ecosystems as well as on developing tools for predicting when they will occur, allowing for early warnings of these events. Although more research is required to quantify the differences in the outputs from the OISST and OSTIA datasets and their relative confidence levels, the similarity of the results strengthens the argument that these events are not just a feature of their input dataset.

It also demonstrates the potential of using OSTIA for future MHW–MCS investigations. Research carried out by Yang et al. (2021) showed that the full-resolution OSTIA was superior to OISST in resolving smaller oceanic features. Unfortunately, fundamental limitations in the R programming language prevented us from using the full-resolution OSTIA dataset in this investigation. However, this presents an excellent topic for a follow-up investigation using the full-resolution dataset (using a Python version of the MHW code) to determine whether this brings about improvements in MHW–MCS detection or delivers greater insights into their formation and behaviour.

Data availability. Publicly available datasets were used and are available from CMEMS (Table 1).

Author contributions. MW generated the initial datasets for the period 1982–2020 required for the investigation. RP processed the data to produce the results outlined above and wrote the first draft of the report. When data for 2021 became available, MW then updated the results with the latest data and performed the necessary rewrites for the review and submission process. SG also reviewed and edited the report.

Competing interests. The contact author has declared that none of the authors has any competing interests.

Disclaimer. Publisher's note: Copernicus Publications remains neutral with regard to jurisdictional claims in published maps and institutional affiliations.

Acknowledgements. The authors would like to acknowledge the following contributors: Robert Schlegel and Albertus Smit for their support with adapting the heatwaveR package to process global data and more generally making their excellent software available to the wider research community so that we can all benefit and Owen Embury of Reading University who made available his verification software, which was used in order to check that the code used to regrid the OSTIA dataset did not degrade the quality of the data. The OSTIA and OISST datasets were compared to independent in situ SST measurements and found to be similar. The results of this investigation were not included in this report since it was a quality control check rather than a research investigation. More information can be obtained from the authors on request.

Financial support. This work was partly funded by the CMEMS SST Thematic Assembly Centre (21001-COP-TAC Lot 3).

Review statement. This paper was edited by Johannes Karstensen and reviewed by two anonymous referees.

References

Abram, N., Gagan, M., McCulloch, M., Chappell, J., and Hantoro, W.: Coral Reef Death during the 1997 Indian Ocean Dipole Linked to Indonesian Wildfires, Science, 301, 952–955, https://doi.org/10.1126/science.1083841, 2003.

Armour, K., Marshall, J., Scott, J., Donohoe, A., and Newsom, E.: Southern Ocean warming delayed by circumpolar upwelling and equatorward transport, Nature Geosci., 9, 549–554, https://doi.org/10.1038/ngeo2731, 2016.

Auger, M., Morrow, R., Kestenare, E., Sallée, J., and Cowley, R.: Southern Ocean in-situ temperature trends over 25 years emerge from interannual variability, Nat. Commun., 12, 514, https://doi.org/10.1038/s41467-020-20781-1, 2021.

Cheung, W. W. L., Frölicher, T. L., Lam, V. W. Y., Oyinlola, M. A., Reygondeau, G., Sumaila, U. R., Tai, T. C., Teh, L. C. L., and Wabnitz, C. C. C.: Marine high temperature extremes amplify the impacts of climate change on fish and fisheries, Sci. Adv., 7, eabh0895, https://doi.org/10.1126/sciadv.abh0895, 2021.

Darmaraki, S., Somot, S., Sevault, F., and Nabat, P.: Past variability of Mediterranean Sea marine heatwaves, Geophys. Res. Lett., 46, 9813–9823, https://doi.org/10.1029/2019GL082933, 2019.

Duchez, A., Frajka-Williams, E., Josey, S., Evans, D., Grist, J., Marsh, R., McCarthy, G., Sinha, B., Berry, D., and Hirschi, J.: Drivers of Exceptionally Cold North Atlantic Ocean Temperatures and Their Link to the 2015 European Heat Wave, Environ. Res. Lett., 11, 74004, https://doi.org/10.1088/1748-9326/11/7/074004, 2016.

EU Copernicus Marine Service Product: Global Ocean OSTIA Sea Surface Temperature and Sea Ice Reprocessed, Mercator Ocean International [data set], https://doi.org/10.48670/moi-00168, 2022.

Frölicher, T. L. and Laufkötter, C.: Emerging risks from marine heat waves, Nat. Commun., 9, 650, https://doi.org/10.1038/s41467-018-03163-6, 2018.

Frölicher, T. L., Fischer, E. M., and Gruber, N.: Marine heatwaves under global warming, Nature, 560, 360–364, https://doi.org/10.1038/s41586-018-0383-9, 2018.

Genin, A., Lazar, B., and Brenner, S.: Vertical mixing and coral death in the Red Sea following the eruption of Mount Pinatubo, Nature, 377, 507–510, https://doi.org/10.1038/377507a0, 1995.

Good, S., Fiedler, E., Mao, C., Martin, M., Maycock, A., Reid, R., Roberts-Jones, J., Searle, T., Waters, J., While, J., and Worsfold, M.: The Current Configuration of the OSTIA System for Operational Production of Foundation Sea Surface Temperature and Ice Concentration Analyses, Remote Sensing, 12, 1–20, https://doi.org/10.3390/rs12040720, 2020.

Group for High Resolution Sea Surface Temperature (GHRSST): Products, GHRSST, https://www.ghrsst.org/ghrsst-data-services/products/, last access: 1 December 2022.

Hobday, A., Alexander, L., Perkins, S., Smale, D., Straub, S., Oliver, E., Benthuysen, J., Burrows, M., Donat, M., Feng, M., Holbrook, N., Moore, P., Scannell, H., Sen Gupta, A., and Wernberg, T.: A Hierarchical Approach to Defining Marine Heatwaves, Prog. Oceanogr., 141, 227–238, https://doi.org/10.1016/j.pocean.2015.12.014, 2016.

Hobday, A., Oliver, E., Sen Gupta, A., Benthuysen, J., Burrows, M., Donat, M., Holbrook, N., Moore, P., Thomsen, M., Wernberg, T., and Smale, D.: Categorizing and Naming MARINE HEATWAVES, Oceanography, 31, 162–173, https://www.jstor.org/stable/26542662, 2018.

Holbrook, N. J., Scannell, H. A., and Sen Gupta, A.: A global assessment of marine heatwaves and their drivers, Nat. Commun., 10, 2624, https://doi.org/10.1038/s41467-019-10206-z, 2019.

Huang, B., Liu, C., Banzon, V., Freeman, E., Graham, G., Hankins, B., Smith, T., and Zhang, H: Improvements of the Daily Optimum Interpolation Sea Surface Temperature (DOISST) Version 2.1, J. Climate, 34, 1–47, https://doi.org/10.1175/JCLI-D-20-0166.1, 2020.

IPCC Climate Change 2021: The Physical Science Basis. Contribution of Working Group I to the Sixth Assessment Report of the Intergovernmental Panel on Climate Change, Cambridge University Press, 1227–1228, https://www.ipcc.ch/report/ar6/wg1/ (last access: 18 November 2022), 2021.

Johnson, K. S., Chavez, F. P., Elrod, V. A., Fitzwater, S. E., Pennington, J. T., Buck, K. R., and Walz, P. M.: The annual cycle of iron and the biological response in central California coastal waters, Geophys. Res. Lett., 28, 1247–1250, https://doi.org/10.1029/2000GL012433, 2001.

Laufkötter, C., Zscheischler, J., and Frölicher, T. L.: High-impact marine heatwaves attributable to human-induced global warming, Science, 369, 1621–1625, https://doi.org/10.1126/science.aba0690, 2020.

Le Traon, P. Y. and Morrow, R.: Chapter 3 Ocean Currents and Eddies, in: Satellite Altimetry and Earth Sciences, edited by: Lee-Lueng, F. and Anny, B. T., International Geophysics Cazenave, 69:171–xi, Academic Press, https://doi.org/10.1016/S0074-6142(01)80148-0, 2001.

Lirman, D., Schopmeyer, S., Manzello, D., Gramer, L., Precht, W., Muller-Karger, F., Banks, K., Barnes, B., Bartels, E., Bourque, A., Byrne, J., Donahue, S., Duquesnel, J., Fisher, L., Gilliam, D., Hendee, J., Johnson, M., Maxwell, K., McDevitt, E., Monty, J., Rueda, D., Ruzicka, R., and Thanner S.: Severe 2010 Cold-Water Event Caused Unprecedented Mortality to Corals of the Florida Reef Tract and Reversed Previous Survivorship Patterns, PloS One, 6, e23047–e23047, https://doi.org/10.1371/journal.pone.0023047, 2011.

Oliver, E. C. J.: Mean warming not variability drives marine heatwave trends, Clim. Dynam., 53, 1653–1659, https://doi.org/10.1007/s00382-019-04707-2, 2019.

Oliver, E. C. J., Donat, M., Burrows, M. T., Moore, P., Smale, D., Alexander, L., Benthuysen, J., Feng, M., Sen Gupta, A., Hobday, A., Holbrook, N., Perkins- Kirkpatrick, S., Scannell, H., Straub, S., and Wernberg, T.: Longer and more frequent marine heatwaves over the past century, Nat. Commun., 9, 1324, https://doi.org/10.1038/s41467-018-03732-9, 2018.

Mills, K., Pershing, A., Brown, C., Chen, Y., Holland, D,. Lehuta, S., Nye, J., Sun, J., Thomas, A., and Richard, W.:Fisheries Management in a Changing Climate: Lessons From the 2012 Ocean Heat Wave in the Northwest Atlantic, Oceanography, 26, 191–195, https://doi.org/10.5670/oceanog.2013.27, 2013.

Mogensen, K., Balmaseda M., Weaver, A., Martin, M., and Vidard, A.: NEMOVAR: A Variational Data Assimilation System for the NEMO Ocean Model, ECMWF Newsletter, 120, 17–21, https://doi.org/10.21957/3yj3mh16iq, 2009.

NOAA: NOAA Declares Third Ever Global Coral Bleaching Event, https://www.noaa.gov/media-release/noaa-declares-third-ever-global-coral-bleaching-event (last access: June 2022), 2015.

Rye, C. D., Marshall, J., Kelley, M., Russell, G., Nazarenko, L. S., Kostov, Y., Schmidt, G., and Hansen, J.: Antarctic glacial melt as a driver of recent Southern Ocean climate trends, Geophys. Res. Lett., 47, e2019GL086892, https://doi.org/10.1029/2019GL086892, 2020.

Schlegel, R. and Smit, A.: HeatwaveR: A Central Algorithm for the Detection of Heatwaves and Cold-Spells, J. Open Source Softw., 3, 821, https://doi.org/10.21105/joss.00821, 2018.

Schlegel, R., Oliver, E., Wernberg, T., and Smit, A.: Nearshore and Offshore Co-Occurrence of Marine Heatwaves and Cold-Spells, Prog. Oceanogr., 151, 189–205, https://doi.org/10.1016/j.pocean.2017.01.004, 2017.

Schlegel, R., Sofia Darmaraki, S., Benthuysen, J., Filbee-Dexter, K., and Oliver, E.: Marine cold-spells, Prog. Oceanogr., 198, 102684, https://doi.org/10.1016/j.pocean.2021.102684, 2021.

Smale, D. A., Wernberg, T., Oliver, E. C. J., Thomsen, M., Harvey, B., Straub, S., Burrows, M., Alexander, L., Benthuysen, J., Donat, M., Feng, M., Hobday, A., Holbrook, N., Perkins-Kirkpatrick, S., Scannell, H., Sen Gupta, A., Payne, B., and Moore, P.: Marine heatwaves threaten global biodiversity and the provision of ecosystem services, Nat. Clim. Chang., 9, 306–312, https://doi.org/10.1038/s41558-019-0412-1, 2019.

Smith, K. E., Burrows, M. T., Hobday, A. J., Sen Gupta, A., Moore, P. J., Thomsen, M., Wernberg, T., and Smale, D. A.: Socioeconomic impacts of marine heatwaves: Global issues and opportunities, Am. Assoc. Adv. Sci., 374, https://doi.org/10.1126/science.abj3593, 2021.

Trenberth, K. E.: The Definition of El Niño, B. Am. Meteorol. Soc., 78, 2771–2778, https://doi.org/10.1175/1520-0477(1997)078<2771:TDOENO>2.0.CO;2, 1997.

Wakelin, S., Townhill, B., Engelhard, G., Holt, J., and Renshaw, R.: Marine Heatwaves and Cold-Spells, and Their Impact on Fisheries in the North Sea, Copernicus Marine Service Ocean State Report, Issue 5, J. Oper. Oceanogr., 14(sup1), 1–185, https://doi.org/10.1080/1755876X.2021.1946240, 2021.

Wang, Y., Kajtar, J. B., Alexander, L. V., Pilo, G. S., and Holbrook, N. J.: Understanding the changing nature of marine cold-spells, Geophys. Res. Lett., 49, e2021GL097002, https://doi.org/10.1029/2021GL097002, 2022.

Wernberg, T., Smale, D., Tuya, F., Thomsen, M., Langlois, T., de Bettignies, T., Bennett, S., and Rousseaux, C.: An Extreme Climatic Event Alters Marine Ecosystem Structure in a Global Biodiversity Hotspot, Nat. Clim. Change, 3, 78–82, https://doi.org/10.1038/nclimate1627, 2013.

Wernberg, T., Bennett, S., Babcock, R., de Bettignies, T., Cure, K., Depczynski, M., Dufois, F., Fromont, J., Fulton, C., Hovey,

R., Harvey, E., Holmes, T., Kendrick, G., Radford, B., Santana-Garcon, J., Saunders, B., Smale, D., Thomsen, M., Tuckett, C., Tuya, F., Vanderklift, M., and Wilson S.: Climate-Driven Regime Shift of a Temperate Marine Ecosystem, Science, 353, 169–172, https://doi.org/10.1126/science.aad8745, 2016.

Worsfold, M., Good, S., McLaren, A., Fiedler, E., Roberts-Jones, J., and Martin, M.: EU Copernicus Marine Service QUALITY INFORMATION DOCUMENT for Global Ocean OSTIA Sea Surface Temperature Reprocessing product, SST-GLO-SST-L4-REP-OBSERVATIONS-010-011, Issue: 3, Mercator Ocean International, https://catalogue.marine.copernicus.eu/documents/QUID/CMEMS-SST-QUID-010-011.pdf (last access: 5 April 2023), 2022a.

Worsfold, M., Good, S., Martin, M., McLaren, A., Roberts-Jones, J., and Fiedler, E.: EU Copernicus Marine Service PRODUCT USER MANUAL for the Global Ocean OSTIA Sea Surface Temperature Reprocessing product, SST-GLO-SST-L4-REP-OBSERVATIONS-010-011, Issue: 1.4, Mercator Ocean International, https://catalogue.marine.copernicus.eu/documents/PUM/CMEMS-SST-PUM-010-011.pdf (last access: 5 April 2023), 2022b.

Yang, C., Leonelli, F. E., Marullo, S., Artale, V., Beggs, H., Nardelli, B. B., Chin, T. M., De Toma, V., Good, S., Huang, B., Merchant, C. J., Sakurai, T., Santoleri, R., Vazquez-Cuervo, J., Zhang, H., and Pisano, A.: Sea Surface Temperature Intercomparison in the Framework of the Copernicus Climate Change Service (C3S), J. Climate, 34, 5257–5283, https://doi.org/10.1175/JCLI-D-20-0793.1, 2021.

State Planet, 1-osr7, 4, 2023
https://doi.org/10.5194/sp-1-osr7-4-2023

South Atlantic overturning and heat transport variations in ocean reanalyses and observation-based estimates

Jonathan Andrew Baker[1], Richard Renshaw[1], Laura Claire Jackson[1], Clotilde Dubois[2], Doroteaciro Iovino[3], Hao Zuo[4], Renellys C. Perez[5], Shenfu Dong[5], Marion Kersalé[6], Michael Mayer[7,4], Johannes Mayer[7], Sabrina Speich[8], and Tarron Lamont[9,10,11]

[1]Met Office, Exeter, UK
[2]Mercator Ocean International, Toulouse, France
[3]Centro Euro-Mediterraneo sui Cambiamenti Climatici, Bologna, Italy
[4]European Centre for Medium-Range Weather Forecasts, Reading, UK
[5]Atlantic Oceanographic and Meteorological Laboratory, National Oceanic and Atmospheric Administration, Miami, USA
[6]Direction Générale de l'Armement, Ingénierie des projets, Paris, France
[7]University of Vienna, Vienna, Austria
[8]Laboratoire de Météorologie Dynamique–IPSL, Ecole Normale Supérieure, Paris, France
[9]University of Cape Town, Cape Town, South Africa
[10]Department of Environment, Forestry and Fisheries, Oceans and Coasts Research Branch, Cape Town, South Africa
[11]Bayworld Centre for Research and Education, Cape Town, South Africa

Correspondence: Jonathan Andrew Baker (jonathan.baker@metoffice.gov.uk)

Received: 1 August 2022 – Discussion started: 30 September 2022
Revised: 15 March 2023 – Accepted: 31 March 2023 – Published: 27 September 2023

Abstract. The variability in the South Atlantic Meridional Overturning Circulation (MOC) and meridional heat transport measured across 34.5° S during 2013–2017 differs significantly between observational and ocean reanalysis estimates. Variability in an ocean reanalysis ensemble and an eddy-resolving reanalysis is similar to an altimeter-based estimate but smaller than energy-budget and mooring-based estimates. Over 1993–2020, there is no long-term trend in the ensemble-mean overturning and heat transport, although there are inter-model differences, whereas the altimeter-based and energy-budget estimate transports increase over this period. Time-mean overturning volume transport (and the depth of maximum overturning) across 34.5° S in the ensemble and observations are similar, whereas the corresponding mean heat transports differ by up to 0.3 PW. The seasonal cycle of these transports varies between estimates, due to differences in the methods for estimating the geostrophic flow and the sampling characteristics of the observational approaches. The baroclinic, barotropic, and Ekman MOC components tend to augment each other in mooring-based estimates, whereas in other estimates they tend to counteract each other, so the monthly-mean, interannual, and seasonal MOC anomalies have a greater magnitude in the mooring-based estimates. Thus, the mean and variation in real-world South Atlantic transports and the amplitude of their fluctuations are still uncertain. Ocean reanalyses are useful tools to identify and understand the source of these differences and the mechanisms that control volume and heat transport variability in the South Atlantic, a region critical for determining the global overturning pathways and inter-basin transports.

Published by Copernicus Publications.

https://doi.org/10.5194/sp-1-osr7-4-2023

Table 1. Data products used in this study, including documentation where available.

Product ref. no.	Product ID and type	Data access	Documentation
1	GLOBAL_REANALYSIS_PHY_001_031 (C-GLORSv7 and GLORYS2V4) [1993–2020]; numerical models	EU Copernicus Marine Service Product (2022a)	Quality Information Document (QUID): Desportes et al. (2022) Product User Manual (PUM): Gounou et al. (2022)
2	ORAP6 global ocean reanalysis [1993–2020]	Updated version of product ref. 1, EU Copernicus Marine Service Product (2022a).	In progress for Copernicus Marine implementation, Zuo et al. (2021)
3	GloRanV14 global ocean reanalysis [1993–2021]	Updated version of FOAM/GloSea5 from product ref. 1, EU Copernicus Marine Service Product (2022a).	In progress for Copernicus Marine implementation
4	GLOBAL_MULTIYEAR_PHY_001_030 (GLORYS12V1) [1993–2019]; numerical models	EU Copernicus Marine Service Product (2022b)	QUID: Drévillon et al. (2022a) PUM: Drévillon et al. (2022b)
5	South Atlantic Meridional Overturning Circulation – Basin-wide Array (SAMBA) observations for 2013–2017	Data from the Southwest Atlantic MOC project (SAM) are funded by the DOC-NOAA Climate Program Office – Ocean Observation and Monitoring Division and the Atlantic Oceanographic and Meteorological Laboratory. These data are freely available via http://www.aoml.noaa.gov/phod/research/moc/samoc/sam/ (last access: 1 December 2022).	Kersalé et al. (2020) for MOC Kersalé et al. (2021) for MHT
6	Blended in situ and satellite altimeter estimates for 1993–2021 (Dong et al., 2021)		Dong et al. (2021)
7	Energy-budget estimates of Mayer et al. (2022) [1993–2017]	Atmospheric energy budgets using ERA5 available at https://doi.org/10.24381/cds.c2451f6b (Mayer et al., 2021b) TOA radiation data from the University of Reading: Liu and Allan (2020)	Mayer et al. (2022) Liu et al. (2020)
8	Energy-budget estimates of Trenberth et al. (2019a) [2000–2016]	Trenberth et al. (2019a)	Trenberth et al. (2019b)

1 Introduction

The Meridional Overturning Circulation (MOC) modulates climate on seasonal to millennial timescales via its meridional transport of freshwater, heat, and carbon through the global ocean (Rahmstorf, 2015; Weijer et al., 2019; Buckley and Marshall, 2016). It is therefore important to understand how the Atlantic MOC (AMOC), which dominates the upper cell of the global MOC, is changing. Changes in overturning in the South Atlantic are particularly important because they play a crucial role in determining the pathways of the global overturning circulation (Baker et al., 2021, 2020; Xu et al., 2022; Nadeau and Jansen, 2020), while freshwater transports in the South Atlantic impact the stability of the AMOC (Garzoli and Matano, 2011; Hawkins et al., 2011; Weijer et al., 2019, 2002). Transport changes here could determine the rate at which the AMOC weakens in response to increased greenhouse gas emissions (Weijer et al., 2020; Collins et al., 2019), beyond the weakening that may already have occurred over the past century (Caesar et al., 2018; Rahmstorf, 2015; Thornalley et al., 2018).

From September 2013 to July 2017, the expanded nine-site South Atlantic Meridional Overturning Circulation – Basinwide Array (SAMBA) (Fig. 1c) has collected measurements from which both daily meridional transports of heat and volume across 34.5° S can be estimated (Kersalé et al., 2020, 2021). Volume transports were also estimated during 2009–2010 using the two-site pilot configuration of the SAMBA array (Meinen et al., 2018, 2013). These studies have improved our understanding of the variability in the overturning circulation and meridional heat transport (MHT) in this region. The SAMBA array has improved mooring coverage since 2021 (Chidichimo et al., 2023), but data recorded after 2017 have yet to be incorporated into published AMOC or MHT estimates.

Since MOC and MHT estimates are currently only available from SAMBA during 2013–2017, longer-term variations must be inferred using model-based and alternative observation-based estimates (Garzoli et al., 2013; Goes et al., 2015; Dong et al., 2009; Mignac et al., 2018; Biastoch et al., 2021; Caínzos et al., 2022). This includes transport estimates derived from satellite sea level anomalies (SLAs) and in situ data (Dong et al., 2015; Majumder et al., 2016). Although Majumder et al. (2016) found large differences between ocean reanalyses and their observation-based estimate from 2000–2014, ocean reanalyses agree better with observations than free-running models (Mignac et al., 2018). Dong et al. (2021) generated MOC and MHT estimates over 1993–2021 from a synthetic method combining in situ and satellite data (updated from Dong et al., 2015) that agreed well with expendable bathythermograph (XBT)-derived MOC and MHT estimates in the South Atlantic. The MHT estimates from Dong et al. (2021), however, differed significantly from energy-budget MHT estimates produced by Trenberth et al. (2019b). All of the aforementioned transport estimates vary less than the nine-site SAMBA array estimates (Kersalé et al., 2021, 2020).

We aim to build upon these studies by comparing an ensemble of global ocean reanalyses (product refs. 1, 2, 3) directly against the observation-based estimates available over the SAMBA (2013–2017) and the altimetry (1993–2020) time periods. We also compare the reanalyses with new energy-budget MHT estimates at 34.5° S, which are analogous to an estimate at 26° N in the North Atlantic of Mayer et al. (2022), which is well correlated with observed transports across the RAPID array. While SAMBA array studies have primarily focused on daily-to-seasonal variability, here we focus on monthly-to-interannual variability. All of the time series were averaged to represent monthly values prior to further analysis.

Ocean reanalyses may provide realistic three-dimensional estimates of past changes in the South Atlantic overturning and heat transport (Mignac et al., 2018) and thus could be a useful tool to infer the nature and cause of past MOC and MHT variability. An earlier version of the reanalysis ensemble used in this study provides a good representation of the subtropical and subpolar North Atlantic overturning circulation (Jackson et al., 2018, 2019; Baker et al., 2022); thus, it may also accurately simulate changes in the South Atlantic.

2 Data and methods

2.1 Data

We use an ensemble of eddy-permitting (1/4° horizontal resolution) global ocean reanalyses. These are GloRanV14 (an improvement on GloSea5; MacLachlan et al., 2015), C-GLORSv7 (Storto et al., 2016), GLORYS2V4 (Lellouche et al., 2013), and ORAP6 (Zuo et al., 2021). Together, these four reanalyses form a new Copernicus Marine Environment Monitoring Service (CMEMS) reanalysis ensemble, updating product ref. 1 (see Table 1). We also use an eddy-resolving (1/12°) global ocean reanalysis: GLORYS12V1 (product ref. 4). Each reanalysis uses the NEMO (Nucleus for European Modelling of the Ocean) model, but the sea-ice model and data assimilation techniques differ. Each reanalysis is constrained by observations and is driven by atmospheric forcing from either ERA5 (Hersbach et al., 2020) or ERA-Interim (Dee et al., 2011) over the period 1993–2020, with GloRan extended to December 2021. They all assimilate satellite SLA, sea-ice concentrations, and in situ temperature and salinity, and they either assimilate satellite sea surface temperature (SST) or implement SST nudging.

We compare the MOC and MHT from the ensemble with the SAMBA-based estimates of Kersalé et al. (2020, 2021), the altimeter-based estimate of Dong et al. (2021), and the energy-budget MHT estimates of Trenberth et al. (2019b) and Mayer et al. (2022).

The energy-budget estimates of Mayer et al. (2022) calculate the net surface heat flux using top-of-the-atmosphere

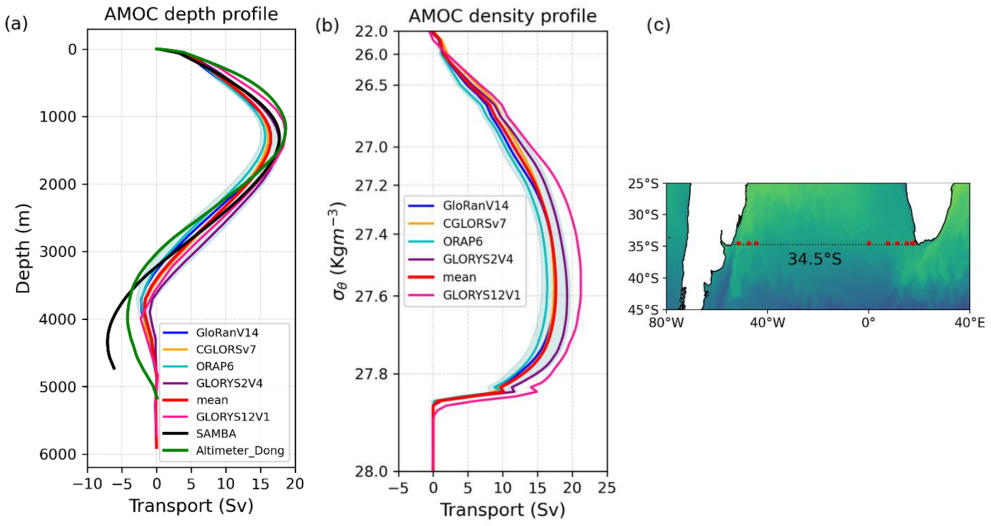

Figure 1. Vertical profile of the overturning transport across 34.5° S in **(a)** depth space and **(b)** density space, averaged over the 2013–2017 period of SAMBA observations, from September 2013 to July 2017. The reanalysis ensemble mean (red line; product refs. 1, 2, 3) and spread (light cyan background shading) are plotted, along with each ensemble member (blue, orange, cyan and purple lines), the GLORYS12V1 reanalysis (pink line; product ref. 4), the SAMBA estimate of Kersalé et al. (2020; black line; product ref. 5), and an altimeter-based estimate of Dong et al. (2021; green line; product ref. 6). The ensemble spread is defined as 2 times the standard deviation across the ensemble members. **(c)** Map showing the location of the SAMBA moorings (red dots) along 34.5° S.

radiative fluxes from CERES-EBAF (Loeb et al., 2018) with a backward extension (Liu et al., 2020) and atmospheric energy-budget quantities from ERA5 (see Mayer et al., 2021a, for methods). These are combined with ocean heat content (OHC) tendencies from ocean reanalyses to infer the MHT. Mayer et al. (2022) use OHC tendencies from ORAP6 ("Mayer_ORAP6" in figures); here we use an additional (unpublished) ORAS5-based estimate ("Mayer_ORAS5"), using OHC tendencies from ORAS5 (Zuo et al., 2019), the same as that used in the Trenberth et al. (2019b) estimate. For further details, see the Supplement. We note that energy-budget estimates may accumulate errors at southern latitudes, since they are integrated southward from high, northern latitudes (Dong et al., 2021).

2.2 Methods

Ensemble mean and spread and the time mean of the altimeter-based and Mayer energy-budget estimates are calculated over 1993–2020 and over the 2013–2017 SAMBA observational period. We calculate monthly-mean MOC across 34.5° S in depth coordinates, using commonly applied methods (e.g. Frajka-Williams et al., 2019), integrating monthly-mean velocity from coast to coast and from the surface down to the seafloor with a zero-net-volume transport constraint applied. Without this constraint, the ensemble mean has a net southward transport through the section over the observational period of 1.14 Sv (as do the individual reanalyses), and GLORYS12V1 has a net southward transport of 3.1 Sv, but the constraint only has a small impact on MOC estimates (Table 1). For the reanalysis, the MHT is calculated by integrating the product of monthly-mean model velocity and temperature (scaled by density and specific heat coefficient) across the whole section with a zero-net-volume transport constraint applied. Each observational product applies its own constraint to reference the flow due to differences in their geostrophic techniques. The altimeter-based dataset references the flow to the time-mean YoMaHA velocities at 1000 m (Katsumata and Yoshinari, 2010; Lebedev et al., 2007) and uses a zero-net-mass transport constraint (Dong et al., 2021). Kersalé et al. (2020) use models to reference the time-mean barotropic component at 1500 db, and bottom pressure measurements from the moorings provide the time-varying barotropic velocity component.

We calculate the overturning profiles, the monthly-to-interannual variation, and the seasonal cycles of the upper-cell MOC and the total MHT in each dataset. We separate the transports into their Ekman and geostrophic components. In the reanalyses, the Ekman component is calculated using the ERA5 or ERA-Interim wind stress, and for MHT, the zonal-mean SST across the section is used, assuming SST is representative of the Ekman layer temperature. The geostrophic component is calculated as a residual of the total and Ekman transports.

We also calculate the baroclinic and barotropic components of the ensemble's geostrophic MOC. We use thermal wind balance and the model's geopotential height anomalies to estimate the baroclinic velocities (see, e.g., Perez et al., 2011), integrating these from the deep ocean to the surface. The reference level is set $\sim$1000 m above the ocean floor,

above the unphysically large zonal gradients in geopotential height anomaly that exist in the deepest layers of the model. Thus, the reference level depth varies spatially (∼ 2000 to ∼ 4000 m deep) due to the bathymetry, but it is constant in time. The reference velocity is not required to calculate the baroclinic MOC anomalies, so we set the baroclinic velocity to 0 at the reference level depth. A visual inspection confirmed that the large month-to-month spatial variations in the baroclinic velocity field are in good agreement with the associated changes in the total velocity field. We tested the method using different reference level depths that generated similar monthly-mean MOC anomalies (not shown). We calculate the baroclinic component of the MOC by integrating the baroclinic velocities from the surface down to the depth of the time-mean total MOC maximum in each reanalysis (∼ 1250 m over 2013–2017). We calculate the barotropic component as a residual of the geostrophic and baroclinic MOC anomalies. The baroclinic and barotropic MOC anomalies in the reanalyses and in SAMBA estimates are not directly comparable because the reference levels differ. However, our baroclinic MOC anomaly estimate in the reanalyses accounts for baroclinic velocity variations from around 1000 m above the ocean floor to the surface over which the velocities are greatest and have large monthly variation.

3 Results

3.1 MOC profiles and statistics of variability

The ensemble of reanalyses captures the main structure of the observed overturning profile (Fig. 1a). The depth and strength of the maximum overturning is similar among all estimates with a range of ∼ 15–18 Sv (Fig. 1a). The profiles diverge in the deeper ocean, with a weaker than observed lower overturning cell and southward flow in the ensemble (i.e. the MOC decreases more gradually with depth). The reanalyses are less accurate at depth due to there being fewer observations to constrain the flow. The overturning profiles of the ensemble and GLORYS12V1 in density space have no negative transport (i.e. no abyssal cell), and their MOC is stronger than in depth space (Fig. 1b). The temporal variability in their upper MOC strength at 34.5° S, however, is fairly insensitive to the vertical coordinate system used for integration (Fig. S1 in the Supplement). We therefore focus on the MOC in depth space because the reanalyses can then be directly compared with the observational estimates.

We analyse the basic statistics of the variability in the maximum MOC strength and the MHT by looking at their time mean and standard deviation over 2013–2017 and 1993–2020. The time-mean MOC estimates have a range of 15.5–18.7 Sv, with the ensemble mean (labelled "mean" in figures) being only slightly weaker than the altimeter-based estimate and that observed across SAMBA (crosses in Fig. 2a). The time-mean MHT estimates have a range of 0.31–0.61 PW (crosses in Fig. 2c). Relative to the ensemble-mean values (MOC: 16.56 Sv; MHT: 0.36 PW), the time-mean MHT range has a 75 % increase from its minimum to its maximum value (excluding the energy-budget estimates) compared to only a 20 % increase for the time-mean MOC range. These ranges are within the documented uncertainty in SAMBA (Table 2). The ensemble-mean MHT is similar to the energy-budget estimates based on Mayer et al. (2022) (Fig. 2c). While there is inter-model spread in the ensemble time-mean transports (crosses in Fig. 2b, d), the spread is smaller than the uncertainty in SAMBA (Table 2), although it is more comparable for the MHT than for the MOC.

Monthly-mean variability (i.e. the standard deviation) of MOC and MHT in the ensemble is similar to the altimeter-based estimate over 2013–2017 and 1993–2020, whereas variability observed from SAMBA is much greater (Figs. 2a, c and 3a–d; Table 2), with significant differences ($p < 0.05$ in an F test for the equality of two variances). Similarly, the ensemble-mean time series is significantly ($p < 0.05$) correlated with the altimeter-based estimate ($r = 0.63$ for MOC; $r = 0.77$ for MHT; both over 2013–2017), but it is not well correlated with SAMBA ($r < 0.1$). The monthly-mean SAMBA estimates (Fig. 3a, b) and the Mayer energy-budget MHT estimates have high-frequency variations of comparable magnitude (Fig. 3b, d and Table 2), although their variability is uncorrelated. Mayer_ORAP6 is weakly correlated with the ensemble mean and altimeter-based estimate ($r = 0.14$ and $r = 0.19$ over 1993–2017 and $r = 0.28$ and $r = 0.32$ over 2013–2017, for the respective datasets). Mayer_ORAS5 has a higher correlation with the ensemble mean and altimeter-based estimate ($r = 0.30$ and $r = 0.32$ over 1993–2017 and $r = 0.52$ and $r = 0.57$ over 2013–2017, for the respective datasets). The GloRan reanalysis run with and without assimilating altimetry data (not shown) has a similar correlation with the altimeter-based estimate ($r = 0.52$ vs. $r = 0.56$ for MOC over 2013–2017). Thus, the strong correlation between ensemble mean and altimeter-based estimates is not dependent on directly assimilating altimetry data. The experimental reanalysis does, however, still assimilate in situ and satellite temperature and salinity data, which would serve to constrain thermosteric and halosteric contributions, respectively, to sea level. In the 12-month running mean estimates (Fig. 3e, f), the ensemble mean is only weakly correlated with the altimeter-based estimate ($r = 0.24$ for MOC; $r = 0.25$ for MHT), so their high monthly-mean correlation is largely due to similar seasonal variability.

The GLORYS12V1 reanalysis has a larger time-mean MOC and MHT than the ensemble mean (and GLORYS2V4). It has similar monthly-mean variability to the lower-resolution reanalyses: slightly larger than the ensemble mean but smaller than GLORYS2V4 (Table 2). It is also significantly correlated with the ensemble mean ($r = 0.80$ for MOC and $r = 0.84$ for MHT over 1993–2019). Thus, fully resolving (as opposed to only permitting) eddies in the ocean reanalyses considered here is important to infer the time-

https://doi.org/10.5194/sp-1-osr7-4-2023

Table 2. Time mean and uncertainty (or ensemble spread) and monthly-mean variability and trends of the maximum MOC and the MHT across 34.5° S, for the ensemble mean (product refs. 1, 2, 3), GLORYS12V1 (product ref. 4), SAMBA observations (product ref. 5), an altimeter-based estimate (product ref. 6), and energy-budget estimates (product refs. 7 and 8). All volume transports are referenced to 0 at the surface. The time-mean MOC and monthly-mean variability calculated in the reanalyses using no net-zero-transport constraint is added in parentheses. Time-mean values are calculated over the 2013–2017 SAMBA observational period and over the full 1993–2020 ensemble period if available. Uncertainty in the ensemble mean is defined as the standard error in the time-mean transport across the ensemble (note: this is smaller than the true uncertainty in the estimate). Monthly-mean variability (i.e. a measure of the deviation of monthly-mean data from the time mean) is defined as the standard deviation of the monthly-mean transports over the time series. Methods used to calculate SAMBA observational uncertainty (Kersalé et al., 2021, 2020) are described in Meinen et al. (2013) and Kersalé et al. (2021). Trends that are statistically insignificant ($p > 0.05$) are labelled NS.

Variable	Statistic	Ocean reanalyses		South Atlantic MOC estimates		Energy-budget estimates		
		Ensemble	GLORYS12V1	SAMBA	Altimeter Dong	Trenberth	Mayer ORAS5	Mayer ORAP6
MOC (Sv)	Mean ± uncertainty (2013–2017)	16.56 ± 0.37 (16.29)	18.72 (18.02)	17.29 ± 5.0	18.69	–	–	–
	Monthly-mean variability	2.67 (3.20)	2.90 (2.70)	11.35	3.25	–	–	–
	Mean ± uncertainty (1993–2020)	16.38 ± 0.66 (16.11)	19.23 (18.51)	–	18.34	–	–	–
	Monthly-mean variability	3.00 (3.53)	3.30 (3.14)	–	3.48	–	–	–
	Trends (Sv per decade) (1993–2020)	0.17 (NS)	−0.08 (NS)	–	0.66	–	–	–
MHT (PW)	Mean ± uncertainty (2013–17)	0.36 ± 0.03	0.44	0.50 ± 0.23	0.61	–	0.31	0.31
	Monthly-mean variability	0.19	0.20	0.55	0.20	–	0.46	0.43
	Mean ± uncertainty (1993–2020)	0.37 ± 0.04	0.49	–	0.58	0.33 (2000–2016)	0.33 (1993–2017)	0.34 (1993–2017)
	Monthly-mean variability	0.20	0.23	–	0.21	–	0.40	0.44
	Trends (PW per decade) (1993–2020)	−0.001 (NS)	−0.007 (NS)	–	0.036	−0.010 (2000–16)	0.086 (1993–2016)	0.094 (1993–2016)

Variable	Statistic	Ensemble			
		GloRanV14	C-GLORSv7	ORAP6	GLORYS2V4
MOC (Sv)	Trends (Sv per decade) (1993–2020)	1.18	−0.32	0.41	−0.60
MHT (PW)	Trends (PW per decade) (1993–2020)	0.042	−0.014 (NS)	−0.012 (NS)	−0.016 (NS)

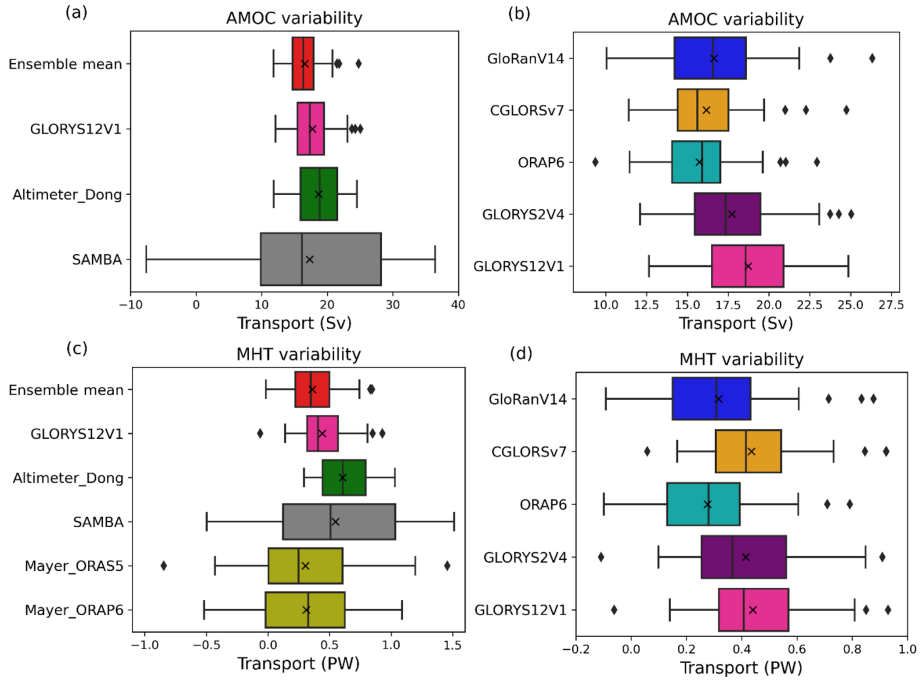

Figure 2. Whisker–box plots of the monthly-mean MOC **(a, b)** and MHT **(c, d)** across 34.5° S over the SAMBA observational period (2013–2017), using the same products as in Fig. 1. Energy-budget estimates Mayer_ORAP6 and Mayer_ORAS5 (yellow; product ref. 7) are also used for the MHT. Reanalyses analysed are shown in **(b)** and **(d)** with a reduced scale to highlight the differences between models. Boxes represent the interquartile range (IQR) with the median (line) and mean (crosses) shown. Whiskers cover a range of values up to 1 IQR beyond the upper and lower quartiles, and diamonds are outlying values beyond this range. Note: the x-axis scale changes between panels **(a)** and **(c)**, on the one hand, and **(b)** and **(d)**, on the other.

mean transports across 34.5° S, but it has minimal impact on the variation in the monthly-mean transports.

The 12-month running mean MOC and MHT in the ensemble over 1993–2020 are relatively stable (Fig. 3e, f), with similar ensemble-mean values to those during 2013–2017 (Table 2) and no significant trend over 1993–2020. However, the individual reanalyses have significant ($p < 0.05$) trends in the MOC over 1993–2020 with differing sign and magnitude (Table 2). In contrast, only GloRan has a significant (increasing) trend in MHT (~ 0.042 PW per decade). GLORYS12V1 has no significant trend in MOC or MHT. Hence, there is uncertainty in the long-term trends amongst the reanalyses.

The altimeter-based estimate has significant ($p < 0.05$) increases in MOC (~ 0.66 Sv per decade) and MHT (~ 0.036 PW per decade) over 1993–2020. The aforementioned MHT trends are similar over 1993–2016 (GloRanV14: ~ 0.047 PW per decade; altimeter: ~ 0.032 PW per decade). There is a significant increase in MHT over 1993–2016 in both the ORAS5-based (~ 0.086 PW per decade) and the ORAP6-based (~ 0.094 PW per decade) Mayer estimates. The Trenberth estimate has a significant but weak decline (~ -0.010 PW per decade) over 2000–2016; the Mayer estimates also decline over this period, but the trend is insignificant.

The 12-month running mean from SAMBA is entirely different to other estimates (Fig. 3e, f), with a rapid increase in the MOC (~ 14 Sv) and MHT (~ 0.7 PW) from March 2014 to June 2016, followed by a rapid decline. Although an extended time series is needed to determine longer timescale variations, the interannual variability captured by SAMBA over 2013–2017 exceeds that of other estimates. Only the Mayer MHT estimates have interannual variations of comparable magnitude, but those variations occur before 2013 (Fig. 3f).

3.2 Seasonal cycles

There is a predominantly annual cycle in the ensemble mean and altimeter-based transports, unlike the SAMBA seasonal cycle that has a stronger semi-annual variability (Fig. 3c, d). While we show the ensemble mean and altimeter-based seasonal cycles over 2013–2017 (Fig. 4), the seasonal cycles derived over the full record lengths are similar (not shown). The ensemble and altimeter-based overturning are weakest in austral summer, but the ensemble is strongest in May/June, peaking 2 months after the altimeter-based estimate (Fig. 4a, b). In contrast, the MOC in SAMBA is dominated by a semi-annual signal, with minima in April and September and maxima in August and December. There are year-to-year vari-

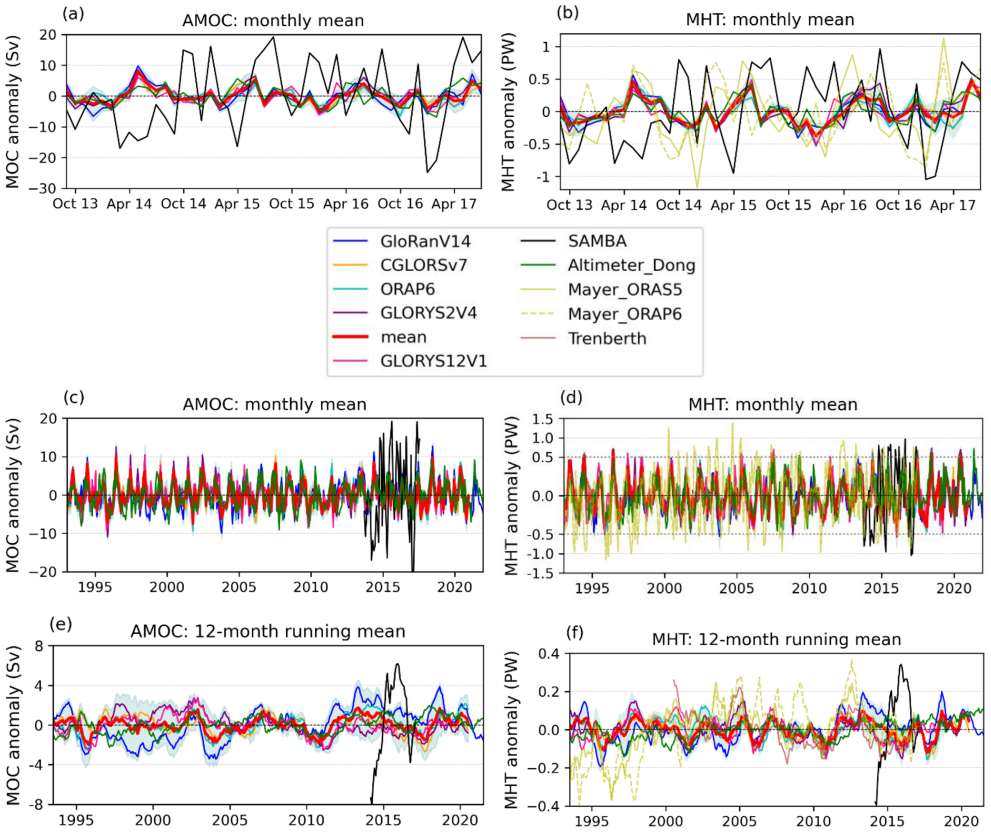

Figure 3. Time series of the monthly overturning **(a, c, e)** and heat transport **(b, d, f)** anomalies nominally across 34.5° S, with monthly-mean values from September 2013 to July 2017 **(a, b)** and over 1993–2021 **(c, d)** and 12-month running mean values over 1993–2021 **(e, f)** in the four reanalyses of the ensemble, ensemble mean (red), GLORYS12V1 (pink), SAMBA observations (black), an altimeter-based estimate (green), and energy-budget estimates (yellow and brown, product ref. 8). Labels, shading, and product information as in Fig. 1. The horizontal grey dotted lines in **(d)** divide the y axis into two linear scales, with the y axis compressed above the line. Note: Trenberth energy-budget estimate is for latitude 33.5° S.

ations in the annual cycles of all estimates (not shown), with variations in phase, shape, and magnitude. In SAMBA, 4 years of observations are not long enough to examine the sensitivity of the seasonal cycle to changing the time period, but given the strong high-frequency variations, the seasonal cycle based on 4 years of data is unlikely to be robust.

The shape of the seasonal cycle in MHT is similar to that of the MOC for each estimate as expected given the high correlation between the monthly-mean MHT and MOC ($r = 0.90$, $r = 0.91$, and $r = 0.96$ for the ensemble mean, altimeter-based estimate, and SAMBA, respectively, over 2013–2017). The Mayer energy-budget estimates have seasonal cycles dominated by an annual signal, with a larger magnitude range than other estimates. They are similar to the Trenberth estimate but with greater month-to-month variability. However, when averaged over the 2000–2016 period used in the Trenberth estimate rather than 2013–2017, they become smoother and closer to the ensemble ("Mayer_ORAS5_2000–16" in Fig. 4).

Year-to-year variations in the annual cycles of each estimate over 2013–2017 (not shown) and differences in the climatological seasonal cycle between each estimate (Fig. 4) stem from their geostrophic differences (Fig. 4e, f) because the Ekman annual cycles are similar year to year (not shown) and for all estimates (Fig. 4c, d). Differences between estimates are clearer in the geostrophic component, peaking before the ensemble mean in the altimeter-based estimate and after the ensemble mean in SAMBA. Thus, the Ekman and geostrophic components tend to counteract each other in the altimeter-based estimate and augment each other in SAMBA. This causes a greater increase in the magnitude of the total MOC and MHT seasonal cycles (relative to their geostrophic components) in SAMBA than it does in the altimeter-based estimate but a greater change in the seasonal cycle phase and shape in the altimeter-based estimate (cf. Fig. 4a, b and e, f). The relative contribution of the Ekman component to the total MOC and MHT in the ensemble is nonetheless significantly greater than in SAMBA. In the ensemble mean (and in GLORYS12V1 and SAMBA), the geostrophic component of the MOC (Fig. 4e) has a second peak in November or December (i.e. austral spring or summer) and thus has a semi-annual signal. Although the increase in the MOC to

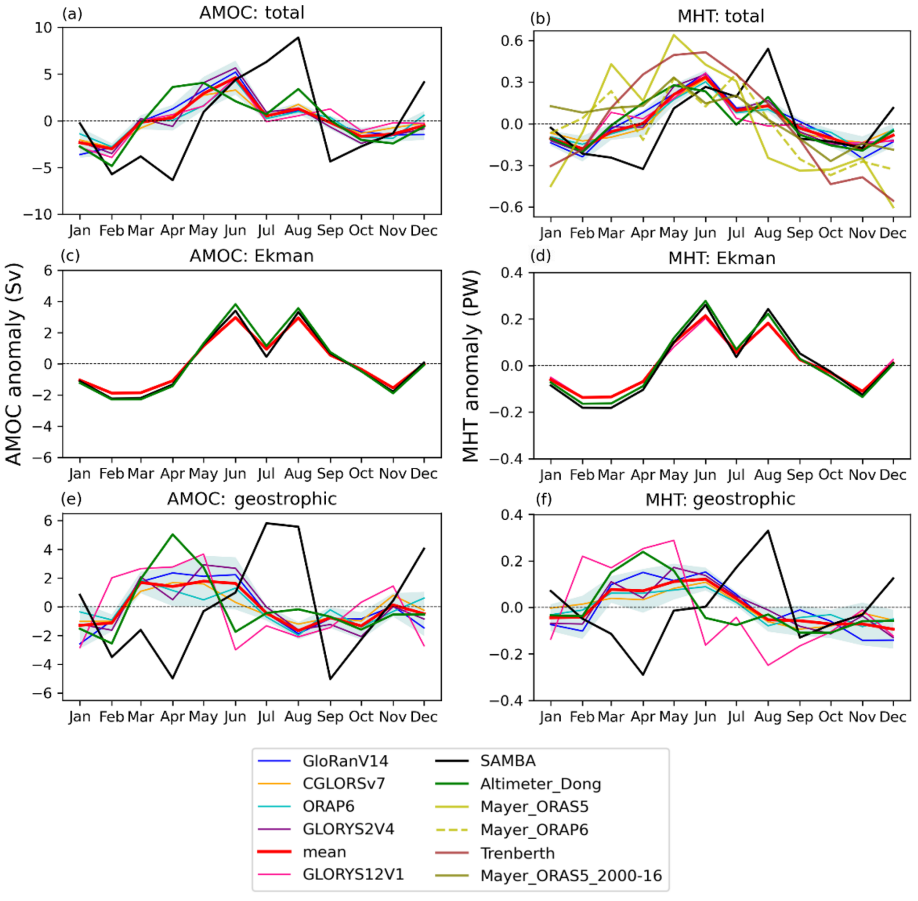

Figure 4. Seasonal cycles of **(a, c, e)** the overturning and **(b, d, f)** the MHT anomalies across 34.5° S, averaged over the SAMBA observational period from September 2013 to July 2017. The exception is the energy-budget MHT estimate of Trenberth et al. (2019b), which is averaged over 2000–2016, and also the ORAS5-based Mayer energy-budget estimate, "Mayer_ORAS5_2000–16" (olive), which is averaged over the same period for comparison. The total **(a, b)**, Ekman **(c, d)**, and geostrophic **(e, f)** components of these transports are plotted. Labels, shading, and product information are as in Figs. 1 and 3.

this end-of-year peak relative to the magnitude of decrease from the preceding peak is smaller in the ensemble mean than in SAMBA, it is noteworthy, increasing by 52 % of the preceding decrease (and by 77 % in the seasonal cycle over 1993–2020) compared to 84 % in SAMBA. The altimeter-based estimate has no significant increase in the geostrophic component in austral spring, and there is also no increase in the ensemble-mean MHT, unlike in SAMBA (Fig. 4f).

3.3 Baroclinic and barotropic components

We investigate possible causes of the difference in variability between SAMBA and the ensemble by separating the geostrophic MOC anomalies into their baroclinic and barotropic components. The baroclinic and barotropic components of the MOC are not directly comparable between the ensemble and SAMBA due to differences in the reference level depth, but this probably has little impact on the differences between these estimates (see Sect. 2.2). The seasonal cycles of these components largely counteract each other in the ensemble, with their sum equal to the geostrophic component (Fig. 5). By contrast, these components tend to augment each other in SAMBA (Fig. 5), so their geostrophic seasonal cycle has variations of a greater magnitude. The baroclinic component tends to dominate in both datasets, primarily controlling the phase of the geostrophic MOC seasonal cycle (Fig. 5). Although the barotropic component tends to counteract the baroclinic component in the ensemble, it has a notable effect on the phase of the geostrophic MOC seasonal cycle over 2013–2017 unlike over 1993–2020. Thus, while differences in the seasonality of the baroclinic MOC component account for most of the difference in the seasonality of the geostrophic MOC, differences in the barotropic component between the ensemble and SAMBA also play a role.

We also analyse the monthly-mean and interannual variations in the baroclinic and barotropic components of the MOC anomalies (Fig. 6). Both the baroclinic and the barotropic components of the MOC have similar monthly-

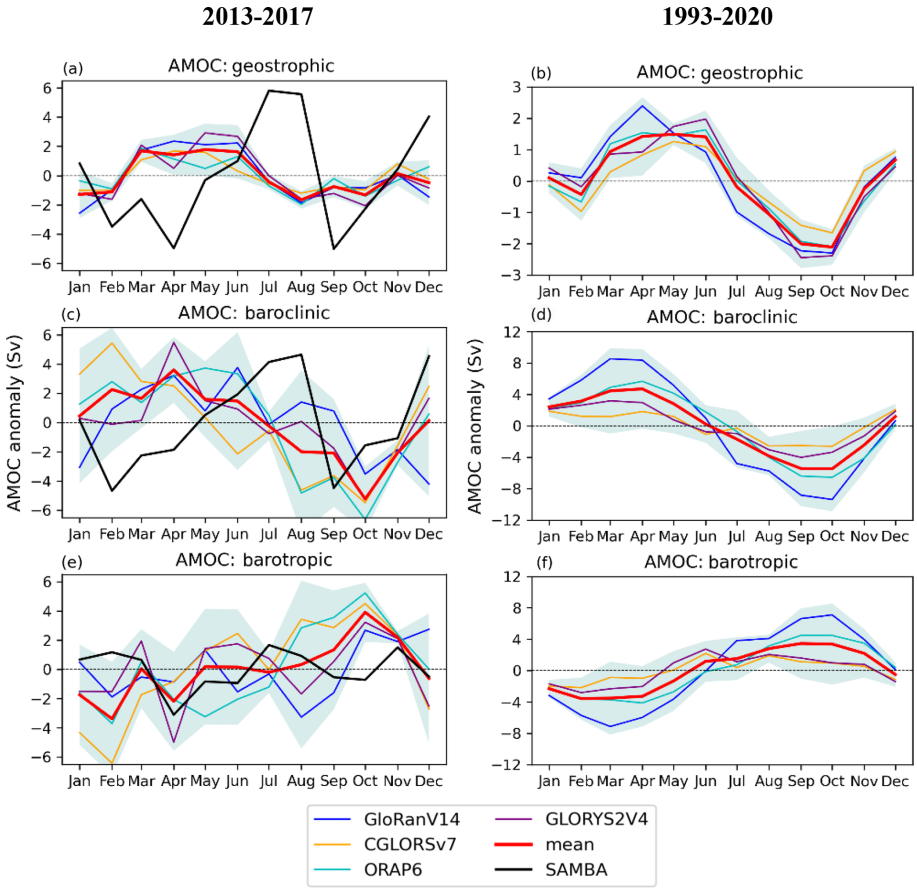

Figure 5. Seasonal cycles of the MOC anomalies across 34.5° S, averaged over the **(a, c, e)** the SAMBA observational period from September 2013 to July 2017 and **(b, d, f)** the 1993–2020 period of the reanalyses. The geostrophic **(a, b)**, baroclinic **(c, d)**, and barotropic **(e, f)** components of these transports are plotted. Labels, shading, and product information are as in Figs. 1 and 3.

mean variability in the ensemble and in SAMBA over 2013–2017 (Fig. 6d, e), although the baroclinic variability is slightly higher in SAMBA (7.5 Sv vs. 5.3 Sv). Similarly, the interannual variability in the baroclinic and barotropic components has similar peak-to-trough magnitudes over 2013–2017 in the ensemble and SAMBA (Fig. 6f). However, since the barotropic component counteracts the baroclinic component in the ensemble, the geostrophic and total MOC anomalies in the ensemble have much smaller monthly-mean and interannual variability than in SAMBA (Fig. 6a, b, f and Table 2). The monthly-mean and 12-month running mean baroclinic and barotropic components in the ensemble have even larger variability over 1993–2020, but these components counteract each other over the whole period (Fig. 6f).

4 Discussion

Seasonal variations in the baroclinic component of the MOC in the ensemble over 1993–2020 are caused by seasonal variations in both the eastern and western boundary volume transports, with variations in the western boundary tending to dominate. Over 2013–2017, there is much larger spatial variability in the seasonal transport, with significant contributions to the seasonal variations from the interior as well as from the boundaries. Therefore, differences in the MOC seasonality between datasets is likely caused by seasonal variations in both the boundary currents and the interior baroclinic transports. A spatial analysis of the baroclinic transports in SAMBA could determine the regions responsible for the seasonality of this component and thus why it differs from the ensemble.

The altimeter-based estimate uses reference velocities at 1000 m depth that are constant in time. Thus, the barotropic component has no temporal variability, so the geostrophic MOC anomalies only account for baroclinic transport anomalies above 1000 m. Given the baroclinic component primarily determines the shape of the seasonal cycle in the ensemble and SAMBA, the fact the barotropic component is constant in the altimeter-based estimate may not significantly impact its estimate of the MOC's seasonal cycle phase. However, the magnitude of its monthly, interannual, and seasonal variability may be affected if temporal changes

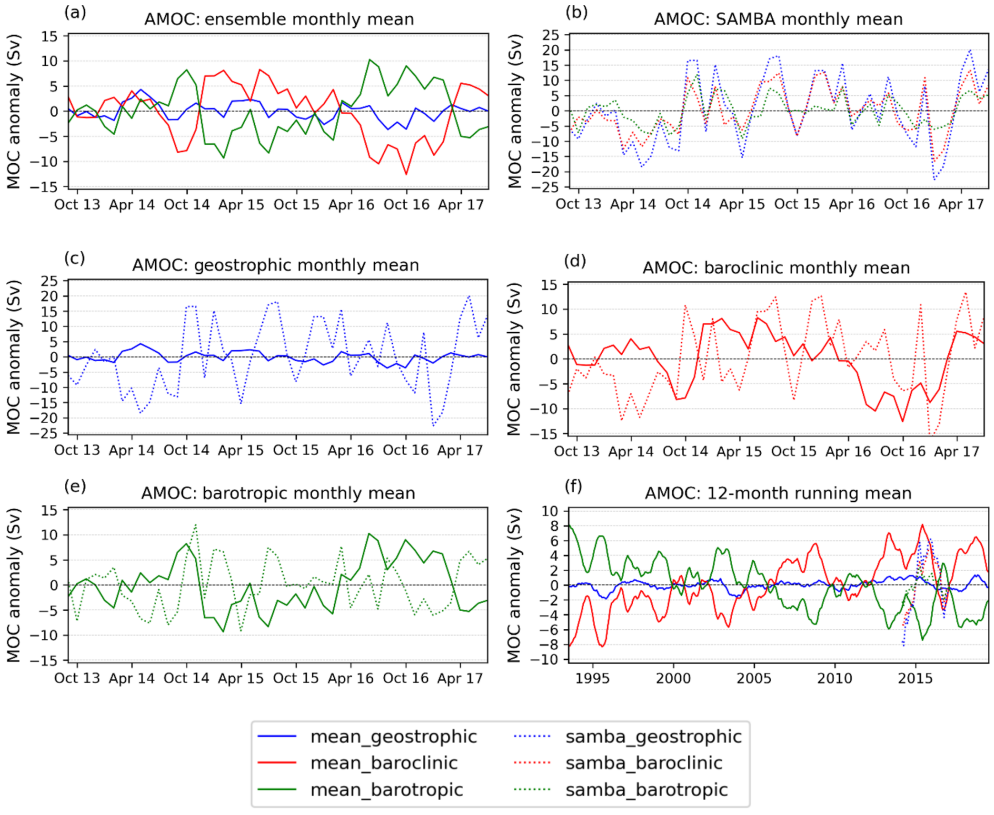

Figure 6. Time series of **(a–e)** monthly-mean (2013–2017) and **(f)** 12-month running mean (1993–2019) MOC anomalies showing the geostrophic (blue), baroclinic (red), and barotropic (green) components in **(a)** the ensemble, **(b)** SAMBA, and **(c–f)** both the ensemble (solid lines) and SAMBA (dashed lines).

in the barotropic component are important, as suggested by the ensemble and SAMBA estimates of this component. The reference level depth used in the reanalyses (i.e. not in our baroclinic and barotropic component estimates but that implemented in the models and thus in the geostrophic estimate) is the ocean floor, closer to the depths used to estimate the time-varying barotropic component in SAMBA. Thus, differences in the reference level are unlikely to cause the differences in the geostrophic component between SAMBA and the ensemble. However, differences in the methods used to estimate the barotropic velocity at that reference level could cause some of the difference.

We have shown that the monthly-mean MOC variability (i.e. standard deviation) is greater in SAMBA than in the ensemble and altimeter-based estimate, primarily because the Ekman, barotropic, and baroclinic components augment each other in SAMBA, whereas they tend to counteract each other in the ensemble and altimeter-based estimates. While the standard deviation provides an insight into the month-to-month fluctuations, it does not determine the frequency of these fluctuations. Both the baroclinic and barotropic components have more frequent monthly fluctuations in SAMBA than in the ensemble (Fig. 5). These high-frequency variations could be caused by ocean eddy variability and variations that were previously under-resolved with only two mooring sites and are now better resolved but likely still aliased with nine sites.

5 Conclusions

An ensemble of global ocean reanalyses from CMEMS provides a useful estimate of the magnitude and variability in the South Atlantic MOC and MHT, although it differs substantially from estimates based on SAMBA array data at 34.5° S, observed between 2013 and 2017. The ensemble is compared with several other estimates of the MOC and MHT, which differ in many aspects from – but also have similarities with – the reanalyses.

The ensemble-mean (and 1/12° GLORYS12V1 reanalysis) transports have no long-term trend over 1993–2020, although the trends in the individual reanalyses differ, and observational estimates increase over this period. All estimates of the time-mean MOC are similar (∼ 15.5–18.7 Sv), but relative to the ensemble-mean value there is greater spread in the MHT (0.31–0.61 PW), with the ensemble mean weaker than SAMBA observations. Monthly-mean MOC and MHT in the ensemble, the 1/12° GLORYS12V1 reanalysis, and an altimeter-based estimate (Dong et al., 2021) vary signif-

icantly less than those from the SAMBA array. In contrast, energy-budget estimates of MHT (Mayer et al., 2022) have a large monthly-mean variability comparable to SAMBA. Both the monthly-mean MOC and MHT in the ensemble are significantly correlated with the altimeter-based estimate across the whole 1993–2020 period (although most of the skill is from the seasonal cycle), whereas correlations with SAMBA estimates are not significant.

While there is interannual variability in the reanalyses and altimeter-based estimate over 1993–2020, SAMBA observations and some energy-budget MHT estimates have much larger interannual variability. The climatological seasonal cycles of the MOC and MHT vary considerably in phase and magnitude between estimates due to differences in the geostrophic flow, with good agreement in the Ekman contributions among all datasets considered. Differences in the baroclinic component of the MOC are most important for determining the phase of the seasonal cycle in both the reanalyses and SAMBA, although the barotropic component also plays a role. The baroclinic, barotropic, and Ekman MOC components tend to augment each other in SAMBA, whereas they tend to counteract each other in the ensemble and altimeter-based estimate. Thus, in SAMBA the monthly-mean, interannual, and seasonal MOC anomalies have a greater magnitude than in the ensemble and altimeter-based estimate. This causes a large increase in the monthly-mean standard deviation of the total MOC in SAMBA. The baroclinic and barotropic MOC anomalies also have more frequent monthly-mean fluctuations in SAMBA.

Further insight into the cause of the similarities and differences between the ensemble, SAMBA and the altimeter-based estimate might be found by comparing the monthly-mean density profiles of these estimates. This could show how contributions from the baroclinic velocity to the geostrophic MOC anomalies vary between the datasets, including their spatial variations, and how these lead to differences in seasonality. Similarly, the barotropic velocity (vertically averaged velocity) in the reanalyses can be compared with that used by the in situ altimetry and SAMBA methods to reference the flow. We also suggest exploring the horizontal resolution of SAMBA moorings used on the boundaries since it may alias variability here, with too few sites over steeply sloping topography. The impact of array resolution on SAMBA could be inferred by recalculating the baroclinic and barotropic components of the MOC in the ensemble using only a subset of their vertical density profiles. Reanalyses could therefore provide information on whether modifications to the observational density across the SAMBA array may provide more robust observational transport estimates. Use of the expanded set of moorings will also allow us to determine the importance of the aliasing of variability on the boundaries. Since the reanalyses are in reasonable agreement with altimeter-based estimates but not with SAMBA, this prompts closer inspection of the methodologies used to make the computations.

To summarise, an ensemble of ocean reanalyses appears to be a useful tool to understand changes in the South Atlantic MOC and MHT and to identify differences between observational estimates. Reanalyses also enable examination of variations prior to the SAMBA array record. Comparisons of reanalyses and observational estimates can be used together to refine methodologies and sampling approaches and ultimately improve our understanding and estimations of ocean transports in the South Atlantic.

Data availability. All data products used in this paper are listed in Table 1, along with their corresponding documentation and online availability.

Supplement. The supplement related to this article is available online at: https://doi.org/10.5194/sp-1-osr7-4-2023-supplement.

Author contributions. JAB conceived the study, performed the analysis, and wrote the manuscript. All authors provided data for analysis, discussed the results, and edited or commented on the manuscript.

Competing interests. The contact author has declared that none of the authors has any competing interests.

Disclaimer. Publisher's note: Copernicus Publications remains neutral with regard to jurisdictional claims in published maps and institutional affiliations.

Acknowledgements. We thank two anonymous reviewers for their constructive comments that improved this study.

Review statement. This paper was edited by Pierre Brasseur and reviewed by two anonymous referees.

References

Baker, J., Renshaw, R., Jackson, L., Dubois, C., Iovino, D., and Zuo, H.: Overturning variations in the subpolar North Atlantic in an ocean reanalyses ensemble, in: Copernicus Marine Service Ocean State Report, Issue 6, Supplement, J. Oper. Oceanogr., 15, S16–S20, https://doi.org/10.1080/1755876X.2022.2095169, 2022.

Baker, J. A., Watson, A. J., and Vallis, G. K.: Meridional overturning circulation in a multibasin model. Part I: Dependence on southern ocean buoyancy forcing, J. Phys. Oceanogr., 50, 1159–1178, https://doi.org/10.1175/JPO-D-19-0135.1, 2020.

Baker, J. A., Watson, A. J., and Vallis, G. K.: Meridional Overturning Circulation in a Multibasin Model. Part II: Sensitivity to Diffusivity and Wind in Warm and Cool Climates, J.

Phys. Oceanogr., 51, 1813–1828, https://doi.org/10.1175/JPO-D-20-0121.1, 2021.

Biastoch, A., Schwarzkopf, F. U., Getzlaff, K., Rühs, S., Martin, T., Scheinert, M., Schulzki, T., Handmann, P., Hummels, R., and Böning, C. W.: Regional imprints of changes in the Atlantic Meridional Overturning Circulation in the eddy-rich ocean model VIKING20X, Ocean Sci., 17, 1177–1211, https://doi.org/10.5194/os-17-1177-2021, 2021.

Buckley, M. W. and Marshall, J.: Observations, inferences, and mechanisms of the Atlantic Meridional Overturning Circulation: A review, Rev. Geophys., 54, 5–63, https://doi.org/10.1002/2015RG000493, 2016.

Caesar, L., Rahmstorf, S., Robinson, A., Feulner, G., and Saba, V.: Observed fingerprint of a weakening Atlantic Ocean overturning circulation, Nature, 556, 191–196, https://doi.org/10.1038/s41586-018-0006-5, 2018.

Caínzos, V., Hernández-Guerra, A., McCarthy, G. D., McDonagh, E. L., Cubas Armas, M., and Pérez-Hernández, M. D.: Thirty Years of GOSHIP and WOCE Data: Atlantic Overturning of Mass, Heat, and Freshwater Transport, Geophys. Res. Lett., 49, e2021GL096527, https://doi.org/10.1029/2021GL096527, 2022.

Chidichimo, M. P., Perez, R. C., Speich, S., Kersalé, M., Sprintall, J., Dong, S., Lamont, T., Sato, O. T., Chereskin, T. K., Hummels, R., and Schmid, C.: Energetic overturning flows, dynamic interocean exchanges, and ocean warming observed in the South Atlantic, Communications Earth & Environment, 4, 1–20, https://doi.org/10.1038/s43247-022-00644-x, 2023.

Collins, M., Sutherland, M., Bouwer, L., Cheong, S.-M., Fro¨licher, T., Jacot Des Combes, H., Koll Roxy, M., Losada, I., McInnes, K., Ratter, B., Rivera-Arriaga, E., Susanto, R., Swingedouw, D., and Tibig, L.: Extremes, Abrupt Changes and Managing Risk, in: IPCC Special Report on the Ocean and Cryosphere in a Changing Climate, edited by: Po¨rtner, H.-O., Roberts, D. C., Masson-Delmotte, V., Zhai, P., Tignor, M., Poloczanska, E., Mintenbeck, K., Alegri´a, A., Nicolai, M., Okem, A., Petzold, J., Rama, B., and Weyer, N. M., Cambridge University Press, Cambridge, UK and New York, NY, USA, 589–655, https://doi.org/10.1017/9781009157964.008, 2019.

Dee, D. P., Uppala, S. M., Simmons, A. J., Berrisford, P., Poli, P., Kobayashi, S., Andrae, U., Balmaseda, M. A., Balsamo, G., Bauer, P., Bechtold, P., Beljaars, A. C. M., van de Berg, L., Bidlot, J., Bormann, N., Delsol, C., Dragani, R., Fuentes, M., Geer, A. J., Haimberger, L., Healy, S. B., Hersbach, H., Hólm, E. v., Isaksen, L., Kållberg, P., Köhler, M., Matricardi, M., McNally, A. P., Monge-Sanz, B. M., Morcrette, J.-J., Park, B.-K., Peubey, C., de Rosnay, P., Tavolato, C., Thépaut, J.-N., and Vitart, F.: The ERA-Interim reanalysis: configuration and performance of the data assimilation system, Q. J. Roy. Meteor. Soc., 137, 553–597, https://doi.org/10.1002/qj.828, 2011.

Desportes, C., Garric, G., Régnier, C,, Drévillon, M., Parent, L., Drillet, Y., Masina, S., Storto, A., Mirouze, I., Cipollone, A., Zuo, H., Balmaseda, M., Peterson, D., Wood, R., Jackson, L., Mulet, S., Greiner, E., and Gounou, A.: EU Copernicus Marine Service Quality Information Document for the Global Ocean Reanalysis Multi-model Ensemble Products, GLOBAL-REANALYSIS-PHY-001-031, Issue 1.1, Mercator Ocean International, https://catalogue.marine.copernicus.eu/documents/QUID/CMEMS-GLO-QUID-001-031.pdf (last access: 5 April 2023), 2022.

Dong, S., Garzoli, S., Baringer, M., Meinen, C., and Goni, G.: Interannual variations in the Atlantic meridional overturning circulation and its relationship with the net northward heat transport in the South Atlantic, Geophys. Res. Lett., 36, L20606, https://doi.org/10.1029/2009GL039356, 2009.

Dong, S., Goni, G., and Bringas, F.: Temporal variability of the South Atlantic Meridional Overturning Circulation between 20° S and 35° S, Geophys. Res. Lett., 42, 7655–7662, https://doi.org/10.1002/2015GL065603, 2015.

Dong, S., Goni, G., Domingues, R., Bringas, F., Goes, M., Christophersen, J., and Baringer, M.: Synergy of In Situ and Satellite Ocean Observations in Determining Meridional Heat Transport in the Atlantic Ocean, J. Geophys. Res.-Oceans, 126, e2020JC017073, https://doi.org/10.1029/2020JC017073, 2021.

Drévillon, M., Lellouche, J. M., Régnier, C., Garric, G., Bricaud, C., Hernandez, O., and Bourdallé-Badie, R.: EU Copernicus Marine Service Quality Information Document for the Global Ocean Physical Multi Year Product, GLOBAL_MULTIYEAR_PHY_001_030, Issue 1.6, Mercator Ocean International, https://catalogue.marine.copernicus.eu/documents/QUID/CMEMS-GLO-QUID-001-030.pdf (last access: 5 April 2023), 2022a.

Drévillon, M., Fernandez, E., and Lellouche, J. M.: EU Copernicus Marine Service Product User Manual for the Global Ocean Physical Multi Year Product, GLOBAL_MULTIYEAR_PHY_001_030, Issue 1.4, Mercator Ocean International, https://catalogue.marine.copernicus.eu/documents/PUM/CMEMS-GLO-PUM-001-030.pdf (last access: 5 April 2023), 2022b.

EU Copernicus Marine Service Product: Global Ocean Ensemble Reanalysis, Mercator Ocean International [data set], https://doi.org/10.48670/moi-00024, 2022a.

EU Copernicus Marine Service Product: Global Ocean Physics Reanalysis, Mercator Ocean International [data set], https://doi.org/10.48670/moi-00021, 2022b.

Frajka-Williams, E., Ansorge, I. J., Baehr, J., Bryden, H. L., Chidichimo, M. P., Cunningham, S. A., Danabasoglu, G., Dong, S., Donohue, K. A., Elipot, S., Heimbach, P., Holliday, N. P., Hummels, R., Jackson, L. C., Karstensen, J., Lankhorst, M., le Bras, I. A., Susan Lozier, M., McDonagh, E. L., Meinen, C. S., Mercier, H., Moat, B. I., Perez, R. C., Piecuch, C. G., Rhein, M., Srokosz, M. A., Trenberth, K. E., Bacon, S., Forget, G., Goni, G., Kieke, D., Koelling, J., Lamont, T., McCarthy, G. D., Mertens, C., Send, U., Smeed, D. A., Speich, S., van den Berg, M., Volkov, D., and Wilson, C.: Atlantic meridional overturning circulation: Observed transport and variability, Front. Mar. Sci., 6, 260, https://doi.org/10.3389/FMARS.2019.00260, 2019.

Garzoli, S. L. and Matano, R.: The South Atlantic and the Atlantic Meridional Overturning Circulation, Deep-Sea Res. Pt. II, 58, 1837–1847, https://doi.org/10.1016/J.DSR2.2010.10.063, 2011.

Garzoli, S. L., Baringer, M. O., Dong, S., Perez, R. C., and Yao, Q.: South Atlantic meridional fluxes, Deep-Sea Res. Pt. I, 71, 21–32, https://doi.org/10.1016/J.DSR.2012.09.003, 2013.

Goes, M., Goni, G., and Dong, S.: An optimal XBT-based monitoring system for the South Atlantic meridional overturning circulation at 34° S, J. Geophys. Res.-Oceans, 120, 161–181, https://doi.org/10.1002/2014JC010202, 2015.

Gounou, A., Drévillon, M., and Clavier, M.: EU Copernicus Marine Service Product User Manual for the Global Ocean

Reanalysis Multi-model Ensemble Products, GLOBAL-REANALYSIS-PHY-001-031, Issue 1.1, Mercator Ocean International, https://catalogue.marine.copernicus.eu/documents/PUM/CMEMS-GLO-PUM-001-031.pdf (last access: 5 April 2023), 2022.

Hawkins, E., Smith, R. S., Allison, L. C., Gregory, J. M., Woollings, T. J., Pohlmann, H., and de Cuevas, B.: Bistability of the Atlantic overturning circulation in a global climate model and links to ocean freshwater transport, Geophys. Res. Lett., 38, L10605, https://doi.org/10.1029/2011GL047208, 2011.

Hersbach, H., Bell, B., Berrisford, P., Hirahara, S., Horányi, A., Muñoz-Sabater, J., Nicolas, J., Peubey, C., Radu, R., Schepers, D., Simmons, A., Soci, C., Abdalla, S., Abellan, X., Balsamo, G., Bechtold, P., Biavati, G., Bidlot, J., Bonavita, M., de Chiara, G., Dahlgren, P., Dee, D., Diamantakis, M., Dragani, R., Flemming, J., Forbes, R., Fuentes, M., Geer, A., Haimberger, L., Healy, S., Hogan, R. J., Hólm, E., Janisková, M., Keeley, S., Laloyaux, P., Lopez, P., Lupu, C., Radnoti, G., de Rosnay, P., Rozum, I., Vamborg, F., Villaume, S., and Thépaut, J. N.: The ERA5 global reanalysis, Q. J. Roy. Meteor. Soc., 146, 1999–2049, https://doi.org/10.1002/QJ.3803, 2020.

Jackson, L., Dubois, C., Masina, S., Storto, A., and Zuo, H.: Atlantic Meridional Overturning Circulation, in: the Copernicus Marine Service Ocean State Report, Issue 2, edited by: von Schuckmann, K., Le Traon, P.-Y., Smith, N., Pascual, A., Brasseur, P., Fennel, K., and Djavidnia, S., Supplement, J. Oper. Oceanogr., 11, S1–S142, https://doi.org/10.1080/1755876X.2018.1489208, 2018.

Jackson, L. C., Dubois, C., Forget, G., Haines, K., Harrison, M., Iovino, D., Köhl, A., Mignac, D., Masina, S., Peterson, K. A., Piecuch, C. G., Roberts, C. D., Robson, J., Storto, A., Toyoda, T., Valdivieso, M., Wilson, C., Wang, Y., and Zuo, H.: The Mean State and Variability of the North Atlantic Circulation: A Perspective From Ocean Reanalyses, J. Geophys. Res.-Oceans, 124, 9141–9170, https://doi.org/10.1029/2019JC015210, 2019.

Katsumata, K. and Yoshinari, H.: Uncertainties in global mapping of Argo drift data at the parking level, J. Oceanogr., 66, 553–569, https://doi.org/10.1007/S10872-010-0046-4, 2010.

Kersalé, M., Meinen, C. S., Perez, R. C., le Hénaff, M., Valla, D., Lamont, T., Sato, O. T., Dong, S., Terre, T., van Caspel, M., Chidichimo, M. P., van den Berg, M., Speich, S., Piola, A. R., Campos, E. J. D., Ansorge, I., Volkov, D. L., Lumpkin, R., and Garzoli, S. L.: Highly variable upper and abyssal overturning cells in the South Atlantic, Sci. Adv., 6, eaba7573, https://doi.org/10.1126/sciadv.aba7573, 2020.

Kersalé, M., Meinen, C. S., Perez, R. C., Piola, A. R., Speich, S., Campos, E. J. D., Garzoli, S. L., Ansorge, I., Volkov, D. L., le Hénaff, M., Dong, S., Lamont, T., Sato, O. T., and van den Berg, M.: Multi-Year Estimates of Daily Heat Transport by the Atlantic Meridional Overturning Circulation at 34.5° S, J. Geophys. Res.-Oceans, 126, e2020JC016947, https://doi.org/10.1029/2020JC016947, 2021.

Lebedev, K., Yoshinari, H., Maximenko, N. A., and Hacker, P. W.: YoMaHa'07: Velocity data assessed from trajectories of Argo floats at parking level and at the sea surface, IPRC Technical Note No. 4, 16 pp., 2007.

Lellouche, J.-M., Le Galloudec, O., Drévillon, M., Régnier, C., Greiner, E., Garric, G., Ferry, N., Desportes, C., Testut, C.-E., Bricaud, C., Bourdallé-Badie, R., Tranchant, B., Benkiran, M., Drillet, Y., Daudin, A., and De Nicola, C.: Evaluation of global monitoring and forecasting systems at Mercator Océan, Ocean Sci., 9, 57–81, https://doi.org/10.5194/os-9-57-2013, 2013.

Liu, C. and Allan, R.: Reconstructions of the radiation fluxes at the top of the atmosphere and net surface energy flux over 1985–2017 – DEEP-C Version 4.0, University of Reading [data set], https://doi.org/10.17864/1947.271, 2020.

Liu, C., Allan, R. P., Mayer, M., Hyder, P., Desbruyères, D., Cheng, L., Xu, J., Xu, F., and Zhang, Y.: Variability in the global energy budget and transports 1985–2017, Clim. Dynam., 55, 3381–3396, https://doi.org/10.1007/S00382-020-05451-8, 2020.

Loeb, N. G., Doelling, D. R., Wang, H., Su, W., Nguyen, C., Corbett, J. G., Liang, L., Mitrescu, C., Rose, F. G., and Kato, S.: Clouds and the Earth's Radiant Energy System (CERES) Energy Balanced and Filled (EBAF) Top-of-Atmosphere (TOA) Edition-4.0 Data Product, J. Climate, 31, 895–918, https://doi.org/10.1175/JCLI-D-17-0208.1, 2018.

MacLachlan, C., Arribas, A., Peterson, K. A., Maidens, A., Fereday, D., Scaife, A. A., Gordon, M., Vellinga, M., Williams, A., Comer, R. E., Camp, J., Xavier, P., and Madec, G.: Global Seasonal forecast system version 5 (GloSea5): a high-resolution seasonal forecast system, Q. J. Roy. Meteor. Soc., 141, 1072–1084, https://doi.org/10.1002/qj.2396, 2015.

Majumder, S., Schmid, C., and Halliwell, G.: An observations and model-based analysis of meridional transports in the South Atlantic, J. Geophys. Res.-Oceans, 121, 5622–5638, https://doi.org/10.1002/2016JC011693, 2016.

Mayer, J., Mayer, M., and Haimberger, L.: Consistency and Homogeneity of Atmospheric Energy, Moisture, and Mass Budgets in ERA5, J. Climate, 34, 3955–3974, https://doi.org/10.1175/JCLI-D-20-0676.1, 2021a.

Mayer, J., Mayer, M., and Haimberger, L.: Mass-consistent atmospheric energy and moisture budget monthly data from 1979 to present derived from ERA5 reanalysis, Copernicus Climate Change Service (C3S) Climate Data Store (CDS) [data set], https://doi.org/10.24381/cds.c2451f6b, 2021b.

Mayer, J., Mayer, M., Haimberger, L., and Liu, C.: Comparison of Surface Energy Fluxes from Global to Local Scale, J. Climate, 1, 1–55, https://doi.org/10.1175/JCLI-D-21-0598.1, 2022.

Meinen, C. S., Speich, S., Perez, R. C., Dong, S., Piola, A. R., Garzoli, S. L., Baringer, M. O., Gladyshev, S., and Campos, E. J. D.: Temporal variability of the meridional overturning circulation at 34.5° S: Results from two pilot boundary arrays in the South Atlantic, J. Geophys. Res.-Oceans, 118, 6461–6478, https://doi.org/10.1002/2013JC009228, 2013.

Meinen, C. S., Speich, S., Piola, A. R., Ansorge, I., Campos, E., Kersalé, M., Terre, T., Chidichimo, M. P., Lamont, T., Sato, O. T., Perez, R. C., Valla, D., van den Berg, M., le Hénaff, M., Dong, S., and Garzoli, S. L.: Meridional Overturning Circulation Transport Variability at 34.5° S During 2009–2017: Baroclinic and Barotropic Flows and the Dueling Influence of the Boundaries, Geophys. Res. Lett., 45, 4180–4188, https://doi.org/10.1029/2018GL077408, 2018.

Mignac, D., Ferreira, D., and Haines, K.: South Atlantic meridional transports from NEMO-based simulations and reanalyses, Ocean Sci., 14, 53–68, https://doi.org/10.5194/os-14-53-2018, 2018.

Nadeau, L. P. and Jansen, M. F.: Overturning Circulation Pathways in a Two-Basin Ocean Model, J. Phys. Oceanogr., 50, 2105–2122, https://doi.org/10.1175/JPO-D-20-0034.1, 2020.

Perez, R. C., Garzoli, S. L., Meinen, C. S., and Matano, R. P.: Geostrophic Velocity Measurement Techniques for the Meridional Overturning Circulation and Meridional Heat Transport in the South Atlantic, J. Atmos. Ocean. Tech., 28, 1504–1521, https://doi.org/10.1175/JTECH-D-11-00058.1, 2011.

Rahmstorf, S.: Exceptional twentieth-century slowdown in Atlantic Ocean overturning circulation, Nat. Clim. Chang., 5, 475–480, https://doi.org/10.1038/nclimate2554, 2015.

Storto, A., Masina, S., and Navarra, A.: Evaluation of the CMCC eddy-permitting global ocean physical reanalysis system (C-GLORS, 1982–2012) and its assimilation components, Q. J. Roy. Meteor. Soc., 142, 738–758, https://doi.org/10.1002/qj.2673, 2016.

Thornalley, D. J. R., Oppo, D. W., Ortega, P., Robson, J. I., Brierley, C. M., Davis, R., Hall, I. R., Moffa-Sanchez, P., Rose, N. L., Spooner, P. T., Yashayaev, I., and Keigwin, L. D.: Anomalously weak Labrador Sea convection and Atlantic overturning during the past 150 years, Nature, 556, 227–230, https://doi.org/10.1038/s41586-018-0007-4, 2018.

Trenberth, K. E., Zhang, Y., Fasullo, J. T., and Cheng, L.: Ocean Meridional Heat Transport Values, Version 1.0, UCAR/NCAR – GDEX, https://doi.org/10.5065/9v3y-fn61, 2019a.

Trenberth, K. E., Zhang, Y., Fasullo, J. T., and Cheng, L.: Observation-Based Estimates of Global and Basin Ocean Meridional Heat Transport Time Series, J. Climate, 32, 4567–4583, https://doi.org/10.1175/JCLI-D-18-0872.1, 2019b.

Weijer, W., de Ruijter, W. P. M., Sterl, A., and Drijfhout, S. S.: Response of the Atlantic overturning circulation to South Atlantic sources of buoyancy, Glob. Planet. Change, 34, 293–311, https://doi.org/10.1016/S0921-8181(02)00121-2, 2002.

Weijer, W., Cheng, W., Drijfhout, S. S., Fedorov, A. V., Hu, A., Jackson, L. C., Liu, W., McDonagh, E. L., Mecking, J. V., and Zhang, J.: Stability of the Atlantic Meridional Overturning Circulation: A Review and Synthesis, J. Geophys. Res.-Oceans, 124, 5336–5375, https://doi.org/10.1029/2019JC015083, 2019.

Weijer, W., Cheng, W., Garuba, O. A., Hu, A., and Nadiga, B. T.: CMIP6 Models Predict Significant 21st Century Decline of the Atlantic Meridional Overturning Circulation, Geophys. Res. Lett., 47, e2019GL086075, https://doi.org/10.1029/2019GL086075, 2020.

Xu, X., Chassignet, E. P., Dong, S., and Baringer, M. O.: Transport Structure of the South Atlantic Ocean Derived From a High-Resolution Numerical Model and Observations, Front. Mar. Sci., 9, 175, https://doi.org/10.3389/FMARS.2022.811398, 2022.

Zuo, H., Balmaseda, M. A., Tietsche, S., Mogensen, K., and Mayer, M.: The ECMWF operational ensemble reanalysis–analysis system for ocean and sea ice: a description of the system and assessment, Ocean Sci., 15, 779–808, https://doi.org/10.5194/os-15-779-2019, 2019.

Zuo, H., Balmaseda, M. A., de Boisseson, E., Tietsche, S., Mayer, M., and de Rosnay, P.: The ORAP6 ocean and sea-ice reanalysis: description and evaluation, EGU General Assembly 2021, online, 19–30 April 2021, EGU21-9997, https://doi.org/10.5194/egusphere-egu21-9997, 2021.

State Planet, 1-osr7, 5, 2023
https://doi.org/10.5194/sp-1-osr7-5-2023

Satellite monitoring of surface phytoplankton functional types in the Atlantic Ocean over 20 years (2002–2021)

Hongyan Xi[1], Marine Bretagnon[2], Svetlana N. Losa[1,3], Vanda Brotas[4], Mara Gomes[4], Ilka Peeken[1], Leonardo M. A. Alvarado[1], Antoine Mangin[2], and Astrid Bracher[1,5]

[1]Alfred Wegener Institute, Helmholtz Centre for Polar and Marine Research, Bremerhaven, Germany
[2]ACRI-ST, Sophia Antipolis CEDEX, France
[3]Shirshov Institute of Oceanology, Russian Academy of Sciences, Moscow, Russia
[4]MARE/ARNET – Marine and Environmental Sciences Centre, Faculdade de Ciências, Universidade de Lisboa, Campo Grande, Lisbon, Portugal
[5]Institute of Environmental Physics, University of Bremen, Bremen, Germany

Correspondence: Hongyan Xi (hongyan.xi@awi.de)

Received: 30 July 2022 – Discussion started: 30 September 2022
Revised: 24 January 2023 – Accepted: 17 March 2023 – Published: 27 September 2023

Abstract. An analysis of multi-satellite-derived products of four major phytoplankton functional types (PFTs – diatoms, haptophytes, prokaryotes and dinoflagellates) was carried out to investigate the PFT time series in the Atlantic Ocean between 2002 and 2021. The investigation includes the 2-decade trends, climatology, phenology and anomaly of PFTs for the whole Atlantic Ocean and its different biogeochemical provinces in the surface layer that optical satellite signals can reach. The PFT time series over the whole Atlantic region showed mostly no clear trend over the last 2 decades, except for a small decline in prokaryotes and an abrupt increase in diatoms during 2018–2019, which is mainly observed in the northern Longhurst provinces. The phenology of diatoms, haptophytes and dinoflagellates is very similar: at higher latitudes bloom maxima are reached in spring (April in the Northern Hemisphere and October in the Southern Hemisphere), in the oligotrophic regions in winter time and in the tropical regions during May to September. In general, prokaryotes show opposite annual cycles to the other three PFTs and present more spatial complexity. The PFT anomaly (in percent) of 2021 compared to the 20-year mean reveals mostly a slight decrease in diatoms and a prominent increase in haptophytes in most areas of the high latitudes. Both diatoms and prokaryotes show a mild decrease along coastlines and an increase in the gyres, while prokaryotes show a clear decrease at mid-latitudes to low latitudes and an increase on the western African coast (Canary Current Coastal Province, CNRY and Guinea Current Coastal Province, GUIN) and southwestern corner of North Atlantic Tropical Gyral Province (NATR). Dinoflagellates, as a minor contributor to the total biomass, are relatively stable in the whole Atlantic region. This study illustrated the past and current PFT state in the Atlantic Ocean and acted as the first step to promote long-term consistent PFT observations that enable time series analyses of PFT trends and interannual variability to reveal potential climate-induced changes in phytoplankton composition on multiple temporal and spatial scales.

Published by Copernicus Publications.

Table 1. Products used.

Product ref. no.	Product ID and type	Data access	Documentation
1	OCEANCOLOUR_GLO_BGC_L4_MY_009_104; satellite observations	EU Copernicus Marine Service Product (2022)	Quality Information Document (QUID): Garnesson et al. (2022); Product User Manual: Colella et al. (2022)
2	PFTs derived from SeaWiFS-/MODIS-/MERIS-merged products for the period of January 2012 to April 2012; satellite observations	Our own archive	Xi et al. (2021)
3	PFTs derived from Sentinel 3A OLCI product for the period of May 2016 to December 2016; satellite observations	Our own archive	Xi et al. (2021)
4	In situ PFT data; in situ observations	Xi et al. (2023)	Xi et al. (2023)

1 Introduction

Phytoplankton in the sunlit layer of the ocean act as the base of the marine food web fueling fisheries and also regulate key biogeochemical processes. Climate-induced changes causing temperature rise, ocean acidification and ocean deoxygenation stress the ocean's contemporary biogeochemical cycles and ecosystems, thereby impacting the phytoplankton communities (Gruber, 2011; Gruber et al., 2021; Bindoff et al., 2019). Related to this, the changing nutrient and light availability, particularly in the polar oceans, is also critical for the development of phytoplankton communities (Käse and Geuer, 2018). In the past decades, satellite observations of ocean color (OC) information, especially the surface chlorophyll *a* concentration (chl *a*) as a proxy for phytoplankton biomass, have been able to revolutionize our understanding of biogeochemical processes and provide insights into the changes in phytoplankton and inferred productivity driven by climate change (e.g., Antoine et al., 2005; Gregg and Rousseaux, 2014; McClain, 2009; Behrenfeld et al., 2016; Kulk et al., 2020). However, phytoplankton biomass does not provide a full description of the complex nature of phytoplankton community and function. Phytoplankton composition varies across ocean biomes, and the different phytoplankton groups influence marine ecosystem and biogeochemical processes differently (Bracher et al., 2017). Continuous monitoring of phytoplankton composition is important not only to understand the biogeochemical processes such as nutrient uptake and carbon and energy transfer, but also for fisheries, ocean environment, water quality and even human health when certain species cause, for example, harmful algal blooms (Quéré et al., 2005; Bindoff et al., 2019; Bracher et al., 2022).

Phytoplankton diversity is very high, summarized in phytoplankton functional types (PFTs) as prokaryotes (cyanobacteria) and eukaryotes, including diatoms, haptophytes and dinoflagellates. Depending on area, season and size class, different PFTs can act as dominating organisms in the food web and, therefore, regulate the seasonality of the predators (Käse and Geuer, 2018). Diatoms, known as major silicifiers, have silica frustules that surround and protect the cells and sink rapidly out of the surface layer of the ocean, contributing to the transport of carbon, nitrogen and silica to deeper waters (IOCCG, 2014). Haptophytes are another very abundant PFT in the global ocean occurring mainly in the middle-sized (2–20 µm) range. The prominent subgroup within haptophytes consists of coccolithophores, which have been considered a critical component of marine environments because of their dual capacity to fix environmental carbon via biomineralization (calcium carbonate, calcite) and through photosynthesis (Reyes-Prieto et al., 2009). Dinoflagellates are also one of the largest groups of marine eukaryotes, although most species are, on average, smaller than the average of diatom species. The majority of dinoflagellate species are autotrophic and tend to thrive under stable conditions. Due to their motility and ability to regulate their position in the water column, they can outcompete other phytoplankton and sometimes accumulate rapidly, resulting in a visible coloration of the water, known as harmful algal blooms (IOCCG, 2014). Prokaryotes as picophytoplankton are abundant in many ocean regions (notably at mid-latitudes to low latitudes but also others) and also account for a substantial fraction of marine primary production, with the two taxa being *Synechococcus* and *Prochlorococcus* in tropical regions (Flombaum et al., 2013).

PFTs have been the focus of various studies carried out worldwide as well as in the Atlantic Ocean, providing rich and valuable knowledge of PFT assessments in terms of their

abundance, distribution, phenology, roles in the primary production, and relationship to other physical and biological parameters (e.g., Head and Pepin, 2010; Brotas et al., 2013, 2022; Soppa et al., 2016; Brewin et al., 2017; Moisan et al., 2017; Bolaños et al., 2020; Yang et al., 2020). Information of phytoplankton composition with respect to the functional types and size classes can be retrieved by ocean color algorithms based on different types of input data. However, most of the studies focus on either a certain PFT (e.g., Lange et al., 2020), a short time period or a limited spatial coverage (e.g., Bracher et al., 2020; Brotas et al., 2022). A complete, systematic frame for the long-term monitoring of multiple PFTs on a wide scale is yet to be established. Previously, we have developed and further improved an approach (referred to as EOF-PFT) consisting of a set of empirical-orthogonal-function-based PFT algorithms thanks to a large global in situ PFT data set based on HPLC (high-performance liquid chromatography)-measured pigments (Xi et al., 2020, 2021). These algorithms use multi-spectral reflectance data from OC satellites and sea surface temperature data to estimate chl *a* concentration of six major phytoplankton groups. Here, we focus only on four PFTs, which on the whole account for the major part of the biomass in the Atlantic Ocean. Applied to multi-sensor merged products and Sentinel 3A Ocean and Land Colour Instrument (OLCI) data, the algorithms enable us to generate global PFT products, which have been available from the EU Copernicus Marine Service since 2020 and are updated regularly, providing global chl *a* data with per-pixel uncertainty for diatoms, haptophytes, dinoflagellates, chlorophytes and phototrophic prokaryotes spanning the period from 2002 until today.

In this section, we combine these PFT data sets of different sensors, covering various lifespans and radiometric characteristics, into consistent long-term satellite PFT products. The 2-decade quality-assured global PFT data sets for the Atlantic Ocean (50° S to 50° N, 60° W to 10° E) are derived by correcting the input-sensor-specific PFT products using inter-sensor comparisons with uncertainty estimations, which then allow us to (1) evaluate Copernicus Marine Service PFT products and improve their continuity along the products derived from different satellite sensors and (2) analyze PFT time series in the last 2 decades in terms of climatology, trends, anomaly and phenology of multiple PFTs in the Atlantic Ocean and its different biogeochemical provinces (Longhurst, 2007).

2 Data and method

2.1 PFT products from Copernicus Marine Service

Satellite data used in this study are listed in Table 1. Multiple PFT chl *a* products with per-pixel uncertainty have been available from the Copernicus Marine Service since May 2020, with updates in 2021 and 2022, and were derived from three sets of OC products (product ref. no. 1 in Table 1): (1) merged remote sensing reflectance (Rrs) products at 9 bands from SeaWiFS, MODIS and MERIS from July 2002 to December 2011; (2) merged Rrs products at 9 bands from MODIS and VIIRS from January 2012 to December 2016; and (3) Rrs products at 11 bands from Sentinel 3A OLCI from January 2017 to December 2021 (Table 1; Xi et al., 2021). In this section, monthly PFT products with 25 km resolution in the open ocean (depth > 200 m) are used for spatiotemporal analysis in the Atlantic Ocean spanning the period from July 2002 to December 2021.

Consistency of satellite data is checked with the following details. As the product developer we have additionally generated PFT retrievals from different sensor combinations but with overlapping time periods. PFT products from SeaWiFS-/MODIS-/MERIS-merged data and that from MODIS-/VIIRS-merged data have a 4-month overlap from January to April 2012 (product ref. no. 2 in Table 1), and MODIS-/VIIRS-derived PFTs are overlapped with the OLCI-derived PFTs since May 2016 (product ref. no. 3 in Table 1). To produce consistent PFT products over the last 2 decades for the Atlantic Ocean, we compare PFT retrievals within these overlapped periods to identify the systematic differences between two data sources and then set up the correction functions through linear regressions by taking into account the per-pixel uncertainty. Sections 2.3 and 3.3 in Xi et al. (2021) may be referred to for a detailed description of the per-pixel uncertainty assessment of the PFT products. Similar to how the OC-CCI chl *a* product was merged (Jackson, 2020), one of the three sets of PFT products that has been verified to have the lowest uncertainties (produced on a pixel basis) and smallest biases when evaluated by in situ data will be chosen as the reference product. The other two sets of PFT products will be corrected to it. In the EOF-PFT approach development stage (Xi et al., 2020, 2021), we noticed that the PFT products derived from SeaWiFS-/MODIS-/MERIS-merged Rrs data show the lowest per-pixel uncertainties for nearly all the PFT quantities because their corresponding algorithms were trained based on a larger and more widely covered matchup data set between the satellite and in situ observations. Therefore, we take SeaWiFS-/MODIS-/MERIS-derived PFTs as a reference to correct the other two PFT data sets derived from MODIS-/VIIRS-merged data and OLCI data, respectively.

2.2 In situ PFT data and matchup extraction

To evaluate the satellite PFT products, we use in situ HPLC pigment data from past expeditions between 2009 and 2019 covering the whole Atlantic pole-to-pole region (65° S to 80° N), which included 11 expeditions from the North Atlantic to the Arctic Fram Strait (PS74, PSS76, PS78, PS80, PS85, PS93.2, PS99.1, PS99.2, PS106, PS107, PS121), four expeditions in the Atlantic Ocean (PS113, PS120, AMT28 and AMT29) and one expedition in the Southern Ocean (PS103). All pigment data were quality-controlled by apply-

ing the method by Aiken et al. (2009). Diagnostic pigment analysis was carried out to determine the in situ PFT chl *a* concentrations with newly tuned weighting coefficients by Alvarado et al. (2022), according to Vidussi et al. (2001) and Uitz et al. (2006), modified as in Hirata et al. (2011) and Brewin et al. (2015). In situ PFT data (product ref. no. 1 in Table 1) are then used to validate the corrected PFTs by extracting matchups between daily 4 km PFT products from the Copernicus Marine Service and the in situ data. For each in situ measurement a matchup of 3×3 pixels around the in situ location on the same day was extracted. Averaged data based on 3×3 pixels were computed following the matchup protocol as in Xi et al. (2020, 2021), including only matchups containing at least 50 % of valid pixels with a coefficient of variation (CV) of the valid pixel values lower than 0.15.

2.3 Time series analysis

We focus on preliminary explorations of the calibrated PFT products to reveal and understand the trends of and variations in Atlantic PFTs in the last 2 decades. We derive the PFT time series of the whole Atlantic region, on different regional scales and also at the per-pixel level. For regional scales, PFT data of the Atlantic Ocean are partitioned into smaller regions using Longhurst's geographic classification system of biomes and provinces (Longhurst, 2007; Flanders Marine Institute, 2009). We determine the annual cycle (climatology) based on both pixel data and regional log-based mean values and derive anomalies to observe the interannual changes and detect trends reflected by the satellite observations. Time series analysis is done both per pixel and for the whole region or province. We investigate the trends in the PFTs for the last 20 years using linear regression in the format of $Y = SX + I$, where Y is the monthly PFT chl *a* either per pixel or of the regional log-based mean, X is the time on a monthly basis, S is the slope of the regression, and I is the intercept. Only trends with statistically significant correlations of the regression ($p < 0.05$) are shown. Indicators of PFT phenology and the anomaly of 2021 (the last year of the considered time period) are also extracted in order to identify potential changes/shifts in PFTs. Abundance maxima time, as one of the phenology indicators, is identified for each pixel by finding the month when the maximum PFT chl *a* occurred during the year. Anomaly in percent is determined by computing the relative difference between the PFT state of 2021 and the average state of the last 2 decades (i.e., climatology).

3 Results

3.1 Inter-sensor corrections of PFT products and validation with in situ data

Figure 1 shows the comparison between monthly PFTs from SeaWiFS-/MODIS-/MERIS-merged and MODIS-/VIIRS-merged data for the overlapped 4 months (January–April 2012). PFT retrievals from different satellite sensors show some differences but overall correlate well with each other ($R^2 > 0.82$). Type II linear regression between the retrievals from two satellite data sources is determined for each PFT by accounting for the per-pixel uncertainty. The slope and intercept values are then used to correct the MODIS-/VIIRS-derived PFTs to the SeaWiFS-/MODIS-/MERIS-derived ones so that they are overall consistent, though the pixelwise discrepancy still exists. The same is applied to the Sentinel 3A OLCI-derived PFTs by comparing them to the corrected MODIS-/VIIRS-derived PFTs for the overlapped period April–December 2016 so that all PFT data from both MODIS/VIIRS and OLCI are now referenced to SeaWiFS-/MODIS-/MERIS-derived PFTs. Though R^2 is slightly weaker (R^2 between 0.77 and 0.83) compared to that from the MODIS-/VIIRS- versus SeaWiFS-/MODIS-/MERIS-derived PFTs (R^2 between 0.82 and 0.98), OLCI-derived PFTs still showed overall good correlations to the corrected MODIS/VIIRS data, with regression slopes between 0.83 and 1.03, despite prokaryote chl *a* retrievals from OLCI data being higher in general.

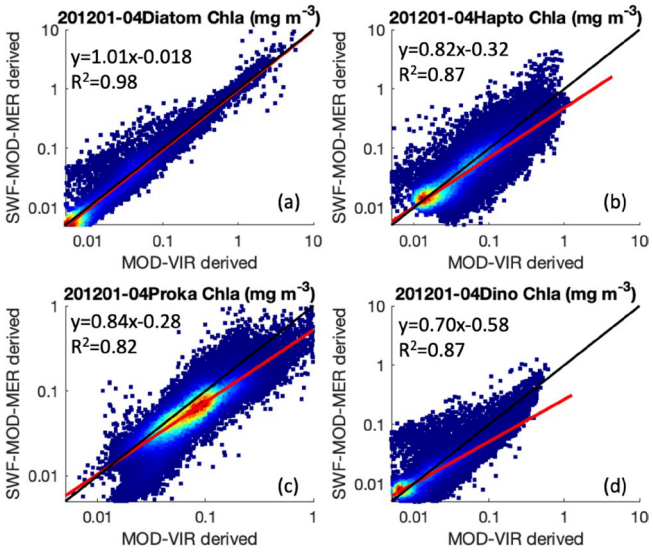

Figure 1. Scatterplots of monthly PFTs derived from SeaWiFS-/MODIS-/MERIS-merged and MODIS-/VIIRS-merged Rrs data for the overlapping period January–April 2012. **(a)** Diatoms, **(b)** haptophytes, **(c)** prokaryotes and **(d)** dinoflagellates. The 1 : 1 line is shown in black and the linear regression line (using type II regression with per-pixel uncertainty) in red. R^2, slopes and offsets determined in log-10 scale are also presented.

Validation was carried out by comparing the collocated satellite PFTs with the in situ PFTs using the extracted matchup data. Statistical results of the validation in Table 2 in general show acceptable agreement between the in situ and satellite-derived PFTs. Median percent differences (MDPDs) are consistent with the median satellite PFT uncertain-

ties (relative error in percent) estimated through Monte Carlo simulation and error propagation in Xi et al. (2021), and for dinoflagellates they are notably lower. A higher MDPD is found for prokaryotes due to a systematic overestimation of the picophytoplankton in the retrieval algorithms for all the three sets of satellite OC sensors; however, no significant bias of satellite prokaryote products is detected between different sensors. Therefore the overestimation should have minor influence on the time series data of prokaryotes. In addition, a coarser evaluation by directly comparing the monthly satellite PFTs (which have better spatial coverage) to the in situ PFTs for the whole cruise track has shown that the PFT variation regarding regional phytoplankton dynamics observed by the in situ PFT is very well revealed by satellite PFT maps (images not shown). These evaluations assure the quality of the satellite PFTs for time series analysis.

3.2 PFT climatology (2002–2021)

Figure 2 shows the climatology (2002–2021) of the four PFTs generated using satellite monthly PFT products, depicting differences and similarities in terms of PFT chl *a* magnitude and spatial variation among different PFTs. Diatoms, as major silicifiers, are typically large-celled (> 20 µm, though species with smaller cells also exist) and highly dependent on nutrient levels. They are sensitive to the global temperature, especially to the Equator–pole temperature gradient. The 2-decade climatology of diatoms in the Atlantic region shows a clearly higher abundance at high latitudes and in coastal regions and the lowest abundance (or even undetectable) in the vast subtropical gyres. Similarly, haptophytes, which are mostly classified as nanophytoplankton (2–20 µm), also have a higher abundance at high latitudes and in coastal regions but span a larger coverage than diatoms. Enhanced abundance level is also found in the equatorial belt. The lowest abundance of haptophytes is also found in the gyres, but their abundance is not as low as that of diatoms. Prokaryotes, commonly referred to as picophytoplankton (< 2 µm), show the highest abundance at mid-latitudes to low latitudes of the open Atlantic Ocean. Though spatially showing the lowest abundance in the gyres, prokaryotes are still the most dominant phytoplankton group in the majority of these regions. Dinoflagellates as a relatively minor contributor to the total biomass follow a similar distribution pattern to diatoms but are much lower in abundance at higher latitudes.

3.3 PFT trends during 2002–2021 in the Atlantic Ocean

Following the climatology study, the annual cycles of the four PFTs over the whole Atlantic Ocean are also derived by extracting the mean biomass of the 2 decades for each month (Fig. 3a). Prokaryotes are clearly the most dominant group, showing the highest mean of the chl *a* (0.062–0.072 mg m^{-3}) over the Atlantic all year round, followed by haptophyte chl *a*, which varies from 0.03 to 0.045 mg m^{-3}. Diatom chl *a*

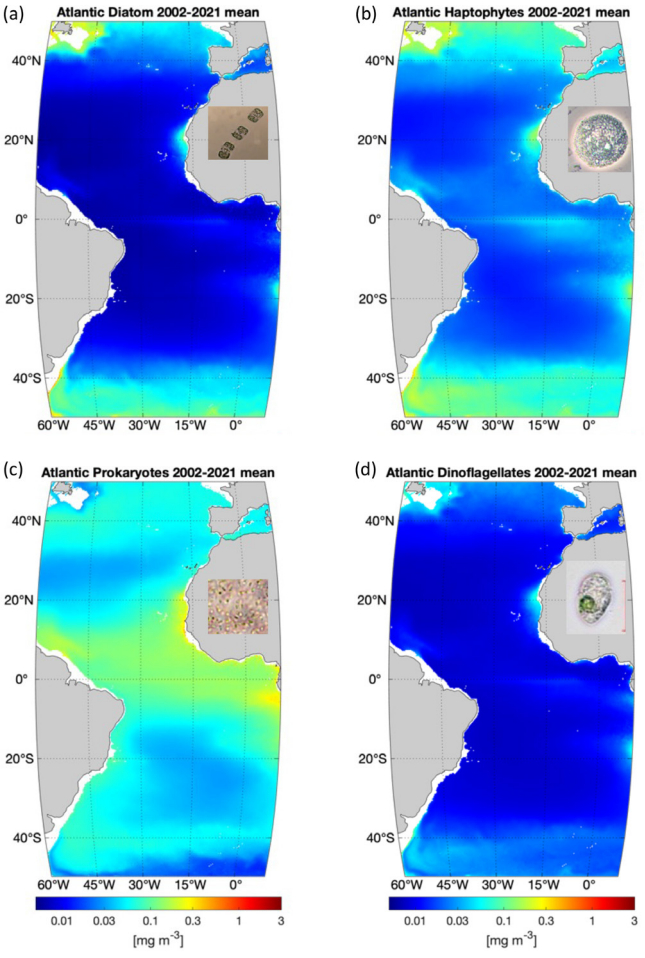

Figure 2. PFT climatology based on monthly PFT chl *a* products from 2002 to 2021: **(a)** diatoms, **(b)** haptophytes, **(c)** prokaryotes and **(d)** dinoflagellates. Microscopic photos of the representative species for the four PFTs are presented (photo credit: Alfred Wegener Institute).

varies from 0.017 to 0.026 mg m^{-3}, and dinoflagellates, with the lowest mean chl *a*, are below 0.015 mg m^{-3}. Despite different magnitudes, diatoms, haptophytes and dinoflagellates present very similar annual cycles, with two biomass peaks in April and November, indicating the spring blooming especially at high latitudes in both the Northern Hemisphere and Southern Hemisphere. In contrast, prokaryotes show a distinct biomass peak in June–July and a less prominent increase in December–January due to the suppressed growth of the other PFTs in these periods.

Time series of the monthly PFT data averaged for the whole Atlantic are shown in Fig. 3b, depicting a significant decrease (0.0001 chl *a* mg m^{-3} per month, $p < 0.01$) in prokaryote chl *a*, but no significant trend is observed for the other three PFTs, although some interannual changes are visible. Between the time window of 2003 and 2008, a slight decline in prokaryote chl *a* is observed, followed by a 2-year

Table 2. Statistical validation results of satellite-derived PFT chl *a* (after inter-mission correction) as a function of in situ PFT chl *a* using least square fit in logarithmic scale. N: number of matchups; R^2: coefficient of determination; MDPD: median percent difference; RMSD: root mean square difference; for a definition of equations of these terms please refer to Xi et al. (2020). Note that slope, intercept and R^2 were calculated based on a logarithmic scale. Median uncertainties calculated based on satellite per-pixel PFT uncertainty (equivalent to relative error in percent, adapted from Xi et al., 2021) are also shown in the last column.

	N	Slope	Intercept	R^2	MDPD (%)	RMSD (mg m^{-3})	Median satellite PFT uncertainty (%)
Diatoms	192	0.71	−0.27	0.76	60.5	0.30	57.3
Haptophytes	191	0.95	−0.007	0.41	58.9	0.18	41.5
Prokaryotes	187	0.71	0.12	0.36	185	0.06	86.5
Dinoflagellates	144	1.07	0.04	0.66	59.1	0.07	74.3

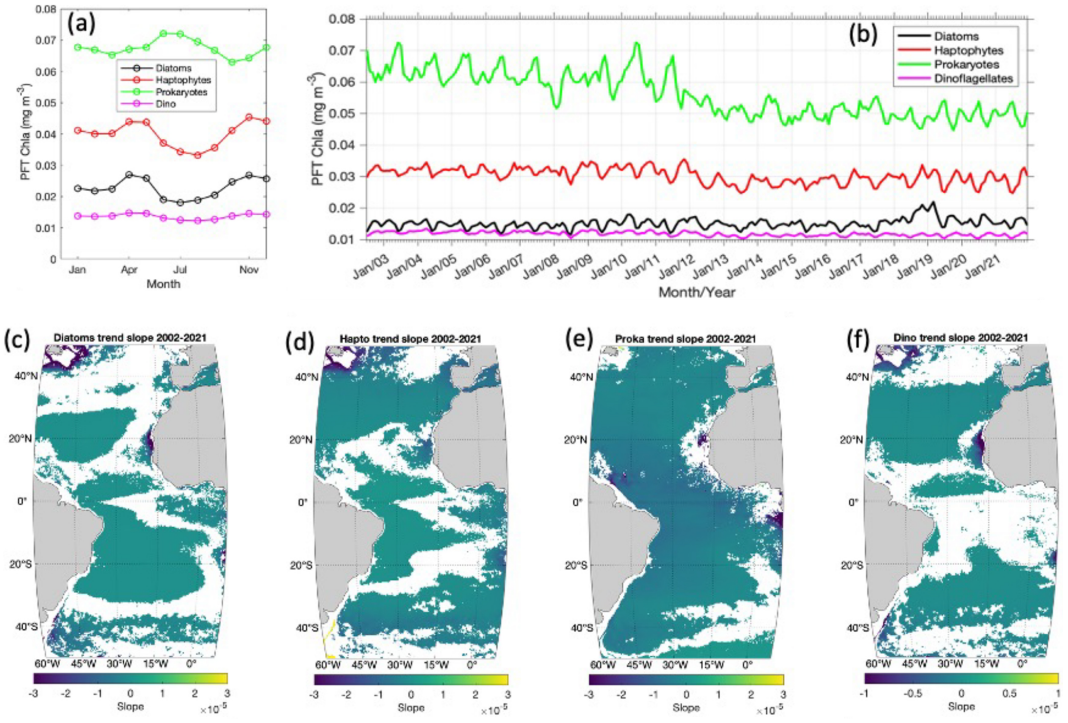

Figure 3. **(a)** Annual cycle of the four PFTs of diatoms, haptophytes, prokaryotes and dinoflagellates in the Atlantic Ocean (−50° S to 50° N, 60° W to 10° E); **(b)** 20-year time series from 2002 to 2021; and **(c)** per-pixel slope based on monthly chl *a* products of diatoms, **(d)** haptophytes, **(e)** prokaryotes and **(f)** dinoflagellates from 2002 to 2021 (where $p < 0.05$ is shown; slope unit: chl *a* mg m^{-3} per month).

increase (2009–2010), but from 2011 onwards a continuous decline is again observed. The per-pixel trend of prokaryotes in Fig. 3e shows that the decreasing trend of prokaryotes is mainly found at low latitudes and particularly on the west coast of Africa (Canary Current Coastal Province, CNRY, and Guinea Current Coastal Province, GUIN; refer to Fig. 4 for Longhurst provinces). Haptophyte time series show the lowest abundance during 2013–2015, which is then elevated slightly from 2016 (Fig. 3b). A slight increasing trend of haptophytes on the pixel level is found at mid-latitudes to low latitudes, and a decrease is found near the coast at higher latitudes (Fig. 3d). Diatom chl *a* is rather stable until 2017, with an abrupt increase in 2018–2019 and then a decrease in 2020–2021 to the average level of the last 20 years (Fig. 3b). The per-pixel time series in Fig. 3c shows that a significant decrease is found only on the west coast of Africa (CNRY), northwest of the North Atlantic (Northwest Atlantic Shelves Province, NWCS) and on the Patagonian coast. A very slight increasing trend of diatoms is presented in the gyres and equatorial region. Dinoflagellate chl *a* contributes a very minor proportion to the total biomass (< 10 %) and has been relatively stable over the last 2 decades in the whole Atlantic region (Figs. 3b and f).

Time series of diatom chl *a* in different Longhurst provinces of the Atlantic are further extracted in order to investigate whether the abrupt increase in diatoms during

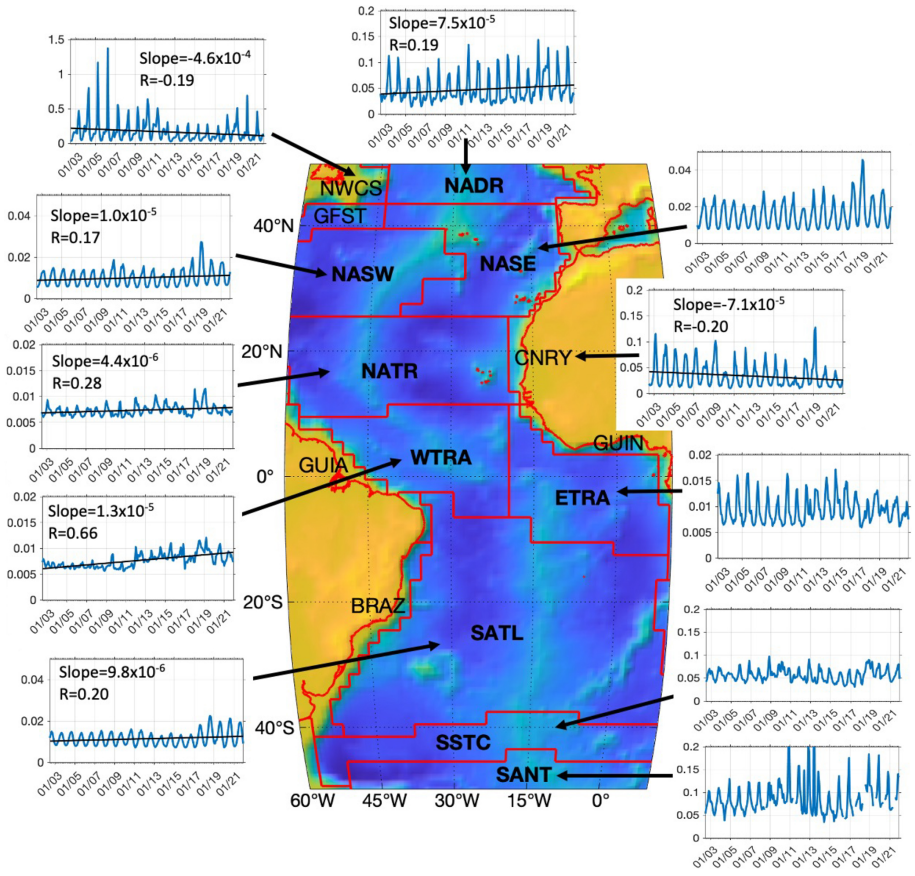

Figure 4. Time series of diatom chl *a* (mg m^{-3}) in 11 Longhurst provinces in the Atlantic Ocean with bathymetric information based on ETOPO1 bathymetry (Amante and Eakins, 2009). Provinces according to Longhurst (2007) are NADR for North Atlantic Drift Province, NWCS for Northwest Atlantic Shelves Province, NASW for North Atlantic Subtropical Gyral Province (West), NASE for North Atlantic Subtropical Gyral Province (East), NATR for North Atlantic Tropical Gyral Province, CNRY for Canary Current Coastal Province, GUIN for Guinea Current Coastal Province, WTRA for Western Tropical Atlantic Province, ETRA for Eastern Tropical Atlantic Province, SATL for South Atlantic Gyral Province, SSTC for South Subtropical Convergence Province and SANT for Subantarctic Water Ring Province, respectively. Trend lines with slopes (chl *a* mg m^{-3} per month) and correlation coefficients are shown for provinces with significant trends ($p < 0.05$).

2018–2019 took place in the whole Atlantic or only in some regions. Figure 4 presents large variability in the diatoms in different regions in terms of both magnitudes of chl *a* and temporal trends. In general, high latitudes and coastal regions, where diatom chl *a* is higher, present high interannual variation compared to the open ocean at lower latitudes. For instance, diatoms on the west coast of Africa (CNRY) have in general decreased in the last 2 decades except for a dramatic increase in late 2018 and spring 2019, followed by a 2-year decrease in 2020–2021. Despite an obvious elevation in diatoms during 2018–2020, a significant decline in diatoms in the last 2 decades is still found in the NWCS, consistent with the trend map shown in Fig. 3c. A slight increase is found in provinces in the gyres and equatorial region (North Atlantic Subtropical Gyral Province (West), NASW; NATR; Western Tropical Atlantic Province, WTRA; and South Atlantic Gyral Province, SATL), with very low diatom chl *a* (mean chl *a* < 0.02 mg m^{-3}), and also in the Southern Ocean South Subtropical Convergence Province (SSTC). The prominent increase observed during 2018–2019 is mostly contributed by the North Atlantic Ocean CNRY, North Atlantic Subtropical Gyral Province (East) (NASE) and NASW. Other provinces such as in the gyres, with elevated diatom chl *a* since 2018, also contribute, but only slightly, to this increase due to much lower diatom chl *a* there compared to the other regions.

3.4 PFT phenology and anomaly of 2021

The status of the PFTs in the Atlantic Ocean is investigated specifically in 2021 to reflect the Atlantic ecological state and changes for this year as compared to the previous years. To better understand the yearly transition and shifting between different PFTs in the Atlantic Ocean, one of the phenology indicators, abundance maxima time, is mapped per-

pixel for the four PFTs (Fig. 5). Diatoms in the North Atlantic ($> 35°$ N) reach the abundance maxima during late spring (April–May) but earlier (January–February) in the North Atlantic gyre. In the equatorial region the maxima months vary between May and August, with the Equator reaching the maxima the earliest (around May). In the Southern Hemisphere, diatoms reach maxima on average 6 months later than in the Northern Hemisphere, i.e., in the South Atlantic gyre in July–August (austral winter) and in October–December (late spring) in most of the Southern Ocean, which corresponds well with the maxima seasons in the Northern Hemisphere. Haptophytes and dinoflagellates show similar patterns to diatoms but on average bloom 1 month later than diatoms, indicating PFT dominance succession between diatoms and haptophytes in late spring and early summer. Prokaryotes over the whole Atlantic show a more complex and distinct seasonal cycle compared to the other three PFTs. The per-pixel phenology map shows that prokaryotes reach an abundance maximum from autumn to winter at latitudes $> 20°$ N, and their maxima time is delayed with decreasing latitude. In other regions the per-pixel maxima month normally spans a wider time window of 3 to 5 months, such as in the equatorial region from January to May, the South Atlantic gyre from April to August, the western sector of the Southern Ocean from January to April and the eastern sector from November to January. Though geographically prokaryotes show more variation in the phenology, an overall inverse seasonal cycle is presented compared to diatoms, haptophytes and dinoflagellates, as depicted in Fig. 3a.

Anomalies in percent of the four PFTs in 2021 compared to the average state of the last 2 decades are shown in Fig. 6. The diatom anomaly presents changes mainly at high latitudes and in gyres and some coastal regions (such as CNRY). The anomaly shows mostly lower diatom chl *a* at high latitudes, except for NWCS and the southeastern part of NADR, where diatom chl *a* is increased. In contrast to that, diatom chl *a* of 2021 in the gyres is generally higher ($\sim 30\,\%$) compared to the 20-year average state. Note that changes are shown in percent instead of the absolute values to enhance the visibility of small absolute changes, which in the gyres can be very sensitive, as diatom chl *a* is extremely low there (< 0.01 mg m^{-3}). The haptophyte anomaly presents changes in similar regions to diatoms but reversely at high latitudes, especially in the Southern Ocean, where a more prominent increase and also larger coverage are observed. An increase in haptophytes in the area north of the Equator in WTRA is more significant than diatoms. Different from diatoms and haptophytes, prokaryotes reveal a very slight decrease in 2021, mostly at low latitudes within 20° N–20° S, with higher prokaryote chl *a* on the west coast of Africa, especially CNRY, whereas only a mild increase ($< 20\,\%$) is found at high latitudes. Dinoflagellates show the most stable state in 2021 among the four PFTs, with only a slight increase in chl *a* in the North Atlantic Ocean above 40° N and a small decrease in CNRY.

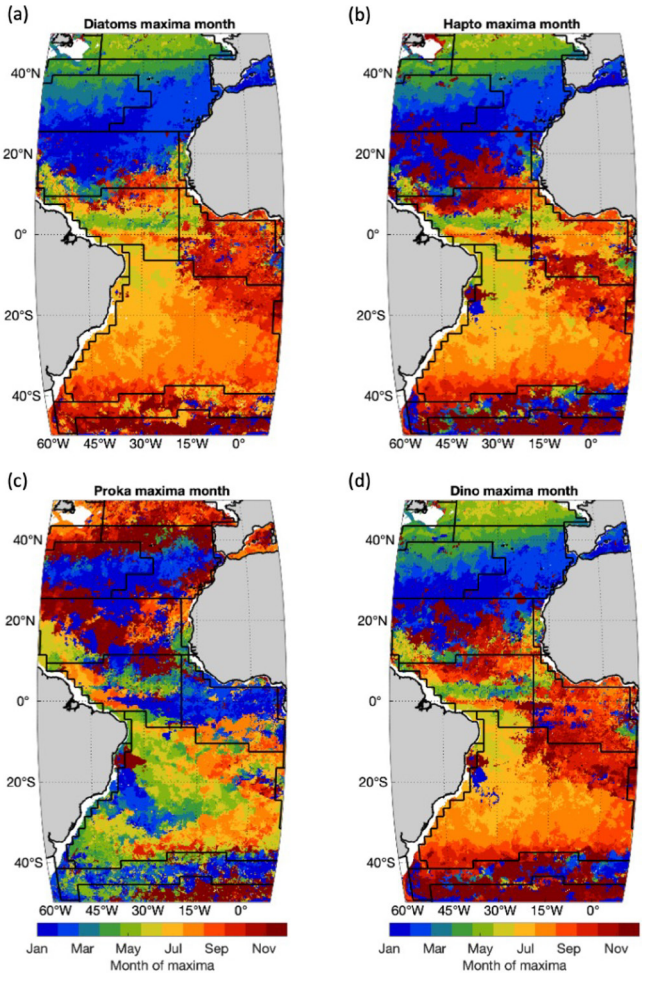

Figure 5. Occurrence month of PFT chl *a* maxima of 2021 in different provinces for **(a)** diatoms, **(b)** haptophytes, **(c)** prokaryotes and **(d)** dinoflagellates. Black lines indicate boundaries of Longhurst provinces as in Fig. 4.

4 Discussion, conclusions and outlook

A systematic time series analysis of PFTs in the Atlantic Ocean is carried out showing high potential of the Copernicus Marine Service satellite PFTs in monitoring the ecological state of the ocean at different scales. Due to different life spans and radiometric characteristics of satellite sensors, there are often inconsistencies and gaps between the same quantities retrieved from different sensors. Data continuity and quality assurance are therefore necessary to provide sound and continuous satellite observations enabling time series studies (Mélin and Franz, 2014; Sathyendranath et al., 2019). As preparatory work for such a study aiming at long-term monitoring of PFTs in the vast Atlantic Ocean, we applied a straightforward inter-mission bias correction as a preliminary trial using overlapped PFT products between the three sets of satellite data. Validation using in situ data shows no significant biases of PFTs derived from different sensors,

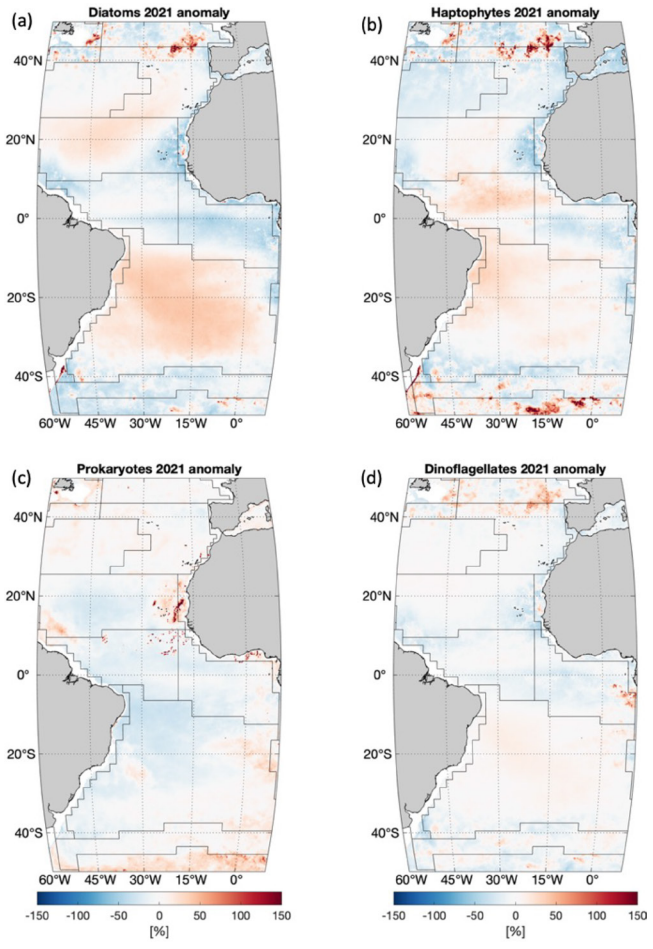

Figure 6. PFT anomaly in percent (%) of 2021 compared to the 20-year mean for **(a)** diatoms, **(b)** haptophytes, **(c)** prokaryotes and **(d)** dinoflagellates. Anomaly in percent is defined as (PFT_{2021} − climatology)/climatology × 100. Black lines indicate boundaries of Longhurst provinces as in Fig. 4.

indicating that the inter-mission offset was effectively corrected. Retrievals of chl *a* of different PFTs are more upscaled products compared to bulk satellite OC products such as total chl *a*, colored dissolved organic matter (CDOM) and absorption properties. It is especially still challenging to accurately retrieve prokaryotic phytoplankton because in the open ocean these dominate in the low-chl *a* areas, where the satellite signals are weaker. Therefore, higher uncertainties exist in these products (e.g., Brewin et al., 2017; Losa et al., 2017; Xi et al., 2021) as compared to uncertainties for other PFTs (see Table 2). In summary, our statistical results of PFT validation are comparable to the evaluations of satellite PFT products derived from different approaches, according to the Quality Information Documents (QUID) that have been published by the Copernicus Marine Service (Pardo et al., 2020; Garnesson et al., 2022). It is noteworthy that the bias correction only targeted the Atlantic Ocean and might not be applicable to other ocean regions, which leads us to further explore a more generic method in the future for the global ocean. However, with these first investigations this study paves the way to promote satellite PFT products into long-term time series studies.

Satellite PFT products provide robust spatial distributions which are comparable to in situ data. The 20-year mean of the four PFTs has presented a trustworthy overview of how different PFTs vary and are distributed spatially in the surface layer of the Atlantic Ocean. Diatoms, haptophytes and dinoflagellates share similar geographic patterns, showing higher abundance at high latitudes and in coastal and equatorial upwelling regions, where the nutrient level is generally high, and minimum abundance in the gyres, especially for diatoms and dinoflagellates. Prokaryotes are more dominant in the gyres and at low latitudes but contribute much less to the total biomass at high latitudes. The findings are consistent with previous studies of phytoplankton group and size classes (e.g., Hirata et al., 2011; Brewin et al., 2015; Losa et al., 2017) and are justified in detail in Xi et al. (2020). More recent studies by Bracher et al. (2020) and Brotas et al. (2022) based on in situ observations have also revealed similar PFT latitudinal distribution to our satellite observations. Furthermore, Brotas et al. (2022) point out that dinoflagellates can be underestimated in the pigment approach, due to their pigment variability; some species do not have the diagnostic pigment peridinin, and there are several heterotrophic species where the pigments are absent or strongly reduced.

PFT time series of the last 2 decades are for the first time generated from multi-satellite observations. For the whole Atlantic Ocean, no significant trend was found for diatoms, haptophytes and dinoflagellates over the last 20 years, but a decline in prokaryotes was observed. However, the per-pixel trend maps revealed that regional trends are different from province to province, such as for diatoms; a significant decrease was found at latitudes above 40° and on the west coast of Africa (CNRY). This was similarly found for haptophytes as well. There is a clear shift for prokaryotes in 2012: from 2003 to 2012, the average value is higher ($0.064\,mg\,m^{-3}$), and the seasonality is clearly defined, whereas from 2013 to 2020, seasonal variations are softened, and the mean value is lower ($0.053\,mg\,m^{-3}$). The retreat of MERIS in 2012 should not influence the prokaryote data set very much for the following reasoning: firstly, such a decline was not found in other PFTs; secondly, MERIS observed more pixels on the coast and at high latitudes, whereas we focus on the open ocean and have excluded the coastal regions with bathymetry < 200 m, and this study covers the Atlantic Ocean between 50° N to 50° S. The main reason might be the relatively lower retrieval accuracy of prokaryotes compared to other PFTs as discussed above in the validation. Our previous work showed that all of the retrieval models for the three sets of sensors have poorer performance for prokaryotic phytoplankton than for other PFT retrievals. This may cause weaker consistency of prokaryotes for the 2-decade pe-

riod even after inter-mission correction. Nevertheless, coverage variability among different satellite missions should be taken into consideration in analyzing long-time-series studies as the ability of the sensors to observe certain waters may differ (van Oostende et al., 2022). These findings in terms of 20-year trends still need to be evaluated further with both in situ measurements and numerical models, though available matchup data between in situ and satellite data are very sparse, and disagreements between models and satellite observations also exist (Gregg and Rousseaux, 2014). Indeed, a period of 20 years is not considered to be long enough for a robust trend analysis as the decadal variability might be too dominant, and for the Atlantic Ocean on average at least 35 years is needed to detect a climate-driven trend in chlorophyll concentration as indicated in Henson et al. (2010, 2016). Nonetheless, the 20-year-long time series provides the opportunity to observe interesting patterns, such as the diatom increase during 2018–2019. Therefore, further investigation of biophysical interactions and linkage to climate is necessary to find evidence and interpret the findings extracted from PFT time series.

Phenology maps of the four PFTs correspond well with their mean annual cycles. Prokaryotes have distinct phenology compared to the other three PFTs, which present similar annual cycles and close bloom maxima time on a general scale despite haptophytes and dinoflagellates reaching biomass maxima a bit later than diatoms in some regions. This section has chooses only one coarse phenological index, the time of the maxima, using monthly satellite products, which has shown the capability of the Copernicus Marine Service satellite PFTs in revealing PFT shifting and growth state at a larger scale than traditional means that rely on extensive ship-based measurements and long-term monitoring stations (e.g., Bracher et al., 2020; Nöthig et al., 2020; Yang et al., 2020). More phenological indices, including the PFT growth duration, biomass amplitude and start and ending dates, could be considered using higher-temporal-resolution products to fully understand the patterns of and interannual variability in the PFT phenology (Soppa et al., 2016).

The PFT anomaly of 2021 compared to the 20-year mean reveals mostly a slight decrease in diatoms above 40° N/S (except for the southeastern part of NADR) and a significant increase in haptophytes in most areas of the high latitudes, which corresponds well with the hypothesis of "Atlantification" proposing that smaller phytoplankton are expanding to high latitudes (e.g., Nöthig et al., 2015; Neukermans et al., 2018; Oziel et al., 2020). A decline in silicate and nitrate concentrations might contribute to the decrease in diatoms in the North Atlantic as indicated in the Copernicus Ocean State Report 5 by von Schuckmann et al. (2021). In contrast to this, most changes in the Southern Ocean were found at latitudes higher than 40° S, which is the region of the Great Calcite Belt. Deppeler and Davidson (2017) pointed out that climate-induced changes such as higher temperature and shallow mixed-layer depth are expected to alter the structure and function of phytoplankton communities in the Southern Ocean. Diatoms and haptophytes as two major groups there may be severely subject to these changes. Interestingly, an increase in haptophytes and decrease in diatoms indicated that the phytoplankton community structure has been altered in recent years, which cannot be easily captured with observations other than satellite PFT time series.

In summary, this study illustrates the past and current PFT state in the Atlantic Ocean and acts as the first step to promote long-term PFT observations serving as ocean monitoring indicators (OMIs) implemented in the Copernicus Marine Service that enable time series analyses of PFT trends and interannual variability to reveal potential climate-induced changes in phytoplankton composition on multiple temporal and spatial scales.

Data availability. Data and products used in this study, as well as their availabilities and documentations, are summarized in Table 1. In situ HPLC pigment and PFT data used for the validation of Copernicus Marine Service PFT products are available on PANGAEA (https://doi.org/10.1594/PANGAEA.954738; Xi et al., 2023).

Author contributions. HX, AB and AM conceptualized the study. HX designed and carried out the experiments. MB provided support in satellite products and matchup data extraction. VB, MG and IP contributed to in situ data compilation for validation. SNL and LMAA helped with data analysis. HX drafted and revised the manuscript with contributions from all co-authors.

Competing interests. The contact author has declared that none of the authors has any competing interests.

Disclaimer. Publisher's note: Copernicus Publications remains neutral with regard to jurisdictional claims in published maps and institutional affiliations.

Acknowledgements. We thank the European Union's Horizon 2020 Research and Innovation Programme under grant agreement 810139 for the project Portugal Twinning for Innovation and Excellence in Marine Science and Earth Observation – PORTWIMS and the Copernicus Marine Service Evolution project GLOPHYTS (grant no. 21036L05B-COP-INNO SCI-9000) for funding. Copernicus Marine Service is implemented by Mercator Ocean International in the framework of a delegation agreement with the European Union. Astrid Bracher and Svetlana N. Losa were supported by the DFG (German Research Foundation) Transregional Collaborative Research Center ArctiC Amplication: Climate Relevant Atmospheric and SurfaCe Processes, and Feedback Mechanisms (AC)3 (Project C03, grant no. 268020496 – TRR 172) and by the ESA S5P+Innovation Theme 7 Ocean Colour (S5POC) project (grant no. 4000127533/19/I-NS). Svetlana N. Losa's work was also

partly made in the framework of the state assignment of the Federal Agency for Scientific Organizations (FASO) Russia (theme FMWE-2021-0014). The contribution by Leonardo M. A. Alvarado was supported by the Federal Ministry of Economics and Technology (BMWi) and German Aerospace Center (DLR) (grant no. 50EE1915) within the project TypSynSat. We also thank Gavin Tilstone (PML), Giorgio Dall'Olmo (OGS) and Robert Brewin (University of Exeter) for AMT28 and AMT29 pigment data. Thanks to NASA, ESA and EUMETSAT for the SeaWiFS, MODIS, VIIRS, MERIS and OLCI data and especially the ACRI-ST GlobColour team for providing OLCI and merged ocean colour L3 products. The captain, crew and expedition scientists are also acknowledged for their support during the expeditions. We finally thank Sorin Constantin and the other two anonymous reviewers who helped to improve this work by providing constructive comments.

Financial support. This research has been supported by the H2020 European Research Council (grant no. 810139), European Commission (EC) (grant no. 21036L05B-COP-INNO SCI-9000), the Deutsche Forschungsgemeinschaft (grant no. 268020496), European Space Agency (grant no. 4000127533/19/I-NS-S5P+I-OC), Federal Agency for Scientific Organizations (FASO) Russia (grant no. FMWE-2021-0014), and Federal Ministry of Economics and Technology (BMWi) and German Aerospace Center (DLR) (grant no. 50EE1915).

Review statement. This paper was edited by Marilaure Grégoire and reviewed by Sorin Constantin and two anonymous referees.

References

Aiken, J., Pradhan, Y., Barlow, R., Lavender, S., Poulton, A., Holligan, P., and Hardman-Mountford, N.: Phytoplankton pigments and functional types in the Atlantic Ocean: A decadal assessment, 1995–2005, Deep-Sea Res. Pt. II, 56, 899–917, https://doi.org/10.1016/j.dsr2.2008.09.017, 2009.

Alvarado, L. M. A., Soppa, M. A., Gege, P., Losa, S. N., Dröscher, I., Xi, H., and Bracher, A.: Retrievals of the main phytoplankton groups at Lake Constance using OLCI, DESIS, and evaluated with field observations, 12th EARSeL Workshop on Imaging Spectroscopy, Potsdam, Germany, 22–24 June 2022, https://elib.dlr.de/189789, 2022.

Amante, C. and Eakins, B. W.: ETOPO1 1 Arc-Minute Global Relief Model: Procedures, data sources and analysis, NOAA technical memorandum NESDIS NGDC-24, National Geophysical Data Center, NOAA [data set], https://doi.org/10.7289/V5C8276M, 2009.

Antoine, D., Morel, A., Gordon, H. R., Banzon, V. F., and Evans, R. H.: Bridging ocean color observations of the 1980s and 2000s in search of long-term trends, J. Geophys. Res.-Oceans, 110, C06009, https://doi.org/10.1029/2004JC002620, 2005.

Behrenfeld, M. J., O'Malley R. T., Boss, E. S., Westberry, T. K., Graff, J. R., Halsey, K. H., Milligan, A. J., Siegel, D. A., and Brown, M. B.: Revaluating ocean warming impacts on global phytoplankton, Nat. Clim. Change, 6, 3223–3330, https://doi.org/10.1038/nclimate2838, 2016.

Bindoff, N. L., Cheung, W. W. L., Kairo, J. G., Arístegui, J., Guinder, V. A., Hallberg, R., Hilmi, N., Jiao, N., Karim, M. S., Levin, L., O'Donoghue, S., Purca Cuicapusa, S. R., Rinkevich, B., Suga, T., Tagliabue, A., and Williamson, P.: Changing Ocean, Marine Ecosystems, and Dependent Communities, in: IPCC Special Report on the Ocean and Cryosphere in a Changing Climate, edited by: Pörtner, H.-O., Roberts, D. C., Masson-Delmotte, V., Zhai, P, Tignor, M., Poloczanska, E., Mintenbeck, K., Alegría, A., Nicolai, M., Okem, A., Petzold, J., Rama, B., and Weyer, N. M., Cambridge University Press, Cambridge, UK and New York, NY, USA, 447–587, https://doi.org/10.1017/9781009157964.007, 2019.

Bolaños, L. M., Karp-Boss, L., Choi, C. J., Worden, A. Z., Graff., J. R., Haëntjens, N., Chase, A. P., Della Penna, A., Gaube, P., Morison, F., Menden-Deuer, S., Westberry, T. K., O'Malley, R. T., Boss, E., Behrenfeld, M. J., and Glovannoni, S. J.: Small phytoplankton dominate western North Atlantic biomass, The ISME Journal, 14, 1663–1674, https://doi.org/10.1038/s41396-020-0636-0, 2020.

Bracher, A., Bouman, H. A., Brewin, R. J. W., Bricaud, A., Brotas, V., Ciotti, A. M., Clementson, L., Devred, E., Di Cicco, A., Dutkiewicz, S., Hardman-Mountford, N. J., Hickman, A. E., Hieronymi, M., Hirata, T., Losa, S. N., Mouw, C. B., Organelli, E., Raitsos, D. E., Uitz, J., Vogt, M., and Wolanin, A.: Obtaining phytoplankton diversity from ocean color: a scientific roadmap for future development, Front. Mar. Sci., 4, 1–15, https://doi.org/10.3389/fmars.2017.00055, 2017.

Bracher, A., Xi, H., Dinter, T., Mangin, A., Strass, V. H., von Appen, W.-J., and Wiegmann, S.: High resolution water column phytoplankton composition across the Atlantic Ocean from ship-towed vertical undulating radiometry, Front. Mar. Sci., 7, 235, https://doi.org/10.3389/fmars.2020.00235, 2020.

Bracher, A., Brewin, R. J. W., Ciotti, A. M., Clementson, L. A., Hirata, T., Kostadinov, T., Mouw, C. B., and Organelli, E.: Applications of satellite remote sensing technology to the analysis of phytoplankton community structure on large scales, in: Advances in Phytoplankton Ecology, edited by: Clementson, L. A., Eriksen, R. S., and Willis, A., Elsevier, 217–244, https://doi.org/10.1016/B978-0-12-822861-6.00015-7, 2022.

Brewin, R. J. W., Sathyendranath, S., Jackson, T., Barlow, R., Brotas, V., Airs, R., and Lamont, T.: Influence of light in the mixed-layer on the parameters of a three-component model of phytoplankton size class, Remote Sens. Environ., 168, 437–450, https://doi.org/10.1016/j.rse.2015.07.004, 2015.

Brewin, R. J. W., Tilstone, G. H., Jackson, T., Cain, T., Miller, P. I., Lange, P. K., Misra, A., and Airs, R. L.: Modelling size-fractionated primary production in the Atlantic Ocean from remote sensing, Prog. Oceanogr., 158, 130–149, https://doi.org/10.1016/j.pocean.2017.02.002, 2017.

Brotas, V., Brewin, R. J. W., Sa, C., Brito, A. C., Silva, A., Mendes, C. R., Diniz, T., Kaufmann, M., Tarran, G., Groom, S. B., Platt, T., and Sathyendranath, S.: Deriving phytoplankton size classes from satellite data: Validation along a trophic gradient in the eastern Atlantic Ocean, Remote Sens. Environ., 134, 66–77, https://doi.org/10.1016/j.rse.2013.02.013, 2013.

Brotas, V., Tarran, G. A., Veloso, V., Brewin, R. J. W., Woodward, E. M. S., Airs, R., Beltran, C., Ferreira, A., and Groom, S. B.: Complementary Approaches to Assess Phytoplankton Groups and Size Classes on a Long Tran-

sect in the Atlantic Ocean, Front. Mar. Sci., 8, 682621, https://doi.org/10.3389/fmars.2021.682621, 2022.

Colella, S., Böhm, E., Cesarini, C., Garnesson, P., Netting, J., and Calton, B.: EU Copernicus Marine Service Product User Manual for Ocean Colour Products, Issue 3.0, Mercator Ocean International, https://catalogue.marine.copernicus.eu/documents/PUM/CMEMS-OC-PUM.pdf (last access: 22 March 2023), 2022.

Deppeler, S. L. and Davidson, A. T.: Southern Ocean Phytoplankton in a Changing Climate, Front. Mar. Sci., 4, 40, https://doi.org/10.3389/fmars.2017.00040, 2017.

EU Copernicus Marine Service Product: Global Ocean Colour (Copernicus-GlobColour), Bio-Geo-Chemical, L4 (monthly and interpolated) from Satellite Observations (1997-ongoing), Mercator Ocean International [data set], https://doi.org/10.48670/moi-00281, 2022.

Flanders Marine Institute: Longhurst Provinces, Marine Regions, Flanders Marine Institute [data set], https://www.marineregions.org/sources.php#longhurst (last access: 5 May 2022), 2009.

Flombaum, P., Gallegos, J. L., Gordillo, R. A., Rincon, J., Zabala, L. L., Jiao, N., Karl, D. M., Li, W. K. W., Lomas, M. W., Veneziano, D., Vera, C. S., Vrugt, J. A., and Martiny, A. C.: Present and future global distributions of the marine Cyanobacteria Prochlorococcus and Synechococcus, P. Natl. Acad. Sci. USA, 110, 9824–9829, https://doi.org/10.1073/pnas.1307701110, 2013.

Garnesson, P., Mangin, A., Bretagnon, M., and Jutard, Q.: EU Copernicus Marine Service Quality Information Document (QUID) for OC TAC Products OCEANCOLOUR OBSERVATIONS GlobColour, Issue 3.0, Mercator Ocean International, https://catalogue.marine.copernicus.eu/documents/QUID/CMEMS-OC-QUID-009-101to104-111-113-116-118.pdf (last access: 22 March 2023), 2022.

Gregg, W. W. and Rousseaux, C. S.: Decadal trends in global pelagic ocean chlorophyll: A new assessment integrating multiple satellites, in situ data, and models, J. Geophys. Res.-Oceans, 119, 5921–5933, https://doi.org/10.1002/2014JC010158, 2014.

Gruber, N.: Warming up, turning sour, losing breath: Ocean biogeochemistry under global change, Philos. T. Roy. Soc. A, 369, 1980–1996, https://doi.org/10.1098/rsta.2011.0003, 2011.

Gruber, N., Boyd, P. W., Frölicher T. L., and Vogt, M.: Biogeochemical extremes and compound events in the ocean, Nature, 600, 395–407, https://doi.org/10.1038/s41586-021-03981-7, 2021.

Head, E. J. H. and Pepin, P.: Monitoring changes in phytoplankton abundance and composition in the Northwest Atlantic: a comparison of results obtained by continuous plankton recorder sampling and colour satellite imagery, J. Plankton Res., 32, 1649–1660, https://doi.org/10.1093/plankt/fbq120, 2010.

Henson, S. A., Sarmiento, J. L., Dunne, J. P., Bopp, L., Lima, I., Doney, S. C., John, J., and Beaulieu, C.: Detection of anthropogenic climate change in satellite records of ocean chlorophyll and productivity, Biogeosciences, 7, 621–640, https://doi.org/10.5194/bg-7-621-2010, 2010.

Henson, S. A., Beaulieu, C., and Lampitt, R.: Observing climate change trends in ocean biogeochemistry: when and where, Glob. Change Biol., 22, 1561–1571, https://doi.org/10.1111/gcb.13152, 2016.

Hirata, T., Hardman-Mountford, N. J., Brewin, R. J. W., Aiken, J., Barlow, R., Suzuki, K., Isada, T., Howell, E., Hashioka, T., Noguchi-Aita, M., and Yamanaka, Y.: Synoptic relationships between surface Chlorophyll-*a* and diagnostic pigments specific to phytoplankton functional types, Biogeosciences, 8, 311–327, https://doi.org/10.5194/bg-8-311-2011, 2011.

IOCCG: Phytoplankton Functional Types from Space, in: Reports of International Ocean Colour Coordinating Group (IOCCG), Report Number 15, edited by: Sathyendranath, S., IOCCG, Dartmouth, Nova Scotia, Canada, 154 pp., https://doi.org/10.25607/OBP-106, 2014.

Jackson, T.: ESA Ocean Colour Climate Change Initiative – Phase 3 Product, User Guide for v5.0 Dataset, Issue 1.0, ESA/ESRIN, https://docs.pml.space/share/s/okB2fOuPT7Cj2r4C5sppDg (last access: 30 March 2023), 2020.

Käse, L. and Geuer, J. K.: Phytoplankton Responses to Marine Climate Change – An Introduction, in: YOUMARES 8 – Oceans Across Boundaries: Learning from each other, edited by: Jungblut, S., Liebich, V., and Bode B., SpringerOpen, Cham, Switzerland, 55–71, https://doi.org/10.1007/978-3-319-93284-2, 2018.

Kulk, G., Platt, T., Dingle, J., Jackson, T., Jönsson, B. F., Bouman, H. A., Babin, M., Brewin, R. J. W., Doblin, M., Estrada, M., Figueiras, F. G., Furuya, K., González-Benítez, N., Gudfinnsson, H. G., Gudmundsson, K., Huang, B., Isada, T., Kovac, Z., Lutz, V. A., Maranon, E., Raman, M., Richardson, K., Rozema, P. D., van de Poll, W. H., Segura, V., Tilstone, G. H., Uitz, J., van Dongen-Vogels, V., Yoshikawa, T., and Sathyendranath, S.: Primary Production, an Index of Climate Change in the Ocean: Satellite-Based Estimates over Two Decades, Remote Sens.-Basel, 12, 826, https://doi.org/10.3390/rs12050826, 2020.

Lange, P. K., Werdell, P. J., Erickson, Z. K., Dall'Olmo, G., Brewin, R. J. W., Zubkov, M. V., Tarran, G. A., Bouman, H. A., Slade, W. H., Craig, S. E., Poulton, N. J., Bracher, A., Lomas, M. W., and Cetinić, I.: Radiometric approach for the detection of picophytoplankton assemblages across oceanic fronts, Opt. Express, 28, 25682–25705, https://doi.org/10.1364/OE.398127, 2020.

Longhurst, A. R.: Ecological Geography of the Sea, Academic Press, Cambridge, Massachusetts, U.S.A., 542 pp., https://doi.org/10.1016/B978-0-12-455521-1.X5000-1, 2007.

Losa, S. N., Soppa, M. A., Dinter, T., Wolanin, A., Brewin, R. J. W., Bricaud, A., Oelker, J., Peeken, I., Gentili, B., Rozanov, V., and Bracher, A.: Synergistic Exploitation of Hyper- and Multi-Spectral Precursor Sentinel Measurements to Determine Phytoplankton Functional Types (SynSenPFT), Front. Mar. Sci., 4, 1–22, https://doi.org/10.3389/fmars.2017.00203, 2017.

McClain, C. R.: A decade of satellite ocean color observations, Annu. Rev. Mar. Sci., 1, 19–42, https://doi.org/10.1146/annurev.marine.010908.163650, 2009.

Mélin, F. and Franz, B. A.: Chapter 6.1 – Assessment of satellite ocean colour radiometry and derived geophysical products, Experimental Methods in the Physical Sciences, 47, 609–638, https://doi.org/10.1016/B978-0-12-417011-7.00020-9, 2014.

Moisan, T. A., Rufty, K. M., Moisan, J. R., and Linkswiler, M. A.: Satellite Observations of Phytoplankton Functional Type Spatial Distributions, Phenology, Diversity, and Ecotones, Front. Mar. Sci., 4, 189, https://doi.org/10.3389/fmars.2017.00189, 2017.

Neukermans, G., Oziel, L., and Babin, M.: Increased intrusion of warming Atlantic water leads to rapid expansion of temperate phytoplankton in the Arctic, Glob. Change Biol., 24, 2545–2553, https://doi.org/10.1111/gcb.14075, 2018.

Nöthig, E. M., Bracher, A., Engel, A., Metfies, K., Niehoff, B., Peeken, I., Bauerfeind, E., Cherkasheva, A., Gäbler-Schwarz, S., Hardge, K., Kilias, E., Kraft, A., Kidane, Y. M., La-

lande, C., Piontek, J., Thomisch, K., and Wurst, M.: Summertime plankton ecology in Fram Strait – a compilation of long- and short-term observations, Polar Res., 34, 23349, https://doi.org/10.3402/polar.v34.23349, 2015.

Nöthig, E. M., Ramondenc, S., Haas, A., Hehemann, L., Walter, A., Bracher, A., Lalande, C., Metfies, K., Peeken, I., Bauerfeind, E., and Boetius, A.: Summertime Chlorophyll a and Particulate Organic Carbon Standing Stocks in Surface Waters of the Fram Strait and the Arctic Ocean (1991–2015), Front. Mar. Sci., 7, 350, https://doi.org/10.3389/fmars.2020.00350, 2020.

Oziel, L., Baudena, A., Ardyna, M., Massicotte, P., Randelhoff, A., Sallée, J.-B., Ingvaldsen, R. B., Devred, E., and Babin, M.: Faster Atlantic currents drive poleward expansion of temperate phytoplankton in the Arctic Ocean, Nat. Commun., 11, 1705, https://doi.org/10.1038/s41467-020-15485-5, 2020.

Pardo, S., Jackson, T., Taylor, B., Netting, J., Calton, B., and Howey, B.: EU Copernicus Marine Service Quality Information Document (QUID) for OC TAC Products – Atlantic and Arctic Observation Products, Issue 2.2, Mercator Ocean International, https://catalogue.marine.copernicus.eu/documents/QUID/CMEMS-OC-QUID-009-066-067-068-069-088-091.pdf (last access: 22 March 2022), 2020.

Quéré, C. L., Harrison, S. P., Colin Prentice, I., Buitenhuis, E. T., Aumont, O., Bopp, L., Claustre, H., Cotrim Da Cunha, L., Geider, R., Giraud, X., Klaas, C., Kohfeld, K. E., Legendre, L., Manizza, M., Platt, T., Rivkin, R. B., Sathyendranath, S., Uitz, J., Watson, A. J., and Wolf-Gladrow, D.: Ecosystem dynamics based on plankton functional types for global ocean biogeochemistry models, Glob. Change Biol., 11, 2016–2040, https://doi.org/10.1111/j.1365-2486.2005.1004.x, 2005.

Reyes-Prieto, A., Yoon, H. S., and Bhattacharya, D.: Marine Algal Genomics and Evolution, in: Encyclopedia of Ocean Sciences, 2nd edn., edited by: Steele, J. H., Academic Press, 552–559, https://doi.org/10.1016/B978-012374473-9.00779-7, 2009.

Sathyendranath, S., Brewin, R. J. W., Brockmann, C., Brotas, V., Calton, B., Chuprin, A., Cipollini, P., Couto, A. B., Dingle, J., Doerffer, R., Donlon, C., Dowell, M., Farman, A., Grant, M., Groom, S., Horseman, A., Jackson, T., Krasemann, H., Lavender, S., Martinez-Vicente, V., Mazeran, C., Mélin, F., Moore, T. S., Müller, D., Regner, P., Roy, S., Steele, C., Steinmetz, F., Swinton, J., Taberner, M., Thompson, A., Valente, A., Zühlke, M., Brando, V. E., Feng, H., Feldman, G., Franz, B. A., Frouin, R., Gould, R. W., Hooker, S. B., Kahru, M., Kratzer, S., Mitchell, B. G., Muller-Karger, F. E., Sosik, H. M., Voss, K. J., Werdell, J., and Platt, T.: An ocean-colour time series for use in climate studies: The experience of the Ocean-Colour Climate Change Initiative (OC-CCI), Sensors, 19, 4285, https://doi.org/10.3390/s19194285, 2019.

Soppa, M. A., Völker, C., and Bracher, A.: Diatom Phenology in the Southern Ocean: Mean Patterns, Trends and the Role of Climate Oscillations, Remote Sens.-Basel, 8, 420, https://doi.org/10.3390/rs8050420, 2016.

Uitz, J., Claustre, H., Morel, A., and Hooker, S. B.: Vertical distribution of phytoplankton communities in open ocean: An assessment based on surface chlorophyll, J. Geophys. Res.-Oceans, 111, C08005, https://doi.org/10.1029/2005JC003207, 2006.

van Oostende, M., Hieronymi, M., Krasemann, H., Baschek, B., and Röttgers, R.: Correction of inter-mission inconsistencies in merged ocean colour satellite data, Front. Remote Sens., 3, 1–17, https://doi.org/10.3389/frsen.2022.882418, 2022.

Vidussi, F., Claustre, H., Manca, B. B., Luchetta, A., and Marty, J.-C.: Phytoplankton pigment distribution in relation to upper thermocline circulation in the eastern Mediterranean Sea during winter, J. Geophys. Res.-Oceans, 106, 19939–19956, https://doi.org/10.1029/1999JC000308, 2001.

von Schuckmann, K., Le Traon, P.., Smith, N., Pascual, N., Samuel Djavidnia, S., Gattuso, J., and Grégoire, M. (Eds.): Copernicus Marine Service Ocean State Report, Issue 5 Supplement, J. Oper. Oceanogr., 14, 1–185, https://doi.org/10.1080/1755876X.2021.1946240, 2021.

Xi, H., Losa, S. N., Mangin, A., Soppa, M. A., Garnesson, P., Demaria, J., Liu, Y., d'Andon, O. H. F., and Bracher, A.: A global retrieval algorithm of phytoplankton functional types: Towards the applications to CMEMS GlobColour merged products and OLCI data, Remote Sens. Environ., 240, 111704, https://doi.org/10.1016/j.rse.2020.111704?, 2020.

Xi, H., Losa, S. N., Mangin, A., Garnesson, P., Bretagnon, M., Demaria, J., Soppa, M. A., d'Andon, O. H. F., and Bracher, A.: Global chlorophyll *a* concentrations of phytoplankton functional types with detailed uncertainty assessment using multi-sensor ocean color and sea surface temperature satellite products, J. Geophys. Res.-Oceans, 126, e2020JC017127, https://doi.org/10.1029/2020JC017127, 2021.

Xi, H., Peeken, I., Gomes, M., Brotas, V., Tilstone, G., Brewin, R. J. W., Dall'Olmo, G., Tracana, A., Alvarado, L. M. A., Murawski, S., Wiegmann, S., and Bracher, A.: Phytoplankton pigment concentrations and phytoplankton groups measured on water samples collected from various expeditions in the Atlantic Ocean from 71° S to 84° N, PANGAEA [data set], https://doi.org/10.1594/PANGAEA.954738, 2023.

Yang, B., Boss, E. S., Haëntjens, N., Long, M. C., Behrenfeld, M. J., Eveleth, R., and Doney, S. C.: Phytoplankton phenology in the North Atlantic: Insights from profiling float measurements, Front. Mar. Sci., 7, 139, https://doi.org/10.3389/fmars.2020.00139, 2020.

State Planet, 1-osr7, 6, 2023
https://doi.org/10.5194/sp-1-osr7-6-2023

The dynamical role of upper layer salinity in the Mediterranean Sea

Ali Aydogdu[1], Pietro Miraglio[1], Romain Escudier[2], Emanuela Clementi[1], and Simona Masina[1]

[1]Ocean Modeling and Data Assimilation Division, Fondazione Centro Euro-Mediterraneo sui Cambiamenti Climatici, Bologna, Italy
[2]Observations pour Les Systèmes D'analyse et de Prévision, Mercator Ocean International, Toulouse, France

Correspondence: Ali Aydogdu (ali.aydogdu@cmcc.it)

Received: 25 August 2022 – Discussion started: 26 September 2022
Revised: 14 April 2023 – Accepted: 2 May 2023 – Published: 27 September 2023

Abstract. The Mediterranean Sea (MED) is a semi-enclosed basin with an excess amount of evaporation compared to the water influx through precipitation at the surface and river runoff on the land boundaries. The deficit in the water budget is balanced by the inflow in the Strait of Gibraltar and Turkish Straits System connecting the Mediterranean with the less saline Atlantic Ocean and the Black Sea, respectively. There is evidence that the Mediterranean region is a hotspot in a warming climate, which will possibly change the water cycle significantly, but with large uncertainties. Therefore, it is inevitable to monitor the evolution of the essential ocean variables (EOVs) to respond to the associated risks and mitigate the related problems. In this work, we evaluate the evolution of the salinity content and anomaly between 0–300 m in the Mediterranean Sea during the last decades using the Copernicus Marine Service reanalysis and in situ objective analysis products. The results show an increasing mean salinity with a stronger trend in the eastern Mediterranean (EMED) basin. The spread of the products implies a larger variability in the western Mediterranean (WMED) basin, while the standard deviation is lower in the eastern side, especially in the Ionian and the Levantine basins.

1 Introduction

The Mediterranean Sea (MED) is warming (Pisano et al., 2020). It is evaporating more and more (Skliris et al., 2018; Jordà et al., 2017) with marine heat waves increasing in intensity, duration and frequency (Juza et al., 2022; Dayan et al., 2022). The Mediterranean region is a hotspot with global warming (Tuel and El Tahir, 2020) that will likely alter the water cycle (Cos et al., 2022). Tracking the changes of the essential ocean variables (EOVs) is crucial in order to understand the impact of climate change. Two of these EOVs are linked to the ocean salinity at the surface and subsurface, which will be affected significantly by the surface heat and freshwater fluxes. The global water cycle modulating the ocean salinity is a key element of the Earth's climate (Cheng et al., 2020). In the Mediterranean Sea, freshwater fluxes through the land (rivers) and atmosphere (evaporation and precipitation) are balanced by two sea straits, namely Gibraltar and Dardanelles, from which the less saline Atlantic Ocean and Black Sea waters flow into the basin with an annual net inflow of 0.78 ± 0.05 Sv (Soto-Navarro et al., 2010) and 0.05 ± 0.04 Sv (Jarosz et al., 2013), respectively. These density contrasts contribute to the wind-driven circulation and generate a highly energetic anti-estuarine circulation (Cessi et al., 2014). The salinity of the Atlantic Waters (AW) entering through the Straight of Gibraltar is about 36.2 psu. The salinity of the Dardanelles Strait can vary significantly and it can be as low as 27 psu (Aydogdu et al., 2018; Sannino et al., 2017). Recently, Fedele et al. (2022) studied the characterisation of the Atlantic Waters and Levantine intermediate waters (LIW) from the Argo profiles in the last 20 years. Their conclusion is a clear salinification and warming trend which characterised both AW and LIW over the last 2 decades. Skliris et al. (2018) argue that the Mediterranean basin salinification is driven by changes in the regional water cycle rather than by changes in salt transports at the straits, as it is shown by the water mass transformation

Published by Copernicus Publications.

Table 1. Products from Copernicus Marine Service used in this study.

Product ref. no.	Product ID and type	Data access	Documentation
1	MEDSEA_MULTIYEAR_PHY_006_004 (MEDREA24, multi-year product) [1987–2021], numerical models	EU Copernicus Marine Service Product (2022a)	Quality Information Document (QUID): Escudier et al. (2022) Product User Manual (PUM): Lecci et al. (2022)
2	MEDSEA_MULTIYEAR_PHY_006_004 (MEDREA24, INTERIM product) [2021], numerical models	EU Copernicus Marine Service Product (2022b)	QUID: Escudier al. (2022) PUM: Lecci et al. (2022)
3	GLOBAL_REANALYSIS_PHY_001_031 (GREP) [1993–2019], numerical models	EU Copernicus Marine Service Product (2022c)	QUID: Desportes et al. (2022) PUM: Gounou et al. (2022)
4	INSITU_GLO_PHY_TS_OA_MY_013_052 (CORA) [1993–2020], in situ observations	EU Copernicus Marine Service Product (2022d)	QUID: Szekely (2022a) PUM: Szekely (2022b)
5	MULTIOBS_GLO_PHY_TSUV_3D_ MYNRT_015_012 (ARMOR3D) [1993–2020], in situ observations and satellite observations	EU Copernicus Marine Service Product (2021)	QUID: Grenier et al. (2021) PUM: Guinehut (2021)

distribution in salinity coordinates. However, we will show that there is a bigger uncertainty compared to most of the basin in the radius of influence of both the Gibraltar and Dardanelles straits. In Sect. 2, the data and methods used in this study are presented. In Sect. 3, the results are shown and discussed, while in Sect. 4, the conclusions are drawn.

2 Data and methods

In this study, the Copernicus Marine Service global and regional reanalyses as well as observational gridded products are used to explore the role of the salinity variability in the 0–300 m depth among different estimates as well as temporal and spatial anomalies against a mean.

The Mediterranean $1/24°$ resolution regional reanalysis (hereinafter, MEDREA24; Escudier et al., 2021) from the Copernicus Marine Service is used as a regional high-resolution product. In this work, MEDREA24 and its interim extension until the end of 2021 are included. Moreover, the $1/4°$ resolution Global Reanalysis Ensemble Product (hereinafter, GREP) is also used. It consists of the global reanalysis from Mercator Ocean's GLORYS2V4 (Lellouche et al., 2013), UK MetOffice's GLOSEA5v13 (MacLachlan et al., 2014) using the Forecasting Ocean Assimilation Model (FOAM) system (Blockley et al., 2014), CMCC C-GLORSv7 (Storto et al., 2016) and ECMWF's ORAS5 (Zuo et al., 2017). A study on the ocean heat content and steric sea level representation in the GREP ensemble can be found in Storto et al. (2019a). A more general status of the global ocean reanalysis is reviewed in Storto et al. (2019b). The period covered by the GREP is 1993–2019.

As observational products, the gridded reconstructions of CORA (Szekely et al., 2019) and ARMOR3D (Guinehut et al., 2012) are adopted. Both datasets are available between 1993 and 2020. In the CORA, the objective analysis is performed on measurements' anomalies relative to a first guess provided by monthly climatology for different decades in the World Ocean Atlas 2013 to accurately reproduce the climate tendencies; it is interpolated and centred on the 15th of each month. Instead, in ARMOR3D, the first guess is adopted from World Ocean Atlas 2018. Both products use an objective analysis method proposed by Bretherton et al. (1976).

The investigation is performed in the entire Mediterranean Sea (MED) as well as in the eastern (EMED) and western (WMED) basins, which have very different characteristics. The salinity mean ($\overline{S}$) is computed using Eq. (1) as the monthly volume (V) average of each product between 0 and 300 m depth, i.e. excluding the shelf areas close to the coast with a depth less than 300 m.

$$\overline{S} = \frac{1}{V}\int_V S dV \tag{1}$$

The mean of different products and their standard deviation are evaluated in the common period 1993–2019. Besides this time frame, the CORA and ARMOR3D time series are available until 2020, while the MEDREA24 time series is provided up to 2021 (last 6 months extended in interim mode).

The salinity anomalies are computed using Eq. (2). The difference of the salinity, S, with a reference salinity, S_{ref},

is normalised by the depth of the water column, which is constant in our case with $z_2 = 300$ m and $z_1 = 0$ m.

$$S_A = \int_{z_1}^{z_2} \frac{S - S_{ref}}{z_2 - z_1} dz \quad (2)$$

Equation (2) is a modified version of the one proposed in Boyer et al. (2007), which uses the salinity as a proxy for the equivalent freshwater content. This method has been later adopted in various studies including, among the others, Holliday et al. (2020), with a density weight to account for baroclinic properties of the water column. The formulation in Boyer et al. (2007) is based on a reference salinity. As an example, mean values of a basin (Aagaard and Carmack, 1989) is a widely used choice for S_{ref} in global freshwater content calculations. However, it is argued that since a reference value can be chosen arbitrarily, this would bring ambiguity (Schauer and Losch, 2019) in computing the equivalent freshwater content. Therefore, in this study, we propose to evaluate the salinity content and anomaly following Eq. (2) by choosing S_{ref} as a monthly climatology of each dataset computed from each product separately between 1993 and 2014. This period is chosen to be consistent with the Ocean Monitoring Indicators produced previously in the Mediterranean Sea and other Copernicus Marine domains. Furthermore, the calculations are performed in the entire Mediterranean Sea (MED) as well as in its western (WMED) and eastern (EMED) subbasins, separated at the Sicily Strait. In Fig. 1, we present the monthly variation of the S_{ref} as an example only, the one from MEDREA24, which shows a clear difference in the seasonality in the EMED and WMED, with a maximum in March and December, respectively. It is also evident that the Mediterranean monthly salinity reference shows a seasonal cycle much similar to the one of the eastern basin (but with different magnitude) characterised by lower salinity during the summer period and larger values at the end of the year.

3 Results and discussion

The Copernicus Marine Service products described in the previous section allow the assessment of the salinity content of the Mediterranean Sea along with its anomalies and trends during the last decades.

In Fig. 2, we present the time series of the mean salinity content in the first 300 m derived from the analysed products (MEDREA24 in red, GREP ensemble mean in blue, GREP ensemble members in thin light blue, CORA in dark green, ARMOR3D in light green) and their overall mean (in black) and spread (shaded grey).

During the early 1990s in the entire Mediterranean Sea (Fig. 2a), there is a large spread in salinity with the observations showing a higher salinity, while the reanalysis products present relatively lower salinity. This is the case until 2005. Coinciding with the global coverage of the Argo profilers in the early 2000s following the efforts in the Global Ocean Data Assimilation (GODAE) together with the Climate Variability and Predictability Programme (CLIVAR) and the Global Climate Observing System/Global Ocean Observing System (GCOS/GOOS), the spread among different products narrows. Possibly, the reanalyses are better constrained through data assimilation with this novel observation type (Johnson et al., 2022), which provides high-resolution and high-frequency temperature and salinity profiles all over the world's oceans, while the observation-based gridded products become more confident. The maximum spread between the period 1993–2019 occurs in the 1990s with a value of 0.096 psu, and it decreases to as low as 0.009 psu by the end of the 2010s. The mean salinity computed in the entire Mediterranean Sea from all products varies between approximately 38.5 and 38.6 psu with a spatiotemporal mean of 38.57 psu (Table 2).

Table 2. The temporal mean salinity (in psu) and trend (in psu per year) in the 0–300 m between the common period 1993–2019 for separate products and their overall mean in Fig. 2.

psu (psu yr^{-1})	MED	WMED	EMED
MEDREA24	38.58 (0.0070)	38.15 (0.0055)	38.83 (0.0078)
GREP	38.48 (0.0110)	38.01 (0.0111)	38.87(0.0106)
CORA	38.61 (0.0020)	38.21(0.0019)	38.84 (0.0024)
ARMOR3D	38.64 (0.0027)	38.24 (0.0020)	38.75(0.0032)
Mean	38.57 (0.0056)	38.16 (0.0049)	38.87 (0.0061)

In the western Mediterranean (Fig. 2b), the overall mean is centred around 38.16 psu with a larger spread – with a maximum and minimum of 0.172 psu and 0.026, respectively – occurring in the early 2000s. An increase of the mean salinity in 2005 is evident from all the reanalysis products and, to a lesser extent, from the CORA dataset, for which one of the many possible reasons is the regime shift as discussed in Schroeder et al. (2016), corresponding to a major deep-water formation event at the beginning of the Western Mediterranean Transition (Zunino et al., 2012).

In the eastern Mediterranean (Fig. 2c), the overall mean is centred around 38.87 psu with a lower spread compared to the western basin, with a maximum and minimum of 0.086 psu and 0.003, respectively.

Overall, for the period between 1993–2019, we note that the observational products, gridded using optimal interpolation statistical techniques, show a higher average salinity compared to the reanalysis products that are dynamically integrated and corrected through data assimilation. The spread is representing the offset of the products more than their variability in the entire Mediterranean Sea, as well as in its eastern and western subdomains.

All the products show a positive trend between 1993–2019 (in parenthesis in Table 2). The trend in the mean of all products is calculated as 0.0056 psu yr^{-1}. This trend is consistent with the estimates between 1950–2002 of Skliris et al. (2018)

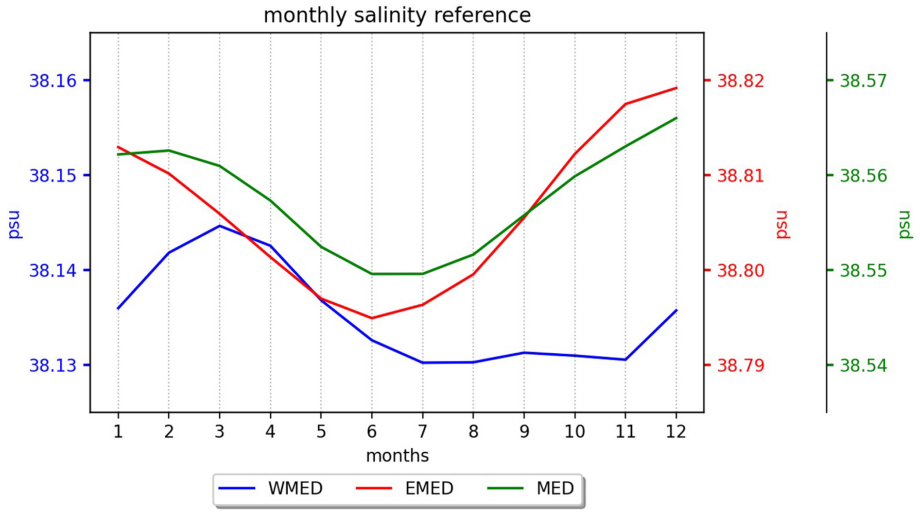

Figure 1. The monthly reference salinity S_{ref} estimates calculated from the MEDREA24 in the period 1993–2014. The green, blue and red curves show the MED, WMED and EMED regions, respectively on its corresponding vertical axis. The same calculation is done for each product separately (not shown) to evaluate Eq. (2) to compute salinity anomaly.

from the EN4 and MEDATLAS datasets, which show a trend of 0.0096 ± 0.0077 and 0.0088 ± 0.0092, respectively, in the first 150 m while showing a trend of 0.0067 ± 0.0040 and 0.0067 ± 0.0036 between 150–600 m. The differences in trend in different products that we used are mainly due to the discrepancies at the beginning of the time series. The weak consistency among the reanalyses visible during the first decade is likely due to the lack of observations not sufficient to constrain the different models, which use different physics and initialisation (e.g. Masina and Storto, 2017). The reduction of the spread among the products evolves in parallel to the increase of the observational coverage after the advent of the Argo network. The observational products will be impacted from the scarcity of the observations in the 1990s, since they rely on statistical methods. The trend calculated for each grid point from the MEDREA24, which is the analysed product covering the longest period, is presented in Fig. 2d. The dominant signal in the entire basin is positive with a larger amplitude in the Balearic Sea, Ionian Sea, Adriatic Sea, Western Levantine and with a less evident signal in the Gulf of Lions, Northern Aegean Sea and Eastern Levantine Basin. A small negative trend zone appears in the Alboran Sea. The trend in the entire analysed period is about 0.0049 psu yr^{-1} in the western basin. This is below the rate of the basin-wide trend, which is larger due to the trend in the eastern basin (0.0061 psu yr^{-1}). Differences among different products, especially the objectively analysed observations and GREP, for the trend is larger in the western basin. They are more confined around the mean in the eastern basin, which may also explain the lower spread in this area as discussed below in Fig. 3b.

For 2020, CORA and ARMOR3D products are available, and both continue to sustain the positive trend even though it is less evident in the western basin. Along with its interim extension, MEDREA24 shows an increasing mean salinity until the end of 2021. All products present larger values after 2016 and a maximum in 2018.

The spatial mean, computed between 1993–2014 from all products in the first 300 m (Fig. 3a), shows a gradual increase in the upper ocean integrated salinity from west to east. Minimum salinity occurs close to river mouths, such as in the North Adriatic Sea due to the freshwater input from the Po River, and on the pathways of the outflow of the Dardanelles and Gibraltar straits. The Atlantic Waters, modified through its route, can be traced till the eastern basin from its low salinity. The spread deduced from all the products (Fig. 3b) implies that they agree more, meaning lower spread, in the Levantine and Ionian Seas and to a lesser degree between the Balearic, Sardinia and Corsica islands. The spread is larger especially in the northern Aegean and Adriatic Sea and southwestern coast between the Gulf of Gabes and Strait of Gibraltar. This uncertainty or mismatch in the products is possibly due to the different volume fluxes through the rivers and straits.

In Fig. 4a–c, we show the time series of the salinity anomaly estimates in the western (Fig. 4a), eastern (Fig. 4b) and entire (Fig. 4c) basin from each product using Eq. (2). We recall that the salinity reference is computed for each product per se. Moreover, the salinity anomaly map in 2021 from MEDREA24 is depicted in Fig. 4d, computed against the overall mean between 1993–2014, which is shown in Fig. 3a.

The anomalies have a larger range in the reanalysis products. There is a negative anomaly within the first decade in GREP and MEDREA24 which turns to positive first in the western Mediterranean (Fig. 4a) and followed by the eastern

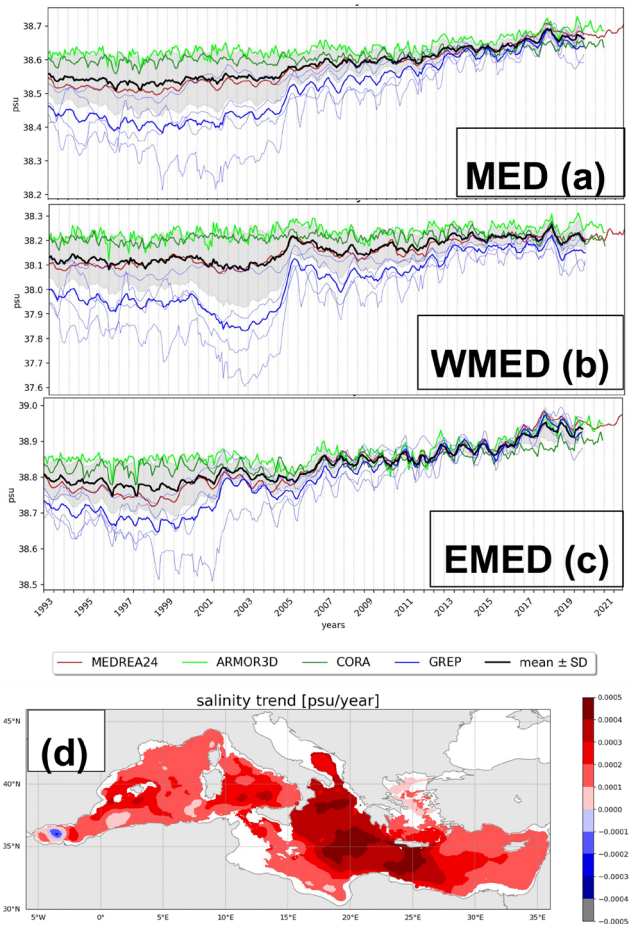

Figure 2. Time series of mean salinity in the upper 300 m in the **(a)** entire Mediterranean Sea, **(b)** western Mediterranean basin and **(c)** eastern Mediterranean basin between the period 1993 and 2021 from MEDREA24, until the end of 2020 for ARMOR3D and CORA, and until the end of 2019 for GREP. The mean of all the products is drawn in black with their standard deviation shaded around the mean. The GREP ensemble members are depicted in thin blue curves. The GREP product covers the period until 2019, while the observational products CORA and ARMOR3D cover the period until 2020. The time series for MEDREA24 is extended until 2021 using the interim products. Panel **(d)** shows the salinity trend in the first 300 m from the MEDREA24 practical salinity unit (psu) per year.

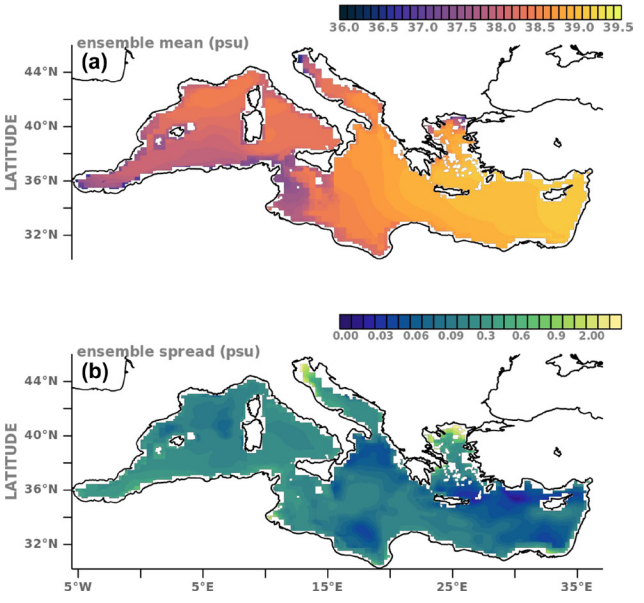

Figure 3. The maps of the **(a)** mean and **(b)** spread of integrated salinity in the period between 1993–2014 in 0–300 m computed from the GREP ensemble mean, CORA, ARMOR3D and MEDREA24 products. We refer to the text for the information on the data products used. The analysis is performed only if the water column is deeper than 300 m. Note that in **(b)**, the colour scale is not linear to show the smaller standard deviation.

Table 3. The temporal mean salinity anomaly (in psu) in the 0–300 m between the common period 1993–2019 for separate products and their average in Fig. 3.

psu	MED	WMED	EMED
MEDREA24	0.026	0.027	0.025
GREP	0.042	0.056	0.034
CORA	0.001	−0.008	0.007
ARMOR3D	0.001	−0.009	0.008
Mean	0.018	0.017	0.019

basin (Fig. 4b) after 2006. In the CORA and ARMOR3D, instead, there is a clear increase in the salinity anomaly in the eastern Mediterranean and the entire basin with a less evident positive trend in the western basin. We summarise the mean salinity anomalies in Table 3.

In 2021, the anomaly is mostly positive, with some negative anomaly structures on the path of the Atlantic Waters (Fig. 4d), Alboran Sea and upwelling favouring the Balearic Islands. Fedele et al. (2022) reports a positive salinity trend in the modified Atlantic and Levantine intermediate waters using 18-year-long (2001–2019) Argo profiles, which in general agrees with the anomaly map to a large extent. However, we note that the spread on the pathway of the water entering from the Strait of Gibraltar and reaching the Levantine basin has a relatively larger spread compared to the deeper areas (see Fig. 3b).

4 Conclusions

In this study, we presented the salinity characteristics of the Mediterranean Sea in the upper 300 m deduced from various products including reanalysis and gridded observational datasets released by the Copernicus Marine Service. The products with dynamically constructed ocean reanalysis and objectively analysed observations show significantly large spread at the beginning of the period of investigation, while

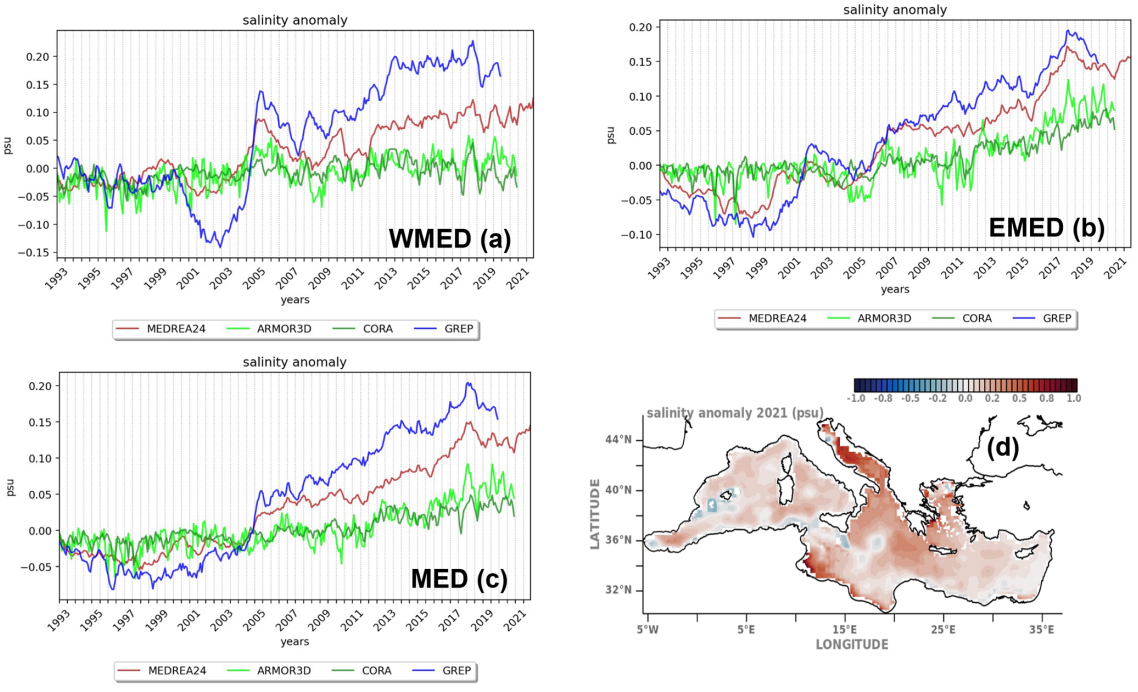

Figure 4. Time series of the salinity anomaly from the MEDREA24, GREP, ARMOR3D and CORA products in the **(a)** western Mediterranean Sea, **(b)** eastern Mediterranean basin and **(c)** entire Mediterranean basin computed with respect to the monthly reference salinity estimates in the corresponding area in Fig. 1 calculated from the MEDREA24 in the period 1993–2014. The GREP products cover the period until 2019, while the observational products CORA and ARMOR3D cover the period until 2020. The time series for MEDREA24 is extended until 2021 using the interim products. Panel **(d)** shows the salinity anomaly in 2021 in the Mediterranean Sea against the mean of salinity in Fig. 3a.

the uncertainty is possibly reduced with the emergence of Argo profilers, which allowed wider spatial sampling and a higher frequency of sampling in the ocean. The mean salinity with its anomaly and trend is computed and analysed in the entire basin as well as in the western and eastern basins for all the datasets separately and averaged. The spatial maps of the mean and the spread of the salinity are depicted and discussed. The overall results show a salinification of the Mediterranean Sea agreeing with earlier studies (e.g. Skliris et al., 2018). The subbasin-scale investigation shows negative salinity anomalies in the western basin in the upwelling regions, which may imply stronger upwelling events, and waterway following the North African coast, which may be a consequence of the freshening North Atlantic water masses (Holliday et al., 2020). There is a large spread in the salinity estimates among different products, which is reduced with the introduction of the Argo profilers in the data assimilation components of the reanalysis systems. Besides the large spread, considering the reported discrepancies in the salinity measurements after 2016 (Barnoud et al., 2021), it is essential to use all available information sources for a more accurate state estimate and uncertainty quantification.

Data availability. All datasets used in this article can be obtained from the Copernicus Marine Service catalogues as described in Table 1 with their names, temporal coverages and documentation.

Author contributions. AA and PM have done the investigation, developed the methodology and performed the data analysis. AA wrote the initial draft. All the authors reviewed and edited the paper.

Competing interests. The contact author has declared that none of the authors has any competing interests.

Disclaimer. Publisher's note: Copernicus Publications remains neutral with regard to jurisdictional claims in published maps and institutional affiliations.

Acknowledgements. We would like to express our thanks to Katrin Schroeder and one anonymous referee for their useful comments, which helped us to improve the paper. We thank to Piero Lionello for his editorial suggestions. Finally, we would like to thank to Karina von Schuckmann for very useful discussions during course of the study.

Financial support. This study has been conducted using EU Copernicus Marine Service Information. This work has been funded through the EU Copernicus Marine Med-MFC Service, lot no. 21002L5-COP-MFC MED-5500.

Review statement. This paper was edited by Piero Lionello and reviewed by Katrin Schroeder and one anonymous referee.

References

Aagaard, K. and Carmack, E. C.: The role of sea ice and other fresh water in the Arctic circulation, J. Geophys. Res.-Oceans, 94, 14485–14498, 1989.

Aydoğdu, A., Pinardi, N., Özsoy, E., Danabasoglu, G., Gürses, Ö., and Karspeck, A.: Circulation of the Turkish Straits System under interannual atmospheric forcing, Ocean Sci., 14, 999–1019, https://doi.org/10.5194/os-14-999-2018, 2018.

Barnoud, A., Pfeffer, J., Guérou, A., Frery, M.-L., Siméon, M., Cazenave, A., Chen, J., Llovel, W., Thierry, V., Legeais, J. F., and Ablain, M.: Contributions of altimetry and Argo to non-closure of the global mean sea level budget since 2016, Geophys. Res. Lett., 48, e2021GL092824, https://doi.org/10.1029/2021GL092824, 2021.

Blockley, E. W., Martin, M. J., McLaren, A. J., Ryan, A. G., Waters, J., Lea, D. J., Mirouze, I., Peterson, K. A., Sellar, A., and Storkey, D.: Recent development of the Met Office operational ocean forecasting system: an overview and assessment of the new Global FOAM forecasts, Geosci. Model Dev., 7, 2613–2638, https://doi.org/10.5194/gmd-7-2613-2014, 2014.

Boyer, T., Levitus, S., Antonov, J., Locarnini, R., Mishonov, A., Garcia, H., and Josey, S. A.: Changes in freshwater content in the North Atlantic Ocean 1955–2006, Geophys. Res. Lett., 34, L16603, https://doi.org/10.1029/2007GL030126, 2007.

Bretherton, F. P., Davis, R. E., and Fandry, C. B.: A technique for objective analysis and design of oceanographic experiments applied to MODE-73, Deep-Sea Res., 23, 559–582, 1976.

Cessi, P., Pinardi, N., and Lyubartsev, V.: Energetics of semienclosed basins with two-layer flows at the strait, J. Phys. Oceanogr., 44, 967–979, 2014.

Cheng, L., Trenberth, K. E., Gruber, N., Abraham, J. P., Fasullo, J. T., Li, G., Mann, M. E., Zhao, X., and Zhu, J.: Improved Estimates of Changes in Upper Ocean Salinity and the Hydrological Cycle, J. Climate, 33, 10357–10381, https://doi.org/10.1175/JCLI-D-20-0366.1, 2020.

Cos, J., Doblas-Reyes, F., Jury, M., Marcos, R., Bretonnière, P.-A., and Samsó, M.: The Mediterranean climate change hotspot in the CMIP5 and CMIP6 projections, Earth Syst. Dynam., 13, 321–340, https://doi.org/10.5194/esd-13-321-2022, 2022.

Dayan, H., McAdam, R., Masina, S., and Speich, S.: Diversity of marine heatwave trends across the Mediterranean Sea over the last decades, in: Copernicus marine service ocean state report, issue 6, J. Oper. Oceanogr., 15, 49–56, 2022.

Desportes, C., Garric, G., Régnier, C., Drévillon, M., Parent, L., Drillet, Y., Masina, S., Storto, A., Mirouze, I., Cipollone, A., Zuo, H., Balmaseda, M., Peterson, D., Wood, R., Jackson, L., Mulet, S., Grenier, E., and Gounou, A.: EU Copernicus Marine Service Quality Information Document for the Global Ocean Ensemble Physics Reanalysis, GLOBAL_REANALYSIS_PHY_001_031, Issue 1.1, Mercator Ocean International, https://catalogue.marine.copernicus.eu/documents/QUID/CMEMS-GLO-QUID-001-031.pdf (last access: 3 May 2023), 2022.

Escudier, R., Clementi, E., Cipollone, A., Pistoia, J., Drudi, M., Grandi, A., Lyubartsev, V., Lecci, R., Aydogdu, A., Delrosso, D., Omar, M., Masina, S., Coppini, G., and Pinardi, N.: A High Resolution Reanalysis for the Mediterranean Sea, Front. Earth Sci., 9, 702285, https://doi.org/10.3389/feart.2021.702285, 2021.

Escudier, R., Clementi, E., Nigam, T., Aydogdu, A., Fini, E., Pistoia, J., Grandi, A., and Miraglio, P.: EU Copernicus Marine Service Quality Information Document for the Mediterranean Sea Physics Reanalysis, MEDSEA_MULTIYEAR_PHY_006_004, Issue 2.3, Mercator Ocean International, https://catalogue.marine.copernicus.eu/documents/QUID/CMEMS-MED-QUID-006-004.pdf (last access: 3 May 2023), 2022.

EU Copernicus Marine Service Product: Multi Observation Global Ocean 3D Temperature Salinity Height Geostrophic Current and MLD, Mercator Ocean International [data set], https://doi.org/10.48670/moi-00052, 2021.

EU Copernicus Marine Service Product: Mediterranean Sea Physics Reanalysis, Mercator Ocean International [data set], https://doi.org/10.25423/CMCC/MEDSEA_MULTIYEAR_PHY_006_004_E3R1, 2022a.

EU Copernicus Marine Service Product: Mediterranean Sea Physics Reanalysis INTERIM, Mercator Ocean International [data set], https://doi.org/10.25423/CMCC/MEDSEA_MULTIYEAR_PHY_006_004_E3R1I, 2022b.

EU Copernicus Marine Service Product: Global Ocean Ensemble Physics Reanalysis, Mercator Ocean International [data set], https://doi.org/10.48670/moi-00024, 2022c.

EU Copernicus Marine Service Product: Global Ocean-Delayed Mode gridded CORA – In-situ Observations objective analysis in Delayed Mode, INSITU_GLO_PHY_TS_OA_MY_013_052, Mercator Ocean International [data set], https://doi.org/10.17882/46219, 2022d.

Fedele, G., Mauri, E., Notarstefano, G., and Poulain, P. M.: Characterization of the Atlantic Water and Levantine Intermediate Water in the Mediterranean Sea using 20 years of Argo data, Ocean Sci., 18, 129–142, https://doi.org/10.5194/os-18-129-2022, 2022.

Gounou, A., Drevillon, M., and Clavier, M.: EU Copernicus Marine Service Product User Manual for the Global Ocean Ensemble Physics Reanalysis, GLOBAL_REANALYSIS_PHY_001_031, Issue 1.1, Mercator Ocean International, https://catalogue.marine.copernicus.eu/documents/PUM/CMEMS-GLO-PUM-001-031.pdf (last access: 3 May 2023), 2022.

Grenier, E., Verbrugge, N., Mulet, S., and Guinehut, S.: EU Copernicus Marine Service Quality Information Document for the Multi Observation Global Ocean 3D Temperature Salinity Height Geostrophic Current and MLD, MULTIOBS_GLO_PHY_TSUV_3D_MYNRT_015_012, Issue 1.1, Mercator Ocean International, https://catalogue.marine.copernicus.eu/documents/QUID/CMEMS-MOB-QUID-015-012.pdf (last access: 3 May 2023), 2021.

Guinehut, S.: EU Copernicus Marine Service Product User Manual for the Multi Observation Global Ocean 3D Temperature Salinity Height Geostrophic Current and MLD, MULTIOBS_GLO_PHY_TSUV_3D_MYNRT_015_012, Issue 1.1, Mercator Ocean International, https://catalogue.marine.copernicus.eu/documents/PUM/CMEMS-MOB-PUM-015-012.pdf (last access: 3 May 2023), 2021.

Guinehut, S., Dhomps, A.-L., Larnicol, G., and Le Traon, P.-Y.: High resolution 3-D temperature and salinity fields derived from in situ and satellite observations, Ocean Sci., 8, 845–857, https://doi.org/10.5194/os-8-845-2012, 2012.

Holliday, N. P., Bersch, M., Berx, B., Chafik, L., Cunningham, S., Florindo-López, C., Hátún, H., Johns, W., Josey, S. A., Larsen, K. M., and Mulet, S.: Ocean circulation causes the largest freshening event for 120 years in eastern subpolar North Atlantic, Nat. Commun., 11, 585, https://doi.org/10.1038/s41467-020-14474-y, 2020.

Jarosz, E., Teague, W. J., Book, J. W., and Beşiktepe, Ş. T.: Observed volume fluxes and mixing in the Dardanelles Strait, J. Geophys. Res.-Oceans, 118, 5007–5021, 2013.

Johnson, G. C., Hosoda, S., Jayne, S. R., Oke, P. R., Riser, S. C., Roemmich, D., Suga, T., Thierry, V., Wijffels, S. E., and Xu, J.: Argo-two decades: global oceanography, revolutionized, Annu. Rev. Mar. Sci., 14, 379–403, 2022.

Jordà, G., Von Schuckmann, K., Josey, S. A., Caniaux, G., García-Lafuente, J., Sammartino, S., Özsoy E., Polcher J., Notarstefano, G., Poulain, P. M., Adloff, F., Salat, J., Naranjo, C., Schroeder, K., Chiggiato, J., Sannino, G., and Macías, D.: The Mediterranean Sea heat and mass budgets: Estimates, uncertainties and perspectives, Prog. Oceanogr., 156, 174–208, https://doi.org/10.1016/j.pocean.2017.07.001, 2017.

Juza, M., Fernández-Mora, À., and Tintoré, J.: Sub-Regional Marine Heat Waves in the Mediterranean Sea From Observations: Long-Term Surface Changes, Sub-Surface and Coastal Responses, Front. Mar. Sci., 9, 785771, https://doi.org/10.3389/fmars.2022.785771, 2022.

Lecci, R., Drudi, M., Grandi, A., Cretì, S., and Clementi, E.: EU Copernicus Marine Service Product User Manual for the Mediterranean Sea Physics Reanalysis, MEDSEA_MULTIYEAR_PHY_006_004, Issue 2.3, Mercator Ocean International, https://catalogue.marine.copernicus.eu/documents/PUM/CMEMS-MED-PUM-006-004.pdf (last access: 3 May 2023), 2022.

Lellouche, J.-M., Le Galloudec, O., Drévillon, M., Régnier, C., Greiner, E., Garric, G., Ferry, N., Desportes, C., Testut, C.-E., Bricaud, C., Bourdallé-Badie, R., Tranchant, B., Benkiran, M., Drillet, Y., Daudin, A., and De Nicola, C.: Evaluation of global monitoring and forecasting systems at Mercator Océan, Ocean Sci., 9, 57–81, https://doi.org/10.5194/os-9-57-2013, 2013.

MacLachlan, C., Arribas, A., Peterson, K. A., Maidens, A., Fereday, D., Scaife, A. A., Gordon, M., Vellinga, M., Williams, A., Comer, R. E., Camp, J., Xavier, P., and Madec, G.: Global seasonal forecast system version 5 (GloSea5): A high-resolution seasonal forecast system, Q. J. Roy. Meteorol. Soc., 141, 1072–1084, https://doi.org/10.1002/qj.2396, 2014.

Masina, S. and Storto, A.: Reconstructing the recent past ocean variability: status and perspective, J. Mar. Res., 75, 727–764, 2017.

Pisano, A., Marullo, S., Artale, V., Falcini, F., Yang, C., Leonelli, F. E., Santoleri, R., and Buongiorno Nardelli, B.: New Evidence of Mediterranean Climate Change and Variability from Sea Surface Temperature Observations, Remote Sens., 12, 132, https://doi.org/10.3390/rs12010132, 2020.

Sannino, G., Sözer, A., and Özsoy, E.: A high-resolution modelling study of the Turkish Straits System, Ocean Dynam., 67, 397–432, 2017.

Schauer, U. and Losch, M.: "Freshwater" in the ocean is not a useful parameter in climate research, J. Phys. Oceanogr., 49, 2309–2321, 2019.

Schroeder, K., Chiggiato, J., Bryden, H. L., Borghini, M., and Ben Ismail, S.: Abrupt climate shift in the Western Mediterranean Sea, Scientific reports, 6, 1–7, 2016.

Skliris, N., Zika, J. D., Herold, L., Josey, S. A., and Marsh, R.: Mediterranean sea water budget long-term trend inferred from salinity observations, Clim. Dynam., 51, 2857–2876, https://doi.org/10.1007/s00382-017-4053-7, 2018.

Soto-Navarro, J., Criado-Aldeanueva, F., García-Lafuente, J., and Sánchez-Román, A.: Estimation of the Atlantic inflow through the Strait of Gibraltar from climatological and in situ data, J. Geophys. Res.-Oceans, 115, C10023, https://doi.org/10.1029/2010JC006302, 2010.

Storto, A., Masina, S., and Navarra, A.: Evaluation of the CMCC eddy-permitting global ocean physical reanalysis system (C-GLORS, 1982–2012) and its assimilation components, Q. J. R. Meteorol. Soc., 142, 738–758, https://doi.org/10.1002/qj.2673, 2016.

Storto, A., Masina, S., Simoncelli, S., Iovino, D., Cipollone, A., Drevillon, M., Drillet, Y., von Schuckman, K., Parent, L., Garric, G., and Greiner, E.: The added value of the multi-system spread information for ocean heat content and steric sea level investigations in the CMEMS GREP ensemble reanalysis product, Clim. Dynam., 53, 287–312, https://doi.org/10.1007/s00382-018-4585-5, 2019a.

Storto, A., Alvera-Azcárate, A., Balmaseda, M. A., Barth, A., Chevallier, M., Counillon, F., Domingues, C. M., Drevillon, M., Drillet, Y., Forget, G., Garric, G., Haines, K., Hernandez, F., Iovino, D., Jackson, L. C., Lellouche, J.-M., Masina, S., Mayer, M., Oke, P. R., Penny, S. G., Peterson, K. A., Yang, C., and Zuo, H.: Ocean reanalyses: recent advances and unsolved challenges, Front. Mar. Sci., 6, 418, https://doi.org/10.3389/fmars.2019.00418, 2019b.

Szekely, T.: EU Copernicus Marine Service Quality Information Document for the Global Ocean-Delayed Mode gridded CORA – In-situ Observations objective analysis in Delayed Mode, INSITU_GLO_PHY_TS_OA_MY_013_052, issue 1.2, Mercator Ocean International, https://catalogue.marine.copernicus.eu/documents/QUID/CMEMS-INS-QUID-013-052.pdf (last access: 4 April 2023), 2022a.

Szekely, T.: EU Copernicus Marine Service Product User Manual for the Global Ocean-Delayed Mode gridded CORA – In-situ Observations objective analysis in Delayed Mode, INSITU_GLO_PHY_TS_OA_MY_013_052, issue 1.10, Mercator Ocean International, https://catalogue.marine.copernicus.eu/documents/PUM/CMEMS-INS-PUM-013-002-052.pdf (last access: 4 April 2023), 2022b.

Szekely, T., Gourrion, J., Pouliquen, S., and Reverdin, G.: The CORA 5.2 dataset for global in situ temperature and salinity measurements: data description and validation, Ocean Sci., 15, 1601–1614, https://doi.org/10.5194/os-15-1601-2019, 2019.

Tuel, A. and Eltahir, E. A. B.: Why Is the Mediterranean a Climate Change Hot Spot?, J. Climate, 33, 5829–5843, https://journals.ametsoc.org/view/journals/clim/33/14/JCLI-D-19-0910.1.xml (retrieved 25 Jannuary 2022), 2020.

Zunino, P., Schroeder, K., Vargas-Yáñez, M., Gasparini, G. P., Coppola, L., García-Martínez, M. C., and Moya-Ruiz, F.: Effects of the Western Mediterranean Transition on the resident water masses: Pure warming, pure freshening and pure heaving, J. Mar. Syst., 15, 96–97, https://doi.org/10.1016/j.jmarsys.2012.01.011, 2012.

Zuo, H., Balmaseda, M. A., and Mogensen, K.: The new eddy-permitting ORAP5 ocean reanalysis: description, evaluation and uncertainties in climate signals, Clim. Dynam., 49, 791–811, https://doi.org/10.1007/s00382-015-2675-1, 2017.

State Planet, 1-osr7, 7, 2023
https://doi.org/10.5194/sp-1-osr7-7-2023

Baltic Sea freshwater content

Urmas Raudsepp, Ilja Maljutenko, Amirhossein Barzandeh, Rivo Uiboupin, and Priidik Lagemaa

Department of Marine Systems, Tallinn University of Technology, Tallinn, 12618, Estonia

Correspondence: Ilja Maljutenko (ilja.maljutenko@taltech.ee)

Received: 1 September 2022 – Discussion started: 29 September 2022
Revised: 8 August 2023 – Accepted: 29 August 2023 – Published: 27 September 2023

Abstract. The Baltic Sea is a brackish shallow sea, the state of which is determined by the mixing of freshwater from net precipitation and runoff with the salty water from the North Sea inflows. The freshwater content (FWC) of the Baltic Sea is calculated from the Copernicus regional reanalysis data covering the period 1993–2021. The FWC in the Baltic Sea has shown a steady decrease over the past 2 decades, with a linear trend of 23.9 km^3 yr^{-1}; however, the trend has significant spatial variability. The Gulf of Bothnia has a positive FWC tendency, while the Baltic Proper has a negative FWC tendency. Temporal changes of FWC are opposite between the Bothnian Bay in the north and the southern Baltic Proper. In the Bothnian Bay, interannual changes of FWC are positively correlated with river runoff and net precipitation and negatively correlated with salt transport. In the southern Baltic Proper, the variations of FWC and salt transport through the Danish straits are negatively correlated from 1993 until 2010 but positively correlated thereafter. The seasonal freshwater content reflects the specific hydrophysical conditions of each sub-basin, with northern basins being influenced by seasonal river runoff and ice formation and melting, while the southern basins are more responsive to subsurface salinity changes due to salt transport through the Danish straits.

1 Introduction

Climate warming has resulted in the intensification of the global hydrological cycle but not necessarily on the regional scale (Pratap and Markonis, 2022). The increase in net precipitation over land and sea areas, decrease in ice cover, and increase in river runoff are the main components of the global hydrological cycle that increase freshwater content (FWC) in the ocean (Boyer et al., 2007) and decrease ocean salinity. All the components can be directly estimated but might have significant uncertainties. Instead, the ocean salinity change can be used as a marker of the water cycle change (Durack et al., 2012).

In the case of an open part of the ocean, for example, a regional sea, using salinity as a proxy for FWC includes an additional blurring aspect, which is water transport through the open boundaries between the basin under consideration and its surrounding area. The impact of water exchange on the changes of FWC is significant if not dominant. In that case, changes of FWC may not represent the actual changes of freshwater input from the above-mentioned sources.

The Baltic Sea is one of the marginal seas where water salinity and FWC are strongly influenced by the water exchange with the North Sea. The major Baltic inflows (MBIs) are the most voluminous event-type sources of saline water to the Baltic Sea (Mohrholz, 2018). The frequency and intensity of the MBIs and other large volume inflows have no long-term trends but do have a multidecadal variability of about 30 years (Mohrholz, 2018; Lehmann and Post, 2015; Lehmann et al., 2017; Radtke et al., 2020). Smaller barotropic and baroclinically driven inflows transport saline water into the halocline or below it, depending on the density of the inflow water (Reissmann et al., 2009). The inflows of saline water are forced by winds from the west and outflows by winds from the east.

Direct total input of freshwater to the Baltic Sea consists of river runoff and net precipitation. The total river runoff from the Baltic Sea catchment area shows no statistically significant trend but a variability of about 30 years (Meier et al., 2019a, b) and a pronounced decadal variability of accumulated anomaly of runoff (Lehmann et al., 2022). The variations in runoff explain about 50 % of the long-term variability

Published by Copernicus Publications.

Table 1. CMEMS and non-CMEMS products used in this study, including information on data documentation.

Product ref. no.	Product ID & type	Data access	Documentation
1	BALTICSEA_REANALYSIS_PHY_003_011; numerical models	EU Copernicus Marine Service Product (2023)	Quality Information Document (QUID): Liu et al. (2019) Product User Manual (PUM): Axell (2021)
2	ERA5; numerical models	Hersbach et al. (2023)	Hersbach et al. (2020)
3	IOW-THREDDS-BMIP_bmip_rivers_2019-10-10-1; numerical models and observations	IOW THREDDS (2019)	Väli et al. (2019)
4	EMODNET_CHEMISTRY_Baltic_Sea_aggregated_eutrophication_and_acidity_datasets_1902-2017_v2018; observations	SMHI (2023)	Buga et al. (2018), Giorgetti et al. (2020)

in volume-averaged Baltic Sea salinity (Meier and Kauker, 2003; Lehmann et al., 2022), while the direct dilution of the Baltic Sea water by freshwater accounts for 27 % of the interannual variations (Radtke et al., 2020). During 1950–2018, precipitation averaged over the Baltic Sea catchment area had a trend of 1.44 mm yr^{-1} (Meier et al., 2022).

Thus, the long-term salinity of the Baltic Sea is determined by saline water inflows from the North Sea (wind forcing) and its dilution with freshwater originating from numerous rivers across the Baltic coast and net precipitation (Winsor et al., 2001; Meier and Kauker, 2003; Gustafsson and Omstedt, 2009; Schimanke and Meier, 2016; Lehmann et al., 2022). There is no clear long-term trend of the mean salinity of the Baltic Sea, but there are multidecadal oscillations of about 30 years (Kniebusch et al., 2019). A 30-year variability has been found for the salinity, river runoff, and saltwater inflows (Radtke et al., 2020). The Baltic Sea salinity also has a natural centennial variability (Kniebusch et al., 2019).

A specific feature of the Baltic Sea is the large difference in sea surface salinity, ranging from about 20 g kg^{-1} in the Kattegat to 2 g kg^{-1} in the Bothnian Bay (Leppäranta and Myrberg, 2009). Kniebusch et al. (2019) found a positive trend of centennial changes in the north–south gradient of the surface salinity and river runoff in the northern catchment area. Multidecadal oscillations control the long-term variations of surface salinity and its meridional gradient with a period of about 30 years (Radtke et al., 2020).

A common approach is to use salinity to describe the energy and water cycles in the Baltic Sea (Lehmann et al., 2022; Meier et al., 2022). In this study, instead of using spatially mean salinity of the Baltic Sea, we suggest the concept of FWC (Boyer et al., 2007) for the description of the physical state of the Baltic Sea. Previously, a concept of FWC has been used to estimate the freshwater budget of the Baltic Sea (Winsor et al., 2001) and for the geographical spreading of spring-time river runoff (Eilola and Stigebrandt, 1998).

The aim of this study is to analyse the changes of the Baltic Sea FWC during the period of 1993–2021. The MBI in 1993 ended the stagnation period with no MBIs that lasted for about 10 years (1983–1993). During the stagnation period, salinity was below average, stratification weakened, and hypoxic area decreased (Lehmann et al., 2022). The period of 1993–2021 includes the third largest MBI in 2014 (Mohrholz et al., 2015) and several of the other barotropic large volume inflows (Mohrholz, 2018). We focus on the changes of the FWC in the whole Baltic Sea as well as its sub-basins. We investigate the trends in FWC and observe its seasonal changes. A qualitative explanation of the physical processes behind the dynamics of FWC is provided.

2 Data and methods

The BALMFC CMEMS reanalysis product (data ref. 1, Table 1) is calculated using the Nemo-Nordic 1.0 ocean model (Hordoir et al., 2019). The horizontal resolution of the model is approximately 2 nmi, and there are 56 vertical levels. Vertical resolution varies from 3 m at the surface to 10 m below the 100 m depth. The model without data assimilation has been thoroughly validated (Hordoir et al., 2019). The Copernicus model system uses the local singular evolutive interpolated Kalman filter data assimilation method (Liu and Fu, 2018). A detailed quality assessment of the reanalysis product (data ref. 1, Table 1), using the K-means clustering algorithm (Raudsepp and Maljutenko, 2022), is provided in Appendix A.

The FWC is calculated according to Boyer et al. (2007):

$$\mathrm{FWC} = \frac{\rho\left(S_{\mathrm{ref}}, T_{\mathrm{ref}}, p\right)}{\rho\left(0, T_{\mathrm{ref}}, p\right)} \frac{S_{\mathrm{ref}} - S}{S}, \tag{1}$$

where $S(x, y, z, t)$ and $S_{\mathrm{ref}}(x, y, z)$ are actual salinity and reference salinity, respectively, and x, y, z, and t are zonal, meridional, vertical, and temporal coordinates, respectively. The density, ρ, is calculated according to the TEOS10 (IOC

et al., 2010). The key issue of FWC calculations lies in how the reference salinity is defined. The climatological range of salinity in the Baltic Sea varies from the freshwater conditions in the northern and eastern parts to the oceanic water conditions in the Kattegat. We follow the Boyer et al. (2007) formulation and calculate the climatological FWC from the three-dimensional temperature (T_{ref}) and salinity (S_{ref}) fields averaged over the period of 1993–2020.

The other widely used formulation of FWC is as follows (e.g. Gustafsson and Stigebrandt, 1996):

$$\mathrm{FWC} = \frac{\rho\left(S_{\mathrm{ref}}, T_{\mathrm{ref}}, p\right)}{\rho\left(0, T_{\mathrm{ref}}, p\right)} \frac{S_{\mathrm{ref}} - S}{S_{\mathrm{ref}}}. \quad (2)$$

Both formulations are derived from the concept of the mixing of two water masses with different salinities using conservation of salt but have different mechanistic approaches, which are explained in detail in Appendix B.

The total volume of freshwater needed to dilute the water with salinity S_{ref} to the salinity S, if $S < S_{\mathrm{ref}}$ or should be removed to obtain water with the salinity S, if $S > S_{\mathrm{ref}}$ is

$$\mathrm{FWC}(t) = \iiint_V \mathrm{FWC}(x, y, z, t)\,\mathrm{d}x\,\mathrm{d}y\,\mathrm{d}z \quad (\mathrm{m}^3\,\mathrm{m}^{-3}).$$

A vertical distribution of the FWC is calculated as

$$\mathrm{FWC}(z, t) = \iint_A \mathrm{FWC}(x, y, z, t)\,\mathrm{d}x\,\mathrm{d}y \quad (\mathrm{m}^2\,\mathrm{m}^{-3}),$$

and horizontal distribution of the FWC is calculated as

$$\mathrm{FWC}(x, y, t) = \int_D \mathrm{FWC}(x, y, z, t)\,\mathrm{d}z \quad (\mathrm{m}\,\mathrm{m}^{-3}).$$

V and A correspond to the volume and area of the Baltic Sea or its sub-region, as shown in Fig. 1. D corresponds to depth from surface to bottom at a specific location.

The sea ice volume, V_{i}, is calculated from the same BALMFC CMEMS reanalysis product (data ref. 1, Table 1), based on the LIM3 model configuration (Pemberton et al., 2017). The V_{i} is calculated for each model grid cell (x, y) using total ice thickness, H_{i}, and ice concentration, C_{i}:

$$V_{\mathrm{i}}(x, y, t) = H_{\mathrm{i}}(x, y, t) \times C_{\mathrm{i}}(x, y, t) \times \mathrm{d}A(x, y),$$

where $\mathrm{d}A$ is the area of each grid cell.

Hourly precipitation and evaporation data have been extracted from the ERA5 reanalysis (data ref. 2, Table 1) from the period of 1993–2020. Net precipitation was calculated by subtracting evaporation from precipitation. Thereafter, the net precipitation was interpolated onto a reanalysis model grid, and total net precipitation was estimated for the wet grid cells of each sub-basin (Fig. 1). The net precipitation anomalies were calculated relative to the period 1993–2020.

The total runoff from the Baltic Sea rivers was estimated from the river discharge database (data ref. 3, Table 1) of the Baltic Model Intercomparison Project (Gröger et al., 2022). The runoff to each sub-basin was calculated by summing the runoffs from each river discharging to the corresponding sub-basin (Fig. 1). The runoff data covered the period 1993–2018, and the anomalies were calculated relative to the same reference period.

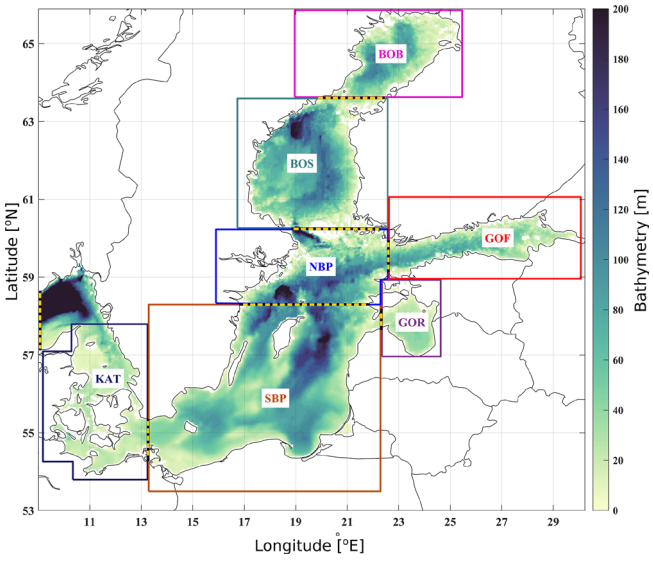

Figure 1. Map of the Baltic Sea depth distribution (data ref. 1, Table 1). Boxes indicate the boundaries used to calculate the freshwater content for different sub-basins. The transects used to calculate salt transport between sub-basins are represented by dashed yellow–black lines. The abbreviations for the sub-basins are as follows: KAT (Kattegat), SBP (southern Baltic Proper), NBP (northern Baltic Proper), BOS (Bothnian Sea), BOB (Bay of Bothnia), GOF (Gulf of Finland), and GOR (Gulf of Riga).

Salt transport was estimated by calculating the salt flux at the boundaries of each sub-basin (see Fig. 1 for the location of the transects). Daily salt transport through each transect was calculated as a salinity and perpendicular velocity product. The annual mean salt transports were calculated by averaging the transects of daily transports over each year and later integrated over the vertical and corresponding horizontal dimension. The positive direction is determined according to the estuarine transport definition; i.e. inflow is from the ocean and outflow is from the head of the estuary.

3 Results

Time series of the FWC and linear trends of the Baltic Sea and its sub-basins are presented in Fig. 2. Even if the calculated trends are not statistically significant, they provide information about the tendency of FWC changes. The FWC of the Baltic Sea has a negative trend of $-23.9 \pm 0.7\,\mathrm{km}^3\,\mathrm{yr}^{-1}$ ($p < 10^{-3}$) superimposed by irregular decadal variations (Fig. 2a). The trends are variable over the whole Baltic Sea (Fig. 2). It changes sign from positive in the northern sub-

basins to neutral in the eastern sub-basins and to negative in the central and southern sub-basins (Fig. 2). The decrease in the FWC in the southern Baltic Proper (Fig. 2) contributes the most to the overall decreasing trend in the Baltic Sea. If we look at the continuous distribution of the trends in the Baltic Sea, we see opposite temporal regimes of the FWC in the Bothnian Bay and in the Baltic Proper, with the Bothnian Sea being the transition area (Fig. 3). Although there is no trend in the Gulf of Finland as a whole (Fig. 2), the eastern part has a small negative tendency, while the western part shows a small positive tendency. The shallow Gulf of Riga has a negligible trend. The trends vanish in the southwestern Baltic Sea and in the Kattegat area (Fig. 3).

The spatial distribution of the trends indicates a possible coherence of salinity dynamics in different sub-basins, which is checked further on by calculating correlation coefficients between the basins. The correlation coefficients calculated pairwise between detrended FWC time series (Table 2) show a high positive value between the southern and northern Baltic Proper ($R = 0.8$) and between the Bothnian Bay and the Bothnian Sea ($R = 0.6$), while the correlation between the Bothnian Bay and southern and northern Baltic Proper is negative ($R = -0.6$). This suggests that although temporal variability is opposite, the dynamics of FWC are linked over the Baltic Sea.

Horizontal transition of the trends from positive to negative points to the three-dimensional structure of the FWC variability field. Therefore, time–depth variations of the FWC in each sub-basin were calculated (Fig. 4). Vertically, in the whole Baltic Sea, FWC is the most variable in the halocline layer and beneath it (Fig. 4a). Vertical distribution of the trends shows the absence of the trend in the upper layer of 50 m but a strong negative trend within and below the halocline. Thus, the decrease in the FWC in the whole Baltic Sea is mostly contributed by the drop of the FWC below the upper mixed layer. The variability as well as negative trends is strongest in the southern and the northern Baltic Proper (Fig. 4e, c). Moving further northward and eastward in the Baltic Sea, we can notice that the negative tendencies are only present in the deeper layer (deeper than 50 m) of the Gulf of Finland and the Bothnian Sea (Fig. 4f, d). On the other side, there is a strong positive trend of the FWC in the Bothnian Bay and in the upper 50 m layer of the Bothnian Sea (Fig. 4b, d). It is relevant to note that a positive tendency in the FWC is seen in the layer of 10–50 m in the Gulf of Finland (Fig. 4f). In the northern Baltic Proper, the trend is absent in the upper layer of 30 m but turns negative in the surface layer of the southern Baltic Proper. In the Gulf of Riga, the variability is low, and the trends are negligible and do not show systematic vertical distribution.

FWC exhibits noticeable irregular decadal variations over time, as shown in Figs. 2 and 4. To understand the interannual variability of FWC, we calculated a time series of river runoff, net precipitation, and salt transport through the cross-sections between the sub-basins of the Baltic Sea (Fig. 1; Supplement). Our aim is to examine the co-variability of these factors and the FWC response of both the entire Baltic Sea as well as its sub-basins. To accomplish this, we present a time series of detrended standardized yearly variables in Fig. 5.

For the entire Baltic Sea, the study period can be divided into two sub-periods. From 1993 to 2003, i.e. the first period, changes in the FWC of the Baltic Sea correlated with freshwater sources, namely net precipitation and river runoff (Fig. 5a). A prominent example is the period from 1997 to 2003. Meanwhile, the salt transport to the Baltic Sea remained relatively low. Since 2004, i.e. the second period, we have observed a coherent relationship between salt transport and the FWC in the Baltic Sea, which is difficult to explain. We may speculate that an increase in net precipitation might trigger an increase in the FWC between 2007 and 2012, while river runoff has no effect.

The changes in the FWC of the entire Baltic Sea are influenced by the changes occurring in its sub-basins, resulting in a complex integrated effect. This is illustrated by the simultaneous positive trend of FWC in the northern Baltic Sea and negative trend in the southern Baltic Sea (Fig. 2) as well as their negative correlation (Table 2). Hence, it is necessary to examine the changes in variables separately for each sub-basin. It is important to note that while the FWC, net precipitation, and river runoff for the entire Baltic Sea represent the sum of contributions from each sub-basin, the net salt flux does not represent an integrated value.

We specifically focus on two sub-basins: the southern Baltic Proper, which is characterized by saltwater dominance, and the Bothnian Bay, which is characterized by freshwater dominance. The variations in the southern Baltic Proper differ in several features from the variations in the whole Baltic Sea. The southern Baltic Proper exhibits two distinct periods (Fig. 5e), which is qualitatively similar to the entire Baltic Sea, but the periods do not coincide temporally. The first period spans from 1993 to 2007, while the second period extends from 2008 until the end of recorded data. In the first period, FWC, net precipitation, and river runoff show positive covariation, while the flux exhibits a negative covariation pattern. In the second period, there is positive covariation between FWC and salt flux and partially net precipitation, but the pattern is reversed for river runoff. In the Bothnian Bay, there is positive covariation between FWC, net precipitation, and river runoff but negative covariation with salt flux (Fig. 5b). In the northern Baltic Proper and the Bothnian Sea, the main pattern is negative covariation between FWC and salt flux (Fig. 5c and d). Changes in net precipitation and river runoff generally support changes in FWC, but the variability pattern remains complex.

The Gulf of Finland (Fig. 5f) and the Gulf of Riga (Fig. 5g) do not exhibit a well-defined pattern in the variability of the variables. In the latter basin, the changes in FWC align with the changes in river runoff from 1993 to 2009 but not thereafter.

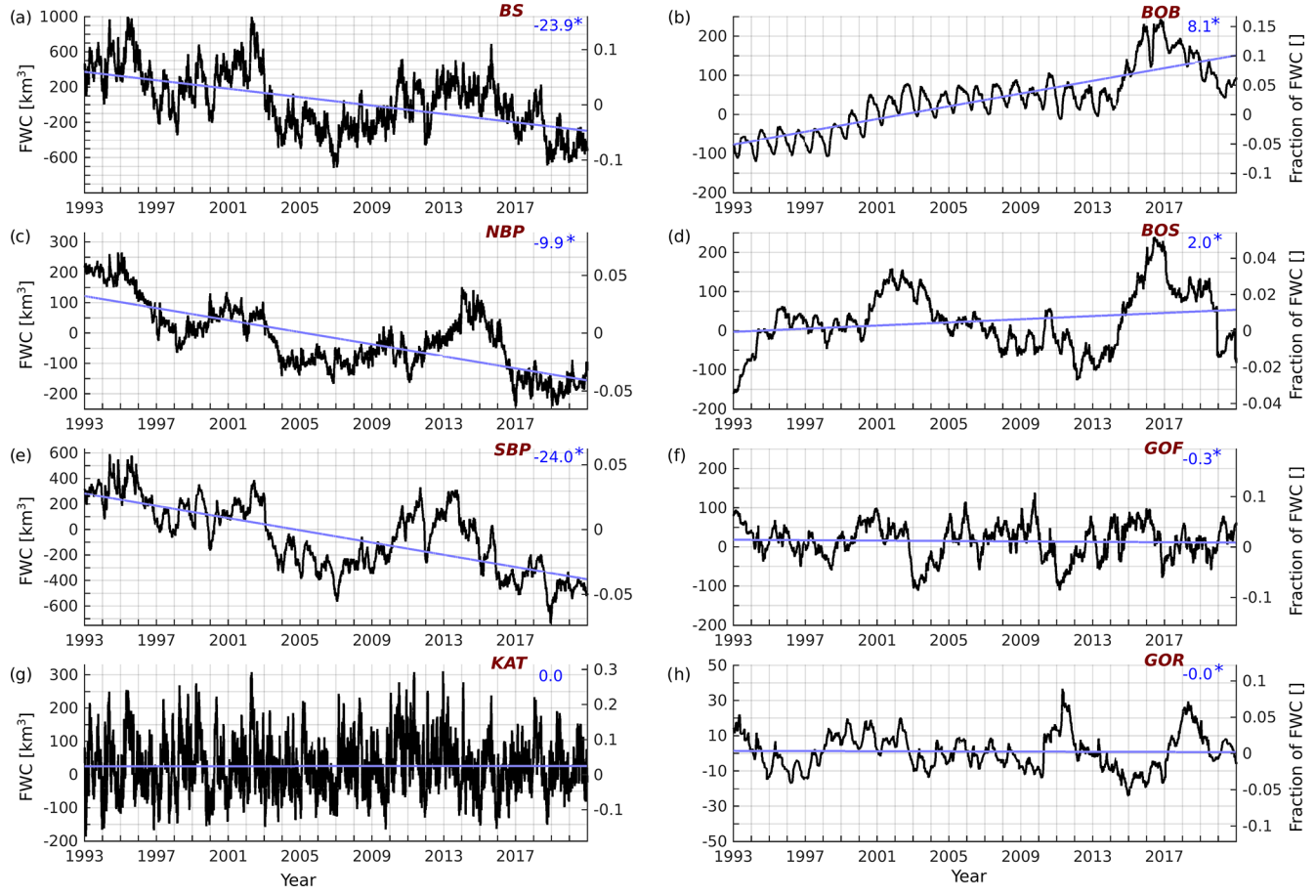

Figure 2. Freshwater content time series in the Baltic Sea **(a)** and in different sub-basins **(b–h)**. The trend of FWC in the corresponding basin is shown in the upper-right corner ($km^3\ yr^{-1}$, asterisk $p > 0.05$) and plotted using the blue line. The abbreviations for the sub-basins are as follows: BS (Baltic Sea), NBP (northern Baltic Proper), SBP (southern Baltic Proper), KAT (Kattegat), BOB (Bay of Bothnia), BOS (Bothnian Sea), GOF (Gulf of Finland), and GOR (Gulf of Riga) (data ref. 1, Table 1).

Table 2. Correlation table of the FWC between the sub-basins (Fig. 1) of the Baltic Sea (data ref. 1, Table 1). The abbreviations for the sub-basins are as follows: KAT (Kattegat), SBP (southern Baltic Proper), NBP (northern Baltic Proper), BOS (Bothnian Sea), BOB (Bay of Bothnia), GOF (Gulf of Finland), and GOR (Gulf of Riga).

	BS	BOB	BOS	GOF	GOR	KAT	NBP	SBP
BS	1.00							
BOB	−0.38	1.00						
BOS	0.06	0.57	1.00					
GOF	0.11	0.01	−0.08	1.00				
GOR	0.13	−0.03	−0.07	−0.09	1.00			
KAT	0.42	−0.04	−0.03	−0.10	0.30	1.00		
NBP	0.78	−0.64	−0.22	0.28	−0.17	0.01	1.00	
SBP	0.88	−0.65	−0.25	−0.08	0.13	0.21	0.79	1.00

The seasonal dynamics of FWC further emphasize the effect of freshwater discharge in the northern basins and salt transport in the southern basins of the Baltic Sea (Fig. 6). In the whole Baltic Sea, FWC is low in autumn and winter but high in spring and summer (Fig. 6a). Qualitatively, low FWC could be explained by high salt transport in autumn and winter (Fig. 7c) accompanied by low river runoff (Fig. 7a), but this is interfered with by high precipitation in autumn (Fig. 7b). Contrarily, the high FWC could be explained by high river runoff and low or even negative salt transport in

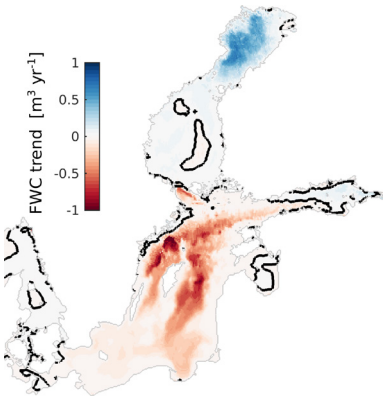

Figure 3. Spatial distribution of depth normalized FWC trends, with the zero isoline highlighted in black.

spring and summer. Indeed, net precipitation is low in that period. The Gulf of Bothnia has low FWC in winter and early spring and high FWC in summer and autumn (Fig. 6b, d). The seasonal course is more pronounced in the Bothnian Bay (Fig. 6b) than in the Bothnian Sea (Fig. 6d). In the Gulf of Bothnia, the decrease in FWC in winter could be associated with the freezing of seawater (Fig. 7f). An increase in the FWC in the Bothnian Bay in spring coincides with the melting of sea ice (Fig. 7f), high river runoff (Fig. 7a), and negative salt transport (Fig. 7e).

In the southern Baltic Proper, FWC is low in winter and high in summer (Fig. 6e), while in the Gulf of Finland the situation is opposite (Fig. 6f). Similarly, net salt transport to these basins is opposite in time (Fig. 7c, d). The seasonal course of FWC is almost absent in the northern Baltic Proper (Fig. 6c) where the influence from adjacent sub-basins, the southern Baltic Proper and the Gulf of Finland, which have opposite FWC seasonality, could compensate for each other. In the Gulf of Riga, FWC is at its maximum in spring and decreases monotonically until winter (Fig. 6h). Surprisingly, the seasonal course of the FWC in the Kattegat (Fig. 6g) is like the seasonal course of the FWC in the Gulf of Riga (Fig. 6h). Dynamically, these two areas cannot be interlinked due to their geographical separation.

4 Discussion

A distinct feature of the Baltic Sea salinity evolution over the period 1993–2021 was the decreasing trend of the FWC in the southern Baltic Proper and increasing trend in the Bothnian Bay (Fig. 2). Overall, the FWC in the whole Baltic Sea had a statistically significant negative trend (Fig. 2). Salt transport to the Baltic Sea, net precipitation, and total river runoff to the sea (Supplement) did not explain the calculated trends. No steady increase in the salt transport to the Baltic Sea has been reported elsewhere, although deepwater salinity has increased in the Gotland Basin from 1993 to 2018 (Lehmann et al., 2022). The rate of 0.2–0.25 g kg^{-1} per decade was estimated for the period 1979–2018 (Lehmann et al., 2022). In the Baltic Sea, there was no trend in net precipitation, nor river runoff. Therefore, the decrease in FWC should be explained by accumulated salt flux from the North Sea to the Baltic Sea due to the major Baltic inflows (Mohrholz, 2018), large barotropic inflows (Lehmann et al., 2017), and smaller inflows of barotropic origin (Lehmann et al., 2022). Our estimations of the annual salt transport to the southern Baltic Proper did not show an increase in the salt flux (Supplement). In our reanalysis model data, the salt flux at the Danish straits could have large uncertainty due to relatively high salinity errors there (Appendix A). Inside the Baltic Sea area, as reanalysis model data have been calculated using assimilation of the observations, the estimates of FWC have low uncertainty due to low salinity errors (Appendix A).

Net precipitation and river runoff increased over the Bothnian Bay (Supplement), which contributed to the increase in the FWC (Fig. 2b). An increase in FWC was fastest at the surface of the bay and monotonically slowed down with depth (Fig. 4b). We would like to note that there are no studies that support or refute our findings on the increase in the FWC or the decrease in salinity in the Gulf of Bothnia.

The trends of FWC are present in our data, but this could be characteristic of the period of our study. An increase in the salinity in the central Baltic Proper since 1993 has been reported by Lehmann et al. (2022), which is consistent with our results about the decline of FWC. Going back further in time, the positive salinity trend becomes weaker (Lehmann et al., 2022) until it vanishes (Radtke et al., 2020). The study by Radtke et al. (2020) was prolonged into the past until 1850 but does not cover the last 15 years.

Many authors have reported dominant 30-year variability in mean, surface, and bottom salinity of the Baltic Sea as well as river runoff into the Baltic Sea and even salt transport across Darss sill (Kniebusch et al., 2019; Radtke et al., 2020; Lehmann et al., 2022). Our time series of 28 years are short to reveal 30-year variability in FWC, river runoff, or net precipitation with a statistical significance. Visual inspection of the time series of FWC does not hint at the presence of a 30-year cycle (Fig. 2). We admit the presence of decadal variability in the time series, which has also been reported by Lehmann et al. (2022). The trends and multi-scale variability of FWC are opposite in the Baltic Proper and in the Bothnian Bay (Fig. 2, Table 1). This raises the following question: if FWC has opposite changes in the southern and northern Baltic Sea, how could changes in river runoff explain the opposite variability? Our analysis showed that there are multi-year periods when river runoff is in phase or out of phase with the FWC. An example of an in-phase period in the whole Baltic Sea is 1993–2009 and an out-of-phase period 2010–2018 (Fig. 5a). In the Bothnian Bay, we mostly have river runoff and the FWC in phase and out of phase with salt transport.

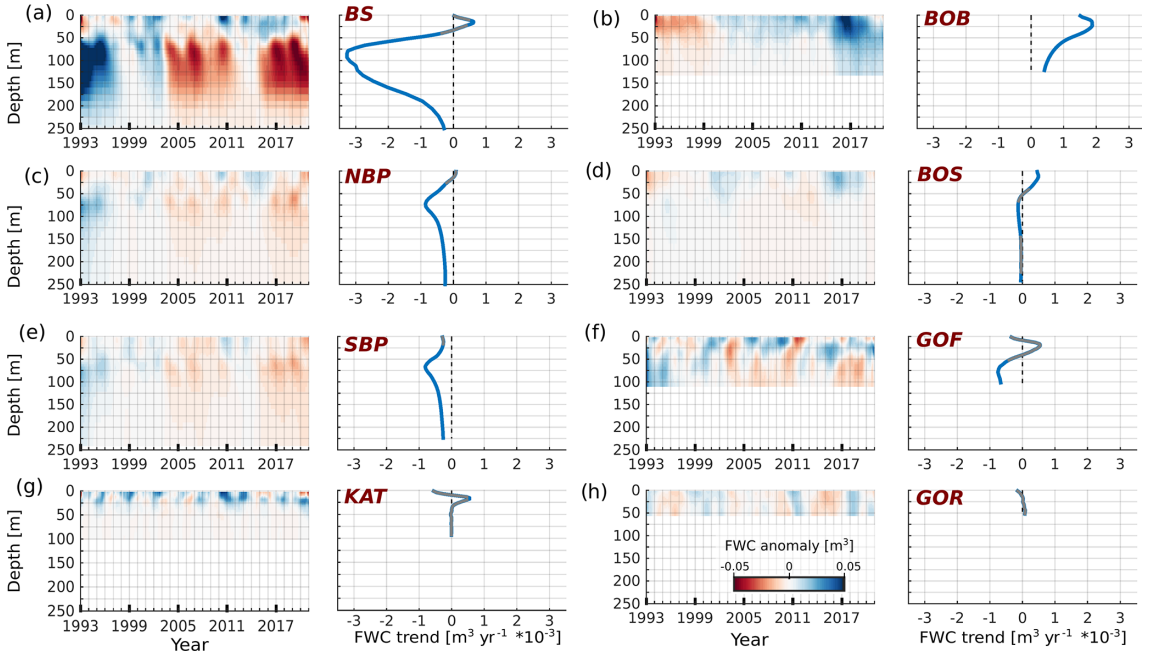

Figure 4. Vertical distribution of the horizontal mean FWC anomaly and corresponding trends for each Baltic Sea sub-basin. Trends with statistical significance less than 5 % (p value < 0.05) are shown as grey line segments. The abbreviations for the sub-basins are as follows: BS (Baltic Sea), NBP (northern Baltic Proper), SBP (southern Baltic Proper), KAT (Kattegat), BOB (Bay of Bothnia), BOS (Bothnian Sea), GOF (Gulf of Finland), and GOR (Gulf of Riga) (data ref. 1, Table 1).

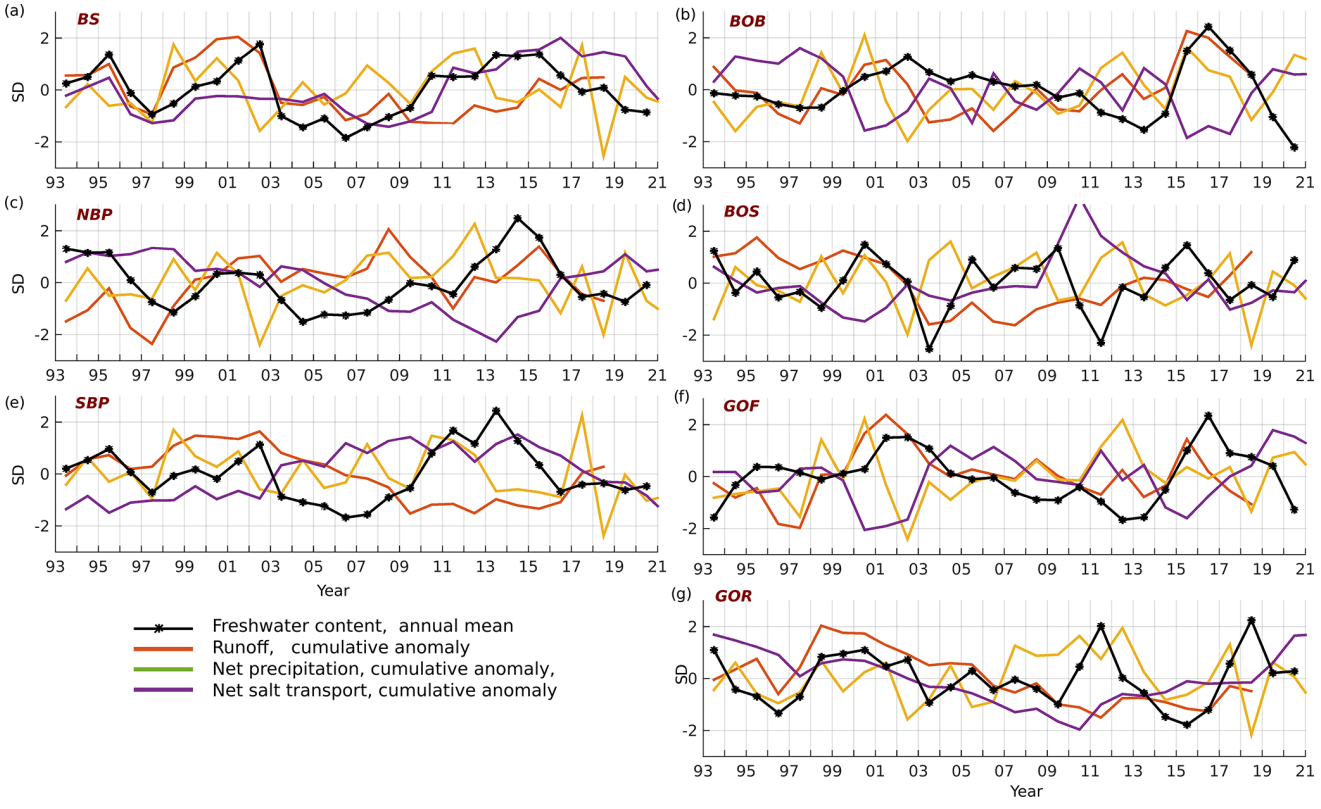

Figure 5. Normalized time series of detrended annual mean FWC (black asterisk), runoff, net precipitation, and net salt fluxes. The abbreviations for the sub-basins are as follows: BS (Baltic Sea), NBP (northern Baltic Proper), SBP (southern Baltic Proper), BOB (Bay of Bothnia), BOS (Bothnian Sea), GOF (Gulf of Finland), and GOR (Gulf of Riga) (data ref. 1, 2, 3, 1; Table 1).

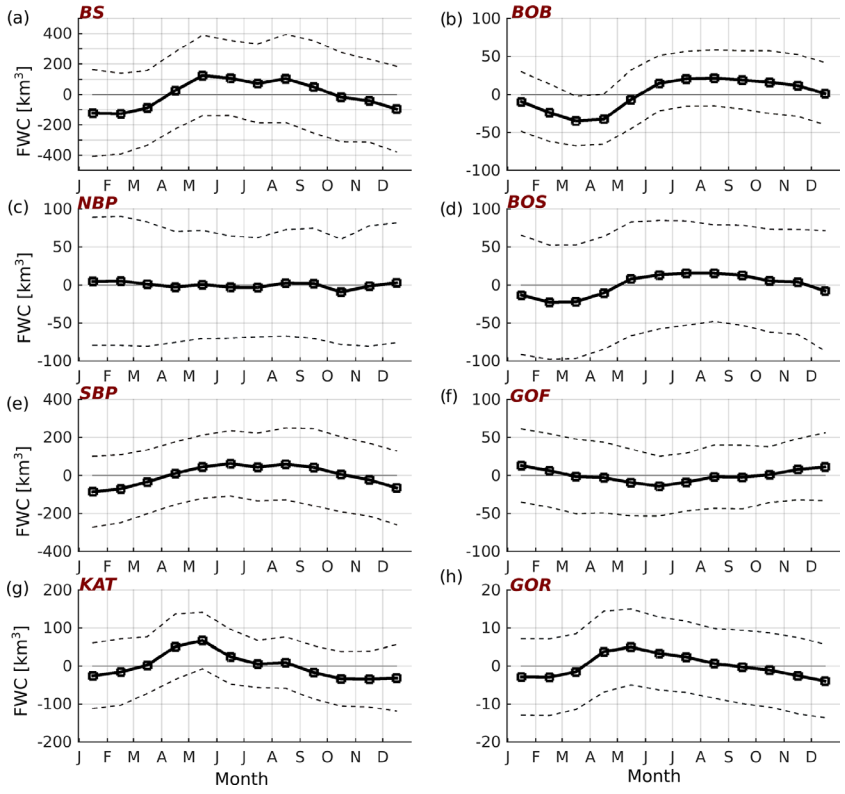

Figure 6. Seasonality of detrended FWC in the different Baltic Sea sub-basins. The abbreviations for the sub-basins are as follows: BS (Baltic Sea), NBP (northern Baltic Proper), SBP (southern Baltic Proper), KAT (Kattegat), BOB (Bay of Bothnia), BOS (Bothnian Sea), GOF (Gulf of Finland), and GOR (Gulf of Riga) (data ref. 1, Table 1).

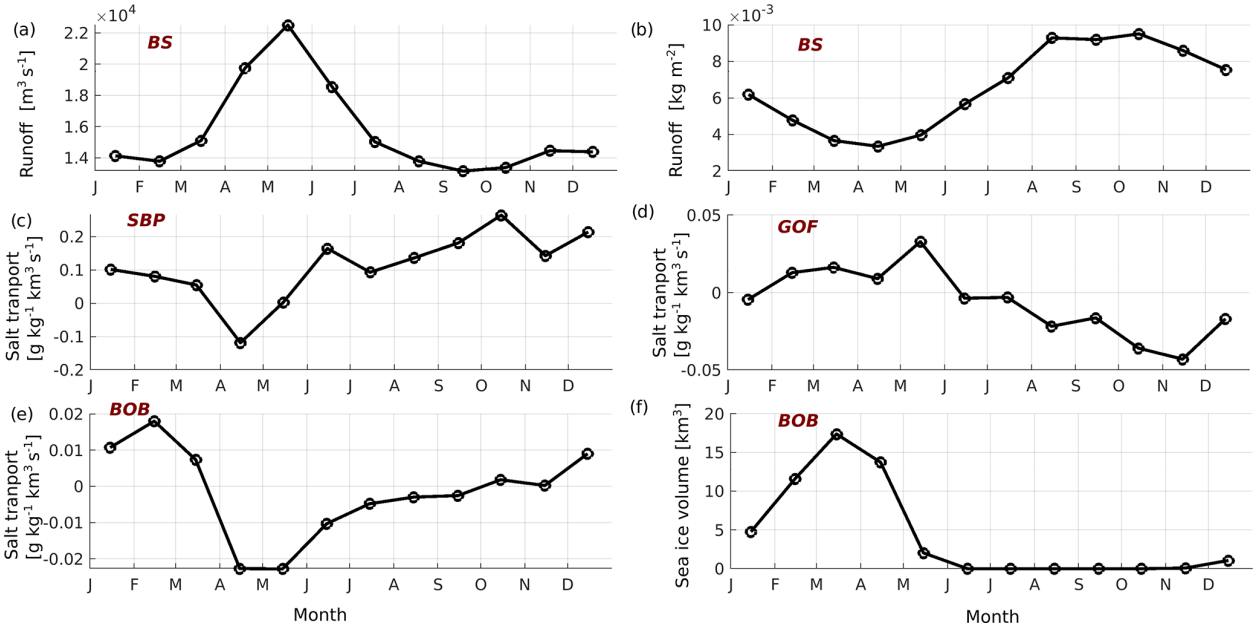

Figure 7. Seasonality of runoff and net precipitation over the Baltic Sea (BS) **(a, b)**; salt transport through the western boundary of the southern Baltic Proper (SBP) **(c)**, the Gulf of Finland (GOF) **(d)**, and the southern boundary of the Bothnian Bay (BOB) **(e)**; and the sea ice volume in the Bothnian Bay **(f)**.

Future climate model scenarios could provide insight into how combinations of different factors affect long-term salinity changes in the Baltic Sea, although the uncertainties in the climate projections are high. Three main factors that affect salinity and FWC are the wind fields over the Baltic Sea region (Lass and Matthäus, 1996), river runoff to the Baltic Sea (Schinke and Matthäus, 1998), and global mean sea level rise (Meier et al., 2017, 2021). With increasing precipitation and river runoff, the salinity in the Baltic Sea decreases (Saraiva et al., 2019). Mean sea level rise, in turn, tends to increase salinity because saltwater imports through the Danish straits are larger (Meier et al., 2017, 2021). An increasing westerly wind could block the freshwater flow out of the Baltic Sea, causing reduced salt transport to the Baltic Sea (Meier and Kauker, 2003), but Schimanke et al. (2014) showed that the intensity and frequency of MBIs were projected to slightly increase due to changes in the wind fields. In summary, different factors affect salinity and FWC differently, so the observed effect cannot be explained in a simple way. For instance, Meier et al. (2021) stated that no changes in the Baltic Sea salinity were found because river runoff and sea level rise approximately compensated each other. Therefore, also in our study, we could not explain the trends and multidecadal variations, although we have considered the main factors that affect the FWC of the Baltic Sea.

5 Conclusion

Temporal variability of the FWC at different timescales has an opposite pattern in the northern and southern sub-basins of the Baltic Sea. The Gulf of Bothnia shows positive tendencies of FWC, while in the Baltic Proper, negative tendencies can be witnessed. The total FWC of the Baltic Sea has decreased steadily with a rate of $23.9\,\mathrm{km^3\,yr^{-1}}$ over the years 1993–2021. There is no solid explanation for what caused it because different drivers could compensate for each other to a certain extent.

Interannual variations of the FWC in the Bothnian Bay are supported by interannual variability of river runoff, net precipitation, and salt transport from the Bothnian Sea, the latter being opposite to the changes of FWC. In the Bothnian Sea and northern Baltic Proper, interannual variations of the FWC and net salt flux to the basins are opposite to each other. The changes in river runoff and net precipitation have a complex contribution to the changes of FWC. In the southern Baltic Proper, the changes of FWC, river runoff, net precipitation, and net salt flux have rather complex relationships. A separate study is needed to understand the interplay of these factors, especially seeing as the variations of salt transport and FWC are opposite to each other from 1993 until 2010 but positively correlated thereafter.

The seasonal course of FWC in different sub-basins highlights the local dynamics and explains the FWC dynamics in relation to the local sources of freshwater and salt transport through the sections that border the corresponding sub-basin. Seasonal changes of sea ice volume affect the seasonal cycle of the FWC in the Gulf of Bothnia.

By taking into consideration the spatial and temporal tendencies of the FWC shown in each separate sub-basin, we can characterize the Baltic Sea as a typical estuarine system with a strengthening exchange flow in time. Geographically, the system spans from the Danish straits in the south to the Bothnian Bay in the north. The southern part corresponds to the estuary mouth, where saltwater transport from the ocean prevails and leads to a decrease in FWC. At the other end, the Bothnian Bay is a typical estuary head characterized by a significant influence of freshwater discharge, resulting in an increase in FWC over time. The northern Baltic Proper and the Bothnian Sea converge in the transitional zone between the saltwater-dominated region and the freshwater-dominated region. In terms of vertical distribution, the freshwater-influenced area extends towards the estuary mouth in the upper layer, while the saltwater-dominated area extends towards the estuary head in the lower layer. Moving eastward, the Gulf of Finland represents a branch of the main estuarine system and shares general characteristics of a transition zone, although it possesses its own unique estuarine structure and dynamics (Maljutenko and Raudsepp, 2019; Westerlund et al., 2019; Liblik et al., 2018).

Appendix A

We utilize a clustering method to assess the accuracy of the hydrodynamic model. This method provides insights into the overall model accuracy by clustering the errors. The clustering process employs the K-means algorithm, which is a form of unsupervised machine learning (Jain, 2010). The original description of this method can be found in the work of Raudsepp and Maljutenko (2022). In our assessment, all available data within the model domain and simulation period are included, even if the verification data are unevenly distributed or occasionally sparse. This approach allows us to evaluate the model quality at each specific location and time instance where measurements have been obtained.

The first step of the method is the formation of a two-dimensional error space of two simultaneously measured parameters. A two-dimensional error space $(\mathrm{d}S, \mathrm{d}T)$, where $\mathrm{d}S = (S_{\mathrm{mod}} - S_{\mathrm{obs}})$ and $\mathrm{d}T = (T_{\mathrm{mod}} - T_{\mathrm{obs}})$, of simultaneously measured temperature and salinity values was formed as the basis for the clustering. The dataset utilized in this validation study was obtained from the EMODnet dataset compiled by SMHI (SMHI, 2023; data ref. 4, Table 1). It comprises a total of 651 565 observations that align with the CMEMS reanalysis simulation period, encompassing the years 1993 to 2021. We extracted the nearest model values from the reanalysis dataset for each observation.

The second step is the selection of the number of clusters. For simplicity, we preselected five clusters. The third step

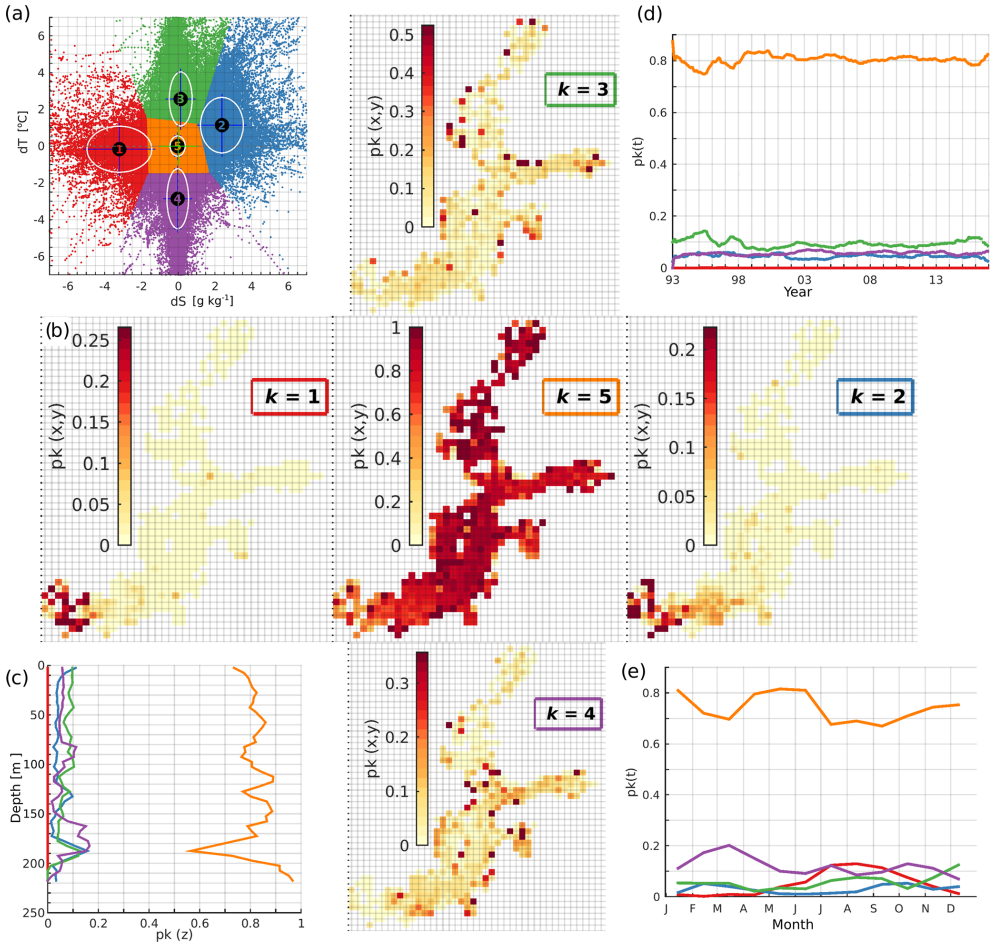

Figure A1. Distribution of normalized error clusters for $k = 5$ (**a**). The spatial distribution (**b**, shaded sub-plots), vertical distribution **(c)**, temporal distribution **(d)**, and seasonal distribution **(e)** of the share of error points belonging to the five different clusters.

Table A1. The share (%), bias, root-mean-square error (RMSE), standard deviation (SD), and correlation coefficient (Corr) for each of the five clusters.

	Shares	Bias		SD		RMSE		Corr		
k	%	dS (g kg^{-1})	dT (°C)	S (g kg^{-1})	T (°C)	S (g kg^{-1})	T (°C)	S	T	dSdT
1	2.8	−3.201	−0.169	1.763	1.250	3.654	1.261	0.950	0.721	−0.155
2	5.5	2.379	1.140	1.164	1.508	2.649	1.891	0.983	0.626	0.206
3	8.0	0.137	2.567	0.621	1.465	0.636	2.955	0.994	0.637	0.030
4	6.7	−0.026	−2.859	0.587	1.630	0.587	3.291	0.985	0.693	−0.006
5	77.0	−0.029	0.006	0.412	0.549	0.413	0.549	0.994	0.907	0.113

is to perform a K-means clustering of the 2-dimensional errors. The clustering is applied to the normalized errors. Normalization was done for temperature and salinity errors separately using corresponding standard deviations of the errors. The K-means algorithm finds the location of the centroids of a predefined number of clusters in the error space. The location of the centroids represents the bias of the set of errors for each cluster. The fourth step is the calculation of statistical metrics of non-normalized clustered errors. Common statistics, like SD, RMSE, and correlation coefficient, can be calculated for the parameters belonging to each cluster.

The fifth step is the analysis of spatio-temporal distributions of the errors belonging to different clusters. In the formation of the error space, we retained the coordinates of each error point $(\mathrm{d}S, \mathrm{d}T)(x, y)$, which enables us to map the errors belonging to each cluster back to the location where the mea-

surements were performed. In order to do that, the model domain is divided into horizontal grid cells (i, j) of $1 \times 1\,\mathrm{km}^2$ in size. Subsequently, the number of error points belonging to different clusters at each grid cell (i, j) is counted. The total number of error points belonging to the grid cell (i, j) is the sum of the points of each cluster. The share of error points in each grid cell belonging to cluster k is the ratio of the number of error points of cluster k and the total number of error points in each grid cell.

Figure A1 displays the results of the K-means clustering for non-normalized errors. Table A1 presents the corresponding metrics. Within cluster $k = 5$, the salinity and temperature values closely align with the observations, with a bias of $\mathrm{d}S = -0.03\,\mathrm{g\,kg}^{-1}$ and $\mathrm{d}T = 0.006\,^{\circ}\mathrm{C}$, respectively. This cluster encompasses 77 % of all data points. The points are distributed throughout the entire Baltic Sea, with a dominant share exceeding 0.5 (Fig. A1b). Clusters $k = 3$ and $k = 4$ exhibit relatively even spatial distributions over the Baltic Sea, accounting for 8 % and 7 % of the points, respectively. These clusters are particularly noteworthy due to their small salinity biases and variability, which are crucial for estimating the freshwater content (FWC) directly impacted by salinity. Collectively, approximately 92 % of all validation points exhibit relatively low salinity bias, standard deviation (SD), and root-mean-square error (RMSE) (Table A1). Consequently, we anticipate that the model reanalysis data provide sufficiently accurate information for calculating the FWC of the Baltic Sea.

Appendix B

The mixing of two water masses (M_{ref}, M_{f}) with different salinities (S_{ref}, S_{f}) results in the mixture ($M_{\mathrm{ref}} + M_{\mathrm{f}}$) with unknown salinity S:

$$M_{\mathrm{ref}} S_{\mathrm{ref}} + M_{\mathrm{f}} S_{\mathrm{f}} = (M_{\mathrm{ref}} + M_{\mathrm{f}})\, S. \tag{B1}$$

If one of the water masses, M_{f}, is freshwater with $S_{\mathrm{f}} = 0$, and we assume that the densities of the water masses of different salinities have negligible difference, then Eq. (B1) simplifies to

$$V_{\mathrm{ref}} S_{\mathrm{ref}} = V_{\mathrm{ref}} S + V_{\mathrm{f}} S, \tag{B2}$$

where V_{ref} and V_{f} are the volumes of reference water and freshwater, respectively. The formulation of Boyer et al. (2007) for freshwater content (FWC) follows directly from Eq. (B2), where the volume of freshwater in the total volume of the mixture is

$$V_{\mathrm{f}} = V_{\mathrm{ref}} \left(\frac{S_{\mathrm{ref}} - S}{S} \right). \tag{B3}$$

In the derivation of Eq. (B3), the volume of the mixture of two water masses is not limited.

The formulation (B3) answers the question of how much freshwater (V_{f}) is needed to dilute the water (V_{ref}) with salinity S_{ref} to the salinity S if $S < S_{\mathrm{ref}}$. The volume of water with S will be $(V_{\mathrm{ref}} + V_{\mathrm{f}})$. If $S > S_{\mathrm{ref}}$, then Eq. (B3) shows how much freshwater should be removed from the volume of water (V_{ref}) with the salinity S_{ref} to obtain water with the salinity S. In this case, the volume of resulting water with S will be $(V_{\mathrm{ref}} - V_{\mathrm{f}})$.

We would like to note that the relationship (B3) is not a linear relationship between salinity and V_{f}. There are straightforward conclusions that can be drawn from Eq. (B3). First, to obtain water with a salinity close to zero, an infinite amount of freshwater is needed, independent of the S_{ref},

$$\lim_{S \to 0} V_{\mathrm{f}} = \infty.$$

Second, no freshwater is needed to add to the water V_{ref} if the mixture has a salinity equal to S_{ref}. Third, if

$$\lim_{S \to \infty} V_{\mathrm{f}} = -V_{\mathrm{ref}},$$

then all water should be removed from the mixture.

In its practical application, the formulation (Eq. B3) means that a fixed volume equal to V_{ref} was initially filled with the water of salinity S_{ref}. Then, V_{f} is the volume of freshwater that was needed to dilute the water to the observed salinity S. In this case, the volume of the mixture $(V_{\mathrm{ref}} + V_{\mathrm{f}})$ with salinity S is larger than the initial volume V_{ref}. This means that the amount of water in the mixture, V_{f}, with salinity S should be removed from the system after the mixing is complete. If $S > S_{\mathrm{ref}}$, then $V_{\mathrm{f}} < 0$, and this is the volume of freshwater that was removed from the system to obtain water with the salinity S. In such a case, the volume of the mixture $(V_{\mathrm{ref}} - V_{\mathrm{f}})$ with salinity S is smaller than the initial volume V_{ref}. This means that the amount of water in the mixture, V_{f} with salinity S, should be added to the system.

In the natural system, water volume and salinity are conserved when volume and salt exchange with the outside system is allowed. First, we assume that the natural system is initially filled with water V_{ref} with salinity S_{ref}. Then, if at some time instance we observe that water salinity has decreased to S, so that $S < S_{\mathrm{ref}}$, then V_{f} was added to the system either by river runoff or net precipitation. (Without losing generality, we neglect the presence of ice in the system and variations of the water volume of the system.) At the same time, to fix the volume of the natural system, the amount of water V_{f} with salinity S must be removed from the system due to outflow through the open boundary, for instance. If water salinity has increased to S, so that $S > S_{\mathrm{ref}}$, then the amount of freshwater V_{f} has been removed from the system either by evaporation or outflow through the open boundary. Simultaneously, to conserve the volume of water in the natural system, the amount of water V_{f} with salinity S must be transported to the system due to inflow from the open boundary. We would like to note that in the current argumentation, the actual inflow/outflow volume and salt transport through the open boundary cannot be estimated from knowing the V_{f}.

The derivation of the formulation by Gustafsson and Stigebrandt (1996) is based on the conservation of salt in mixing

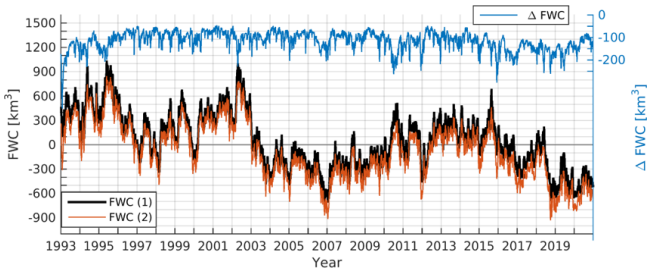

Figure B1. Time series of FWC in the Baltic Sea as calculated according to Eq. (B3) (black line, 1) and Eq. (B5) (brown line, 2) and difference between Eqs. (B5) and (B3) (blue).

of two water masses; i.e. Eqs. (B1) and (B2) are valid. Additionally, the assumption behind their formulation is that the water volume of the mixture, $V = V_f + V_{ref}$, is known, while V_{ref} is an unknown volume. Thus, in addition to Eq. (B2), the unknown volume can be expressed as

$$V_{ref} = V - V_f. \tag{B4}$$

Substituting Eq. (B4) into Eq. (B2), we can express FWC as

$$V_f = V\frac{(S_{ref} - S)}{S_{ref}}. \tag{B5}$$

The relationship between salinity and V_f is linear in Eq. (B5). Now some conclusions will be drawn from Eq. (B5). First, if the salinity is $S = 0$, then $V_f = V$; i.e. all water in the mixture is freshwater. Second, if $S = S_{ref}$, then $V_f = 0$; i.e. there is no freshwater in the mixture. If $S > S_{ref}$, then we obtain that $V_f < 0$, which means that a fraction of the water in the mixture becomes negative. Therefore, in its initial applications (Gustafsson and Stigebrandt, 1996; Eilola and Stigebrandt, 1998; Winsor et al., 2001), the relationship (B5) is bounded to zero when $S > S_{ref}$. The argumentation about the dynamics of the freshwater content is not applicable to the formulation by Gustafsson and Stigebrandt (1996). In the applicability range $S \leq S_{ref}$, Eq. (B5) can be interpreted as follows: initially, a fixed volume, V, is filled in with the water with salinity S_{ref}, and, then, the amount of water V_f with salinity S_{ref} is removed from the fixed volume and replaced with freshwater with volume V_f to obtain the mixture with salinity S.

Technically, Eq. (B5) can also be used for the calculation of V_f if $S > S_{ref}$. We have calculated FWC for the whole Baltic Sea using Eqs. (B3) and (B5) (Fig. B1). The difference of the calculated FWC of the Baltic Sea is around 100 km^3 and rarely exceeds 200 km^3, while the FWC anomaly of the Baltic Sea varies in the range of $\pm$1000 km^3. The estimates used by either formulation are between 10 %–20 %. We would like to point out that FWC calculated by Eq. (B3) (Boyer et al., 2007) is always larger than FWC calculated by Eq. (B5) (Gustafsson and Stigebrandt, 1996):

$$\Delta\text{FWC} \equiv \text{Eq. (B5)} - \text{Eq. (B3)} = \frac{-(S - S_{ref})^2}{S S_{ref}}. \tag{B6}$$

From Eq. (B6) we can see that the difference in FWC of two formulations increases with the increase in the difference between reference water salinity and the salinity of the mixture.

Data availability. This study is based on public databases and the references are listed in Table 1.

Supplement. The supplement related to this article is available online at: https://doi.org/10.5194/sp-1-osr7-7-2023-supplement.

Author contributions. In the study, UR was responsible for conceptualizing the research, developing the methodology, conducting the investigation, performing formal analysis, and writing the original draft of the paper. IM carried out formal analyses, conducted data curation, and handled data visualization, while also participating in the initial drafting of the manuscript. AB was involved in formal analysis, investigation, and data visualization. RU and PL obtained funding and managed project administration tasks. All authors collaborated in the review and editing of the manuscript.

Competing interests. The contact author has declared that none of the authors has any competing interests.

Disclaimer. The Copernicus Marine Service offering is regularly updated to ensure it remains at the forefront of user requirements. In this process, some products may undergo replacement or renaming, leading to the removal of certain product IDs from our catalogue.

If you have any questions or require assistance regarding these modifications, please feel free to reach out to our user support team for further guidance. They will be able to provide you with the necessary information to address your concerns and find suitable alternatives, maintaining our commitment to delivering top-quality services.

Publisher's note: Copernicus Publications remains neutral with regard to jurisdictional claims in published maps and institutional affiliations.

Review statement. This paper was edited by Pierre Brasseur and reviewed by three anonymous referees.

References

Axell, L.: EU Copernicus Marine Service Product User Manual for Baltic Sea Physical Reanalysis Product, BALTICSEA_REANALYSIS_PHY_003_011, Issue 2.1, Mercator Ocean International, https://doi.org/10.5281/zenodo.7935113, 2021.

Boyer, T., Levitus, S., Antonov, J., Locarnini, R., Mishonov, A., Garcia, H., and Josey, S. A.: Changes in freshwater content in

the North Atlantic Ocean 1955–2006, Geophys. Res. Lett., 34, L16603, https://doi.org/10.1029/2007GL030126, 2007.

Buga, L., Sarbu, G., Fryberg, L., Magnus, W., Wesslander, K., Gatti, J., Leroy, D., Iona, S., Larsen, M., Koefoed Rømer, J., Østrem, A. K., Lipizer, M., and Giorgetti A.: EMODnet Chemistry Eutrophication and Acidity aggregated datasets v2018, EMODnet, Thematic Lot no. 4/SI2.749773, https://doi.org/10.6092/EC8207EF-ED81-4EE5-BF48-E26FF16BF02E, 2018.

Durack, P. J., Wijffels, S. E., and Matear, R. J.: Ocean Salinities Reveal Strong Global Water Cycle Intensification during 1950 to 2000, Science, 336, 6080455–6080458, https://doi.org/10.1126/science.1212222, 2012.

Eilola, K. and Stigebrandt, A.: Spreading of juvenile freshwater in the Baltic proper, J. Geophys. Res., 103, 27795–27807, https://doi.org/10.1029/98JC02369, 1998.

EU Copernicus Marine Service Product: Baltic Sea Physics Reanalysis, cmems_mod_bal_phy_my_P1D-m, Mercator Ocean International [data set], https://doi.org/10.48670/moi-00013, 2023.

Giorgetti, A., Lipizer, M., Molina Jack, M. E., Holdsworth, N., Jensen, H. M., Buga, L., Sarbu, G., Iona, A., Gatti, J., Larsen, M., and Fyrberg, L.: Aggregated and Validated Datasets for the European Seas: The Contribution of EMODnet Chemistry, Front. Mar. Sci., 7, 583657, https://doi.org/10.3389/fmars.2020.583657, 2020.

Gröger, M., Placke, M., Meier, H. E. M., Börgel, F., Brunnabend, S.-E., Dutheil, C., Gräwe, U., Hieronymus, M., Neumann, T., Radtke, H., Schimanke, S., Su, J., and Väli, G.: The Baltic Sea Model Intercomparison Project (BMIP) – a platform for model development, evaluation, and uncertainty assessment, Geosci. Model Dev., 15, 8613–8638, https://doi.org/10.5194/gmd-15-8613-2022, 2022.

Gustafsson, B. and Stigebrandt, A.: Dynamics of the freshwater influenced surface layers in the Skagerrak, J. Sea Res., 35, 39–53, https://doi.org/10.1016/S1385-1101(96)90733-9, 1996.

Gustafsson, E. and Omstedt, A.: Sensitivity of Baltic Sea deep water salinity and oxygen concentration to variations in physical forcing, Boreal Environ. Res., 14, 18–30, 2009.

Hersbach, H., Bell, B., Berrisford, P., Hirahara, S., Horányi, A., Muñoz-Sabater, J., Nicolas, J., Peubey, C., Radu, R., Schepers, D., and Simmons, A.: The ERA5 global reanalysis, Q. J. Roy. Meteor., 146, 1999–2049, 2020.

Hersbach, H., Bell, B., Berrisford, P., Biavati, G., Horányi, A., Muñoz Sabater, J., Nicolas, J., Peubey, C., Radu, R., Rozum, I., Schepers, D., Simmons, A., Soci, C., Dee, D., and Thépaut, J.-N.: ERA5 hourly data on single levels from 1940 to present, Copernicus Climate Change Service (C3S) Climate Data Store (CDS) [data set], https://doi.org/10.24381/cds.adbb2d47, 2023.

Hordoir, R., Axell, L., Höglund, A., Dieterich, C., Fransner, F., Gröger, M., Liu, Y., Pemberton, P., Schimanke, S., Andersson, H., Ljungemyr, P., Nygren, P., Falahat, S., Nord, A., Jönsson, A., Lake, I., Döös, K., Hieronymus, M., Dietze, H., Löptien, U., Kuznetsov, I., Westerlund, A., Tuomi, L., and Haapala, J.: Nemo-Nordic 1.0: a NEMO-based ocean model for the Baltic and North seas – research and operational applications, Geosci. Model Dev., 12, 363–386, https://doi.org/10.5194/gmd-12-363-2019, 2019.

IOC, SCOR and IAPSO: The international thermodynamic equation of seawater – 2010: calculation and use of thermodynamic properties. Intergovernmental Oceanographic Commission, Manuals and Guides No. 56, UNESCO, 196 pp., http://www.teos-10.org (last access: 11 October 2021), 2010.

IOW THREDDS: The IOW thredds at Leibniz Institute for Baltic Sea Research Warnemuende, IOW THREDDS [data set], https://thredds-iow.io-warnemuende.de/thredds/catalogs/projects/bmip/catalog_bmip_rivers.html (last access: 7 March 2023), 2019.

Jain, A. K.: Data clustering: 50 years beyond *K*-means, Pattern Recogn. Lett., 31, 651–666, https://doi.org/10.1016/j.patrec.2009.09.011, 2010.

Kniebusch, M., Meier, H. E. M., and Radtke, H.: Changing salinity gradients in the Baltic Sea as a consequence of altered freshwater budgets, Geophys. Res. Lett., 46, 9739–9747, https://doi.org/10.1029/2019GL083902, 2019.

Lass, H. U. and Matthäus, W.: On temporal wind variations forcing salt water inflows into the Baltic Sea, Tellus A, 48, 663–671, https://doi.org/10.1034/j.1600-0870.1996.t01-4-00005.x, 1996.

Lehmann, A. and Post, P.: Variability of atmospheric circulation patterns associated with large volume changes of the Baltic Sea, Adv. Sci. Res., 12, 219–225, https://doi.org/10.5194/asr-12-219-2015, 2015.

Lehmann, A., Höflich, K., Post, P., and Myrberg, K.: Pathways of deep cyclones associated with large volume changes (LVCs) and major Baltic inflows (MBIs), J. Marine Syst., 167, 11–18, https://doi.org/10.1016/j.jmarsys.2016.10.014, 2017.

Lehmann, A., Myrberg, K., Post, P., Chubarenko, I., Dailidiene, I., Hinrichsen, H.-H., Hüssy, K., Liblik, T., Meier, H. E. M., Lips, U., and Bukanova, T.: Salinity dynamics of the Baltic Sea, Earth Syst. Dynam., 13, 373–392, https://doi.org/10.5194/esd-13-373-2022, 2022.

Leppäranta M. and Myrberg, K.: Physical Oceanography of the Baltic Sea, Springer-Verlag, 378 pp., ISBN 978-3-540-79702-9, 2009.

Liblik, T., Naumann, M., Alenius, P., Hansson, M., Lips, U., Nausch, G., Tuomi, L., Wesslander, K., Laanemets, J., and Viktorsson, L.: Propagation of impact of the recent Major Baltic Inflows from the Eastern Gotland basin to the Gulf of Finland, Front. Mar. Sci., 5, 222, https://doi.org/10.3389/fmars.2018.00222, 2018.

Liu, Y. and Fu, W.: Assimilating high-resolution sea surface temperature data improves the ocean forecast potential in the Baltic Sea, Ocean Sci., 14, 525–541, https://doi.org/10.5194/os-14-525-2018, 2018.

Liu, Y., Axell, L., Jandt-Scheelke S., Lorkowski, I., Lindenthal, A., Verjovkina S., and Schwichtenberg, F.: EU Copernicus Marine Service Quality Information Document for Baltic Sea Physical Reanalysis Product, BALTICSEA_REANALYSIS_PHY_003_011, Issue 2.5, Mercator Ocean International, https://doi.org/10.5281/zenodo.7935113, 2019.

Maljutenko, I. and Raudsepp, U.: Long-term mean, interannual and seasonal circulation in the Gulf of Finland – The wide salt wedge estuary or gulf type ROFI, J. Marine Syst., 195, 1–19, https://doi.org/10.1016/j.jmarsys.2019.03.004, 2019.

Meier, H. E. M. and Kauker, F.: Modeling decadal variability of the Baltic Sea: 2. Role of freshwater inflow and large-scale atmospheric circulation for salinity, J. Geophys. Res., 108, 3368, https://doi.org/10.1029/2003JC001799, 2003.

Meier, H. E. M., Höglund, A., Eilola, K., and Almroth-Rosell, E.: Impact of accelerated future global mean sea level rise on hypoxia in the Baltic Sea, Clim. Dynam., 49, 163–172, https://doi.org/10.1007/s00382-016-3333-y, 2017.

Meier, H. E. M., Eilola, K., Almroth-Rosell, E., Schimanke, S., Kniebusch, M., Höglund, A., Pemberton, P., Liu, Y., Väli, G., and Saraiva, S.: Disentangling the impact of nutrient load and climate changes on Baltic Sea hypoxia and eutrophication since 1850, Clim. Dynam., 53, 1145–1166, https://doi.org/10.1007/s00382-018-4296-y, 2019a.

Meier, H. E. M., Eilola, K., Almroth-Rosell, E., Schimanke, S., Kniebusch, M., Höglund, A., Pemberton, P., Liu, Y., Väli, G., and Saraiva, S.: Correction to: Disentangling the impact of nutrient load and climate changes on Baltic Sea hypoxia and eutrophication since 1850, Clim. Dynam., 53, 1167–1169. https://doi.org/10.1007/s00382-018-4483-x, 2019b.

Meier, H. E. M., Dieterich, C., and Gröger, M.: Natural variability is a large source of uncertainty in future projections of hypoxia in the Baltic Sea, Commun. Earth Environ., 2, 50, https://doi.org/10.1038/s43247-021-00115-9, 2021.

Meier, H. E. M., Kniebusch, M., Dieterich, C., Gröger, M., Zorita, E., Elmgren, R., Myrberg, K., Ahola, M. P., Bartosova, A., Bonsdorff, E., Börgel, F., Capell, R., Carlén, I., Carlund, T., Carstensen, J., Christensen, O. B., Dierschke, V., Frauen, C., Frederiksen, M., Gaget, E., Galatius, A., Haapala, J. J., Halkka, A., Hugelius, G., Hünicke, B., Jaagus, J., Jüssi, M., Käyhkö, J., Kirchner, N., Kjellström, E., Kulinski, K., Lehmann, A., Lindström, G., May, W., Miller, P. A., Mohrholz, V., Müller-Karulis, B., Pavón-Jordán, D., Quante, M., Reckermann, M., Rutgersson, A., Savchuk, O. P., Stendel, M., Tuomi, L., Viitasalo, M., Weisse, R., and Zhang, W.: Climate change in the Baltic Sea region: a summary, Earth Syst. Dynam., 13, 457–593, https://doi.org/10.5194/esd-13-457-2022, 2022.

Mohrholz, V.: Major Baltic inflow statistics–revised, Front. Mar. Sci., 5, 384, https://doi.org/10.3389/fmars.2018.00384, 2018.

Mohrholz, V., Naumann, M., Nausch, G., Krüger, S., and Gräwe, U.: Fresh oxygen for the Baltic Sea – An exceptional saline inflow after a decade of stagnation, J. Marine Syst., 148, 152–166, https://doi.org/10.1016/j.jmarsys.2015.03.005, 2015.

Pemberton, P., Löptien, U., Hordoir, R., Höglund, A., Schimanke, S., Axell, L., and Haapala, J.: Sea-ice evaluation of NEMO-Nordic 1.0: a NEMO–LIM3.6-based ocean–sea-ice model setup for the North Sea and Baltic Sea, Geosci. Model Dev., 10, 3105–3123, https://doi.org/10.5194/gmd-10-3105-2017, 2017.

Pratap, S. and Markonis, Y.: The response of the hydrological cycle to temperature changes in recent and distant climatic history, Prog. Earth Planet. Sci., 9, 30, https://doi.org/10.1186/s40645-022-00489-0, 2022.

Radtke, H., Brunnabend, S.-E., Gräwe, U., and Meier, H. E. M.: Investigating interdecadal salinity changes in the Baltic Sea in a 1850–2008 hindcast simulation, Clim. Past, 16, 1617–1642, https://doi.org/10.5194/cp-16-1617-2020, 2020.

Raudsepp, U. and Maljutenko, I.: A method for assessment of the general circulation model quality using the K-means clustering algorithm: a case study with GETM v2.5, Geosci. Model Dev., 15, 535–551, https://doi.org/10.5194/gmd-15-535-2022, 2022.

Reissmann, J. H., Burchard, H., Feistel,R., Hagen, E., Lass, H. U., Mohrholz, V., Nausch, G., Umlauf, L., and Wieczorek, G.: Vertical mixing in the Baltic Sea and consequences for eutrophication a review, Progr. Oceanogr., 82, 47–80, https://doi.org/10.1016/j.pocean.2007.10.004, 2009.

Saraiva, S., Meier, H. E. M., Andersson, H., Höglund, A., Dieterich, C., Gröger, M., Hordoir, R., and Eilola, K.: Uncertainties in Projections of the Baltic Sea Ecosystem Driven by an Ensemble of Global Climate Models, Front. Earth Sci., 6, 244, https://doi.org/10.3389/feart.2018.00244, 2019.

Schimanke, S. and Meier, H. E. M.: Decadal to centennial variability of salinity in the Baltic Sea, J. Climate, 29, 7173–7188, https://doi.org/10.1175/JCLI-D-15-0443.1, 2016.

Schimanke, S., Dieterich, C., and Meier, H. E. M.: An algorithm based on sea-level pressure fluctuations to identify major Baltic inflow events, Tellus A, 66, 23452, https://doi.org/10.3402/tellusa.v66.23452, 2014.

Schinke, H. and Matthäus, W.: On the causes of major Baltic inflows – an analysis of long time series, Cont. Shelf Res., 18, 67–97, https://doi.org/10.1016/S0278-4343(97)00071-X, 1998.

SMHI: Baltic Sea – Eutrophication and Acidity aggregated datasets 1902/2017 v2018, Swedish Meteorological and Hydrological Institute, EMODnet Chemistry [data set], https://doi.org/10.6092/595D233C-3F8C-4497-8BD2-52725CEFF96B, 2023.

Väli, G., Meier, M., Dieterich, C., and Placke, M.: River runoff forcing for ocean modeling within the Baltic Sea Model Intercomparison Project, Meereswiss. Ber., Warnemünde, Marine Science Reports No. 113, https://doi.org/10.12754/msr-2019-0113, 2019.

Westerlund, A., Tuomi, L., Alenius, P., Myrberg, K., Miettunen, E., Vankevich, R. E., and Hordoir, R.: Circulation patterns in the Gulf of Finland from daily to seasonal timescales, Tellus A, 71, 1627149, https://doi.org/10.1080/16000870.2019.1627149, 2019.

Winsor, P., Rodhe, J., and Omstedt, A.: Baltic Sea ocean climate: an analysis of 100 yr of hydrographic data with focus on the freshwater budget, Clim. Res., 18, 5–15, https://doi.org/10.3354/cr018005, 2001.

State Planet, 1-osr7, 8, 2023
https://doi.org/10.5194/sp-1-osr7-8-2023

High-frequency radar-derived coastal upwelling index

Pablo Lorente[1], Anna Rubio[2], Emma Reyes[3], Lohitzune Solabarrieta[2], Silvia Piedracoba[4], Joaquín Tintoré[3,5], and Julien Mader[2]

[1]Puertos del Estado, Madrid, 28042, Spain
[2]AZTI Marine Research, Basque Research and Technology Alliance (BRTA), Pasaia, 20110, Spain
[3]Balearic Islands Coastal Ocean Observing and Forecasting System (SOCIB), Palma, 07122, Spain
[4]CETMAR (Centro Tecnológico del Mar), Vigo, 36208, Spain
[5]Mediterranean Institute for Advanced Studies (IMEDEA), Esporles, 07190, Spain

Correspondence: Pablo Lorente (plorente@puertos.es)

Received: 30 July 2022 – Discussion started: 30 September 2022
Revised: 24 March 2023 – Accepted: 30 May 2023 – Published: 27 September 2023

Abstract. Coastal upwelling has been extensively studied since it plays a critical role in the connectivity between offshore waters and coastal ecosystems, which has impacts on water quality, fisheries, and aquaculture production. Significant efforts have been devoted to the quantification of the intensity, duration, and variability of this phenomenon by means of coastal upwelling indexes (CUIs), derived from wind, sea level pressure, or sea surface temperature data. Although valuable, first-order descriptors, such classical indexes have been reported to present some limitations. As one of the major shortcomings is the omission of the direct influence of ocean circulation, this work introduces a novel CUI, generated from remotely sensed hourly surface current observations provided by a high-frequency radar (HFR). The consistency of the proposed index (CUI-HFR) is assessed in two different oceanographic areas during two distinct time periods: in the north-western Iberian (NWI) peninsula for 2021 and in the Bay of Biscay (BOB) for 2014. To this aim, CUI-HFR is compared against a traditional CUI based on hourly wind observations (CUI-WIND) provided by two buoys. Likewise, the skill of CUI-HFR to identify upwelling and downwelling processes is also qualitatively evaluated. Complementarily, the prognostic capabilities of the GLOBAL analysis and forecasting system to accurately reproduce upwelling and downwelling events in the NWI area are also analysed (CUI-GLOBAL). Results obtained in these two pilot areas revealed the following: (i) noticeable agreement between CUI-HFR and CUI-WIND, with correlation coefficients above 0.67; and (ii) a proven ability of CUI-HFR and CUI-GLOBAL to categorize a variety of upwelling and downwelling episodes, which highlights their potential applicability for direct upwelling monitoring over any coastal area of the global ocean.

1 Introduction

Since coastal waters encompass many unique habitats and support a wide range of anthropogenic activities (tourism, transportation, fisheries, etc.), accurate monitoring is required for efficient marine resources management, the preservation of vulnerable ecosystems, and the sustained development of the so-called blue economy (Trincardi et al., 2020).

Cutting-edge technology that has been steadily gaining worldwide recognition as an effective shore-based remote sensing instrument is high-frequency radar – HFR (Roarty et al., 2019). HFR networks have become an essential component of ocean observatories as they collect, in near-real time, fine-resolution maps of the upper-layer flow over broad coastal areas, providing a dynamical framework for other traditional in situ observation platforms (Lorente et al., 2022; Rubio et al., 2017). HFR-derived surface circulation is a reliable source of information for search-and-rescue operations and oil spill tracking, among other practical applications (Reyes et al., 2022; Roarty et al., 2019; Rubio et al., 2017). Equally, it can be used for a detailed investiga-

Published by Copernicus Publications.

Table 1. Products from the Copernicus Marine Service used in this study, including the Product User Manual (PUM) and QUality Information Document (QUID). Last access for all web pages cited in this table: 2 June 2023.

Product ref. no.	Product ID and type	Data access	Documentation
1	INSITU_GLO_PHY_UV_DISCRETE_NRT_013_048, in situ observations	EU Copernicus Marine Service Product (2022a)	PUM: Verbrugge et al. (2022a); QUID: Verbrugge et al. (2022b)
2	INSITU_GLO_PHY_UV_DISCRETE_MY_013_044, in situ observations	EU Copernicus Marine Service Product (2023a)	PUM: Etienne et al. (2022); QUID: Etienne et al. (2023)
3	INSITU_IBI_PHYBGCWAV_DISCRETE_MYNRT_013_033, in situ observations	EU Copernicus Marine Service Product (2022b)	PUM: Copernicus Marine In Situ Tac Data Management Team (2021); QUID: Wehde et al. (2022)
4	GLOBAL_ANALYSISFORECAST_PHY_001_024, numerical models	EU Copernicus Marine Service Product (2022c)	PUM: Le Galloudec et al. (2022); QUID: Lellouche et al. (2022)
5	SST_GLO_SST_L4_REP_OBSERVATIONS_010_011, satellite observations	EU Copernicus Marine Service Product (2023b)	PUM: Worsfold et al. (2022); QUID: Worsfold et al. (2023)
6	OCEANCOLOUR_GLO_BGC_L4_MY_009_104, satellite observations	EU Copernicus Marine Service Product (2022d)	PUM: Colella et al. (2022); QUID: Garnesson et al. (2022)

tion of upwelling (UPW) and downwelling (DOW) processes that modulate the connectivity between offshore waters and coastal ecosystems (Lorente et al., 2020; Paduan et al., 2018; Kaplan and Largier, 2006). It occurs when alongshore winds and the Coriolis effect (due to Earth's rotation) combine to drive a near-surface layer of water offshore, a process referred to as Ekman transport (Ekman, 1905). Such cross-shelf transport is compensated for by the vertical uplift of cold and enriched waters that fertilize the uppermost layer. Conversely, during DOW events winds induce net onshore displacement and subduction of surface coastal waters that foster the retention of organic matter and pollutants onto the shoreline with a subsequent impact on residence times and water renewal mechanisms.

Nowadays, there is an emerging question about the impact of anthropogenic pressures on future changes in coastal UPW ecosystems and the potential implications for biodiversity conservation (IPCC, 2022; Abrahams et al., 2021a; Xiu et al., 2018; Bakun et al., 2015; Cropper et al., 2014; Di Lorenzo, 2015). It has been hypothesized that climate change could promote greater land–sea temperature gradients together with stronger alongshore winds, eventually resulting in intensified wind-driven coastal UPW (Di Lorenzo, 2015; Varela et al., 2015; Barton et al., 2013). In Wang et al. (2015), results from an ensemble of climate models showed relevant changes in the timing, duration, intensity, and spatial heterogeneity of coastal UPW in response to future warming in most eastern boundary upwelling systems.

Since there is no available ground-truth observation of vertical currents, diverse coastal upwelling indexes (CUIs) have been derived from historical estimations of other met-ocean parameters (e.g. wind, sea level pressure, or sea surface temperature) to indirectly infer seasonal trends of UPW along the shoreline (Gunduz et al., 2022; Mourre et al., 2023; Abrahams et al., 2021a, b; González-Nuevo et al., 2014; Benazzouz et al., 2014; Wooster et al., 1976; Bakun, 1973). Despite being valuable first-order descriptors, such classical indexes have been reported to provide an incomplete picture of coastal UPW due to a number of limitations, encompassing uncertainties related to the estimation of wind stress or derived from the coarse spatio-temporal resolution of the atmospheric pressure fields used (Jacox et al., 2018).

As one of the major shortcomings is the omission of the direct influence of ocean circulation, the present work intends to fill this gap by introducing a novel CUI, generated from HFR-derived hourly surface current observations (CUI-HFR). Although such an ocean-based index was firstly presented in Lorente et al. (2020) as a proof-of-concept investigation, here we gain further insight into the credibility of the proposed approach by analysing two different regions (Fig. 1a), the north-western Iberian (NWI) peninsula upwelling system and the Bay of Biscay (BOB), for distinct time periods (2021 and 2014, respectively).

In the NWI region, which extends from 40 to 44° N (Fig. 1a), the ocean dynamics are regulated by the relative changes in the strength and position of the Azores high-pressure system with respect to the Iceland low-pressure system, defining two largely wind-driven oceanographic seasons (Lorente et al., 2020). The UPW season is predominant from March to October when northerly winds prevail and induce a south-westward surface flow. The upward flux of cold deep waters supplies nutrients to the euphotic zone, resulting in an elongated alongshore strip of maximum concentration of chlorophyll (Fig. 1b). During the rest of the year, the predominant DOW season is characterized by (i) prominent southerly winds that drive the surface circulation northwards and (ii) low biological productivity, with nutrient concentrations confined in shallower coastal areas (Fig. 1c).

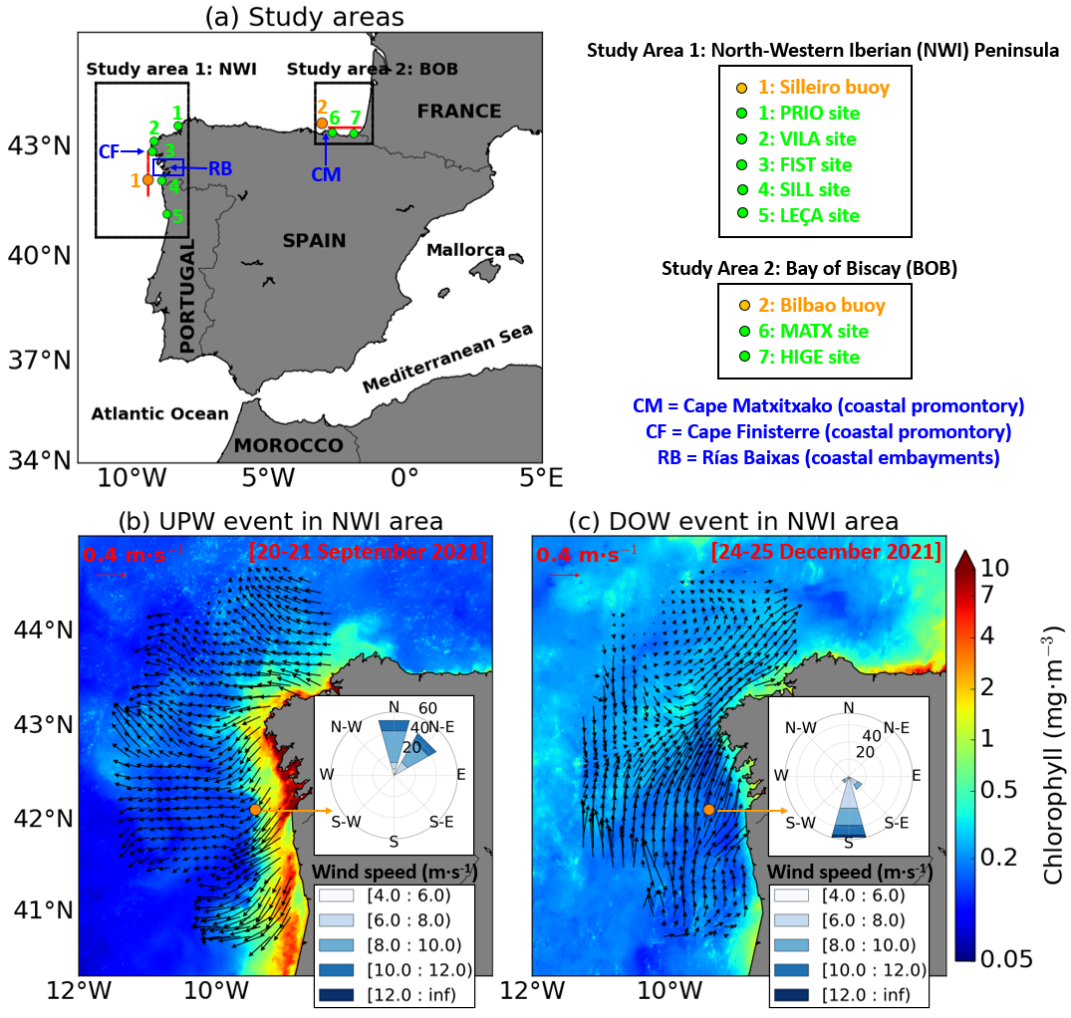

Figure 1. **(a)** Study areas are marked with black squares: the north-western Iberian (NWI) peninsula upwelling system and the Bay of Biscay (BOB), where two high-frequency radars (HFRs) are deployed – product ref. nos. 1 and 2 (Table 1). Green dots denote HFR sites, while orange dots represent the Silleiro buoy and Bilbao buoy locations (product ref. no. 3) (Table 1), moored within the NWI and BOB areas, respectively. Red lines indicate selected transects: HFR-derived surface circulation and satellite-derived chlorophyll distribution – product ref. no. 6 (Table 1) – during a 2 d **(b)** summer upwelling event and **(c)** winter downwelling event in the NWI area, when intense northerly and southerly winds were predominant, respectively.

The south-eastern BOB (Fig. 1a) is characterized by complex topography wherein a combination of different temporal and spatial ocean processes (i.e. slope currents, eddies) governs the local hydrodynamics (Llope et al., 2006). Coastal UPW and DOW processes depict a marked seasonal variability, linked to seasonal changes in the wind regime (Prego et al., 2012; Botas et al., 1990). During autumn and winter, south-westerly winds are prevalent and induce DOW events. In spring and summer, winds are less intense and more variable, with the dominance of easterlies and northeasterlies driving weak but frequent UPW episodes (Fontán et al., 2008). Although UPW (whenever present) can be considered weak in comparison with typical UPW areas worldwide (Borja et al., 2008), this phenomenon has been investigated in the BOB region as they are significantly correlated with the recruitment of commercial fish species (Caballero et al., 2018). In particular, 55 % of the recruitment variability of anchovy fisheries can be explained by upwelling over the spawning area (Borja et al., 2008). Therefore, the HFR deployed in this region might be very useful to monitor the surface circulation and characterize the UPW variability by means of a CUI (Caballero et al., 2018).

The main goal of this contribution is twofold: firstly, to assess the validity of the proposed ocean-based CUI-HFR through its comparison against a traditional CUI based on hourly wind observations (CUI-WIND) provided by adjacent in situ buoys (Fig. 1a). Likewise, the skill of CUI-HFR to categorize UPW and DOW events was also qualitatively evaluated. The second part of the goal is to infer the prognostic capabilities of the GLOBAL analysis and forecasting system

(Lellouche et al., 2018) to accurately reproduce UPW and DOW events previously detected in the NWI region. In this context, hydrodynamic models can serve as ancillary tools for gappy HFR surface current maps by offering a seamless predictive picture of the ocean state.

This work is structured as follows: Sect. 2 outlines the observational and modelled data sources. Section 3 describes the methodology adopted. Results are presented and discussed in Sect. 4. Finally, principal conclusions are drawn in Sect. 5.

2 Data

All the observational and modelled products used in this study are gathered in Table 1 and thoroughly described below.

2.1 The HFR system deployed in NWI

A five-site CODAR SeaSonde HFR network, deployed along the Galician–Portuguese coast (Fig. 1b) since 2004, was used in this work (product ref. nos. 1 and 2 in Table 1). The network is jointly operated by Puertos del Estado, INTECMAR–Xunta de Galicia, and the Portuguese Hydrographic Institute. While the southernmost HFR site operates at 13.5 MHz, the other four sites operate at a central frequency of 4.86 MHz, providing hourly radial vectors that are representative of the currents moving toward or away from the site. All radial current vectors (from two or several sites) within a predefined search radius of 25 km are geometrically combined to estimate hourly total current vectors on a Cartesian regular mesh of 6×6 km horizontal resolution and 200 km range (Lorente et al., 2015, 2020). Data are quality-controlled and delivered freely through the European HFR Node, which oversees the harvesting, harmonization, formatting, and distribution of HFR data (Corgnati et al., 2021).

HFR-derived data used in this study were collected from August to December 2021, once the southernmost site (LEÇA) was calibrated and integrated into the pre-existing network. During this 5-month period, the five sites were simultaneously operational, and the spatial coverage was at its maximum extent. The specific geometry of the HFR domain and, hence, the intersection angles of radial vectors handicap the accuracy of the total current vectors resolved at each grid point. Such a source of uncertainty is quantified by a dimensionless parameter called geometrical dilution of precision – GDOP (Chapman et al., 1997; Barrick, 2006), which typically increases with the distance from the HFR sites. In this work, a cut-off filter of 3 was imposed for the GDOP to get rid of estimations affected by higher uncertainties (Fig. A1a).

2.2 The HFR system deployed in BOB

This HFR system, deployed in the south-eastern BOB since 2009 and owned by Euskalmet (product ref. nos. 1 and 2 in Table 1), is a two-site CODAR SeaSonde network (Fig. 1a) that operates at a central frequency of 4.46 MHz, providing hourly current maps (representative of the first 1.5 m of the water column) with a spatial resolution of 5 km in an area up to 150 km from the coast (Solabarrieta et al., 2014). The consistent performance of this system and its potential for the study of ocean processes and transport patterns have already been demonstrated by previous works (Manso-Narvarte et al., 2018; Solabarrieta et al., 2014, 2015, 2016; Rubio et al., 2011, 2018).

Data are collected, processed, and quality-controlled following standard recommendations (Mantovani et al., 2020). They are later distributed in near-real time through the European HFR Node as part of the Copernicus Marine Service products. Again, a cut-off filter of 3 was imposed for the GDOP parameter to mitigate the impact of geometrical uncertainties on total current vectors accuracy (Fig. A1b). Finally, HFR-derived current estimations used in this work were collected from April to August 2014, when the system operated consistently and provided the longest data series (Solabarrieta et al., 2015).

2.3 In situ buoys

Basic features of two deep-ocean buoys (product ref. no. 3 in Table 1), deployed within each HFR footprint (Fig. 1a) and operated by Puertos del Estado, are gathered in Table 2. Both in situ devices collect quality-controlled estimations of sea surface temperature, salinity, and currents, among other physical parameters. Furthermore, both buoys are equipped with a wind sensor, providing hourly averaged wind vectors at 3 m height.

2.4 GLOBAL analysis and forecasting system

The operational Mercator global ocean analysis and forecast system provides 10 d of 3D global ocean forecasts updated daily. This product (product ref. no. 4 in Table 1), named GLOBAL_ANALYSIS_FORECAST_PHY_001_024 and freely available through the Copernicus Marine Service catalogue, includes daily and monthly mean files of temperature, salinity, currents, sea level, mixed layer depth, and ice parameters from the surface to seafloor (5500 m depth) over the global ocean. It also includes hourly mean surface fields for sea level height, temperature, and currents. The global ocean output files are displayed on 50 vertical levels with a $1/12°$ horizontal resolution over a regular latitude and longitude equirectangular projection. This product presents temporal coverage from November 2020 to the present.

The system is based on the Nucleus for European Modelling of the Ocean (NEMO) v3.1 ocean model (Madec and the NEMO team, 2008) and is forced with 3-hourly atmospheric fields provided by the European Centre for Medium-Range Weather Forecasts. The GLOBAL system does not include tides or pressure forcing. Altimeter data, in situ tem-

Table 2. Description of the buoys (product ref. no. 3 in Table 1) deployed within the coverage of each HFR system (product ref. no. 1 and no. 2 in Table 1), as shown in Fig. 1. More information on products can be found in the text and in the product table.

Name (area)	Type	Deployment	Longitude	Latitude	Depth	Sampling	Coriolis parameter
Silleiro (NWI)	Seawatch	1998	9.44° W	42.12° N	600 m	1 h	$9.75 \times 10^{-5}\ s^{-1}$
Bilbao (BOB)	Seawatch	1990	3.04° W	43.64° N	580 m	1 h	$10 \times 10^{-5}\ s^{-1}$

perature and salinity vertical profiles, and satellite sea surface temperature data are jointly assimilated to estimate the initial conditions for numerical ocean forecasting. For further details, the reader is referred to the GLOBAL Product User Manual (Le Galloudec et al., 2022) and to Lellouche et al. (2018).

2.5 Satellite-derived data

Surface fields of temperature and chlorophyll (product ref. nos. 5 and 6 in Table 1, respectively) provided by satellite missions were downloaded from the Copernicus Marine Service catalogue and used to analyse the impact of UPW and DOW events on their spatial distribution.

3 Methodology

Bakun (1973, 1975) proposed a CUI (the so-called Bakun index) based on Ekman theory (Ekman, 1905) and available estimates of atmospheric conditions to derive estimates of cross-shore Ekman transport as a proxy for coastal UPW. Following the same approach, in the present contribution two CUIs were computed (as benchmarks to compare CUI-HFR against) from hourly wind estimations provided by in situ buoys moored within each HFR coverage (Fig. 1a). Then, the CUI-WIND is defined as follows.

For the NWI region:

$$U_{\mathrm{Ekman}} = \mathrm{CUI-WIND}\left(\frac{\mathrm{m}^3}{\mathrm{s\,km}}\right) = -\frac{\rho_{\mathrm{a}} \cdot C_{\mathrm{d}} \cdot \sqrt{u^2+v^2} \cdot v \cdot 1000}{f \cdot \rho_{\mathrm{w}}} \quad (1)$$

For the BOB region:

$$V_{\mathrm{Ekman}} = \mathrm{CUI-WIND}\left(\frac{\mathrm{m}^3}{\mathrm{s\,km}}\right) = -\frac{\rho_{\mathrm{a}} \cdot C_{\mathrm{d}} \cdot \sqrt{u^2+v^2} \cdot u \cdot 1000}{f \cdot \rho_{\mathrm{w}}} \quad (2)$$

Here, ρ_{a} is the air density at standard temperature and pressure conditions ($1.22\,\mathrm{kg\,m^{-3}}$), ρ_{w} is the seawater density ($1025\,\mathrm{kg\,m^{-3}}$), C_{d} is a dimensionless empirical drag coefficient (1.4×10^{-3}), and f is the latitude-dependent Coriolis parameter (whose values are shown in Table 2). In this case, u and v denote the hourly time series of zonal and meridional wind at 3 m height, respectively, as measured by each buoy. The sign is changed to define positive (negative) magnitudes of CUI-WIND as a response to the predominant equatorward (poleward) wind over NWI and the predominant westward (eastward) wind over BOB.

Assuming the prompt and direct reaction of the upper ocean layer to intense and prolonged wind forcing in NWI (Herrera et al., 2005) and BOB (Solabarrieta et al., 2015), it seems reasonable to develop an ocean-based indicator for UPW and DOW conditions. Analogously, the CUI-HFR is defined as follows.

For the NWI region:

$$U_{\mathrm{Ekman}} = \mathrm{CUI-HFR}\left(\frac{\mathrm{m}^3}{\mathrm{s\,km}}\right) = -\frac{\rho_{\mathrm{a}} \cdot C_{\mathrm{d}} \cdot \sqrt{u^2+v^2} \cdot v \cdot 1000}{f \cdot \rho_{\mathrm{w}}} \cdot C \quad (3)$$

For the BOB region:

$$V_{\mathrm{Ekman}} = \mathrm{CUI-HFR}\left(\frac{\mathrm{m}^3}{\mathrm{s\,km}}\right) = -\frac{\rho_{\mathrm{a}} \cdot C_{\mathrm{d}} \cdot \sqrt{u^2+v^2} \cdot u \cdot 1000}{f \cdot \rho_{\mathrm{w}}} \cdot C \quad (4)$$

Here, u and v represent the filtered hourly time series of zonal and meridional surface current velocities ($\mathrm{m\,s^{-1}}$) provided by the HFR, respectively. A 25 h running-mean filter was used to smooth time series data by suppressing the main diurnal and semidiurnal tidal constituents (Shirahata et al., 2016), particularly the M2 signal, which is the largest harmonic constituent in the study area. Furthermore, C represents a dimensionless parameter that acts as a proportionality constant between wind and surface current observations, assuming a direct relationship between the two parameters (Lorente et al., 2020; Solabarrieta et al., 2015). The value of this parameter, which depends on the selected study area, can be easily derived from the best linear fit against CUI-WIND. For instance, C is equal to 2300 (3500) for the NWI (BOB) region.

In order to obtain a single time series of CUI-HFR, which is representative of the entire study area, hourly 2D maps

were spatially averaged over a delimited HFR spatial subdomain (see Fig. A1). In particular, two prerequisites were imposed to select such a subdomain: (i) it should be between 60 and 1200 m bathymetric depths to represent coastal waters while avoiding shallow water effects and the potential impact of impulsive-type freshwater discharges on the coastal circulation, and (ii) a predefined threshold of 3 was established for the GDOP parameter to minimize geometrical uncertainties in the remotely sensed currents. Finally, as a rough approximation, we also assumed that the local coastline was perfectly aligned in the south–north axis for the NWI region and in the east–west axis for the BOB region, which implies that v and u surface current components were parallel to the coastline.

Representative UPW and DOW episodes were selected for each study area to analyse the prevailing met-ocean conditions (wind and surface circulation, among others) along with the spatial distribution of CUI. In the case of the NWI area, a CUI was also derived from the surface currents predicted by the GLOBAL analysis and forecast system (Lellouche et al., 2018) following Eq. (3). CUI-GLOBAL and CUI-HFR were intercompared to infer strengths and weaknesses of each index and infer the potential of the GLOBAL model as a predictive tool for UPW conditions in this specific region. To this aim, a variety of outcomes were computed, ranging from 2D maps, time series, and the best linear fit of scatter plots to Hovmöller diagrams, which are the common way of plotting met-ocean data to depict changes over time of scalar quantities such as the CUI (Benazzouz et al., 2014).

4 Results

To quantify the consistency of both CUI-HFR and CUI-GLOBAL in the NWI area, hourly time series were compared against CUI-WIND, derived from wind estimations provided by the Silleiro buoy (Fig. 2a–b). The visual resemblance between the three different CUIs was noticeable, with significantly high correlation coefficients: (i) 0.72 and 0.74 between CUI-GLOBAL and CUI-WIND for the entirety of 2021 and for August–December 2021, respectively, as reflected by their best linear fit of scatter plots (Fig. A2a–b); (ii) 0.80 between CUI-HFR and CUI-WIND for August–December 2021 (Fig. A2c); (iii) 0.91 between CUI-GLOBAL and CUI-HFR for August–December 2021 (Fig. A2d). According to the statistical results in Fig. A2a–c, we can state that (i) the slope and intercept values were close to 1 and moderately low, respectively, and (ii) ocean-based CUI and CUI-WIND are strongly correlated, likely due to the role of alongshore wind stress as a primary driver of UPW conditions in the NWI area. Hourly alongshore winds (from Silleiro buoy) and HFR-derived alongshore currents (at the grid point closest to the buoy) are highly correlated (0.80) for August–December 2021 (not shown). It is also worth highlighting the ability of the GLOBAL model to capture many of the most relevant UPW (positive values) and DOW (negative values) episodes such as those observed during February 2021, whose values were higher than $3000\,m^3\,s^{-1}\,km^{-1}$ and lower than $-5000\,m^3\,s^{-1}\,km^{-1}$, respectively (Fig. 2a).

With regard to the 5-month period (August–December 2021) of concurrent CUI estimations (Fig. 2b), the degree of agreement was rather satisfactory. Both ocean-based CUIs were able to reproduce the temporal variability, capturing the most prominent events fairly well (marked and denoted in black). Hovmöller diagrams of CUI were computed at a selected transect of constant longitude (9.43° W, shown in Fig. 1a) to infer its spatio-temporal evolution (Fig. 2c–d). There were clear similarities (in terms of intensity and timing) between CUI-HFR and CUI-GLOBAL during the entire 5-month period, with a predominance of UPW (DOW) events during the summer and autumn (early winter) of 2021.

The Hovmöller diagrams of sea surface temperature (SST) and chlorophyll a (Chl) concentration at the same transect corroborated the consistency of the proposed approach (Fig. 2e–f). An abrupt cooling (with SST below 14 °C) and a relevant peak of Chl (with values above $2\,mg\,m^{-3}$) were observed by mid-August 2021, coincident with the UPW-1 event previously categorized (Fig. 2b–d). Equally, the moderate UPW episode that took place on 20 September 2021 (denoted as UPW-2 in Fig. 2b) could also be related to a local drop in SST (Fig. 2e) and a maximum of Chl (Fig. 2f) at the northernmost sector of the transect, in the vicinity of Cape Finisterre (Fig. 1a), which has been largely documented to act as the locus of frequent UPW (Lorente et al., 2020; Torres et al., 2003). Finally, the intense DOW event identified by CUI-HFR and CUI-GLOBAL for 21 December 2021 (denoted as DOW-1 in Fig. 2b) was coincident with a general minimum of Chl concentration (Fig. 2f), resulting in reduced primary production. These findings confirm the strong connection between the wind-induced circulation, coastal UPW, and the modulation of SST and Chl fields at the uppermost layer, in line with previous works. For instance, Alvarez et al. (2012) postulated that the high seasonal variability of Chl in NWI was mainly related to UPW episodes during spring and summer, while Chl variations depended on other additional factors (such as the input of nutrients from land runoff) during autumn and winter.

To gain further insight into the three specific events previously identified (Fig. 2b), daily averaged maps of CUI and circulation patterns were computed from current estimations provided by both HFR and the GLOBAL model (Fig. 3). During the UPW-1 (Fig. 3a–b) and UPW-2 (Fig. 3c–d) events, intense northerlies (with gusts above $10\,m\,s^{-1}$) were predominant over the study area according to the wind roses derived from Silleiro buoy observations. Despite the observed discrepancies in magnitude and direction, maps of wind-induced surface currents shared some common features: (i) the prevailing S-SW surface circulation (as a response to northerly winds) along with the typical offshore deflection of the flow, associated with UPW-favourable con-

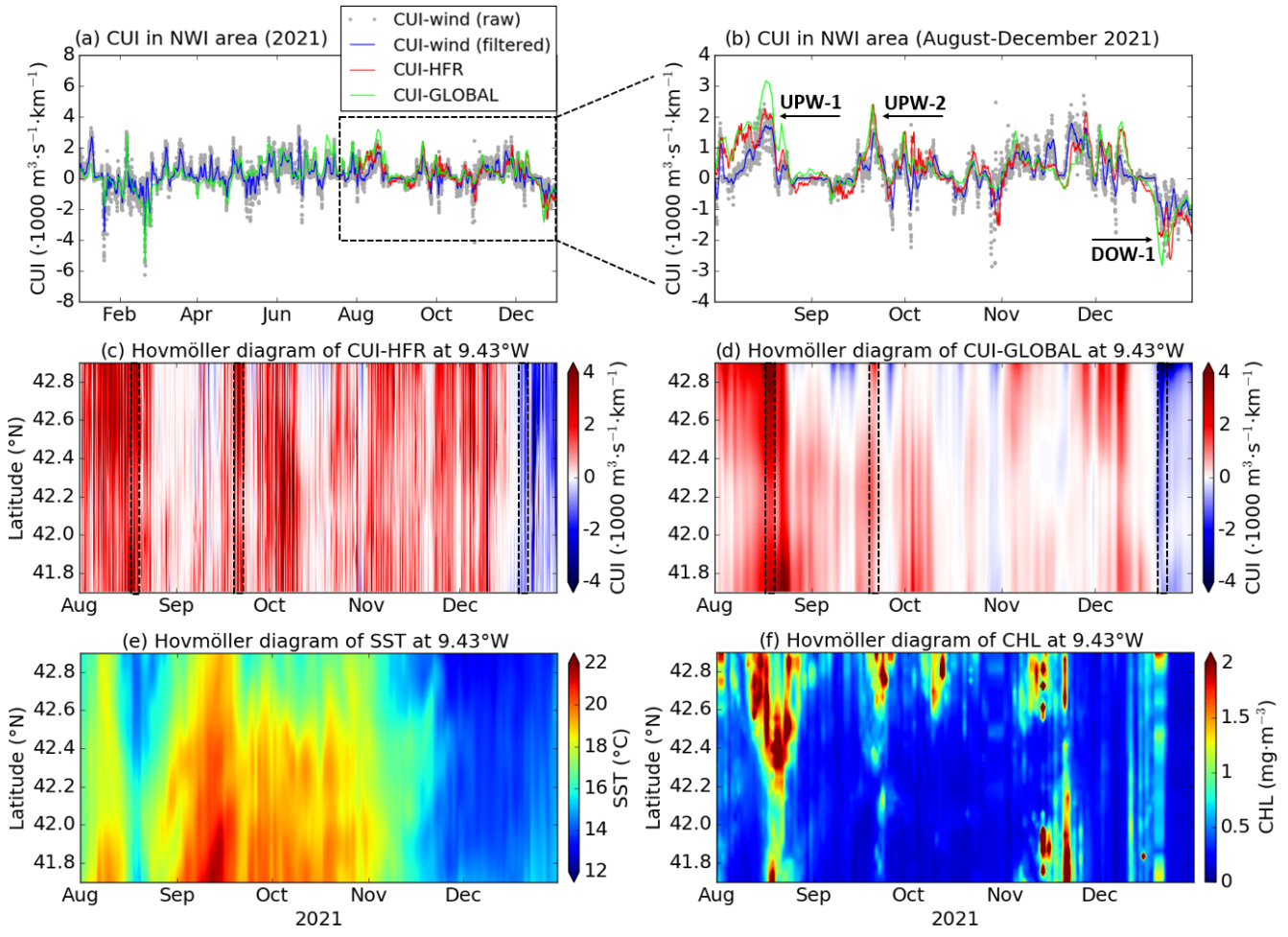

Figure 2. Time series of diverse hourly coastal upwelling index (CUI) in the north-western Iberia (NWI) region **(a)** for the entirety of 2021 and **(b)** for August–December 2021, as derived from wind observations from the Silleiro buoy (CUI-WIND) (product ref. no. 3; Table 1), HFR surface currents (CUI-HFR) (product ref. nos. 1 and 2; Table 1), and modelled surface currents (CUI-GLOBAL) (product ref. no. 4; Table 1). CUI-WIND raw (grey dots) was filtered by applying a 24 h moving mean (blue line). Hovmöller diagrams of **(c)** CUI-HFR, **(d)** CUI-GLOBAL, **(e)** sea surface temperature (SST) (product ref. no. 5; Table 1), and **(f)** chlorophyll (Chl) (product ref. no. 6; Table 1) concentration during the period August–December 2021 for a selected transect of constant longitude (9.43° W), depicted in Fig. 1a.

ditions; (ii) the rather uniform circulation westwards (southwestwards) to the north (south) of Cape Finisterre (indicated in Fig. 1a); (iii) the absence of submesoscale structures (i.e. eddies, small meanders) due to the strong wind-induced homogenization. It is also worth mentioning that the GLOBAL model predicted a more pronounced alongshore circulation (i.e. a more intense meridional – v – velocity component) to the south of this coastal promontory, which probably gave rise to higher CUI values (Fig. 3b) than those derived from HFR current estimations (Fig. 3a), according to Eq. (3). Indeed, this could be also observed in Fig. 2b where the peak of CUI-GLOBAL (green line) was higher than the concomitant peak of CUI-HFR (red line) during the UPW-1 episode. By contrast, local maximums of CUI-GLOBAL and CUI-HFR time series during the UPW-2 event were rather alike in terms of timing and strength (Fig. 2b). Analogously, the spatial distribution of CUI was quite similar for HFR (Fig. 3c) and GLOBAL (Fig. 3d), with a core of maximum UPW observed to the south of Rías Baixas (several coastal embayments characterized by high biodiversity, denoted in Fig. 1a). The main discrepancy between the two patterns was that in the case of GLOBAL, the peak appeared in the form of an elongated belt of positive values of CUI (confined landward close to the shoreline), whereas the HFR-derived pattern revealed a wider dipole-like structure, with two main cores of maximum CUI-HFR (close to 4000 $m^3\ s^{-1}\ km^{-1}$). The drop in CUI-HFR is consistent (in timing and location) with the drop in Chl concentration shown in Fig. 1b, supporting this HFR pattern, which was already documented in Lorente et al. (2020). Finally, during the DOW-1 event (Fig. 2b), both HFR and GLOBAL captured the so-called Iberian poleward current fairly well, a narrow surface poleward flow along the

NWI shelf edge (Torres and Barton, 2006). As reflected in Fig. 3e–f, DOW-favourable southerly winds induced a net flow to the north that settled in the continental shelf and circuited the western and northern Iberia margins. Again, the main difference resided in the existence of both a longitudinal gradient and a narrow strip of very negative CUI values close to the coastline in the case of GLOBAL (Fig. 3f), while the HFR-derived map of CUI exhibited a dipole-like distribution wherein the values were not so negative (Fig. 3e). This was also evidenced in the spatially averaged hourly time series of CUI shown in Fig. 2b, where the drop in CUI-GLOBAL was sharper than observed in CUI-HFR.

To further verify the validity of the proposed methodology, a similar CUI was generated for a 5-month period (April–August 2014) from an hourly surface current estimation provided by another HFR system deployed in the BOB since 2009 (Solabarrieta et al., 2014). This CUI-HFR was validated against a CUI-WIND based on hourly estimations provided by the Bilbao buoy (located within the HFR footprint and depicted in Fig. 1a), used here as a reference benchmark (Fig. 4a). The visual resemblance between the two time series was significantly high, with a correlation coefficient and a slope of 0.68 and 1, respectively, for a set of 3672 hourly data (Fig. A2e). During the analysed period, DOW events (5) were predominant with respect to UPW episodes (1). It seemed that CUI-HFR tended to slightly underestimate the intensity of some DOW events (i.e. DOW-2, DOW-3, and DOW-4), while it clearly overestimated the strength of the UPW-1 episode (Fig. 4a).

A Hovmöller diagram of CUI-HFR was computed at a selected transect of constant latitude (43.54° N, denoted in Fig. 1a) to deduce its spatio-temporal variability (Fig. 4b). The six events previously categorized were clearly observed and marked in the diagram, where the UPW and DOW features were evidenced throughout the entire transect. A number of secondary UPW events could be observed: although relevant in strength and duration, they were spatially confined to the westernmost sector of the transect (coincident with Cape Matxitxako, denoted in Fig. 1a) during the beginning of April, late July, and early August 2014. This fact highlighted the importance of coastal promontories as modulators of UPW processes by inducing important wind stress variations and zones of retention (Pitcher et al., 2010).

During DOW-1 event (Fig. 4c), intense westerly winds (up to 10–12 $m\,s^{-1}$) were dominant and a counterclockwise recirculation pattern prevailed, revealing the associated mechanisms of convergence and subduction (and the subsequent vertical mixing), especially in the vicinity of Cape Matxitxako (denoted in Fig. 1a) where a local minimum of CUI (down to $-3000\,m^3\,s^{-1}\,km^{-1}$) was detected. By contrast, weak north-easterly winds induced a general surface flow to the west during UPW-1 (Fig. 4d). Two local cores of UPW (ranging from 1000 to 1500 $m^3\,s^{-1}\,km^{-1}$) could be observed: one on the south-western French coast and a secondary one near Cape Matxitxako. The rest of the DOW events denoted in Fig. 4a (not shown) were very similar to the DOW-1 case shown here (Fig. 4c), sharing common circulation features and comparable spatial distributions of CUI. Most of the surface current patterns were clearly related to specific wind patterns that are recurrent in the study area, in line with Borja et al. (2008) and Solabarrieta et al. (2015).

5 Conclusions

Over the last decades, relevant efforts have been dedicated to the indirect quantification of the intensity, duration, and variability of UPW since it seriously impacts biogeochemical cycles and ecosystem productivity (Lachkar and Gruber, 2011). Diverse CUIs have been traditionally derived from wind or sea level pressure estimations, but they present some limitations such as the omission of the direct influence of ocean circulation (Jacox et al., 2018). In the present contribution, attention was placed on the development of a purely ocean-based CUI for the NWI and BOB regions (Fig. 1a), constructed from reliable hourly surface current maps provided by two different HFR remote sensing systems.

In this context, the proposed CUI-HFR presents additional advantages with respect to previous traditional CUIs, namely the following.

i. It takes into consideration the direct influence of coastal waters dynamics, thereby providing a more complete portrait of this phenomenon.

ii. It provides high-resolution two-dimensional maps that can aid in elucidating the spatial distribution and magnitude of the coastal, together with the potential existence of recurrent patterns and/or filaments in intricate regions with complex geometry configurations. The small-scale belt of UPW, confined in shallower coastal areas and evidenced in Fig. 3a and c, is consistent with HFR-derived maps of horizontal divergence previously published in Lorente et al. (2020). In this previous work, it was suggested that positive divergence, localized at the tip of Cape Finisterre, induced topographic UPW and then upwelled waters were advected southwards away from the promontory. Similar initiatives with HFR current observations were effectively addressed on the west coast of the USA (Roughan et al., 2005), proposing that confined areas of semi-persistent UPW were not due to local or remote wind forcing but rather to the divergence of the prevailing southerly flow as it passed the Point Loma headland.

iii. It is generated from consistent remotely sensed hourly surface current observations, not from coarse-resolution atmospheric forecasts, which are probably affected by higher uncertainties. This interpretation is supported by the fact that operational atmospheric and ocean models include assimilation schemes in which remote observations are routinely ingested to improve their pre-

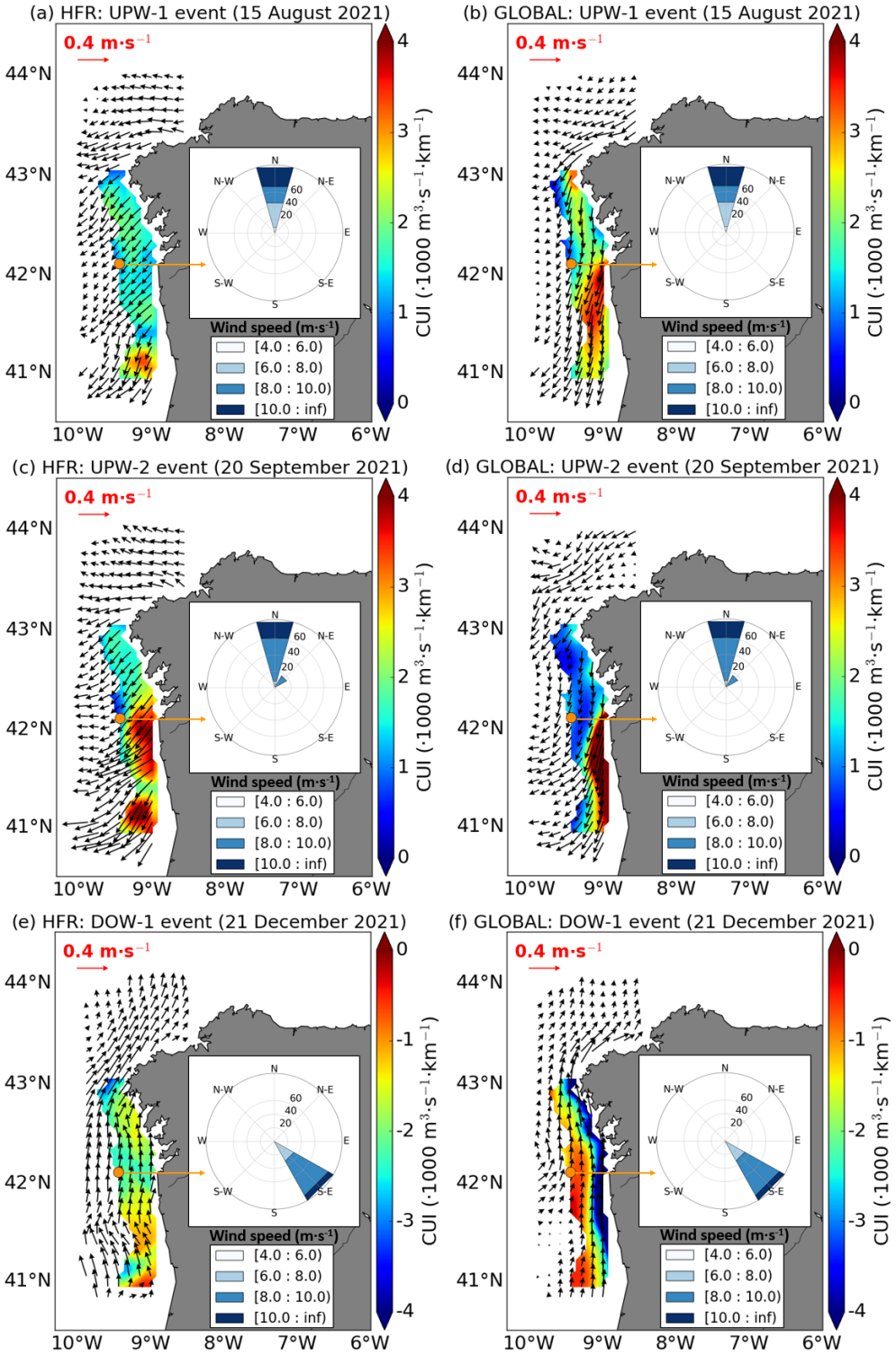

Figure 3. Daily averaged maps of circulation and coastal upwelling index (CUI) as derived from surface current estimations provided by a high-frequency radar (HFR, left column, product ref. no. 1 and no. 2 in Table 1) and the GLOBAL model (right column, product ref. 4) for each specific upwelling (UPW) and downwelling (DOW) episode categorized in Fig. 2b. Daily wind roses derived from hourly wind estimations from the Silleiro buoy (represented by an orange dot, product ref. no. 3 in Table 1) are also provided, indicating incoming wind direction and speed.

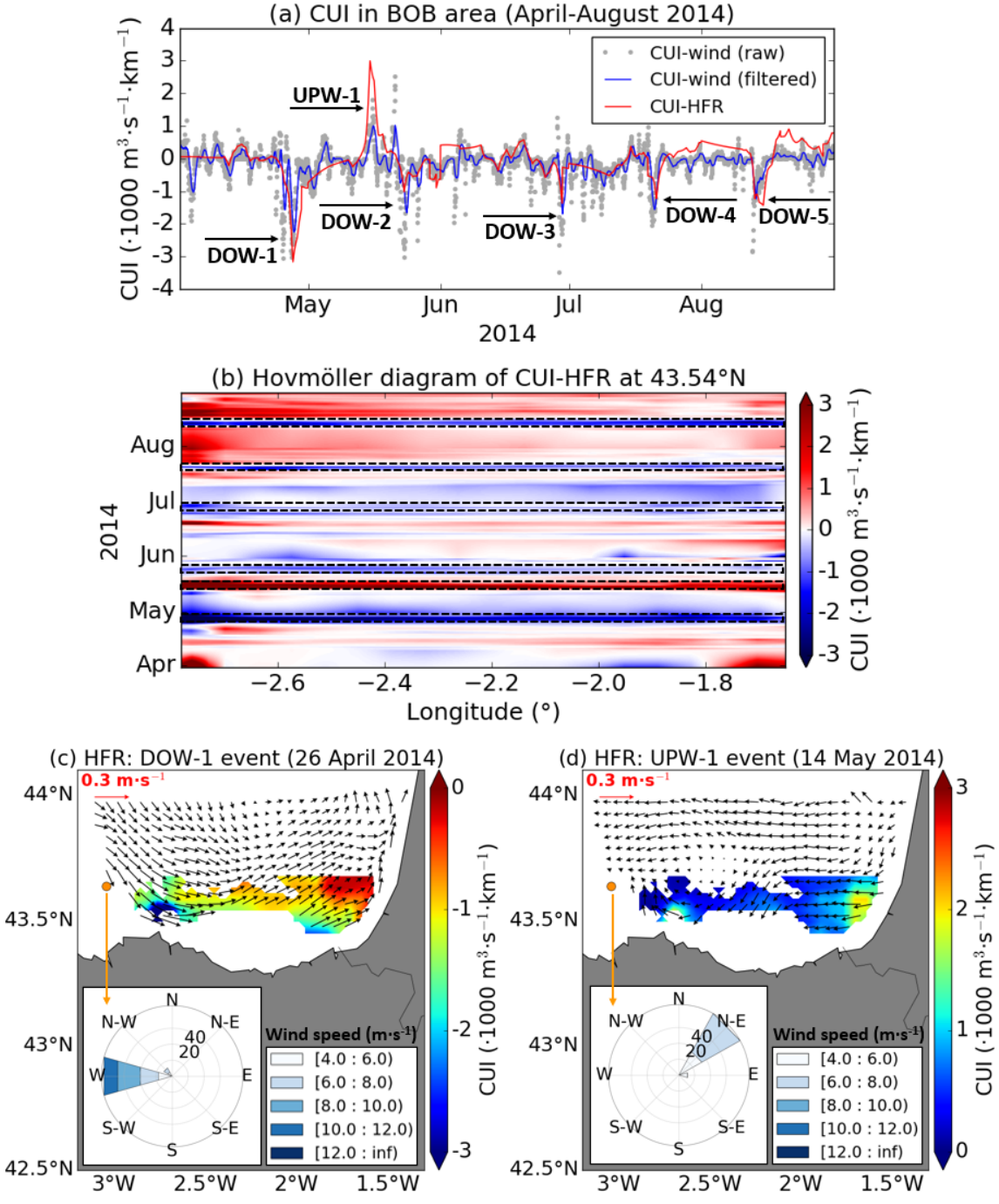

Figure 4. **(a)** Coastal upwelling indexes (CUIs) in the Bay of Biscay (April–August 2014) based on hourly wind observations (from the Bilbao buoy, product ref. no. 3 in Table 1) and hourly surface currents (from an HFR system, product ref. no. 1 and no. 2 in Table 1). CUI-WIND raw (grey dots) was filtered by applying a 24 h moving mean (blue line). Identification of six UPW–DOW events. **(b)** Hovmöller diagram of CUI-HFR for a transect of constant latitude, where UPW (DOW) events are marked with black dotted squares. **(c–d)** Daily averaged maps of surface circulation and CUI-HFR for two events. Daily wind roses from the Bilbao buoy (represented by an orange dot, product ref. no. 3 in Table 1) are also provided, indicating incoming wind direction and speed.

dictive skills (Wilczak et al., 2019; Hernandez-Lasheras et al., 2021).

To assess the credibility of the proposed CUI-HFR indexes, they were spatially averaged over specific subdomains (Fig. A1) and later validated against CUI-WIND time series, based on hourly wind observations collected by two in situ buoys moored within each HFR footprint, during two distinct time periods: in NWI for August–December 2021 (Fig. 2) and in BOB for April–August 2014 (Fig. 4), respectively. The results obtained evidenced the significant agreement between CUI-HFR and CUI-WIND, with correlation coefficients of 0.80 (Fig. A2c) and 0.68 (Fig. A2e), respectively, for these two pilot areas. Furthermore, CUI-HFRs were able to adequately identify a variety of UPW and DOW episodes, regardless of their length and intensity, corroborating the recurrent relationship between the surface circulation and predominant wind patterns in NWI (Herrera et al., 2005) and BOB (Solabarrieta et al., 2015). Thanks to the computation of Hovmöller diagrams at selected transects, coastal promontories such as Cape Finisterre (NWI) and Cape Matxitxako (BOB) were revealed as important modulators of UPW processes, in line with previous works that acknowledged that capes and bays may induce significant variations in wind stress (Torres and Barton, 2006; Enriquez and Friehe, 1995).

The strong link between HFR-derived wind-induced circulation and the modulation of surface fields of temperature and chlorophyll (provided by two independent satellite missions) was also shown in the NWI area, coherent with prior literature (Picado et al., 2013). Intense northerly winds and the general flow induced to the south-west are closely associated with the cooling and fertilization of coastal waters with nutrients, fuelling high primary production that ultimately supports the notable biological diversity in this region. Within this framework, future investigations should explore the connection between ocean dynamics and marine communities as well as how the latter respond to persistent changes in the former. This could be achieved by analysing the relationship between the proposed CUI-HFRs and food availability, which is often represented by recruitment indexes (Borja et al., 1996, 2008).

As a proof-of-concept investigation, the prognostic capabilities of the GLOBAL analysis and forecasting system to accurately reproduce UPW–DOW events in the NWI area were also assessed (Figs. 2 and 3). Following the same approach, CUI-GLOBAL demonstrated significant consistency, with annual correlation coefficients of 0.74 and 0.72 for 2020 (Fig. A3) and 2021 (Fig. 2a). From a qualitative perspective, the daily maps of surface circulation and spatial patterns of CUI-GLOBAL presented similarities with those derived from HFR remotely sensed observations, namely (i) the rather uniform S-SW surface circulation as well as the related offshore deflection of the main flow during UPW-favourable conditions (Fig. 3a–d) and (ii) the narrow surface poleward flow along the NWI shelf edge during DOW-favourable conditions (Fig. 3e–f). The discrepancies detected between CUI-HFR and CUI-GLOBAL maps in this specific subregion could be attributed to the fact that coastal and shelf phenomena are still poorly replicated or even misrepresented as the model grid mesh is too coarse (e.g. nominal $1/12°$). This is especially true for complex geometry regions like semi-enclosed coastal embayments where the coastline, seamounts, and bottom topography are not well resolved. In this context, mixing schemes, river inflows, and atmospheric forcings have been traditionally identified as areas of further research in global ocean modelling (Holt et al., 2017). Nevertheless, this comparison potentially opens future pathways for the design of fit-for-purpose metrics that quantify the model skill in reproducing specific ocean processes and their seasonal variability.

Therefore, the obtained outcomes support the potential implementation of a predictive application to infer UPW–DOW conditions even 10 d ahead, which is the maximum forecast horizon provided by the GLOBAL ocean model. Complementarily, the methodology proposed in this work could also be applied to the GLOBAL ocean physics reanalysis product (which covers the period 1 January 1993–31 December 2020) to analyse long-term seasonal trends in both study areas, as extremely active and persistent UPW and DOW episodes might negatively impact coastal ecosystems. During periods of increased offshore advection, some fish and invertebrate populations are exported from coastal habitats and exhibit reduced recruitment success (Bjorkstedt and Roughgarden, 1997). Moreover, an excessive enrichment of surface waters inshore may support the proliferation of harmful algal blooms (Pitcher et al., 2010). By contrast, the opposite-phase circulation patterns during DOW-favourable wind conditions might be related to the transport and retention of pollutants onto the shoreline, with subsequent biological and socioeconomic consequences.

In summary, results seem to suggest that the HFR performances were sound and credible for the two distinct periods and areas analysed, providing reliable surface current estimations that could be effectively used for coastal monitoring and the characterization of recurring UPW and DOW episodes. Future research endeavours should include the synergetic combination of HFRs and GLOBAL model products to implement a valuable long-term ocean monitoring indicator that might be used over any coastal area of the global ocean for wise decision-making to mitigate adverse effects of climate change.

Appendix A

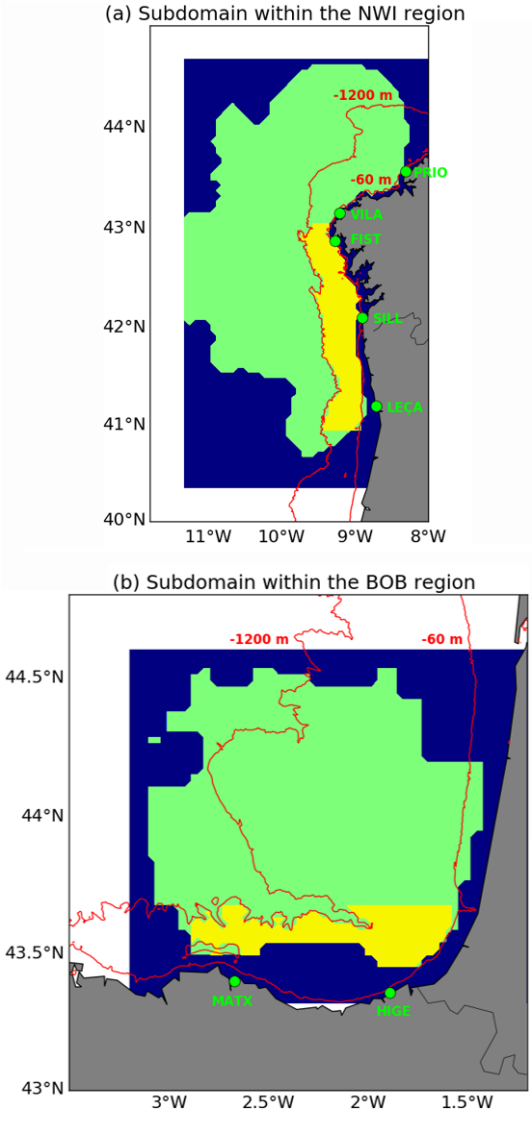

Figure A1. Selection of subdomains within each HFR coverage – product ref. nos. 1 and 2 (Table 1). The blue area represents the entire HFR spatial grid, while the green area denotes the subdomain where the value of the dimensionless GDOP parameter is below 3. The yellow area is the selected HFR subdomain to compute the coastal upwelling index (CUI) and must fulfil two requirements: (i) GDOP must be below 3, and (ii) it must be between bathymetric contours (red lines) of 60 and 1200 m depth. Green dots represent the HFR sites that compose each network deployed in the NWI **(a)** and BOB **(b)** regions.

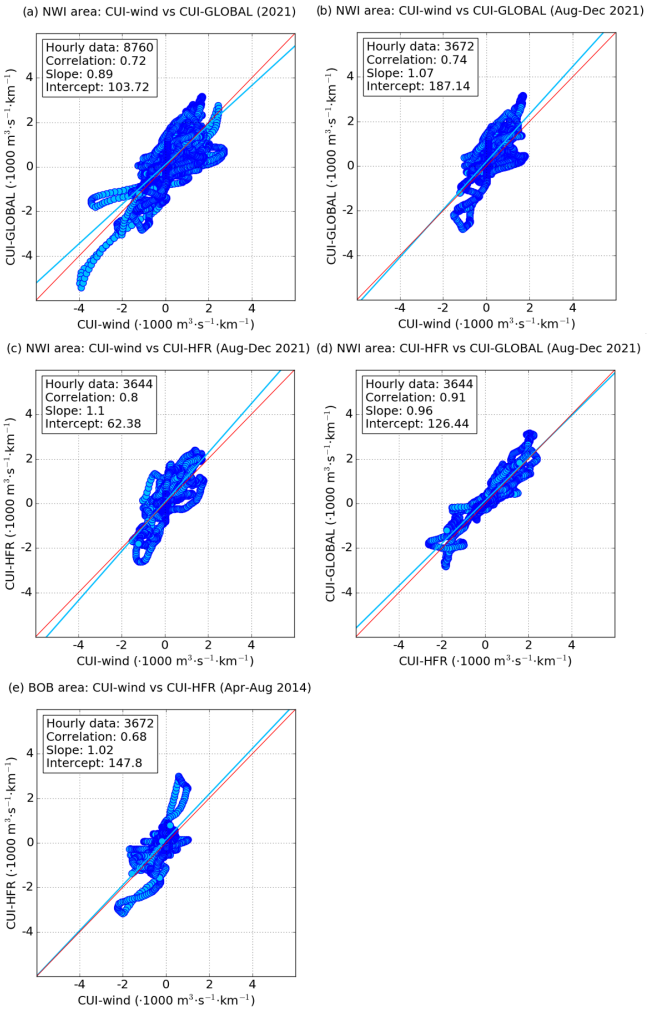

Figure A2. Best linear fit of scatter plots between the following: **(a–b)** CUI-GLOBAL (product ref. no. 4 in Table 1) and CUI-WIND (filtered), product ref. no. 3 (Table 1), in the NWI area for the entirety of 2021 and August–December 2021; **(c)** CUI-HFR, product ref. nos. 1 and 2 (Table 1), and CUI-WIND (filtered), product ref. no. 2 (Table 1), in the NWI area for August–December 2021; **(d)** CUI-GLOBAL, product ref. no. 4 (Table 1), and CUI-HFR, product ref. nos. 1 and 2 (Table 1) in the NWI area for August–December 2021; **(e)** CUI-HFR, product ref. nos. 1 and 2 (Table 1), and CUI-WIND (filtered), product ref. no. 3 (Table 1), in the BOB area for April–August 2014. Statistical metrics are gathered in white boxes.

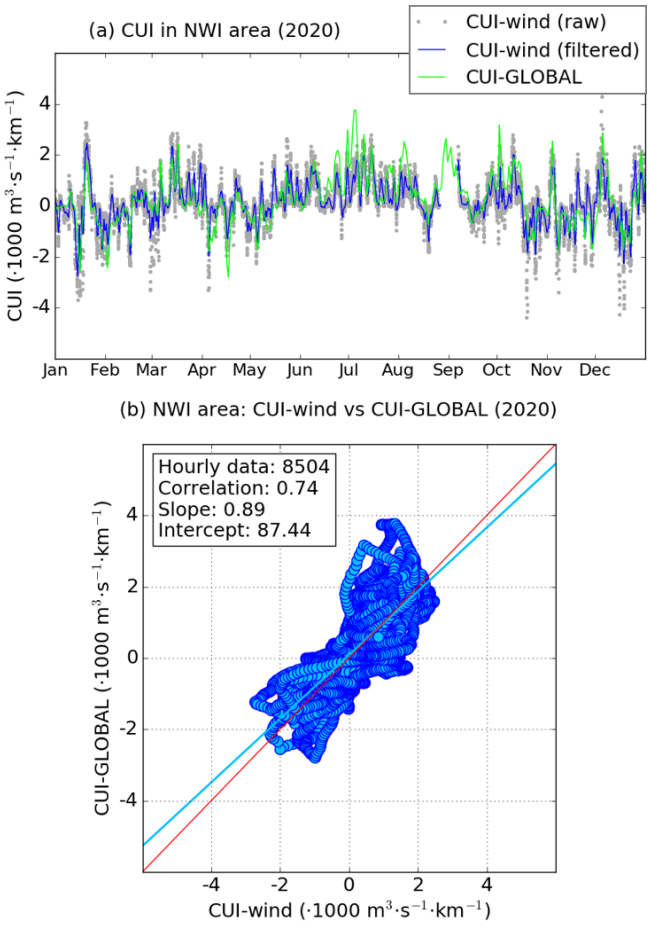

Figure A3. **(a)** Time series of hourly coastal upwelling index (CUI) in the north-western Iberia (NWI) region for the entirety of 2020 as derived from wind observations from Silleiro Buoy (CUI-WIND), product ref. no. 3 (Table 1), and from modelled surface currents (CUI-GLOBAL), product ref. no. 4 (Table 1). CUI-WIND raw (grey dots) was filtered by applying a 25 h moving mean (blue line); **(b)** best linear fit of the scatter plot between CUI-GLOBAL and CUI-WIND (filtered). Statistical metrics are gathered in the white box.

Data availability. The model and observation products used in this study from both the Copernicus Marine Service and other sources are listed in Table 1.

Author contributions. PL, AR, ER, LS, JT, SP, and JM conducted the pilot study through fruitful discussions in the framework of working team meetings. PL, SP, LS, and ER created the figures. PL prepared a first version of the draft with inputs from all co-authors. AR and LS analysed HF radar and in situ observations from the Bay of Biscay, while ER, PL, and SP provided expertise in the definition of upwelling indices. All authors participated in the iterations and revision of the paper.

Competing interests. The contact author has declared that none of the authors has any competing interests.

Disclaimer. Publisher's note: Copernicus Publications remains neutral with regard to jurisdictional claims in published maps and institutional affiliations.

Acknowledgements. This study has been developed in the framework of the Work Package WP3 of EuroSea project (https://eurosea.eu/, last access: 29 June 2023), which is aimed at improving and integrating the European ocean observing and forecasting system. The authors acknowledge the financial support of the EU H2020 Programme's JERICO-S3 project. It is also worth mentioning that this work builds upon a previous proof-of-concept investigation conducted within the context of the RADAR_ON_RAIA project (Interreg V, a Spain–Portugal programme). Finally, the authors are grateful to INTECMAR–Consellería do Mar–Xunta de Galicia and the Hydrographic Institute of Portugal for the strong cooperation to jointly operate the Galician HFR network. Equally, the authors thank the Emergencies and Meteorology Directorate (Security Department) of the Basque Government for public data provision from the Basque Operational Oceanography System EuskOOS. This study has been conducted using EU Copernicus Marine Service Information.

Financial support. This research has been partially funded through the EU H2020 Programme's JERICO-S3 project (grant agreement no. 871153).

Review statement. This paper was edited by Joanna Staneva and reviewed by Charles-Antoine Guerin and one anonymous referee.

References

Abrahams, A., Schlegel, R. W., and Smit, A. J.: Variation and change of upwelling dynamics detected in the world's eastern boundary upwelling systems, Frontiers in Marine Science, 8, 626411, https://doi.org/10.3389/fmars.2021.626411, 2021a.

Abrahams, A., Schlegel, R. W., and Smit, A. J.: A novel approach to quantify metrics of upwelling intensity, frequency, and duration, PLoS ONE, 16, e0254026, https://doi.org/10.1371/journal.pone.0254026, 2021b.

Alvarez, I., Lorenzo, M. N., and deCastro, M.: Analysis of chlorophyll *a* concentration along the Galician coast: seasonal variability and trends, ICES J. Mar. Sci., 69, 728–738, https://doi.org/10.1093/icesjms/fss045, 2012.

Bakun, A.: Coastal upwelling indices, west coast of North America, 1946-71, NOAA technical report NMFS SSRF; 671, https://repository.library.noaa.gov/view/noaa/9041 (last access: 29 June 2023), 1973.

Bakun, A.: Daily and weekly upwelling indices, west coast of North America, 1967-73, NOAA technical report NMFS SSRF; 693, https://repository.library.noaa.gov/view/noaa/15387 (last access: 29 June 2023), 1975.

Bakun, A., Black, B. A., Bograd, S. J., García-Reyes, M., Miller, A. J., Rykaczewski, R. R., and Sydeman, W. J.: Anticipated effects of climate change on coastal upwelling ecosystems, Current Climate Change Reports, 1, 85–93, https://doi.org/10.1007/s40641-015-0008-4, 2015.

Barrick, D.: Geometrical Dilution of Statistical Accuracy (GDOSA) in Multi-Static HF Radar Networks, CODAR Ocean Sensors Ltd., Mountain View, CA, USA, http://www.codar.com/images/about/2006Barrick_GDOSA.pdf (last access: 29 June 2023), 2006.

Barton, E. D., Field, D. B., and Roy, C.: Canary current upwelling: More or less?, Prog. Oceanogr., 116, 167–178, 2013.

Benazzouz, A., Mordane, S., Orbi, A., Chagdali, M., Hilmi, K., Atillah, A., Pelegrí, J. L., and Hervé, D.: An improved coastal upwelling index from sea surface temperature using satellite-based approach – The case of the Canary Current upwelling system, Cont. Shelf Res., 81, 38–54, https://doi.org/10.1016/j.csr.2014.03.012, 2014.

Bjorkstedt, E. and Roughgarden, J.: Larval transport and coastal upwelling: An application of HF radar in ecological research, Oceanography, 10, 64–67, 1997.

Borja, A., Uriarte, A., Valencia, V., Motos, I., and Uriarte, A.: Relationship between anchovy (*Engraulis encrasicolus* L.) recruitment and the environment in the Bay of Biscay, Sci. Mar., 60, 179–192, 1996.

Borja, A., Fontán, A., Sáenz, J., and Valencia, V.: Climate, oceanography, and recruitment: the case of the Bay of Biscay anchovy (*Engraulis encrasicolus*), Fish. Oceanogr., 17, 477–493, https://doi.org/10.1111/j.1365-2419.2008.00494.x, 2008.

Botas, J. A., Fernández, E., Bode, A., and Anadón, R.: A persistent upwelling off the Central Cantabrian coast (Bay of Biscay), Estuar. Coast. Shelf S., 30, 185–199, 1990.

Caballero, A., Rubio, A., and Manso, I.: Exploring the potential of HF radar data to monitor upwelling events in the SE Bay of Biscay, EGU General Assembly, Vienna, Austria, 4–13 April 2018, EGU2018-13624, 2018.

Chapman, R. D., Shay, L. K., Graber, H. C., Edson, J. B., Karachintsev, A., Trump, C. L., and Ross, D. B.: On the accuracy of HF radar surface current measurements: Intercomparisons with ship-based sensors, J. Geophys. Res.-Oceans, 102, 18737–18748, https://doi.org/10.1029/97JC00049, 1997.

Colella, S., Böhm, E., Cesarini, C., Garnesson, P., Netting, J., and Calton, B.: EU Copernicus Marine Service Product User Manual for the Global Ocean Colour (Copernicus-GlobColour), Bio-Geo-Chemical, L4 (monthly and interpolated) from Satellite Observations (1997-ongoing), OCEANCOLOUR_GLO_BGC_L4_MY_009_104, Issue: 3.0, Mercator Ocean International, https://catalogue.marine.copernicus.eu/documents/PUM/CMEMS-OC-PUM.pdf (last access: 2 June 2023), 2022.

Corgnati, L., Mantovani, C., Rubio, A., Reyes, E., Rotllan, P., Novellino, A., Gorringe, P., Solabarrieta, L., Griffa, A., and Mader, J.: The Eurogoos High Frequency radar task team: a success story of collaboration to be kept alive and made growing, in 9th EuroGOOS International conference, Shom, Ifremer, EuroGOOS AISBL, May 2021, Brest, France, 467–474, Brest, France, https://hal.archives-ouvertes.fr/hal-03328829 (last access: 27 June 2023), 2021.

Cropper, T. E., Hanna, E., and Bigg, G. R.: Spatial and temporal seasonal trends in coastal upwelling off Northwest Africa, 1981-2012, Deep-Sea Res. Pt. I, 86, 94–111, https://doi.org/10.1016/j.dsr.2014.01.007, 2014.

Di Lorenzo, E.: The future of coastal ocean upwelling, Nature, 518, 310–311, https://doi.org/10.1038/518310a, 2015.

Ekman, W.: On the influence of the Earth's rotation on ocean currents, Ark. Mat. Astr. Fys., 2, 1–52, 1905.

Enriquez, A. G. and Friehe, C. A.: Effects of wind stress and wind stress curl variability on coastal upwelling, J. Phys. Oceanogr., 25, 1651–1671, 1995.

Etienne, H., Boone, C., Verbrugge, N., Reyes, E., Rotllán, P., Rubio, A., Solabarrieta, L., Corgnati, L., Mantovani, C., Mader, J., and Carval, T.: EU Copernicus Marine Service Product User Manual for the Global Ocean-Delayed Mode in-situ Observations of surface (drifters and HFR) and subsurface (vessel-mounted ADCPs) water velocity, INSITU_GLO_PHY_UV_DISCRETE_MY_013_044, Issue: 3.3, Mercator Ocean International, https://catalogue.marine.copernicus.eu/documents/PUM/CMEMS-INS-PUM-013-044.pdf (last access: 2 June 2023), 2022.

Etienne, H., Verbrugge, N., Boone, C., Rubio, A., Solabarrieta, L., Corgnati, L., Mantovani, C., Reyes, E., Chifflet, M., Mader, J., and Carval, T.: EU Copernicus Marine Service Quality Information Document for the Global Ocean-Delayed Mode in-situ Observations of surface (drifters and HFR) and subsurface (vessel-mounted ADCPs) water velocity, INSITU_GLO_PHY_UV_DISCRETE_MY_013_044, Issue: 3.4, Mercator Ocean International, https://catalogue.marine.copernicus.eu/documents/QUID/CMEMS-INS-QUID-013-044.pdf (last access: 2 June 2023), 2023.

EU Copernicus Marine Service Product: Global Ocean- in-situ Near real time observations of ocean currents, Mercator Ocean International [data set], https://doi.org/10.48670/moi-00041, 2022a.

EU Copernicus Marine Service Product: Atlantic Iberian Biscay Irish Ocean- In-Situ Near Real Time Observations, Mercator Ocean International [data set], https://doi.org/10.48670/moi-00043, 2022b.

EU Copernicus Marine Service Product: Global Ocean Physics Analysis and Forecast, Mercator Ocean International [data set], https://doi.org/10.48670/moi-00016, 2022c.

EU Copernicus Marine Service Product: Global Ocean Colour (Copernicus-GlobColour), Bio-Geo-Chemical, L4 (monthly and interpolated) from Satellite Observations (1997–ongoing), Mercator Ocean International [data set], https://doi.org/10.48670/moi-00281, 2022d.

EU Copernicus Marine Service Product: Global Ocean-Delayed Mode in-situ Observations of surface (drifters and HFR) and sub-surface (vessel-mounted ADCPs) water velocity, Mercator Ocean International [data set], https://doi.org/10.17882/86236, 2023a.

EU Copernicus Marine Service Product: Global Ocean OSTIA Sea Surface Temperature and Sea Ice Reprocessed, Mercator Ocean International [data set], https://doi.org/10.48670/moi-00168, 2023b.

Fontán, A., Valencia, V., Borja, A., and Goikoetxea, N.: Oceanometeorological conditions and coupling in the south-eastern Bay of Biscay, for the period 2001-2005: A comparison with the past two decades, J. Marine Syst., 72, 167–177, 2008.

Garnesson, P., Mangin, A., Bretagnon, M., and Jutard, Q.: EU Copernicus Marine Service Quality Information Document for the Global Ocean Colour (Copernicus-GlobColour), Bio-Geo-Chemical, L4 (monthly and interpolated) from Satellite Observations (1997-ongoing), OCEANCOLOUR_GLO_BGC_L4_MY_009_104, Issue: 3.0, Mercator Ocean International, https://catalogue.marine.copernicus.eu/documents/QUID/CMEMS-OC-QUID-009-101to104-111-113-116-118.pdf (last access: 2 June 2023), 2022.

González-Nuevo, G., Gago, J., and Cabanas, J. M.: Upwelling Index: A powerful tool for marine research in the NW Iberian upwelling system, J. Oper. Oceanogr., 7, 47–57, 2014.

Gunduz, M., Causio, S., Bonino, G., Vandenbulcle, L., Gtregorie, M., Lima, L., Ciliberti, S., LLicak, M., Aydogdu, A., Masina, S., Coppini, G. H., and Pinardi, N.: Coastal upwelling along the Turkish coast of the black Sea: its role in the distribution of the hydrographic properties, J. Oper. Oceanogr., Special Issue: Ocean State Report 6, Sect. 4.8, 205–210, 2022.

Hernandez-Lasheras, J., Mourre, B., Orfila, A., Santana, A., Reyes, E., and Tintoré, J.: Evaluating high-frequency radar data assimilation impact in coastal ocean operational modelling, Ocean Sci., 17, 1157–1175, https://doi.org/10.5194/os-17-1157-2021, 2021.

Herrera, J. L., Piedracoba, S., Varela, R., and Rosón, G.: Spatial analysis of the wind field on the western coast of Galicia (NW Spain) from in situ measurements, Cont. Shelf Res., 25, 1728–1748, 2005.

Holt, J., Hyder, P., Ashworth, M., Harle, J., Hewitt, H. T., Liu, H., New, A. L., Pickles, S., Porter, A., Popova, E., Allen, J. I., Siddorn, J., and Wood, R.: Prospects for improving the representation of coastal and shelf seas in global ocean models, Geosci. Model Dev., 10, 499–523, https://doi.org/10.5194/gmd-10-499-2017, 2017.

Copernicus Marine In Situ Tac Data Management Team: Product User Manual for multiparameter Copernicus In Situ TAC (PUM), https://doi.org/10.13155/43494, 2021.

IPCC, 2022: Climate Change 2022: Impacts, Adaptation and Vulnerability. Contribution of Working Group II to the Sixth Assessment Report of the Intergovernmental Panel on Climate Change, edited by: Pörtner, H.-O., Roberts, D. C., Tignor, M., Poloczanska, E. S., Mintenbeck, K., Alegría, A., Craig, M., Langsdorf, S., Löschke, S., Möller, V., Okem, A., and Rama, B., Cambridge University Press, Cambridge, UK and New York, NY, USA, 3056 pp., https://doi.org/10.1017/9781009325844, 2022.

Jacox, M. G., Edwards, C. A., Hazen, E. L., and Bograd, S. J.: Coastal upwelling revisited: Ekman, Bakun, and improved upwelling indices for the U.S. West Coast, J. Geophys. Res.-Oceans, 123, 7332–7350, https://doi.org/10.1029/2018JC014187, 2018.

Kaplan, D. M. and Largier, J. L.: HF radar-derived origin and destination of surface waters off Bodega Bay, California, Deep-Sea Res. Pt. II, 53, 2906–2930, 2006.

Lachkar, Z. and Gruber, N.: What controls biological production in coastal upwelling systems? Insights from a comparative modeling study, Biogeosciences, 8, 2961–2976, https://doi.org/10.5194/bg-8-2961-2011, 2011.

Le Galloudec, O., Law Chune, S., Nouel, L., Fernandez, E., Derval, C., Tressol, M., Dussurget, R., Biardeau, A., and Tonani, M.: EU Copernicus Marine Service Product User Manual for the Global Ocean Physics Analysis and Forecast, GLOBAL_ANALYSISFORECAST_PHY_001_024, Issue: 1.9, Mercator Ocean International https://catalogue.marine.copernicus.eu/documents/PUM/CMEMS-GLO-PUM-001-024.pdf (last access: 2 June 2023), 2022.

Lellouche, J.-M., Le Galloudec, O., Regnier, C., Van Gennip, S., Law Chune, S., Levier, B., Greiner, E., Drevillon, M., and Szczypta, C.: EU Copernicus Marine Service Quality Information Document for the Global Ocean Physics Analysis and Forecast, GLOBAL_ANALYSISFORECAST_PHY_001_024, Issue: 1.0, https://catalogue.marine.copernicus.eu/documents/QUID/CMEMS-GLO-QUID-001-024.pdf (last access: 2 June 2023), 2022.

Lellouche, J.-M., Greiner, E., Le Galloudec, O., Garric, G., Regnier, C., Drevillon, M., Benkiran, M., Testut, C.-E., Bourdalle-Badie, R., Gasparin, F., Hernandez, O., Levier, B., Drillet, Y., Remy, E., and Le Traon, P.-Y.: Recent updates to the Copernicus Marine Service global ocean monitoring and forecasting real-time 1/12° high-resolution system, Ocean Sci., 14, 1093–1126, https://doi.org/10.5194/os-14-1093-2018, 2018.

Llope, M., Anadón, R., Viesca, L., Quevedo, M., González-Quirós, R., and Stenseth, N. C.: Hydrography of the southern Bay of Biscay shelf-break region: Integrating the multiscale physical variability over the period 1993–2003, J. Geophys. Res., 111, C09021, https://doi.org/10.1029/2005JC002963, 2006.

Lorente, P., Piedracoba, S., and Álvarez-Fanjul, E.: Validation of high-frequency radar ocean surface current observations in the NW of the Iberian Peninsula, Cont. Shelf Res., 92, 1–15, 2015.

Lorente, P., Piedracoba, S., Montero, P., Sotillo, M.G., Ruiz, M.I. and Álvarez-Fanjul, E.: Comparative analysis of summer upwelling and downwelling events in NW Spain: a model-observations approach, Remote Sens., 12, 2762, https://doi.org/10.3390/rs12172762, 2020.

Lorente, P., Aguiar, E., Bendoni, M., Berta, M., Brandini, C., Cáceres-Euse, A., Capodici, F., Cianelli, D., Ciraolo, G., Corgnati, L., Dadić, V., Doronzo, B., Drago, A., Dumas, D., Falco, P., Fattorini, M., Gauci, A., Gómez, R., Griffa, A., Guérin, C.-A., Hernández-Carrasco, I., Hernández-Lasheras, J., Ličer, M., Magaldi, M. G., Mantovani, C., Mihanović, H., Molcard, A., Mourre, B., Orfila, A., Révelard, A., Reyes, E., Sánchez, J., Saviano, S., Sciascia, R., Taddei, S., Tintoré, J., Toledo, Y., Ursella, L., Uttieri, M., Vilibić, I., Zambianchi, E., and Cardin, V.: Coastal high-frequency radars in the Mediterranean – Part 1: Status of operations and a framework for future development, Ocean Sci., 18, 761–795, https://doi.org/10.5194/os-18-761-2022, 2022.

Madec, G. and the NEMO team: NEMO ocean engine, Note du Pôlede modélisation, Institut Pierre-Simon Laplace (IPSL), France, No 27, ISSN 1288-1619, 2008.

Manso-Narvarte, I., Caballero, A., Rubio, A., Dufau, C., and Birol, F.: Joint analysis of coastal altimetry and high-frequency (HF) radar data: observability of seasonal and mesoscale ocean dynamics in the Bay of Biscay, Ocean Sci., 14, 1265–1281, https://doi.org/10.5194/os-14-1265-2018, 2018.

Mantovani, C., Corgnati, L., Horstmann, J., Rubio, A., Reyes, E., Quentin, C., Cosoli, S., Asensio, J. L., Mader, J., and Griffa, A.: Best practices on High Frequency Radar deployment and operation for ocean current measurement, Frontiers in Marine Science, 7, 210, https://doi.org/10.3389/fmars.2020.00210, 2020.

Mourre, B., Reyes, E., Lorente, P., Santana, A., Hernández-Lasheras, J., Hernández-Carrasco, I., Garcia-Jove, M., and Zarokanellos, N. D.: Intense wind-driven coastal upwelling in the Balearic Islands in response to Storm Blas (November 2021), in: 7th edition of the Copernicus Ocean State Report (OSR7), edited by: von Schuckmann, K., Moreira, L., Le Traon, P.-Y., Grégoire, M., Marcos, M., Staneva, J., Brasseur, P., Garric, G., Lionello, P., Karstensen, J., and Neukermans, G., Copernicus Publications, State Planet, 1-osr7, 15, https://doi.org/10.5194/sp-1-osr7-15-2023, 2023.

Paduan, J. D., Cook, M. S., and Tapia, V. M.: Patters of upwelling and relaxation around Monterrey Bay based on long-term observations of surface currents from High Frequency radar, Deep-Sea Res. Pt. II, 151, 129–136, 2018.

Picado, A., Álvarez, I., Vaz, N., and Dias, J. M.: Chlorophyll concentration along the north-western coast of the Iberian Peninsula vs. atmosphere-ocean-land conditions, J. Coast. Res., 65, 2047–2052, 2013.

Pitcher, G. C., Figueiras, F. G., Hickey, B. M., and Moita, M. T.: The physical oceanography of upwelling systems and the development of harmful algal blooms, Prog. Oceanogr., 85, 5–32, 2010.

Prego, R., Varela, M., deCastro, M., Ospina-Alvarez, N., Garcia-Soto, C., and Gómez-Gesteira, M.: The influence of summer upwelling at the western boundary of the Cantabrian coast. Estuarine, Coast. Shelf Sci., 98, 138–144, 2012.

Reyes, E., Aguiar, E., Bendoni, M., Berta, M., Brandini, C., Cáceres-Euse, A., Capodici, F., Cardin, V., Cianelli, D., Ciraolo, G., Corgnati, L., Dadić, V., Doronzo, B., Drago, A., Dumas, D., Falco, P., Fattorini, M., Fernandes, M. J., Gauci, A., Gómez, R., Griffa, A., Guérin, C.-A., Hernández-Carrasco, I., Hernández-Lasheras, J., Ličer, M., Lorente, P., Magaldi, M. G., Mantovani, C., Mihanović, H., Molcard, A., Mourre, B., Révelard, A., Reyes-Suárez, C., Saviano, S., Sciascia, R., Taddei, S., Tintoré, J., Toledo, Y., Uttieri, M., Vilibić, I., Zambianchi, E., and Orfila, A.: Coastal high-frequency radars in the Mediterranean – Part 2: Applications in support of science priorities and societal needs, Ocean Sci., 18, 797–837, https://doi.org/10.5194/os-18-797-2022, 2022.

Roarty, H., Cook, T., Hazard, L., Harlan, J., Cosoli, S., Wyatt, L., Fanjul, E. A., Terrill, E., Otero, M., Largier, J., Glenn, S., Ebuchi, N., Whitehouse, B., Bartlett, K., Mader, J., Rubio, A., Corgnati, L. P., Mantovani, C., Griffa, A., Reyes, E., Lorente, P., Flores-Vidal, X., Rogowski, P., Prukpitikul, S., Lee, S. H., Lai, J. W., Guerin, C., Sanchez, J., Hansen, B., Grilli, S., and Matta, K. S.: The Global High Frequency Radar Network, Frontiers in Marine Science, 6, 164, https://doi.org/10.3389/fmars.2019.00164, 2019.

Roughan, M., Terril, E. J., Largier, J. L., and Otero, M.: Observations of divergence and upwelling around Point Loma, California, J. Geophys. Res., 110, C04011, https://doi.org/10.1029/2004JC002662, 2005.

Rubio, A., Reverdin, G., Fontán, A., González, M., and Mader, J.: Mapping near-inertial variability in the SE Bay of Biscay from HF radar data and two offshore moored buoys, Geophys. Res. Lett., 38, L19607, https://doi.org/10.1029/2011GL048783, 2011.

Rubio, A., Mader, J., Corgnati, L., Mantovani, C., Griffa, A., Novellino, A., Quentin, C., Wyatt, L., Schulz-Stellenfleth, J., Horstmann, J., Lorente, P., Zambianchi, E., Hartnett, M., Fernandes, C., Zervakis, V., Gorringe, P., Melet, A., and Puillat, I.: HF radar activity in European coastal seas: next steps towards a pan-European HF radar network, Frontiers in Marine Science, 4, 8, https://doi.org/10.3389/fmars.2017.00008, 2017.

Rubio, A., Caballero, A., Orfila, A., Hernández-Carrasco, I., Ferrer, L., González, M., Solabarrieta, L., and Mader, J.: Eddy-induced cross-shelf export of high Chl-a coastal waters in the SE Bay of Biscay, Remote Sens. Environ., 205, 290–304, https://doi.org/10.1016/j.rse.2017.10.037, 2018.

Shirahata, K., Yoshimoto, S., Tsuchihara, T., and Ishida, S. Digital Filters to Eliminate or Separate Tidal Components in Groundwater Observation Time-Series Data, JARQ-Jpn. Agr. Res. Q., 50, 241–252, https://doi.org/10.6090/jarq.50.241, 2016.

Solabarrieta, L., Rubio, A., Castanedo, S., Medina, R., Charria, G., and Hernández, C.: Surface water circulation patterns in the southeastern Bay of Biscay: New evidences from HF radar data, Cont. Shelf Res., 74, 60–76, https://doi.org/10.1016/j.csr.2013.11.022, 2014.

Solabarrieta, L., Rubio, A., Cárdenas, M., Castanedo, S., Esnaola, G., Méndez, F. J., Medina, R., and Ferrer, L.: Probabilistic relationships between wind and surface water circulation patterns in the SE Bay of Biscay, Ocean Dynam., 65, 1289–1303, https://doi.org/10.1007/s10236-015-0871-5, 2015.

Solabarrieta, L., Frolov, S., Cook, M., Paduan, J., Rubio, A., González, M., Mader, J., and Charria, G.: Skill assessment of HF radar–derived products for lagrangian simulations in the Bay of Biscay, J. Atmos. Ocean. Tech., 33, 2585–2597, https://doi.org/10.1175/JTECH-D-16-0045.1, 2016.

Torres, R. and Barton, E. D.: Onset and development of the Iberian poleward flow along the Galician coast, Cont. Shelf Res., 26, 1134–1153, 2006.

Torres, R., Barton, E. D., Miller, P., and Álvarez-Fanjul, E.: Spatial patterns of wind and sea surface temperature in the Galician upwelling region, J. Geophys. Res., 108, 3130, https://doi.org/10.1029/2002JC001361, 2003.

Trincardi, F., Cappelletto, M., Barvanti, A., Cadiou, J.-F., Bataille, A., Campillos Llanos, M., Chacón Campollo, E., and Trujillo Quintela, A.: BlueMED, Preliminary implementation plan D2.9 (Core Document), European Union's Horizon 2020, https://ec.europa.eu/research/participants/documents/downloadPublic?documentIds=080166e5d180fcbd&appId=PPGMS (last access: 28 June 2023), 2020.

Varela, R., Álvarez, I., Santos, F., deCastro, M., and Gómez-Gesteira, M.: Has upwelling strengthened along worldwide coasts over 1982–2010?, Scientific Reports, 5, 10016, https://doi.org/10.1038/srep10016, 2015.

Verbrugge, N., Etienne, H., Boone, C., Corgnati, L., Mantovani, C., Reyes, E., Solabarrieta, L., Rubio, A., Rotllán, P., Carval, T., Mader, J., and Drouineau, L.: EU Copernicus Marine Service Product User Manual for the Global Ocean- in-situ Near real time observations of ocean currents, INSITU_GLO_PHY_UV_DISCRETE_NRT_013_048, Issue: 2.2, Mercator Ocean International, https://catalogue.marine.copernicus.eu/documents/PUM/CMEMS-INS-PUM-013-048.pdf (last access: 2 June 2023), 2022a.

Verbrugge, N., Etienne, H., Corgnati, L., Mantovani, C., Reyes, E., Solabarrieta, L., Rubio, A., Carval, T., Mader, J., and Drouineau, L.: EU Copernicus Marine Service Quality Information Document for the Global Ocean-in-situ Near real time observations of ocean currents,

INSITU_GLO_PHY_UV_DISCRETE_NRT_013_048, Issue: 2.2, Mercator Ocean International, https://catalogue.marine.copernicus.eu/documents/QUID/CMEMS-INS-QUID-013-048.pdf (last access: 2 June 2023), 2022b.

Wang, D., Gouhier, T., Menge, B., and Ganguly, A. R.: Intensification and spatial homogenization of coastal upwelling under climate change, Nature, 518, 390–394, https://doi.org/10.1038/nature14235, 2015.

Wehde, H., Schuckmann, K. V., Pouliquen, S., Grouazel, A., Bartolome, T., Tintore, J., De Alfonso Alonso-Munoyerro, M., Carval, T., Racapé, V., and the INSTAC team: EU Copernicus Marine Service Quality Information Document for the Atlantic Iberian Biscay Irish Ocean- In-Situ Near Real Time Observations, INSITU_IBI_PHYBGCWAV_DISCRETE_MYNRT_013_033, Issue 2.2, Mercator Ocean International, https://catalogue.marine.copernicus.eu/documents/QUID/CMEMS-INS-QUID-013-030-036.pdf (last access: 2 June 2023), 2022.

Wilczak, J. M., Olson, J. B., Djalalova, I., Bianco, L., Berg, L. K., Shaw, W. J., Coulter, R. L., Eckman, R. M., Freedman, J., Finley, C., and Cline, J.: Data assimilation impact of in situ and remote sensing meteorological observations on wind power forecasts during the first Wind Forecast Improvement Project (WFIP), Wind Energy, 22, 932–944, https://doi.org/10.1002/we.2332, 2019.

Wooster, W. S., Bakun, A., and McLain, D. R.: Seasonal upwelling cycle along eastern boundary of North-Atlantic, J. Mar. Res., 34, 131–141, 1976.

Worsfold, M., Good, S., Martin, M., McLaren, A., Roberts-Jones, J., and Fiedler, E.: EU Copernicus Marine Service Product User Manual for the Global Ocean OSTIA Sea Surface Temperature Reprocessing, SST-GLO-SST-L4-REP-OBSERVATIONS-010-011, Issue: 1.4, Mercator Ocean International, https://catalogue.marine.copernicus.eu/documents/PUM/CMEMS-SST-PUM-010-011.pdf (last access: 2 June 2023), 2022.

Worsfold, M., Good, S., McLaren, A., Fiedler, E., Roberts-Jones, J., and Martin, M.: EU Copernicus Marine Service Quality Information Document for the Global Ocean OSTIA Sea Surface Temperature Reprocessing, SST-GLO-SST-L4-REP-OBSERVATIONS-010-011, Issue: 3.0, Mercator Ocean International, https://catalogue.marine.copernicus.eu/documents/QUID/CMEMS-SST-QUID-010-011.pdf (last access: 2 June 2023), 2023.

Xiu, P., Chai, F., Curchitser, E. N., and Castruccio, F. S.: Future changes in coastal upwelling ecosystems with global warming: The case of the California Current System, Scientific Reports, 8, 2866, https://doi.org/10.1038/s41598-018-21247-7, 2018.

State Planet, 1-osr7, 9, 2023
https://doi.org/10.5194/sp-1-osr7-9-2023

Ocean heat content in the Iberian–Biscay–Ireland regional seas

Álvaro de Pascual-Collar[1], Roland Aznar[1], Bruno Levier[2], and Marcos García-Sotillo[1]

[1]Nologin Consulting, Avda. de Ranillas 1D, 50018 Zaragoza, Spain
[2]Mercator Ocean, 8-10, rue Hermès, 31520, Ramonville Saint-Agne, France

Correspondence: Álvaro de Pascual-Collar (alvaro.depascual@nologin.es)

Received: 28 July 2022 – Discussion started: 23 September 2022
Revised: 12 April 2023 – Accepted: 23 April 2023 – Published: 27 September 2023

Abstract. The ocean has the largest heat capacity of any single component of the climate system and plays a key dominant role in global heat content changes. To analyse ocean heat content (OHC) variability in the Iberia–Biscay–Ireland (IBI) region, several Copernicus Marine reanalysis and observational products are used together to provide multi-product estimations of OHC anomalies over the water column (at upper layers 150, 700, and 2000 m). This work provides a study of spatial and temporal variability of OHC in the northeastern Atlantic region through the analysis of area-averaged time series, trend maps, and trends linked with the main water masses found in the IBI region.

The work states the key role that subsurface water masses play in the OHC trends in the IBI region. The study shows that, although no significant trends are detected for the surface water layers, the intermediate and deep water layers show significant trends (with rates of $+0.40\,\mathrm{W\,m^{-2}}$). However, the high interannual variability of the subsurface water masses masks these trends. Two of the main water masses described in the region (i.e. Sub-Arctic Intermediate Water and Mediterranean Outflow Water) are found to explain more than 50 % of the OHC variability. Since the variability of both water masses is linked to the North Atlantic Oscillation, the work shows the mechanisms by which atmospheric forcing is able to affect the subsurface water layers without showing a signal in the surface.

1 Introduction

It is well established that the main storage (> 90 %) of extra heat from increasing greenhouse gases is absorbed by the oceans; consequently, oceans are the dominant source of changes in global warming (Levitus et al., 2005, 2012; Trenberth et al., 2014; Cheng et al., 2017; von Schuckmann et al., 2020; Gulev et al., 2021). Additionally, the heat stored in oceans has increased during the last decades at basin and global scales (Gulev et al., 2021; Abraham et al., 2013). Therefore, ocean heat content (OHC) is one of the six global climate indicators recommended by the World Meteorological Organization for Sustainable Development Goal 13 implementation (WMO, 2017).

Ideally, the estimations of OHC are integrated over the full depth of the ocean, but for limitations related to the observing system, this is typically done from the ocean's surface down to a reduced depth (such as 700 or 2000 m). The choice of these levels is due to the fact before the year 2000, temperature measurements were most often taken in the upper 700 m of the water column, but by about 2005 the Argo array had sufficient space–time sampling to yield an improved measurement of OHC down to a depth of 2000 m (von Schuckmann et al., 2016; Abraham et al., 2013; Cheng et al., 2022, 2017).

The Copernicus Marine service provides marine data covering the global ocean and European seas, splitting them into six different regions. One of those, the Iberian–Biscay–Ireland (IBI) region, covers the northeastern Atlantic from the Canary Islands (26° N) up to Ireland (55° N), being limited by the 20° W meridian and the continental margin. Among the variety of hydrographic processes taking place

Published by Copernicus Publications.

Table 1. List of Copernicus Marine products used for the computation of ocean heat content (OHC) in the Iberia–Biscay–Ireland region (IBI).

Product ref. no.	Product ID/acronym/type	Data access	Documentation QUID: Quality Information Document PUM: Product User Manual
1	IBI_MULTIYEAR_PHY_005_002 (IBI-REA) Numerical models	EU Copernicus Marine Service Product (2022a)	QUID: Levier et al. (2022) PUM: Amo-Baladrón et al. (2022)
2	GLOBAL_MULTIYEAR_PHY_001_030 (GLO-REA) Numerical models	EU Copernicus Marine Service Product (2022b)	QUID: Drévillon et al. (2022a) PUM: Drévillon et al. (2022b)
3	INSITU_GLO_PHY_TS_OA_MY_013_052 (CORA) In situ observations	EU Copernicus Marine Service Product (2022c)	QUID: Szekely (2022a) PUM: Szekely (2022b)
4	MULTIOBS_GLO_PHY_TSUV_3D_MYNRT_015_012 (ARMOR) In situ observations and Satellite observations	EU Copernicus Marine Service Product (2021a)	QUID: Greiner et al. (2021) PUM: Guinehut (2021)
5	GLOBAL_OMI_OHC_trend (GLO-OMI-trend) Numerical models, in situ observations, and satellite observations	EU Copernicus Marine Service Product (2021b)	QUID: von Schuckmann et al. (2021) PUM: Monier et al. (2021)

in the IBI region we could mention the northern limit of the Canary Current, the upwelling system that influences the Iberian Peninsula and African coasts, the spreading Mediterranean waters that influence the intermediate hydrographic properties and promote the formation of long-lasting eddies, and the influence of the eastern closure of the subtropical gyre that brings warm waters from the Gulf Stream, influencing the climate of western Europe. In this region, the literature describes a number of water masses but three groups of salinity extrema mainly determine the intermediate hydrographic structure: a subsurface salinity minima connected with Sub-Arctic Intermediate Water (SAIW) at potential density anomalies $27.3 < \sigma_\theta$ kg m^{-3}, salinity maxima connected with Mediterranean Outflow Water (MOW) at the neutral density $27.25 < \sigma_\theta < 27.45$ kg m^{-3}, and salinity minima connected with Labrador Sea Water (LSW) underneath the isopycnal $27.8 > \sigma_\theta$ kg m^{-3} (Talley and McCarney, 1982; Iorga and Lozier, 1999a, b; van Aken, 2000; Prieto et al., 2013; de Pascual-Collar et al., 2019). The density ranges for these water masses show considerable overlap, which allows both diapycnal and isopycnal mixing.

Among the Copernicus Marine Service products are the Ocean Monitoring Indicators (OMIs), which are free downloadable trends and datasets covering the past quarter of a century. These are indicators that allow us to track the vital health signs of the ocean and changes in line with climate change. These OMIs are proposed to cover the blue ocean, e.g. the mean volume transport across sections from Reanalysis OMI (GLOBAL_OMI_WMHE_voltrp); the green ocean, e.g. the chlorophyll *a* time series and trends from Observations Reprocessing OMI (OMI_HEALTH_CHL_GLOBAL_OCEANCOLOUR_trend); and the white ocean, e.g. the sea ice extent OMI (ARCTIC_OMI_SI_extent). Among the multiple OMIs provided by Copernicus Marine, an important family includes the indicators focused on evaluating OHC trends and variability. Particularly, the indicator GLOBAL_OMI_OHC_trend (see Tables 1 and 2 for more details on the product; hereafter this product will be referred to as GLO-OMI-trend) provides a global map of trends of OHC integrated in the upper 2000 m. Attending to the spatial variability of trends in the IBI region, this global OMI shows spatial variability of trends, ranging from negative trends of -5 W m^{-2} northward of the parallel 40° N up to positive trends of 2.5 W m^{-2} observed westward of the Gulf of Cádiz. However, this global information should be treated cautiously when looking at regions close to coastal areas and marked by the combination of on-shelf and open waters, such as occurs in the IBI domain.

In the last decades, the upper North Atlantic Ocean experienced a reversal of climatic trends for temperature and salinity. While the period 1990–2004 is characterised by decadal-scale ocean warming, the period 2005–2014 shows a substantial cooling and freshening (González-Pola et al., 2020; Holliday et al., 2020; Somavilla et al., 2009). Such changes are discussed to be linked to ocean internal dynamics and air–sea interactions (Fox-Kemper et al., 2021; Collins et al., 2019; Robson et al., 2016), together with changes linked to the connectivity between the North Atlantic Ocean and the Mediterranean Sea (Masina et al., 2022). Previous works show a consistency of regional OHC with this decadal-scale variability in the IBI region (von Schuckmann et al., 2016, 2018); however, in spite of the year-to-year variability, a long-term warming trend of 0.9 ± 0.4 W m^{-2} in the upper 700 m of the IBI region is also detected. These studies concluded that the

Table 2. Spatial and temporal coverage of products.

Product reference	Resolution	Temporal coverage	Vertical coverage
1. IBI-REA	0.083° × 0.083°	1993–2020	0–5500 m (50 levels)
2. GLO-REA	0.083° × 0.083°	1993–2020	0–5500 m (50 levels)
3. CORA	∼ 0.36° × 0.5°	1993–2021	0–2000 m (152 levels)
4. ARMOR	0.25° × 0.25°	1993–2021	0–5500 m (50 levels)
5. GLO-OMI-trend	0.25° × 0.25°	2005–2009	Integrated 0–2000 (1 level)

Earth's positive energy imbalance dominates the observed regional changes around Europe, but the year-to-year variability in the region potentially masks the long-term warming trend.

Since the distribution of various water masses is one of the main sources of variability (spatial and temporal) in the IBI region, analysis of the heat stored by them can provide information on OHC trends at regional and local scales. For example, Potter and Lozzier (2004), based on 50 years of hydrographic data, studied the temperature and salinity trends of the MOW, finding positive trends that lead to a heat content gain in the MOW reservoir that surpasses the average gain of the North Atlantic basin. Nonetheless, the literature on OHC variability of specific water masses in the IBI region is rather limited. Alternatively, since several studies have concentrated efforts on assessing the thermohaline variability of water masses, they may provide some clues as to what can be expected with respect to OHC.

Regarding the SAIW, Leadbetter et al. (2007) studied the temperature variability of the water column in the period 1981–2005 in a section at 36° N, concluding that the variability in the SAIW is consistent with the displacement of neutral density surfaces driven by changes in surface wind forcing and linked with North Atlantic Oscillation (NAO).

Several studies have focused on the temporal variability of MOW. The analysis of hydrographic properties in the MOW core concluded that changes in MOW properties are not dominated by changes in Mediterranean Sea Water properties (Lozier and Sindlinger, 2009; Bozec et al., 2011). However, the variability of MOW is strongly influenced by year-to-year processes. Some studies described the MOW interannual variability as an oscillation of the water tongue shifting the dominant spreading pathway and interacting with the underlying water masses such as North Atlantic Deep Water and LSW (Bozec et al., 2011; de Pascual-Collar et al., 2019); this variability is also correlated with NAO.

The interannual variability of LSW has been described in previous works, concluding that some of the variability in the water mass can be explained by diapycnal mixing with the overlying MOW (van Aken, 2000) as well as changes in the source regions over the North Atlantic basin (Leadbetter et al., 2007). Additionally, Bozec et al. (2011) studied the distribution of LSW and MOW from 1950 to 2006, observing a coupling between the spreading areas of both water masses and the NAO index.

The present work pursues two main objectives: on one hand, the availability of higher-resolution specific regional products allows us to refine the study of OHC trends in the IBI region; thus, this work explores the spatial and temporal variability of OHC trends in the region as well as explaining its causes in the period 1993–2021, providing a better understanding of the processes controlling such trends. Additionally, since OMIs are simplified indicators that statistically summarise ocean information, a study of the oceanographic processes behind each indicator is needed to have a proper understanding of the changes represented by the OMI. Thus, the work analyses the use and interpretation of OHC OMIs on regional scales and its sources of variability and uncertainty.

This paper is organised as follows: Sect. 2 presents the datasets used, as well as the methodology applied, to compute the OHC in the IBI region. In Sect. 3 the time series of OHC averaged over the whole IBI region are discussed to provide a general view of the regional trends estimated. Section 4 is devoted to showing and discussing maps of trends computed in the same way as the ones provided in the GLO-OMI-trend product. Section 5 analyses the vertical profiles of OHC trends, studying the variability associated with different water masses. Section 6 summarises the availability of the data used in this article. Finally, main conclusions are summed up in Sect. 7.

2 Data and methods

Following the same methodology as in previous Copernicus Marine Ocean State Report contributions (Lima et al., 2020; Mayer et al., 2021), the estimates of OHC anomalies were computed in the IBI region according to the follow equation:

$$\mathrm{OHC} = \int_{z_1}^{z_2} \rho_0 C_p \left(T_\mathrm{m} - T_\mathrm{clim}\right) \mathrm{d}z, \tag{1}$$

where ρ_0 is the density at a reference depth ($\rho_0 = 1020\,\mathrm{kg\,m^{-3}}$), C_p is the specific heat capacity ($C_p = 4181.3\,\mathrm{J\,kg^{-1}\,°C^{-1}}$), z_1 and z_2 are the range of depths to compute the total OHC, T_m is the monthly average

potential temperature at a specific depth, and T_{clim} is the climatological potential temperature of the corresponding month and depth.

As can be seen in Eq. (1), the OHC anomalies are obtained from integrated differences between the monthly temperature and the climatological one along a vertical profile in the ocean. In the present work the anomalies have been referenced to the monthly climatology computed between 1993 and 2019. Additionally, the OHC is presented for the typical depths of 700 and 2000 m, but also for the upper 150 m to analyse the OHC variability in the upper layer.

In order to allow assessing uncertainties of results, different Copernicus products were used to provide multi-product estimations of OHC; therefore, all results were previously computed for a collection of Copernicus products and combined to give an ensemble mean and the standard deviation of the ensemble. Since the objective of this work is the analysis of OHC in the IBI region integrating results from the surface down to a maximum of 2000 m depth, this study has included all Copernicus Marine products that deliver gridded data on potential temperature with vertical coverage from the surface down to at least 2000 m. As shown in Tables 1 and 2, four different products meet these stated conditions: two model reanalyses (the global and regional ones: GLO-REA and IBI-REA, respectively) and two observation-based products (CORA and ARMOR). It is worth mentioning that when OHC was computed, the GLO-REA product did not cover the year 2020, so that year was not considered in the mentioned product.

Each product used is supplied for specific vertical levels with specific thickness; all vertical integrations were computed taking into consideration the thickness of each product level. Similarly, since most of the products used are provided with regular lat–long grids, the surface of each grid cell depends on the latitude, and the spatial averages (when used in this study) were computed considering the specific surface of each product grid cell.

This work shows different results of OHC, mixing different products with specific spatial resolutions (see Table 2). The OHC has been computed for all products using Eq. (1) on the grid of the distributed products and integrating results (from the surface down to 150, 700, and 2000 m) using the product layer thicknesses. The presentation of the results as time series or as maps implies a difference in the way the results are averaged to compute the ensemble mean and spread. Regarding the time series of OHC, anomalies were calculated referenced to the climatic mean of the period 1993–2019. Then the vertical integrations and spatial average were obtained, preserving the service grid of each product. Therefore, the ensemble time series are averaged from time series computed over the service grid of each product. However, to compute ensemble results that comprise spatial information (i.e. results presented as maps), each ensemble member must be interpolated to obtain all estimations on the same grid. Since IBI-REA and GLO-REA products share the same grid, it was considered to be the reference grid; thus, CORA and ARMOR products were spatially interpolated. This interpolation was made over the OHC integrated on the respective layer before averaging the ensemble. The comparison of interpolated and non-interpolated results of each ensemble member did not show relevant changes in the field structure or mathematical artefacts.

This paper focuses on the analysis of OHC trends in the IBI regions. For this purpose, OHC trends are analysed on different time periods within the registry. The selection of time periods corresponds to different criteria such as the detection of trend changes, comparison of results with other works, or selection of periods representative of large-scale patterns. In the case of the analysis of vertical trend profiles (Sect. 5), the time record 1993–2021 has been divided into two periods characterised by a differentiated behaviour of the NAO (NOAA, 2022), considering that (i) the NAO index in 1994 was moderately positive and (ii) it has a minimum in 2010 and (iii) a maximum in 2018; the periods 1993–2010 and 2010–2019 were selected as representative of NAO changes in phase from positive to negative (period 1993–2010) and vice versa, from negative to positive (period 2010–2019; see Fig. S1 in the Supplement).

3 Analysis of OHC time series

Figure 1 shows combined results of products IBI-REA, GLO-REA, CORA, and ARMOR (listed in Tables 1 and 2), with panels displaying the ensemble mean and the ensemble standard deviation of OHC for the period 1993–2021. Corresponding to the ensemble spread, time series reveal an increase in uncertainties when deeper layers are included (0–700 and 0–2000 m); this result can be explained by the decrease in observational data available in deeper levels. It is worth noting the decrease in uncertainties observed after 2003 in the time series integrated over the upper 2000 m. These differences in uncertainties are explained considering the remarkable improvement in the global ocean observing system achieved with the implementation of the global Argo array in 2005 (von Schuckmann et al., 2016; Abraham et al., 2013; Cheng et al., 2022, 2017). The period 1999–2001 shows larger uncertainties observed in the record. This indicates larger discrepancies between ensemble members in representing the minimum of OHC observed in this period. These discrepancies affect both the year when the minimum is reached (while GLO-PHY-REA estimates the minimum in 2000, the other products reach the minimum in 2001) and the magnitude of the minimum values (with all products agreeing on observed negative anomalies during this year).

Trends of time series obtained in Fig. 1 show a barely significant warming of the IBI region in the upper (0–700 m; $0.39 \pm 0.27\,W\,m^{-2}$) and intermediate to deep layers (0–2000 m; $0.40 \pm 0.39\,W\,m^{-2}$); conversely, such a trend does not affect the surface layer, where the trend is not signifi-

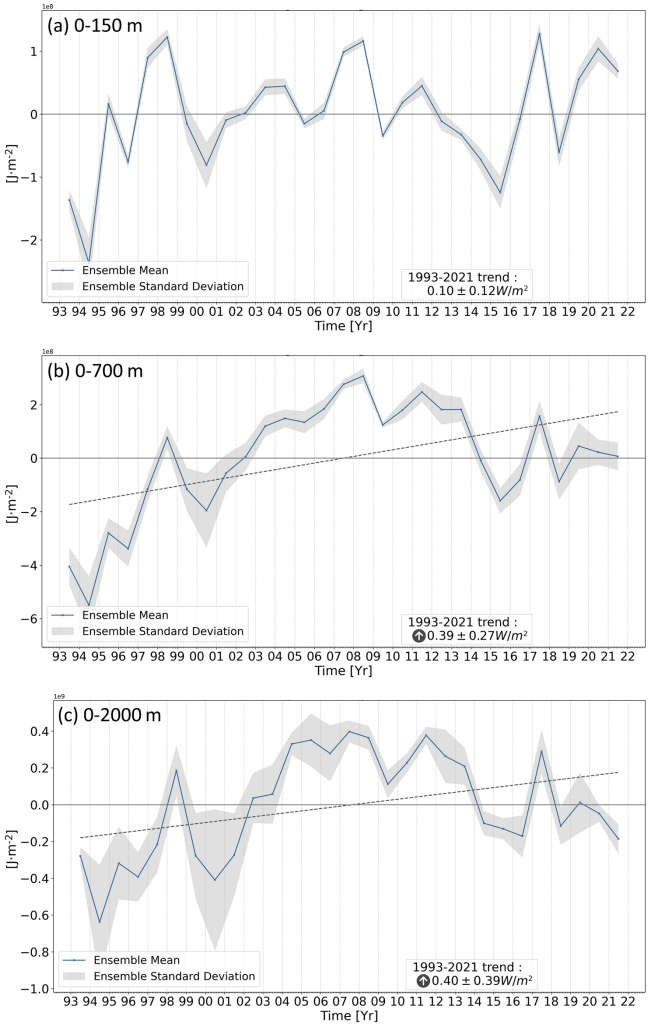

Figure 1. OHC averaged in the IBI domain integrated from the ocean's surface down to 150 m **(a)**, 700 m **(b)**, and 2000 m **(c)**. Time series computed from four Copernicus Marine products (i.e. IBI-REA, GLO-REA, CORA, and ARMOR), providing a multi-product approach. The blue line represents the ensemble mean, and shaded grey areas represent the standard deviation of the ensemble. The analysis of trends (at 95 % confidence interval) computed in the period 1993–2020 is included (bottom right box). Trend lines (dashed line) are only included in the figures when a significant trend is obtained.

cant. Considering that the trend integrated at 0–2000 m is at the limit of significance, we can consider this to be a mathematical result; thus, results suggest a dominance of the variability at intermediate levels over the OHC trend. It is worth mentioning that, despite the positive trends observed in the whole period (1993–2020) of time series integrated down to 700 and 2000 m, a change in trends of these time series after the year 2005 can be appreciated. Table 3 shows the trend analysis by dividing the time record into two halves: the period 1993–2005 and the period 2005–2021. While the results show a significant warming of integration depths 0–700 and

Table 3. Mean OHC trends (in $W\,m^{-2}$) averaged in the IBI domain and integrated from the ocean's surface down to 150, 700, and 2000 m. The confidence interval of trends is computed with 95 % confidence. In bold are the values for which the absolute trend exceeds the confidence interval.

Integration depth (m)	OHC trend ($W\,m^{-2}$) computed in period		
	1993–2005	2005–2021	1993–2021
0–150	0.36 ± 0.46	0.03 ± 0.25	0.10 ± 0.12
0–700	$\mathbf{1.6 \pm 0.57}$	$\mathbf{-0.56 \pm 0.35}$	$\mathbf{0.39 \pm 0.27}$
0–2000	$\mathbf{1.86 \pm 1.09}$	$\mathbf{-1.02 \pm 0.48}$	$\mathbf{0.40 \pm 0.39}$

0–2000 in the period 1993–2005, the period 2005–2021 is characterised by a cooling of both integration layers. This result is consistent with the decadal-scale warming and freshening observed in the North Atlantic Ocean in the period 1990–2020 (González-Pola et al., 2020; Holliday et al., 2020; Somavilla et al., 2009). Additionally, this reversal of the trend explains the discrepancies observed between the long-term trends estimated in this work and the ones observed at 0–700 m in von Schuckmann et al. (2016) ($0.8 \pm 0.3\,W\,m^{-2}$) and von Schuckmann et al. (2018) ($0.9 \pm 0.4\,W\,m^{-2}$) for the periods 1993–2015 and 1993–2016, respectively. The cited works exclude the last years, which have a large influence on the overall trend.

4 Analysis of regional trends of OHC

Figure 2 shows trend maps of OHC computed at 0–2000 m for the IBI region. The figure includes the computation of trends considering two different periods. The period 2005–2019 was selected to allow comparison of results obtained in this work (Fig. 2a) with those obtained with the product GLO-OMI-trend (Fig. 2b), computed for the same period and cropped in the figure to only show the study region. On the other hand, the period 1993–2021 was selected to study the spatial distribution of long-term trends in the IBI region (Fig. 2c). The comparison of results obtained in this work with the GLO-OMI-trend (Fig. 2a and b) shows a high level of agreement, with differences mostly being related to the different resolution. Thus, both figures estimate a negative trend that mainly affects the offshore ocean north of 38° N and a tongue between 31 and 38° N that shows warming trends.

It worth mentioning that the higher resolutions of the products used in this work allow computing OHC trends along the northwestern European shelf, showing a significant warming of the region. This warming may seem low when compared with the values observed in open ocean, but it should be considered that this warming is affected by the shallower depths in the region. For the sake of brevity, Fig. 2 only shows results for the 0–2000 m layer; however, as occurred in the

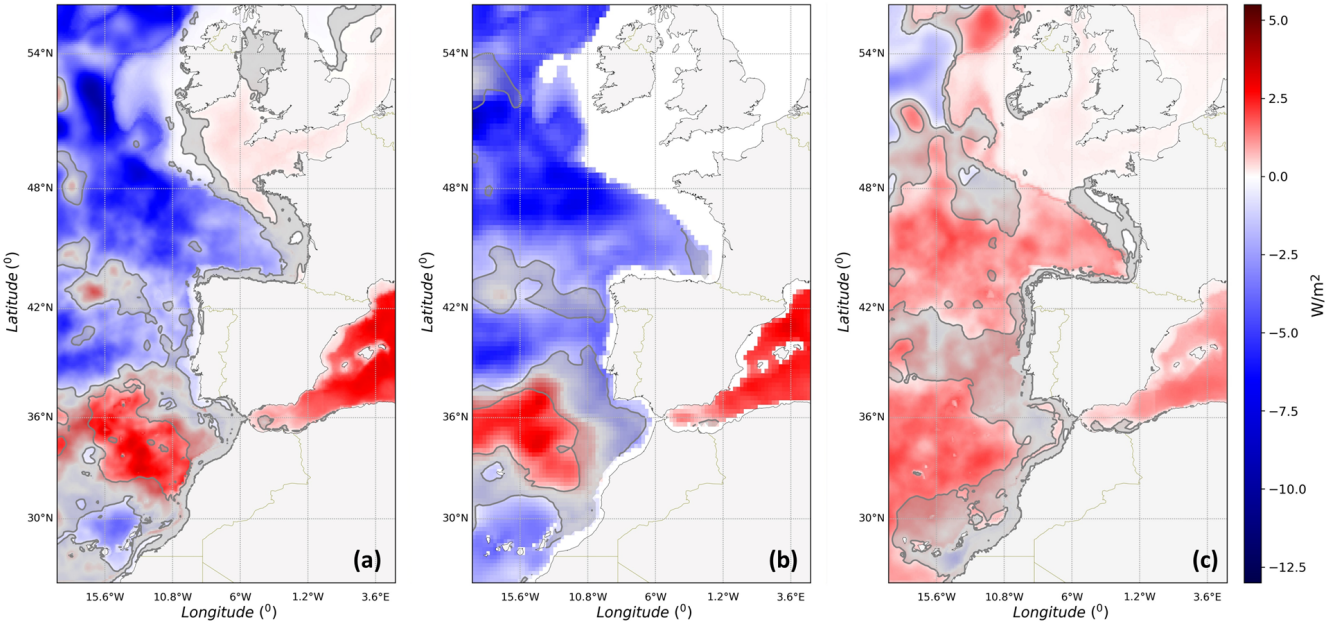

Figure 2. Regional maps of OHC trend computed at 0–2000 m **(a)** over the periods 2005–2019 and **(c)** 1993–2021. Trends computed using the four Copernicus Marine products (IBI-REA, GLO-REA, CORA, and ARMOR), providing a multi-product approach. Shaded colours represent mean trends (using all products), while shaded grey indicates areas with less robust signatures (where the noise – ensemble standard deviation of trends – exceeds the signal – ensemble mean). **(b)** Same as panels **(a)** and **(c)** but obtained from the product GLO-OMI-trend over the period 2005–2019.

time series analysed in the previous section, the observed trends (positive and negative) are subsurface-intensified, so the larger the integration depth, the larger the observed trend (results not shown). Such intensification of trends suggests that both signals are stronger underneath the upper layer, suggesting that they are more related to the evolution of intermediate and deep water masses than to the year-to-year interaction with the atmosphere.

Examining trends computed for the whole time record (Fig. 2c) we conclude that, as estimated by the averaged time series in the previous section, the trend calculated for the whole time record indicates a generalised warming of the IBI area. However, the significance of such warming is smaller, existing in regions with no evidence of OHC trend.

As occurred with the analysis of time series, trend maps show a dependence of the results on the time period selected for the analysis (comparing Fig. 2a and c). This suggests a strong influence of interannual processes on the observed trends. However, it is worth mentioning that the warming trend of the region around 34° N latitude is consistent for both analyses.

5 Analysis of OHC trends across different water masses

Since it has been observed in the data that OHC trends are accentuated in depth, the following section analyses the vertical profile of trends in the region. However, this analysis cannot be carried out for all products and for all points of the grid. Therefore, it has been decided to study the trend profile obtained from the IBI-REA product for two characteristic subregions centred at 35 and 48° N (Fig. 3a and b). Hereafter these subregions will be referred to as 35N and 48N, respectively.

The IBI-REA product was selected for this purpose because it assimilates observational (in situ and satellite) data and uses the GLO-REA product as initial and boundary conditions, therefore indirectly incorporating from the parent products information from the other products. On the other hand, the subregions chosen were selected to provide a detailed analysis of the main features described in the previous section. A first analysis has shown that, as seen with vertically integrated data, the resulting trends show a dependency on the selected period. Hence, as explained in the "Data and methods" section (Sect. 2), in order to provide information on the temporal variability of the water bodies in the IBI area, the trend analysis has been performed by dividing the time period into two periods representative of the positive and negative trend of the NAO index: the period 1993–2010 when the NAO evolves from positive to negative and the period 2010–2019 representing the NAO transition from negative to positive.

The analysis of OHC trend maps for these two periods shows that during the transition to negative NAO phases (Fig. 3a), the water masses in the region undergo signifi-

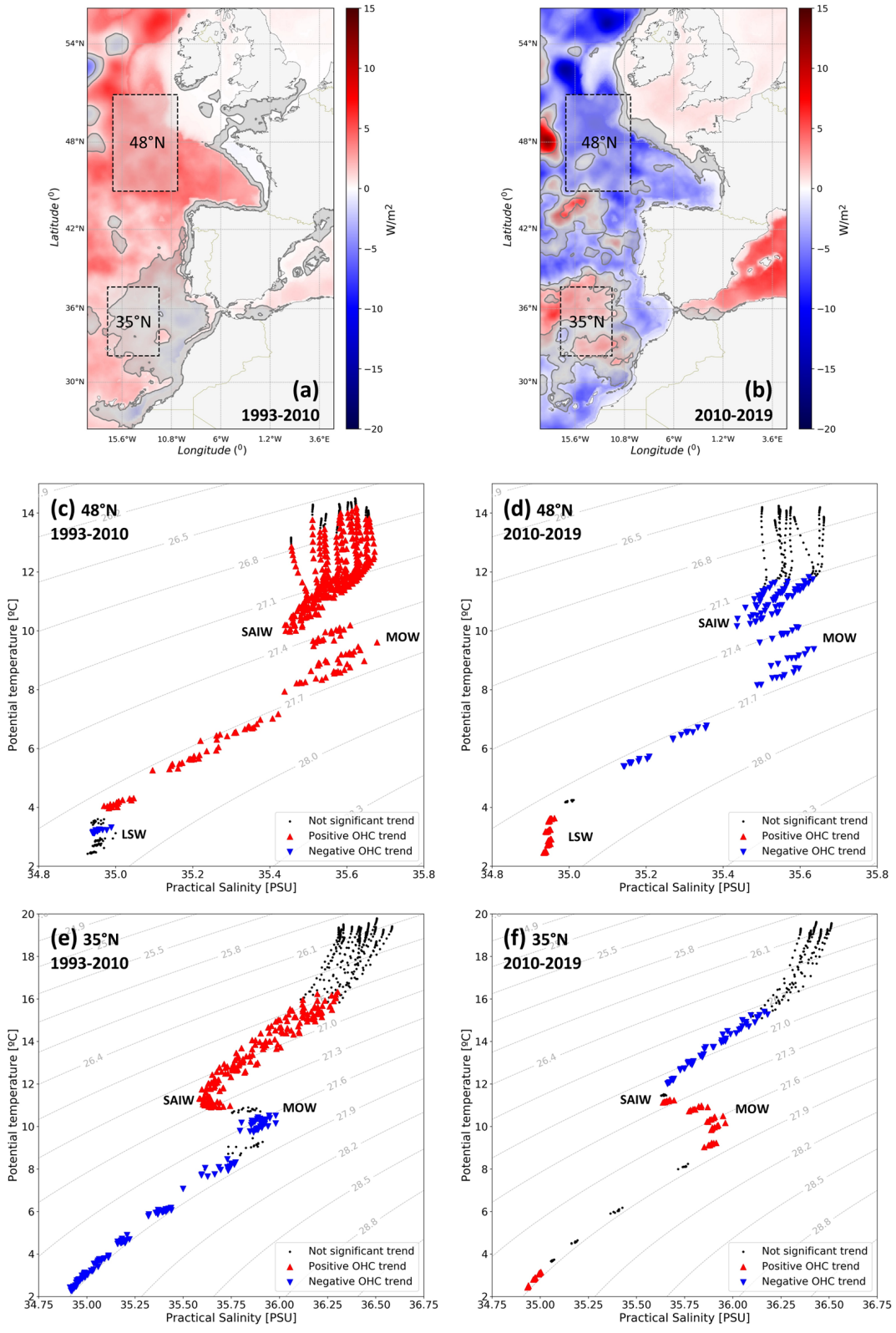

Figure 3. **(a, b)** Maps of regional trends of OHC (0–2000 m) over the periods 1993–2010 **(a)** and 2010–2019 **(b)** derived from the IBI-REA product. Grey shaded areas represent regions where the trend is not significant (95 % confidence). Dashed rectangles denote the subregions 35 and 48° N where θ/S diagrams are averaged in other panels. **(c–f)** θ/S diagrams averaged in subregions (35 and 48° N) and over the periods 1993–2010 and 2010–2019. **(c)** Region 48° N period 1993–2010, **(d)** region 48° N period 2010–2019, **(e)** region 35° N period 1993–2010, and **(f)** region 35° N period 2010–2019.

cant warming over almost the entire IBI area. However, this warming is not significant in part of the southern half of the domain, in the vicinity of the Gulf of Cádiz and the Seine and Horseshoe Abyssal Plains. In contrast, the trend map associated with the NAO transition period towards positive values (Fig. 3b) reveals a generalised cooling pattern with a warming trend around the Horseshoe region similar to that observed in Fig. 2b. Take into account, however, the fact that Figs. 2b and 3b are not directly comparable, since temporal coverage differs.

The trends of OHC averaged for the subregions defined at 35N and 48N have been computed at each level to obtain a vertical profile of trends. These trend profiles are presented in Fig. 3c, d, e, and f combined with the temperature and salinity data on a yearly basis. Each profile shown in the θ/S diagrams corresponds to the annual mean temperature and salinity observed in the selected period (1993–2010 or 2010–2021) and averaged over the corresponding study region (35N or 48N). The different markers used correspond to the different OHC trends observed for each depth. Therefore, the shown θ/S diagrams allow discussing the trends of OHC at each layer, linking these results with the different water masses observed in the region.

The θ/S profiles shown in Fig. 3c, d, e, and f are consistent with the water masses that the literature has described in the northeastern Atlantic: the SAIW characterised by a salinity minima at potential density $\sigma_\theta = 27.2\,\mathrm{kg\,m^{-3}}$, the salinity maxima connected with MOW at the neutral density surface $\sigma_\theta = 27.6\,\mathrm{kg\,m^{-3}}$, and a deeper salinity minima corresponding to LSW underneath the isopycnal $\sigma_\theta = 27.8\,\mathrm{kg\,m^{-3}}$ (Talley and McCarney, 1982; Iorga and Lozier, 1999a, b; van Aken, 2000; Prieto et al., 2013; de Pascual-Collar et al., 2019); however, the core of LSW is only clearly visible in subregion 48N where this water mass has a greater presence.

Regarding the OHC variability of SAIW, results in Fig. 3 show a similar behaviour of the water mass at 48N and 35N. Thus, at both latitudes, the SAIW shows a warming (cooling) associated with the negative (positive) NAO transition. On the contrary, the OHC trends of MOW shows an inverse behaviour between the subregions 35N and 48N. Thus, while in subregion 35N, the MOW experiences a cooling (warming) associated with the negative (positive) NAO transition (periods 1993–2010 and 2010–2021, respectively), in subregion 48N the opposite occurs, and a warming (cooling) of the MOW associated with the negative (positive) NAO transition is observed. These are consistent with the processes described in the literature. Thus, the SAIW trends are coherent with the changes in wind forcing associated with NAO as described by Hurrel (1995) and Leadbetter et al. (2007), and the MOW results are consistent with studies that observed a significant anticorrelation between the westward and northward transport of MOW (Bozec et al., 2011) as well as works that describe the east–west shift of water mass boundaries in the Horseshoe basin (de Pascual-Collar et al., 2019).

Table 4. Mean thermic trends (in $\mathrm{W\,m^{-2}}$) of SAIW, MOW, and 0–2000 m in the IBI subregions (35N and 48N) computed for the period 1993–2021 with the product IBI-REA. Significance of trends computed with 95 % confidence.

Water type	Averaged trend ($\mathrm{W\,m^{-2}}$) in IBI subregions (1993–2021)	
	35N	48N
Sub-Arctic Intermediate Water (SAIW)	+0.52 (44 %)	+0.40 (27 %)
Mediterranean Outflow Water (MOW)	+0.52 (44 %)	+0.36 (24 %)
Total (0–2000 m)	+1.18	+1.46

Apart from the estimation of density levels defining each water mass (shown in Fig. 3), an estimation of the heat trends for each water mass was done for the entire study period of 1993–2021 (see results in Table 4). It is observed that, in line with the results shown in Fig. 2, the overall OHC trends in both regions are positive. Considering that each water mass has different thickness (SAIW approximately 300 m and MOW approximately 400–500 m), we must conclude that although the total trend shown in Table 4 is of the same magnitude for both water masses, the heat gain per cubic metre is higher for SAIW than for MOW. Additionally, the relative influence should be noted that both water masses have on the water column trends down to 2000 m, explaining the sum of the two water masses (a layer approximately 700–800 m thick): 88 % (51 %) of the OHC trend in 35N (48N), respectively.

6 Conclusions

The present work uses several Copernicus Marine products to generate a multi-product OMI of ocean heat content from the surface down to a set of depths over the period 1993–2021. These indicators are able to detect decadal trends of OHC. Specifically, the IBI region presents a warming of $+0.39\,\mathrm{W\,m^{-2}}$ in the upper 700 m. However, the study of both time series trends and spatial distribution of trends shows a high sensitivity to the time period selected, and therefore the high inter-decadal variability detected makes these trends not very significant. On the other hand, the OMIs integrated up to 150 and 2000 m does not allow detecting clear significant trends of results, which suggest that OHC variability in the upper 2000 m may be mainly controlled by intermediate levels.

Although the regional analysis of OHC trends integrated in different depths may provide some clues about the origin of such trends, a finer analysis focusing on the different water masses involved concludes that the vertically integrated trend is the result of different trends (positive and negative) contributing at different layers. The analysis of water masses in the region shows the existence of three water masses (well referenced in the literature): SAIW, MOW, and

LSW. Since the LSW is found in the depth limit established here (2000 m), we put the focus on studying the temporal variability of the heat stored by the other two involved water masses: the SAIW and MOW. The study states that the IBI-REA can simulate the OHC behaviour of SAIW and MOW in a consistent way, with the OHC variability being associated with the NAO, consistent with the variability described in the literature.

Despite the results showing a strong relationship between the variability of the NAO and the OHC of SAIW and MOW, both water masses show a differentiated behaviour. While SAIW shows a homogeneous behaviour over the whole IBI area (OHC trends associated with NAO have the same sign in subregions 35N and 48N), MOW shows an anticorrelated behaviour between subregions 35N and 48N (when the trend is positive in 35N, in 48N it is negative and vice versa).

The work states the key role that subsurface water masses play in the OHC trends in the IBI region by computing the OHC trends for SAIW and MOW over the period 1993–2021. The results show that, despite high interannual variability, both water masses have experienced significant warming in the study period. Additionally, the relative influence that these two water masses have on the integrated OHC trends down to 2000 m is remarkable. Thus, it is found that the sum of both water masses accounts for up to 88 % of the integrated OHC variability from the surface down to 2000 m. However, at more northerly latitudes, this relative influence decreases to 50 %. The greater presence of LSW in the northern regions of the IBI domain suggests that this water mass may share relevance with respect to OHC trends with SAIW and MOW; however, this hypothesis has not been demonstrated in the present work.

Code availability. The code developed for the current work is the property of Nologin Consulting. The code can be accessed by request to Nologin Consulting, Avda. de Ranillas 1D, 50018 Zaragoza, Spain, or by email to the main author (alvaro.depascual@nologin.es).

Data availability. All data used in this article can be downloaded from the Copernicus Marine Environment Monitoring Service web page (https://doi.org/10.48670/moi-00052, EU Copernicus Marine Service Product, 2021a; https://doi.org/10.48670/moi-00236, EU Copernicus Marine Service Product, 2021b; https://doi.org/10.48670/moi-00028, EU Copernicus Marine Service Product, 2022a: https://doi.org/10.48670/moi-00021, EU Copernicus Marine Service Product, 2022b; and https://doi.org/10.17882/46219, EU Copernicus Marine Service Product, 2022c). A description of the data products, as well as their names, spatial and temporal coverages, and documentation, is summarised in Table 1.

Supplement. The supplement related to this article is available online at: https://doi.org/10.5194/sp-1-osr7-9-2023-supplement.

Author contributions. This work was conceptualised through the participation of all authors. Data analysis and drafting of the first version were carried out by AdPC. Additionally, RA, BL, and MGS contributed to the final writing and subsequent revisions of the manuscript.

Competing interests. The contact author has declared that none of the authors has any competing interests.

Disclaimer. Publisher's note: Copernicus Publications remains neutral with regard to jurisdictional claims in published maps and institutional affiliations.

Acknowledgements. The authors thank the Copernicus Marine Environment Monitoring Service for providing the data for the article. Additionally, the helpful comments of Karina von Schuckmann and the other referees are gratefully acknowledged.

Review statement. This paper was edited by Marta Marcos and reviewed by Carolina M. L. Camargo and Cesar Gonzalez-Pola.

References

Abraham, J. P., Baringer, M., Bindoff, N. L., Boyer, T., Cheng, L. J., Church, J. A., Conroy, J. L., Domingues, C. M., Fasullo, J. T., Gilson, J., Goni, G., Good, S. A., Gorman, J. M., Gouretski, V., Ishii, M., Johnson, G. C., Kizu, S., Lyman, J. M., Macdonald, A. M., Minkowycz, W. J., Moffitt, S. E., Palmer, M. D., Piola, A. R., Reseghetti, F., Schuckmann, K., Trenberth, K. E., Velicogna, I., and Willis, J. K.: A review of global ocean temperature observations: Implications for ocean heat content estimates and climate change, Rev. Geophys., 51, 450–483, 2013.

Amo-Baladrón, A., Levier, B., Aznar, R., and Sotillo, M. G.: EU Copernicus Marine Service Product User Manual for the Atlantic-Iberian Biscay Irish-Ocean Physics Reanalysis, IBI_MULTIYEAR_PHY_005_002, issue 4.1, Mercator Ocean International, https://catalogue.marine.copernicus.eu/documents/PUM/CMEMS-IBI-PUM-005-002.pdf (last access: 4 April 2023), 2022.

Bozec, A., Lozier, M. S., Chasignet, E. P., and Halliwel, G. R.: On the variability of the Mediterranean Outflow Water in the North Atlantic from 1948 to 2006, J. Geophys. Res.-Oceans, 116, C09033, https://doi.org/10.1029/2011JC007191, 2011.

Cheng, L., Trenberth, K. E., Fasullo, J., Boyer, T., Abraham, J., and Zhu, J.: Improved estimates of ocean heat content from 1960–2015, Sci. Adv., 3, e1601545, https://doi.org/10.1126/sciadv.1601545, 2017.

Cheng, L., Foster, G., Hausfather, Z., Trenberth, K. E., and Abraham, J.: Improved quantification of the rate of ocean warming,

J. Climate, 35, 1–37, https://doi.org/10.1175/JCLI-D-21-0895.1, 2022.

Collins, M., Sutherland, M., Bouwer, L., Cheong, S.-M., Frölicher, T., Jacot Des Combes, H., Koll Roxy, M., Losada, I., McInnes, K., Ratter, B., Rivera-Arriaga, E., Susanto, R. D., Swingedouw, D., and Tibig, L.: Extremes, Abrupt Changes and Managing Risk, in: IPCC Special Report on the Ocean and Cryosphere in a Changing Climate, edited by: Pörtner, H.-O., Roberts, D. C., Masson-Delmotte, V., Zhai, P., Tignor, M., Poloczanska, E., Mintenbeck, K., Alegría, A., Nicolai, M., Okem, A., Petzold, J., Rama, B., and Weyer, N. M., Cambridge University Press, Cambridge, UK and New York, NY, USA, 589–655, https://doi.org/10.1017/9781009157964.008, 2019.

de Pascual-Collar, Á., G. Sotillo, M., Levier, B., Aznar, R., Lorente, P., Amo-Baladrón, A., and Álvarez-Fanjul, E.: Regional circulation patterns of Mediterranean Outflow Water near the Iberian and African continental slopes, Ocean Sci., 15, 565–582, https://doi.org/10.5194/os-15-565-2019, 2019.

Drévillon, M., Lellouche, J. M., Régnier, C., Garric, G., Bricaud, C., Hernandez, O., and Bourdalé-Badie, R.: EU Copernicus Marine Service Quality Information Document for the Global Ocean Physics Reanalysis, GLOBAL_REANALYSIS_PHY_001_030, issue 1.6, Mercator Ocean International, https://catalogue.marine.copernicus.eu/documents/QUID/CMEMS-GLO-QUID-001-030.pdf (last access: 4 April 2023), 2022a.

Drévillon, M., Fernandez, E., and Lellouche, J. M.: EU Copernicus Marine Service Product User Manual for the Global Ocean Physics Reanalysis, GLOBAL_REANALYSIS_PHY_001_030, Issue 1.4, Mercator Ocean International, https://catalogue.marine.copernicus.eu/documents/PUM/CMEMS-GLO-PUM-001-030.pdf (last access: 4 April 2023), 2022b.

EU Copernicus Marine Service Product: Multi Observation Global Ocean 3D Temperature Salinity Height Geostrophic Current and MLD, Mercator Ocean International [data set], https://doi.org/10.48670/moi-00052, 2021a.

EU Copernicus Marine Service Product: Global Ocean Heat Content trend map from Reanalysis & Multi-Observations Reprocessing, Mercator Ocean International [data set], https://doi.org/10.48670/moi-00236, 2021b.

EU Copernicus Marine Service Product: Atlantic-Iberian Biscay Irish-Ocean Physics Reanalysis Forecast, Mercator Ocean International [data set], https://doi.org/10.48670/moi-00028, 2022a.

EU Copernicus Marine Service Product: Global Ocean Physics Reanalysis, Mercator Ocean International [data set], https://doi.org/10.48670/moi-00021, 2022b.

EU Copernicus Marine Service Product: Global Ocean – Delayed Mode gridded CORA – In-situ Observations objective analysis in Delayed Mode, Mercator Ocean International [data set], https://doi.org/10.17882/46219, 2022c.

Fox-Kemper, B., Hewitt, H. T., Xiao, C., Aðalgeirsdóttir, G., Drijfhout, S. S., Edwards, T. L., Golledge, N. R., Hemer, M., Kopp, R. E., Krinner, G., Mix, A., Notz, D., Nowicki, S., Nurhati, I. S., Ruiz, L., Sallée, J.-B., Slangen, A. B. A., and Yu, Y.: Ocean, Cryosphere and Sea Level Change, in: Climate Change 2021: The Physical Science Basis. Contribution of Working Group I to the Sixth Assessment Report of the Intergovernmental Panel on Climate Change, edited by: Masson-Delmotte, V., Zhai, P., Pirani, A., Connors, S. L., Péan, C., Berger, S., Caud, N., Chen, Y., Goldfarb, L., Gomis, M. I., Huang, M., Leitzell, K., Lonnoy, E., Matthews, J. B. R., Maycock, T. K., Waterfield, T., Yelekçi, O., Yu, R., and Zhou, B., Cambridge University Press, Cambridge, United Kingdom and New York, NY, USA, 1211–1362, 2021.

González-Pola, C., Larsen, K. M. H., Fratantoni, P., and Beszczynska-Möller, A. (Eds.): ICES Report on Ocean Climate 2019, ICES Cooperative Research Reports No. 350, 136 pp., https://doi.org/10.17895/ices.pub.7537, 2020.

Greiner, E., Verbrugge, N., Mulet, S., and Guinehut, S.: EU Copernicus Marine Service Quality Information Document for the Multi Observation Global Ocean 3D Temperature Salinity Heights Geostrophic Currents and MLD Product, MULTIOBS_GLO_PHY_TSUV_3D_MYNRT_015_012, issue 1.1, Mercator Ocean International, https://catalogue.marine.copernicus.eu/documents/QUID/CMEMS-MOB-QUID-015-012.pdf (last access: 4 April 2023), 2021.

Guinehut, S.: EU Copernicus Marine Service Product User Manual for the Multi Observation Global Ocean 3D Temperature Salinity Heights Geostrophic Currents and MLD Product, MULTIOBS_GLO_PHY_TSUV_3D_MYNRT_015_012, issue 1.1, Mercator Ocean International, https://catalogue.marine.copernicus.eu/documents/PUM/CMEMS-MOB-PUM-015-012.pdf (last access: 4 April 2023), 2021.

Gulev, S. K., Thorne, P. W., Ahn, J., Dentener, F. J., Domingues, C.M., Gerland, S., Gong, D., Kaufman, D. S., Nnamchi, H. C., Quaas, J., Rivera, J. A., Sathyendranath, S., Smith, S. L., Trewin, B., von Schuckmann, K., and Vose, R. S.: Changing State of the Climate System, in: Climate Change 2021: The Physical Science Basis. Contribution of Working Group I to the Sixth Assessment Report of the Intergovernmental Panel on Climate Change, edited by: Masson Delmotte, V., Zhai, P., Pirani, A., Connors, S. L., Péan, C., Berger, S., Caud, N., Chen, Y., Goldfarb, L., Gomis, M. I., Huang, M., Leitzell, K., Lonnoy, E., Matthews, J. B. R., Maycock, T. K., Waterfield, T., Yelekçi, O., Yu, R., and Zhou, B., Cambridge University Press, Cambridge, United Kingdom and New York, NY, USA, 287–422, 2021.

Holliday, N. P., Bersch, M., Berx, B., Chafik, L., Cunningham, S., Florindo-López, C., Hátún, H., Johns, W., Josey, S. A., Larsen, K. M. H., Mulet, S., Oltmanns, M., Reverdin, G., Rossby, T., Thierry, V., Valdimarsson, H., and Yashayaev, I.: Ocean circulation causes the largest freshening event for 120 years in eastern subpolar North Atlantic, Nat. Commun., 11, 585, https://doi.org/10.1038/s41467-020-14474-y, 2020.

Hurrell, J.: Decadal trends in the North Atlantic Oscillation: Regional temperatures and precipitation, Science, 269, 676–679, 1995.

Iorga, M. C. and Lozier, M. S.: Signatures of the Mediterranean outflow from a North Atlantic climatology 1. Salinity and density fields, J. Geophys. Res., 104, 25985–26009, 1999a.

Iorga, M. C. and Lozier, M. S.: Signatures of the Mediterranean outflow from a North Atlantic climatology 2. Diagnostic velocity fields, J. Geophys. Res., 104, 26011–26029, 1999b.

Leadbetter, S. J., Williams, R. G., McDonagh, E. L., and King, B. A.: A twenty year reversal in water mass trends in the subtropical North Atlantic, Geophys. Res. Lett., 34, 1–6, https://doi.org/10.1029/2007GL029957, 2007.

Levier, B., Reffray, G., and Sotillo, M. G.: EU Copernicus Marine Service Quality Information Document for the Atlantic-Iberian Biscay Irish-Ocean Physics Reanalysis, IBI_MULTIYEAR_PHY_005_002, issue 5.1, Mercator Ocean International, https://catalogue.marine.copernicus.eu/documents/QUID/CMEMS-IBI-QUID-005-002.pdf (last access: 4 April 2023), 2022.

Levitus, S., Antonov, J., and Boyer, T.: Warming of the world ocean, 1955–2003, Geophys. Res. Lett., 32, L02604, https://doi.org/10.1029/2004GL021592, 2005.

Levitus, S., Antonov, J. I., Boyer, T. P., Baranova, O. K., Garcia, H. E., Locarnini, R. A., Mishonov, A. V., Reagan, J. R., Seidov, D., Yarosh, E. S., and Zweng, M. M.: World ocean heat content and thermosteric sea level change (0–2000 m), 1955–2010, Geophys. Res. Lett., 39, L10603, https://doi.org/10.1029/2012GL051106, 2012.

Lima, L., Peneva, E., Ciliberti, E., Masina, S., Lemieux, B., Storto, A., and Chtirkova, B.: Ocean heat content in the Black Sea, in: Copernicus marine service ocean state report, issue 4, edited by: von Schuckmann, K., Le Traon, P. Y., Smith, N., Pascual, A., Djavidnia, S., Gattuso, J. P., Grégoire, M., Nolan, G., Aaboe, S., Álvarez-Fanjul, E., Aouf, L., Aznar, R., Badewien, T. H., Behrens, A., Berta, M., Bertino, L., Blackford, J., Bolzon, G., Borile, F., Bretagnon, M., Brewin, R. J. W., Canu, D., Cessi, P., Ciavatta, S., Chapron, B., Trang Chau, T. T., Chevallier, F., Chtirkova, B., Ciliberti, S., Clark, J. R., Clementi E., Combot, C., Comerma, E., Conchon, A., Coppini, G., Corgnati, L., Cossarini, G., Cravatte, S., de Alfonso, M., de Boyer Montégut, C., De Lera Fernández, C., de los Santos, F. J., Denvil-Sommer, A., de Pascual-Collar, A., Dias Nunes, P. A. L., Di Biagio, V., Drudi, M., Embury, O., Falco, P., Fanton d'Andon, O., Ferrer, L., Ford, D., Freund, H., García León, M., García-Sotillo. M., García-Valdecasas, J. M., Garnesson, P., Garric, G., Gasparin, F., Gehlen, M., Genua-Olmedo, A., Geyer, G., Ghermandi, A., Good, S. A., Gourrion, J., Greiner, E., Griffa, A., González, M., Hernández-Carrasco, I., Isoard, E., Kenned, J. J., Kay. S., Korosov, A., Laanemäe, K., Land, P. E., Lavergne, T., Lazzari, P., Legeais, J. F., Lemieux, B., Levier, B., Llovel, W., Lyubartsev, V., Le Traon, P. Y., Lien, V. S., Lima, L., Lorente, P., Mader, J., Magaldi, M. G., Maljutenko, I., Mangin, A., Mantovani, C., Marinova, V., Masina, S., Mauri, E., Meyerjürgens, J., Mignot, A., McEwan, R., Mejia, C., Melet, A., Menna, M., Meyssignac, B., Mouche, A., Mourre, B., Müller, M., Notarstefano, G., Orfila, A., Pardo, S., Peneva, E., Pérez-Gómez, B., Perruche, C., Peterlin, M., Poulain, PM., Pinardi, N., Quilfen, Y., Raudsepp, U., Renshaw, R., Révelard, A., Reyes-Reyes, E., Ricker, M., Rodríguez-Rubio, P., Rotllán, P., Royo Gelabert, E., Rubio, A., Ruiz-Parrado, I., Sathyendranath, S., She, J., von Schuckmann, K., Solidoro, C., Stanev, E.V., Staneva, J., Storto, A., Su, J., Tajalli Bakhsh, T., Tilstone, G. H., Tintoré, J., Toledano, C., Tournadre, J., Tranchant, B., Uiboupin, R., Valcarcel, A., Valcheva, N., Verbrugge, N., Vrac, M., Wolff, J. O., Zambianchi, E., Zielinski, O., Zinck, A. S., and Zunino, S., J. Oper. Oceanogr., 13, S1–S172, https://doi.org/10.1080/1755876X.2020.1785097, 2020.

Lozier, M. S. and Sindlinger, L.: On the Source of Mediterranean OverflowWater Property Changes, J. Phys. Oceanogr., 39, 1800–1817, https://doi.org/10.1175/2009JPO4109.1, 2009.

Masina, S., Pinardi, N., Cipollone, A., Banerjee, D. S., Lyubartsev, V., von Schuckmann, K., Jackson, L., Escudier, R., Clementi, E., Aydogdu, A., and Iovino D.: The Atlantic Meridional Overturning Circulation forcing the mean se level in the Mediterranean Sea through the Gibraltar transport, in: Copernicus Ocean State Report, Issue 6, edited by: von Schuckmann, K. and Le Traon, P.-Y., J. Oper. Oceanogr., 15, s119–s126, https://doi.org/10.1080/1755876X.2022.2095169, 2022.

Mayer, M., Lien, V. S., Mork, K. A., von Schuckmann, K., Monier, M., and Greiner, E.: Ocean heat content in the High North, in: Copernicus Marine Service Ocean State Report, Issue 5, edited by: von Schuckmann, K., Le Traon, P. Y., Smith, N., Pascual, A., Djavidnia, S., Gattuso, J. P., Grégoire, M., Aaboe, S., Alari, V., Alexander, B. E., Alonso-Martirena, A., Aydogdu, A., Azzopardi, J., Bajo, M., Barbariol, F., Batistić, M., Behrens, A., Ben Ismail, S., Benetazzo, A., Bitetto, I., Borghini, M., Bray, L., Capet, A., Carlucci, R., Chatterjee, S., Chiggiato, J., Ciliberti, S., Cipriano, G., Clementi, E., Cochrane, P., Cossarini, G., D'Andrea, L, Davison, S., Down, E., Drago, A., Druon, J. N., Engelhard, G., Federico, I., Garić, R., Gauci, A., Gerin, R., Geyer, G., Giesen, R., Good, S., Graham, R., Grégoire, M., Greiner, E., Gundersen, K., Hélaouët, P., Hendricks, S., Heymans, J. J., Holt, J., Hure, M., Juza, M., Kassis, D., Kellett, P., Knol-Kauffman, M., Kountouris, P., Kõuts, M., Lagemaa, P., Lavergne, T., Legeais, J. F., Le Traon, P. Y., Libralato, S., Lien, V. S., Lima, L., Lind, S., Liu, Y., Macías, D., Maljutenko, I., Mangin, A., Männik, A., Marinova, V., Martellucci, R., Masnadi, F., Mauri, E., Mayer, M., Menna, M., Meulders, C., Møgster, J. S., Monier, M., Arne Mork, K., Müller, M., Øie Nilsen, J. E., Notarstefano, G., Oviedo, J. L., Palerme, C., Palialexis, A., Panzeri, D., Pardo, S., Peneva, E., Pezzutto, P., Pirro, A., Platt, T., Poulain, P. M., Prieto, L., Querin, S., Rabenstein, L., Raj, R. P., Raudsepp, U., Reale, M., Renshaw, R., Ricchi, A., Ricker, R., Rikka, S., Ruiz, J., Russo, T., Sanchez, J., Santoleri, R., Sathyendranath, S., Scarcella, G., Schroeder, K., Sparnocchia, S., Spedicato, M. T., Stanev, E., Staneva, J., Stocker, A., Stoffelen, A., Teruzzi, A., Townhill, B., Uiboupin, R., Valcheva, N., Vandenbulcke, L., Vindenes, H., von Schuckmann, K., Vrgoč, N., Wakelin, S., and Zupa, W., J. Oper. Oceanogr., 14, 1–185, https://doi.org/10.1080/1755876X.2021.1946240, 2021.

Monier, M., Derval, C., and Fernandez, E.: EU Copernicus Marine Service Product User Manual for the Global Ocean Heat Content trend map from Reanalysis and Multi-Observations Reprocessing, GLOBAL_OMI_OHC_trend, issue 4.0, Mercator Ocean International, https://catalogue.marine.copernicus.eu/documents/PUM/CMEMS-OMI-PUM-GLO-OHC.pdf (last access: 4 April 2023), 2021.

NOAA: North Atlantic Oscillation (NAO), NOAA, https://www.ncei.noaa.gov/access/monitoring/nao/, last access: December 2022.

Potter, R. A. and Lozier, M. S.: On the warming and salinification of the Mediterranean outflow waters in the North Atlantic, Geophys. Res. Lett., 31, 1–4, https://doi.org/10.1029/2003GL018161, 2004.

Prieto, E., González-Pola, C., Lavín, A., Sánchez, R. F., and Ruiz-Villarreal, M.: Seasonality of intermediate waters hydrography west of the Iberian Peninsula from an 8 yr semiannual time series of an oceanographic section, Ocean Sci., 9, 411–429, https://doi.org/10.5194/os-9-411-2013, 2013.

Robson, J., Ortega, P., and Sutton, R.: A reversal of climatic trends in the North Atlantic since 2005, Nat. Geosci., 9, 513–517, https://doi.org/10.1038/ngeo2727, 2016.

Somavilla, R., González-Pola, C., Rodriguez, C., Josey, S. A., Sánchez, R. F., and Lavín, A.: Large changes in the hydrographic structure of the Bay of Biscay after the extreme mixing of winter 2005, J. Geophys. Res.-Oceans, 114, C01001, https://doi.org/10.1029/2008JC004974, 2009.

Szekely, T.: EU Copernicus Marine Service Quality Information Document for the Global Ocean – Delayed Mode gridded CORA – In-situ Observations objective analysis in Delayed Mode, INSITU_GLO_PHY_TS_OA_MY_013_052, issue 1.2, Mercator Ocean International, https://catalogue.marine.copernicus.eu/documents/QUID/CMEMS-INS-QUID-013-052.pdf (last access: 4 April 2023), 2022a.

Szekely, T.: EU Copernicus Marine Service Product User Manual for the Global Ocean – Delayed Mode gridded CORA – In-situ Observations objective analysis in Delayed Mode, INSITU_GLO_PHY_TS_OA_MY_013_052, issue 1.10, Mercator Ocean International, https://catalogue.marine.copernicus.eu/documents/PUM/CMEMS-INS-PUM-013-002-052.pdf (last access: 4 April 2023), 2022b.

Talley, L. D. and McCartney, M. S.: Distribution and Circulation of Labrador Sea Water, J. Phys. Oceanogr., 12, 1189–1205, https://doi.org/10.1175/1520-0485(1982)012<1189:DACOLS>2.0.CO;2, 1982.

Trenberth, K. E., Fasullo, J. T., and Balmaseda, M.: Earth's energy imbalance, J. Climate, 27, 3129–3144, https://doi.org/10.1175/JCLI-D-13-00294.1, 2014.

van Aken, H. M.: The hydrography of the mid-latitude Northeast Atlantic Ocean II: The intermediate water masses, Deep-Sea Res., 47, 789–824, https://doi.org/10.1016/S0967-0637(99)00112-0, 2000.

von Schuckmann, K., Balmaseda, M., and Simoncelli, S.: Ocean Heat Content, in: The Copernicus Marine Environment Monitoring Service Ocean State Report, Journal of Operational Oceanography, Volume 9 – Issue sup2, edited by: von Schuckmann, K., Le Traon, P. Y., Alvarez-Fanjul, E., Axell, L., Balmaseda, M., Breivik, L. A., Brewin, R. J. W., Bricaud, C., Drevillon, M., Drillet, Y., Dubois, C., Embury, O., Etienne, H., García-Sotillo, M., Garric, G., Gasparin, F., Gutknecht, E., Guinehut, S., Hernandez, F., Juza, M., Karlson, B., Korres, G., Legeais, J. F., Levier, B., Lien, V. S., Morrow, R., Notarstefano, G., Parent, L., Pascual-Collar, A., Pérez-Gómez, B., Perruche, C., Pinardi, N., Pisano, A., Poulain, P. M., Pujol, I. M., Raj, R. P., Raudsepp, U., Roquet, H., Samuelsen, A., Sathyendranath, S., She, J., Simoncelli, S., Solidoro, C., Tinker, J., Tintoré, J., Viktorsson, J., Ablain, M., Almroth-Rosell, E., Bonaduce, A., Clementi, E., Cossarini, G., Dagneaux, Q., Desportes, C., Dye, S., Fratianni, C., Good, S., Greiner, E., Gourrion, J., Hamon, M., Holt, J., Hyder, P., Kennedy, J., Manzano-Muñoz, F., Melet, A, Meyssignac, B., Mulet, S., Buongiorno Nardelli, B., O'Dea, E., Olason, E., Paulmier, A., Pérez-González, I., Reid, R., Racault, M. F., Raitsos, D. E., Ramos, A., Sykes, P., Szekely, T., and Verbrugge, N., The Copernicus Marine Environment Monitoring Service Ocean, https://doi.org/10.1080/1755876X.2016.1273446, 2016.

von Schuckmann, K., Storto, A., Simoncelli, S., Raj, R. P., Samuelsen, A., Pascual-Collar, A., Garcia-Sotillo, M., and Szerkely, T.: Ocean Heat Content, in: Copernicus Marine Service Ocean State Report, edited by: von Schuckmann, K., Le Traon, P. Y., Smith, N., Pascual, A., Brasseur, P., Fennel, K., Djavidnia, S., Aaboe, S., Fanjul, E. A., Autret, E., Axell, L., Aznar, R., Benincasa, M., Bentamy, A., Boberg, F., Bourdallé-Badie, R., Nardelli, B. B., Brando, V. E., Bricaud, C., Breivik, L. A., Brewin, R. J. W., Capet, A., Ceschin, A., Ciliberti, S., Cossarini, G., de Alfonso, M., Pascual-Collar, A., de Kloe, J., Deshayes, J., Desportes, C., Drévillon, M., Drillet, Y., Droghei, R., Dubois, C., Embury, O., Etienne, E., Fratianni, C., García Lafuente, J., Garcia-Sotillo, M., Garric, G., Gasparin, F., Gerin, R., Good, S., Gourrion, J., Grégoire, M., Greiner, E, Guinehut, S., Gutknecht, E., Hernandez, F., Hernandez, O., Høyer, J., Jackson, L., Jandt, S., Josey, S., Juza, M., Kennedy, J., Kokkini, Z., Korres, G., Kõuts, M., Lagemaa, P., Lavergne, T., le Cann, B., Legeais, J. F., Lemieux-Dudon, B., Levier, B., Lien, V., Maljutenko, I., Manzano, F., Marcos, M., Marinova, V., Masina, S., Mauri, E., Mayer, M., Melet, A., Mélin, F., Meyssignac, B., Monier, M., Müller, M., Mulet, S., Naranjo, C., Notarstefano, G., Paulmier, A., Pérez Gomez, B., Pérez Gonzalez, I., Peneva, E., Perruche, C., Peterson, K. A., Pinardi, N., Pisano, A., Pardo, S., Poulain, P. M., Raj, R. P., Raudsepp, U., Ravdas, M., Reid, R., Rio, M. H., Salon, S., Samuelsen, A., Sammartino, M., Sammartino, S., Britt Sandø, A., Santoleri, R., Sathyendranath, S., She, J., Simoncelli, S., Solidoro, C., Stoffelen, A., Storto, A., Szerkely, T., Tamm, S., Tietsche, S., Tinker, J., Tintore, J., Trindade, A., van Zanten, D., Vandenbulcke, L., Verhoef, A., Verbrugge, N., Viktorsson, L., Wakelin, S. L., Zacharioudaki, A., and Zuo, H., J. Oper. Oceanogr., 11, S1–S142, https://doi.org/10.1080/1755876X.2018.1489208, 2018.

von Schuckmann, K., Cheng, L., Palmer, M. D., Hansen, J., Tassone, C., Aich, V., Adusumilli, S., Beltrami, H., Boyer, T., Cuesta-Valero, F. J., Desbruyères, D., Domingues, C., García-García, A., Gentine, P., Gilson, J., Gorfer, M., Haimberger, L., Ishii, M., Johnson, G. C., Killick, R., King, B. A., Kirchengast, G., Kolodziejczyk, N., Lyman, J., Marzeion, B., Mayer, M., Monier, M., Monselesan, D. P., Purkey, S., Roemmich, D., Schweiger, A., Seneviratne, S. I., Shepherd, A., Slater, D. A., Steiner, A. K., Straneo, F., Timmermans, M.-L., and Wijffels, S. E.: Heat stored in the Earth system: where does the energy go?, Earth Syst. Sci. Data, 12, 2013–2041, https://doi.org/10.5194/essd-12-2013-2020, 2020.

von Schuckmann, K., Monier, M., and Drévillon, M.: EU Copernicus Marine Service Quality Information Document for the Global Ocean Heat Content trend map from Reanalysis & Multi-Observations Reprocessing, GLOBAL_OMI_OHC_trend, issue 1.0, Mercator Ocean International, https://catalogue.marine.copernicus.eu/documents/QUID/CMEMS-OMI-QUID-GLO-OHC.pdf (last access: 4 April 2023), 2021.

WMO: Weather ready, Climate smart – Supporting the 2030 Agenda for Sustainable Development, World Meteorological Organisation Bulletin, 66, edited by: Mananekova, E. and Castonguay, S., World Meteorological Organisation, Geneva, Switzerland, https://library.wmo.int/?lvl=notice_display&id=20022 (last access: May 2023), 2017.

State Planet, 1-osr7, 10, 2023
https://doi.org/10.5194/sp-1-osr7-10-2023

Dissolved oxygen as an indicator of multiple drivers of the marine ecosystem: the southern Adriatic Sea case study

Valeria Di Biagio, Riccardo Martellucci, Milena Menna, Anna Teruzzi, Carolina Amadio, Elena Mauri, and Gianpiero Cossarini

National Institute of Oceanography and Applied Geophysics – OGS, Trieste, Italy

Correspondence: Valeria Di Biagio (vdibiagio@ogs.it)

Received: 22 July 2022 – Discussion started: 30 September 2022
Revised: 13 March 2023 – Accepted: 31 March 2023 – Published: 27 September 2023

Abstract. Oxygen is essential to all aerobic organisms, and its dynamics in the ocean involve interconnected physical and biological processes that form the basis of the functioning of the marine ecosystem. The study of dissolved oxygen (DO) variations under multiple drivers is currently one of the main goals of climate and marine-ecological scientific communities, and the quantification of DO levels is essential for the assessment of the environmental status, especially in coastal areas.

We investigate the 1999–2021 interannual variability in DO in the southern Adriatic Sea, a marginal area of the Mediterranean Sea, where deep-water formation processes occur, contributing significantly to the ventilation of the eastern Mediterranean Basin. Following the Marine Strategy Framework Directive, which promotes the integration of different observational platforms, we use DO modelled by the Copernicus Marine Mediterranean Sea biogeochemical reanalysis, which assimilates satellite chlorophyll concentrations and to which we apply a bias correction using DO Argo float measurements in 2014–2020. A correlation analysis of the time series of the first three modes of variability (86 % of the total variance) of the DO profiles extracted from the bias-corrected reanalysis with key meteo-marine indicators shows a link with (i) net heat fluxes related to oxygen solubility, (ii) vertical mixing, (iii) biological production at the surface and in subsurface layers, and (iv) circulation associated with the entrance of northern Adriatic waters. The alternating entrance of Levantine and Atlantic waters through the North Ionian Gyre (NIG) appears to be the driver of the fourth mode of variability, which explains 8 % of the total variance. Moreover, we find that the first temporal mode of variability is the main driver of the negative anomaly of DO in the 0–600 m layer in 2021 with respect to the 1999–2020 climatology. We ascribe the lower content of DO in 2021 to a negative anomaly of the subsurface biological production in the same year, in agreement with the previous correlation analysis, but not to heat fluxes. Indeed, in agreement with previous studies, we observe a sharp increase in salinity favoured by the cyclonic circulation of NIG from 2019 onwards. We interpret this as a possible regime shift that is not captured by the time series analysis and whose possible consequences for Ionian–Adriatic system ventilation and for marine organisms should be carefully monitored in the near future.

Published by Copernicus Publications.

Table 1. Products used in the present work. Prod. ref. nos. 4 and 5 are a forcing for prod. ref. nos. 1 and 2, and prod. ref. no. 8 is a forcing for prod. ref. nos. 4 and 5.

Prod. ref. no.	Product ID and type	Data access	Documentation
1	MEDSEA_MULTIYEAR_BGC_006_008 (multi-year product), numerical models	EU Copernicus Marine Service Product (2022a)	Quality Information Document (QUID): Teruzzi et al. (2022); Product User Manual (PUM): Lecci et al. (2022a)
2	MEDSEA_MULTIYEAR_BGC_006_008 (INTERIM product), numerical models	EU Copernicus Marine Service Product (2022b)	QUID: Teruzzi et al. (2022); PUM: Lecci et al. (2022a)
3	INSITU_MED_PHYBGCWAV_DISCRETE _MYNRT_013_035, in situ observations	EU Copernicus Marine Service Product (2022c)	QUID: Wehde et al. (2022); PUM: Pouliquen et al. (2022)
4	MEDSEA_MULTIYEAR_PHY_006_004 (multi-year product), numerical models	EU Copernicus Marine Service Product (2022d)	QUID: Escudier et al. (2022); PUM: Lecci et al. (2022b)
5	MEDSEA_MULTIYEAR_PHY_006_004 (INTERIM product), numerical models	EU Copernicus Marine Service Product (2022e)	QUID: Escudier et al. (2022); PUM: Lecci et al. (2022b)
6	SEALEVEL_EUR_PHY_L4_MY_008_068, satellite observations	EU Copernicus Marine Service Product (2023b)	QUID: Pujol et al. (2023); PUM: Pujol (2022)
7	SEALEVEL_EUR_PHY_L4_NRT _OBSERVATIONS_008_060, satellite observations	EU Copernicus Marine Service Product (2023a)	QUID: Pujol et al. (2023) PUM: Pujol (2022)
8	ERA5 hourly data on single levels from 1940 to present, global climate and weather reanalysis	https://doi.org/10.24381/cds.adbb2d47, EU Copernicus Climate Change Service Product (2023)	Hersbach et al. (2023)

1 Introduction

Dissolved oxygen (DO) is a key indicator for monitoring the marine ecosystem functioning because it is the result of several atmospheric, hydrodynamic, and biogeochemical driving processes (such as air–sea fluxes, vertical convection and mixing, horizontal transport, and biological production and consumption; Keeling and Garcia, 2002; Oschlies et al., 2018; Pitcher et al., 2021). Indeed, DO is currently being studied under the global warming scenarios by climate and marine-ecological scientific communities (e.g. IPCC, 2019; Kwiatkowski et al., 2020; Garcia-Soto et al., 2021), as oxygen depletion has been observed in the global ocean as well as at the local scale (Breitburg et al., 2018). Climate models predict a reduction in global-ocean dissolved oxygen content (Matear et al., 2000; Oschlies et al., 2008; Stramma et al., 2010; Reale et al., 2022), so this parameter is of primary interest, especially in those areas where oceanic processes connect surface and deep layers.

The southern Adriatic Sea (SAdr; Fig. 1a) is one of these areas, as it is an area of deep-water formation (Gačić et al., 2002; Pirro et al., 2022) and represents one of the deep engines of the eastern Mediterranean thermohaline circulation (Malanotte-Rizzoli et al., 1999), which is crucial for the eastern basin ventilation. The Adriatic Sea (Fig. 1a) is an elongated, semi-enclosed, and roughly north–south-oriented basin characterized by a shallow northern shelf (shallower than 80 m) and a deep pit in its southern part (maximum depth of approximately 1200 m) which is connected to the Ionian Sea (central Mediterranean Basin) through the Otranto Strait (with a maximum depth of 800 m). The Adriatic Sea is characterized by a cyclonic circulation governed by several drivers: river runoff, wind stress, surface buoyancy fluxes, and mass exchanges through the Otranto Strait (Cushman-Roisin et al., 2013).

The SAdr is strongly influenced by the inflow of water masses from the northern Adriatic Sea (i.e. North Adriatic Dense Water; Querin et al., 2016) and the Ionian Sea. In particular, the inflow of southern water masses is triggered by the periodic reversal of North Ionian Gyre circulation (Gačić et al., 2002; Civitarese et al., 2010; Menna et al., 2019; Gačić et al., 2021). This oscillating system, called the Adriatic–Ionian Bimodal Oscillating System (BiOS), changes the circulation of the North Ionian Gyre from cyclonic to anticyclonic and vice versa, modulating the advection of water masses in the Adriatic Sea (Gačić et al., 2010; Rubino et al., 2020). The cyclonic circulation of the North Ionian Gyre causes the advection of saline water masses of Levantine origin (i.e. Levantine Intermediate Water, LIW; Cretan Intermediate Water; Ionian Surface Water; and Levantine Surface

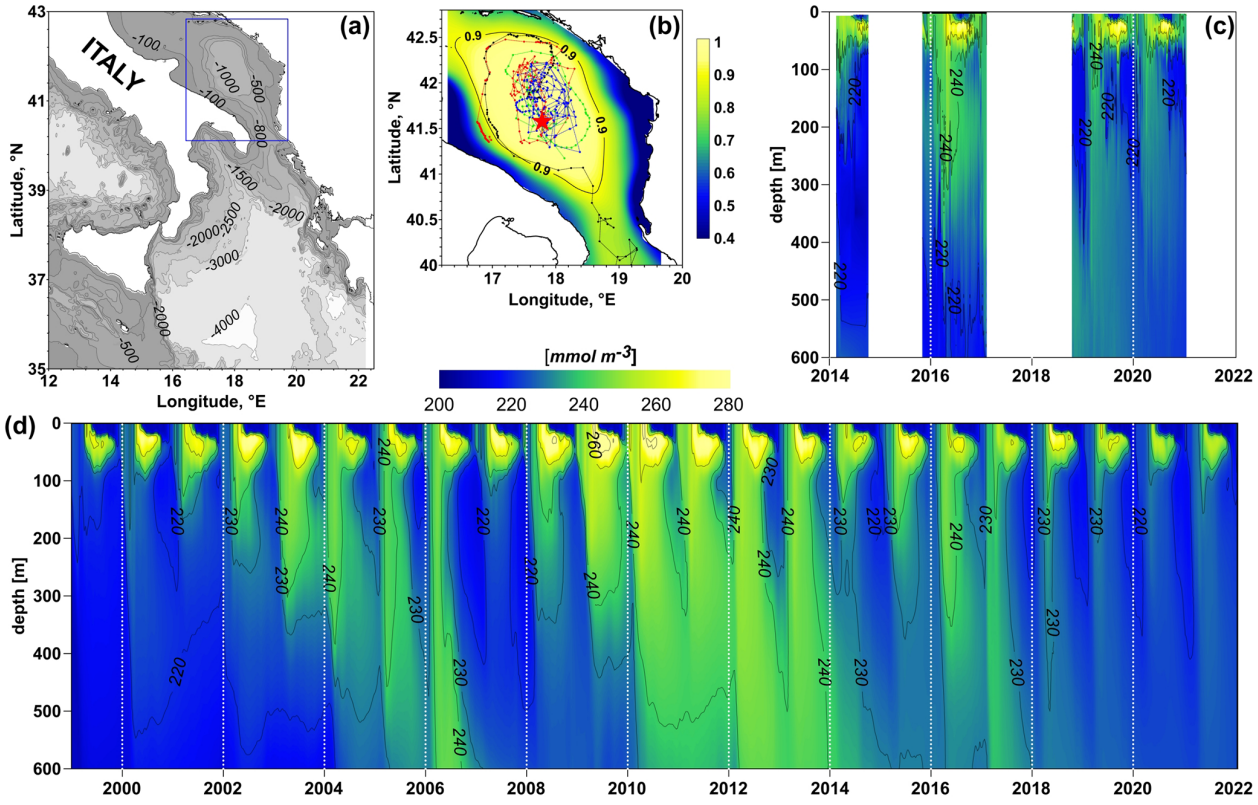

Figure 1. **(a)** Southern Adriatic area (blue square) within the Mediterranean Sea. **(b)** Cross-correlation map of surface oxygen, nitrate, and chlorophyll concentration provided by Copernicus biogeochemical reanalysis (prod. ref. nos. 1 and 2, Table 1) in the southern Adriatic area with respect to the central point of the pit indicated by the red star; the black contour line delimits the area with cross-correlation equal to or higher than 0.9; dashed lines indicate the trajectories of BGC-Argo floats (in situ TAC data, prod. ref. no. 3) passing the area. **(c)** Hovmöller diagrams of the dissolved oxygen concentration from in situ TAC data (prod. ref. no. 3) within the 0.9 cross-correlation area **(b)**. Data have been interpolated for readability of the plot. **(d)** Hovmöller diagrams of dissolved oxygen concentration from Copernicus biogeochemical reanalysis (prod. ref. nos. 1 and 2), spatially averaged within the area of cross-correlation equal to 0.9 **(a)** in the time period of 1999–2021, after the bias correction procedure based on in situ TAC data (prod. ref. no. 3).

Water; Manca et al., 2006), while the anticyclonic circulation favours the inflow of Atlantic Water and a relative decrease in salinity in the SAdr (Gačić et al., 2011; Menna et al., 2022a). This feature has a strong influence on the biogeochemical properties of the SAdr, affecting nutrient availability (Civitarese et al., 2010), phytoplankton blooms (Gačić et al., 2002; Civitarese et al., 2010), and species composition (Batistić et al., 2014; Mauri et al., 2021).

While hydrodynamic and biogeochemical properties of the SAdr have been widely described in several studies (e.g. Civitarese et al., 2010; Cushman-Roisin et al., 2013; Lipizer et al., 2014; Kokkini et al., 2018, 2020; Mavropoulou et al., 2020; Mihanović et al., 2021; Menna et al., 2022b), to the best of our knowledge DO dynamics in the area in connection with relevant driving processes over decadal timescales have not been addressed yet.

Investigating the DO multidecadal variability is crucial for quantifying the state of the marine environment (Marine Strategy Framework Directive, MSFD: EU-COM, 2008; Oesterwind et al., 2016) and for understanding anthropogenic impacts on the marine environment (IPCC, 2022). The emerging ecosystem-based management method proposed by the MSFD (2008/56/EC) promotes the use of different observational platforms, allowing information on the space-time distribution of important parameters related to water quality to be synoptically collected (Martellucci et al., 2021).

In this context, the present work integrates the state-of-the-art approach of in situ measurements (in 2014–2020, distributed by Copernicus In Situ Thematic Centre, INS TAC) with the Copernicus biogeochemical reanalysis in the Mediterranean Sea at high resolution (Cossarini et al., 2021) with the aim of characterizing the DO dynamics in the SAdr in the time period of 1999–2021. In particular, we aim to assess DO interannual variability in an area (SAdr) sensitive to multiple drivers (e.g. atmospheric forcing, Mediterranean circulation, and biological processes) and to evaluate the relative importance of the different drivers in this area.

2 Data and methods

In the present study the DO concentration in the SAdr area (Fig. 1a) was assessed by combining data from the Copernicus biogeochemical reanalysis in the Mediterranean Sea (product reference numbers – prod. ref. nos. – 1 and 2 in Table 1; Cossarini et al., 2021) in 1999–2021 and the Copernicus in situ dataset (prod. ref. no. 3), available for the period 2014-2020 (Figs. 1b-c). The temporal evolution of the combined model–in situ DO concentration profile in the time period of 1999–2021 is shown in Fig. 1d.

In particular, we used the Biogeochemical Argo (BGC-Argo) float measurements of in situ DO to compute a bias correction of the daily DO concentrations simulated by the biogeochemical reanalysis at $1/24°$ horizontal resolution. In fact, the biogeochemical reanalysis does not include BGC-Argo float DO assimilation and displays an average RMSD (root mean square difference) of $15\,\mathrm{mmol\,m^{-3}}$ for DO in the 0–600 m depth layer with respect to the observations in the area (Cossarini et al., 2021; Teruzzi et al., 2022). Quantile mapping, a technique largely used for climate simulations (e.g. Hopson and Webster, 2010; Jakob Themeßl et al., 2011; Gudmundsson et al., 2012), was adopted to perform the reanalysis bias correction. The quantile mapping technique adjusts the cumulative distribution of the data simulated for the past or future period by applying a transformation between the quantiles of the simulated and observed data in the present. In our application, we adapted the code publicly provided by Beyer et al. (2020) at https://doi.org/10.17605/OSF.IO/8AXW9 (Beyer, 2023) and included available in situ data of daily DO (Fig. 1c) within a representative area (Fig. 1b) of the southern Adriatic in the period 2014–2020 and DO reanalysis data for the same days of measurements. The representative area was identified by applying a spatial cross-correlation analysis (Martellucci et al., 2021) to the biogeochemical reanalysis centred on the SAdr pit and selecting the correlation threshold of 0.9 (Fig. 1b). Specifically, we considered the cross-correlation between the surface data of DO, nitrate, and chlorophyll concentrations in the central point of the pit and those at each spatial grid point in the domain to identify the area that displayed the same dynamics at the surface from a phenomenological perspective. Further details of the quantile mapping bias correction are included in Appendix A.

We then applied the empirical orthogonal function (EOF) analysis (e.g. Thomson and Emery, 2014) to the vertical profiles in Fig. 1d to describe DO variability in the SAdr area in the period 1999–2021. The EOF analysis allows us to identify the spatial patterns of variability (i.e. EOF vertical patterns), describe how they change in time by means of time series (i.e. EOF time series), and associate the explained variance with each mode.

Finally, we performed a Pearson correlation analysis between the EOF time series in 1999–2021 and the following series of forcing indexes (reported in Fig. 2), providing evidence of the mechanisms driving oxygen concentration and dynamics in the area:

- heat fluxes in the SAdr as a proxy for thermal and mixing and stratification cycles (from prod. ref. no. 8 in Table 1; Fig. 2a);
- mixed-layer depth in the SAdr as a proxy for both local vertical mixing and water residence times in the pit (prod. ref. nos. 4 and 5; Escudier et al., 2021; Fig. 2b);
- chlorophyll concentration at the surface and in the subsurface in the SAdr as a proxy for biological production in spring and late spring–summer, respectively (prod. ref. nos. 1 and 2; Fig. 2c–d);
- heat fluxes in the northern Adriatic Sea (NAdr), as a proxy for oxygen-rich dense-water formation in the NAdr and its transport into the pit (prod. ref. no. 8; Fig. 2e);
- North Ionian Gyre (NIG) vorticity derived from satellite altimetry, as a proxy for the inflow of Levantine waters and Atlantic Water (AW) (prod. ref. nos. 6 and 7; Fig. 2f).

In particular, the temporal phases of the NIG are defined as cyclonic and anticyclonic, respectively, when the vorticity field is positive and negative, as highlighted by the deseasonalized time series in Fig. 2f.

Mixed-layer depth (computed in prod. ref. nos. 4 and 5 considering the $0.03\,\mathrm{kg\,m^{-3}}$ density difference with respect to the near-surface value at 10 m depth) and the chlorophyll at the surface and in the subsurface (30–80 m, where the deep chlorophyll maximum is located) were spatially averaged in the SAdr area (41.6–42.1° N, 17.6–18.1° E; to consider the whole volume of the pit); heat fluxes were calculated in both the SAdr area and in the NAdr area (44.5–45.5° N, 13–13.5° E), while current vorticity was computed in the northern Ionian Sea (37–39° N, 17–19.5° E).

In the correlation analysis, the time series of the heat fluxes in the NAdr (Fig. 2e) has been temporally lagged by 2 months as an estimated mean time for the entrance in the SAdr pit of waters originating in the northern Adriatic area (Vilibić and Mihanović, 2013; Querin et al., 2016; Mihanović et al., 2021). Moreover, we tested the significance of the correlation coefficients between EOF and driver time series using a parametric t test (with a reference significance level of 0.05).

3 Results

3.1 Temporal scales of variability in connection with drivers

Dissolved oxygen in the southern Adriatic area (Fig. 1a) shows in the subsurface layers an alternation between periods of enrichment (in 2004–2006, 2010–2013, 2016–2017)

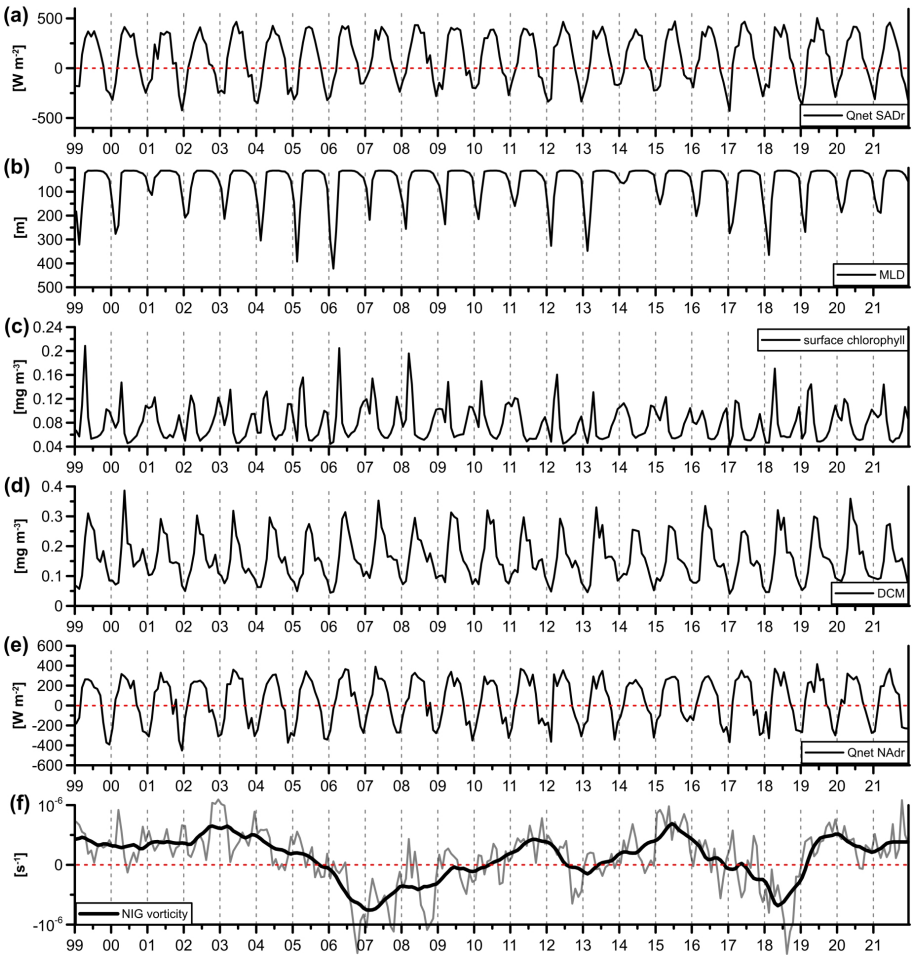

Figure 2. Time series of the main forcing in the time period of 1999–2021: **(a)** net heat fluxes in SAdr (prod. ref. no. 8 in Table 1), **(b)** mixed-layer depth (prod. ref. nos. 4 and 5), **(c)** surface chlorophyll concentration (prod. ref. nos. 1 and 2), **(d)** subsurface chlorophyll concentration (30–80 m layer in which deep chlorophyll maximum, DCM, is located; prod. ref. nos. 1 and 2), **(e)** net heat fluxes in the NAdr (prod. ref. no. 8), and **(f)** NIG current vorticity (grey line) and de-seasonalized time series as obtained by applying a low-pass filter of 13 months (thick black line) (prod. ref. nos. 6 and 7).

and sharp declines that impacted the oxygen minimum layer (OML), located between 100 and 300 m. Low concentration values are also observed in the years between 1999 and 2003.

The EOF analysis was performed on the vertical profiles of the oxygen anomaly, derived by removing the mean profile in the period 1999–2021 and then normalized dividing by their standard deviation.

The time series of the first four EOF modes, which explain up to 95 % of the oxygen variability in the water column, are shown along with the corresponding vertical patterns in Fig. 3a, c, e, g and Fig. 3b, d, f, h, respectively.

The EOFs are interpreted considering the correlation of the EOF time series (Fig. 3a, c, e, g) with the time series of the forcing indicators shown in Fig. 2 (see Table 2), with heat fluxes in the northern Adriatic Sea time-lagged by 2 months as the estimated time of entry of the NAdr dense water in the SAdr pit.

The first mode (Fig. 3a–b), accounting for 48.9 % of the explained variance, can be associated with the seasonal cycle of oxygen concentration in the upper layers: its vertical pattern mainly affects the first levels (Fig. 3b), the corresponding time series shows relative maximum values in spring (Fig. 3a), and it shows a statistically significant but moderate correlation ($r = 0.56$) with heat flux and a lower correlation with the subsurface chlorophyll concentration ($r = 0.43$) in the SAdr area (first column in Table 2).

The second and third modes (Fig. 3c–d and Fig. 3e–f, respectively), describing 19.7 % and 17.7 % of the variance, respectively, affected both the upper and deeper layers. Both modes display relative maximum values in summer, but they have different correlation coefficients with the explanatory factors. The time series of the second mode (second column in Table 2) shows a significant but low correlation with multiple drivers, exceeding 0.4 only for surface chloro-

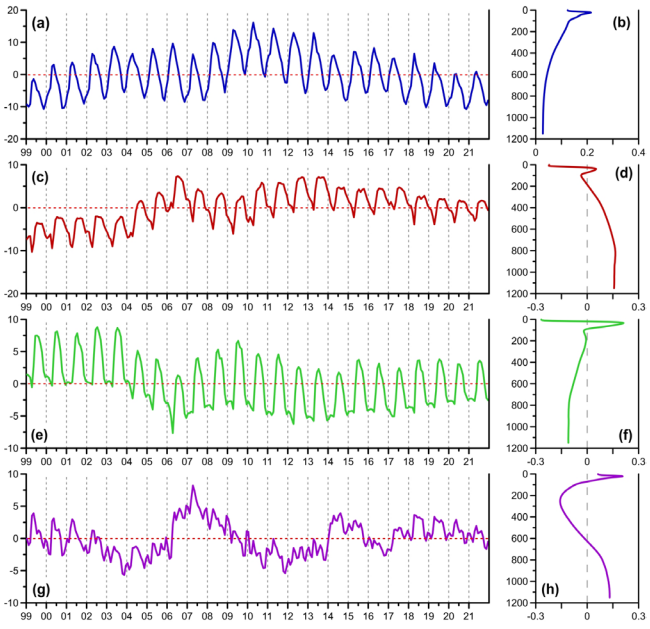

Figure 3. EOF time series **(a, c, e, g)** and vertical patterns **(b, d, f, h)** of the first four modes computed on the bias-corrected dissolved oxygen concentration in the southern Adriatic area shown in Fig. 1d. The explained variances of the four modes are 48.9 %, 19.7 %, 17.7 %, and 8.4 %.

Table 2. Correlations between the first four temporal modes of EOFs of DO (Fig. 3a, c, e, g) and the forcing fields (with heat fluxes in the northern Adriatic Sea time-lagged by 2 months; Fig. 2). Non-statistically significant correlations are identified by a significance level higher than 0.05 and indicated by "n.s." in the table.

	Mode 1	Mode 2	Mode 3	Mode 4
Heat flux (SAdr)	0.56	0.15	0.51	0.32
Mixed-layer depth (SAdr)	n.s.	−0.28	−0.41	−0.25
Surface chlorophyll (SAdr)	n.s.	−0.41	−0.61	n.s.
Subsurface chlorophyll (SAdr)	0.43	0.13	0.48	0.34
Heat flux (NAdr, 2-month lag)	n.s.	0.48	0.68	0.16
NIG vorticity (North Ionian)	n.s.	−0.40	n.s.	−0.37

phyll ($r = -0.41$) and waters from the NAdr area ($r = 0.48$). The time series of the third mode (third column, same table) is moderately correlated with both surface chlorophyll ($r = -0.61$) and NAdr waters ($r = 0.68$ correlation), but also with heat fluxes in the area ($r = 0.51$) and, to a lower extent, with mixed-layer depth ($r = -0.41$) and subsurface chlorophyll ($r = 0.48$).

The fourth mode (Fig. 3g–h), which describes 8 % of the variance, can be ascribed mainly to the vorticity of the NIG ($r = -0.37$, last column in Table 2), which affects the oxygen concentration in the intermediate layer (100–500 m depth), filled by LIW, and acts in the opposite direction in the upper and deeper layers (Fig. 3h).

Analysing the four modes in order of decreasing explained variance, we ascribe the seasonal variability connected with solubility mainly to the first mode, whereas we associate the biological contribution to oxygen dynamics to multiple interacting modes. In fact, the first mode explains the onset of the subsurface oxygen maximum (SOM) in spring, while the summer dynamics of the SOM are partially related to the third mode. The second mode, whose time series is correlated with surface chlorophyll evolution among other factors, can explain that part of the oxygen variability that is related to winter surface productivity.

The SOM, evident in summer oxygen profiles in Fig. 1c–d at about 40 m depth, is a feature that has already been observed in a great part of oligotrophic oceans (Riser and Johnson, 2008; Yasunaka et al., 2022) and of the Mediterranean Sea (e.g. Kress and Herut, 2001; Copin-Montégut and Bégovic, 2002; Manca et al., 2004; Cossarini et al., 2021; Di Biagio et al., 2022), and it represents an emerging property resulting from multiple interacting ecosystem processes (i.e. air–sea interactions, transport, mixing, and biological production and consumption) and is, indeed, captured by multiple modes.

The third mode, which also describes the high concentration values in the deep layers in the period 2005–2006 and 2012–2014, is also moderately associated with a multiannual signal of the inflow of deep, denser, and oxygenated water from the northern Adriatic Sea ($r = 0.68$, third column in Table 2; Querin et al., 2016). Finally, it is worth noting that an EOF analysis of detrended DO time series (not shown) yields fairly similar results but with the third mode only weakly correlated with the forcing indexes ($r < 0.4$). Indeed, we can conclude that the third mode captures a signal of long-term evolution of oxygen concentration associated with changes in heat fluxes and chlorophyll concentration.

3.2 The 2021 anomaly

The year 2021 shows an overall negative anomaly in the oxygen concentration profile (Fig. 4b) compared to the 1999–2020 climatological profiles (Fig. 4a). In particular, the anomaly affects a layer that thinned during the year, moving from 0–600 m depth in winter–early spring to 30–400 m in late spring–summer and 0–80 m in autumn. The (absolute) maximum values correspond to 25–30 mmol m^{-3} at the surface in spring and at the SOM depth in summer.

We verified that, among the EOF modes, the negative anomaly of the first mode is the main contributor to the 2021 negative oxygen anomaly (not shown). The time series of the first mode (Fig. 3a) is actually negative from 2019 and cor-

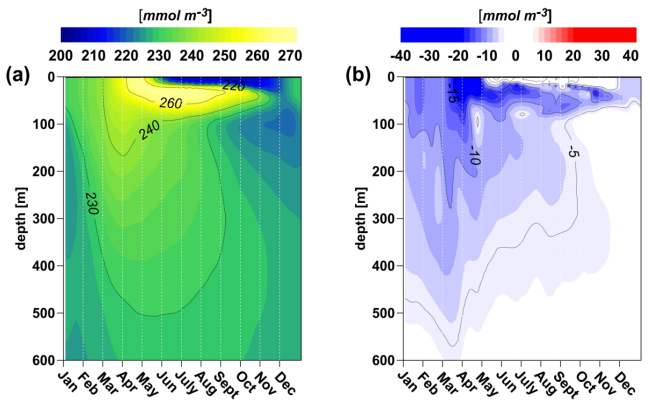

Figure 4. Hovmöller diagrams of 1999–2020 mean of daily oxygen concentration computed from Copernicus biogeochemical reanalysis (prod. ref. nos. 1 and 2, Table 1) after the bias correction procedure based on in situ TAC data (prod. ref. no. 3) **(a)** and anomaly in 2021 with respect to the period of 1999–2020 **(b)**.

responds to the negative anomaly of only one of its drivers (Table 2), i.e. subsurface chlorophyll (Fig. 2d), and not heat fluxes (Fig. 2a). In particular, we estimated a mean negative anomaly approximately equal to 6 % with respect to the climatological mean (1999–2020) for subsurface chlorophyll in 2021.

One of the causes of the decrease in total oxygen concentration in the SAdr could be due to the exceptional salinization observed in the SAdr since 2017 (Mihanović et al., 2021; Menna et al., 2022b). This increase was related to the inflow of new, warmer, and noticeably saltier water masses from the north-eastern Ionian Sea (Mihanović et al., 2021; Menna et al., 2022b). The inflow of saltier and warmer water masses is also evident by observing the temporal evolution of these parameters through the Strait of Otranto (Fig. B1). In particular, in the upper layer (0–150 m) both temperature and salinity show an overall positive trend throughout the period 1999–2021, whereas the decrease observed in 2006–2011 and 2017–2018 can be associated with the inflow of less saline AW, triggered by the anticyclonic circulation of the NIG (Fig. 2f). In the intermediate layer (150–600 m), salinity shows a positive trend in 1999–2021, while no clear trend is observed for temperature. Moreover, a sharp increase in salinity (~ 0.1) is observed in 2019. This increase occurred after the NIG inversion from anticyclonic to cyclonic (Fig. 2f), resulting in a further increase in salinity due to both the decrease in AW advection and the increase in LIW inflow.

4 Conclusions

Merging the Copernicus biogeochemical reanalysis in the Mediterranean Sea with in situ TAC data of biogeochemical Argo floats allowed us to characterize the interannual variability in dissolved oxygen in the southern Adriatic Sea in the time period of 1999–2021 and the 2021 anomaly with respect to the mean over 1999–2020. This study enriches our knowledge of the dissolved oxygen state and long-term dynamics in the area by proposing a seamless time and space perspective that is complementary to previous climatologies and data aggregation information (e.g. Lipizer et al., 2014) and adding an explanatory framework for the driving mechanisms in the marine environment.

The EOF statistical analysis that we conducted on the vertical oxygen profiles yielded two key results. First, in contrast with a climatological view, the analysis was able to capture most of the interannual oxygen variability associated with variability in the main drivers (i.e. heat fluxes affecting solubility, biological productivity, vertical mixing). We do not detect a clear deoxygenation trend in the subsurface layer, while the multiannual variability is characterized by an alternation of enrichment and reduction phases, whose dominant correlations with the drivers for each EOF time series are in the (absolute) range of 0.40–0.70. The possibility of observing such cyclic signals is enhanced by the relatively small volume and short residence time of the SAdr pit waters (Querin et al., 2016) with respect to other Mediterranean areas (Coppola et al., 2018). This feature makes the SAdr a potential efficient probe to detect a rapid response to changes in its meteo-marine drivers, i.e. circulation and atmospheric patterns.

Indeed, as our second result, the variability that is not explained by the EOF decomposition appears to be connected with a possible regime shift, associated with the entrance of new water masses that are warmer, markedly saltier, and less oxygenated which were not previously observed in the analysed time period.

The exceptional increase in salinity occurring after 2019 has already been documented (Mihanović et al., 2021; Menna et al., 2022b) and also observed north of the SAdr pit. Further monitoring of such anomalously high salinity values and assessment of their potential impact on the marine food web are of great importance, as picoplankton groups are sensitive to this environmental variable (Mella-Flores et al., 2011), and changes in biomass and production due to salinity have already been observed in previous studies in the Adriatic Sea (Beg Paklar et al., 2020; Mauri et al., 2021). Moreover, if such a strong negative oxygen anomaly as that observed in 2021 were to persist, it could have direct impacts on local marine organisms, as well as on the cycling of dissolved chemical elements (Conley et al., 2009), potentially altering the energy flux towards the higher trophic levels (Ekau et al., 2010). The importance of the relationship between dissolved oxygen and the catch distribution of some marine species has already been proved in the Adriatic Sea (Chiarini et al., 2022).

By integrating model and in situ data, our study demonstrates the importance of following up the oxygen content in a seamless spatial and temporal way, as it is a fundamental indicator of good environmental status (GES; Oesterwind et

al., 2016) and a factor that significantly affects fishing activities and the economy.

Appendix A: Quantile mapping bias correction of DO concentration profiles

Figures A1 and A2 show the modelled DO concentration profiles and histogram distributions before and after the quantile mapping bias correction, respectively, conducted by using the BGC-Argo float measurements available in 2014–2020 (Fig. 1c). The quantile mapping, better than other methods (i.e. additive delta change, multiplicative delta change, and variance scaling; results not shown), acted on the profiles by modifying the values of the concentrations (as indicated by the different colour bars in Fig. A1a and A1b) but, at the same time, maintaining the main dynamics observed before the correction: mixing and stratification at the surface during the year, subsurface oxygen maximum onset in spring and development in summer, and interannual variability related to the mixed-layer-depth dynamics in the intermediate layers. The distributions of the values of the model output before and after the quantile mapping bias correction and the values from BGC-Argo floats are displayed in Fig. A2. The correction actually changed the modelled values (Fig. A2a) to reproduce the shape of the distribution of the observations (Fig. A2c). In particular, after the correction (Fig. A2b) the modelled data show higher variability and a more skewed distribution toward the higher values, similarly to the observations.

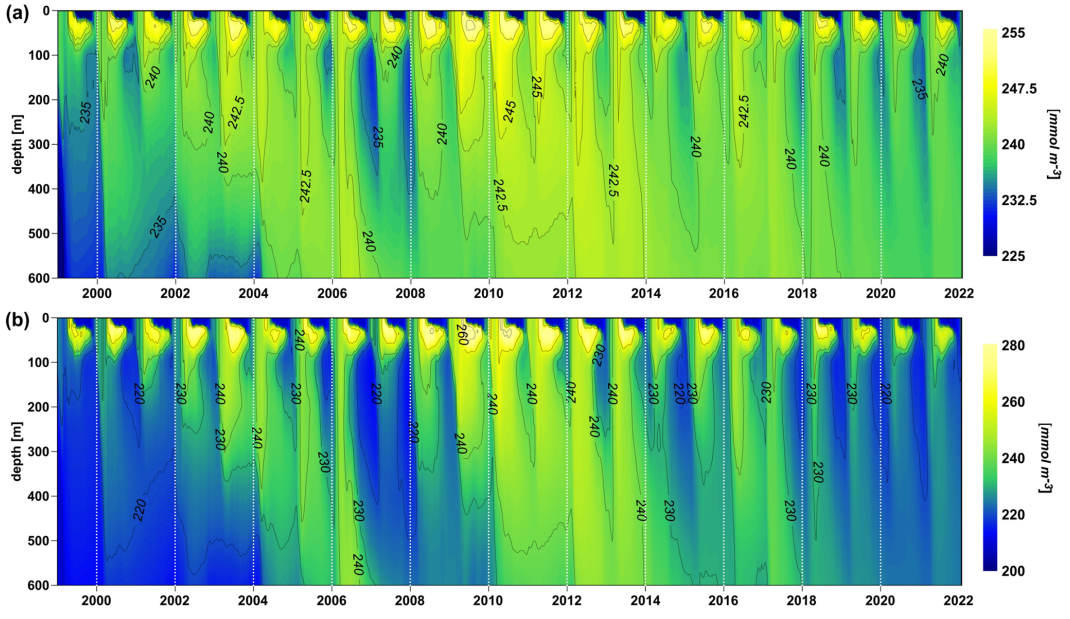

Figure A1. Hovmöller diagram of the modelled oxygen concentrations spatially averaged within the area of autocorrelation equal to 0.9, indicated in Fig. 1b, before the bias correction by quantile mapping **(a)** and after the procedure **(b)**.

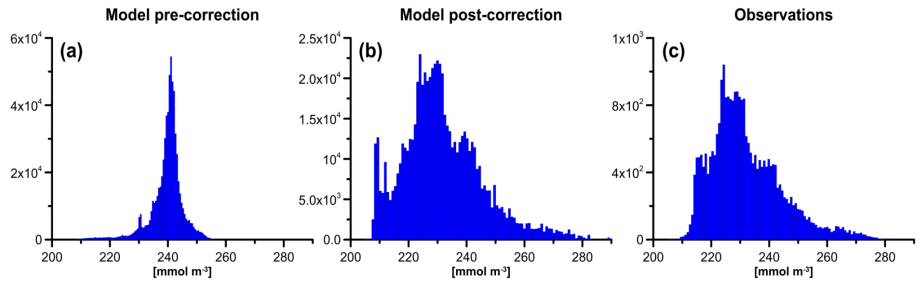

Figure A2. Frequency histogram of modelled oxygen concentrations before the bias correction by quantile mapping **(a)** and after the procedure **(b)**, compared with BGC-Argo observations **(c)**.

Appendix B: Time series of surface and intermediate temperature and salinity at the Otranto Strait

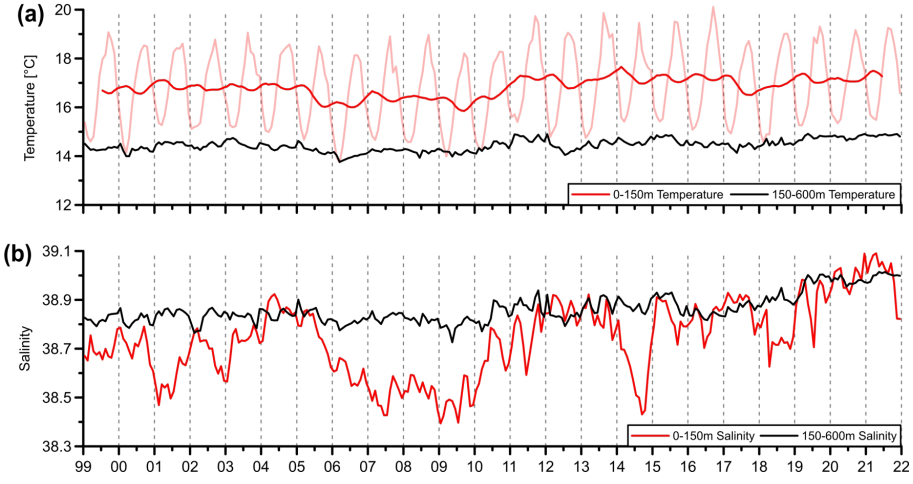

Figure B1. Time series of temperature **(a)** and salinity **(b)**, averaged in the vertical layers 0–150 m (red lines) and 150–600 m (black lines) of the Otranto Strait (39.8° N, 18.5–19.5° E) in the time period of 1999–2021. In panel **(a)**, light red and dark red indicate data before and after de-seasonalization, respectively. Data are provided by Copernicus physical reanalysis (prod. ref. nos. 4 and 5, Table 1).

Data availability. Publicly available datasets were analysed in this study. Modelling and in situ data can be found at the Copernicus Marine Service, with references and DOIs indicated in Table 1 of the paper.

Author contributions. VDB and GC conceived the idea. VDB, RM, and MM conducted the analysis. VDB, RM, and GC wrote the first draft, with contributions from the other co-authors. All the authors discussed and reviewed the submitted manuscript.

Competing interests. The contact author has declared that none of the authors has any competing interests.

Disclaimer. Publisher's note: Copernicus Publications remains neutral with regard to jurisdictional claims in published maps and institutional affiliations.

Acknowledgements. This study has been conducted using EU Copernicus Marine Service Information.

Financial support. This study has been partly funded by the Copernicus Mediterranean – Monitoring Forecasting Centre (contract LOT reference: 21002L5-COP-MFC MED-5500, issued by Mercator Ocean) within the framework of the Marine Copernicus Service.

Review statement. This paper was edited by Marilaure Grégoire and reviewed by three anonymous referees.

References

Batistić, M., Garić, R., and Molinero, J. C.: Interannual variations in Adriatic Sea zooplankton mirror shifts in circulation regimes in the Ionian Sea, Clim. Res., 61, 231–240, https://doi.org/10.3354/cr01248, 2014.

Beg Paklar, G., Vilibić, I., Grbec, B., Matić, F., Mihanović, H., Džoić, T., Šantić, D., Šestanović, S., Šolić, M., Ivatek-Šahdan, S., and Kušpilić, G.: Record-breaking salinities in the middle Adriatic during summer 2017 and concurrent changes in the microbial food web, Prog. Oceanogr., 185, 102345, https://doi.org/10.1016/j.pocean.2020.102345, 2020.

Beyer, R.: BiasCorrection (ClimPast), OSF [code], https://doi.org/10.17605/OSF.IO/8AXW9, 2023.

Beyer, R., Krapp, M., and Manica, A.: An empirical evaluation of bias correction methods for palaeoclimate simulations, Clim. Past, 16, 1493–1508, https://doi.org/10.5194/cp-16-1493-2020, 2020.

Breitburg, D., Levin, L. A., Oschlies, A., Grégoire, M., Chavez, F. P., Conley, D. J., Garçon, V., Gilbert, D., Gutiérrez, D., Isensee, K., Jacinto, G. S., Limburg, K. E., Montes, I., Naqvi, S. W. A., Pitcher, G. C., Rabalais, N. N., Roman, M. R., Rose, K. A., Seibel, B. A., Telszewski, M., Yasuhara, M., and Zhang, J.: Declining oxygen in the global ocean and coastal waters, Science, 359, eaam7240, https://doi.org/10.1126/science.aam7240 , 2018.

Chiarini, M., Guicciardi, S., Angelini, S., Tuck, I. D., Grilli, F., Penna, P., Domenichetti, F., Canduci, G., Belardinelli, A., Santojanni, A., Arneri, E., Milone, N., Medvešek, D., Isajlović, I., Vrgoč, N., and Martinelli, M.: Accounting for environmental and fishery management factors when standardizing CPUE data from a scientific survey: A case study for *Nephrops norvegicus* in the Pomo Pits area (Central Adriatic Sea), PloS ONE, 17, e0270703, https://doi.org/10.1371/journal.pone.0270703, 2022.

Civitarese, G., Gačić, M., Lipizer, M., and Eusebi Borzelli, G. L.: On the impact of the Bimodal Oscillating System (BiOS) on the biogeochemistry and biology of the Adriatic and Ionian Seas (Eastern Mediterranean), Biogeosciences, 7, 3987–3997, https://doi.org/10.5194/bg-7-3987-2010, 2010.

Conley, D. J., Björck, S., Bonsdorff, E., Carstensen, J., Destouni, G., Gustafsson, B. G., Hietanen, S., Kortekaas, M., Kuosa, H., Markus Meier, H. E., Müller-Karulis, B., Nordberg, K., Norkko, A., Nürnberg, G., Pitkänen, H., Rabalais, N. N., Rosenberg, R., Savchuk, O. P., Slomp, C. P., Voss, M., Wulff, F., and Zillén, L.: Hypoxia-related processes in the Baltic Sea, Environ. Sci. Technol., 43, 3412–3420, https://doi.org/10.1021/es802762a, 2009.

Copin-Montégut, C. and Bégovic, M.: Distributions of carbonate properties and oxygen along the water column (0–2000 m) in the central part of the NW Mediterranean Sea (dyfamed site): Influence of winter vertical mixing on air–sea CO_2 and O_2 exchanges, Deep-Sea Res. Pt. II, 49, 2049–2066, https://doi.org/10.1016/S0967-0645(02)00027-9, 2002.

Coppola, L., Legendre, L., Lefevre, D., Prieur, L., Taillandier, V., and Diamond Riquier, E.: Seasonal and inter-annual variations of dissolved oxygen in the northwestern Mediterranean Sea (DYFAMED site), Prog. Oceanogr., 162, 187–201, https://doi.org/10.1016/j.pocean.2018.03.001, 2018.

Cossarini, G., Feudale, L., Teruzzi, A., Bolzon, G., Coidessa, G., Solidoro, C., Di Biagio, V., Amadio, C., Lazzari, P., Brosich, A., and Salon, S.: High-resolution reanalysis of the Mediterranean Sea biogeochemistry (1999–2019), Frontiers in Marine Science, 8, 741486, https://doi.org/10.3389/fmars.2021.741486, 2021.

Cushman-Roisin, B., Gacic, M., Poulain, P. M., and Artegiani, A. (Eds.): Physical oceanography of the Adriatic Sea: past, present and future. Springer Science & Business Media, https://doi.org/10.1007/978-94-015-9819-4, 2013.

Di Biagio, V., Salon, S., Feudale, L., and Cossarini, G.: Subsurface oxygen maximum in oligotrophic marine ecosystems: mapping the interaction between physical and biogeochemical processes, Biogeosciences, 19, 5553–5574, https://doi.org/10.5194/bg-19-5553-2022, 2022.

Ekau, W., Auel, H., Pörtner, H.-O., and Gilbert, D.: Impacts of hypoxia on the structure and processes in pelagic communities (zooplankton, macro-invertebrates and fish), Biogeosciences, 7, 1669–1699, https://doi.org/10.5194/bg-7-1669-2010, 2010.

Escudier, R., Clementi, E., Cipollone, A., Pistoia, J., Drudi, M., Grandi, A., Lyubartsev, V., Lecci, R., Aydogdu, A., Delrosso, D., Omar, M., Masina, S., Coppini, G., and Pinardi, N.: A High Resolution Reanalysis for the Mediterranean Sea, Frontiers in Marine Science, 9, 702285, https://doi.org/10.3389/feart.2021.702285, 2021.

Escudier, R., Clementi, E., Nigam, T., Aydogdu, A., Fini, E., Pistoia, J., Grandi, A., and Miraglio, P.: EU Copernicus Marine Service Quality Information Document for the Mediterranean Sea Physics Reanalysis, MEDSEA_MULTIYEAR_PHY_006_004, Issue 2.3, Mercator Ocean International, https://catalogue.marine.copernicus.eu/documents/QUID/CMEMS-MED-QUID-006-004.pdf (last access: 6 March 2023), 2022.

EU-COM: Directive 2008/56/EC of the European Parliament and of the Council establishing a framework for community action in the field of marine environmental policy (Marine Strategy Framework Directive), Official J. Eur. Union, L164, 19–40, 2008.

EU Copernicus Climate Change Service Product: ERA5 hourly data on single levels from 1940 to present, Copernicus Climate Change Service (C3S) Climate Data Store (CDS) [data set], https://doi.org/10.24381/cds.adbb2d47, 2023.

EU Copernicus Marine Service Product: Mediterranean Sea Biogeochemical Reanalysis, Mercator Ocean International [data set], https://doi.org/10.25423/CMCC/MEDSEA_MULTIYEAR_BGC_006_008_MEDBFM3, 2022a.

EU Copernicus Marine Service Product: Mediterranean Sea Biogeochemical Reanalysis INTERIM, Mercator Ocean International [data set], https://doi.org/10.25423/CMCC/MEDSEA_MULTIYEAR_BGC_006_008_MEDBFM3I, 2022b.

EU Copernicus Marine Service Product: Mediterranean Sea- In-Situ Near Real Time Observations, Mercator Ocean International [data set], https://doi.org/10.48670/moi-00044, 2022c.

EU Copernicus Marine Service Product: Mediterranean Sea Physics reanalysis, Mercator Ocean International [data set], https://doi.org/10.25423/CMCC/MEDSEA_MULTIYEAR_PHY_006_004_E3R1, 2022d.

EU Copernicus Marine Service Product: Mediterranean Sea Physics reanalysis INTERIM, Mercator Ocean International [data set],

https://doi.org/10.25423/CMCC/MEDSEA_MULTIYEAR_PHY_006_004_E3R1I, 2022e.

EU Copernicus Marine Service Product: European Seas Gridded L 4 Sea Surface Heights And Derived Variables Nrt, Mercator Ocean International [data set], https://doi.org/10.48670/moi-00142, 2023a.

EU Copernicus Marine Service Product: European Seas Gridded L 4 Sea Surface Heights And Derived Variables Reprocessed 1993 Ongoing, Mercator Ocean International [data set], https://doi.org/10.48670/moi-00141, 2023b.

Gačić, M., Civitarese, G., Miserocchi, S., Cardin, V., Crise, A., and Mauri, E.: The open-ocean convection in the Southern Adriatic: a controlling mechanism of the spring phytoplankton bloom, Cont. Shelf Res., 22, 1897–1908, https://doi.org/10.1016/S0278-4343(02)00050-X, 2002.

Gačić, M., Borzelli, G. L. E., Civitarese, G., Cardin, V., and Yari, S.: Can internal processes sustain reversals of the ocean upper circulation? The Ionian Sea example, Geophys. Res. Lett., 37, L09608, https://doi.org/10.1029/2010GL043216, 2010.

Gačić, M., Civitarese, G., Eusebi Borzelli, G. L., Kovačević, V., Poulain, P.-M., Theocharis, A., Menna, M., Catucci, A., and Zarokanellos, N.: On the relationship between the decadal oscillations of the northern Ionian Sea and the salinity distributions in the eastern Mediterranean, J. Geophys. Res.-Oceans, 116, C12002, https://doi.org/10.1029/2011JC007280, 2011.

Gačić, M., Ursella, L., Kovačević, V., Menna, M., Malačič, V., Bensi, M., Negretti, M.-E., Cardin, V., Orlić, M., Sommeria, J., Viana Barreto, R., Viboud, S., Valran, T., Petelin, B., Siena, G., and Rubino, A.: Impact of dense-water flow over a sloping bottom on open-sea circulation: laboratory experiments and an Ionian Sea (Mediterranean) example, Ocean Sci., 17, 975–996, https://doi.org/10.5194/os-17-975-2021, 2021.

Garcia-Soto, C., Cheng, L., Caesar, L., Schmidtko, S., Jewett, E. B., Cheripka, A., Rigor, I., Caballero, A., Chiba, S., Báez, J. C., Zielinski, T., and Abraham, J. P.: An overview of ocean climate change indicators: Sea surface temperature, ocean heat content, ocean pH, dissolved oxygen concentration, arctic sea ice extent, thickness and volume, sea level and strength of the AMOC (Atlantic Meridional Overturning Circulation), Frontiers in Marine Science, 8, 642372, https://doi.org/10.3389/fmars.2021.642372, 2021.

Gudmundsson, L., Bremnes, J. B., Haugen, J. E., and Engen-Skaugen, T.: Technical Note: Downscaling RCM precipitation to the station scale using statistical transformations – a comparison of methods, Hydrol. Earth Syst. Sci., 16, 3383–3390, https://doi.org/10.5194/hess-16-3383-2012, 2012.

Hersbach, H., Bell, B., Berrisford, P., Biavati, G., Horányi, A., Muñoz Sabater, J., Nicolas, J., Peubey, C., Radu, R., Rozum, I., Schepers, D., Simmons, A., Soci, C., Dee, D., Thépaut, J.-N.: ERA5 hourly data on single levels from 1940 to present, Copernicus Climate Change Service (C3S) Climate Data Store (CDS) [data set], https://doi.org/10.24381/cds.adbb2d47, 2023.

Hopson, T. M. and Webster, P. J.: A 1–10-day ensemble forecasting scheme for the major river basins of Bangladesh: Forecasting severe floods of 2003–07, J. Hydrometeorol., 11, 618–641, https://doi.org/10.1175/2009JHM1006.1, 2010.

IPCC: IPCC Special Report on the Ocean and Cryosphere in a Changing Climate, edited by: Pörtner, H. O., Roberts, D. C., Masson-Delmotte, V., Zhai, P., Tignor, M., Poloczanska, E., Mintenbeck, K., Alegría, A., Nicolai, M., Okem, A., Petzold, J., Rama, B., and Weyer, N. M., Cambridge University Press, Cambridge, UK and New York, NY, USA, 755 pp., https://doi.org/10.1017/9781009157964, 2019.

IPCC: Climate Change 2022: Impacts, Adaptation, and Vulnerability. Contribution of Working Group II to the Sixth Assessment Report of the Intergovernmental Panel on Climate Change, edited by: Pörtner, H. O., Roberts, D. C., Tignor, M., Poloczanska, E. S., Mintenbeck, K., Alegría, A., Craig, M., Langsdorf, S., Löschke, S., Möller, V., Okem, A., and Rama, B., Cambridge University Press, Cambridge University Press, Cambridge, UK and New York, NY, USA, 3056 pp., https://doi.org/10.1017/9781009325844, 2022.

Jakob Themeßl, M., Gobiet, A., and Leuprecht, A.: Empirical-statistical downscaling and error correction of daily precipitation from regional climate models, Int. J. Climatol., 31, 1530–1544, https://doi.org/10.1002/joc.2168, 2011.

Keeling, R. F. and Garcia, H. E.: The change in oceanic O_2 inventory associated with recent global warming, P. Natl. Acad. Sci. USA, 99, 7848–7853, https://doi.org/10.1073/pnas.122154899, 2002.

Kokkini, Z., Notarstefano, G., Poulain, P.-M., et al.: Unusual salinity pattern in the South Adriatic Sea, Copernicus Marine Service Ocean State Report 2018-09-08, J. Oper. Oceanogr., 11, S1–S142, https://doi.org/10.1080/1755876X.2018.1489208, 2018.

Kokkini, Z., Mauri, E., Gerin, R., Poulain, P.-M., Simoncelli, S., and Notarstefano, G.: On the salinity structure in the South Adriatic as derived from float and glider observations in 2013–2016, Deep-Sea Res. Pt. II, 171, 104625, https://doi.org/10.1016/j.dsr2.2019.07.013, 2020.

Kress, N. and Herut, B.: Spatial and seasonal evolution of dissolved oxygen and nutrients in the Southern Levantine Basin (Eastern Mediterranean Sea): chemical characterization of the water masses and inferences on the N:P ratios, Deep-Sea Res. Pt. I, 48, 2347–2372, https://doi.org/10.1016/S0967-0637(01)00022-X, 2001.

Kwiatkowski, L., Torres, O., Bopp, L., Aumont, O., Chamberlain, M., Christian, J. R., Dunne, J. P., Gehlen, M., Ilyina, T., John, J. G., Lenton, A., Li, H., Lovenduski, N. S., Orr, J. C., Palmieri, J., Santana-Falcón, Y., Schwinger, J., Séférian, R., Stock, C. A., Tagliabue, A., Takano, Y., Tjiputra, J., Toyama, K., Tsujino, H., Watanabe, M., Yamamoto, A., Yool, A., and Ziehn, T.: Twenty-first century ocean warming, acidification, deoxygenation, and upper-ocean nutrient and primary production decline from CMIP6 model projections, Biogeosciences, 17, 3439–3470, https://doi.org/10.5194/bg-17-3439-2020, 2020.

Lecci, R., Salon, S., Bolzon, G., and Cossarini, G.: EU Copernicus Marine Service Product User Manual for the Mediterranean Sea Biogeochemistry Reanalysis, MEDSEA_MULTIYEAR_BGC_006_008, Issue 3.2, Mercator Ocean International, https://catalogue.marine.copernicus.eu/documents/PUM/CMEMS-MED-PUM-006-008.pdf (last access: 6 March 2023), 2022a.

Lecci, R., Drudi, M., Grandi, A., Cretì, S., and Clementi, E.: EU Copernicus Marine Service Product User Manual for the Mediterranean Sea Physics Reanalysis, MEDSEA_MULTIYEAR_PHY_006_004, Issue 2.3, Mercator Ocean International, https://catalogue.marine.copernicus.eu/

documents/PUM/CMEMS-MED-PUM-006-004.pdf (last access: 6 March 2023), 2022b.

Lipizer, M., Partescano, E., Rabitti, A., Giorgetti, A., and Crise, A.: Qualified temperature, salinity and dissolved oxygen climatologies in a changing Adriatic Sea, Ocean Sci., 10, 771–797, https://doi.org/10.5194/os-10-771-2014, 2014.

Malanotte-Rizzoli, P., Manca, B. B., d'Alcala, M. R., Theocharis, A., Brenner, S., Budillon, G., and Ozsoy, E. The Eastern Mediterranean in the 80s and in the 90s: the big transition in the intermediate and deep circulations, Dynam. Atmos. Oceans, 29, 365–395, https://doi.org/10.1016/S0377-0265(99)00011-1, 1999.

Manca, B., Burca, M., Giorgetti, A., Coatanoan, C., Garcia, M. J., and Iona, A.: Physical and biochemical averaged vertical profiles in the Mediterranean regions: an important tool to trace the climatology of water masses and to validate incoming data from operational oceanography, J. Marine Syst., 48, 83–116, https://doi.org/10.1016/j.jmarsys.2003.11.025, 2004.

Manca, B., Ibello, V., Pacciaroni, M., Scarazzato, P., and Giorgetti, A.: Ventilation of deep waters in the Adriatic and Ionian Seas following changes in thermohaline circulation of the Eastern Mediterranean, Clim. Res., 31, 239–256, https://doi.org/10.3354/cr031239, 2006.

Martellucci, R., Salon, S., Cossarini, G., Piermattei, V., and Marcelli, M.: Coastal phytoplankton bloom dynamics in the Tyrrhenian Sea: Advantage of integrating in situ observations, large-scale analysis and forecast systems, J. Marine Syst., 218, 103528, https://doi.org/10.1016/j.jmarsys.2021.103528, 2021.

Matear, R. J., Hirst, A. C., and McNeil, B. I.: Changes in dissolved oxygen in the Southern Ocean with climate change, Geochem. Geophy. Geosy., 1, 1050, https://doi.org/10.1029/2000GC000086, 2000.

Mauri, E., Menna, M., Garić, R., Batistić, M., Libralato, S., Notarstefano, G., Martellucci, R., Gerin, R., Pirro, A., Hure, M., and Poulain, P.-M.: Recent changes of the salinity distribution and zooplankton community in the South Adriatic Pit, Copernicus Marine Service Ocean State Report, Issue 5, J. Oper. Oceanogr., 14, 1–185, https://doi.org/10.1080/1755876X.2021.1946240, 2021.

Mavropoulou, A. M., Vervatis, V., and Sofianos, S.: Dissolved oxygen variability in the Mediterranean Sea, J. Marine Syst., 208, 103348, https://doi.org/10.1016/j.jmarsys.2020.103348, 2020.

Mella-Flores, D., Mazard, S., Humily, F., Partensky, F., Mahé, F., Bariat, L., Courties, C., Marie, D., Ras, J., Mauriac, R., Jeanthon, C., Mahdi Bendif, E., Ostrowski, M., Scanlan, D. J., and Garczarek, L.: Is the distribution of *Prochlorococcus* and *Synechococcus* ecotypes in the Mediterranean Sea affected by global warming?, Biogeosciences, 8, 2785–2804, https://doi.org/10.5194/bg-8-2785-2011, 2011.

Menna, M., Reyes-Suarez, N. C., Civitarese, G., Gačić, M., Poulain, P.-M., and Rubino, A.: Decadal variations of circulation in the Central Mediterranean and its interactions with the mesoscale gyres, Deep-Sea Res. Pt. II, 164, 14–24, https://doi.org/10.1016/j.dsr2.2019.02.004, 2019.

Menna, M., Gačić, M., Martellucci, R., Notarstefano, G., Fedele, G., Mauri, E., Gerin, R., and Poulain, P.-M.: Climatic, decadal and interannual variability in the upper layer of the Mediterranean Sea using remotely sensed and in-situ data, Remote Sens., 14, 1322, https://doi.org/10.3390/rs14061322, 2022a.

Menna, M., Martellucci, R., Notarstefano, G., Mauri, E., Gerin, R., Pacciaroni, M., Bussani, A., Pirro, A., and Poulain, P.-M.: Record-breaking high salinity in the South Adriatic Pit in 2020, Copernicus Marine Service Ocean State Report 6, J. Oper. Oceanogr., 15, 1–220, https://doi.org/10.1080/1755876X.2022.2095169, 2022b.

Mihanović, H., Vilibić, I., Šepić, J., Matić, F., Ljubešić, Z., Mauri, E., Gerin, R., Notarstefano, G., and Poulain, P. M.: Observation, Preconditioning and Recurrence of Exceptionally High Salinities in the Adriatic Sea, Frontiers in Marine Science, 8, 672210, https://doi.org/10.3389/fmars.2021.672210, 2021.

Oesterwind, D., Rau, A., and Zaiko, A.: Drivers and pressures–untangling the terms commonly used in marine science and policy, J. Environ. Manage., 181, 8–15, https://doi.org/10.1016/j.jenvman.2016.05.058, 2016.

Oschlies, A., Schulz, K. G., Riebesell, U., and Schmittner, A.: Simulated 21st century's increase in oceanic suboxia by CO2-enhanced biotic carbon export, Global Biogeochem. Cy., 22, GB4008, https://doi.org/10.1029/2007GB003147, 2008.

Oschlies, A., Brandt, P., Stramma, L., and Schmidtko, S.: Drivers and mechanisms of ocean deoxygenation, Nat. Geosci., 11, 467–473, https://doi.org/10.1038/s41561-018-0152-2, 2018.

Pirro, A., Mauri, E., Gerin, R., Martellucci, R., Zuppelli, P., and Poulain, P. M.: New insights on the formation and breaking mechanism of convective cyclonic cones in the South Adriatic Pit during winter 2018. J. Phys. Oceanogr., 52, 2049–2068, https://doi.org/10.1175/JPO-D-21-0108.1, 2022.

Pitcher, G. C., Aguirre-Velarde, A., Breitburg, D., Cardich, J., Carstensen, J., Conley, D. J., Dewitte, B., Engel, A., Espinoza-Morriberón, D., Flores, G., Garçon, V., Graco, M., Grégoire, M., Gutiérrez, D., Hernandez-Ayon, J. M., Huang, H.-H. M., Isensee, K., Jacinto, M. E., Levin, L., Lorenzo, A., Machu, E., Merma, L., Montes, I., SWA, N., Paulmier, A., Roman, M., Rose, K., Hood, R., Rabalais, N. N., Salvanes, A. G. V., Salvatteci, R., Sánchez, S., Sifeddine, A., Tall, A., W., van der Plas, A. K., Yasuhara, M., Zhang, J., and Zhu, Z. Y.: System controls of coastal and open ocean oxygen depletion, Prog. Oceanogr., 197, 102613, https://doi.org/10.1016/j.pocean.2021.102613, 2021.

Pouliquen, S., Carval, T., Petit de la Villéon, L., Tarot, S., and In Situ TAC partners: EU Copernicus Marine Service Product User Manual for the Mediterranean Sea- In-Situ Near Real Time Observations, INSITU_MED_PHYBGCWAV_DISCRETE_MYNRT_013_035, Issue 1.14, Mercator Ocean International, https://catalogue.marine.copernicus.eu/documents/PUM/CMEMS-INS-PUM-013-030-036.pdf (last access: 6 March 2023), 2022.

Pujol, M.-I.: EU Copernicus Marine Service Product User Manual for the European Seas Gridded L4 Sea Surface Heights And Derived Variables Reprocessed 1993 Ongoing, SEALEVEL_EUR_PHY_L4_MY_008_068 and SEALEVEL_EUR_PHY_L4_NRT_OBSERVATIONS_008_060, Issue 7.0, Mercator Ocean International, https://catalogue.marine.copernicus.eu/documents/PUM/CMEMS-SL-PUM-008-032-068.pdf (last access: 6 March 2023), 2022.

Pujol, M.-I., Taburet, G., and SL-TAC team: EU Copernicus Marine Service Quality Information Document for the European Seas Gridded L4 Sea Surface

Heights And Derived Variables Reprocessed 1993 Ongoing, SEALEVEL_EUR_PHY_L4_MY_008_068 and SEALEVEL_EUR_PHY_L4_NRT_OBSERVATIONS_008_060, Issue 8.2, Mercator Ocean International, https://catalogue.marine.copernicus.eu/documents/QUID/CMEMS-SL-QUID-008-032-068.pdf (last access: 6 March 2023), 2023.

Querin, S., Bensi, M., Cardin, V., Solidoro, C., Bacer, S., Mariotti, L., Stel, F., and Malačič, V.: Saw-tooth modulation of the deep-water thermohaline properties in the southern Adriatic Sea, J. Geophys. Res.-Oceans, 121, 4585–4600, https://doi.org/10.1002/2015JC011522, 2016.

Reale, M., Cossarini, G., Lazzari, P., Lovato, T., Bolzon, G., Masina, S., Solidoro, C., and Salon, S.: Acidification, deoxygenation, and nutrient and biomass declines in a warming Mediterranean Sea, Biogeosciences, 19, 4035–4065, https://doi.org/10.5194/bg-19-4035-2022, 2022.

Riser, S. C. and Johnson, K. S.: Net production of oxygen in the subtropical ocean, Nature, 451, 323–325, https://doi.org/10.1038/nature06441, 2008.

Rubino, A., Gačić, M., Bensi, M., Kovačević, V., Malačič, V., Menna, M., Negretti, M. E., Sommeria, J., Zanchettin, D., Barreto, R. V., Ursella, L., Cardin, V., Civitarese, G., Orlić, M., Petelin, B., and Siena, G.: Experimental evidence of long-term oceanic circulation reversals without wind influence in the North Ionian Sea, Sci. Rep.-UK, 10, 1905, https://doi.org/10.1038/s41598-020-57862-6, 2020.

Teruzzi, A., Di Biagio, V., Feudale, L., Bolzon, G., Lazzari, P., Salon, S., Coidessa, G., and Cossarini, G.: EU Copernicus Marine Service Quality Information Document for the Mediterranean Sea Biogeochemistry Reanalysis, MEDSEA_MULTIYEAR_BGC_006_008, Issue 3.2, Mercator Ocean International,https://catalogue.marine.copernicus.eu/documents/QUID/CMEMS-MED-QUID-006-008.pdf (last access: 6 March 2023), 2022.

Stramma, L., Schmidtko, S., Levin, L. A., and Johnson, G. C.: Ocean oxygen minima expansions and their biological impacts, Deep-Sea Res. Pt. I, 57, 587–595, https://doi.org/10.1016/j.dsr.2010.01.005, 2010.

Thomson, R. E. and Emery, W. J.: Data analysis methods in physical oceanography, Newnes, ISBN: 978-0-12-387782-6, 2014.

Vilibić, I., and Mihanović, H.: Observing the bottom density current over a shelf using an Argo profiling float, Geophys. Res. Lett., 40, 910–915, https://doi.org/10.1002/grl.50215, 2013.

Wehde, H., Schuckmann, K. V., Pouliquen, S., Grouazel, A., Bartolome, T., Tintore, J., De Alfonso Alonso-Munoyerro, M., Carval, T., Racapé, V., and the INSTAC team: EU Copernicus Marine Service Quality Information Document for the Mediterranean Sea- In-Situ Near Real Time Observations, INSITU_MED_PHYBGCWAV_DISCRETE_MYNRT_013_035, Issue 2.2, Mercator Ocean International, https://catalogue.marine.copernicus.eu/documents/QUID/CMEMS-INS-QUID-013-030-036.pdf (last access: 6 March 2023), 2022.

Yasunaka, S., Ono, T., Sasaoka, K., and Sato, K.: Global distribution and variability of subsurface chlorophyll *a* concentrations, Ocean Sci., 18, 255–268, https://doi.org/10.5194/os-18-255-2022, 2022.

State Planet, 1-osr7, 11, 2023
https://doi.org/10.5194/sp-1-osr7-11-2023

Characterization of the organic vs. inorganic fraction of suspended particulate matter in coastal waters based on ocean color radiometry remote sensing

Hubert Loisel[1], Lucile Duforêt-Gaurier[1], Trung Kien Tran[1], Daniel Schaffer Ferreira Jorge[1], François Steinmetz[2], Antoine Mangin[3], Marine Bretagnon[3], and Odile Hembise Fanton d'Andon[3]

[1]Université du Littoral Côte d'Opale, CNRS, Univ. Lille, IRD, UMR 8187 – LOG – Laboratoire d'Océanologie et de Géosciences, 62930 Wimereux, France
[2]HYGEOS, Euratechnologies, 165 avenue de Bretagne, 59000 Lille, France
[3]ACRI-ST, 260 Route du Pin Montard, 06904 Sophia-Antipolis, France

Correspondence: Hubert Loisel (hubert.loisel@univ-litoral.fr)

Received: 30 August 2022 – Discussion started: 30 September 2022
Revised: 14 February 2023 – Accepted: 27 February 2023 – Published: 27 September 2023

Abstract. Knowledge of the organic and inorganic particulate fraction of suspended material in coastal waters is essential for the study of particle dynamics and biogeochemical cycles in these complex and highly variable environments. Thanks to the availability of appropriate spatial sensors and to the considerable improvements in algorithms dedicated to the satellite observation of coastal waters from ocean color radiometry (OCR) achieved in the last 2 decades, various optical and biogeochemical parameters can now be routinely monitored over coastal waters. Here we show that a proxy for particulate composition (PPC) can be estimated from OCR observations. The present algorithm, based on a neural network approach, has been validated using a broad range of biogeochemical data collected in various contrasted coastal waters and has been applied to MERIS observations over the global coastal ocean at a 1 km × 1 km spatial resolution from 2002 to 2012. The relevance of the temporal occurrence of PPC in a given water pixel has been illustrated over the global coastal ocean, and its pertinence has been discussed in depth for the English Channel and the southern North Sea, which are characterized by a well-documented variability in suspended particulate matter composition. The present algorithm can directly be applied to all OCR sensors.

1 Introduction

Water quality parameters display large spatiotemporal variability in coastal waters as these areas are the location of strong coupling between aquatic and terrestrial systems and are under pressure from great natural and anthropogenic forcing. The characterization of the spatiotemporal distribution of biological, biogeochemical, and physical parameters in coastal waters is of fundamental importance for a variety of applications dedicated to coastal management, which often involves economic interests, and for improving our understanding of the dynamics of the coastal ecosystems and their associated biogeochemical cycles.

Among the large set of water quality parameters sampled in coastal waters, the concentration of the suspended particulate matter (SPM) or equivalent parameters (e.g., the turbidity) has been intensively studied by the scientific community as a key parameter for understanding sediment transport, downstream sedimentation, and coastal geomorphological processes (Velegrakis et al., 1997; Lahet and Stramski, 2010; Vantrepotte et al., 2012; Loisel et al., 2014; Anthony et al., 2015; Marchesiello et al., 2019). For instance, combining SPM spatiotemporal products with wave data allows resuspension areas to be identified (Loisel et al., 2014). While the SPM spatiotemporal patterns provide relevant information on the suspended particulate dynamics, the variation in the composition (i.e., chemical nature) of SPM may disclose rel-

Published by Copernicus Publications.

Table 1. CMEMS and non-CMEMS products used in this study, including information on data documentation.

Product ref. no.	Product ID and type	Data access	Documentation
1	RRS (remote-sensing reflectance), satellite observations	https://www.globcolour.info/ (last access: 28 April 2023)	Product User Guide: https://www.globcolour.info/CDR_Docs/GlobCOLOUR_PUG.pdf (last access: 28 April 2023)
2	PPC, satellite observations	It will be introduced in GlobColour and in the Copernicus Marine Service (EU Copernicus Marine Service Product, 2022)	Quality Information Document (QUID): Garnesson et al. (2022); Product User Manual (PUM): Colella et al. (2022)

evant information on the complex chemical, physical, and biological processes occurring in coastal waters. For instance, the portion of particulate organic matter (POM) in SPM is of particular interest when investigating the adsorption of trace elements on particles, abrupt changes in water quality due to pelagic or benthic blooms, or the fate of suspended matter between the water column and sediments. Modeling particulate transport requires specific modules coupled with hydrodynamical models. For example, in the SUBSTANCE module (Mengual et al., 2017), which can be coupled with CROCO, a French code built upon the well-known Regional Oceanic Modeling System (Shchepetkin and McWilliams, 2005), conservative and non-conservative (i.e., biological) particulate substances have to be defined by their own density and/or settling velocity, depending on the nature of the SPM (mineral vs. organic). The settling and flocculation processes, closely linked to the organic fraction of SPM and to the transport of particulate variables in the water column, are also considered in these modules.

Particulate organic carbon (POC) encompasses living (phytoplankton, heterotrophic bacteria, and viruses) and non-living (i.e., detritus) organic particles in suspension. Information on the SPM and POC variability represents crucial input for the initiation and validation of sediment transport models (Douillet et al., 2001; Ford and Fox, 2014; Wu et al., 2020) and biogeochemical models (Aumont et al., 2015). While the analysis of the variation in the absolute values of SPM and POC concentrations brings relevant information for our understanding of the carbon cycle and marine particulate dynamics in coastal waters, the dimensionless POC / SPM ratio is used in many studies to describe the temporal variability in the particulate matter pool composition and origin (Coynel et al., 2005; Emmerton et al., 2008; Doxaran et al., 2012, 2015; Ehn et al., 2019), which is often related to variation in the regional environmental forcing (e.g., water discharge, phytoplankton bloom dynamics). This ratio is also used to better interpret the in situ optical measurements (Babin et al., 2003; Loisel et al., 2007; Woźniak et al., 2011; Doxaran et al., 2012; Neukermans et al., 2016; Reynolds et al., 2016; Reynolds and Stramski, 2019) and satellite ocean color radiometry (OCR) observations (Vantrepotte et al., 2011). From in situ data collected in the near-shore marine environment at Imperial Beach in California, Woźniak et al. (2010) set threshold values for the POC / SPM ratio to identify changes in the particulate assemblage from the dominance of mineral particles (POC / SPM < 0.06) to the dominance of organic particles (POC / SPM > 0.25) and for mixed particulate assemblages ($0.25 <$ POC / SPM < 0.6). Neukermans et al. (2016) and Reynolds et al. (2016) followed the approach of Woźniak et al. (2010) to partition their Arctic seawater datasets into these three broad compositional classes.

Due to the high variability in the physical and biogeochemical processes occurring in coastal waters, traditional approaches such as oceanographic cruises and in situ time series, although essential, are very time-consuming and expensive, and it is sometimes uncertain whether they will yield meaningful results for the studied phenomena. Satellite observation of OCR is now well-recognized as a powerful tool to monitor the spatiotemporal distribution of biogeochemical and optical parameters in coastal waters (IOCCG, 2000; Loisel et al., 2013; IOCCG, 2018; Groom et al., 2019). Over the past decades, various OCR bio-optical algorithms have shown that SPM (Ahn et al., 2006; Nechad et al., 2010; Feng et al., 2014; Han et al., 2016; Balasubramanian et al., 2020; Pahlevan et al., 2022) and POC concentrations (Liu et al., 2015; Hu et al., 2016; Woźniak et al., 2016; Le et al., 2017; Tran et al., 2019) can be estimated over coastal waters.

The objective of this study is to provide a proxy for particulate composition (PPC) from remote sensing. For that purpose, the POC / SPM ratio value is used as an intermediate product which allows the PPC, composed of three different classes (i.e., organically dominated, mineral-dominated, and mixed), to be estimated. We will re-examine the relevance of the POC / SPM threshold values of Woźniak et al. (2010), developed to assess the organic vs. mineral fraction of the bulk particulate matter. This will be done through the examination of the relationship between the POC / SPM ratio

and the b_{bp}/c_p optical ratio, which is an indicator of the bulk particulate assemblage chemical composition (Twardowski et al., 2001; Loisel et al., 2007). An extensive in situ dataset collected in a biogeochemically contrasted environment has been gathered for that purpose. A neural network (NN) algorithm will be developed and validated against a large in situ dataset collected in various coastal environments to assess PPC from OCR. The new algorithm will then be applied to MERIS (MEdium Resolution Imaging Spectrometer) observations (2002–2012) over global coastal waters at a 1 km^2 spatial resolution to discuss the significance of this new product. A specific focus will be on the English Channel and the southern North Sea, for which the temporal occurrence of the organic vs. inorganic fraction for a given pixel, built from 10-year temporal series, will be discussed.

2 Materials and methods

2.1 Dataset description

2.1.1 In situ datasets

In situ measurements were collected between 1997 and 2014 in the southeastern Beaufort Sea (Bélanger et al., 2008), French Guiana (Vantrepotte et al., 2012, 2015), European coastal waters (the English Channel, North Sea, Bay of Biscay) (Lubac and Loisel, 2007; Lubac et al., 2008; Neukermans et al., 2012; Bonato et al., 2016; Novoa et al., 2017), and the South China Sea/Vietnam East Sea (Loisel et al., 2014, 2017). The sampling strategies, the field measurement protocols, and data processing are described in related papers. Measurements include concentrations of POC and SPM ($\mu g\,L^{-1}$), remote-sensing reflectances (R_{rs}, sr^{-1}), the particulate backscattering coefficient (b_{bp}), and the particulate attenuation coefficient (c_p) (m^{-1}) at 650 nm. The samples cover a wide range of biogeochemical variability as POC and SPM concentrations span 4 and 3 orders of magnitude, respectively. The first in situ database, named DS0, includes 300 coincident POC, SPM, b_{bp}, and c_p measurements (Table 2). In Sect. 2.3, DS0 will be used to examine the empirical relationship between b_{bp}/c_p and POC / SPM. The POC / SPM ratio ranges between 1.1×10^{-3} and 8.7×10^{-1}. In comparison, Woźniak et al. (2010) collected 44 samples in the near-shore area off Imperial Beach (California) with POC / SPM values between 2.3×10^{-2} and 4.2×10^{-1}. The second in situ database, referred to as DS, is made of 325 coincident POC, SPM, and R_{rs} measurements, with $3.9 \times 10^{-4} \leq \mathrm{POC/SPM} \leq 5.6 \times 10^{-1}$ (Table 2). It will be used to test the performance of POC / SPM estimates from the neural network algorithm (Sect. 3.1).

2.1.2 The global coastal MERIS R_{rs} and match-up datasets

MERIS level 1 data were used to study the PPC spatial and temporal distribution (Sect. 3.2) and for the match-up ex-

Table 2. Information on the in situ data used in this study: mean [minimum, maximum] and standard deviation (SD).

Dataset	Region	No. of data	Years	In situ $\frac{POC}{SPM}$	$\frac{POC}{SPM}$ derived from satellite R_{rs}	$\frac{POC}{SPM}$ derived from in situ R_{rs}	$\frac{b_{bp}(650)}{c_p(550)}$
DS0	European coastal waters	300	2010–2014	0.1136 [0.0001, 0.8700] (0.1465)	– – –	– – –	0.0162 [0.0013, 0.519] (0.0076)
DS	European coastal waters, French Guiana, Beaufort Sea, Vietnam East Sea	325	1997–2018	0.0895 [0.0004, 0.5606] (0.1046)	– – –	0.0894 [0.0026, 0.5382] (0.1024)	– – –
DSM	French coastal waters, European coastal waters	101	2002–2018	0.0801 [< 0.0001, 0.5606] (0.1074)	0.1116 [0.0002, 0.5574] (0.1117)	– – –	– – –

ercise (Sect. 3.1). MERIS level 1 data (∼ 1 km pixel resolution) over the 2002–2012 period were processed using the polymer atmospheric correction algorithm (Steinmetz et al., 2011; Steinmetz and Ramon, 2018), which was adapted for coastal waters within the framework of the GlobCoast project. Following Mélin and Vantrepotte (2015), only pixels presenting a distance to the coast lower than 200 km and with a bottom depth not deeper than 4000 m are selected (Loisel et al., 2017). A third dataset, named DSM (for DataSet Match-up), was composed of collocated MERIS data with in situ data points of POC and SPM (Table 2), collected within the framework of the French Coastal Monitoring Network SOMLIT (Service d'Observation en Milieu Littoral, https://www.somlit.fr/en/, last access: 22 March 2023). The criteria considered for the match-up selection are described in Bailey and Werdell (2006). Due to the absence of organically dominated match-up data points using the MERIS sensor, complementary match-up data points were added to DSM by looking at SeaWiFS (Sea-Viewing Wide Field-of-View Sensor) match-up with DS. We only kept the match-up data points with a good R_{rs} retrieval (only possible using DS). For that purpose, only data points with R_{rs}(in situ) / R_{rs}(satellite) values from 412 to 560 nm, below 0.5, or above 1.5 are selected. The DSM dataset is composed of 101 matched points after the application of these criteria. The POC / SPM mean value is 0.0801 for DSM instead of 0.1136 and 0.0895 for DS0 and DS, respectively.

2.2 Algorithm development

Two different approaches were initially tested to estimate PPC from R_{rs}. For the first approach, SPM is estimated by the Han et al. (2016) algorithm (referred to as HA16) which consists of semi-analytical relationships between SPM and R_{rs} in the red or NIR bands, according to the level of turbidity. The typical band–ratio relationship using the red to blue–green bands is used to assess POC from the algorithm of Tran et al. (2019) (referred to as TR19). Once POC and SPM are derived, the POC / SPM ratio is calculated, and PPC is estimated using the different threshold values (see Sect. 2.3). However, Tran et al. (2019) showed that POC concentration can be overestimated in the presence of mineral waters. The result is that the POC / SPM ratio is also overestimated when mineral-dominated waters dominate (not shown). Moreover, the errors in both POC and SPM estimations are additive when the POC / SPM ratio is finally calculated. To limit this error propagation, we focus on the development of a single algorithm to derive the POC / SPM ratio from R_{rs} in one step.

For that purpose, a neural network approach has been selected as a second approach. We used a feed-forward network with log-sigmoid hidden neurons and linear output neurons coupled to a Levenberg–Marquardt algorithm allowing an efficient back propagation through the training procedure (Lv et al., 2018; Hagan et al., 1996). The DS dataset was randomly divided into three datasets to develop, train, and validate this NN. Overall, 60 % of the observations were used to construct and train the NN, 20 % were used for its validation, and 20 % were used to test its performance independently. The training and validation phases are performed jointly, allowing us to stop the training procedure when the generalization of the NN stops improving. We tested several combinations of R_{rs} bands (412, 443, 490, 510, 560, and 665 nm) to best predict the POC / SPM ratio. The final NN architecture was best trained using R_{rs} at 412, 490, 510, and 560 nm as the input layer, two hidden layers (8 and 10 neurons), and one output layer (POC / SPM ratio). The metrics used to evaluate the performance of the NN optimization are described in Portillo Juan and Negro Valdecantos (2022).

2.3 Determination of the organic, mineral, and mineral–organic mixed fraction

As previously explained, the POC / SPM ratio is an indicator of the particle assemblage and can be used to partition in situ data into three water types as defined by Woźniak et al. (2010). In addition, some theoretical and field studies showed that the variability in the ratio b_{bp}/b_p can be related to the particle composition (Boss et al., 2004; Twardowski et al., 2001; Loisel et al., 2007; Duforêt-Gaurier et al., 2018). Low b_{bp}/b_p values are observed for a particle population dominated by low refractive-index material such as phytoplankton. In contrast, high b_{bp}/b_p values are generally observed in the presence of a relatively high concentration of inorganic particles. At 650 nm, c_p is dominated by the scattering, and the optical ratio b_{bp}/c_p can be used instead of b_{bp}/b_p (Loisel et al., 2007).

The objective here is to re-examine the pertinence of the POC / SPM threshold values of Woźniak et al. (2010) on a larger in situ coastal dataset (DS0) (covering a wider range of optical and biogeochemical variability) through the examination of the POC / SPM to b_{bp}/c_p relationship. As expected, b_{bp}/c_p decreases when POC / SPM increases, that is when we move from a mineral-dominated to an organically dominated environment, with b_{bp}/c_p values typically lower than 0.010–0.012 (Twardowski et al., 2001; Loisel et al., 2007) (Fig. 1). The regression line (b_{bp}/c_p vs. POC / SPM; black line) is plotted, and the estimated regression coefficients are indicated with their standard error (Fig. 1). The threshold values are first fixed according to the b_{bp}/c_p values (as a given range of b_{bp}/c_p values corresponds to a given range of the refractive index of the bulk particulate matter) and then adjusted, with a careful examination of each data point for which ancillary data (i.e., chlorophyll a, counted cells, phytoplankton to particulate absorption ratio, and R_{rs} spectra) are used to better characterize the bulk particulate matter. The first threshold value has been shifted to 0.08 (corresponding to a b_{bp}/c_p value of 0.012) to encompass data points collected in mineral-dominated environments (close to river mouths). An asymptote is reached at high POC / SPM values (above 0.2) and concerns data points with low b_{bp}/c_p (below

0.075) values typical of phytoplankton-dominated environments. The new threshold value of POC / SPM for organically dominated waters is set to 0.2 (i.e., $b_{bp}/c_p < 0.075$) to encompass in situ data points collected during bloom events. This value is, however, very similar to the value previously obtained by Woźniak et al. (2010) (0.25). Data points located along the asymptote are therefore associated with organically dominated waters.

The thresholds are applied to monthly POC / SPM values derived from MERIS data, and the frequency of dominance is computed for each pixel of the scene over the 10 years (2002–2012) as detailed below. A pixel geographically located at a given latitude and longitude is named the k pixel ($k = 1, S_{tot}$). S_{tot} is the total number of pixels over the selected geographical area. For each k pixel, we computed the number of valid pixels (N^k_{tot}) over the period that corresponds to 120 months ($N^k_{tot} \leq 120$). The term "valid pixel" means a non-flag pixel for which the R_{rs} value is provided in order to derive POC / SPM with the neural network. Then, for the k pixel, we calculate how many times the class i is identified over N^k_{tot}: n^k_i is the class occurrence, and $i = 1, 2$, or 3 with 1 for mineral-dominated, 2 for organically dominated, and 3 for mixed water classes. The frequency of dominance is defined as the ratio of the occurrence to the number of valid pixels:

$$D^k = \frac{\text{maximum}\left(n^k_1, n^k_2, n^k_3\right)}{N^k_{tot}} \times 100\,(\%). \quad (1)$$

Eq. (1) is repeated S_{tot} times to compute the frequency of dominance over the whole scene and provide maps in Sect. 3.2.

3 Results

3.1 Validation of the classification

In situ measurements of R_{rs} from DS are used as input for the neural network algorithm to test the performance of the estimation of algorithm-derived values, named NN POC / SPM (Fig. 2a). The NN algorithm achieves a good performance over the whole range of POC / SPM (Fig. 2a). The median absolute percentage difference (MAPD) is 24 %, the median ratio (MR) is 1.06, and the bias is 0.004. The slope of the type II (log-transformed) regression is 0.90. The same classification is obtained for 88.5 % of data points between the in situ and model-derived values. About 10.9 % of data points are misclassified in the adjacent group and only 0.62 % are misclassified in a non-adjacent group. SeaWiFS and MERIS match-ups on both the independent SOMLIT in situ dataset (for which no in situ R_{rs} values are available) and DS in situ data (for which in situ R_{rs} values are available) are shown in Fig. 2b. Compared to the results obtained using in situ measurements (Fig. 2a), the data points are much more scattered around the 1 : 1 line when POC / SPM is derived from satellite R_{rs} (Fig. 2b). This strongly emphasizes the impact of atmospheric correction on PPC, which is a common feature of OCR products. In Fig. 2b, all mineral-dominated data are from the SOMLIT dataset. As the in situ R_{rs} values are not available for SOMLIT data, we cannot apply the criteria described in Sect. 2.1.2 to remove inaccurate satellite R_{rs} retrievals. Removing such R_{rs} values will certainly allow us to identify strongly misclassified patterns. In Fig. 2b, 68.4 % of mineral-dominated data, 44.4 % of mixed data, and 73.7 % of organically dominated data are well-classified. Due to atmospheric correction uncertainties, a proper estimation of POC / SPM values from remote sensing is still very challenging, while the estimation of PPC can still be performed with a reasonable accuracy. Extra match-up data points, including both in situ R_{rs} and POC / SPM measurements, are, however, needed to definitely support this conclusion.

3.2 Global and regional PPC patterns

The PPC algorithm has been applied to MERIS monthly $R_{rs}(\lambda)$ data over the 2002–2012 time period, and the maximum occurrence of PPC has been calculated over this 10-year time period as described in Sect. 2.3 (Fig. 3a). As expected, we observe a well-marked near-shore–off-shore gradient from mineral-dominated waters to organically dominated waters with a transition zone corresponding to mixed particulate assemblages. Large deltas and estuaries characterized by intense sediment discharge, such as the Amazon Estuary, Mekong Delta, Huanghe (Yellow River) Delta, Yangtze Estuary, or Ganges–Brahmaputra Delta, present a very high occurrence of mineral-dominated waters (70 %–90 %). These areas can extend much further from the river outlet, depending on the bathymetry and the surface currents, as for instance in the central part of the Yellow Sea at the Yangtze Estuary. Values of POC / SPM of 0.12–0.15, depicting mix-dominated particulate assemblages, have been measured in the East China Sea region (124–126° E, 30–32° N) in great agreement with our present finding (Hung et al., 2007). The dominance of mineral-dominated waters is generally persistent throughout the considered time period as depicted by the relatively low (20 %–30 %) coefficient of variation observed at the outlet of these different estuaries and deltas (Fig. 3b). In contrast, at the Amazon and Yangtze estuaries and the Huanghe Delta, some off-shore areas with a high (70 %) coefficient of variation depict the impact of seasonal and interannual interactions between the continental (river and sediment discharges) and oceanic forcing (tide, wind, surface current, sub-mesoscale structures) and the bathymetry. For example, close interaction between the Amazon plume dominated by mineral particles and the retroflection of the North Brazil Current carrying oceanic particulate organic matter occurs in the region at the Amazon Estuary where the slope in the continental shelf drastically changes (Gensac et al., 2016; Varona et al., 2019), causing a significant temporal variation in the PPC. In contrast to the

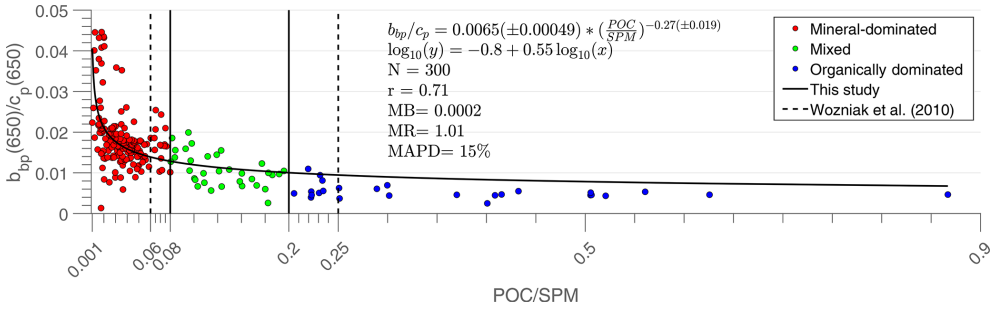

Figure 1. Relationships between b_{bp}/c_p (650 nm) and POC / SPM from DS0. The black curve is the power regression. The vertical dashed lines represent the thresholds delimiting the water types according to Woźniak et al. (2010). The vertical solid lines show the new thresholds defined in the present study. The linear regression (in log space) between derived (named y) and in situ b_{bp}/c_p (named x) is given, as are the regression coefficient (r), the median absolute percentage difference (MAPD), the median ratio (MR), and the mean bias (MB). These statistical indicators (MAPD, MR, and MB) are calculated in normal space as described in Jorge et al. (2021).

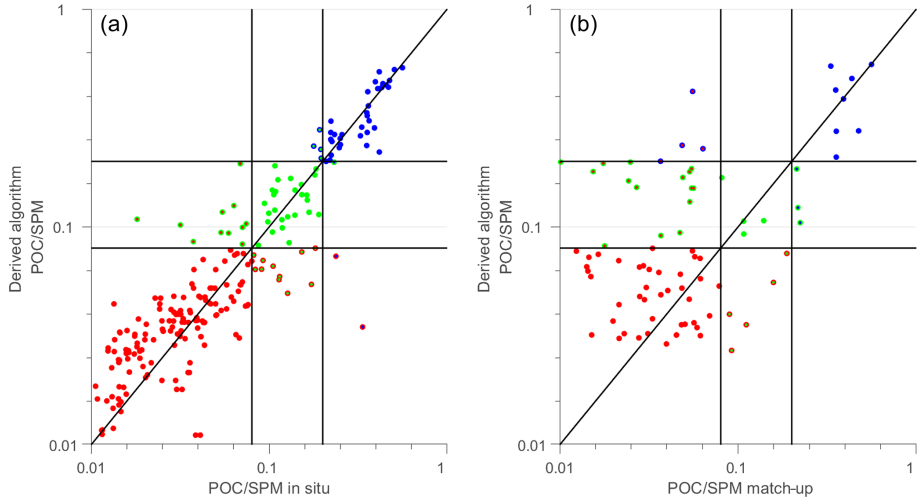

Figure 2. Comparison of in situ and derived POC / SPM from neural network algorithm (NN POC / SPM) **(a)** for DS (i.e., in situ R_{rs} values are used by NN POC / SPM) and **(b)** for DSM (i.e., satellite R_{rs} values are used by NN POC / SPM). The dashed line is the 1 : 1 line. Red, blue, and green colors are for mineral-dominated, organically dominated, and mixed waters, respectively. For both panels, the vertical and horizontal solid lines indicate the thresholds (0.08 and 0.2) used to partition the water types. Dots are color-coded according to the values of the in situ POC / SPM, whereas the circles are color-coded according to the values of POC / SPM derived from NN. When circles and dots are of the same color, it means that the retrieved values belong to the same class as the in situ ones.

previously mentioned rivers and despite the Congo River being the world's second-largest river in terms of both drainage area and water discharge, only a small PPC signature (mainly organically dominated) can be seen at the outlet of its estuary (not visible in Fig. 3a), except in the coefficient of variation (Fig. 3b). This is coherent with the fact that the sediment discharge of the Congo River is very low, in contrast to the dissolved part of the discharge, and that most of the particulate assemble is organic (Coynel et al., 2005). A specific zoom on this area reveals the dominance of organic matter even at the outlet of the estuary, in good agreement with in situ data reported in Coynel et al. (2005).

While an extensive investigation of the different spatiotemporal patterns presented in Fig. 3 are is beyond the scope of the present paper, a specific focus illustrating the pertinence of the PPC product is conducted over the eastern English Channel (EEC) and the southern North Sea (SNS), for which the biogeochemical and physical processes driving the suspended particulate matter composition are relatively well-documented. The eastern English Channel and southern North Sea coastal region is known for its strong hydrodynamics marked by intense tidal currents. This shallow-water region, therefore largely impacted by resuspension effects, is also largely influenced by freshwater discharges from different rivers, the most important ones being the Seine and the Somme along the French coast of the EEC and the Thames and the Scheldt along the SNS. Strong spring and early summer phytoplankton blooms of diatoms and *Phaeocystis globosa* occurred in this region at different times of the year, depending on the nutrient and light (i.e., season and turbidity

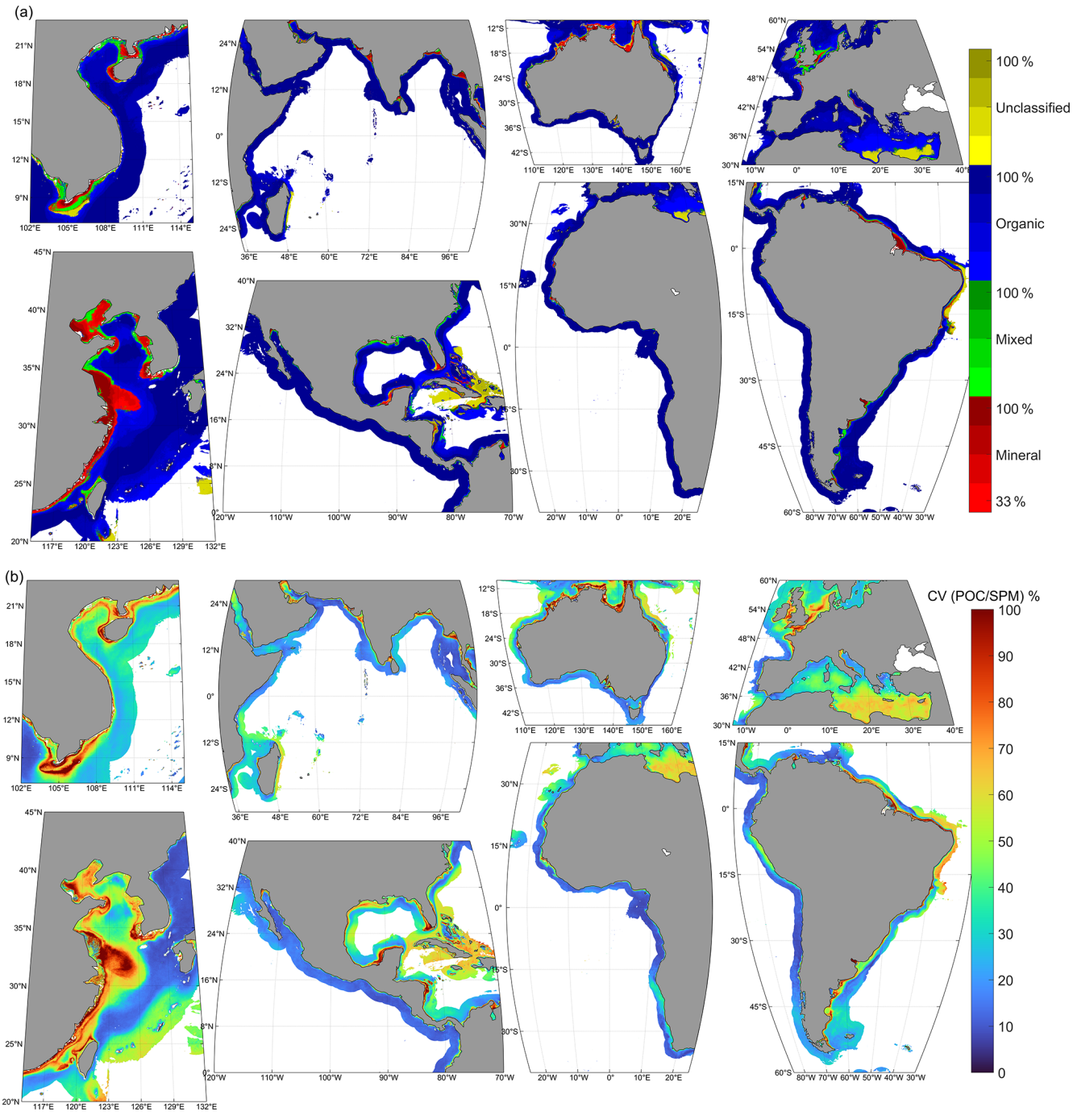

Figure 3. **(a)** Frequency (%) of dominant water type (red for mineral-dominated, green for mixed, blue for organically dominated) over the MERIS time period of 2002–2012. The yellow color corresponds to unclassified pixels, which means pixels for which the retrieved value of POC / SPM is non-valid (i.e., negative). **(b)** Coefficient of variation in POC / SPM over the MERIS period of 2002–2012.

level) availability (Breton et al., 2000; Antajan et al., 2004; Sazhin et al., 2007). For these different reasons, the composition of the suspended particulate matter in this area is strongly variable, as already stressed by different field studies based on optical and biogeochemical measurements (Loisel et al., 2007; Vantrepotte et al., 2007; Lubac et al., 2008). The monthly occurrence of each PPC class is in excellent agreement with our present knowledge of this area (Fig. 4). Between mid-fall and winter (from October to February), the particulate matter pool of the EEC and the SNS is characterized by mineral and mix-dominated assemblages, mainly due to sediment river inputs and resuspension effects from strong

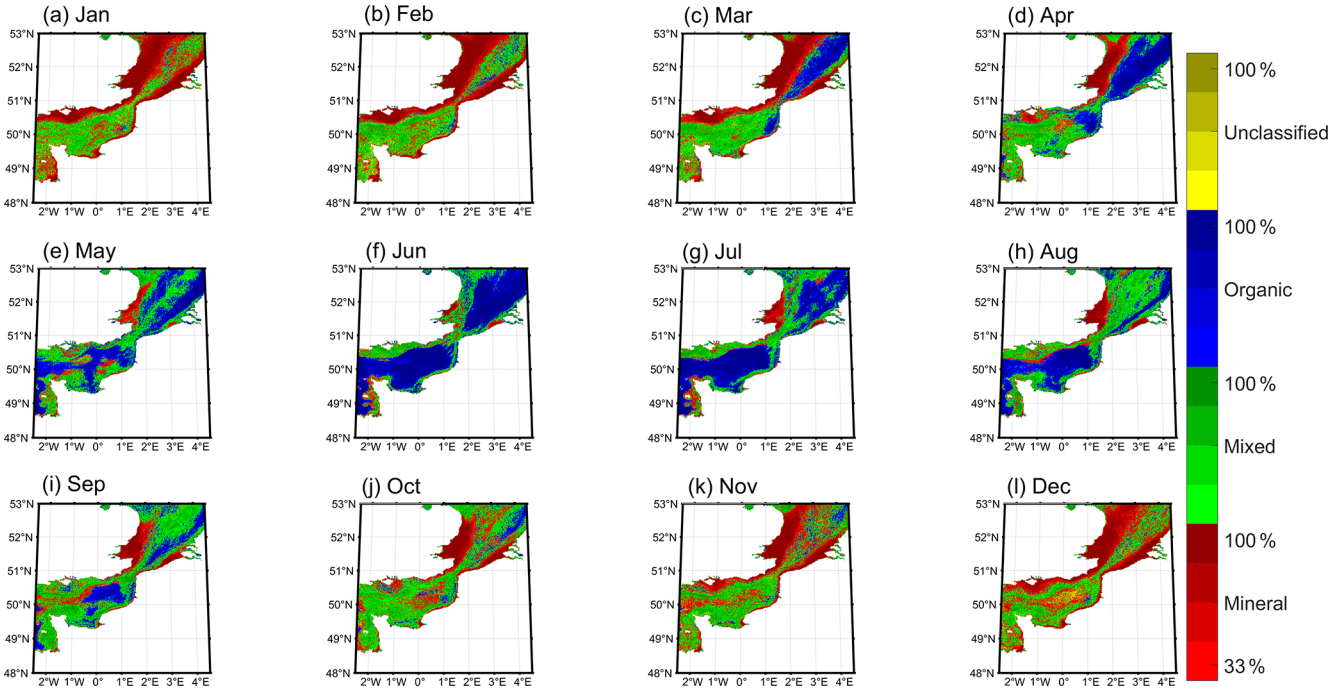

Figure 4. Frequency of dominance (%) for mineral-dominated (red), mixed (green), organically dominated (blue), or unclassified (yellow) waters over the MERIS period of 2002–2012 in the eastern English Channel and the southern North Sea.

physical (i.e., waves) forcing (Lesourd et al., 2003; Lancelot et al., 2007; Gohin, 2011; Renosh et al., 2014). This is consistent with the results of Vantrepotte et al. (2012), who observed that the relative contribution of the particulate matter assemblage with a strong proportion of mineral particles increases significantly during the winter time. In March, organically dominated pixels appear in the SNS coastal region and at the Somme River area in the EEC. Then, while the organically dominated particle assemblage areas are developing in the SNS from March to July, similar particulate assemblages start developing from May to July in off-shore waters of the EEC and along the EEC coast from June. The timing of the development of organic matter areas in the EEC and the SNS is in perfect agreement with phytoplankton bloom dynamics in these regions, which first develop in the Bay of the Somme area and the SNS, followed by another bloom which develops south in the area of the Bay of the Seine (Brunet et al., 1996; Vantrepotte et al., 2007; Joint and Pomroy, 1993; Van der Zande et al., 2012; Gohin et al., 2019). Finally, areas covered by organically dominated pixels are at a maximum in June and July, and then mixed assemblages start developing in the northern part of the domain to fully cover the whole region in October. Mixed assemblages are more likely dominated by aggregates of mineral particles and detrital matter (non-living organic particles) which developed during the senescence of the bloom (Vantrepotte et al., 2007; Loisel et al., 2007; Gohin, 2011; Grattepanche et al., 2011).

4 Concluding remarks

The PPC can be used as an appropriate indicator for characterizing the nature of bulk suspended particulate matter from satellite OCR remote sensing. The MERIS spatiotemporal patterns of this new indicator are consistent with general features documented in the literature. Due to the visible bands used, common to all OCR sensors, the PPC algorithm can be applied to all OCR satellite sensors, allowing us to assess the long-term trend of suspended particulate matter over the global coastal ocean. The application of this algorithm to the satellite Copernicus Marine Environment Monitoring Service (CMEMS) data is underway to assess the different temporal patterns (seasonal, trend, and irregular) using the Census X-11 approach (Vantrepotte et al., 2011).

Data availability. DS0, DS, and DSM can be obtained on request.

Author contributions. HL, as the recipient of most of the funding, proposed the idea of the work, gave permission to use data in LOG, was involved in the algorithm development and data analysis, and co-wrote the paper. LDG was involved in the algorithm development, supervised the analysis and visualization of the data, and was involved in paper organization and co-writing. TKT analyzed and visualized the in situ and satellite data, developed and tested the algorithms, and developed the codes to process images. DSFJ supported the development of the MATLAB-processed images, provided the final plots and statistics, and revised the paper.

FS provided the Polymer algorithm to perform atmospheric corrections to process satellite images in coastal waters. AM, MB, and OHFd'A gave suggestions and comments.

Competing interests. The contact author has declared that none of the authors has any competing interests.

Disclaimer. Publisher's note: Copernicus Publications remains neutral with regard to jurisdictional claims in published maps and institutional affiliations.

Acknowledgements. This study was realized with support from the French Space Agency (CNES) through the COYOTE project (CNES/TOSCA program). MERIS data were processed within the framework of the GlobCoast project funded by the French Agence Nationale de la Recherche (grant no. ANR-11-BS56-0018). Some of the in situ measurements used in this study were collected from different cruises performed in Vietnam coastal waters, French Guiana, and the eastern English Channel through various projects funded by CNES. The authors are grateful to all the people that contributed to data provided by the Service d'Observation en Milieu Littoral (SOMLIT), INSU-CNRS. We also thank our many colleagues who participated in the collection of the various datasets cited in this study. We thank Arnaud Cauvin and Xavier Mériaux, who conducted field missions at LOG, processed field biogeophysical data, and were in charge of LOG database management. We express our gratitude to Roy Elhourany for his advice concerning the neural network algorithm. The authors thank the reviewers, who helped to improve the paper with their comments and suggestions.

Financial support. This research has been supported by the Centre National d'Etudes Spatiales (TOSCA/COYOTE project) and the Agence Nationale de la Recherche (grant no. ANR-11-BS56-0018).

Review statement. This paper was edited by Griet Neukermans and reviewed by two anonymous referees.

References

Ahn, Y. H., Shanmugam, P., and Moon, J. E.: Retrieval of ocean colour from high resolution multi-spectral imagery for monitoring highly dynamic ocean features, Int. J. Remote Sens., 27, 367–392, https://doi.org/10.1080/01431160500300479, 2006.

Antajan, E., Chrétiennot-Dinet, M.-J., Leblanc, C., Daro, M.-H., and Lancelot, C.: 19'-hexanoyloxyfucoxanthin may not be the appropriate pigment to trace occurrence and fate of Phaeocystis: the case of *P. globosa* in Belgian coastal waters, J. Sea Res., 52, 165–177, https://doi.org/10.1016/j.seares.2004.02.003, 2004.

Anthony, E. J., Brunnier, G., Besset, M., Goichot, M., Dussouillez, P., and Nguyen, V. L.: Linking rapid erosion of the Mekong River delta to human activities, Sci. Rep.-UK, 5, 14745, https://doi.org/10.1038/srep14745, 2015.

Aumont, O., Ethé, C., Tagliabue, A., Bopp, L., and Gehlen, M.: PISCES-v2: an ocean biogeochemical model for carbon and ecosystem studies, Geosci. Model Dev., 8, 2465–2513, https://doi.org/10.5194/gmd-8-2465-2015, 2015.

Babin, M., Morel, A., Fournier-Sicre, V., Fell, F., and Stramski, D.: Light scattering properties of marine particles in coastal and open ocean waters as related to the particle mass concentration, Limnol. Oceanogr., 48, 843–859, https://doi.org/10.4319/lo.2003.48.2.0843, 2003.

Bailey, S. W. and Werdell, P. J.: A multi-sensor approach for the on-orbit validation of ocean color satellite data products, Remote Sens. Environ., 102, 12–23, https://doi.org/10.1016/j.rse.2006.01.015, 2006.

Balasubramanian, S. V., Pahlevan, N., Smith, B., Binding, C., Schalles, J., Loisel, H., Gurlin, D., Greb, S., Alikas, K., Randla, M., Bunkei, M., Moses, W., Nguy\^{e}˜n, H., Lehmann, M. K., O'Donnell, D., Ondrusek, M., Han, T.-H., Fichot, C. G., Moore, T., and Boss, E.: Robust algorithm for estimating total suspended solids (TSS) in inland and nearshore coastal waters, Remote Sens. Environ., 246, 111768, https://doi.org/10.1016/j.rse.2020.111768, 2020.

Bonato, S., Breton, E., Didry, M., Lizon, F., Cornille, V., Lécuyer, E., Christaki, U., and Artigas, L. F.: Spatio-temporal patterns in phytoplankton assemblages in inshore–offshore gradients using flow cytometry: A case study in the eastern English Channel, J. Marine Syst., 156, 76–85, https://doi.org/10.1016/j.jmarsys.2015.11.009, 2016.

Boss, E., Pegau, W. S., Lee, M., Twardowski, M., Shybanov, E., Korotaev, G., and Baratange, F.: Particulate backscattering ratio at LEO 15 and its use to study particle composition and distribution, J. Geophys. Res., 109, C01014, https://doi.org/10.1029/2002JC001514, 2004.

Breton, E., Brunet, C., Sautour, B., and Brylinski, J.-M.: Annual variations of phytoplankton biomass in the Eastern English Channel: comparison by pigment signatures and microscopic counts, J. Plankton Res., 22, 1423–1440, https://doi.org/10.1093/plankt/22.8.1423, 2000.

Brunet, C., Brylinski, J., Bodineau, L., Thoumelin, G., Bentley, D., and Hilde, D.: Phytoplankton Dynamics During the Spring Bloom in the South-eastern English Channel, Estuar. Coast. Shelf S., 43, 469–483, https://doi.org/10.1006/ecss.1996.0082, 1996.

Bélanger, S., Babin, M., and Larouche, P.: An empirical ocean color algorithm for estimating the contribution of chromophoric dissolved organic matter to total light absorption in optically complex waters, J. Geophys. Res., 113, C04027, https://doi.org/10.1029/2007JC004436, 2008.

Colella, S., Böhm, E., Cesarini, C., Garnesson, P., Netting, J., and Calton, B.: EU Copernicus Marine Service Product User Manual for the Copernicus-GlobColour Products, Issue 3.0, Mercator Ocean International, https://catalogue.marine.copernicus.eu/documents/PUM/CMEMS-OC-PUM.pdf (last access: 24 April 2023), 2022.

Coynel, A., Etcheber, H., Abril, G., Maneux, E., Dumas, J., and Hurtrez, J.-E.: Contribution of small mountainous rivers to particulate organic carbon input in the Bay of Biscay, Biogeochemistry, 74, 151–171, https://doi.org/10.1007/s10533-004-3362-1, 2005.

Douillet, P., Ouillon, S., and Cordier, E.: A numerical model for fine suspended sediment transport in the southwest lagoon of New Caledonia, Coral Reefs, 20, 361–372, https://doi.org/10.1007/s00338-001-0193-6, 2001.

Doxaran, D., Ehn, J., Be´langer, S., Matsuoka, A., Hooker, S., and Babin, M.: Optical characterisation of suspended particles in the Mackenzie River plume (Canadian Arctic Ocean) and implications for ocean colour remote sensing, Biogeosciences, 9, 3213–3229, https://doi.org/10.5194/bg-9-3213-2012, 2012.

Doxaran, D., Devred, E., and Babin, M.: A 50 % increase in the mass of terrestrial particles delivered by the Mackenzie River into the Beaufort Sea (Canadian Arctic Ocean) over the last 10 years, Biogeosciences, 12, 3551–3565, https://doi.org/10.5194/bg-12-3551-2015, 2015.

Duforêt-Gaurier, L., Dessailly, D., Moutier, W., and Loisel, H.: Assessing the Impact of a Two-Layered Spherical Geometry of Phytoplankton Cells on the Bulk Backscattering Ratio of Marine Particulate Matter, Appl. Sci.-Basel, 8, 2689, https://doi.org/10.3390/app8122689, 2018.

Ehn, J. K., Reynolds, R. A., Stramski, D., Doxaran, D., Lansard, B., and Babin, M.: Patterns of suspended particulate matter across the continental margin in the Canadian Beaufort Sea during summer, Biogeosciences, 16, 1583–1605, https://doi.org/10.5194/bg-16-1583-2019, 2019.

Emmerton, C. A., Lesack, L. F., and Vincent, W. F.: Nutrient and organic matter patterns across the Mackenzie River, estuary and shelf during the seasonal recession of sea-ice, J. Marine Syst., 74, 741–755, https://doi.org/10.1016/j.jmarsys.2007.10.001, 2008.

EU Copernicus Marine Service Product: Global Ocean Colour (Copernicus-GlobColour), Bio-Geo-Chemical, L3 (daily) from Satellite Observations (1997–ongoing), Mercator Ocean International [data set], https://doi.org/10.48670/moi-00280, 2022.

Feng, L., Hu, C., Chen, X., and Song, Q.: Influence of the Three Gorges Dam on total suspended matters in the Yangtze Estuary and its adjacent coastal waters: Observations from MODIS, Remote Sens. Environ., 140, 779–788, https://doi.org/10.1016/j.rse.2013.10.002, 2014.

Ford, W. I. and Fox, J. F.: Model of particulate organic carbon transport in an agriculturally impacted stream, Hydrol. Process., 28, 662–675, https://doi.org/10.1002/hyp.9569, 2014.

Garnesson, P., Mangin, A., Bretagnon, M., and Jutard, Q.: EU Copernicus Marine Service Quality Information Document for the Copernicus-GlobColour Products, Issue 3.0, Mercator Ocean International, https://catalogue.marine.copernicus.eu/documents/QUID/CMEMS-OC-QUID-009-101to104-111-113-116-118.pdf (last access: 24 April 2023), 2022.

Gensac, E., Martinez, J.-M., Vantrepotte, V., and Anthony, E. J.: Seasonal and inter-annual dynamics of suspended sediment at the mouth of the Amazon river: The role of continental and oceanic forcing, and implications for coastal geomorphology and mud bank formation, Cont. Shelf Res., 118, 49–62, https://doi.org/10.1016/j.csr.2016.02.009, 2016.

Gohin, F.: Annual cycles of chlorophyll-a, non-algal suspended particulate matter, and turbidity observed from space and in-situ in coastal waters, Ocean Sci., 7, 705–732, https://doi.org/10.5194/os-7-705-2011, 2011.

Gohin, F., Van der Zande, D., Tilstone, G., Eleveld, M. A., Lefebvre, A., Andrieux-Loyer, F., Blauw, A. N., Bryère, P., Devreker, D., Garnesson, P., Hernández Fariñas, T., Lamaury, Y., Lampert, L., Lavigne, H., Menet-Nedelec, F., Pardo, S., and Saulquin, B.: Twenty years of satellite and *in situ* observations of surface chlorophyll-*a* from the northern Bay of Biscay to the eastern English Channel. Is the water quality improving?, Remote Sens. Environ., 233, 111343, https://doi.org/10.1016/j.rse.2019.111343, 2019.

Grattepanche, J.-D., Vincent, D., Breton, E., and Christaki, U.: Microzooplankton herbivory during the diatom–Phaeocystis spring succession in the eastern English Channel, J. Exp. Mar. Biol. Ecol., 404, 87–97, https://doi.org/10.1016/j.jembe.2011.04.004, 2011.

Groom, S., Sathyendranath, S., Ban, Y., Bernard, S., Brewin, R., Brotas, V., Brockmann, C., Chauhan, P., Choi, J.-k., Chuprin, A., Ciavatta, S., Cipollini, P., Donlon, C., Franz, B., He, X., Hirata, T., Jackson, T., Kampel, M., Krasemann, H., Lavender, S., Pardo-Martinez, S., Mélin, F., Platt, T., Santoleri, R., Skakala, J., Schaeffer, B., Smith, M., Steinmetz, F., Valente, A., and Wang, M.: Satellite Ocean Colour: Current Status and Future Perspective, Frontiers in Marine Science, 6, 485, https://doi.org/10.3389/fmars.2019.00485, 2019.

Hagan, M. T., Demuth, H. B., and Beale, M. H.: Neural network design, PWS Publishing, Boston, ISBN 10: 0534943322 – ISBN 13: 9780534943325, 1996.

Han, B., Loisel, H., Vantrepotte, V., Mériaux, X., Bryère, P., Ouillon, S., Dessailly, D., Xing, Q., and Zhu, J.: Development of a Semi-Analytical Algorithm for the Retrieval of Suspended Particulate Matter from Remote Sensing over Clear to Very Turbid Waters, Remote Sens.-Basel, 8, 211, https://doi.org/10.3390/rs8030211, 2016.

Hu, S., Cao, W., Wang, G., Xu, Z., Lin, J. F., Zhao, W., Yang, Y., Zhou, W., Sun, Z., and Yao, L.: Comparison of MERIS, MODIS, SeaWiFS-derived particulate organic carbon, and in situ measurements in the South China Sea, Int. J. Remote Sens.-Basel, 37, 1585–1600, https://doi.org/10.1080/01431161.2015.1088673, 2016.

Hung, J.-J., Chan, C.-L., and Gong, G.-C.: Summer distribution and geochemical composition of suspended-particulate matter in the East China Sea, J. Oceanogr., 63, 189–202, https://doi.org/10.1007/s10872-007-0021-x, 2007.

IOCCG: Remote Sensing of Ocean Colour in Coastal, and Other Optically-Complex, Waters, in: Reports of the International Ocean-Colour Coordinating Group, 3, edited by: Sathyendranath, S., International Ocean-Colour Coordinating Group (IOCCG), Dartmouth, NS, Canada, 140 pp., https://doi.org/10.25607/OBP-95, 2000.

IOCCG: Earth Observations in Support of Global Water Quality Monitoring, in: Reports of the International Ocean-Colour Coordinating Group, No. 17, edited by: Greb, S., Dekker, A., and Binding, C., Ocean-Colour Coordinating Group (IOCCG), Dartmouth, NS, Canada, International, 125 pp., https://doi.org/10.25607/OBP-113, 2018.

Joint, I. and Pomroy, A.: Phytoplankton biomass and production in the southern North Sea, Mar. Ecol. Prog. Ser., 99, 169–182, http://www.jstor.org/stable/24837760 (last access: 22 March 2023), 1993.

Jorge, D. S., Loisel, H., Jamet, C., Dessailly, D., Demaria, J., Bricaud, A., Maritorena, S., Zhang, X., Antoine, D., Kutser, T., Bélanger, S., Brando, V. O., Werdell, J., Kwiatkowska, E.,

Mangin, A., and d'Andon, O. F.: A three-step semi analytical algorithm (3SAA) for estimating inherent optical properties over oceanic, coastal, and inland waters from remote sensing reflectance, Remote Sens. Environ., 263, 112537, https://doi.org/10.1016/j.rse.2021.112537, 2021.

Lahet, F. and Stramski, D.: MODIS imagery of turbid plumes in San Diego coastal waters during rainstorm events, Remote Sens. Environ., 114, 332–344, https://doi.org/10.1016/j.rse.2009.09.017, 2010.

Lancelot, C., Gypens, N., Billen, G., Garnier, J., and Roubeix, V.: Testing an integrated river–ocean mathematical tool for linking marine eutrophication to land use: The *Phaeocystis*-dominated Belgian coastal zone (Southern North Sea) over the past 50 years, J. Marine Syst., 216–228, https://doi.org/10.1016/j.jmarsys.2006.03.010, 2007.

Le, C., Lehrter, J. C., Hu, C., MacIntyre, H., and Beck, M. W.: Satellite observation of particulate organic carbon dynamics on the Louisiana continental shelf, J. Geophys. Res.-Oceans, 122, 555–569, https://doi.org/10.1002/2016JC012275, 2017.

Lesourd, S., Lesueur, P., Brun-Cottan, J., Garnaud, S., and Poupinet, N.: Seasonal variations in the characteristics of superficial sediments in a macrotidal estuary (the Seine inlet, France), Estuar. Coast. Shelf S., 58, 3–16, https://doi.org/10.1016/S0272-7714(02)00340-2, 2003.

Liu, D., Pan, D., Bai, Y., He, X., Wang, D., Wei, J.-A., and Zhang, L.: Remote Sensing Observation of Particulate Organic Carbon in the Pearl River Estuary, Remote. Sens.-Basel, 7, 8683–8704, 2015.

Loisel, H., Mériaux, X., Berton, J.-F., and Poteau, A.: Investigation of the optical backscattering to scattering ratio of marine particles in relation to their biogeochemical composition in the eastern English Channel and southern North Sea, Limnol. Oceanogr., 52, 739–752, https://doi.org/10.4319/lo.2007.52.2.0739, 2007.

Loisel, H., Vantrepotte, V., Jamet, C., and Dat, D. N.: Challenges and New Advances in Ocean Color Remote Sensing of Coastal Waters, chap. 4, in: Topics in Oceanography, edited by: Zambianchi, E., IntechOpen, Rijeka, https://doi.org/10.5772/56414, 2013.

Loisel, H., Mangin, A., Vantrepotte, V., Dessailly, D., Ngoc Dinh, D., Garnesson, P., Ouillon, S., Lefebvre, J.-P., Mériaux, X., and Minh Phan, T.: Variability of suspended particulate matter concentration in coastal waters under the Mekong's influence from ocean color (MERIS) remote sensing over the last decade, Remote Sens. Environ., 150, 218–230, https://doi.org/10.1016/j.rse.2014.05.006, 2014.

Loisel, H., Vantrepotte, V., Ouillon, S., Ngoc, D. D., Meriaux, X., Dessailly, D., Jamet, C., Duhaut, T., Nguyen, H. H., and Van Nguyen, T.: Assessment and analysis of the chlorophyll-*a* concentration variability over the vietnamese coastal waters from the meris ocean color sensor (2002–2012), Remote Sens. Environ., 190, 217–232, https://doi.org/10.1016/j.rse.2016.12.016, 2017.

Lubac, B. and Loisel, H.: Variability and classification of remote sensing reflectance spectra in the eastern English Channel and southern North Sea, Remote Sens. Environ., 110, 45–58, https://doi.org/10.1016/j.rse.2007.02.012, 2007.

Lubac, B., Loisel, H., Guiselin, N., Astoreca, R., Artigas, L.-F., and Mériaux, X.: Hyperspectral and multispectral ocean color inversions to detect phaeocystis globosablooms in coastal waters, J. Geophys. Res., 113, C06026, https://doi.org/10.1029/2007JC004451, 2008.

Lv, C., Xing, Y., Zhang, J., Na, X., Li, Y., Liu, T., Cao, D., and Wang, F.-Y.: Levenberg–Marquardt Backpropagation Training of Multilayer Neural Networks for State Estimation of a Safety-Critical Cyber-Physical System, IEEE T. Ind. Inform., 14, 3436–3446, https://doi.org/10.1109/TII.2017.2777460, 2018.

Marchesiello, P., Nguyen, N. M., Gratiot, N., Loisel, H., Anthony, E. J., Dinh, C. S., Nguyen, T., Almar, R., and Kestenare, E.: Erosion of the coastal Mekong delta: Assessing natural against man induced processes, Cont. Shelf Res., 181, 72–89, https://doi.org/10.1016/j.csr.2019.05.004, 2019.

Mengual, B., Hir, P. L., Cayocca, F., and Garlan, T.: Modelling Fine Sediment Dynamics: Towards a Common Erosion Law for Fine Sand, Mud and Mixtures, Water, 9, 564, https://doi.org/10.3390/w9080564, 2017.

Mélin, F. and Vantrepotte, V.: How optically diverse is the coastal ocean?, Remote Sens. Environ., 160, 235–251, https://doi.org/10.1016/j.rse.2015.01.023, 2015.

Nechad, B., Ruddick, K., and Park, Y.: Calibration and validation of a generic multisensor algorithm for mapping of total suspended matter in turbid waters, Remote Sens. Environ., 114, 854–866, https://doi.org/10.1016/j.rse.2009.11.022, 2010.

Neukermans, G., Loisel, H., Mériaux, X., Astoreca, R., and McKee, D.: In situ variability of mass-specific beam attenuation and backscattering of marine particles with respect to particle size, density, and composition, Limnol. Oceanogr., 57, 124–144, https://doi.org/10.4319/lo.2012.57.1.0124, 2012.

Neukermans, G., Reynolds, R., and Stramski, D.: Optical classification and characterization of marine particle assemblage within the western Artic Ocean, Limnol. Oceanogr., 61, 1472–1494, https://doi.org/10.1002/lno.10316, 2016.

Novoa, S., Doxaran, D., Ody, A., Vanhellemont, Q., Lafon, V., Lubac, B., and Gernez, P.: Atmospheric Corrections and Multi-Conditional Algorithm for Multi-Sensor Remote Sensing of Suspended Particulate Matter in Low-to-High Turbidity Levels Coastal Waters, Remote Sens.-Basel, 9, 61, https://doi.org/10.3390/rs9010061, 2017.

Pahlevan, N., Smith, B., Alikas, K., Anstee, J., Barbosa, C., Binding, C., Bresciani, M., Cremella, B., Giardino, C., Gurlin, D., Fernandez, V., Jamet, C., Kangro, K., Lehmann, M. K., Loisel, H., Matsushita, B., Hà, N., Olmanson, L., Potvin, G., Simis, S. G., VanderWoude, A., Vantrepotte, V., and Ruiz-Verdù, A.: Simultaneous retrieval of selected optical water quality indicators from Landsat-8, Sentinel-2, and Sentinel-3, Remote Sens. Environ., 270, 112860, https://doi.org/10.1016/j.rse.2021.112860, 2022.

Portillo Juan, N. and Negro Valdecantos, V.: Review of the application of Artificial Neural Networks in ocean engineering, Ocean Eng., 259, 111947, https://doi.org/10.1016/j.oceaneng.2022.111947, 2022.

Renosh, P., Schmitt, F. G., Loisel, H., Sentchev, A., and Mériaux, X.: High frequency variability of particle size distribution and its dependency on turbulence over the sea bottom during re-suspension processes, Cont. Shelf Res., 77, 51–60, https://doi.org/10.1016/j.csr.2014.01.024, 2014.

Reynolds, R. A. and Stramski, D.: Optical characterization of marine phytoplankton assemblages within surface waters of

the western Arctic Ocean, Limnol. Oceanogr., 64, 2478–2496, https://doi.org/10.1002/lno.11199, 2019.

Reynolds, R. A., Stramski, D., and Neukermans, G.: Optical backscattering by particles in Arctic seawater and relationships to particle mass concentration, size distribution, and bulk composition, Limnol. Oceanogr., 61, 1869–1890, https://doi.org/10.1002/lno.10341, 2016.

Sazhin, A., Artigas, L. F., Nejstgaard, J., and Frischer, M.: The colonization of two Phaeocystis species (Prymnesiophyceae) by pennate diatoms and other protists: A significant contribution to colony biomass, Biogeochemistry, 83, 137–145, https://doi.org/10.1007/s10533-007-9086-2, 2007.

Shchepetkin, A. F. and McWilliams, J. C.: The regional oceanic modeling system (ROMS): a split-explicit, free-surface, topography-following-coordinate oceanic model, Ocean Model., 9, 347–404, https://doi.org/10.1016/j.ocemod.2004.08.002, 2005.

Steinmetz, F. and Ramon, D.: Sentinel-2 MSI and Sentinel-3 OLCI consistent ocean colour products using POLYMER, in: Remote Sensing of the Open and Coastal Ocean and Inland Waters, edited by: Frouin, R. J. and Murakami, H., International Society for Optics and Photonics, SPIE, 10778, 46–55, https://doi.org/10.1117/12.2500232, 2018.

Steinmetz, F., Deschamps, P.-Y., and Ramon, D.: Atmospheric correction in presence of sun glint: application to MERIS, Opt. Express, 19, 9783–9800, https://doi.org/10.1364/OE.19.009783, 2011.

Tran, T. K., Duforêt-Gaurier, L., Vantrepotte, V., Jorge, D. S. F., Mériaux, X., Cauvin, A., Fanton d'Andon, O., and Loisel, H.: Deriving Particulate Organic Carbon in Coastal Waters from Remote Sensing: Inter-Comparison Exercise and Development of a Maximum Band-Ratio Approach, Remote Sens.-Basel, 11, 2849, https://doi.org/10.3390/rs11232849, 2019.

Twardowski, M. S., Boss, E., Macdonald, J. B., Pegau, W. S., Barnard, A. H., and Zaneveld, J. R. V.: A model for estimating bulk refractive index from the optical backscattering ratio and the implications for understanding particle composition in case I and case II waters, J. Geophys. Res., 106, 14129–14142, https://doi.org/10.1029/2000JC000404, 2001.

Van der Zande, D., Lacroix, G., and Ruddick, K.: Observing and explaining the timing of spring/summer algal blooms in the Southern North Sea using ocean colour remote sensing, in: Proceedings of the Ocean Optics XXI, Glasgow, Scotland, 8-12 October 2012.

Vantrepotte, V., Brunet, C., Mériaux, X., Lécuyer, E., Vellucci, V., and Santer, R.: Bio-optical properties of coastal waters in the Eastern English Channel, Estuarine, Coast. Shelf Sci., 72, 201–212, https://doi.org/10.1016/j.ecss.2006.10.016, 2007.

Vantrepotte, V., Loisel, H., Mélin, F., Desailly, D., and Duforêt-Gaurier, L.: Global particulate matter pool temporal variability over the SeaWiFS period (1997–2007), Geophys. Res. Lett., 38, L02605, https://doi.org/10.1029/2010GL046167, 2011.

Vantrepotte, V., Loisel, H., Dessailly, D., and Mériaux, X.: Optical classification of contrasted coastal waters, Remote Sens. Environ., 123, 306–323, https://doi.org/10.1016/j.rse.2012.03.004, 2012.

Vantrepotte, V., Danhiez, F.-P., Loisel, H., Ouillon, S., Mériaux, X., Cauvin, A., and Dessailly, D.: CDOM-DOC relationship in contrasted coastal waters: implication for DOC retrieval from ocean color remote sensing observation., Opt. Express, 23, 33–54, https://doi.org/10.1364/OE.23.000033, 2015.

Varona, H., Veleda, D., Silva, M., Cintra, M., and Araujo, M.: Amazon River plume influence on Western Tropical Atlantic dynamic variability, Dynam. Atmos. Oceans, 85, 1–15, https://doi.org/10.1016/j.dynatmoce.2018.10.002, 2019.

Velegrakis, A., Gao, S., Lafite, R., Dupont, J., Huault, M., Nash, L., and Collins, M.: Resuspension and advection processes affecting suspended particulate matter concentrations in the central English Channel, J. Sea Res., 38, 17–34, https://doi.org/10.1016/S1385-1101(97)00041-5, 1997.

Woźniak, S. B., Stramski, D., Stramska, M., Reynolds, R. A., Wright, V. M., Miksic, E. Y., Cichocka, M., and Cieplak, A. M.: Optical variability of seawater in relation to particle concentration, composition, and size distribution in the nearshore marine environment at Imperial Beach, California, J. Geophys. Res., 115, C08027, https://doi.org/10.1029/2009JC005554, 2010.

Woźniak, S. B., Meler, J., Lednicka, B., Zdun, A., and Stoń-Egiert, J.: Inherent optical properties of suspended particulate matter in the southern Baltic Sea, Oceanologia, 53, 691–729, https://doi.org/10.5697/oc.53-3.691, 2011.

Woźniak, S. B., Darecki, M., Zabłocka, M., Burska, D., and Dera, J.: New simple statistical formulas for estimating surface concentrations of suspended particulate matter (SPM) and particulate organic carbon (POC) from remote-sensing reflectance in the southern Baltic Sea, Oceanologia, 58, 161–175, https://doi.org/10.1016/j.oceano.2016.03.002, 2016.

Wu, Y., Fang, H., Huang, L., and Cui, Z.: Particulate organic carbon dynamics with sediment transport in the upper Yangtze River, Water Res., 184, 116193, https://doi.org/10.1016/j.watres.2020.116193, 2020.

State Planet, 1-osr7, 12, 2023
https://doi.org/10.5194/sp-1-osr7-12-2023

Recent changes in extreme wave events in the south-western South Atlantic

Carolina B. Gramcianinov[1], Joanna Staneva[1], Celia R. G. Souza[2,3], Priscila Linhares[3], Ricardo de Camargo[4], and Pedro L. da Silva Dias[4]

[1]Institute for Coastal Systems Analysis and Modeling, Helmholtz-Zentrum Hereon, Max-Planck-Straße 1, 21502 Geesthacht, Germany
[2]Institute of Environmental Research, Secretariat of Environment, Infrastructure and Logistics of São Paulo State (SEMIL/SP), Rua Joaquim Távora 822, 04015-011, São Paulo – SP, Brazil
[3]Department of Physical Geography, Faculty of Philosophy, Literature and Human Sciences, University of São Paulo (FFLCH/USP), Av. Prof. Lineu Prestes, 338, 05508-000, São Paulo – SP, Brazil
[4]Department of Atmospheric Sciences, Institute of Astronomy, Geophysics and Atmospheric Science, University of São Paulo, Rua do Matão, 1226, 05508-090, São Paulo – SP, Brazil

Correspondence: Carolina B. Gramcianinov (carolina.gramcianinov@hereon.de)

Received: 31 July 2022 – Discussion started: 23 September 2022
Revised: 8 March 2023 – Accepted: 31 March 2023 – Published: 27 September 2023

Abstract. Over the past decades, the South Atlantic Ocean has experienced several changes, including a reported increase in coastal erosion and floods. This study aims to investigate the recent changes in the extreme wave events over the south-western South Atlantic (SWSA) – which hosts the most economically important harbours in South America, high oil and gas production demands, and rich biodiversity. This investigation considers not only the occurrence of extreme wave events but also extreme wave indicators that characterise the potential wave impact on offshore and coastal areas. Extreme wave events are obtained using the averaged monthly 95th percentile of significant wave height (H_s) from 1993 to 2021, combining the CMEMS global wave reanalysis and near-real-time products. Annual and seasonal statistics are derived to analyse mean and extreme wave climate and trends in the study region, focusing on H_s, peak period, and wave power. The analysis gives an overview of the wave climate in the study domain, including a discussion about seasonal differences. For a more direct application to future risk assessment and management, we perform an analysis considering the regional monitoring and warning system division established by the Brazilian Navy. We used a coastal hazard database that covers a portion of the coast to investigate how the trends given by the CMEMS wave products may impact the coastal zone. Our findings showed significant changes in the SWSA mainly associated with an increase in mean values of H_s, wave period, and consequently the wave power. Narrowing down to the coastal impact, we found an increase in the number of coastal hazards in the State of São Paulo associated with waves, which agrees with the increase in the number of extreme wave events in the adjacent ocean sector. However, the increased number of coastal events is also driven by local factors.

Published by Copernicus Publications.

1 Introduction

In recent years, several extreme events have been reported in the South Atlantic Ocean (e.g. Marcello et al., 2018; Dalagnol et al., 2022), thus directly reflecting hazards along the coast. One of the regions that are facing relevant changes is the south-western South Atlantic (SWSA), with an increase in extreme wave and storm surge occurrences (Souza et al., 2019; Gramcianinov et al., 2023). With high economic relevance, the SWSA region hosts strategic harbours in South America, where 7.55×10^8 t of goods were transported in 2021 (ANTAQ, 2022), and promising oil and gas exploration fields. In addition, the region also holds rich biodiversity, including coral reefs and 856 km^2 of mangroves that are crucial for coastal hazard protection, economic activities (e.g. fishery), and the cultural identity of the coastal communities (ICMBio, 2018; Pereira-Filho et al., 2021). The SWSA coastal cities have a dense population, with approximately 20 million people who are extremely vulnerable to coastal erosion and infrastructure damage (Zamboni and Nicolodi, 2008).

Assessing the extreme waves and wave trends in the SWSA with traditional approaches has proven to be challenging for several reasons. The difficulties remain mostly in the still-limited understanding of the local physical processes (e.g. wave–current interaction) and climate variabilities (e.g. the overlapping effect teleconnections). The limited accuracy of long-term integrations and the scarce data availability can make these analyses even more difficult. Some recent studies have revealed changes in the wave pattern in the South Atlantic, usually ascribed to the increase in the extreme waves in the Southern Ocean (SO). In general, previous global or hemisphere-based studies have reported increases in wave height extremes in the Southern Hemisphere (SH) over the past 41 years, and this tendency is expected to continue in the future (Caires and Sterl, 2005; Dobrynin et al., 2012; Lemos et al., 2019). However, when focusing on the SWSA, the mean and extreme wave climate trends present larger uncertainties.

In addition to understanding the significant wave height (H_s) trends, assessing changes in wave event characteristics, such as the mean wave direction and peak period, is of utmost importance. Silva et al. (2020) showed how the oscillation between the southern and eastern dominant wave energy flux directions has led to changes in the coastal morphodynamics at both regional and local scales. Some previous works reported wave power changes under the present climate (Odériz et al., 2021; 1979–2018) and mean wave direction and period changes in both present (Hemer et al., 2010; 1989–2005) and future climate (Lobeto et al., 2021; 2081–2100). These changes directly affect naval and coastal risk assessments, requiring special efforts to properly link the global-scale findings to regional and local wave extremes.

Against such a background, this section aims to report and investigate the recent extreme wave climate trends (1993–

Table 1. Copernicus Marine Service (CMEMS) and non-CMEMS products used in this study, including the Quality Information Document (QUID) and Product User Manual (PUM).

Product ref. no.	Product ID and type	Data access	Documentation
1	GLOBAL_MULTIYEAR_WAV_001_032 (WAVERYS), numerical models	EU Copernicus Marine Service Product (2021)	QUID: Law-Chune et al. (2021b); PUM: Law-Chune (2022)
2	GLOBAL_ANALYSIS_FORECAST_WAV_001_027 (GLO-NRT), numerical models	EU Copernicus Marine Service Product (2022)	QUID: Aouf (2022); PUM: Dalphinet et al. (2022)
3	Baixada Santista Coastal Hazards database (BDe-BS), dataset	Personal contact	Souza et al. (2019, 2022)

2021) in the SWSA while focusing on wave event characteristics such as event frequency, intensity, duration, and peak period. We examined the seasonal statistics and climatic trends using both traditional (i.e. percentile-based) and storm-based approaches to provide new insights into the regional wave climate changes. To obtain results with more direct application to future risk assessment and management, we performed an analysis considering the regional monitoring and warning system, as well as the impact of the recent wave climate changes on the coast.

2 Methods

2.1 Datasets

The main dataset used in this work was the Copernicus Marine Service (CMEMS) global reanalysis, named WAVERYS (product ref. no. 1; Table 1; Law-Chune et al., 2021a), available from 1993 to 2020. To include 2021 in the analysis, the WAVERYS was complemented with data from the CMEMS Global Ocean Waves Analysis Near Real Time product (GLO-NRT; product ref. no. 2; Table 1). The combination (in time) of these two products is hereafter referred to as CMEMS wave products. WAVERYS is available at a $1/5°$ horizontal grid as 3-hourly outputs from 1993 to 2020, while the wave analysis has a $1/12°$ horizontal grid as 3-hourly instantaneous output fields. The GLO-NRT product was interpolated to the 0.20° horizontal grid, so a more consistent analysis can be achieved despite using different sources. Both products are produced using the Météo-France Wave Model (MFWAM) with the dissipation terms developed by Ardhuin et al. (2010). WAVERYS is forced by hourly surface winds and daily sea-ice fraction fields derived from the fifth-generation reanalysis from the European Centre for Medium-Range Weather Forecasts (ECMWF) (ERA5; Hersbach et al., 2020) and ocean currents obtained from the ocean reanalysis Global Ocean Reanalysis and Simulation (GLORYS). The GLO-NRT is forced only by a 6-hourly wind analysis from the IFS-ECMWF atmospheric system.

An evaluation of WAVERYS for the western South Atlantic wave climate was made by Crespo et al. (2022). The authors compared H_s from the WAVERYS, ERA5, and the National Centers for Environmental Prediction (NCEP) wave reanalysis (Chawla et al., 2013) against wave buoy measurements at three locations along the Brazilian coast and found that WAVERYS presented the highest correlation and the lowest root mean square deviation (RMSD). The ERA5 performance in representing the winds is also relevant as the quality of the forcing field is crucial in a wave simulation. Previous works have shown that ERA5 can represent the wind climate, extreme percentiles, and storm variability (e.g. Belmonte Rivas and Stoffelen, 2019; Gramcianinov et al., 2020a; Crespo et al., 2022).

2.2 Percentile computation

In this work, the percentiles were computed using the empirical distribution of the H_s peaks ($H_{s_{peaks}}$) within a given period, thus allowing us to obtain a more detailed view of individual wave events' occurrence. The selected $H_{s_{peaks}}$ must be separated by a minimum of 48 h to guarantee the independence of the peaks. This time window has been widely applied in past studies to ensure the collection of one peak per storm (e.g. Caires and Sterl, 2005; Meucci et al., 2020). Besides that, 48 h is a suitable but not so restrictive time threshold for extreme-wave analysis in the region, particularly considering the differences among the seasons. The 95th percentile was computed based on the monthly $H_{s_{peaks}}$ distribution at each grid point. Using these monthly 95th percentiles, we calculated the annual and seasonal means to analyse trends and proceed with the wave event analysis (Sect. 2.4). The seasonal mean of the monthly 95th percentiles was computed for the summer and winter, using the average December–January–February (DJF) and June–July–August (JJA), respectively, thus having one value per year. The annual percentiles were computed by the average of all monthly percentiles within the year. As a final result, we have a mean annual and seasonal percentile time series at each grid point.

2.3 Trend estimation and testing

Trends were estimated based on Sen's slope estimator (Sen, 1968), which evaluates the magnitude of a time series trend. The significance of Sen's slope was calculated by the Mann–Kendall test (Mann, 1945; Kendall, 1975), considering a p value lower than 0.05. Both methods are non-parametric (distribution-free) procedures and consider the monotonic increase upward or downward of the time series, thus being more robust to climate-based analysis (e.g. Wang et al., 2020).

2.4 Extreme-wave-event analysis

The wave event statistics were derived following the methods developed by Weisse and Günther (2007), in which consecutive points over a specific threshold within a given time series are considered to define extreme wave events. This event-counting process was performed for each grid cell considering its unique severe event threshold (SET), defined herein as the average of the monthly 95th percentile of $H_{s_{peaks}}$ considering the whole period (1993–2021). Notably, there is no widely accepted method for selecting threshold values, and values between the 90th and 99th percentile H_s are often used (De Leo et al., 2020; Gramcianinov et al., 2020b). Moreover, the use of the averaged monthly percentile results in a smoothed field, especially due to the $H_{s_{peaks}}$ variability among the year. In this way, for some locations, the exceedance of events above SET was larger than 5 %.

Following Weisse and Günther (2007), the intensity is equal to the difference between the maximum H_s of the event and the SET at that point. The wave event statistics, such as the number of events, intensity, mean wave direction, and peak period, are presented herein as annual and seasonal means to build the spatial distribution and trends and obtain the spatially averaged time series. The intensity and wave parameters were calculated by averaging all individual events (above SET) within the year or season. The same analysis was applied successfully in the Black Sea by Staneva et al. (2022), allowing a better understanding of the extreme wave events' spatial distribution and trends. More details about these methods can be found in Weisse and Günther (2007).

2.5 Wave power calculation

Following Staneva et al. (2022), we also calculated the wave power in the study domain. Wave power or wave energy flux was obtained following Eq. (1):

$$P = \left(\frac{\rho\ g^2}{64\ \pi}\right)\ {H_s}^2\ T_e, \quad (1)$$

where P is the wave energy flux per unit of wave-crest length (kW m^{-1}), ρ is water density, g is the acceleration due to gravity, H_s is the significant wave height, and T_e is the wave energy period. T_e is directly available in the WAVERYS products (named VTM10) and is defined as the mean wave period obtained by the $T_e \equiv T_{m_{-1,0}} = m_{-1}/m_0$, based on the -1th and 0th moment of the wave spectrum.

2.6 Coastal risk assessment

Warnings and risk assessment in this region are supervised by the Centre of Hydrography of the Brazilian Navy (CHM, from *Centro de Hidrografia da Marinha*), which is recognised by the World Meteorological Organization (WMO) as the issue service for the MetArea V (Atlantic waters west of 7° N–35.8° S, 20° W). According to the CHM monitoring system, the coastal region of SWSA can be divided into four subareas (Fig. 1). These subareas were used to analyse the wave climate trends in the domain, considering the regional specificity and facilitating future discussions about risk management. This analysis may facilitate the applicability of the results found here to improve future monitoring and warning system development.

We used a historical database of coastal hazards in the State of São Paulo, within subarea C, to further investigate coastal impacts. The Baixada Santista Coastal Hazards database (BDe-BS; product ref. no. 3; Table 1) covers the period from 1928 to 2021 and is obtained using the hemerographic method (mostly newspapers) and material from social media (mostly videos), showing coastal impacts caused by strong waves and anomalously high tides (either meteorological or astronomical tides) (Souza et al., 2019; Linhares et al., 2021; Souza et al., 2022). The definition of coastal hazards is mainly based on processes such as coastal erosion and/or coastal inundation, the latter also forced by continental flooding (heavy rainfall) in estuarine areas. Therefore, the coastal hazards registered in the BDe-BS represent events with high intensity since they were brought to the attention of the public due to their significant impact on the beaches, destruction of urban structures, and public and private properties, as well as disruption of the city's day-to-day and port activities. More details regarding the database can be found in Souza et al. (2019).

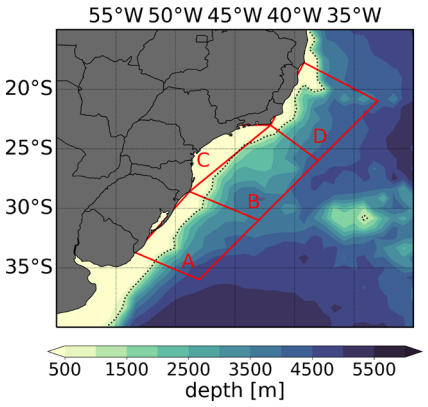

Figure 1. The south-western South Atlantic Ocean with subareas A to D defined by the Brazilian Navy for warning and monitoring operations within MetArea V. Shaded values are the bathymetry from ETOPO1.

Currently, the BDe-BS initiative is maintained by the São Paulo state government through the "Preventive Plan for Coastal Erosion, Coastal Inundation, and Flooding" (adapted from the Portuguese: *Plano Preventivo de Defesa Civil para Erosão Costeira, Inundações Costeiras e Enchentes/Alagamentos causadas por Eventos Meteorológicos-Oceanográficos Extremos como Ressacas do Mar e Marés Altas*). Despite representing a small portion of the coastal area of the SWSA, the number of intense/extreme events reaching the São Paulo state coast can be considered representative of most of the coastal extension of the domain in this study, except for subarea D (see Fig. 1). The reason for this extrapolation is mainly the lack of long-term records in other locations. In addition, the database covers the central portion of the study region in a region with high economic importance.

3 Results

3.1 Extreme-wave-climate characterisation

The 95th percentile distribution, with its gradient towards the south (Fig. 2a, e, i) followed by the concentration of more intense extreme events to the southern portion of the domain (Fig. 2c, g, k), reflects the influence of the South Atlantic

storm track in the region. The storm track controls the extreme wave climate in the SWSA due to the strongest winds associated with the cyclones (e.g. Campos et al., 2018), and it is located between 55 and 30° S (Hoskins and Hodges, 2005; Gramcianinov et al., 2019).

Despite sharing a common extreme-wave-generation source, as is possible to see by the similar mean-wave-direction distribution (Fig. 2d, h, l), summer (DJF) and winter (JJA) present distinct wave patterns due to the southward shift in the storm track in the summertime (Hoskins and Hodges, 2005). Thus, the summer presents smaller values of H_s – and consequently 95th percentile $H_{s_{peaks}}$ ($H_{s_{p95}}$ hereafter) values (Fig. 2e) – in the study domain, which is reflected a lower number of events (Fig. 2f) and weaker events (Fig. 2g) than winter and the whole period. Climatologically, the austral autumn (MAM) presents behaviour closer to the summer pattern, while spring (SON) and winter patterns are similar. In this study, we further analyse the whole period and winter since summer does not present many cases.

During the winter, the main storm track is in its northernmost position (Hoskins and Hodges, 2005), resulting in more wave events than in other seasons (Fig. 2j). Typically, in winter, the region presents relatively long fetches along the coast (south-west-/north-east-oriented) associated with cyclones generated at approximately 35° S (Gramcianinov et al., 2021). These fetches can be widely intensified by rear anticyclones on the western side of the cyclone, thus causing this configuration to be widely related to the most severe cases observed in the domain (e.g. da Rocha et al., 2004; Machado et al., 2010; Dragani et al., 2013).

The high number of events in the northern boundary of the domain (Fig. 2b, j) can be associated with the South Atlantic Subtropical High (SASH), which is also a generating system in the study region (Pianca et al., 2010). The SASH mostly influences the wave climate by generating easterly waves towards central Brazil, northward from 23° S. However, the wave events in this location are associated with relatively small H_s, as is possible to see by the local $H_{s_{p95}}$ values (Fig. 2a, i) and wave event intensities (Fig. 2c, k). For instance, the $H_{s_{p95}}$ values in the northern portion of the domain do not reach 3.5 m in the winter (Fig. 2i).

The overall pattern and values presented in Fig. 2 agree with previous studies, even though methodological differences exist, thus making a straightforward comparison difficult. For instance, Gramcianinov et al. (2020b), using the 90th percentile computed through a spatially varying time window, found a mean of 1.3 and 5.5 extratropical cyclones per year associated with extreme wave events in the region in the summer and winter, respectively. These values are comparable with the number of events presented in the maps of Fig. 2b, g, and l. Regarding the intensity, the same authors found a mean H_s of 6.5 m associated with these cyclone events, which is also comparable to the intensity values (above the percentile) in some locations of the study domain (Fig. 2c, h, m). Moreover, Machado et al. (2010) accessed extreme wave events in the coastal region between 30°S and 32°S and found a mean of 1.33 events per year above the 90th percentile between 1979 and 2008. We also reported this relatively small value at this exact location in Fig. 2b, g, and l. In this way, the method applied herein presents robust results according to what is reported in the region.

3.2 Extreme wave event trends

The monthly $H_{s_{p95}}$ trends present a sparse and weak signal in the study domain, except for the winter (Fig. 3f). The southern coast presents a significant increase in the $H_{s_{p95}}$ values, which are greater than 2 cm yr^{-1} in some locations during the wintertime. When looking at the mean H_s trend, it is possible to see a general increase in this wave parameter along the Brazilian continental shelf, covering the coastal and offshore regions. The magnitude of the mean H_s increase is small (< 0.2 cm yr^{-1}) but significant in the whole period (Fig. 3b). The mean H_s increase in winter is relatively greater (between 0.4 and 0.8 cm yr^{-1}; Fig. 3g). The differences between the mean and $H_{s_{p95}}$ trend signal are in agreement with the findings of Young and Ribal (2019), who showed that the H_s distribution changes in the last years were skewed to the left, with an increase in small waves – which can change the mean without changing the extreme percentiles. The trends in the number of extreme wave events also present sparse behaviour, but with significant increases along the Brazilian coast (Fig. 3c, h). The event increase occurs on most of the coast in the whole-period analysis, while it is confined to some portions of the southern and south-eastern coast during the winter (Fig. 3h). It is important to note that the rise in the number of events does not follow the $H_{s_{p95}}$ trend pattern.

Figure 3 also shows the spatial trends of the mean distribution of the wave peak period and wave power during the events (Fig. 3d, e, i, j). There is a general increase in the peak period in the study domain, confined to the central portion of the coast in the winter (Fig. 3i). The increase in wave period and H_s can lead to important changes in the wave power (Eq. 1). Note that for the wave power calculation, T_e was used, and the trends presented in Fig. 3d and i are based on the T_p. However, considering a JONSWAP wave spectrum, T_e is directly related to T_p ($T_e = 0.9 \times T_p$; Guillou, 2020). The wave power presents a small but significant increase along the coast in the whole period and wintertime (Fig. 3e, j), reaching maximum values (> 0.2 kW m^{-1} yr^{-1}) offshore of the southern Brazilian and Uruguayan coast (30–40° S) in the winter. Following the mean H_s behaviour, the increase in the wave power is larger in the winter than in the whole period – as expected, as wave power is proportional to H_s^2 (Eq. 1). Other extreme event indicators, such as intensity, mean wave direction, and lifetime, did not present a robust trend signal and, therefore, are not shown.

The extreme-event analysis based on each grid point in a high-resolution hindcast provides a more detailed view of pattern changes along the coast. On the other hand, such an

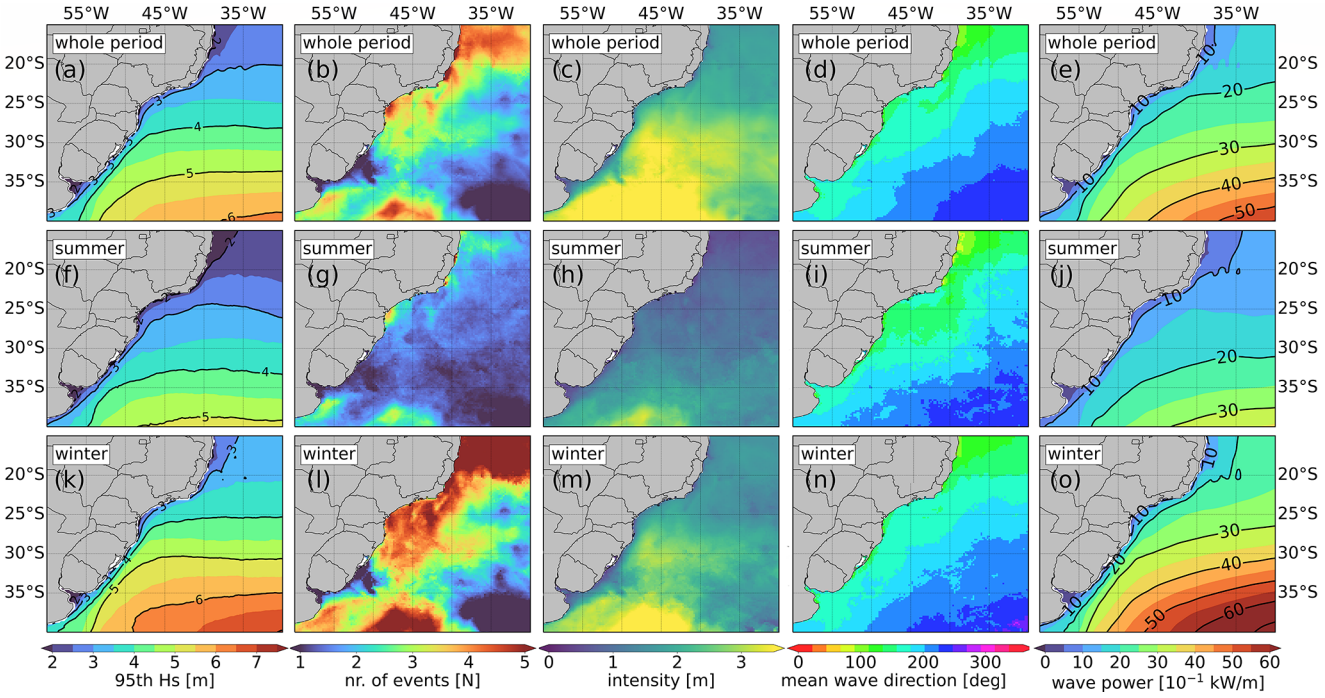

Figure 2. **(a, f, k)** Averaged monthly 95th percentile $H_{s_{peaks}}$ value (m), **(b, g, l)** extreme-wave-event number, **(c, h, m)** intensity (H_s–95th $H_{s_{peaks}}$) (m), **(d, i, n)** mean direction (degrees), and **(e, j, o)** mean wave power (10^{-1} kW m^{-1}) in **(a–e)** the whole period (1993–2021), **(f–j)** summer (DJF), and **(k–o)** winter (JJA) based on the CMEMS wave products (product ref. nos. 1 and 2; Table 1).

analysis can produce sparse results that may not be easily applied to more practical and operational tasks. Therefore, the trends in some event parameters were analysed for each Brazilian Navy monitoring and warning subarea (Fig. 4). For this analysis, we focused on the parameters with significant trends in at least one region and season, although both whole-period and winter trends are presented in Fig. 4 for consistency. Both subareas C and D present a significant increase in the number of events in the whole period. The trends of 0.2 and 0.28 events per year represent an increase of $\sim 20\,\%$ in subareas C and D in 29 years (based on the increase in the annual mean of their series). Together with subarea B, these regions also present an increase in the mean wave power – despite no significant change in the peak period. In the winter, subareas A and C present significant trends in the number of events per year, representing a 27.2 % and 20 % increase, respectively. Subarea C presents a small but significant increase in peak period in the winter, as well as in the wave power. The wave power also increases in subarea D in the winter.

By the time series, it is possible to note a high interannual variability due to large-scale climate modes that affect the regional wave climate through storm track shifts (e.g. Sasaki et al., 2021). The SWSA is affected by many large-scale variability modes that interact, which are widely studied in the atmosphere but not well understood in the wave fields (Godoi et al., 2020; Godoi and Torres Júnior, 2020; Sasaki et al., 2021), which make it difficult to correlate climate indexes with wave parameters directly. However, even considering these variabilities, most parameters present a positive trend, although not always significant. As explained in Sect. 2.3, we consider the Mann–Kendall test to assess the significance of the trends. The sensitivity of the Mann–Kendall test may be related to the large variance of the time series, which directly influences the trend detected by this method (Wang et al., 2020).

3.3 Coastal risk analysis

The Charlies subarea (C) is one of the most affected locations, experiencing an increased number of extreme wave events, peak periods, and wave power in the last years. However, linking the changes in the regional wave climate with coastal hazards is not a straightforward task as the wave systems are modified by bathymetry, and their impact depends on the coastal morphodynamics. Table 2 presents the number of events recorded by the BDe-BS and the computed trends for each type of hazard. The São Paulo coast was affected by 163 hazards between 1993 and 2021, of which 48 % (78) were caused exclusively by storm waves and 30 % (49) by the combination of waves and tides (as a result of either astronomical or meteorological tides). In the winter, 93 % (51) of events are associated with waves, with combined events showing a similar proportion (35 %) of total events com-

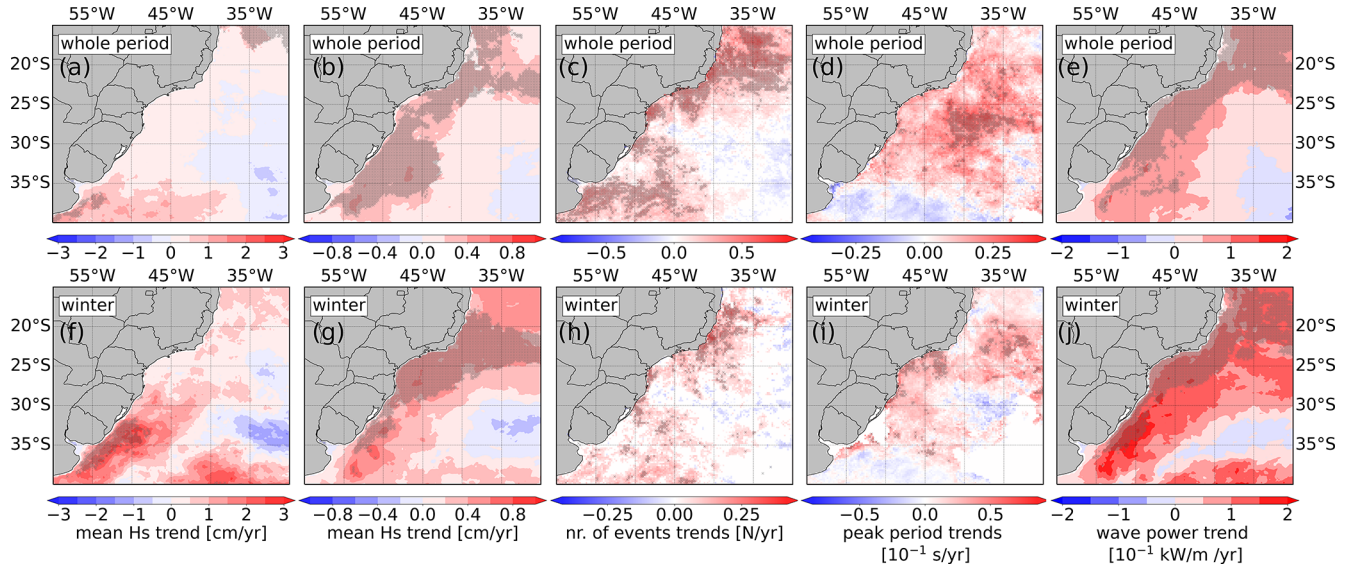

Figure 3. Trends in the **(a, f)** 95th percentile $H_{s_{peaks}}$ (cm per year), **(b, g)** mean H_s (cm per year), **(c, h)** number of extreme wave events (number per year), **(d, i)** peak period of the events (10^{-1} s yr^{-1}), and **(e, j)** mean wave power (10^{-1} kW m^{-1} yr^{-1}) in the **(a–e)** whole period and **(f–j)** winter (JJA) based on the CMEMS wave products (product ref. nos. 1 and 2; Table 1). Grey crosses represent points where the trend is significant (Mann–Kendall test, p value ≤ 0.05).

pared to the whole period (30 %). Thus, the hazards forced exclusively by anomalous tides are rare in the winter, which may be related to the high wave event frequency in this season. The number of events on the coast increased both for the whole period and in winter (JJA). The increase in the number of coastal hazards was mainly led by wave events since events caused only by tidal influence did not present any significant trend. The results show an increase of 120 % and 145 % of total events and wave-forced events on the coast in 29 years, considering the whole-period mean. This high increase is in agreement with Souza et al. (2019), who found a pronounced increase in wave-forced hazards after the decades 2000–2009 and 2010–2019 (226 % compared with the 1928–1999 period) when analysing a longer period of the same database (1928–2016).

Figure 5 shows the time series of the yearly events of coastal hazards from the BDe-BS against the spatial sum of the number of events in subarea C obtained by the wave event analysis (described in Sect. 2.4). Due to the small number of coastal hazards per year, we show the time series and trends for the whole period to obtain more robust statistics. Nevertheless, the winter trends presented the same signal and relation among the event types as the whole period trends (see Table 2). Note that the absolute numbers of events recorded on the coast and obtained in subarea C are not comparable. This analysis aims to evaluate the similarity in the variability and trends of the time series. The number of events presented for subarea C in Fig. 5 is the sum of events in all grid points within defined boundaries.

Most of the coastal hazards reported by the BDe-BS are associated with waves, combined or not with a tidal rise. This is revealed by the numbers not only in Table 2 but also in the time series (Fig. 5a). The trends of all events and events associated with waves are similar, especially considering the trend error. It is possible to compare the trends in the coastal hazards forced by waves (0.22 events per year; Table 2) with the trends of the number of extreme wave events in subarea C (Fig. 5b; 0.20 events per year in Fig. 4a). However, considering the mean number of coastal events forced by waves (4.4 events per year), the increase on the coast corresponds to 145 % in 29 years.

Although there is no total agreement between the extreme events detected in subarea C and hazards reported on the coast in the year-by-year analysis, the trend behaviour is similar. The number of combined events (wave + tides) and the total event trend are superposed in Fig. 5b. These overlaid pictures show that differences in the wave-forced coastal hazards and extreme wave events in subarea C may result from the influence of sea-level-elevation events forced by storms or astronomical tides. For instance, 2002 and 2009 do not present a peak in the extreme wave events within subarea C, but they were marked by a high number of wave-forced coastal hazards related to a higher percentage of combined events. These wave events would not become a hazard if the local sea level elevation did not allow waves to reach further into the continental area. In addition, the disagreement between the coastal and offshore event time series can be addressed for bathymetry and morphology reasons.

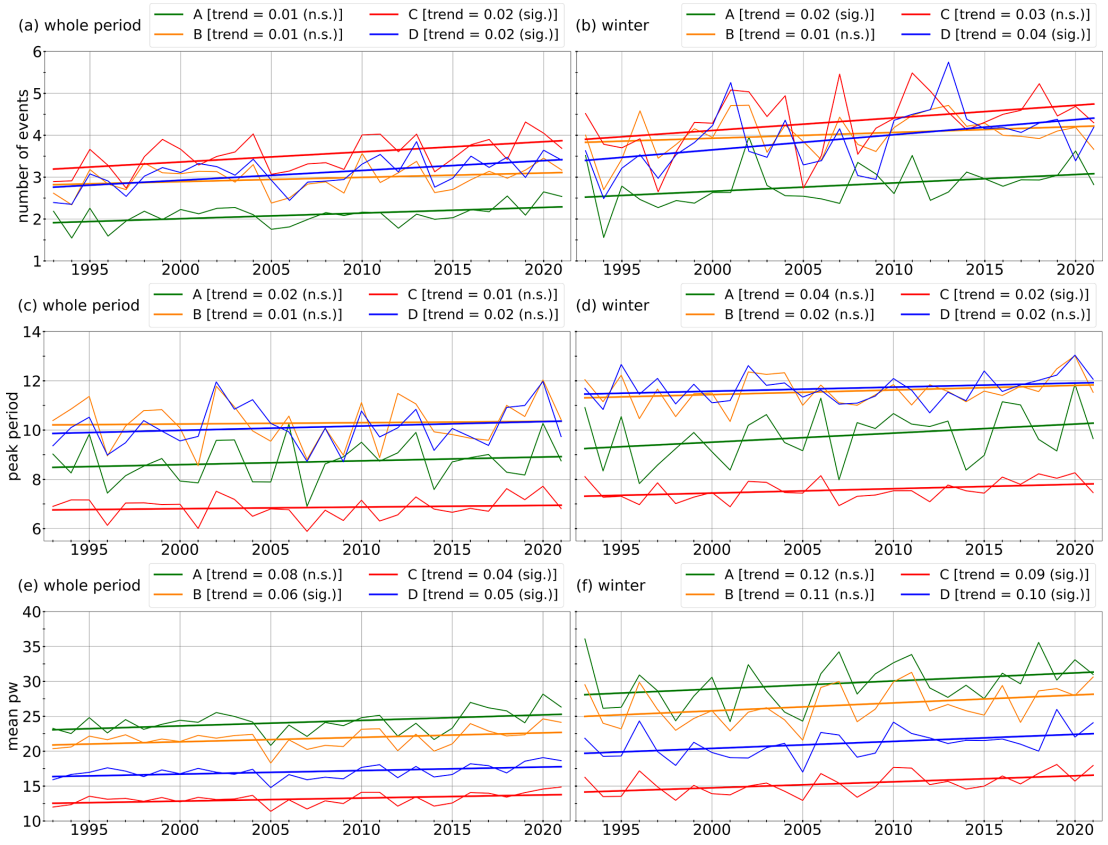

Figure 4. Annual time series and trends for the **(a, b)** number of extreme wave events (number per month), **(c, d)** mean peak period of the events (s), and **(e, f)** mean wave power (10^{-1} kW m^{-1}) in the **(a, c, e)** whole period and **(b, d, f)** winter (JJA) computed for each Brazilian Navy warning subarea along the study domain's coast (Fig. 1) based on the CMEMS wave products (product ref. nos. 1 and 2; Table 1). The trends are presented in the legend, and the units are number per year, 10^{-1} s yr^{-1}, and 10^{-1} kW m^{-1} yr^{-1}, respectively. The abbreviations "n.s." and "sig." in the legend mean "not significant" and "significant", respectively, according to the Mann–Kendall test (p value ≤ 0.05).

Moreover, coastal hazards can also occur after a sequence of events that result in a more vulnerable coast due to the lack of recovery time (Souza et al., 2019). For instance, these additional elements to coastal erosion can explain why the total increase in wave-forced events recorded on the coast in 29 years (145 %) is much larger than the increase in subarea C ($\sim$ 20 %). In this case, the human-made modification of the shoreline may intensify the damaging effects of the increase in extreme wave events (Muehe, 2018).

4 Conclusion

The present work aims to assess changes in the extreme wave climate in the SWSA, giving new insights into offshore coastal risk assessment and management in this domain. Understanding the extreme wave changes is crucial for supporting future projections, which are indispensable for the design and safety control of ship vessels, offshore and coastal structures and maintenance (e.g. oil/gas platforms, aquaculture, wind and wave farms), and coastal infrastructure (e.g. ports, roads, and touristic facilities) (e.g. Bitner-Gregersen et al., 2018; Vettor and Guedes Soares, 2020). Our findings show important changes in the SWSA mainly associated with an increase in the mean H_s values and wave period. These changes directly impact the offshore and coastal zone, increasing the wave power reaching the region and, consequently, aggravating the coastal hazards along the coast.

Even though extreme waves have a major role in coastal flooding and coastal erosion (e.g. Parise et al., 2009; Machado and Calliari, 2016), there still exists a lack of knowledge about how observed large- to regional-scale trends will affect the coast. Most of the Brazilian Navy's monitoring and warning subareas within MetArea V (WMO) require attention regarding wave climate changes. According to the WAVERYS hindcast analysis, the number of extreme wave events (above the 95th percentile $H_{s_{peaks}}$) increased in subareas A, C, and D, and the mean wave power increased in subareas B, C, and D. The trends vary depending on whether the whole period or only wintertime is considered. In this work, we analyse the winter (JJA) since it shows the most extreme wave patterns, but an extension of the analysis to other seasons is recommended for the future as the autumn

Table 2. The number of coastal hazards reported by the BDe-BS (product ref. no. 3; Table 1) in the whole period (1993–2021) and in the winter (JJA). The percentage calculation is based on the total number of events, which represents the sum of events forced only by waves, only by anomalous tides (by either astronomical or meteorological components), or by a combination of both ("waves + tides"). The last row highlights all events associated with waves, with or without tidal influence ("waves"). The trend unit is events per year or season, and bold values denote significance (Mann–Kendall test, p value ≤ 0.05).

	Whole period		Winter (JJA)	
	Number of events	Trend (number per year)	Number of events	Trend (number per season)
Total	163 (100 %)	**0.23**	55 (100 %)	**0.14**
Wave + tides	49 (30 %)	**0.10**	19 (35 %)	**0.06**
Only waves	78 (48 %)	**0.12**	32 (58 %)	**0.06**
Only tides	36 (22 %)	0.01	4 (7 %)	0.01
Waves	127 (78 %)	**0.22**	51 (93 %)	**0.12**

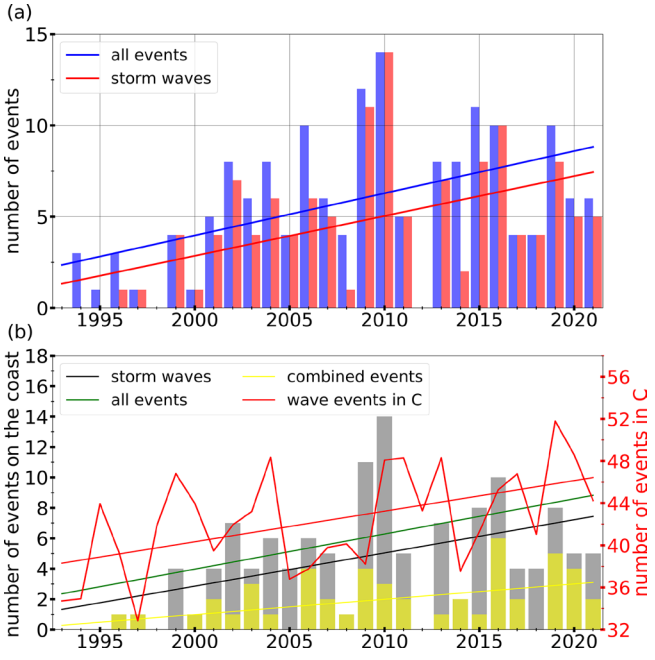

Figure 5. **(a)** Number of coastal hazards per year caused by any forcing (blue) and waves (red) based on BDe-BS (product ref. no. 3; Table 1). **(b)** Numbers and trends of coastal hazards per year associated with waves (grey bars and black line) and combined events (waves + tides; yellow bars and lines) based on BDe-BS and total number and trend of wave events in subarea C (red lines) based on the CMEMS wave products (product ref. nos. 1 and 2; Table 1). The trends presented in these panels are statistically significant (Mann–Kendall test, p value ≤ 0.05), and the values are shown in Table 2.

(MAM) and spring (SON) weather patterns are also able to produce severe waves (e.g. Crespo et al., 2022). By our findings, we recommend special attention to subareas C and D as they present changes in both the number of events and wave power.

Regarding the coastal assessment, we found an increase in the number of coastal hazards in the State of São Paulo. According to our analysis, the increase in coastal hazards in this location is mainly associated with wave forcing and can be related to the increase in the number of extreme wave events in subarea C. Despite the well-known limitation in wave modelling, particularly to extreme waves (e.g. Campos et al., 2018), this finding provides evidence that the WAVERYS hindcast may be useful to assess not only extreme wave climate in the study domain (as shown by Crespo et al., 2022) but also the events reaching the coast in the long to medium term. However, more care is needed for interannual and interseasonal analyses that require year-by-year assessment, especially because a coastal hazard depends not only on the waves. Sea level rise, both in climatic and synoptic scales, and astronomical tides play a large role, potentially turning moderate waves into damaging ones as a high sea level allows waves to propagate and break further into the continent. Souza et al. (2019) highlighted that the most severe coastal hazards reported in the region do not present the highest values of H_s or sea level elevation but a combination of factors. Many other elements, such as coastal vulnerability, precipitation, morphology, and coastline orientation, affect the establishment of a coastal hazard (e.g. Muehe, 2018; Souza et al., 2019), mainly when the hazard is defined by its impact on the coast and not by some pure meteorological and/or oceanographic parameter.

Therefore, a complete assessment of coastal impacts needs more specific analysis considering local information and data, which is impracticable in this work, considering the study domain size. However, the trends derived herein are a valuable factor in identifying areas potentially vulnerable to climate change hazards and are also useful for engineers and stakeholders working towards the sustainable development of maritime activities. These changes may require adaptation measures, such as enhancing coastal protection (e.g. building dikes and establishing harbour protection measures). The findings reported in this work may also support the design of new projects and future assessments that will allow the advancement of the association of large-scale wave climate with coastal impacts.

Code and data availability. The data products used in this article, as well as their names and documentation, are summarised in Table 1. The wave products are available through the Copernicus Marine Service (https://doi.org/10.48670/moi-00022, EU Copernicus Marine Service Product, 2021; https://doi.org/10.48670/moi-00017, EU Copernicus Marine Service Product, 2022). The Baixada Santista Coastal Hazards database (BDe-BS) is available upon request by email to Celia R. G. Souza (celia@sp.gov.br). Codes are available upon request by email to the corresponding author.

Author contributions. CBG: conceptualisation, formal analysis, methodology, visualisation, writing – original draft. JS: conceptualisation, methodology, writing – review and editing, supervision. CRGS and PLS: methodology, writing – review. RC and PLdSD: writing – editing, supervision.

Competing interests. The contact author has declared that none of the authors has any competing interests.

Disclaimer. Publisher's note: Copernicus Publications remains neutral with regard to jurisdictional claims in published maps and institutional affiliations.

Acknowledgements. The authors would like to acknowledge Marcel Ricker for his support with the wave event method implementation. The study was supported by the European Green Deal project "Large scale RESToration of COASTal ecosystems through rivers to sea connectivity" (REST-COAST) (grant no. 101037097). We gratefully acknowledge the project DOORS (grant no. 101000518) and DAM Mission project CostalFuture. Carolina B. Gramcianinov is funded by the Helmholtz European Partnering "Research Capacity Building for healthy, productive and resilient Seas" (SEAReCap) (grant no. PIE-0025). This study also used data and resources from the projects "Resposta Morfodinâmica de Praias do Sudeste Brasileiro aos Efeitos da Elevação do Nível do Mar e Eventos Meteorológico-Oceanográficos Extremos até 2100" (Coordenação de Aperfeiçoamento de Pessoal de Nível Superior – Brazil (CAPES) – finance code 88887.139056/2017-00), "Sistema de Aviso de Ressacas e Inundações Costeiras para o Litoral de São Paulo, com foco em Impactos das Mudanças Climáticas" (São Paulo Research Foundation, FAPESP; grant no. 2018/14601-0), and "Extreme wind and wave modelling and statistics in the Atlantic Ocean" (FAPESP; grant nos. 2018/08057-5 and 2020/01416-0).

Financial support. This research has been supported by the Helmholtz European Partnering programme (grant no. PIE-0025), H2020 Societal Challenges programme (grant nos. 101037097 and 101000518), and the Fundação de Amparo à Pesquisa do Estado de São Paulo (grant nos. 2018/14601-0, 2018/08057-5, and 2020/01416-0).

Review statement. This paper was edited by Marta Marcos and reviewed by Alejandro Orfila and one anonymous referee.

References

ANTAQ: Anuário da Agência Nacional de Transporttes Aquaviários (ANTAQ), Annual Report of the National Water Transportation Agency, Brazil, https://anuario.antaq.gov.br, last access: 12 May 2022 (in Portuguese).

Aouf, L.: EU Copernicus Marine Service Quality Information Document for Global Ocean Waves Analysis and Forecasting Product, GLOBAL_ANALYSISFORECAST_WAV_001_027, Issue 3, Mercator Ocean International, https://catalogue.marine.copernicus.eu/documents/QUID/CMEMS-GLO-QUID-001-027.pdf (last access: 5 April 2023), 2022.

Ardhuin, F., Rogers, E., Babanin, A. V., Filipot, J.-F., Magne, R., Roland, A., van der Westhuysen, A., Queffeulou, P., Lefevre, J.-M., Aouf, L., and Collard, F.: Semiempirical Dissipation Source Functions for Ocean Waves. Part I: Definition, Calibration, and Validation, J. Phys. Oceanogr., 40, 1917–1941, https://doi.org/10.1175/2010jpo4324.1, 2010.

Belmonte Rivas, M. and Stoffelen, A.: Characterizing ERA-Interim and ERA5 surface wind biases using ASCAT, Ocean Sci., 15, 831–852, https://doi.org/10.5194/os-15-831-2019, 2019.

Bitner-Gregersen, E. M., Vanem, E., Gramstad, O., Hørte, T., Aarnes, O. J., Reistad, M., Breivik, Ø., Magnusson, A. K., and Natvig, B.: Climate change and safe design of ship structures, Ocean Eng., 149, 226–237, https://doi.org/10.1016/j.oceaneng.2017.12.023, 2018.

Caires, S. and Sterl, A.: 100-year return value estimates for ocean wind speed and significant wave height from the ERA-40 data, J. Climate, 18, 1032–1048, https://doi.org/10.1175/JCLI-3312.1, 2005.

Campos, R. M., Alves, J. H. G. M., Guedes Soares, C., Guimaraes, L. G., and Parente, C. E.: Extreme wind-wave modeling and analysis in the South Atlantic ocean, Ocean Model., 124, 75–93, https://doi.org/10.1016/j.ocemod.2018.02.002, 2018.

Chawla, A., Spindler, D. M., and Tolman, H. L.: Validation of a thirty year wave hindcast using the Climate Forecast System Reanalysis winds, Ocean Model., 70, 189–206, https://doi.org/10.1016/j.ocemod.2012.07.005, 2013.

Crespo, N. M., da Silva, N. P., Palmeira, R. M. d. J., Cardoso, A. A., Kaufmann, C. L. G., Lima, J. A. M., Andrioni, M., de Camargo, R., and da Rocha, R. P.: Western South Atlantic Climate Experiment (WeSACEx): extreme winds and waves over the Southeastern Brazilian sedimentary basins, Clim. Dynam., 60, 571–588, https://doi.org/10.1007/s00382-022-06340-y, 2022.

Dalagnol, R., Gramcianinov, C. B., Crespo, N. M., Luiz, R., Chiquetto, J. B., Marques, M. T. A., Neto, G. D., de Abreu, R. C., Li, S., Lott, F. C., Anderson, L. O., and Sparrow, S.: Extreme rainfall and its impacts in the Brazilian Minas Gerais state in January 2020: Can we blame climate change?, Climate Resilience and Sustainability, 1, 1–15, https://doi.org/10.1002/cli2.15, 2022.

Dalphinet, A., Aouf, L., Law-Chune, S., Tressol, M., and Fernandez, E.: EU Copernicus Marine Service Product User Manual for Global Ocean Waves Analysis and Forecasting Product, GLOBAL_ANALYSISFORECAST_WAV_001_027, Issue

1.3, Mercator Ocean International, https://catalogue.marine.copernicus.eu/documents/PUM/CMEMS-GLO-PUM-001-027.pdf (last access: 5 April 2023), 2022.

da Rocha, R. P., Sugahara, S., and da Silveira, R. B.: Sea Waves Generated by Extratropical Cyclones in the South Atlantic Ocean: Hindcast and Validation against Altimeter Data, Weather Forecast., 19, 398–410, https://doi.org/10.1175/1520-0434(2004)019<0398:swgbec>2.0.co;2, 2004.

De Leo, F., Solari, S., and Besio, G.: Extreme wave analysis based on atmospheric pattern classification: an application along the Italian coast, Nat. Hazards Earth Syst. Sci., 20, 1233–1246, https://doi.org/10.5194/nhess-20-1233-2020, 2020.

Dobrynin, M., Murawsky, J., and Yang, S.: Evolution of the global wind wave climate in CMIP5 experiments, Geophys. Res. Lett., 39, L18606, https://doi.org/10.1029/2012GL052843, 2012.

Dragani, W. C., Cerne, B. S., Campetella, C. M., Possia, N. E., and Campos, M. I.: Synoptic patterns associated with the highest wind-waves at the mouth of the Río de la Plata estuary, Dynam. Atmos. Oceans, 61–62, 1–13, https://doi.org/10.1016/j.dynatmoce.2013.02.001, 2013.

EU Copernicus Marine Service Product: Global Ocean Waves Reanalysis (WAVERYS), Mercator Ocean International [data set], https://doi.org/10.48670/moi-00022, 2021.

EU Copernicus Marine Service Product: Global Ocean Waves Analysis and Forecasting Product, Mercator Ocean International [data set], https://doi.org/10.48670/moi-00017, 2022.

Godoi, V. A. and Torres Júnior, A. R.: A global analysis of austral summer ocean wave variability during SAM–ENSO phase combinations, Clim. Dynam., 54, 3991–4004, https://doi.org/10.1007/s00382-020-05217-2, 2020.

Godoi, V. A., de Andrade, F. M., Durrant, T. H., and Torres Júnior, A. R.: What happens to the ocean surface gravity waves when ENSO and MJO phases combine during the extended boreal winter?, Clim. Dynam., 54, 1407–1424, https://doi.org/10.1007/s00382-019-05065-9, 2020.

Gramcianinov, C. B., Hodges, K. I., and Camargo, R.: The properties and genesis environments of South Atlantic cyclones, Clim. Dynam., 53, 4115–4140, https://doi.org/10.1007/s00382-019-04778-1, 2019.

Gramcianinov, C. B., Campos, R. M., de Camargo, R., Hodges, K. I., Guedes Soares, C., and da Silva Dias, P. L.: Analysis of Atlantic extratropical storm tracks characteristics in 41 years of ERA5 and CFSR/CFSv2 databases, Ocean Eng., 216, 108111, https://doi.org/10.1016/j.oceaneng.2020.108111, 2020a.

Gramcianinov, C. B., Campos, R. M., Guedes Soares, C., and de Camargo, R.: Extreme waves generated by cyclonic winds in the western portion of the South Atlantic Ocean, Ocean Eng., 213, 107745, https://doi.org/10.1016/j.oceaneng.2020.107745, 2020b.

Gramcianinov, C. B., Campos, R. M., de Camargo, R., and Guedes Soares, C.: Relation between cyclone evolution and fetch associated with extreme wave events in the South Atlantic Ocean, J. Offshore Mech. Arct., 143, 061202, https://doi.org/10.1115/1.4051038, 2021.

Gramcianinov, C. B., de Camargo, R., Campos, R. M., Soares, C. G., and da Silva Dias, P. L.: Impact of extratropical cyclone intensity and speed on the extreme wave trends in the Atlantic Ocean, Clim. Dynam., 60, 1447–1466, https://doi.org/10.1007/s00382-022-06390-2, 2023.

Guillou, N.: Estimating wave energy flux from significant wave height and peak period, Renew. Energ., 155, 1383–1393, https://doi.org/10.1016/j.renene.2020.03.124, 2020.

Hemer, M. A., Church, J. A., and Hunter, J. R.: Variability and trends in the directional wave climate of the Southern Hemisphere, Int. J. Climatol., 30, 475–491, https://doi.org/10.1002/joc.1900, 2010.

Hersbach, H., Bell, B., Berrisford, P., Hirahara, S., Horányi, A., Muñoz-Sabater, J., Nicolas, J., Peubey, C., Radu, R., Schepers, D., Simmons, A., Soci, C., Abdalla, S., Abellan, X., Balsamo, G., Bechtold, P., Biavati, G., Bidlot, J., Bonavita, M., Chiara, G., Dahlgren, P., Dee, D., Diamantakis, M., Dragani, R., Flemming, J., Forbes, R., Fuentes, M., Geer, A., Haimberger, L., Healy, S., Hogan, R. J., Hólm, E., Janisková, M., Keeley, S., Laloyaux, P., Lopez, P., Lupu, C., Radnoti, G., Rosnay, P., Rozum, I., Vamborg, F., Villaume, S., and Thépaut, J.-N.: The ERA5 global reanalysis, Q. J. Roy. Meteor. Soc., 146, 1999–2049, https://doi.org/10.1002/qj.3803, 2020.

Hoskins, B. J. and Hodges, K. I.: A New Perspective on Southern Hemisphere Storm Tracks, J. Climate, 18, 4108–4129, https://doi.org/10.1175/JCLI3570.1, 2005.

ICMBio: Atlas dos Manguezais do Brasil (Brazilian Mangrove Atlas), Instituto Chico Mendes de Conservação da Biodiversidade (ICMBio), Ministério do Meio Ambiente – MMA (Ministry of the Environment), Brazil, https://acervo.socioambiental.org/sites/default/files/documents/17L00001.pdf (last access: 24 April 2023), 2018 (in Portuguese).

Kendall, M.: Rank Correlation Methods, 4th edn., Charles Griffin, London, ISBN-13: 978-01-9520-837-5, 1975.

Law-Chune, S.: EU Copernicus Marine Service Product User Manual for the Global Ocean Wave Multi Year product, GLOBAL_REANALYSIS_WAV_001_032, Issue 1.2, Mercator Ocean International, https://catalogue.marine.copernicus.eu/documents/PUM/CMEMS-GLO-PUM-001-032.pdf (last access: 5 April 2023), 2022.

Law-Chune, S., Aouf, L., Dalphinet, A., Levier, B., Drillet, Y., and Drevillon, M.: WAVERYS: a CMEMS global wave reanalysis during the altimetry period, Ocean Dynam., 71, 357–378, https://doi.org/10.1007/s10236-020-01433-w, 2021a.

Law-Chune, S., Aouf, L., Levier, B., and Dalphinet, A.: EU Copernicus Marine Service Quality Information Document for the Global Ocean Waves Reanalysis, GLOBAL_REANALYSIS_WAV_001_032, Issue 1.3, Mercator Ocean International, https://catalogue.marine.copernicus.eu/documents/QUID/CMEMS-GLO-QUID-001-032.pdf (last access: 5 April 2023), 2021b.

Lemos, G., Semedo, A., Dobrynin, M., Behrens, A., Staneva, J., Bidlot, J.-R., and Miranda, P. M.: Mid-twenty-first century global wave climate projections: Results from a dynamic CMIP5 based ensemble, Global Planet. Change, 172, 69–87, https://doi.org/10.1016/j.gloplacha.2018.09.011, 2019.

Linhares, P. S., Fukai, D. T., and Souza, C. R. G.: Clima de ondas e maré em três eventos meteo-oceanográficos extremos ocorridos em São Paulo, em fevereiro e abril de 2020, in: X Congresso sobre Planejamento e Gestão das Zonas Costeiras nos Países de Expressão Portuguesa, APRH/ABRhidro, 6–10 December 2021, on-line, 2021 (in Portuguese).

Lobeto, H., Menendez, M., and Losada, I. J.: Projections of Directional Spectra Help to Unravel the Future Behavior

of Wind Waves, Frontiers in Marine Science, 8, 655490, https://doi.org/10.3389/fmars.2021.655490, 2021.

Machado, A. A. and Calliari, L. J.: Synoptic systems generators of extreme wind in Southern Brazil: atmospheric conditions and consequences in the coastal zone, J. Coastal Res., 1, 1182–1186, https://doi.org/10.2112/SI75-237.1, 2016.

Machado, A. A., Calliari, L. J., Melo, E., and Klein, A. H. F.: Historical assessment of extreme coastal sea state conditions in southern Brazil and their relation to erosion episodes, Pan-American Journal of Aquatic Sciences, 5, 105–114, https://panamjas.org/pdf_artigos/PANAMJAS_5(2)_277-286.pdf (last access: 24 April 2023), 2010.

Mann, H. B.: Nonparametric Tests Against Trend, Econometrica, 13, 245–259, http://www.jstor.org/stable/1907187 (last access: 24 April 2023), 1945.

Marcello, F., Wainer, I., and Rodrigues, R. R.: South Atlantic Subtropical Gyre Late Twentieth Century Changes, J. Geophys. Res.-Oceans, 123, 5194–5209, https://doi.org/10.1029/2018jc013815, 2018.

Meucci, A., Young, I. R., Hemer, M., Kirezci, E., and Ranasinghe, R.: Projected 21st century changes in extreme wind-wave events, Science Advances, 6, eaaz7295, https://doi.org/10.1126/sciadv.aaz7295, 2020.

Muehe, D.: Panorama da Erosão Costeira no Brasil (Overview of Coastal Erosion in Brazil), Ministério do Meio Ambiente – MMA (Ministry of the Environment), Brazil, ISBN: 978-85-7738-394-8 (on line), 2018 (in Portuguese).

Odériz, I., Silva, R., Mortlock, T. R., Mori, N., Shimura, T., Webb, A., Padilla-Hernández, R., and Villers, S.: Natural Variability and Warming Signals in Global Ocean Wave Climates, Geophys. Res. Lett., 48, e2021GL093622, https://doi.org/10.1029/2021GL093622, 2021.

Parise, C. K., Calliari, L. J., and Krusche, N.: Extreme storm surges in the south of Brazil: atmospheric conditions and shore erosion, Braz. J. Oceanogr., 57, 175–188, 2009.

Pereira-Filho, G. H., Mendes, V. R., Perry, C. T., Shintate, G. I., Niz, W. C., Sawakuchi, A. O., Bastos, A. C., Giannini, P. C. F., Motta, F. S., Millo, C., Paula-Santos, G. M., and Moura, R. L.: Growing at the limit: Reef growth sensitivity to climate and oceanographic changes in the South Western Atlantic, Global Planet. Change, 201, 103479, https://doi.org/10.1016/j.gloplacha.2021.103479, 2021.

Pianca, C., Mazzini, P. L. F., and Siegle, E.: Brazilian offshore wave climate based on NWW3 reanalysis, Braz. J. Oceanogr., 58, 53–70, 2010.

Sasaki, D. K., Gramcianinov, C. B., Castro, B., and Dottori, M.: Intraseasonal variability of ocean surface wind waves in the western South Atlantic: the role of cyclones and the Pacific South American pattern, Weather Clim. Dynam., 2, 1149–1166, https://doi.org/10.5194/wcd-2-1149-2021, 2021.

Sen, P. K.: Estimates of the Regression Coefficient Based on Kendall's Tau, J. Am. Stat. Assoc., 63, 1379–1389, https://doi.org/10.1080/01621459.1968.10480934, 1968.

Silva, A. P., Klein, A. H., Fetter-Filho, A. F., Hein, C. J., Méndez, F. J., Broggio, M. F., and Dalinghaus, C.: Climate-induced variability in South Atlantic wave direction over the past three millennia, Sci. Rep.-UK, 10, 1–12, https://doi.org/10.1038/s41598-020-75265-5, 2020.

Souza, C. R. d. G., Souza, A. P., and Harari, J.: Long Term Analysis of Meteorological-Oceanographic Extreme Events for the Baixada Santista Region, in: Climate Change in Santos Brazil: Projections, Impacts and Adaptation Options, Springer International Publishing, 97–134, https://doi.org/10.1007/978-3-319-96535-2_6, 2019.

Souza, C. R. G., Linhares, P. S., and Morais Silva, V. A.: Histórico de Eventos Meteorológicos-Oceanográficos Intensos/Extremos na Costa de São Paulo (Brasil): 1928–2021, in: Libro Resúmenes. Congreso Latinoamericano de Ciencias del Mar, XIX COLACMAR, Asociación Latinoamericana de Investigadores en Ciencias del Mar, 19 al 23 de septiembre 2022, Ciudad de Panamá, Panamá, 2022 (in Portuguese).

Staneva, J., Ricker, M., Akpınar, A., Behrens, A., Giesen, R., and von Schuckmann, K.: Long-term interannual changes in extreme winds and waves in the Black Sea, J. Oper. Oceanogr., 15, 56–64, https://doi.org/10.1080/1755876X.2022.2095169, 2022.

Vettor, R. and Guedes Soares, C.: A global view on bimodal wave spectra and crossing seas from ERA-Interim, Ocean Eng., 210, 107439, https://doi.org/10.1016/j.oceaneng.2020.107439, 2020.

Wang, F., Shao, W., Yu, H., Kan, G., He, X., Zhang, D., Ren, M., and Wang, G.: Re-evaluation of the Power of the Mann-Kendall Test for Detecting Monotonic Trends in Hydrometeorological Time Series, Frontiers in Earth Science, 8, 14, https://doi.org/10.3389/feart.2020.00014, 2020.

Weisse, R. and Günther, H.: Wave climate and long-term changes for the Southern North Sea obtained from a high-resolution hindcast 1958–2002, Ocean Dynam., 57, 161–172, https://doi.org/10.1007/s10236-006-0094-x, 2007.

Young, I. R. and Ribal, A.: Multiplatform evaluation of global trends in wind speed and wave height, Science, 364, 548–552, https://doi.org/10.1126/science.aav9527, 2019.

Zamboni, A. and Nicolodi, J. L.: Macrodiagnóstico da Zona Costeira e Marinha do Brasil (Macrodiagnosis of the Brazilian Coastal and Marine Zone), Ministério do Meio Ambiente – MMA (Ministry of the Environment), Brazil, ISBN: 978-85-7738-112-8, 2008 (in Portuguese).

State Planet, 1-osr7, 13, 2023
https://doi.org/10.5194/sp-1-osr7-13-2023

Unusual coccolithophore blooms in Scottish waters

Richard Renshaw[1], Eileen Bresnan[2], Susan Kay[1,3], Robert McEwan[4], Peter I. Miller[3], and Paul Tett[5]

[1]Hadley Centre, Met Office, FitzRoy Road, Exeter EX1 3PB, UK
[2]Marine Scotland Marine Laboratory, 375 Victoria Rd, Aberdeen AB11 9DB, UK
[3]Plymouth Marine Laboratory, Prospect Place, Plymouth PL1 3DH, UK
[4]Cefas, Barrack Rd, Weymouth DT4 8UB, UK
[5]Scottish Association for Marine Science, Oban, Argyll PA37 1QA, UK

Correspondence: Richard Renshaw (richard.renshaw@metoffice.gov.uk)

Received: 22 August 2022 – Discussion started: 30 September 2022
Revised: 19 April 2023 – Accepted: 2 May 2023 – Published: 27 September 2023

Abstract. Two unusual blooms were observed in Scottish waters during summer 2021: one in the Clyde Sea and the other by the east coast of the Shetland Islands. Both had the appearance of coccolithophore blooms. Transmission electron microscopy of a sample from the Clyde Sea confirmed the presence there of the coccolithophore *Emiliania huxleyi*. We examine the conditions that led to these unusual blooms. In situ data are scarce, and so we draw inference from satellite data and reanalysis. For Shetland, the bloom can be seen to originate further north on the edge of the continental shelf. It is advected south and then west towards the Shetland coast by surface currents. For the Clyde Sea region, April 2021 was the coldest April of the last 30 years (National Climate Information Centre). We hypothesise that this cold weather restricted the usual spring bloom of diatoms. A restricted spring bloom would mean higher-than-usual concentrations of nutrients in the summer. It might also mean reduced numbers of grazers. These factors would provide ideal conditions for coccolithophores to flourish as temperatures and sunlight increase.

1 Introduction

Coccolithophores belong to a diverse group of phytoplankters (class Prymnesiophyceae) that is widespread in the oceans. The ecological group that includes *Emiliana* is particularly abundant in upwelling and temperate sub-polar regions (Balch et al., 2019). Most coccolithophores are not themselves harmful or toxic, but they are of ecological importance, particularly for carbon cycling and sequestration (Rost and Riebesell, 2004). They typically produce an exoskeleton consisting of several calcium carbonate plates called coccoliths (Young et al., 1999). These coccoliths are not opaque (phytoplankton require light for photosynthesis), but they scatter and polarise light. Coccolith shedding occurs during the later stages of the bloom life cycle, when the cells are threatened, for example by pathogen pressure (Frada et al., 2008). During this stage, the coccoliths are shed and accumulate in the surrounding water. The visual effect is to turn the sea a milky turquoise colour, visible to the human eye and in satellite imagery.

The function of the coccoliths is unclear. They are believed to be protective, either against grazing, against viral or bacterial attack, or as a refractor of light that acts as a sunshade in excessively bright conditions (Monteiro et al., 2016). Johns et al. (2023) show that coccoliths initially provide some protection from viral attack but once shed can mediate such attacks. Müller (2019) suggests that coccolith production may have evolved originally as an efficient mechanism for intracellular Ca^{2+} detoxification at a time of elevated seawater Ca^{2+} concentrations (e.g. during the Cretaceous and Jurassic periods).

Summer 2021 saw milky, turquoise-coloured waters caused by algal blooms in two locations off Scotland, in the Clyde Sea on the west coast and also to the east of the Shetland Islands (Fig. 1). These blooms were visually striking and so unusual that they were reported in the news (e.g. Bradshaw, 2021). Transmission-electron-microscope analysis of

Published by Copernicus Publications.

Table 1. CMEMS and non-CMEMS products used in this study.

Product ref. no.	Product ID and type	Data access	Documentation
1	NWSHELF_MULTIYEAR_PHY _004_009 (1993–2022), numerical models	EU Copernicus Service Product (2021a)	Quality Information Document (QUID): Renshaw et al. (2021); Product User Manual (PUM): Tonani et al. (2022)
2	OCEANCOLOUR_ATL_BGC_L3 _MY_OBSERVATIONS_009_013 (1998–2021), satellite observations	EU Copernicus Service Product (2022)	QUID: Garnesson et al. (2022); PUM: Collela et al. (2022)
3	SST_ATL_SST_L4_REP _OBSERVATIONS_010_026 (1998–2021), satellite observations	EU Copernicus Service Product (2021b)	QUID: Autret et al. (2021a); PUM: Autret et al. (2021b)
4	ERA5 atmospheric reanalysis (1979–2022)	Copernicus Climate Change Service, Climate Data Store (2023) (2023)	Hersbach et al. (2023)

a water sample from the Clyde Sea (Fig. 1d) confirmed the algae to be a morphotype of coccolithophore, *Emiliania huxleyi* (morphotype B). Blooms of this organism are common in spring and early summer in the North Atlantic and occur in some years in the northern North Sea and the western English Channel. However, such striking occurrences have not been reported from the Clyde Sea for many years. Colleagues of one of the authors (PT) recall no such event since 1983, when they remember sampling turquoise waters and coccolithophores in sea lochs of the Firth of Clyde. In this paper we use observations and reanalysis data to look for unusual environmental conditions in 2021 that might have allowed these blooms to thrive.

2 Data

2.1 Ocean colour

Ocean colour (OC) instruments measure water-leaving radiation at various wavelengths in the visible and near-infrared spectrum. Satellite measurements of ocean colour are used here in two forms. One is imagery. The enhanced colour maps from Sentinel-3 OLCI (Ocean and Land Colour Imager) and Sentinel-2 MSI (Multi-Spectral Imager) in Fig. 2 provide visual indications of algal blooms. The other is observation products, point estimates of near-surface chlorophyll concentration derived from multiple sensors. The CMEMS (Copernicus Marine Environment Monitoring Service) product used here (product ref. no. 2, Table 1) estimates chlorophyll concentration for several distinct phytoplankton functional types, including diatoms and nanophytoplankton. The nanophytoplankton category includes *E. huxleyi*.

Several factors make chlorophyll estimation difficult for coastal waters. Bowers et al. (2000) find that dissolved organic matter (DOM) from fresh water is usually the largest optically active constituent in the Clyde Sea. Ocean colour algorithms are designed to minimise errors due to suspended sediment and DOM. The presence of large numbers of coccoliths would also have a strong impact on backscattered radiation (Voss et al., 1998). The estimation process does mask for cloud, sun glint, and coccoliths (OC-CCI, 2020). This masking means there are few OC chlorophyll estimates available for the Clyde Sea during the period of the Clyde bloom (12 June to 7 July 2021). We use the OC product in Fig. 5 not as a measure of absolute value but to show the timing of growth and also how values in 2021 compare to other years.

2.2 North West Shelf reanalysis

The North West Shelf (NWS) reanalysis (product ref. no. 1, Table 1) is based on the physical ocean model NEMO (Madec and Team, 2008) at 7 km horizontal resolution and 51 vertical levels, with tides represented, over a domain that encompasses the North West Shelf (Renshaw et al., 2021). Atmospheric forcing is from the ERA5 atmospheric reanalysis (Hersbach et al., 2023). River discharge volumes for the year 2018 onwards come from a daily climatology. The reanalysis uses NEMOVAR (Mogensen et al., 2012) to assimilate observations of physical variables (satellite sea surface temperature, SST, as well as in situ temperature and salinity profiles; Waters et al., 2015).

Here we use the reanalysis for sea surface temperature and also for near-surface currents in the region of the European Slope Current. Reanalysis SST is strongly constrained by high-quality satellite observations. Variations in surface currents are driven predominantly by surface winds (Röhrs et al., 2023), provided here by ERA5. The slope current itself is forced also by meridional density gradient and steep bathymetry (Marsh et al., 2017). Validation of the reanalysis

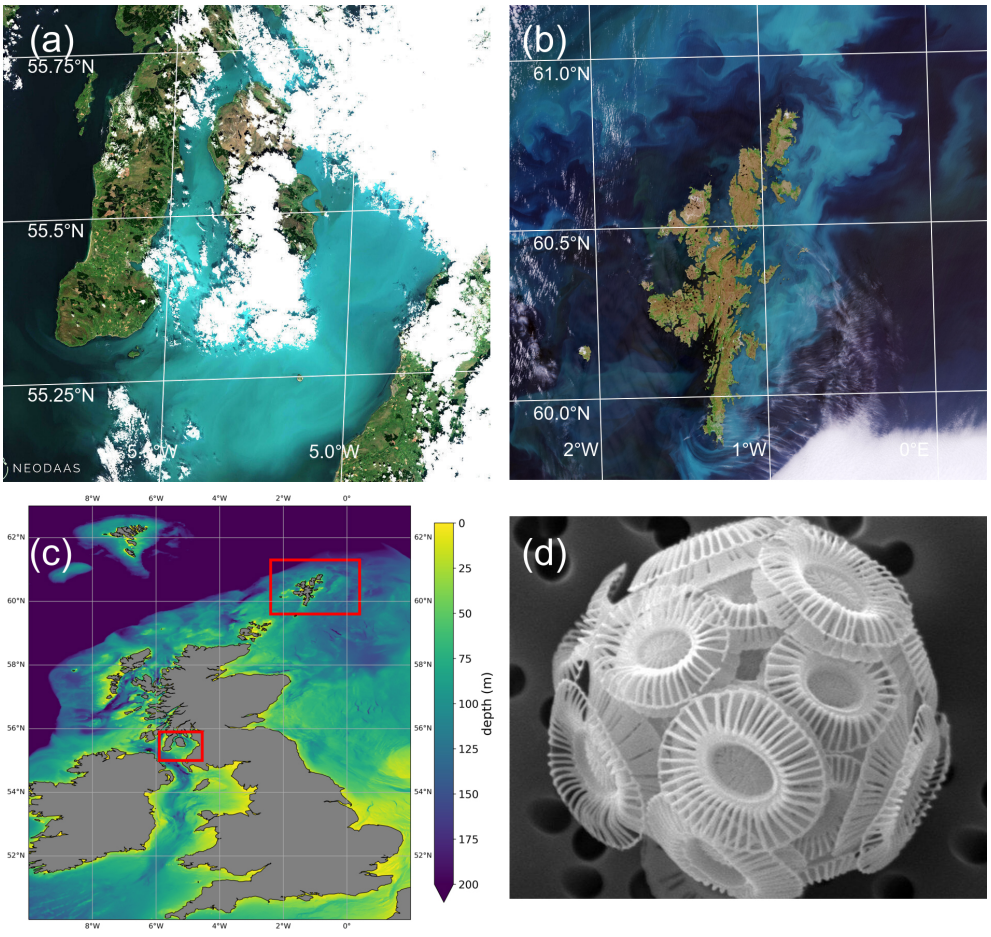

Figure 1. **(a)** Sentinel-2 MSI image of Clyde Sea on 21 June 2021 at 11:35 UTC, true colour with enhanced contrast. Processed by the Natural Environment Research Council Earth Observation Data Acquisition and Analysis Service (NEODAAS) using ACOLITE atmospheric correction. **(b)** Sentinel-2 MSI image of Shetland Islands on 1 July 2021, processed by ESA (https://www.esa.int/ESA_Multimedia/Images, last access: 30 May 2023). **(c)** Bathymetry map with locations of **(a)** and **(b)** marked in red. Shelf edge is visible as transition from light blue (less than 200 m depth) to dark blue (deep water). **(d)** Scanning electron micrograph of sample from the Clyde Sea, June 2021, identified as *E. huxleyi*, morphotype B. Credit: Eileen Bresnan (Marine Scotland Science).

shows that it does produce a realistic slope current (Renshaw et al., 2021).

3 Shetland bloom

Figure 1 shows a bloom on the eastern side of Shetland. There is no information on the species present, but the brightness and turquoise colour of the bloom suggest coccolithophores. Coccolithophore blooms in the North Sea are not unusual. An unusual feature of the 2021 bloom was that it came so close inshore. Examination of imagery for the years 2017 to 2020 from Plymouth Marine Laboratory (PML) (described in Highfield et al., 2014) and of a dataset of coccolithophore blooms for 1998 to 2016 in Kondrik et al. (2019) finds no other examples where blooms intrude among the islands and bays on the eastern side of Shetland.

Kondrik et al. (2019) show that often blooms develop further south and east in the North Sea in spring or early summer and are advected by an anti-clockwise circulation sometimes reaching as far north as Shetland. Sometimes a bloom originates in the north, along the northern edge of the continental shelf, and is advected southwards. Bathymetry in Fig. 1c shows the location of this shelf edge. The European Slope Current flows eastward along this edge, bringing North Atlantic water into the Norwegian Sea. Some of this water flows south past Shetland into the North Sea. Imagery for July 2021 (Fig. 2c, d) seems to show the bloom is of the latter kind, originating along the northern edge of the shelf.

To confirm the bloom's origins and to understand why 2021 was unusual, we used the *OceanParcels* software package (Delandmeter and van Sebille, 2019) to simulate the trajectory of virtual particles in the ocean. Particles were initially positioned at 1 m depth along the slope current (Fig. 3).

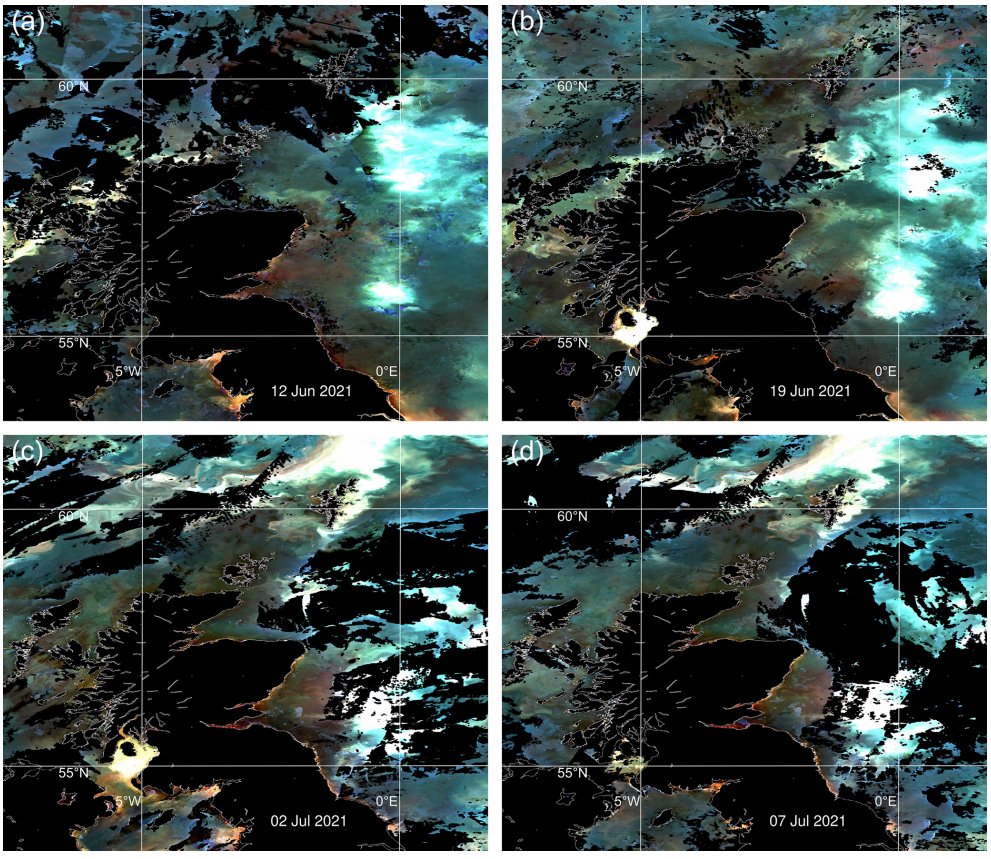

Figure 2. Enhanced ocean colour satellite imagery (provided by PML) from the Sentinel-3 OCLI and Sentinel-2 MSI instruments for 12 and 19 June 2021 and 2 and 7 July 2021. The brightest pixels are indicative of high numbers of coccoliths. Land and cloud are coloured black.

These locations were chosen based on where the speed of the current (from a reanalysis mean climatology for 1993 to 2021) exceeded 0.2 m s^{-1}. *OceanParcels* modelled 3D movement of the particles, advected by daily mean currents from the NWS reanalysis (product ref. no. 1, Table 1) and using a 3 h time step. This was done separately for each year from 1998–2022, starting with particles in initial positions on 3 April and running forward 3 months to predict positions on 3 July (Fig. 3).

In some years nearly all the particles move off beyond the edge of the plots (1999, 2002, 2003, 2009, 2022). In most years all the red particles (those initially at the eastern end of the slope current) disappear in this way. In 2021 it is these red particles that end up close to the eastern side of Shetland on 3 July. The year 2021 was unusual, although not unique, in that easterly winds during spring drove surface currents that pushed particles westward for part of that time. Figure 4 shows 10 m winds (from ERA5) and surface currents (from NWS reanalysis) for May 2021 and for a May climatology. To the east and north of Shetland, climatological winds are westerly, and the surface current is westerly or northerly. For May 2021, winds are north-easterly. These winds induce easterly surface currents (Ekman transport effect).

The years 2012, 2016, and 2019 also experienced easterly winds in spring or early summer (based on ERA5 reanalysis) and similarly show large numbers of red particles still within the plot region on 3 July. Other years see large numbers of other-coloured particles come close inshore, in particular 2007, 2017, and 2020. In the satellite imagery (2017–2020) and Kondrik catalogue (1998–2016), none of these years show coccolithophore blooms that reach into the bays and inlets of eastern Shetland. Imagery for 2020 (not shown) comes the closest, with a bloom 10–20 km away from the coast. The 2020 particle tracking has orange particles in this region, originating from further west on the shelf edge.

We conclude that in some years blooms around Shetland form in water coming from the shelf edge. We cannot conclude that bloom development is always linked to specific locations and timings of source water along the shelf edge.

To understand how the bloom appeared so close inshore, we examined the daily particle trajectories for 2021 (not shown). Particles move south down the eastern side of Shetland during the second half of June. In late June and early July there is a brief period of easterly winds, and the particles are driven in towards the coast. Brief easterlies are not unusual, but these coincided with coccolithophore-laden wa-

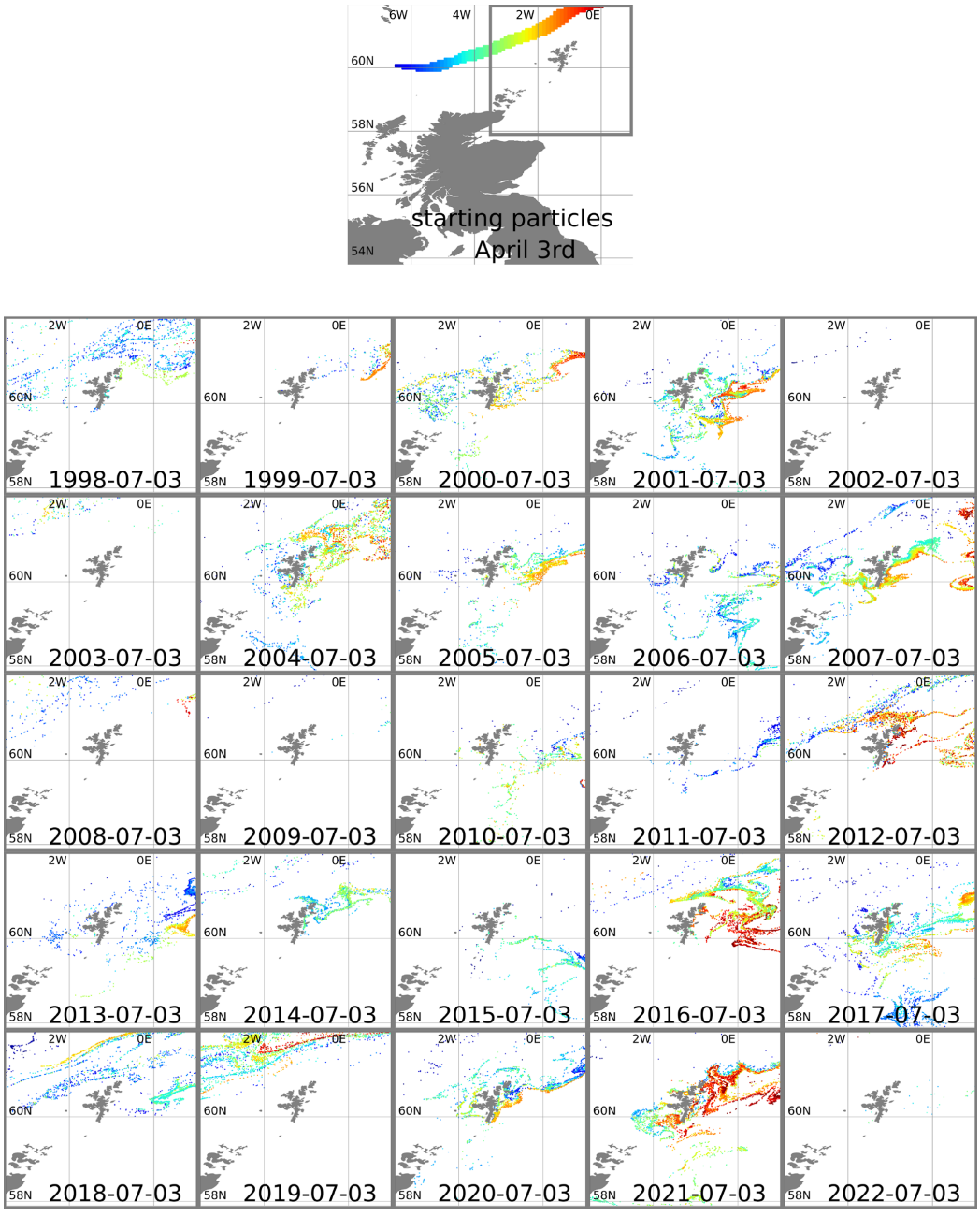

Figure 3. Top plot shows 3 April starting positions for particles positioned along the European Slope Current. The area around Shetland is marked with a grey line. Other plots show particle positions in this area advected forward 3 months, using reanalysis surface currents for each year from 1998–2022. Particles are coloured according to longitude of starting position.

ter near the coast. We suggest that coincidences of timing and weather in 2021 created the unusual phenomenon of a visible coccolithophore bloom on the eastern Shetland coast.

4 Clyde Sea bloom

Analysis of the 2021 bloom in the Clyde Sea is hampered by a paucity of observations. Weather stations provide data on the atmospheric conditions. Satellite instruments provide estimates of SST and of chlorophyll, with caveats discussed below. We have found no in situ measurements of conditions within the Clyde Sea itself. Biogeochemical reanalysis data are available (Kay et al., 2021), but their ability to accurately simulate the Clyde Sea is hampered by a lack of data on river discharge. Freshwater input and nutrient input from rivers are important variables for the biogeochemistry here. In this paper we analyse the data that are available and build from them

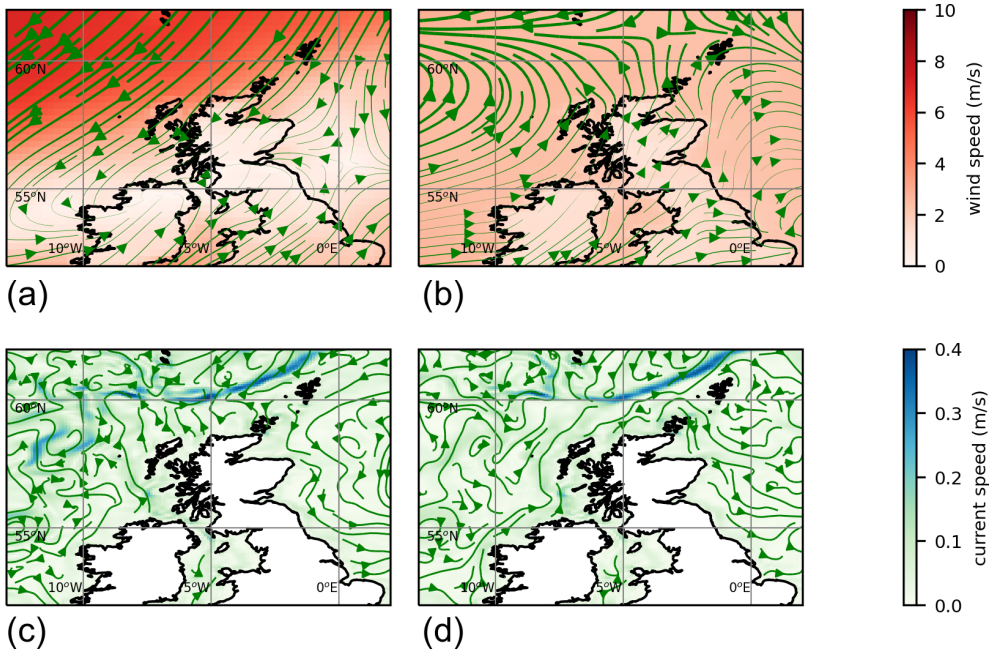

Figure 4. Top: ERA5 monthly mean 10 m winds (product ref. no. 4, Table 1) for **(a)** May 2021 and **(b)** May 1979–2020 climatology. Bottom: surface current for May from reanalysis (product ref. no. 1, Table 1) for **(c)** May 2021 and **(d)** May 1983–2020 climatology.

a plausible storyline. That storyline starts with diatom growth in early spring.

4.1 The Clyde Sea and the annual cycle of diatoms

The Clyde Sea comprises a large tidal estuary with several islands and fjord-like sea lochs. It is the outlet of the River Clyde and other rivers into the Irish Sea. It has a maximum depth of 164 m, with a sill (the "Great Plateau") of approximately 40 m depth where it meets the Irish Sea. Freshwater outflow from rivers and from land drainage tends to maintain stable stratification in the basin (Simpson and Rippeth, 1993). This together with the sill restricts tidal mixing to mostly near-surface waters. Edwards et al. (1986) estimate a residence time of 2 months for surface water in the main body of the Clyde Sea. Nutrient content in the Clyde Sea tends to be higher than adjacent coastal waters (based on measurements of nitrate in Slesser and Turrell, 2013). Tidal currents within the Clyde Sea tend to be weak. Water in the deeper waters below the sill can stagnate, leading to nutrient build-up near the sea bed. Simpson and Rippeth (1993) show that strong winds can sometimes overcome the vertical stability and mix the water column. This would act to replenish nutrients in the surface layers in the event of an algal bloom.

Marshall and Orr (1927) sampled the Clyde Sea and its lochs extensively, finding the following:

> There is a well-marked spring diatom maximum which starts at the end of March or the beginning of April.

A diatom bloom will consume nutrients (Stief et al., 2022), which will tend to inhibit further phytoplankton growth (Elser et al., 2007). Marshall and Orr (1927) also observed a second, smaller summer maximum but noted that diatoms near the surface were less healthy than those several metres deeper. Tests with samples left in direct sunlight and in shade showed that summer light levels were injurious for these diatoms.

Hannah and Boney (1983) assessed extensive and more recent surveys (1976–1978) of the Inner Firth. They found rapid growth in diatoms from late March or early April in each year of the study, dominated by *Skeletonema* spp. and *Thalassiosira nordenskioldii*. They also found *Nitzschia seriata* (now called *Pseudo-nitzschia "seriata* type") and *Chaetoceros* spp. at those times present in considerable numbers. During these spring blooms total chlorophyll was dominated by diatoms. For 1977 they found evidence that the *Skeletonema* were being grazed by microzooplankton (*Ebria*). Bresnan et al. (2016) also report an intense spring bloom dominated by *Skeletonema* during the monitoring period 2005–2013.

4.2 Timing and source of 2021 Clyde coccolithophore bloom

Figure 1 shows the Clyde bloom on 21 June 2021. There are earlier visual reports of bright patches in the sea around the Isle of Arran in the centre of the Clyde Sea on 12 June (Evers-King et al., 2021). Satellite imagery (Fig. 2a) has no bright patch in the Clyde Sea that day, but the sea around Arran is

partly obscured by cloud. Imagery for 13–16 June is almost wholly obscured by cloud, and the first clear satellite image of a bright patch across the whole of the Clyde Sea is from 18 June (Fig. 2b). This patch persists until 5 July and then fades. Figure 2c shows that by this time the bloom is apparent even in the northernmost reaches of Loch Fyne. This sea loch flows into the Clyde Sea but is tidal along its 65 km length.

Transmission electron microscopy of a sample from Millport collected at the end of June revealed the bloom to be comprised of liths and cells of *E. huxleyi* – morphotype B (Fig. 1d), providing the first confirmation of this species in high abundance at this site. *E. huxleyi* morphotypes A and B have been recorded in the waters around Scotland (van Bleijswijk et al., 1991; León et al., 2018). Little is known about the seasonality of *E. huxleyi* morphotypes on the west coast of Scotland. A study at the Marine Scotland Scottish Coastal Observatory (SCObs) monitoring site at Stonehaven on the east coast from 2010–2013 showed a distinct repeated seasonality in the occurrence of different *E. huxleyi* morphotypes (León et al., 2018). Morphotype B was commonly recorded in spring, with morphotype A occurring from June to August followed by an overcalcified form of morphotype A (type AO) in autumn and winter months. The dominance of *E. huxleyi* morphotype B in the 2021 Clyde bloom differs in timing from the seasonality recorded on the east coast.

Coccolithophores have a haplodiplontic life cycle (Keuter et al., 2021). New cells are haploid (one set of chromosomes in the nucleus). These haploid cells develop into diploid cells (two sets of chromosomes in the nucleus). For the genus *Emiliania*, it is only the diploid form that produces coccoliths. Frada et al. (2008) explain its "Cheshire Cat" strategy for resisting viral attack. Giant phycodnaviruses (*Emiliania huxleyi* viruses, EhVs) infect and lyse diploid-phase cells and are heavily implicated in the termination of blooms. The diploid cells transition to haploid cells that are resistant to EhVs, shedding coccoliths as they do. Thus the bloom in the Clyde Sea may have started some time before sufficient coccoliths had accumulated to make it visible.

It is possible that *E. huxleyi* was introduced by tidal mixing into the Clyde Sea from the Irish Sea or that it was already resident. Reverse particle tracking (not shown) excludes immediate seeding from blooms at the Malin shelf break as a likely cause. The satellite imagery shows the bloom mostly confined to the Clyde Sea. We conclude that conditions within the Clyde basin in late May or early June were particularly favourable for *E. huxleyi* to thrive. We aim here to understand exactly which aspects were favourable and what brought them about.

4.3 Physical environment in 2021

Figure 5a shows daily values of sea surface temperature (SST) from the NWS reanalysis averaged over the Clyde Sea for the years 1998–2021. June 2021 values are in the middle of the range. Values for April and May are towards the cold

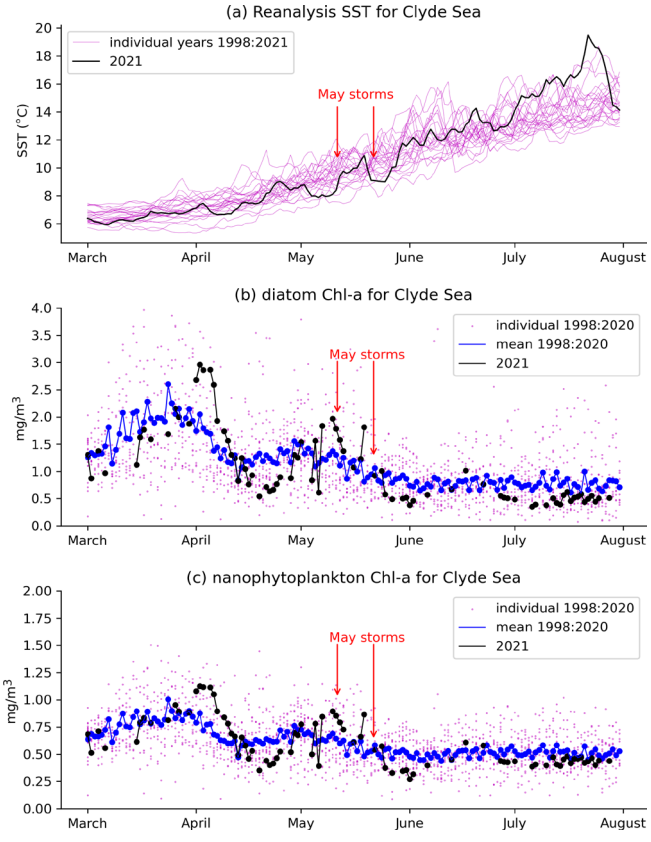

Figure 5. Daily mean values averaged over the Clyde Sea basin of **(a)** reanalysis sea surface temperature for individual years. The year 2021 is in black. Chlorophyll concentrations (product ref. no. 2, Table 1) for the Clyde Sea from ocean colour products for **(b)** diatoms and **(c)** nanophytoplankton are also given. Black dots and lines are ocean colour estimates for 2021. Blue shows mean estimates for 1998 to 2020. Smaller purple dots are values for individual years, showing the year-to-year spread.

end of the range. Statistics from a high-resolution satellite SST product in Table 2 (product ref. no. 3, Table 1) confirm this. Monthly means for April, May, and June 2021 are, respectively, at the 10th, 5th, and 52nd percentiles for those months over the period 1982–2021.

Table 2a has monthly statistics of SST from a satellite SST product (product ref. no. 3, Table 1) for a point within the Clyde Sea (55.27° N, 5.11° W), close to the lower right intersection of grid lines in Fig. 1. April and May 2021 SSTs were unusually cold compared to climatology. June was close to the median. The cold SST can be linked to the weather (Table 2b, c, d). April saw anticyclonic weather that was cold, dry, and exceptionally sunny (Weather Magazine, 2021a). May 2021 had anomalously low atmospheric pressure over the UK, bringing storms, high rainfall, and high winds (Weather Magazine, 2021b). June was drier and warmer than average.

Table 2. Statistics of monthly means from **(a)** CMEMS European area level 4 SST analysis at 55.27° N, 5.11° W, and **(b, c, d)** from weather stations in the Clyde catchment area (National Climate Information Centre, NCIC).

(a) Sea surface temperature			
	Monthly mean (°C)	Anomaly (°C)	Percentile
April	7.53	−0.65	10 %
May	8.81	−1.20	5 %
June	12.24	0.05	52 %
(b) Air temperature			
	Monthly mean (°C)	Anomaly (°C)	Percentile
April	5.5	−1.4	10 %
May	8.4	−1.4	10 %
June	13.4	1.0	83 %
(c) Sunshine hours			
	Total	Percentage of climatology	Percentile
April	236	159 %	100 %
May	151	80 %	19 %
June	174	111 %	76 %
(d) Rainfall			
	Total (mm)	Percentage of climatology	Percentile
April	16	20 %	5 %
May	96	115 %	64 %
June	42	47 %	12 %

Anomalies and percentiles are relative to yearly climatology: **(a)** SST is CMEMS reprocessed level 4 satellite product 1982–2020 (product ref. no. 3, Table 1). **(b, c, d)** Weather station data are for the Clyde catchment area from NCIC for 1980–2021.

There were two severe storms in May 2021, one on 9, 10, and 11 May and a stronger one on 20 and 21 May. These appear to coincide with periods when there is a pause in the rate of increase in SST (Fig. 5a). This suggests the strong winds are mixing the water column.

4.4 Ocean colour estimates of chlorophyll

Figure 5 shows a time series of estimates of chlorophyll *a* from the CMEMS ocean colour product (product ref. no. 2, Table 1) for two plankton functional types, diatoms and nanophytoplankton. Mean values for 1998–2020 (blue line) show similar patterns for diatoms and nanophytoplankton: concentrations rising to a peak in late March and a smaller second peak in early May, although with considerable year-to-year variation (purple dots). Estimates for 2021 are again similar between both functional types. Both have strong peaks in early April, well above the 1998–2020 mean. Values drop rapidly during April, rising again towards the end of that month. Both types also show a fall immediately following the two May storms, around 10 and 20 May.

As discussed in Sect. 2.1, chlorophyll estimation can be difficult in coastal waters. Vertical mixing and river discharge due to the May storms might increase levels of dissolved organic matter and sediment in the water. Vertical mixing might dilute plankton in the surface layers that are sensed by the ocean colour instruments. The presence of coccoliths and cloud mean that much of the data for June have been masked in the estimation process. The ocean colour product includes an estimate of root mean square error (RMSE) following Brewin et al. (2017). For the Clyde Sea, values of RMSE for diatoms and nanophytoplankton in both April and May 2021 are given as approximately 0.5 mg m^{-3}. This is similar in size to the estimates themselves for nanophytoplankton, and so we avoid drawing conclusions from Fig. 5c. Estimated concentrations for diatoms are somewhat larger, and so we have more confidence in drawing conclusions from the diatom time series (Fig. 5b).

4.5 Possible causes of Clyde bloom

Mayers et al. (2019) assessed coccolithophore growth and mortality rates based on samples from the Celtic Sea in April 2015. They identified several conditions that favour coccolithophore blooms. These are considered individually below.

(a) Warm, stratified waters. SST in June 2021 was close to average for that month (Table 2a). Vertical profiles of temperature from the reanalysis for 2021 (not shown) are stably stratified, but this is typical for June. The following conclusion was reached: June 2021 temperatures were not unusual.

(b) Sunlight. June 2021 was sunnier than average (76th percentile, Table 2c). The following conclusion was reached: sunshine might have been a contributory factor in 2021.

(c) Availability of nutrients. We have no direct measurements of nutrients in the Clyde Sea. April 2021 was a dry month (5th percentile, Table 2d), and so river discharge in April would have been low. Rainfall in May was above average. May was also a stormy month, which may have mixed the water column, bringing nutrients from deep water into the photic zone (Pingree et al., 1977). Each of these factors could lead to higher-than-usual nutrient availability by the end of May. Ocean colour estimates of diatoms suggest lower-than-usual diatom growth in April and increased growth during May (Fig. 5b). The following conclusion was reached: observations show low chlorophyll mass in spring 2021. This could be due to the cold water temperatures and limited nutrient input in April 2021. The

wet and stormy conditions in May of both years likely increased nutrient levels in near-surface layers in the Clyde Sea. Both these factors would help produce suitable conditions for a bloom.

(d) Scarcity of predatory microzooplankton. Mayers et al. (2019) found that microzooplankton exert strong top-down control on coccolithophore populations, grazing up to 80 % of daily production in a bloom of *E. huxleyi*. We might hypothesise that fewer diatoms in April and May led to low numbers of microzooplankton during that time, reducing the grazing pressure on *E. huxleyi* in late May and early June. However, growth rates for microzooplankton can be rapid, sometimes more than three doublings per day for tintinnids (Verity, 1986). The following conclusion was reached: this could be a contributory factor, though we have no evidence for this. The ability of microzooplankton to multiply rapidly suggests at least that other factors were also involved.

Advection of a bloom into the region is another possible cause. We consider this unlikely for two reasons. The Clyde Sea is semi-enclosed, with an estimated residence time of 2 months for surface water in the main body of the Clyde Sea (Edwards et al., 1986). This was consistent with reverse tracking (not shown) of a set of virtual particles placed in the Clyde Sea in June and tracked backwards for 60 d to find their source. The majority remained within the Clyde Sea. Also, satellite imagery shows a bloom in the Clyde Sea but not in the adjoining Irish Sea.

5 Discussion

Phytoplankton are of special interest in the waters around Scotland, where aquaculture and fishing are major industries. Through primary production, phytoplankton form the base of a food chain that sustains marine fauna (Frederiksen et al., 2006). Blooms of phytoplankton can be harmful to other marine life and can produce toxins dangerous for human consumers of seafood (Davidson et al., 2011). There is thus increasing interest from policy-makers to understand the diversity dynamics of phytoplankton communities in Scotland and other parts of the North West Shelf (NWS) and to understand its influence on industries and diversity status assessments (Siemering et al., 2016; McQuatters-Gollop et al., 2019).

This paper presents hypotheses to explain two unusual blooms. We suggest that the bloom on the eastern side of Shetland originated in Atlantic water brought north of Shetland by the European Slope Current. The water's passage eastward was retarded by a period of anomalous easterly winds in May, and it was later steered towards the Shetland coast by a shorter period of easterly winds. The timing was such that there were abundant coccoliths present when this water was close inshore. The bloom within the Clyde Sea appears to have developed in place. We hypothesise that environmental factors may have combined to create suitable conditions in the Clyde Sea. A cold and dry April could have restricted spring growth of diatoms, leaving nutrients available for a summer bloom of coccolithophores. A wet and stormy May might also have added to the nutrients.

Our explanations are based on limited evidence (SST and chlorophyll estimates from satellites, modelling by the reanalysis). We do not have in situ measurements from within the blooms to confirm our hypotheses.

For both blooms, we propose the weather as a key factor. Other studies also identify the importance of the weather for algal blooms. Whyte et al. (2014) looked at unusually strong blooms of the biotoxin-producing dinoflagellate *Dinophysis* on the western side of the Shetland Islands in the summers of 2006 and 2013. They found these blooms coincided with periods where the winds, usually more southerly, became westerly. They suggested the westerly winds advected *Dinophysis* populations onshore, resulting in an increase in diarrhetic shellfish toxin levels in farmed mussels (*Mytilus edulis*).

There is evidence that the distribution of coccolithophores has expanded polewards in recent decades (Beaugrand et al., 2013; Winter et al., 2013; Rivero-Calle et al., 2015), due either to changes in ocean temperature or dissolved inorganic carbon. Growth of *E. huxleyi* is also known to be impacted by major changes in ocean pH (Riebesell et al., 2017). Changes in pH observed in seas around the UK (Findlay et al., 2022) are not large enough to explain recent variability in coccolithophore abundance in Scottish waters.

Changing weather patterns have the potential to influence the occurrence of unusual phytoplankton blooms in coastal waters. These changes have the potential to impact higher trophic levels in the marine ecosystem. A better understanding of the processes and dynamics involved will help in forewarning, preparation, and development of adaptation measures for these changes.

This paper shows how use of satellite data and model reanalysis can help to meet the challenge of assessing major events in UK waters, despite a sparsity of in situ observations. However we could be more confident in our findings if we had more information about environmental conditions. More complete data on river discharge would help in simulating biogeochemical and ecosystem variables in the Clyde Sea and other inshore water bodies. Widespread routine monitoring of nutrient levels and phytoplankton components could help greatly in understanding future blooms.

Data availability. The data products used in this article, as well as their names, availability, and documentation, are summarised in Table 1.

Author contributions. RR processed the reanalysis data and wrote much of the text. EB produced the micrograph of the *E. huxleyi* sample. PM produced the ocean colour images. Every author contributed to discussion and development of the hypotheses presented. Every author also added to and reviewed the text.

Competing interests. The contact author has declared that none of the authors has any competing interests.

Disclaimer. Publisher's note: Copernicus Publications remains neutral with regard to jurisdictional claims in published maps and institutional affiliations.

Acknowledgements. We gratefully acknowledge use of the *OceanParcels* code (Delandmeter and van Sebille, 2019) in calculating backward trajectories. We also acknowledge use of collated station statistics from the UK National Climate Information Centre and ERA5 reanalysis data (Hersbach et al., 2023) downloaded from the Copernicus Climate Change Service (C3S) Climate Data Store. We thank ESA for the satellite image in Fig. 1, made available under Creative Commons License BY-SA 3.0 IGO (https://creativecommons.org/licenses/by-sa/3.0/igo/, last access: 30 May 2023). Transmission electron analysis of the Millport water sample was performed at the Microscopy Unit, Institute of Medical Sciences, University of Aberdeen.

Review statement. This paper was edited by Griet Neukermans and reviewed by David Bowers and two anonymous referees.

References

Autret, E., Tandéo, P., Paul, F., and Piollé, J. F.: EU Copernicus Marine Service Quality Information Document for the European North West Shelf/Iberia Biscay Irish Seas – High Resolution L4 Sea Surface Temperature Reprocessed, SST_ATL_SST_L4_REP_OBSERVATONS_010_026, Issue 1.4, Mercator Ocean International, https://catalogue.marine.copernicus.eu/documents/QUID/CMEMS-SST-QUID-010-026.pdf, last access: 12 April 2023, 2021a.

Autret, E., Piollé, J. F., Tandéo, P., and Prévost, C.: EU Copernicus Marine Service Product User Manual for the European North West Shelf/Iberia Biscay Irish Seas – High Resolution L4 Sea Surface Temperature Reprocessed, SST_ATL_SST_L4_REP_OBSERVATONS_010_026, Issue 1.4, Mercator Ocean International, https://catalogue.marine.copernicus.eu/documents/PUM/CMEMS-SST-PUM-010-026.pdf (last access: 12 April 2023), 2021b.

Balch, W. M., Bowler, B. C., Drapeau, D. T., Lubelczyk, L. C., Lyczkowski, E., Mitchell, C., and Wyeth, A.: Coccolithophore distributions of the North and South Atlantic Ocean, Deep Sea Research Part I: Oceanographic Research Papers, 151, 103 066, https://doi.org/10.1016/j.dsr.2019.06.012, 2019.

Beaugrand, G., McQuatters-Gollop, A., Edwards, M., and Goberville, E.: Long-term responses of North Atlantic calcifying plankton to climate change, Nature Climate Change, 3, 263–267, https://doi.org/10.1038/nclimate1753, 2013.

Bowers, D., Harker, G., Smith, P., and Tett, P.: Optical Properties of a Region of Freshwater Influence (The Clyde Sea), Estuarine, Coastal and Shelf Science, 50, 717–726, https://doi.org/10.1006/ecss.1999.0600, 2000.

Bradshaw, H.: Marine algae turned Scotland's water bright blue, BBC News Online, https://www.bbc.co.uk/news/uk-scotland-57720790 (last access: 30 May 2023), 2021.

Bresnan, E., Cook, K., Hindson, J., Hughes, S., Lacaze, J. P., Walsham, P., Webster, L., and Turrell, W. R.: The Scottish coastal observatory 1997-2013 part 2: description of Scotland's coastal waters, Scottish Marine and Freshwater Science, 7, 278, https://doi.org/10.7489/1881-1, 2016.

Brewin, R. J. W., Ciavatta, S., Sathyendranath, S., Jackson, T., Tilstone, G., Curran, K., Airs, R. L., Cummings, D., Brotas, V., Organelli, E., Dall'Olmo, G., and Raitsos, D. E.: Uncertainty in Ocean-Color Estimates of Chlorophyll for Phytoplankton Groups, Front. Mar. Sci., 4, 104, https://doi.org/10.3389/fmars.2017.00104, 2017.

Collela, S., Böhm, E., Cesarini, C., Garnesson, P., Netting, J., and Calton, B.: EU Copernicus Marine Service Product User Manual for North Atlantic Ocean Colour Plankton, Reflectance, Transparency and Optics MY L3 daily observations, Issue 3.0, Mercator Ocean International, https://catalogue.marine.copernicus.eu/documents/PUM/CMEMS-OC-PUM.pdf (last access: 12 April 2023), 2022.

Copernicus Climate Change Service, Climate Data Store: ERA5 hourly data on single levels from 1940 to present, Copernicus Climate Change Service (C3S) Climate Data Store (CDS) [data set], https://doi.org/10.24381/cds.adbb2d47, 2023.

Davidson, K., Tett, P., and Gowen, R.: Chapter 4 Harmful Algal Blooms, in: Marine Pollution and Human Health, pp. 95–127, The Royal Society of Chemistry, https://doi.org/10.1039/9781849732871-00095, 2011.

Delandmeter, P. and van Sebille, E.: The Parcels v2.0 Lagrangian framework: new field interpolation schemes, Geosci. Model Dev., 12, 3571–3584, https://doi.org/10.5194/gmd-12-3571-2019, 2019.

Edwards, A., Baxter, M. S., Ellett, D. J., Martin, J. H. A., Meldrum, D. T., and Griffiths, C. R.: Clyde Sea hydrography, Proc. Roy. Soc. Edinburgh. B, 90, 67–83, https://doi.org/10.1017/S0269727000004887, 1986.

Elser, J. J., Bracken, M. E., Cleland, E. E., Gruner, D. S., Harpole, W. S., Hillebrand, H., Ngai, J. T., Seabloom, E. W., Shurin, J. B., and Smith, J. E.: Global analysis of nitrogen and phosphorus limitation of primary producers in freshwater, marine and terrestrial ecosystems, Ecol. Lett., 10, 1135–1142, https://doi.org/10.1111/j.1461-0248.2007.01113.x, 2007.

EU Copernicus Service Product: Atlantic – European North West Shelf – Ocean Physics Reanalysis, Mercator Ocean International, Copernicus Services [data set], https://doi.org/10.48670/moi-00059, 2021a.

EU Copernicus Service Product: European North West Shelf/Iberia Biscay Irish Seas – High Resolution L4 Sea Surface Temperature Reprocessed, Mercator Ocean International, Copernicus Services [data set], https://doi.org/10.48670/moi-00153, 2021b.

EU Copernicus Service Product: North Atlantic Ocean Colour Plankton, Reflectance, Transparency and Optics MY L3 daily

observations, Mercator Ocean International, Copernicus Services [data set], https://doi.org/10.48670/moi-00286, 2022.

Evers-King, H., Miller, P., Loveday, B., and Wallace, L.: Ocean colour data reveals the extent of beautiful blue waters associated with a phytoplankton bloom observed by hikers around the Isle of Arran in June 2021, EUMETSAT press release, August 2021, https://www.eumetsat.int/big-bloom-firth-clyde (last access: 30 May 2023), 2021.

Findlay, H., Artoli, Y., Birchenough, S., Hartman, S., León, P., and Stiasny, M.: Climate change impacts on ocean acidification relevant to the UK and Ireland, MCCIP Sci. Rev., 2022, 24 pp., https://doi.org/10.14465/2022.reu03.oac, 2022.

Frada, M., Probert, I., Allen, M. J., Wilson, W. H., and de Vargas, C.: The "Cheshire Cat" escape strategy of the coccolithophore *Emiliania huxleyi* in response to viral infection, P. Natl. Acad. Sci. USA, 105, 15944–15949, https://doi.org/10.1073/pnas.0807707105, 2008.

Frederiksen, M., Edwards, M., Richardson, A. J., Halliday, N. C., and Wanless, S.: From plankton to top predators: bottom-up control of a marine food web across four trophic levels, J. An. Ecol., 75, 1259–1268, https://doi.org/10.1111/j.1365-2656.2006.01148.x, 2006.

Garnesson, P., Mangin, A., Bretagnon, M., and Jutard, Q.: EU Copernicus Marine Service Quality Information Document for the North Atlantic Ocean Colour Plankton, Reflectance, Transparency and Optics MY L3 daily observations, OCEANCOLOUR_ATL_BGC_L3_MY_009_113, Issue 3.0, Mercator Ocean International, https://catalogue.marine.copernicus.eu/documents/QUID/CMEMS-OC-QUID-009-111to114-121to124.pdf (last access: 12 April 2023), 2022.

Hannah, F. and Boney, A.: Nanophytoplankton in the Firth of Clyde, Scotland: Seasonal abundance, carbon fixation and species composition, J. Exp. Mar. Biol. Ecol., 67, 105–147, https://doi.org/10.1016/0022-0981(83)90085-0, 1983.

Hersbach, H., Bell, B., Berrisford, P., Biavati, G., Horányi, A., Muñoz-Sabater, J., Nicolas, J., Peubey, C., Radu, R., Rozum, I., Schepers, D., Simmons, A., Soci, C., Dee, D., and Thépaut, J.-N.: ERA5 hourly data on single levels from 1940 to present, Copernicus Climate Change Service (C3S) Climate Data Store (CDS), https://doi.org/10.24381/cds.adbb2d47, 2023.

Highfield, A., Evans, C., Walne, A., Miller, P. I., and Schroeder, D. C.: How many Coccolithovirus genotypes does it take to terminate an Emiliania huxleyi bloom?, Virology, 466–467, 138–145, https://doi.org/10.1016/j.virol.2014.07.017, special issue: Giant Viruses, 2014.

Johns, C., Bondoc-Naumovitz, K., Matthews, A., Matson, P., Iglesias-Rodriguez, M. D., Taylor, A., Fuchs, H., and Bidle, K.: Adsorptive exchange of coccolith biominerals facilitates viral infection, Sci. Adv., 9, eadc8728, https://doi.org/10.1126/sciadv.adc8728, 2023.

Kay, S., McEwan, R., and Ford, D.: EU Copernicus Marine Service Quality Information Document, North West European Shelf Production Centre NWSHELF_MULTIYEAR_BIO_004_011, Issue 5.1, Mercator Ocean International, https://catalogue.marine.copernicus.eu/documents/QUID/CMEMS-NWS-QUID-004-011.pdf (last access: 12 April 2023), 2021.

Keuter, S., Young, J. R., Koplovitz, G., Zingone, A., and Frada, M. J.: Novel heterococcolithophores, holococcolithophores and life cycle combinations from the families Syracosphaeraceae and Papposphaeraceae and the genus *Florisphaera*, J. Micropalaeontol., 40, 75–99, https://doi.org/10.5194/jm-40-75-2021, 2021.

Kondrik, D., Kazakov, E., and Pozdnyakov, D.: A synthetic satellite dataset of the spatio-temporal distributions of Emiliania huxleyi blooms and their impacts on Arctic and sub-Arctic marine environments (1998–2016), Earth Syst. Sci. Data, 11, 119–128, https://doi.org/10.5194/essd-11-119-2019, 2019.

León, P., ad Eileen Bresnan, P. W., Hartman, S., Hughes, S., Mackenzie, K., and Webster, L.: Seasonal variability of the carbonate system and coccolithophore *Emiliania huxleyi* at a Scottish Coastal Observatory monitoring site, Estuarine, Coast. Shelf Sci., 202, 302–314, https://doi.org/10.1016/j.ecss.2018.01.011, 2018.

Madec, G. and Team, N. S.: NEMO ocean engine, Zenodo, https://doi.org/10.5281/zenodo.1464816, 2008.

Marsh, R., Haigh, I. D., Cunningham, S. A., Inall, M. E., Porter, M., and Moat, B. I.: Large-scale forcing of the European Slope Current and associated inflows to the North Sea, Ocean Sci., 13, 315–335, https://doi.org/10.5194/os-13-315-2017, 2017.

Marshall, S. M. and Orr, A. P.: The Relation of the Plankton to some Chemical and Physical Factors in the Clyde Sea Area, J. Mar. Biol. Assoc. UK, 14, 837–868, https://doi.org/10.1017/S0025315400051110, 1927.

Mayers, K., Poulton, A., Daniels, C., Wells, S., Woodward, E., Tarran, G., Widdicombe, C., Mayor, D., Atkinson, A., and Giering, S.: Growth and mortality of coccolithophores during spring in a temperate Shelf Sea (Celtic Sea, April 2015), Prog. Oceanogr., 177, 101928, https://doi.org/10.1016/j.pocean.2018.02.024, shelf Sea Biogeochemistry: Pelagic Processes., 2019.

McQuatters-Gollop, A., Atkinson, A., Aubert, A., Bedford, J., Best, M., Bresnan, E., Cook, K., Devlin, M., Gowen, R., Johns, D. G., Machairopoulou, M., McKinney, A., Mellor, A., Ostle, C., Scherer, C., and Tett, P.: Plankton lifeforms as a biodiversity indicator for regional-scale assessment of pelagic habitats for policy, Ecol. Indic., 101, 913–925, https://doi.org/10.1016/j.ecolind.2019.02.010, 2019.

Mogensen, K., Balmaseda, M. A., and Weaver, A.: The NEMOVAR ocean data assimilation system as implemented in the ECMWF ocean analysis for System 4, ECMWF Technical Memoranda, https://doi.org/10.21957/x5y9yrtm, 2012.

Monteiro, F. M., Bach, L. T., Brownlee, C., Bown, P., Rickaby, R. E. M., Poulton, A. J., Tyrrell, T., Beaufort, L., Dutkiewicz, S., Gibbs, S., Gutowska, M. A., Lee, R., Riebesell, U., Young, J., and Ridgwell, A.: Why marine phytoplankton calcify, Sci. Adv., 2, e1501822, https://doi.org/10.1126/sciadv.1501822, 2016.

Müller, M. N.: On the Genesis and Function of Coccolithophore Calcification, Front. Mar. Sci., 6, https://doi.org/10.3389/fmars.2019.00049, 2019.

OC-CCI: Product User Guide v5.0, Ocean Colour Climate Change Initiative, ESA, D4.2, https://doi.org/10.5285/1dbe7a109c0244aaad713e078fd3059a, 2020.

Pingree, R. D., Maddock, L., and Butler, E. I.: The influence of biological activity and physical stability in determining the chemical distributions of inorganic phosphate, sili-

cate and nitrate, J. Mar. Biolo. Assoc. UK, 57, 1065–1073, https://doi.org/10.1017/S0025315400026138, 1977.

Renshaw, R., Wakelin, S., Golbeck, I., and O'Dea, E.: EU Copernicus Marine Service Quality Information Document for the Atlantic – European North West Shelf – Ocean Physics Reanalysis, NWSHELF_MULTIYEAR_PHY_004_009, Issue 5.2, Mercator Ocean International, https://catalogue.marine.copernicus.eu/documents/QUID/CMEMS-NWS-QUID-004-009.pdf (last access: 12 April 2023), 2021.

Riebesell, U., Bach, L. T., Bellerby, R. G. J., Monsalve, J. R. B., Boxhammer, T., Czerny, J., Larsen, A., Ludwig, A., and Schulz, K. G.: Competitive fitness of a predominant pelagic calcifier impaired by ocean acidification, Nat. Geosci., 10, 19–23, https://doi.org/10.1038/ngeo2854, 2017.

Rivero-Calle, S., Gnanadesikan, A., Castillo, C. E. D., Balch, W. M., and Guikema, S. D.: Multidecadal increase in North Atlantic coccolithophores and the potential role of rising CO_2, Science, 350, 1533–1537, https://doi.org/10.1126/science.aaa8026, 2015.

Röhrs, J., Sutherland, G., Jeans, G., Bedington, M., Sperrevik, A. K., Dagestad, K.-F., Gusdal, Y., Mauritzen, C., Dale, A., and LaCasce, J. H.: Surface currents in operational oceanography: Key applications, mechanisms, and methods, J. Oper. Oceanogr., 16, 60–88, https://doi.org/10.1080/1755876X.2021.1903221, 2023.

Rost, B. and Riebesell, U.: Coccolithophores and the biological pump: responses to environmental changes, 99–125, Springer Berlin Heidelberg, Berlin, Heidelberg, https://doi.org/10.1007/978-3-662-06278-4_5, 2004.

Siemering, B., Bresnan, E., Painter, S. C., Daniels, C. J., Inall, M., and Davidson, K.: Phytoplankton Distribution in Relation to Environmental Drivers on the North West European Shelf Sea, PLOS ONE, 11, 1–24, https://doi.org/10.1371/journal.pone.0164482, 2016.

Simpson, J. and Rippeth, T.: The Clyde Sea: a Model of the Seasonal Cycle of Stratification and Mixing, Estuarine, Coast. Shelf Sci., 37, 129–144, https://doi.org/10.1006/ecss.1993.1047, 1993.

Slesser, G. and Turrell, W.: Annual Cycles of Physical, Chemical and Biological Parameters in Scottish Waters, Scottish Marine and Freshwater Science, 4, 17 pp., https://doi.org/10.7489/1511-1, 2013.

Stief, P., Schauberger, C., Lund, M. B., Greve, A., Abed, R. M. M., Al-Najjar, M. A. A., Attard, K., Bonaglia, S., Deutzmann, J. S., Franco-Cisterna, B., García-Robledo, E., Holtappels, M., John, U., Maciute, A., Magee, M. J., Pors, R., Santl-Temkiv, T., Scherwass, A., Sevilgen, D. S., de Beer, D., Glud, R. N., Schramm, A., and Kamp, A.: Intracellular nitrate storage by diatoms can be an important nitrogen pool in freshwater and marine ecosystems, Commun. Earth Environ., 3, 154–164, https://doi.org/10.1038/s43247-022-00485-8, 2022.

Tonani, M., Ascione, I., and Saulter, A.: EU Copernicus Marine Service Product User Manual for the North West European Shelf Ocean Physical and Biogeochemical Reanalysis NWSHELF_MULTIYEAR_PHY_004_009, NWSHELF_MULTIYEAR_BGC_004_011, Issue 1.3, Mercator Ocean International, https://catalogue.marine.copernicus.eu/documents/PUM/CMEMS-NWS-PUM-004-009-011.pdf (last access: 12 April 2023), 2022.

van Bleijswijk, J., van der Wal, P., Kempers, R., Veldhuis, M., Young, J. R., Muyzer, G., de Vrind-de Jong, E., and Westbroek, P.: Distribution of two types of *Emiliania Huxleyi* (Prymnesiophyceae) in the North East Atlantic region as determined by Immunofluorescence and Coccolith Morphology 1, J. Phycology, 27, 566–570, https://doi.org/10.1111/j.0022-3646.1991.00566.x, 1991.

Verity, P. G.: Growth rates of natural tintinnid populations in Narragansett Bay, Mar. Ecol. Prog. Series, 29, 117–126, https://doi.org/10.3354/meps029117, 1986.

Voss, K. J., Balch, W. M., and Kilpatrick, K. A.: Scattering and attenuation properties of Emiliania huxleyi cells and their detached coccoliths, Limnol. Oceanogr., 43, 870–876, https://doi.org/10.4319/lo.1998.43.5.0870, 1998.

Waters, J., Lea, D. J., Martin, M. J., Mirouze, I., Weaver, A., and While, J.: Implementing a variational data assimilation system in an operational 1/4 degree global ocean model, Q. J. Roy. Meteorol. Soc., 141, 333–349, https://doi.org/10.1002/qj.2388, 2015.

Weather Magazine 2021a: April 2021 Most places cold, sunny and very dry, Weather, 76, i–iv, https://doi.org/10.1002/wea.4005, 2021.

Weather Magazine 2021b: May 2021 Cold, dull and wet, Weather, 76, i–iv, https://doi.org/10.1002/wea.4026, 2021.

Whyte, C., Swan, S., and Davidson, K.: Changing wind patterns linked to unusually high *Dinophysis* blooms around the Shetland Islands, Scotland, Harmful Algae, 39, 365–373, https://doi.org/10.1016/j.hal.2014.09.006, 2014.

Winter, A., Henderiks, J., Beaufort, L., Rickaby, R. E. M., and Brown, C. W.: Poleward expansion of the coccolithophore *Emiliania huxleyi*, J. Plankton Res., 36, 316–325, https://doi.org/10.1093/plankt/fbt110, 2013.

Young, J. R., Davis, S. A., Bown, P. R., and Mann, S.: Coccolith Ultrastructure and Biomineralisation, J. Struct. Biol., 126, 195–215, https://doi.org/10.1006/jsbi.1999.4132, 1999.

State Planet, 1-osr7, 14, 2023
https://doi.org/10.5194/sp-1-osr7-14-2023

Recent variations in oceanic transports across the Greenland–Scotland Ridge

Michael Mayer[1,2,3], Takamasa Tsubouchi[4], Susanna Winkelbauer[1], Karin Margretha H. Larsen[5], Barbara Berx[6], Andreas Macrander[7], Doroteaciro Iovino[8], Steingrímur Jónsson[7,9], and Richard Renshaw[10]

[1]Department of Meteorology and Geophysics, University of Vienna, 1090 Vienna, Austria
[2]Research Department, European Centre for Medium-Range Weather Forecasts (ECMWF), 53175 Bonn, Germany
[3]b.geos, 2100 Korneuburg, Austria
[4]Atmosphere and Ocean Department, Japan Meteorological Agency (JMA), Tokyo, 105-8431, Japan
[5]Faroe Marine Research Institute, Tórshavn, 100, Faroe Islands
[6]Marine Scotland, Aberdeen, AB11 9DB, United Kingdom
[7]Environmental division, Marine and Freshwater Research Institute, Hafnarfjörður, 220, Iceland
[8]Ocean Modeling and Data Assimilation Division, Centro Euro-Mediterraneo sui Cambiamenti Climatici (CMCC), Bologna, 40127, Italy
[9]Faculty of Natural Resource Sciences, University of Akureyri, Akureyri, 600, Iceland
[10]Met Office, Exeter, EX1 3PB, United Kingdom

Correspondence: Michael Mayer (michael.mayer@univie.ac.at)

Received: 25 July 2022 – Discussion started: 7 October 2022
Revised: 20 January 2023 – Accepted: 20 February 2023 – Published: 27 September 2023

Abstract. Oceanic exchanges across the Greenland–Scotland Ridge (GSR) play a crucial role in shaping the Arctic climate and linking with the Atlantic meridional overturning circulation. Most considered ocean reanalyses underestimate the observed 1993–2020 mean net inflow of warm and saline Atlantic Water of 8.0 ± 0.5 Sv by up to 15 %, with reanalyses at 0.25° resolution additionally exhibiting larger biases in the single inflow branches compared to higher-resolution products. The underestimation of Atlantic Water inflow translates into a low bias in mean oceanic heat flux at the GSR of 5 %–22 % in reanalyses compared to the observed value of 280 ± 18 TW. Interannual variations in reanalysis transports correlate reasonably well with observed transports in most branches crossing the GSR. Observations and reanalyses with data assimilation show a marked reduction in oceanic heat flux across the GSR of 4 %–9 % (compared to 1993–2020 means) during a biennial (2-year-long) period centered on 2018, a record low for several products. The anomaly was associated with a temporary reduction in geostrophic Atlantic Water inflow through the Faroe–Shetland branch and was augmented by anomalously cool temperatures of Atlantic Water arriving at the GSR. The latter is linked to a recent strengthening of the North Atlantic subpolar gyre and illustrates the interplay of interannual and decadal changes in modulating transports at the GSR.

Published by Copernicus Publications.

https://doi.org/10.5194/sp-1-osr7-14-2023

Table 1. CMEMS and non-CMEMS products used in this study, including information on data documentation.

Product ref. no.	Product ID and type	Data access	Documentation
1	GLOBAL_REANALYSIS_PHY_001_031 (GREPv2), numerical models	EU Copernicus Marine Service Product (2022a)	Quality Information Document (QUID): Desportes et al. (2022) Product User Manual (PUM): Gounou et al. (2022)
2	GLOBAL_MULTIYEAR_PHY_001_030 (GLORYS12V1), numerical models	EU Copernicus Marine Service Product (2022b)	Quality Information Document (QUID): Drévillon et al. (2022a) Product User Manual (PUM): Drévillon et al. (2022b)
3	Mooring-derived ocean heat transport into Arctic Mediterranean from 1993 updated to July 2021	Data available at http://metadata.nmdc.no/metadata-api/landingpage/0a2ae0e42ef7af767a920811e83784b1 (last access: 21 March 2023); updated time series are available from the authors upon reasonable request.	Tsubouchi et al. (2020, 2021)
	Observational input data for product no. 3		
	Iceland–Faroe branch: January 1993 to December 2020	Data for I-F branch, F-S branch, NIIC, and Faroe Bank Channel are available at OceanSITES (http://www.oceansites.org/tma/gsr.html, last access: 22 March 2023). Data updates are available from the authors upon reasonable request.	Hansen et al. (2015)
	Faroe–Shetland branch: January 1993 to June 2021		Berx et al. (2013)
	North Icelandic Irminger Current: October 1994 to July 2021		Jónsson and Valdimarsson (2012)
	Faroe Bank Channel: December 1995 to April 2021		Hansen et al. (2016)
	Denmark Strait: May 1996 to 2021		Jochumsen et al. (2017)
	Bering Strait: August 1997 to August 2019		Woodgate (2018)
4	SEALEVEL_GLO_PHY_L4_MY_008_047 (DUACS), satellite observations	EU Copernicus Marine Service Product (2023)	Quality Information Document (QUID): Pujol et al. (2023) Product User Manual (PUM): Pujol (2022)
5	Hindcast ocean simulations (no data assimilation) at 0.25° horizontal resolution and 50 vertical levels (GLOB4) and 0.0625° horizontal resolution and 98 vertical levels (GLOB16) provided by CMCC	Data available from the authors upon reasonable request.	Iovino et al. (2023)
6	Ocean reanalysis at 0.25° horizontal resolution and 75 vertical levels provided by UKMO (GloRanV14)	Data available from the authors upon reasonable request.	MacLachlan et al. (2015)

1 Introduction

The Greenland–Scotland Ridge (GSR), encompassing the Denmark Strait, Iceland–Faroe (I-F) branch, Faroe–Shetland (F-S) branch, and European shelf, represents the main oceanic gateway to the so-called Arctic Mediterranean (the ocean bounded by the GSR, Davis Strait, and Bering Strait). Oceanic transports across the GSR play an important role in the Arctic and global climate systems. In the surface layer, the warm and saline Atlantic Water moves northward across the GSR and the light Polar Water flows southward mainly through the Denmark Strait. In the lower layer, the cold and dense water is transported southward at depth into the North Atlantic, contributing to the lower limb of the Atlantic meridional overturning circulation (Hansen and Østerhus, 2000; Buckley and Marshall, 2016).

Transports across the GSR exhibit pronounced interannual variability and thereby play an important role in modulating the heat budget of the Arctic Mediterranean (e.g., Muilwijk et al., 2018; Mayer et al., 2016; Asbjørnsen et al., 2019). Specifically, the inflow of warm and saline Atlantic Water (AW) exhibits a strong co-variability with ocean heat content, especially in the AW layer of the Arctic Mediterranean (M. Mayer et al., 2022). Tsubouchi et al. (2021), using observation-based oceanic transport data (1993–2016), revealed a step change towards stronger oceanic heat transports (OHTs) across the GSR around 2002, suggesting an enhanced contribution of OHT to the observed warming of the Arctic Ocean. M. Mayer et al. (2022) temporally extended the monitoring of OHT at the GSR using ocean reanalyses and found a pronounced reduction in OHT around 2018, which could not be verified with observational data at that time and the causes of which were not explored in detail.

Here, we use observational oceanic transport data at the boundaries of the Arctic Mediterranean updated to 2021 and an extended set of ocean reanalyses to explore the pronounced reduction in OHT in more detail, track it to the main contributing oceanic branch, and relate these changes to larger-scale climate variations on interannual and decadal timescales. An additional aspect of this study is a more detailed validation of reanalysis-based oceanic transports at the GSR at the scale of single branches to further build trust in the usefulness of these products for monitoring Arctic climate and its oceanic drivers.

2 Data and methods

We use monthly data from a comprehensive set of ocean reanalyses to compute oceanic transports across the GSR, Davis Strait, and Bering Strait. The latter two straits are calculated to close the volume budget and obtain unambiguous net heat transport into the Arctic Mediterranean (Schauer and Beszczynska-Möller, 2009). Inflow (positive) has been defined as positive towards the Arctic Mediterranean. The employed products are an updated ensemble based on the Copernicus Marine Environment Monitoring Service Global Reanalysis Ensemble Product (CMEMS GREPv2, product ref 1), consisting of ORAS5, CGLORS, GLORYS2V4, and GloRanV14 (an improvement of GloSea5, also known as the FOAM product, product ref 6; MacLachlan et al., 2015). These are all run at 0.25° horizontal resolution with 75 vertical levels and use atmospheric forcing from ERA-Interim (Dee et al., 2011). The ensemble is complemented with GLORYS12 version 1 (product ref 2), a reanalysis at 0.083° horizontal resolution with 50 vertical levels driven by ERA-Interim atmospheric forcing. Furthermore, two hindcast ocean simulations (i.e., with no data assimilation) at 0.25° horizonal resolution with 50 vertical levels (GLOB4) and 0.0625° horizontal resolution and 98 vertical levels (GLOB16; Iovino et al., 2023) driven by JRA55-do (Tsujino et al., 2018) are employed to investigate the impact of resolution on oceanic volume fluxes. Heat transports from GLOB4 and GLOB16 are not assessed as these are biased due to their setup as forced runs without data assimilation. Transports are computed on the native grid through line integrals similar to Pietschnig et al. (2018).

Observational mass-consistent estimates of oceanic transports (product ref 3) are updated to July 2021 following Tsubouchi et al. (2021; i.e., using the same strategy to infill data gaps, estimate uncertainty, and create a box inverse model to close the volume budget). Temporal coverage and references for the single observational estimates used as input are provided in the data table (Table 1). Surface freshwater inputs by river discharge and precipitation minus evaporation for 1993–2021 used as input to the box inverse model are based on Winkelbauer et al. (2022). The used reanalyses assimilate temperature and salinity profiles available from databases such as Hadley EN4 (Good et al., 2013), which according to our investigations include only a small subset of the mooring data used for our observational transport estimates. Currents are generally not assimilated in ocean reanalyses. Hence, the observation-based volume fluxes represent fully independent data, while temperature fluxes represent largely independent validation data.

We note that quantification methods of oceanic transports in reanalyses and observations are fundamentally different, which needs to be kept in mind when intercomparing. The reanalysis-based estimate is based on surface-to-bottom, coast-to-coast temperature and velocity sections across the Arctic Mediterranean. This ensures conservation of volume and avoids projection of potentially biased positioning of currents in the reanalyses onto the transport estimates. The observational estimate is based on the sum of 11 major ocean current transport estimates categorized into three major water masses – Atlantic Water (AW), Polar Water (PW), and Overflow Water (OW) (Tsubouchi et al., 2021). An assumption is that the 11 major ocean currents represent the major water mass exchanges well across the Arctic Mediterranean. This means it is important that no recirculation, e.g., of AW waters, remains unobserved, as this would introduce

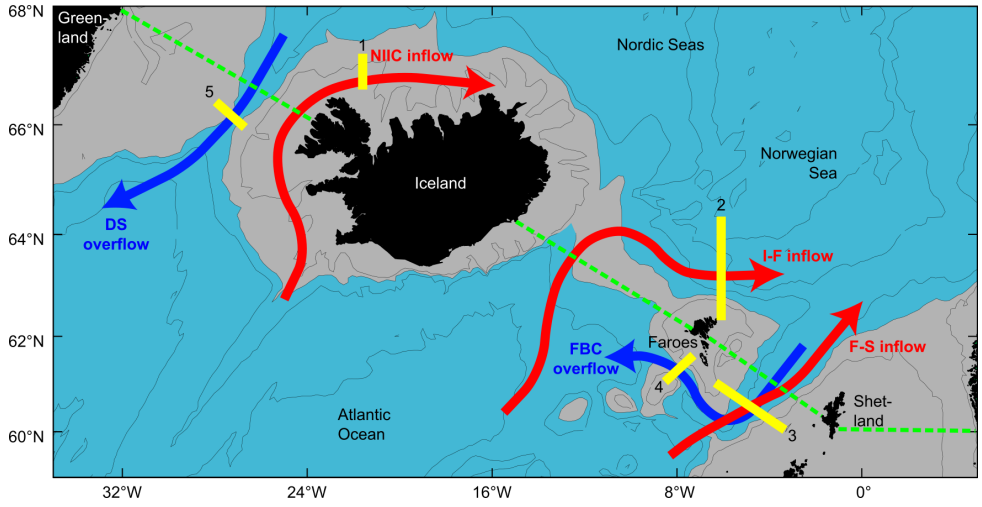

Figure 1. Map of the Greenland–Scotland Ridge region, schematically depicting shallow shelf water and deep water, major AW inflow (red arrows) and OW outflow (blue arrows) branches (DS stands for Denmark Strait, and FBC stands for Faroe Bank Channel), the location of oceanic moorings used for deriving the observation-based transport estimates (yellow bars), and the section used for the computation of transports from ocean reanalyses (dashed green line). Adapted from OceanSITES (http://www.oceansites.org/tma/gsr.html, last access: 20 March 2023, Fig. 1).

biases into the observational estimate. This assumption has been assessed and confirmed many times over the last 2 decades from establishment of sustained hydrographic sections in the GSR in the 1990s (e.g., Dickson et al., 2008) to recent oceanographic surveys to capture ocean circulation in the GSR for AW (e.g., Berx et al., 2013; Hansen et al., 2017; Rossby et al., 2018; Jónsson and Valdimarsson, 2012) and OW (Hansen et al., 2018). We also note that remaining uncertainties arising from potential undersampling are taken into account in the observational estimate obtained through the inverse model. For reference, Fig. 1 shows pathways of major flows across the GSR and the locations of considered oceanic moorings and the sections used for evaluation of reanalyses.

As in M. Mayer et al. (2022), we assume total uncertainties in monthly mean observations (provided in Tsubouchi et al., 2021) to consist of roughly half systematic and half random errors; i.e., the two contributions are the total uncertainty reduced by a factor of $1/\sqrt{2}$. Consequently, the contribution of random errors to uncertainties in long-term mean observational estimates is further reduced by a factor of $1/\sqrt{N}$, where N is the number of years, and deseasonalized anomalies only include the random errors.

Transported water masses at the GSR are decomposed into AW, PW, and OW, largely following Eldevik et al. (2009). PW is defined as $T < 4\,°\mathrm{C}$ and $\sigma_\theta < 27.7\,\mathrm{kg\,m^{-3}}$. OW is defined as $\sigma_\theta > 27.8\,\mathrm{kg\,m^{-3}}$. The rest (i.e., waters with $\sigma_\theta < 27.8\,\mathrm{kg\,m^{-3}}$ with PW taken out) is considered AW. Note that these definitions have been revised from M. Mayer et al. (2022). Water mass decomposition is performed each month based on the monthly temperature and salinity fields in the reanalyses. These definitions are similar to those used for observational products (see references for more details, e.g., Eldevik et al 2009).

We additionally use sea level anomaly (SLA) data provided through CMEMS (product ref 4) for investigating drivers of observed OHT anomalies. The global mean SLA trend is removed before computation of the presented diagnostics.

Deseasonalized anomalies are based on the 1993–2019 climatologies, i.e., the period for which all data are available. Anomaly time series have a 12-monthly temporal smoother applied to emphasize interannual variations. Confidence levels (95 % is set as threshold for significance testing) for temporal correlations take auto-correlation of the involved time series into account (see Oort and Yienger, 1996).

3 Results

3.1 General evaluation of transports of water masses across the GSR

Figure 2 presents mean annual cycles and anomaly time series of relevant oceanic transport quantities at the GSR. It is complemented with long-term averages shown in Table 2 (volume fluxes) and Table 3 (heat fluxes). Observations show seasonally varying AW inflow across the GSR (8.0 ± 0.5 Sv; mean $\pm$ standard deviation of the mean reported throughout, unless explicitly stated) with a maximum in December and minimum in June–July (Fig. 2a). The AW inflow is largely balanced by PW (Fig. 2c; -1.8 ± 0.7 Sv) and OW (Fig. 2b; -5.6 ± 0.3 Sv) outflow, yielding a relatively small net volume flux across the GSR of 0.7 Sv (balanced by flows through Bering and Davis straits). The PW outflow exhibits

an annual cycle balancing the AW inflow (i.e., maximum outflow in boreal winter), while the OW exchange is more stable throughout the year (i.e., small annual cycle).

All reanalyses but one (CGLORS) underestimate AW inflow across the GSR when compared to observations, but the shape of the annual cycle of all estimates is in good agreement with observations. The AW net flow from high-resolution products does not stand out compared to the 0.25° products and is close to the GREP mean. Agreement is also good for the PW outflow, where all products show the observed seasonal maximum flow in boreal winter. The range of reanalysis-based estimates is large in a relative sense, with the observations lying in the middle of the range. There is less coherence across products concerning the OW transports. GLORYS12, GLORYS2V4, and CGLORS are close to observations, with rather persistent overflow on the order of −5.4 Sv and seasonal variations that agree with the observations. Other products tend to have overflows that are too weak (most notably ORAS5), and some also exhibit biases in the representation of the annual cycle (e.g., GloRanV14).

Table 2 additionally includes long-term average volume fluxes in the main AW inflow branches (North Icelandic Irminger Current (NIIC), I-F branch, F-S branch, and European shelf). The reanalysis-based estimates generally agree well with observations. The main discrepancy is the underestimation of I-F inflow and overestimation of F-S inflow by all GREP reanalyses, while the high-resolution products GLORYS12 and GLOB16 are in much better agreement with observations. Direct comparison of GLOB16 to GLOB4 confirms that overestimation of F-S volume flux is reduced when going from 0.25 to 0.0625° resolution. This suggests that increased resolution, along with more realistic bathymetry, improves representation of inflow pathways in the reanalyses. We also note that temporal anomaly correlations with observed I-F volume fluxes are low (Pearson correlation coefficients r range from −0.03 to 0.26 and are statistically insignificant) for all reanalyses but are substantially higher for F-S volume fluxes (r ranges from 0.30 to 0.71 and is statistically significant for all products with data assimilation).

Figure 2d shows the mean annual cycle of heat flux across the GSR, i.e., the sum of sensible heat transported by all waters crossing the GSR. The mean annual cycle of GSR heat fluxes generally follows that of AW volume fluxes, with a minimum between boreal spring and early summer and a maximum in fall and early winter. Seasonal minima and maxima in GSR heat flux co-occur with those of AW volume flux; i.e., seasonal variations in heat flux are largely volume flux driven, and the seasonal cycle in volume-weighted temperatures is in phase.

Since net volume flux across the GSR is small, the ambiguity arising from the choice of reference temperature can be considered small as well. However, for the long-term averages we focus on net heat transport into the Arctic Mediterranean, i.e., the sum of heat fluxes across the GSR, plus those through Bering and Davis straits. Values in Table 3 show that all reanalyses exhibit lower net heat transport (by ∼ 16 % for the GREP mean of 256 ± 19 TW) than that observed (306 ± 19 TW; 311 ± 20 TW when including sea ice). GLORYS12 exhibits a mean net heat flux similar to the GREP mean, but we note that all GREP reanalyses have AW influx that is too strong in the F-S branch (Table 2), where the climatologically warmest waters cross the GSR, and thus enhance the heat flux in those products for the wrong reason.

The net heat transport is clearly related to the strength of AW inflow, but even CGLORS, which has a higher AW mean volume flux (8.3 Sv) than observations, has a negative net heat flux bias. The reason is that all reanalyses exhibit a warm bias in outflowing OW (not shown) and a cold bias in Davis Strait inflow (see Pietschnig et al., 2018). Based on M. Mayer et al. (2022) and taking oceanic storage into account, the energy-budget-based estimate of the net heat boundary transport suggests even higher values (∼ 348 TW) than observations. This inferred value appears high, but we note that this indirect approach has been applied successfully to infer observation-based oceanic transports in the North Atlantic (Trenberth and Fasullo, 2017; Liu et al., 2020; J. Mayer et al., 2022) and the central Arctic (Mayer et al., 2019), and hence it is deemed credible. This estimate at least adds confidence to the conclusion that the observational estimate of oceanic heat transport is not biased high. Table 3 also confirms that long-term averages for heat flux across the GSR are qualitatively very similar to the net heat transport; i.e., heat fluxes across the GSR are the dominant contributor to oceanic heat transport into the Arctic Mediterranean.

Figure 2e shows deseasonalized anomalies of AW volume flux, with a 12-monthly smoother applied to emphasize interannual variability. Typical variability is similar across observations (temporal standard deviation $\sigma = 0.35$ Sv) and reanalyses (σ ranges between 0.22 and 0.47 Sv). Temporal correlations between reanalyzed and observed AW inflow anomalies are moderately high (r ranges between 0.39 and 0.60 and is statistically significant for all products; see the legend of the plot for values).

Figure 2f shows anomalies of total oceanic heat flux across the GSR, which show similar variability to AW volume flux; i.e., the strength of AW inflow modulates not only the seasonal cycle of the total GSR heat flux but also its interannual variations (r ranges from 0.86 to 0.91). GSR total heat flux from reanalyses is in slightly better agreement with observations than AW volume fluxes (r ranges between 0.51 and 0.63 and is statistically significant for all products; see the legend of the plot for values). Figure 2f also shows a prominent negative heat flux anomaly centered around the year 2018, which has already been noted by M. Mayer et al. (2022) for net heat transport into the Arctic Mediterranean.

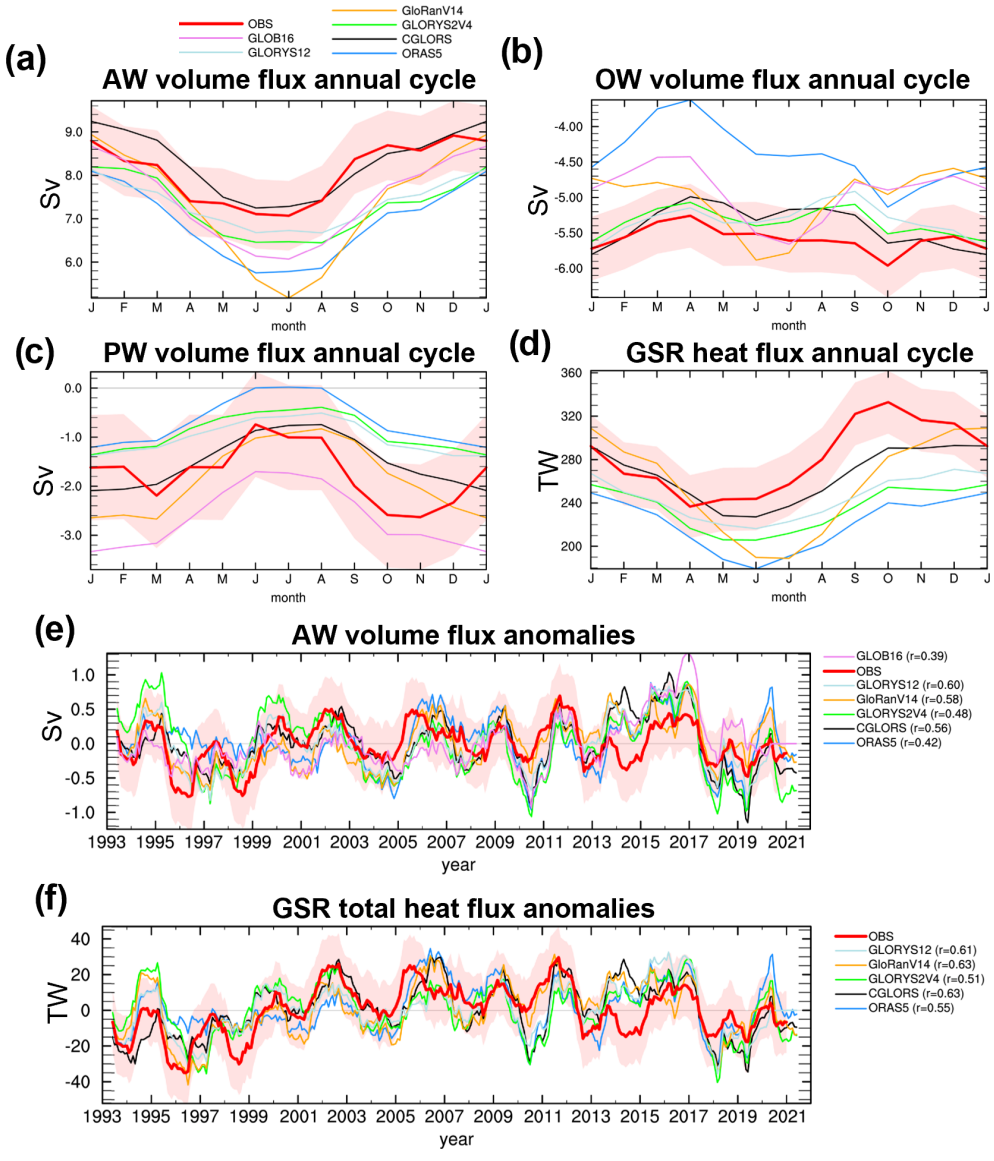

Figure 2. Mean annual cycle of **(a)** AW volume flux, **(b)** OW volume flux, **(c)** PW volume flux, and **(d)** GSR total (AW + PW + OW) heat flux. Temporal anomalies of **(e)** AW volume flux and **(f)** GSR total heat flux. The red shading indicates ±1 standard error in the observational data. Temporal correlations of reanalyses with observations are provided in the legends.

3.2 Spatial structure of the July 2017–June 2019 transport anomaly

To set the scene for further investigation, we present climatological temperatures and currents at the GSR based on GLORYS12 in Fig. 3a and b, respectively. Comparison with analogous figures based on the GREP (shown in M. Mayer et al., 2022) allows us to appreciate the benefits of increased resolution (0.08 vs. 0.25° resolution), including a more distinct representation of inflow and outflow branches and a more spatially variable bathymetry, especially in the I-F branch.

Next, we investigate the recent reduction in AW volume and GSR heat fluxes in more detail. This is most prominent in the biennial (2-year-long) signal of average anomalies in July 2017–June 2019. Figure 3c shows that during this period strong warm anomalies were present over 0–400 m depth in the eastern Denmark Strait, and warm anomalies are also seen in the F-S branch. The latter suggests a temporary deepening of the AW layer. Velocity anomalies for the July 2017–June 2019 period (Fig. 3d) suggest that the positive temperature anomalies in the eastern Denmark Strait are driven by enhanced NIIC transports. The strongest and deepest velocity anomaly in July 2017–June 2019 is located in the eastern part of the F-S branch, where reduced inflow is present from the surface down to the interface at ∼ 600 m, and hence we focus on this branch next. Negative anomalies are also seen in

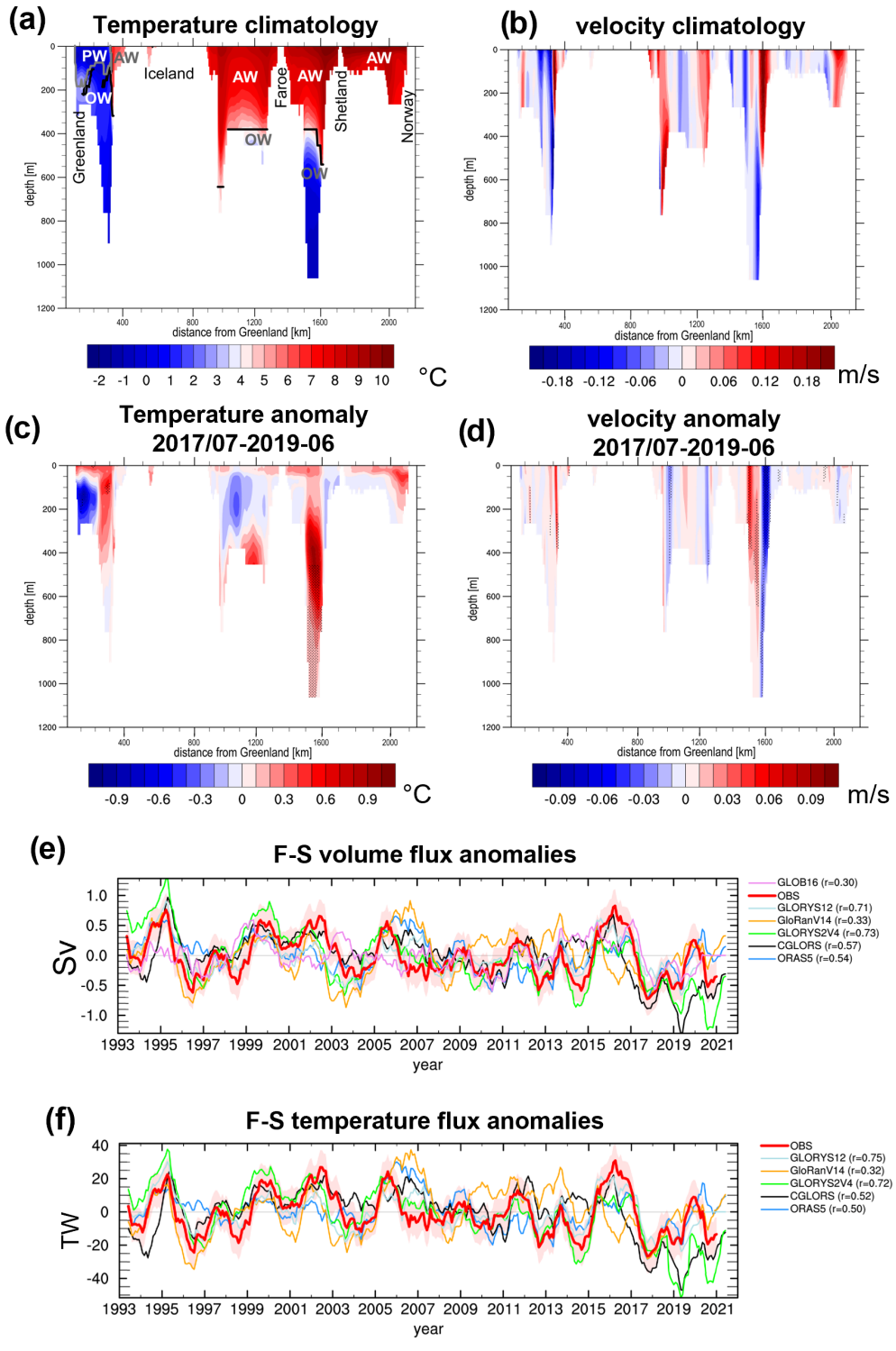

Figure 3. Longitude–depth sections of **(a)** mean temperature (with water mass boundaries indicated), **(b)** mean velocity, **(c)** July 2017–June 2019 anomalous temperature, and **(d)** July 2017–June 2019 anomalous velocity across the GSR based on GLORYS12 (stippling denotes grid cells where anomalies are $> 2\sigma$ of biennial anomalies). Note that the section does not go along the shallowest part of the Denmark Strait and I-F Ridge everywhere, leading to deeper trenches in some places (see also Fig. 1). Time series of **(e)** anomalous volume and **(f)** anomalous temperature flux through the Faroe–Shetland branch, where the red shading indicates ± 1 standard error in the observational data. Temporal correlations of reanalyses with observations are provided in the legends.

Table 2. Long-term mean of volume flux in different water masses and branches across the GSR. Observational European shelf volume fluxes are based on Østerhus et al. (2019). All values are based on 1993–2020 (since observational data do not completely cover 2021) data, except for GLOB16 and GLOB4 (based on 1993–2019 data). Values are given in Sv.

	GSR total	PW	OW	AW	AW NIIC	AW I-F	AW F-S	Shelf
Observations	0.7 ± 0.9	-1.8 ± 0.7	-5.6 ± 0.3	8.0 ± 0.5	0.9 ± 0.1	3.8 ± 0.3	2.7 ± 0.3	0.6 ± 0.3
GREP mean	1.2 ± 0.6	-1.2 ± 0.5	-5.0 ± 0.5	7.4 ± 0.6	0.9 ± 0.2	2.5 ± 0.4	3.5 ± 0.6	0.5 ± 0.2
ORAS5	1.8	−0.6	−4.4	6.8	1.2	2.6	2.8	0.2
CGLORS	1.4	−1.5	−5.4	8.3	0.8	2.8	3.9	0.8
GLORYS2V4	1.0	−0.9	−5.4	7.3	0.8	2.6	3.3	0.6
GloRanV14	0.4	−1.8	−5.0	7.2	0.9	1.9	4.1	0.3
GLORYS12	1.0	−1.0	−5.3	7.3	1.0	3.3	2.4	0.6
GLOB16	−0.2	−2.6	−4.9	7.4	0.6	3.2	3.0	0.6
GLOB4	1.2	−2.7	−4.4	8.3	0.8	3.2	3.7	0.6

Table 3. Long-term mean of total heat flux across the GSR and into the Arctic Mediterranean (total GSR transports plus Bering Strait and Davis Strait transports). The energy-budget-based transport estimate is taken from M. Mayer et al. (2022) and by definition can only be provided for a closed area like the Arctic Mediterranean. All values are based on 1993–2020 data. Values are given in TW.

	GSR total	Arctic Mediterranean
Observations	280 ± 18	306 ± 19
GREP mean	243 ± 21	256 ± 19
ORAS5	219	239
CGLORS	265	276
GLORYS2V4	234	242
GloRanV14	255	269
GLORYS12	243	252
Based on the energy budget	–	348

the overflow from 600 to 1000 m depth. There is some compensation by positive velocity anomalies in the western F-S (meaning reduced southward flow there), but the effect of the eastern F-S anomaly dominates, and the net F-S volume flux anomaly was clearly reduced during this period (see below). We note that these main features are also similar in anomaly sections based on the GREP ensemble mean (not shown).

Observations and all reanalyses show large negative F-S volume inflow anomalies of −0.61, −0.56, −0.34, and −0.24 Sv in the observations, GREP_mean, GLORYS12, and GLOB16, respectively, during July 2017–June 2019 (Fig. 3e). In four out of seven datasets, this is the overall biennial minimum of the 1993–2021 record (not shown). The total AW volume flux anomaly for that period was −0.24, −0.53, −0.37, and +0.08 Sv in the observations, GREP_mean, GLORYS12, and GLOB16, respectively. Thus, F-S volume flux anomalies were partly compensated by other AW branches, with no very clear signal in any of them (not shown). Only GLOB16 exhibits a positive AW volume flux anomaly during that period, which appears to be related to a shift towards generally higher AW volume flux around 2016 (see Fig. 2e). This is not seen in any of the other products.

Temperature transport anomalies in the F-S branch are strongly correlated with volume flux anomalies (compare Fig. 3e and f), and there is a clear reduction in F-S branch temperature flux in July 2017–June 2019 of −21.9, −24.1, and −16.1 TW in the observations, GREP_mean, and GLORYS12, respectively. The contribution of temperature anomalies in the F-S branch during that time was small, with biennial anomalies of observed volume-weighted temperatures between −0.2 and −0.1 K (similar for all products). The total AW heat flux anomaly for July 2017–June 2019 was −11.0, −22.5, and −19.4 TW in observations, GREP_mean, and GLORYS12, respectively. Thus, the reduction in GSR heat transports during that period was mainly driven by a reduction in volume inflow through the F-S branch. It was only partly offset by compensating transport anomalies in other branches. Very similar biennial heat transport anomalies for the total GSR (−11.1, −20.9, and −19.3 TW for observations, GREP_mean, and GLORYS12, respectively) confirm AW as the main driver of heat flux variability across the GSR.

3.3 Relationships between sea level and AW inflow

For a better understanding of mechanisms contributing to the GSR transport anomaly around 2018, we first consider basic statistical relationships between SLA and oceanic quantities. We find a statistically significant temporal correlation of the zonal SLA gradient at GSR with observed AW volume flux anomalies (Fig. 4a), which is plausible in terms of geostrophic balance. The correlation pattern looks very similar when performed with the F-S branch volume flux alone (not shown). The pattern of temporal correlation between the SLA field and observed anomalies of volume-weighted temperature of AW transports (Fig. 4b) is distinct from the relationship with AW volume flux (compare Fig. 4a). It emphasizes SLA in the North Atlantic subpolar gyre (SPG),

with higher SLA in the SPG (i.e., a weaker gyre) associated with higher volume-weighted temperature and vice versa. Although correlations are high (r up to 0.69) in the SPG region, they are not statistically significant. The cause may be the low number of degrees of freedom, as the SLA in the SPG exhibits high temporal auto-correlation (see Fig. 4d discussed below).

Actual SLA anomalies averaged over July 2017–June 2019 (Fig. 4c) indicate a weakened zonal SLA gradient at the GSR, albeit not very strongly pronounced, and anomalously low SLA in the SPG region. According to the correlation patterns discussed above, these two features suggest reduced AW volume flux (as suggested by patterns in Fig. 4a) and anomalously low AW volume-weighted temperatures (as suggested by patterns in Fig. 4b). We also note the positive SLA anomalies north of the GSR with a maximum in the central Nordic Seas.

To put these results in context, we define two SLA-based indices (shown in Fig. 4d) from the correlation patterns found in Fig. 3a and b. The similarity of the correlations in Fig. 4a to the correlations between total OHT at the GSR and SLA shown in M. Mayer et al. (2022) reinforces use of their gradient-based index (i.e., standardized SLA difference between 58–60° N, 2–0° W and 63–67° N, 20–15° W). This index is correlated with AW volume flux anomalies ($r = 0.62$ for observed transports, ranging from 0.47 to 0.70 for reanalyses, which is statistically significant in all cases). The second index uses spatial SLA averages in the North Atlantic region (55–60° N and 40–15° W) as an inverse proxy for SPG strength. This index is correlated with anomalies of volume-weighted temperatures of AW transports. The two indices in Fig. 4d show different characteristics, with the SPG index varying on decadal timescales, while the gradient index shows stronger interannual variations. The SPG index has been negative since $\sim$2014, which suggests a strong SPG and lower inflow temperatures in recent years, in agreement with results by Hátún and Chafik (2018). This SPG index exhibits two minima during the July 2017–June 2019 period, although these are not extreme relative to the entire time series.

Figure 4e shows volume-weighted temperatures of AW waters from different products and confirms their overall decrease in recent years. Comparison with the SPG index in Fig. 4d suggests a generally delayed response of volume-weighted temperature in Atlantic inflow water at the GSR to SPG strength. Lagged correlation analysis indeed suggests positive correlations peaking (at values around 0.3 to 0.5, depending on the dataset) when temperatures are lagging the SPG index $\sim$2–3 years (not shown), but the correlations are not significant due to the high auto-correlation of time series.

4 Conclusions

Reanalysis-based oceanic transports show generally good agreement with observations on the scale of single branches of the GSR, in terms of both mean and variability in volume and heat fluxes. There is some indication that the higher-resolution products have a better representation of AW inflow in the I-F and F-S branches. All considered products underestimate net heat flux into the Arctic Mediterranean. The magnitude of the low bias is correlated with the strength of AW volume flux, but a warm bias in OW and cold bias in Davis Strait inflow further add to the found net heat flux bias. We reiterate that reanalysis-based and observational transport estimates are obtained in different ways (closed line integrations versus measurements from 11 branches with an inverse model applied), but, as elaborated in Sect. 2, we deem this a fair and robust approach for an intercomparison. The energy-budget-based estimate from M. Mayer et al. (2022) suggests even higher net heat flux than oceanic observations, which confirms the underestimation of heat transports by the ocean reanalyses. A much smaller discrepancy was found in an analogous comparison of observed oceanic transports into the central Arctic and an energy-budget-based estimate (Mayer et al., 2019), potentially reflecting the different observational strategies in Fram Strait and the Barents Sea Opening compared to the GSR (see, e.g., Dickson et al., 2008) or potential biases in the employed energy budget fields over the Nordic Seas.

All reanalyses with data assimilation and observations show a pronounced reduction in OHT during the 2-year period July 2017–June 2019, with some recovery after that. Comparison of observed SLA patterns during this period with statistical relationships between SLA and oceanic transports suggests that this reduction arose from a combination of interannual- (i.e., reduced zonal SLA gradient at the GSR) and decadal-scale changes (i.e., strong SPG in recent years). Another potential factor contributing to the OHT reduction during July 2017–June 2019 may have been the positive SLA anomalies centered in the Nordic Seas (Fig. 4c), which Chatterjee et al. (2018) have related to a weakened gyre circulation in the Nordic Seas and may have contributed to the weakened AW inflow as well.

Our results also reveal a delayed response of AW inflow temperatures to SPG strength. This is consistent with earlier studies finding anti-correlation between SPG strength and GSR heat transport (Häkkinen et al., 2011; Hátún et al., 2005). Specifically, the generally weaker SPG during $\sim$1997 and $\sim$2014 (with more pronounced minima in 1997–1998, 2010–2011, and 2003–2006; see Hátún and Chafik, 2018) was associated with warm inflow temperatures and stronger OHT after 2001 (Tsubouchi et al., 2021). After that point, the SPG strengthened and the inflow temperatures declined, which is also consistent with generally reduced oceanic heat transports in recent years.

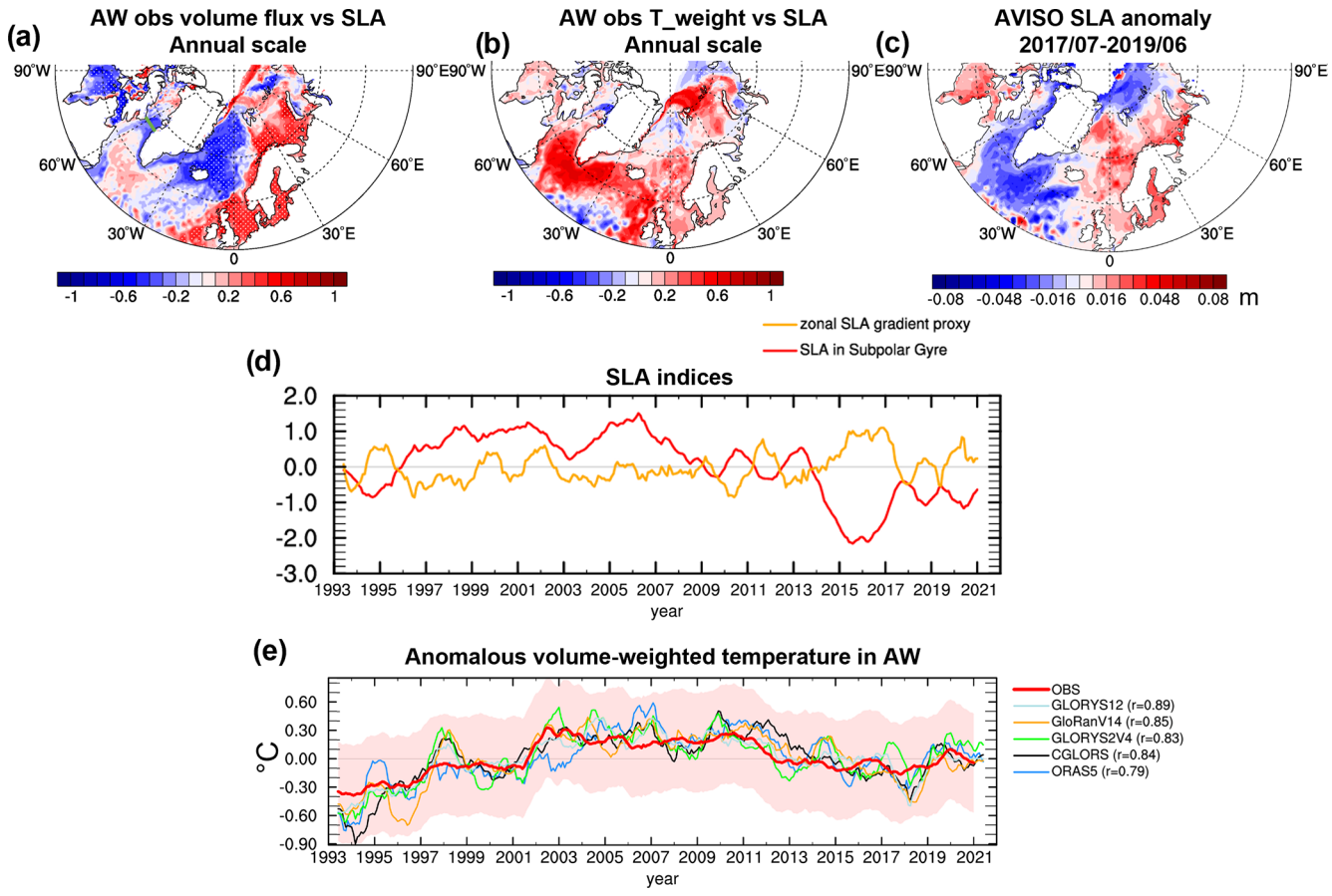

Figure 4. Correlation of observation-based **(a)** AW volume flux and **(b)** AW flux-weighted temperature with SLA with a 12-monthly smoother applied. **(c)** SLA anomaly in July 2017–June 2019. **(d)** Temporal evolution (standardized) of two SLA-based indices based on the zonal SLA gradient at GSR and the SLA in the SPG region. **(e)** Temporal evolution of volume-weighted temperature (T_weight) anomalies of Atlantic waters at the GSR (red shading indicates ±1 standard error in the observational data, and temporal correlations of reanalyses with observations are provided in the legend). Stippling in **(a)** and **(b)** denotes statistically significant correlations on the 95 % confidence level.

The presented results indicate that decadal predictions of the SPG strength, which have been shown to exhibit skill (e.g., Robson et al., 2018; Borchert et al., 2021), may also allow us to infer near-term trends in OHT across the GSR. Another implication is that the strong interannual-to-decadal variability in OHT across the GSR hampers detection of longer-term (forced and unforced) trends in observed OHT, an aspect in which climate simulations show large spread (Burgard and Notz, 2017). Continued in situ monitoring of OHT, complemented with reanalysis efforts, is thus needed to provide observationally constrained time series of sufficient length for climate model validation.

Data availability. The data products used in this article, as well as their names, availability, and documentation, are summarized in Table 1.

Author contributions. MM and TT conceptualized the study. All co-authors were involved with data preparation and analysis, as well as interpretation of results. MM prepared the manuscript with contributions from all co-authors.

Competing interests. The contact author has declared that none of the authors has any competing interests.

Disclaimer. Publisher's note: Copernicus Publications remains neutral with regard to jurisdictional claims in published maps and institutional affiliations.

Acknowledgements. The Iceland–Faroe branch and Faroe Bank Channel overflow data collections received funding from the Danish Ministry of Climate, Energy and Utilities through its climate support program to the Arctic. The Denmark Strait overflow time series was generated by the Institute of Oceanography, Hamburg, and the Marine and Freshwater Research Institute (Iceland). Observational

data collection was further supported through funding from Nordic WOCE, VEINS, MOEN, ASOF-W, NACLIM, RACE II, RACE-Synthese, THOR, AtlantOS, and Blue-Action (EU Horizon 2020 grant agreement no. 727852).

Financial support. This research has been supported by the Austrian Science Fund (grant no. P33177) and Copernicus Marine Service (grant no. 21003-COP-GLORAN Lot 7).

Review statement. This paper was edited by Gilles Garric and reviewed by two anonymous referees.

References

Asbjørnsen, H., Årthun, M., Skagseth, Ø., and Eldevik, T.: Mechanisms of ocean heat anomalies in the Norwegian Sea, J. Geophys. Res.-Oceans, 124, 2908–2923, 2019.

Berx, B., Hansen, B., Østerhus, S., Larsen, K. M., Sherwin, T., and Jochumsen, K.: Combining in situ measurements and altimetry to estimate volume, heat and salt transport variability through the Faroe–Shetland Channel, Ocean Sci., 9, 639–654, https://doi.org/10.5194/os-9-639-2013, 2013.

Borchert, L. F., Menary, M. B., Swingedouw, D., Sgubin, G., Hermanson, L., and Mignot, J.: Improved decadal predictions of North Atlantic subpolar gyre SST in CMIP6, Geophys. Res. Lett., 48, e2020GL091307, https://doi.org/10.1029/2020GL091307, 2021.

Buckley, M. W. and Marshall, J.: Observations, inferences, and mechanisms of the Atlantic Meridional Overturning Circulation: A review, Rev. Geophys., 54, 5–63, 2016.

Burgard, C. and Notz, D.: Drivers of Arctic Ocean warming in CMIP5 models, Geophys. Res. Lett., 44, 4263–4271, 2017.

Chatterjee, S., Raj, R. P., Bertino, L., Skagseth, Ø., Ravichandran, M., and Johannessen, O. M.: Role of Greenland Sea gyre circulation on Atlantic water temperature variability in the Fram Strait, Geophys. Res. Lett., 45, 8399–8406, 2018.

Dee, D. P., Uppala, S. M., Simmons, A. J., Berrisford, P., Poli, P., Kobayashi, S., Andrae, U., Balmaseda, M. A., Balsamo, G., Bauer, P., Bechtold, P., Beljaars, A. C. M., van de Berg, L., Bidlot, J., Bormann, N., Delsol, C., Dragani, R., Fuentes, M., Geer, A. J., Haimberger, L., Healy, S. B., Hersbach, H., Hólm, E. V., Isaksen, L., Kållberg, P., Köhler, M., Matricardi, M., McNally, A. P., Monge-Sanz, B. M., Morcrette, J.-J., Park, B.-K., Peubey, C., de Rosnay, P., Tavolato, C., Thépaut, J.-N., and Vitart, F.: The ERA-Interim reanalysis: Configuration and performance of the data assimilation system, Q. J. Roy. Meteor. Soc., 137, 553–597, 2011.

Desportes, C., Garric, G., Régnier, C., Drévillon, M., Parent, L., Drillet, Y., Masina, S., Storto, A., Mirouze, I., Cipollone, A., Zuo, H., Balmaseda, M., Peterson, D., Wood, R., Jackson, L., Mulet, S., Grenier, E., and Gounou, A.: EU Copernicus Marine Service Quality Information Document for the Global Ocean Ensemble Physics Reanalysis, GLOBAL_REANALYSIS_PHY_001_031, Issue 1.1, Mercator Ocean International, https://catalogue.marine.copernicus.eu/documents/QUID/CMEMS-GLO-QUID-001-031.pdf (last access: 31 March 2023), 2022.

Dickson, R., Meincke, J., and Rhines, P.: Arctic-Subarctic Ocean Fluxes: Defining the Role of the Northern Seas in Climate, Springer, Dordrecht, the Netherlands, ISBN 978-1-4020-6774-7, 2008.

Drévillon, M., Lellouche, J.-M., Régnier, C., Garric, G., Bricaud, C., Hernandez, O., and Bourdallé-Badie, R.: EU Copernicus Marine Service Quality Information Document for the Global Ocean Physics Reanalysis, GLOBAL_REANALYSIS_PHY_001_030, Issue 1.6, Mercator Ocean International, https://catalogue.marine.copernicus.eu/documents/QUID/CMEMS-GLO-QUID-001-030.pdf (last access: 31 March 2023), 2022a.

Drévillon, M., Fernandez, E., and Lellouche, J.-M.: EU Copernicus Marine Service Product User Manual for the Global Ocean Physics Reanalysis, GLOBAL_REANALYSIS_PHY_001_030, Issue 1.4, Mercator Ocean International, https://catalogue.marine.copernicus.eu/documents/PUM/CMEMS-GLO-PUM-001-030.pdf (last access: 31 March 2023), 2022b.

Eldevik, T., Nilsen, J. E. Ø., Iovino, D., Anders Olsson, K., Sandø, A. B., and Drange, H.: Observed sources and variability of Nordic seas overflow, Nat. Geosci., 2, 406–410, 2009.

EU Copernicus Marine Service Product: Global Ocean Ensemble Physics Reanalysis v2, Mercator Ocean International [data set], https://doi.org/10.48670/moi-00024, 2022a.

EU Copernicus Marine Service Product: Global Ocean Physics Reanalysis GLORYS12V1, Mercator Ocean International [data set], https://doi.org/10.48670/moi-00021, 2022b.

EU Copernicus Marine Service Product: Global Ocean Gridded L 4 Sea Surface Heights And Derived Variables Reprocessed 1993 Ongoing, Mercator Ocean International [data set], https://doi.org/10.48670/moi-00148, 2023.

Gounou, A., Drevillon, M., and Clavier, M.: EU Copernicus Marine Service Product User Manual for the Global Ocean Ensemble Physics Reanalysis, GLOBAL_REANALYSIS_PHY_001_031, Issue 1.1, Mercator Ocean International, https://catalogue.marine.copernicus.eu/documents/PUM/CMEMS-GLO-PUM-001-031.pdf (last access: 31 March 2023), 2022.

Good, S. A., Martin, M. J., and Rayner, N. A.: EN4: Quality controlled ocean temperature and salinity profiles and monthly objective analyses with uncertainty estimates, J. Geophys. Res.-Oceans, 118, 6704–6716, 2013.

Häkkinen, S., Rhines, P. B., and Worthen, D. L.: Warm and saline events embedded in the meridional circulation of the northern North Atlantic, J. Geophys. Res., 116, C03006, https://doi.org/10.1029/2010JC006275, 2011.

Hansen, B. and Østerhus, S.: North atlantic–nordic seas exchanges, Prog. Oceanogr., 45.2, 109–208, 2000.

Hansen, B., Larsen, K. M. H., Hátún, H., Kristiansen, R., Mortensen, E., and Østerhus, S.: Transport of volume, heat, and salt towards the Arctic in the Faroe Current 1993–2013, Ocean Sci., 11, 743–757, https://doi.org/10.5194/os-11-743-2015, 2015.

Hansen, B., Húsgarð Larsen, K. M., Hátún, H., and Østerhus, S.: A stable Faroe Bank Channel overflow 1995–2015, Ocean Sci., 12, 1205–1220, https://doi.org/10.5194/os-12-1205-2016, 2016.

Hansen, B., Poulsen, T., Húsgarð Larsen, K. M., Hátún, H., Østerhus, S., Darelius, E., Berx, B., Quadfasel, D., and Jochumsen, K.: Atlantic water flow through the Faroese Channels, Ocean Sci., 13, 873–888, https://doi.org/10.5194/os-13-873-2017, 2017.

Hansen, B., Larsen, K. M. H., Olsen, S. M., Quadfasel, D., Jochumsen, K., and Østerhus, S.: Overflow of cold water across the Iceland–Faroe Ridge through the Western Valley, Ocean Sci., 14, 871–885, https://doi.org/10.5194/os-14-871-2018, 2018.

Hátún, H. and Chafik, L.: On the recent ambiguity of the North Atlantic subpolar gyre index, J. Geophys. Res.-Oceans, 123, 5072–5076, 2018.

Hátún, H., Sandø, A. B., Drange, H., Hansen, B., and Valdimarsson, H.: Influence of the Atlantic subpolar gyre on the thermohaline circulation, Science, 309, 1841–1844, https://doi.org/10.1126/science.1114777, 2005.

Iovino, D., Fogli, P. G., and Masina, S.: Evaluation of the CMCC global eddying ocean model for the Ocean Model Intercomparison Project (OMIP2), EGUsphere [preprint], https://doi.org/10.5194/egusphere-2023-469, 2023.

Jochumsen, K., Moritz, M., Nunes, N., Quadfasel, D., Larsen, K. M. H., Hansen, B., Valdimarsson, H., and Jónsson, S.: Revised transport estimates of the Denmark Strait overflow, J. Geophys. Res.-Oceans, 122, 3434–3450, https://doi.org/10.1002/2017JC012803, 2017 (data available at: https://www.cen.uni-hamburg.de/en/icdc/data/ocean/denmark-strait-overflow.htm, last access: 22 March 2023).

Jónsson, S. and Valdimarsson, H.: Water mass transport variability to the North Icelandic shelf, 1994–2010, ICES J. Mar. Sci., 69, 809–815, https://doi.org/10.1093/icesjms/fss024, 2012.

Liu, C., Allan, R. P., Mayer, M., Hyder, P., Desbruyères, D., Cheng, L., Xu, J., Xu, F., and Zhang, Y.: Variability in the global energy budget and transports 1985–2017, Clim. Dynam., 55, 3381–3396, 2020.

MacLachlan, C., Arribas, A., Peterson, K. A., Maidens, A., Fereday, D., Scaife, A. A., Gordon, M., Vellinga, M., Williams, A., Comer, R. E., Camp, J., Xavier, P., and Madec, G.: Global Seasonal forecast system version 5 (GloSea5): a high-resolution seasonal forecast system, Q. J. Roy. Meteor. Soc., 141, 1072–1084, https://doi.org/10.1002/qj.2396, 2015.

Mayer, J., Mayer, M., Haimberger, L., and Liu, C.: Comparison of Surface Energy Fluxes from Global to Local Scale, J. Climate, 35, 4551–4569, 2022.

Mayer, M., Haimberger, L., Pietschnig, M., and Storto, A.: Facets of Arctic energy accumulation based on observations and reanalyses 2000–2015, Geophys. Res. Lett., 43, 10420–10429, https://doi.org/10.1002/2016GL070557, 2016.

Mayer, M., Tietsche, S., Haimberger, L., Tsubouchi, T., Mayer, J., and Zuo, H.: An improved estimate of the coupled Arctic energy budget, J. Climate, 32, 7915–7934, 2019.

Mayer, M., Tsubouchi, T., von Schuckmann, K., Seitner, V., Winkelbauer, S., Haimberger, L.: Atmospheric and oceanic contributions to observed Nordic Seas and Arctic Ocean Heat Content variations 1993–2020, in: Copernicus Ocean State Report, Issue 6, J. Oper. Oceanogr., 15, s119–s126, https://doi.org/10.1080/1755876X.2022.2095169, 2022.

Muilwijk, M., Smedsrud, L. H., Ilicak, M., and Drange, H.: Atlantic Water heat transport variability in the 20th century Arctic Ocean from a global ocean model and observations, J. Geophys. Res.-Oceans, 123, 8159–8179, 2018.

Oort, A. H. and Yienger, J. J.: Observed interannual variability in the Hadley circulation and its connection to ENSO, J. Climate, 9, 2751–2767, 1996.

Østerhus, S., Woodgate, R., Valdimarsson, H., Turrell, B., de Steur, L., Quadfasel, D., Olsen, S. M., Moritz, M., Lee, C. M., Larsen, K. M. H., Jónsson, S., Johnson, C., Jochumsen, K., Hansen, B., Curry, B., Cunningham, S., and Berx, B.: Arctic Mediterranean exchanges: a consistent volume budget and trends in transports from two decades of observations, Ocean Sci., 15, 379–399, https://doi.org/10.5194/os-15-379-2019, 2019.

Pietschnig, M., Mayer, M., Tsubouchi, T., Storto, A., Stichelberger, S., and Haimberger: Volume transports and temperature distributions in the main Arctic Gateways: A comparative study between an ocean reanalysis and mooring-derived data, EarthArXiv [preprint], https://doi.org/10.31223/osf.io/5hg3z, 2018.

Pujol, M.-I.: EU Copernicus Marine Service Product User Manual for the Global Ocean Gridded L4 Sea Surface Heights And Derived Variables Reprocessed 1993 Ongoing, SEALEVEL_GLO_PHY_L4_ MY_ 008_047, Issue 7.0, Mercator Ocean International, https://catalogue.marine.copernicus.eu/documents/PUM/CMEMS-SL-PUM-008-032-068.pdf, last access: 31 March 2023, 2022

Pujol, M.-I., Taburel, G., and SL-TAC Team: EU Copernicus Marine Service Quality Information Document for the Global Ocean Gridded L4 Sea Surface Heights And Derived Variables Reprocessed 1993 Ongoing, SEALEVEL_GLO_PHY_L4_MY_008_047, Issue 8.2, Mercator Ocean International, https://catalogue.marine.copernicus.eu/documents/QUID/CMEMS-SL-QUID-008-032-068.pdf, last access: 31 March 2023.

Robson, J., Polo, I., Hodson, D. L., Stevens, D. P., and Shaffrey, L. C.: Decadal prediction of the North Atlantic subpolar gyre in the HiGEM high-resolution climate model, Clim. Dynam., 50, 921–937, 2018.

Rossby, T., Flagg, C., Chafik, L., Harden, B., and Søiland, H.: A direct estimate of volume, heat, and freshwater exchange across the Greenland-Iceland-Faroe-Scotland Ridge, J. Geophys. Res.-Oceans, 123, 7139–7153, https://doi.org/10.1029/2018JC014250, 2018.

Schauer, U. and Beszczynska-Möller, A.: Problems with estimation and interpretation of oceanic heat transport – conceptual remarks for the case of Fram Strait in the Arctic Ocean, Ocean Sci., 5, 487–494, https://doi.org/10.5194/os-5-487-2009, 2009.

Trenberth, K. E. and Fasullo, J. T.: Atlantic meridional heat transports computed from balancing Earth's energy locally, Geophys. Res. Lett., 44, 1919–1927, 2017.

Tsubouchi, T., Våge, K., Hansen, B., Larsen, K. M. H, Østerhus, S., Johnson, C., Jónsson, S., and Valdimarsson, H.: Increased ocean heat transport into the Arctic Mediterranean over the period 1993–2016, NMDC [data set], http://metadata.nmdc.no/metadata-api/landingpage/0a2ae0e42ef7af767a920811e83784b1 (last access: 21 March 2023), 2020.

Tsubouchi, T., Våge, K., Hansen, B., Larsen, K. M. H., Østerhus, S., Johnson, C., Jónsson, S., and Valdimarsson, H.: Increased ocean heat transport into the Nordic Seas and Arctic Ocean over the period 1993–2016, Nat. Clim. Change, 11, 21–26, 2021.

Tsujino, H., Urakawa, S., Nakano, H., Small, R. J., Kim, W. M., Yeager, S. G., Danabasoglu, G., Suzuki, T., Bamber, J. L.,

Bentsen, M., Böning, C. W., Bozec, A., Chassignet, E. P., Curchitser, E., Boeira Dias, F., Durack, P. J., Griffies, S. M., Harada, Y., Ilicak, M., Josey, S. A., Kobayashi, C., Kobayashi, S., Komuro, Y., Large, W. G., Le Sommer, J., Marsland, S. J., Masina, S., Scheinert, M., Tomita, H., Valdivieso, M., and Yamazaki, D.: JRA-55 based surface dataset for driving ocean–sea-ice models (JRA55-do), Ocean Model., 130, 79–139, 2018.

Winkelbauer, S., Mayer, M., Seitner, V., Zsoter, E., Zuo, H., and Haimberger, L.: Diagnostic evaluation of river discharge into the Arctic Ocean and its impact on oceanic volume transports, Hydrol. Earth Syst. Sci., 26, 279–304, https://doi.org/10.5194/hess-26-279-2022, 2022.

Woodgate, R. A.: Increases in the Pacific inflow to the Arctic from 1990 to 2015, and insights into seasonal trends and driving mechanisms from year-round Bering Strait mooring data, Prog. Oceanogr., 160, 124–154, https://doi.org/10.1016/j.pocean.2017.12.007, 2018 (data available at: http://psc.apl.washington.edu/HLD/Bstrait/bstrait.html, last access: 22 March 2023).

State Planet, 1-osr7, 15, 2023
https://doi.org/10.5194/sp-1-osr7-15-2023

Intense wind-driven coastal upwelling in the Balearic Islands in response to Storm Blas (November 2021)

Baptiste Mourre[1], Emma Reyes[1], Pablo Lorente[2], Alex Santana[1], Jaime Hernández-Lasheras[1], Ismael Hernández-Carrasco[1], Maximo García-Jove[1], and Nikolaos D. Zarokanellos[1]

[1]SOCIB, Balearic Islands Coastal Observing and Forecasting System, 07122 Palma, Spain
[2]Puertos del Estado, 28042 Madrid, Spain

Correspondence: Baptiste Mourre (bmourre@socib.es)

Received: 3 August 2022 – Discussion started: 30 September 2022
Revised: 10 March 2023 – Accepted: 31 March 2023 – Published: 27 September 2023

Abstract. This article analyses the Balearic Islands wind-driven coastal upwelling in response to the intense and long-lasting Storm Blas, which affected the western Mediterranean Sea in November 2021. The storm was associated with a pronounced pressure low, generating heavy rains and intense winds and showing some characteristics of a tropical cyclone. The Balearic Islands area was particularly affected since the core of the storm was moving over a 1-week-long period from the south-west of this area to just above the islands of Menorca and Mallorca. High-resolution regional forecast models indicated that the intense north-easterly winds blowing over the region during the first days of the storm led to the development of intense upwellings along the north-western coasts of the islands of Mallorca and Ibiza together with a reversal of the surface current. While the clouds associated with the storm prevented the radiometers on board satellites to precisely observe the evolution of the sea surface signature of the upwelling, signals of enhanced chlorophyll concentration were still detected in the upwelling region. The high-resolution Western Mediterranean Operational Prediction System model, which downscales the Copernicus Marine Service Mediterranean predictions, is used to describe the characteristics of this intense coastal-upwelling event, as well as to analyse its singularity over the past-9-year time series through the comparison of different coastal-upwelling indices. The upwelling event is found to have a duration of 3 d (considering its effects on the sea surface temperature) with a spatial offshore extension of around 20 km. It was characterized by intense cold coastal sea surface anomalies of around 6 °C. While it was the most intense event over the past 9 years in terms of local cross-shore sea surface temperature gradients, it is ranked second in terms of the intensity of cross-shelf transports, behind the Storm Gloria upwelling event in January 2020. This study demonstrates the benefits of operational oceanography for the characterization of extreme events through the provision of time series of high-resolution modelling results in the coastal area.

1 Introduction

Storm Blas[1] was an intense Mediterranean cyclone which affected the western Mediterranean Sea from 6 to 18 November 2021. It was first identified on 6 November between the Balearic Islands and Sardinia before moving westwards towards the Balearic archipelago. After the core of the storm looped over the island of Mallorca on 11 November, exhibiting a well-defined, circular, deep (∼ 10 hPa) low-pressure centre, it then moved eastwards while developing a spiral structure resembling that of tropical cyclones. The storm then moved over the islands of Sardinia and Corsica before weakening and dissipating in the Tyrrhenian Sea on 18 November. Figure 1a and b show the distribution of clouds over the affected area on 7 and 13 November, as observed by Sentinel-3 Ocean and Land Colour Instrument (OLCI) satellite true-colour images.

[1]https://www.aemet.es/en/conocermas/borrascas/2021-2022/estudios_e_impactos/blas (last access: 14 April 2023)

Published by Copernicus Publications.

Table 1. Products from the Copernicus Marine Service and other complementary datasets used in this study, including the Product User Manual and quality information. For complementary datasets, the link to the product description, data access and scientific references are provided. Last access for all web pages cited in this table: 14 April 2023.

Product ref. no.	Product ID and type	Data access	Documentation
1	Images from Copernicus Sentinel-3, satellite observations	Sentinel Hub services (EO Browser), https://www.sentinel-hub.com/	Sentinel-3 mission description: https://sentinels.copernicus.eu/web/sentinel/missions/sentinel-3; data acquired by the Ocean and Land Colour Instrument (OLCI)
2	INSITU_MED_PHYBGCWAV_DISCRETE_MYNRT_013_035, in situ observations	EU Copernicus Marine Service Product (2022a)	Quality Information Document (QUID): Wehde et al. (2022); Product User Manual (PUM): Pouliquen et al. (2022)
3	HARMONIE-AROME, numerical models	AEMET, Ministerio para la Transición Ecológica y el Reto Demográfico.	System description: https://www.aemet.es/en/noticias/2017/07/modelo_harmonie-arome (Bengtsson et al., 2017)
4	SOCIB-WMOP, numerical models	SOCIB: http://thredds.socib.es/thredds/catalog/operational_models/oceanographical/hydrodynamics/wmop/catalog.html	Product description: http://socib.es/?seccion=modelling&facility=forecast_system_description (Juza et al., 2016; Mourre et al., 2018; Hernandez-Lasheras and Mourre, 2018; Hernandez-Lasheras et al., 2021)
5	MEDSEA_ANALYSIS_FORECAST_PHY_006_013, numerical models	EU Copernicus Marine Service Product (2022b)	QUID: Goglio et al. (2022); PUM: Lecci et al. (2022)
6	SST_MED_SST_L4_NRT_OBSERVATIONS_010_004, satellite observations	EU Copernicus Marine Service Product (2022c)	QUID: Pisano et al. (2022b); PUM: Pisano et al. (2022a)
7	SEALEVEL_EUR_PHY_L3_NRT_OBSERVATIONS_008_059, satellite observations	EU Copernicus Marine Service Product (2023)	QUID: Pujol et al. (2023); PUM: Pujol (2022)
8	INSITU_GLO_PHY_UV_DISCRETE_NRT_013_048, in situ observations	EU Copernicus Marine Service Product (2022d)	QUID: Verbrugge et al. (2022b); PUM: Verbrugge et al. (2022a)
9	OCEANCOLOUR_MED_BGC_L3_NRT_009_141, satellite observations	EU Copernicus Marine Service Product (2022e)	QUID: Colella et al. (2022b); PUM: Colella et al. (2022a)

This situation created extreme conditions of intense winds and high waves as well as heavy rainfall in the Balearic archipelago. In particular, intense north-easterly winds were blowing over the area during the first phase of the storm from 5 to 7 November (Fig. 1c, d), creating favourable conditions for coastal upwelling along the north-western coasts of the islands of Mallorca and Ibiza. The peak of this wind event occurred on 6 November around 10:00 UTC, with hourly mean values over 17.5 $m\,s^{-1}$ off the island of Mallorca, as represented by the HARMONIE-AROME model (Bengtsson et al., 2017) from the Spanish Meteorological Agency (AEMET).

Coastal upwelling is an oceanic process which generates upward vertical currents at the coast in response to an offshore transport of surface waters produced under the action of an intense or sustained alongshore wind stress. In the Northern Hemisphere, the wind has to blow with the coast on its left-hand side to be favourable to upwelling. By bringing cold and nutrient-rich deep waters close to the surface, the upwelling has significant effects on the physical and biogeochemical characteristics of coastal waters, generally enhancing the local primary productivity and then playing an important role in marine ecosystems (Pauly and Christensen, 1995). In the western Mediterranean Sea, wind-induced upwelling is known to occur along the French coast (Millot et al., 1979; Rey et al., 2000; Bakun and Agostini, 2001), the western and eastern coasts of Sardinia (Olita et al., 2013; Salusti, 1998), and the north-western Alboran Sea (Sarhan

et al., 2000; Macias et al., 2008). Eddy-induced coastal upwelling has also been evidenced in the Ligurian Sea (Casella et al., 2011) and along the Algerian coast (Millot et al., 1985). To our knowledge, no upwelling has been reported yet in the Balearic Islands. While the frequent north-north-westerly mistral wind events do not present the appropriate orientation to generate upwelling along the north-western coast of the Balearic Islands, favourable conditions with intense north-easterly winds are occasionally met during specific storms such as Gloria in January 2020 (Amores et al., 2020; Sotillo et al., 2021; Álvarez-Fanjul et al., 2022) or Blas in November 2021. Notice that these winds blow in the opposite direction of the established Balearic Current, which flows north-eastwards along the north-western coast of the Balearic Islands (Lopez-García et al., 1994).

This study was motivated by the intense sea surface temperature (SST) gradients along the north-western coast of the Balearic Islands seen in high-resolution regional prediction models during the first phase of Storm Blas, together with observations of surface current reversal from high-frequency (HF) radar measurements along the north-western coast of the island of Ibiza. The objective of this study is to characterize this unusually intense upwelling in terms of both its surface signature and its vertical structure, as well as to evaluate its singularity within the time series of different upwelling indices computed over the past decade. The main source of information is a high-resolution numerical prediction model given the very limited number of in situ and satellite observations available during this event.

2 Data and methods

2.1 Numerical models

We analyse the outputs of the Western Mediterranean Operational Prediction System (WMOP[2]; Juza et al., 2016; Mourre et al., 2018) developed at the Balearic Islands Coastal Observing and Forecasting System (SOCIB; Tintoré et al., 2013). The WMOP is a 2 km regional configuration of the Regional Ocean Modeling System (ROMS; Shchepetkin and McWilliams, 2005) implemented over the western Mediterranean Sea. It uses high-resolution (1 h, 2.5 km) atmospheric forcing from the HARMONIE-AROME model (Bengtsson et al., 2017) provided by AEMET. Notice that before February 2019, the HIRLAM model was used as atmospheric forcing with a resolution of 5 km and 1 h (3 h before March 2017). The WMOP downscales the conditions of the Copernicus Marine Service Mediterranean analysis and forecast model (CMEMS-MED; Clementi et al., 2021), which are used as open boundary conditions. It also includes assimilation of observations from satellite SST, along-track sea level anomaly, Argo temperature and salinity profiles as well as surface currents in the Ibiza channel, applying a local multimodel ensemble optimal interpolation approach as described in Hernandez-Lasheras and Mourre (2018) and Hernandez-Lasheras et al. (2021), with a 3 d cycle.

We also consider the outputs of the CMEMS-MED model, which provides a spatial resolution of around 4 km. This system includes variational data assimilation of temperature and salinity vertical profiles and along-track satellite sea level anomaly observations through a 3D-VAR scheme (Dobricic and Pinardi, 2008). The atmospheric forcing is provided by the predictions from the European Centre for Medium-Range Weather Forecasts[3] with a spatial resolution close to 10 km and a temporal resolution of 1 h.

2.2 Ocean colour satellite observations

High-resolution ocean colour imagery was analysed to detect the enhancement of the surface chlorophyll *a* (Chl *a*) concentration during the upwelling. The Level 3 ocean colour product distributed by the Copernicus Marine Service (Volpe et al., 2019) was used. It provides surface Chl *a* concentration from the OLCI on board the Sentinel-3 satellite with a 300 m resolution. Notice that clouds were present over the study area during the storm period, which limited the availability of exploitable high-resolution satellite observations. The Sentinel-3 OLCI observations were the only available satellite data that were found to give relevant information for the detection of the upwelling signature during the study period.

2.3 Upwelling indices

Several upwelling indices (UIs) have been used in the literature with the objective of estimating the intensity of coastal upwelling. These indices are based on either the cross-shore SST differences (Demarcq and Faure, 2000), the alongshore surface current velocities (Lorente et al., 2020) or the cross-shore Ekman transport related to the forcing winds (Bakun, 1973), sometimes also incorporating the effect of cross-shore geostrophic flows (Marchesiello and Estrade, 2010; Rossi et al., 2013; Jacox et al., 2018). This study compares four UIs computed over the 9-year time series of the WMOP operational model outputs:

i. UI_{SST} first quantifies the temperature differences between the coast (SST_{coast}) and a location 25 km offshore ($SST_{offshore}$) off the north-western coast of the island of Mallorca (edges of the magenta cross-shore section illustrated in Fig. 2a). As in Marchesiello and Estrade (2010), the observed differences are normalized by the vertical temperature differences between the surface and 200 m depth ($T^{200\,m}$) at the offshore end of the

[2] https://www.socib.es/?seccion=modellingfacility=forecast (last access: 14 April 2023)

[3] https://www.ecmwf.int (last access: 14 April 2023)

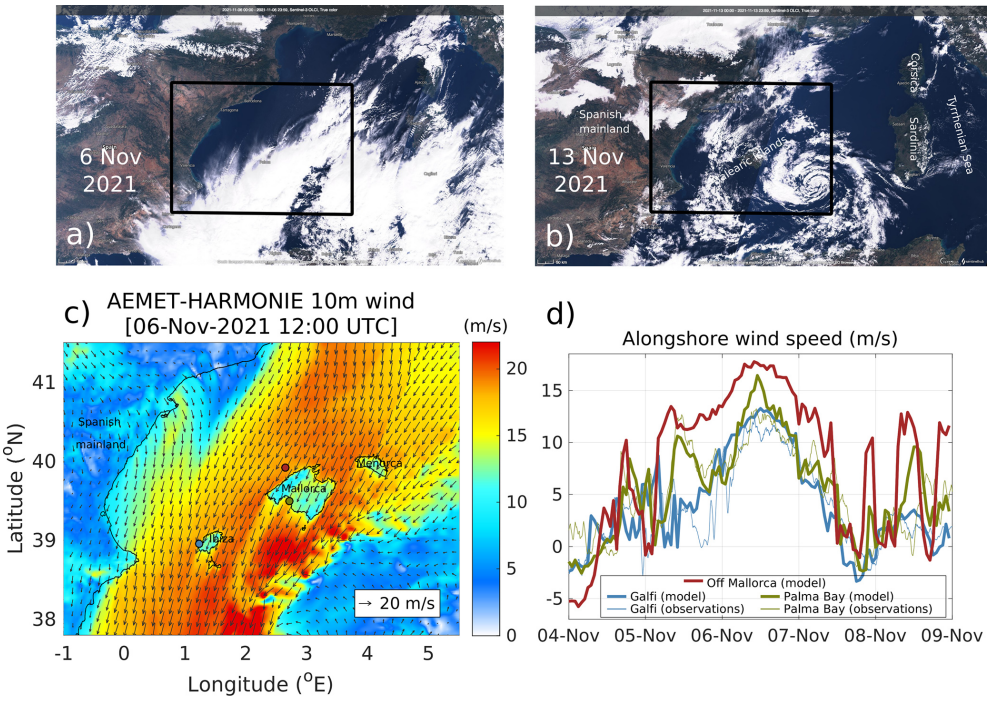

Figure 1. Upper panels: true-colour image from Sentinel-3 OLCI captured over the western Mediterranean Sea on **(a)** 6 November 2021 and **(b)** 13 November 2021. Lower panels: **(c)** 10 m wind map on 6 November 2021 from the AEMET HARMONIE-AROME prediction model over the area delimited by the black rectangles in panels **(a)** and **(b)**, **(d)** time series of alongshore 10 m wind speed from the model and observations at the three locations (1: automatic weather station of Puig des Galfí in Ibiza; 2: oceanographic buoy of Palma Bay in Mallorca; 3: virtual station off the north-western coast of Mallorca) represented in panel **(c)**. "Alongshore" is defined here considering the direction of the north-western coast of the island of Mallorca making an angle of 123° with respect to the north, with positive values south-westwards.

section according to the following formula:

$$\mathrm{UI_{SST}} = \frac{\mathrm{SST_{offshore}} - \mathrm{SST_{coast}}}{\mathrm{SST_{offshore}} - T^{200\,\mathrm{m}}_{\mathrm{offshore}}}. \quad (1)$$

This normalized formulation allows scaling of the horizontal temperature differences by the vertical ones. A value close to 1 indicates a fully developed upwelling with SST values at the coast equal to the temperatures at 200 m depth. Since this formulation of $\mathrm{UI_{SST}}$ generates very high values in situations when the upper ocean is vertically mixed during winter (denominator close to 0), the index is only computed here when the vertical temperature difference is larger than 1 °C.

ii. The second index is based on alongshore surface current velocities, as first proposed in Lorente et al. (2020) as a proof-of-concept investigation. This index was specifically designed to be applied in any coastal area where surface velocities are available from HF radar instruments. It assumes that the alongshore wind stress is the primary driver of upwelling circulation and that the surface currents are highly responsive to local winds (e.g. Paduan and Ronsenfeld, 1996; Kohut et al., 2006). This index is defined here as the average alongshore surface velocity ($V^{\mathrm{surf}}_{\mathrm{alongshore}}$) in the 25 km wide coastal region off the north-western coast of the island of Mallorca, following Eq. (2).

$$\mathrm{UI_{alongshore\ velocity}} = \overline{V^{\mathrm{surf}}_{\mathrm{alongshore}}} \quad (2)$$

The overbar denotes the average over the rectangular box containing the two magenta sections represented in Fig. 2. The alongshore direction is the direction of the corresponding magenta section. It makes an angle of 123° with respect to the north. Positive values denote south-westward flows. Further details about the methodology and application of this index can be found in Lorente et al. (2023; present issue of the Ocean State Report).

iii. The third index is the classical cross-shore Ekman transport index, computed from the alongshore wind stress. It is defined as follows:

$$\mathrm{UI_{Ekman\ transport}} = \int_{x=0}^{x=L} \frac{\tau_{\mathrm{alongshore}}}{\rho\, f}\,\mathrm{d}x\,, \quad (3)$$

where $\tau_{\mathrm{alongshore}}$ is the alongshore wind stress, ρ is the water density, and f is the Coriolis frequency. The integral is computed along the magenta alongshore section over a distance L of 60 km. $\mathrm{UI_{Ekman\ transport}}$ represents

the total transport across this section. Positive values indicate an offshore transport.

Finally, the last index computes the total cross-shore model transport in the upper 50 m across the same section. This depth approximately corresponds to the depth of the Ekman layer as illustrated in Fig. 3. It includes not only the Ekman transport, but also the cross-shore geostrophic transport and other contributions due to the cross-shore wind component and potential effects associated with the spatial variability in the wind stress curl. It is calculated following Eq. (4):

$$\mathrm{UI}_{\text{total transport}} = \int_{z=0}^{z=50\,\mathrm{m}} \int_{x=0}^{x=L} V_{\text{cross-shore}}\,\mathrm{d}x\,\mathrm{d}z\,, \qquad (4)$$

where $V_{\text{cross-shore}}$ is the model horizontal velocity in the cross-shore direction.

3 Surface expression of the upwelling

Figure 2 illustrates the surface circulation patterns and associated SST in the WMOP and CMEMS-MED predictions models on 7 November 2022 at 06:00 UTC (the time with the most significant impact of the upwelling on the SST). The SST exhibits marked upwelling signatures in the WMOP model along the north-western coast of the islands of Mallorca and Ibiza, with the temperature of surface waters around 6 °C colder at the coast compared to 20 km offshore. The surface coastal current flows south-westwards along the wind direction, which is reversed with respect to the direction of the Balearic Current under normal conditions (Lopez-García et al., 1994). The offshore width of the upwelled-water region ranges from 10 to 20 km, which slightly extends off the 200 m isobath. The upwelling is also represented in the CMEMS-MED model, but with a less pronounced signature. It is out of the scope of this short article to investigate these differences between models, but the lower spatial resolution of both the model grid and atmospheric forcing may have an important role in producing these discrepancies. The upwelled water only reaches the surface in the northern half of the north-western coast of the island of Mallorca in CMEMS-MED, yet with a larger offshore extension compared to the WMOP. The event duration based on its effect on the SST was around 3 d, i.e. from 5 November at 15:00 UTC, when the first cross-shore coastal SST gradients were observed, until 8 November at 12:00 UTC, when they vanished.

As illustrated in Fig. 1, the storm was associated with a dense cloud coverage, which only allowed very partial satellite remote sensing information on SST and Chl *a* concentration. Despite this important limitation, the two most relevant ocean colour images illustrated in Fig. 2 hint at the enhancement of the Chl *a* concentration along the north-western coast of the island of Mallorca. While a low concentration of Chl *a* was detected on 4 November before the storm, a significant increase was observed on 7 November. The Chl *a* concentration reached 0.1 mg m^{-3}, a magnitude more than twice as large as that observed 3 d before. While the satellite-derived Chl *a* in coastal areas should be interpreted carefully, particularly under cloudy conditions, no evident errors have been identified in the associated quality index (QI). The QI measures for every pixel the difference between the observation and the climatological average, normalized by the climatological standard deviation. The QI maps for 4 and 7 November are included in the Supplement (Fig. S1), showing values ranging from 1 to 2 in the area of enhanced Chl *a*, with a peak above 4 in the near-coastal zone. Moreover, sediment resuspension is unlikely to affect the quality of the data due to the steep local topography. Also, the Lagrangian analysis of surface water trajectories in the northern part of the island of Mallorca (Fig. S2) allows the hypothesis of a lateral advection of Chl *a* from the northern bay (Alcúdia Bay) towards the north-western coast of the island to be rejected. As a consequence, and within the limitations of both the model and observations, we believe that the spatial consistency between the observed patch of enhanced Chl *a* and the model upwelling area is probably indicative of an upwelling-induced local enhancement of Chl *a*.

4 Vertical structure

Figure 3 illustrates the vertical structure of the temperature and velocity fields along the cross-shore section off the north-western coast of the island of Mallorca, as represented by the WMOP model. While velocities are illustrated on 6 November at 12:00 UTC, corresponding to the maximum wind intensity in this area (Fig. 1), the temperature is displayed 18 h later to illustrate the time with the maximum signature in SST. The temperature section (Fig. 3a) shows a typical pattern of upwelling with an upward tilting of the isotherms towards the coast, which is associated with an upward transport of colder deep waters along the topographic slope. The surface temperature decreases by 6 °C across the upwelling front, varying from 20.6 °C 20 km offshore, where the mixed layer depth is around 50 m, to 14.6 °C at the coast. The cross-shore velocity section (Fig. 3b) shows an offshore displacement of surface waters in the upper 50 m, consistent with the Ekman theory in the presence of alongshore winds. Cross-shore velocities (Fig. 3c) reach 0.3 m s^{-1}. The alongshore velocity along this cross-shelf section is characterized by the intense south-westward coastal jet with surface velocities exceeding 1 m s^{-1}. Upward vertical velocities (Fig. 3d) are enhanced along the topographic slope, with values between 40 and 60 m d^{-1} in the upper 100 m and in the first 12 km from the coast. Overall, these cross-shelf sections illustrate a relatively thin (cross-shore extension around 20 km) but intense upwelling with a significant coastal jet.

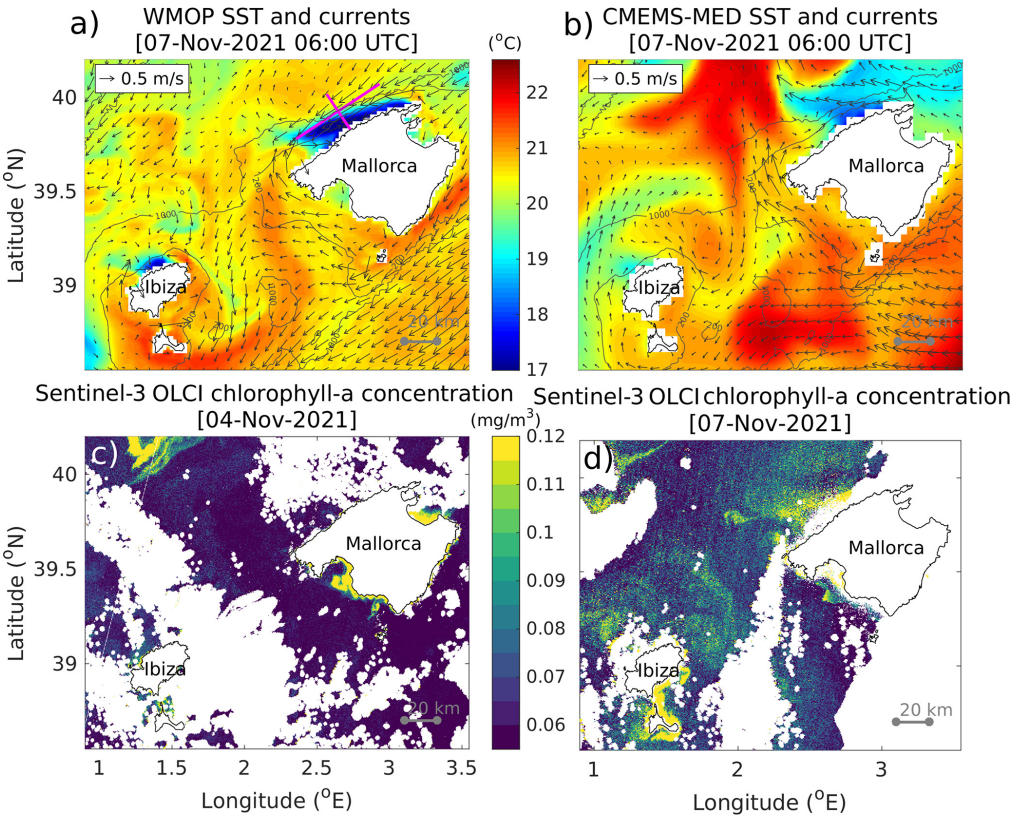

Figure 2. Upper panels: SST and surface currents around the islands of Mallorca and Ibiza on 7 November 2021 at 06:00 UTC as represented by the **(a)** WMOP and **(b)** CMEMS-MED models. In panel **(a)**, the lines in magenta represent the alongshore and cross-shore sections used in Sects. 3 and 4. Lower panels: Chl *a* concentration as observed by Sentinel-3 OLCI on **(c)** 4 November and **(d)** 7 November (i.e. before and during Storm Blas, respectively).

5 Interannual perspective

How singular was this intense wind-driven coastal-upwelling event? To answer this question, we compute here several upwelling indices (described in Sect. 2.3) over the whole WMOP model time series covering the 9-year period between August 2013 and June 2022. The first index, representing the normalized cross-shelf SST gradients, ranks the November 2021 event (i.e. Storm Blas) as the most intense event of the whole time series. It is the only event with a normalized cross-shelf SST gradient exceeding 0.5. The event is also the most intense according to the second index, which measures the intensity of the alongshore surface velocity. However, the Ekman and total cross-shelf transport indices indicate a larger transport during the other extreme event associated with Storm Gloria in January 2020. This is especially true for the total transport, which also accounts for the effects of the wind stress curl and cross-shore geostrophic transport. During both the Gloria and Blas upwelling events, the offshore total transport was enhanced with respect to the Ekman estimate. A third very intense storm in January 2017 (also documented in García-León et al., 2018) led to a slightly larger cross-shore Ekman transport but a lower total transport compared to Blas. The effects on the SST and coastal jet are particularly marked during the Blas upwelling event due to its occurrence in early November, when the surface ocean stratification was still significant. In contrast and despite the intense offshore transport during the upwelling event associated with Storm Gloria, the effects on the SST were hardly noticeable due to the presence of mixed surface waters. Note that the SST index is only computed when the vertical temperature difference between the surface and 200 m depth is larger than 1 °C, which significantly limits the use of the SST-based index during the winter season. However, this was not the case during the Gloria event, which showed values just above 1 °C.

6 Conclusions

This study describes some of the characteristics of a short (5–8 November 2021) but intense wind-driven coastal-upwelling event along the north-western coast of the Balearic Islands, as represented by a high-resolution forecast model during Storm Blas in November 2021. The time series of several upwelling indices illustrate the episodicity of upwelling

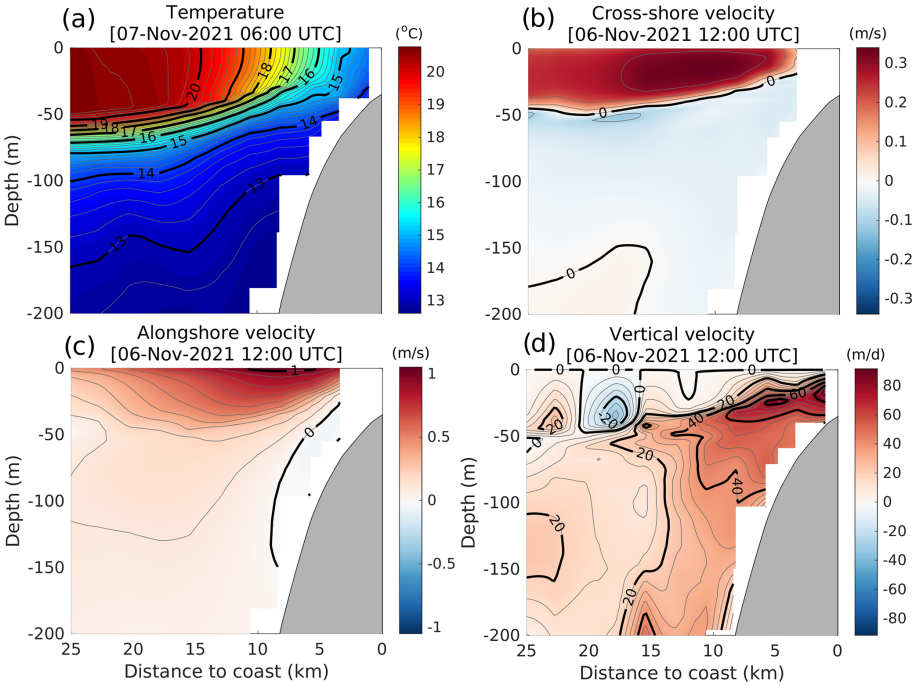

Figure 3. Sections of WMOP model fields along the cross-shore magenta line represented in Fig. 2: **(a)** temperature on 7 November 2021 at 06:00 UTC, **(b)** cross-shore velocity, **(c)** alongshore velocity and **(d)** vertical velocity on 6 November 2021 at 12:00 UTC.

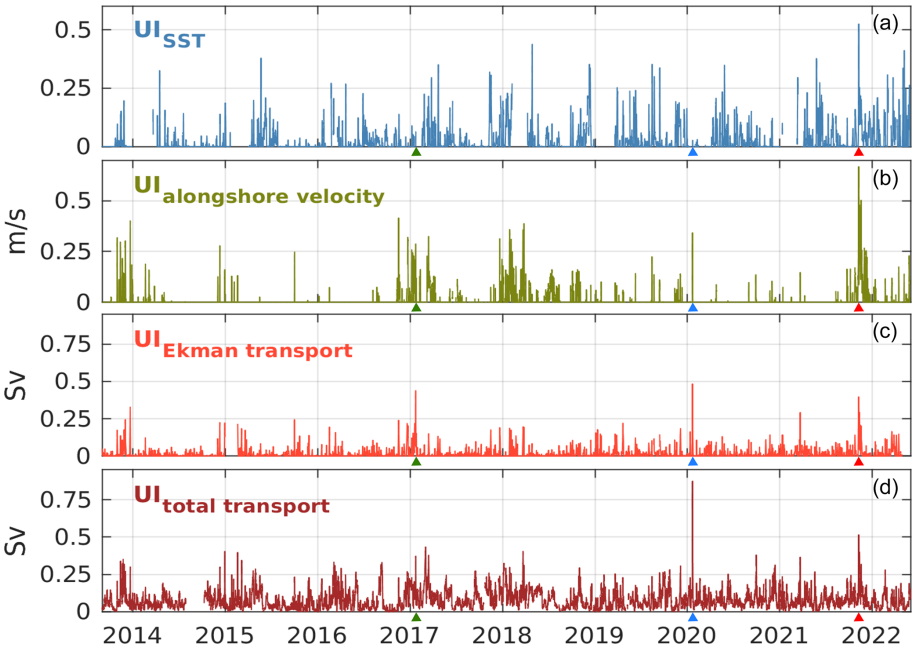

Figure 4. Time series of upwelling indices defined in Sect. 2.3 between August 2013 and June 2022 (3-hourly values are shown after applying a 24 h running average): **(a)** cross-shore normalized SST gradient index, **(b)** alongshore velocity index, **(c)** cross-shore Ekman transport index, **(d)** cross-shore total transport index. The red, blue and green triangles on the *x* axis mark the time of the Blas, Gloria and January 2017 storms, respectively.

events in this area, mainly related to their nature related to the occurrence of storms with intense north-easterly winds.

While the November 2021 Blas-related event was the most intense in terms of the effects on the SST and alongshore velocities over the 9-year-long time series analysed, the induced cross-shelf surface transport was lower than that modelled during Storm Gloria in January 2020, whose effects on the wind, waves, sea level and currents were already reported as a record-breaking event in the literature (Álvarez-Fanjul et al., 2022). This comparison illustrates the difference between upwelling indices for the characterization of the intensity of these events. In particular, the magnitude of SST gradients or alongshore velocity does not necessarily reveal the whole intensity of the underlying offshore transport. A careful analysis of the time series would allow appropriate thresholds to be determined for the different indices so as to define suitable criteria for the identification of the upwelling. The duration would certainly be an additional relevant parameter for the operational definition of these events. Here, for instance, the event duration corresponding to a threshold of 0.25 Sv for the total offshore transport was 42 h for the Blas-related upwelling, 51 h for Gloria and 21 h for the January 2017 event. In the particular case of Blas, this duration is shorter than 3 d, i.e. the value obtained when considering the effect on the SST, highlighting the sensitivity of these metrics to the index and threshold under consideration.

Such storm-driven coastal upwelling is especially difficult to monitor given their short timescale and the absence of in situ observations in this area. The dense cloud coverage associated with the storm also significantly limits the availability of high-resolution satellite observations to characterize the surface signature of the phenomenon. In this context, high-resolution operational regional ocean models help overcome these limitations, providing timely and accurate information to identify and characterize these events. The only available ocean colour image from satellites suggests an increase in primary productivity in a coastal area which corresponds to the area of upwelled water in the model. While the lack of complementary observations prevents the realism of the model fields from being properly evaluated, the consistency between the spatial structure of observed Chl *a* enhancement and model upwelled water seems to indicate a reasonable representation of the effect of the upwelling process in the model. High spatial resolution (close to kilometric) is needed in both the model grid and the atmospheric forcing to describe such coastal phenomena whose cross-shore extension does not exceed 20 km.

Despite its short duration, this phenomenon was found to be sufficient to enhance the surface Chl *a* concentration. A more comprehensive understanding of the impacts of these storm-related upwelling events on local ecosystems would need further investigation requiring dedicated monitoring systems. Underwater gliders equipped with sensors of both physical and biogeochemical parameters can be suitable observation platforms for these studies given their capacity to operate under any weather conditions. In the future, the possible increase in the intensity and duration of the storms affecting the western Mediterranean area (Gaertner et al., 2007; Romero and Emanuel, 2013; González-Alemán et al., 2019) could lead to enhanced impacts of such storm-related upwelling events. While this study presents a first analysis over the last 9 years, it will be important to analyse these events in the longer term with a climate perspective when multi-decadal, kilometre-scale reanalysis simulations become available in the study area.

Data availability. The model and observation products used in this study from both the Copernicus Marine Service and other sources are listed in Table 1.

Supplement. The supplement related to this article is available online at: https://doi.org/10.5194/sp-1-osr7-15-2023-supplement.

Author contributions. BM, ER, AS, JHL, IHC, MGJ and NDZ designed the study through interactive discussions in the framework of working team meetings. BM and ER created the figures. BM prepared the article with contributions from all co-authors. ER analysed HF radar and in situ observations. PL provided expertise in the definition of upwelling indices. AS analysed the atmospheric fields and computed the Ekman transport. NDZ and IHC contributed to the analysis of ocean colour images. JHL and MGJ analysed WMOP and CMEMS-MED model outputs. All authors participated in the iterations and revision of the manuscript.

Competing interests. The contact author has declared that none of the authors has any competing interests.

Disclaimer. Publisher's note: Copernicus Publications remains neutral with regard to jurisdictional claims in published maps and institutional affiliations.

Acknowledgements. This study was conducted using information from the European Union's Copernicus Marine Service. The results of this article were obtained using the HARMONIE-AROME atmospheric fields provided by the Spanish Meteorological Agency (AEMET, Ministerio para la Transición Ecológica y el Reto Demográfico). The authors are very grateful to AEMET for providing these fields. The authors also thank SOCIB and Puertos del Estado for collecting oceanic and atmospheric observations around the Balearic Islands and distributing them through both their institutional websites and the Copernicus database.

Review statement. This paper was edited by Joanna Staneva and reviewed by Riccardo Torres and one anonymous referee.

References

Álvarez-Fanjul, E., Pérez Gómez, M., Alonso-Muñoyerr, M. de A., Jiménez, P. L., Sotillo, M. G., Lin-Ye, J., Lecocq, A., Serna, M. R. G. de la, Rubio, S. P., Clementi, E., Coppini, G., García-León, M., Muñoz, D. S., Rico, M. Y. L., Mestres, M., Molina, R., Tintoré, J., Mourre, B., Masina, S., Mosso, C., Reyes, E., and Santana, A.: Western Mediterranean record-breaking storm Gloria: An integrated assessment based on models and observations, in: Copernicus Ocean State Report, Issue 6, edited by: von Schuckmann, K., Le Traon, P.-Y., Smith, N., Pascual, A., Djavidnia, S., Brasseur, P., and Grégoire, M., J. Oper. Oceanogr., 15, Supplement 1, 1–220, https://doi.org/10.1080/1755876X.2022.2095169, 2022.

Amores, A., Marcos, M., Carrió, D. S., and Gómez-Pujol, L.: Coastal impacts of Storm Gloria (January 2020) over the northwestern Mediterranean, Nat. Hazards Earth Syst. Sci., 20, 1955–1968, https://doi.org/10.5194/nhess-20-1955-2020, 2020.

Bakun, A.: Coastal upwelling indices, west coast of North America, 1946-71, NOAA technical report NMFS SSRF, https://repository.library.noaa.gov/view/noaa/9041 (last access: 14 April 2023), 1973.

Bakun, A. and Agostini, V. N.: Seasonal patterns of wind-induced upwelling/downwelling in the Mediterranean Sea, Sci. Mar., 65, 243–257, 2001.

Bengtsson, L., Andrae, U., Aspelien, T., Batrak, Y., Calvo, J., Rooy, W. de, Gleeson, E., Hansen-Sass, B., Homleid, M., Hortal, M., Ivarsson, Karl-Ivar Lenderink, G., Niemelä, S., Nielsen, K. P., Onvlee, J., Rontu, L., Samuelsson, P., Muñoz, D. S., Subias, A., Tijm, S., Toll, V., Yang, X., and Køltzow, M. Ø.: The HARMONIE–AROME model configuration in the ALADIN–HIRLAM NWP system, Mon. Weather Rev., 145, 1919–1935, 2017.

Casella, E., Molcard, A., and Provenzale, A.: Mesoscale vortices in the Ligurian Sea and their effect on coastal upwelling processes, J. Marine Syst., 88, 12–19, 2011.

Clementi, E., Aydogdu, A., Goglio, A. C., Pistoia, J., Escudier, R., Drudi, M., Grandi, A., Mariani, A., Lyubartsev, V., Lecci, R., Cretí, S., Coppini, G., Masina, S., and Pinardi, N.: Mediterranean Sea Physical Analysis and Forecast (CMEMS MED-Currents, EAS6 system), Version 1, Copernicus Monitoring Environment Marine Service (CMEMS) [data set], https://doi.org/10.25423/CMCC/MEDSEA_ANALYSISFORECAST_PHY_006_013_EAS6, 2021.

Colella, S., Böhm, E., Cesarini, C., Garnesson, P., Netting, J., and Calton, B.: EU Copernicus Marine Service Product User Manual for the Mediterranean Sea Ocean Colour Plankton, Reflectance, Transparency and Optics L3 NRT daily observations, OCEANCOLOUR_MED_BGC_L3_NRT_009_141, Issue 3.0, Mercator Ocean International, https://catalogue.marine.copernicus.eu/documents/PUM/CMEMS-OC-PUM.pdf (last access: 14 April 2023), 2022a.

Colella, S., Brando, V. E., Di Cicco, A., D'Alimonte, D., Forneris, V., and Bracaglia, M.: EU Copernicus Marine Service Quality Information Document for the Mediterranean Sea Ocean Colour Plankton, Reflectance, Transparency and Optics L3 NRT daily observations, OCEANCOLOUR_MED_BGC_L3_NRT_009_141, Issue 2.0, Mercator Ocean International, https://catalogue.marine.copernicus.eu/documents/QUID/CMEMS-OC-QUID-009-141to144-151to154.pdf (last access: 14 April 2023), 2022b.

Demarcq, H. and Faure, V.: Coastal upwelling and associated retention indices derived from satellite SST. Application to *Octopus vulgaris* recruitment, Oceanol. Acta, 23, 391–408, 2000.

Dobricic, S. and Pinardi, N.: An oceanographic three-dimensional variational data assimilation scheme, Ocean Model., 22, 89–105, 2008.

EU Copernicus Marine Service Product: Mediterranean Sea- In-Situ Near Real Time Observations, Mercator Ocean International [data set], https://doi.org/10.48670/moi-00044, 2022a.

EU Copernicus Marine Service Product: Mediterranean Sea Physics Analysis and Forecast, Mercator Ocean International [data set], https://doi.org/10.25423/CMCC/MEDSEA_ANALYSISFORECAST_PHY_006_013_EAS7, 2022b.

EU Copernicus Marine Service Product: Mediterranean Sea High Resolution and Ultra High Resolution Sea Surface Temperature Analysis, Mercator Ocean International [data set], https://doi.org/10.48670/moi-00172, 2022c.

EU Copernicus Marine Service Product: Global Ocean- in-situ Near real time observations of ocean currents, Mercator Ocean International [data set], https://doi.org/10.48670/moi-00041, 2022d.

EU Copernicus Marine Service Product: Mediterranean Sea Ocean Colour Plankton, Reflectance, Transparency and Optics L3 NRT daily observations, Mercator Ocean International [data set], https://doi.org/10.48670/moi-00297, 2022e.

EU Copernicus Marine Service Product: European Seas Along Track L 3 Sea Level Anomalies Nrt Tailored For Data Assimilation, Mercator Ocean International [data set], https://doi.org/10.48670/moi-00140, 2023.

Gaertner, M. A., Jacob, D., Gil, V., Domínguez, M., Padorno, E., Sánchez, E., and Castro, M.: Tropical cyclones over the Mediterranean Sea in climate change simulations, Geophys. Res. Lett., 34, L14711, https://doi.org/10.1029/2007GL029977, 2007.

García-León, M.: Coastal Risk Forecast System: Fostering Proactive Management at the Catalan Coast, Doctoral dissertation, Polytechnic University of Catalonia, Barcelona, http://hdl.handle.net/2117/330131 (last access: 14 April 2023), 2018.

Goglio, A.-C., Clementi, E., Grandi, A., Mariani, A., Giurato, M., and Aydogdu, A.: EU Copernicus Marine Service Quality Information Document for the Mediterranean Sea Physics Analysis and Forecast, MEDSEA_ANALYSISFORECAST_PHY_006_013, Issue 2.3, Mercator Ocean International, https://catalogue.marine.copernicus.eu/documents/QUID/CMEMS-MED-QUID-006-013.pdf (last access: 14 April 2023), 2022.

González-Alemán, J. J., Pascale, S., Gutierrez-Fernandez, J., Murakami, H., Gaertner, M. A., and Vecchi, G. A.: Potential increase in hazard from Mediterranean hurricane activity with global warming, Geophys. Res. Lett., 46, 1754–1764, 2019.

Hernandez-Lasheras, J. and Mourre, B.: Dense CTD survey versus glider fleet sampling: comparing data assimilation performance in a regional ocean model west of Sardinia, Ocean Sci., 14, 1069–1084, https://doi.org/10.5194/os-14-1069-2018, 2018.

Hernandez-Lasheras, J., Mourre, B., Orfila, A., Santana, A., Reyes, E., and Tintoré, J.: Evaluating high-frequency radar data assimilation impact in coastal ocean operational modelling, Ocean Sci., 17, 1157–1175, https://doi.org/10.5194/os-17-1157-2021, 2021.

Jacox, M. G., Edwards, C. A., Hazen, E. L., and Bograd, S. J.: Coastal upwelling revisited: Ekman, Bakun, and improved upwelling indices for the U.S. west coast, J. Geophys. Res., 123, 7332–7350, 2018.

Juza, M., Mourre, B., Renault, L., Gómara, S., Sebastián, K., Lora, S., Beltran, J. P., Frontera, B., Garau, B., Troupin, C., Torner, M., Heslop, E., Casas, B., Escudier, R., Vizoso, G., and Tintoré, J.: SOCIB operational ocean forecasting system and multi-platform validation in the Western Mediterranean Sea, J. Oper. Oceanogr., 9, s155–s166, 2016.

Kohut, J. T., Glenn, S. M., and Paduan, J. D.: Inner-shelf response to tropical storm Floyd. J. Geophys. Res., 111, C09S91, https://doi.org/10.1029/2003JC002173, 2006.

Lecci, R., Drudi, M., Grandi, A., Creti, S., and Clementi, M.: EU Copernicus Marine Service Product User Manual for the Mediterranean Sea Physics Analysis and Forecast, MEDSEA_ANALYSISFORECAST_PHY_006_013, Issue 2.2, Mercator Ocean International, https://catalogue.marine.copernicus.eu/documents/PUM/CMEMS-MED-PUM-006-013.pdf (last access: 14 April 2023), 2022

Lopez-García, M. J., Millot, C., Font, J., and Garcia-Ladona, E.: Surface circulation variability in the Balearic Basin, J. Geophys. Res., 99, 3285–3296, 1994.

Lorente, P., Piedracoba, S., Montero, P., Sotillo, M. G., Ruiz, M. I., and Álvarez-Fanjul, E.: Comparative Analysis of Summer Upwelling and Downwelling Events in NW Spain: A Model-Observations Approach, Remote Sens.-Basel, 2020, 12, 2762, https://doi.org/10.3390/rs12172762, 2020.

Lorente, P., Rubio, A., Reyes, E., Solabarrieta, L., Piedracoba, S., Tintoré, J., and Mader, J.: High-frequency radar-derived coastal upwelling index, in: 7th edition of the Copernicus Ocean State Report (OSR7), edited by: von Schuckmann, K., Moreira, L., Le Traon, P.-Y., Grégoire, M., Marcos, M., Staneva, J., Brasseur, P., Garric, G., Lionello, P., Karstensen, J., and Neukermans, G., Copernicus Publications, State Planet, 1-osr7, 8, https://doi.org/10.5194/sp-1-osr7-8-2023, 2023.

Macías, D., Bruno, M., Echevarría, F., Vázquez, A., and García, C. M.: Meteorologically-induced mesoscale variability of the North-western Alboran Sea (southern Spain) and related biological patterns, Estuar. Coast. Shelf S., 78, 250–266, 2008.

Marchesiello, P. and Estrade, P.: Upwelling limitation by onshore geostrophic flow, J. Mar. Res., 68, 37–62, 2010.

Millot, C.: Wind induced upwellings in the Gulf of Lions, Oceanol. Acta, 2, 261–274, 1979.

Millot, C.: Some features of the Algerian Current, J. Geophys. Res.-Oceans, 90, 7169–7176, 1985.

Mourre B., Aguiar, E., Juza, M., Hernandez-Lasheras, J., Reyes, E., Heslop, E., Escudier, R., Cutolo, E., Ruiz, S., Mason, E., Pascual, A., and Tintoré, J.: Assessment of high-resolution regional ocean prediction systems using multi-platform observations: illustrations in the Western Mediterranean Sea, in: "New Frontiers in Operational Oceanography", edited by: Chassignet, E., Pascual, A., Tintoré, J., and Verron, J., GODAE Ocean View, 663–694, https://doi.org/10.17125/gov2018.ch24, 2018.

Olita, A., Ribotti, A., Fazioli, L., Perilli, A., and Sorgente, R.: Surface circulation and upwelling in the Sardinia Sea: A numerical study, Cont. Shelf Res., 71, 95–108, 2013.

Paduan, J. D. and Rosenfeld, L. K.: Remotely sensed surface currents in Monterey Bay from shore-based HF radar (CODAR), J. Geophys. Res., 101, 20669–20686, 1996.

Pauly, D. and Christensen, V.: Primary production required to sustain global fisheries, Nature, 374, 255–257, 1995.

Pisano, A., Fanelli, C., Buongiorno Nardelli, B., Tronconi, C., Cesarini, C., and La Padula, F.: EU Copernicus Marine Service Product User Manual for Mediterranean Sea High Resolution and Ultra High Resolution Sea Surface Temperature Analysis, SST_MED_SST_L4_NRT_OBSERVATIONS_010_004, Issue 3.0, Mercator Ocean International, https://catalogue.marine.copernicus.eu/documents/PUM/CMEMS-SST-PUM-010-004-006-012-013.pdf, (last access: 14 April 2023), 2022a.

Pisano, A., Fanelli, C., Buongiorno Nardelli, B., Tronconi, C., La Padula, F., and Cesarini, C.: EU Copernicus Marine Service Quality Information Document for Mediterranean Sea High Resolution and Ultra High Resolution Sea Surface Temperature Analysis, SST_MED_SST_L4_NRT_OBSERVATIONS_010_004, Issue 3.0, Mercator Ocean International, https://catalogue.marine.copernicus.eu/documents/QUID/CMEMS-SST-QUID-010-004-006-012-013.pdf, (last access: 14 April 2023), 2022b.

Pouliquen, S., Carval, T., Petit de la Villéon, L., Tarot, S., and In Situ TAC partners: EU Copernicus Marine Service Product User Manual for the Mediterranean Sea- In-Situ Near Real Time Observations, INSITU_MED_PHYBGCWAV_DISCRETE_MYNRT_013_035, Issue 1.14, Mercator Ocean International, https://catalogue.marine.copernicus.eu/documents/PUM/CMEMS-INS-PUM-013-030-036.pdf (last access: 14 April 2023), 2022.

Pujol, M.-I.: EU Copernicus Marine Service Product User Manual for the European Seas Along Track L3 Sea Level Anomalies Nrt Tailored For Data Assimilation, SEALEVEL_EUR_PHY_L3_NRT_OBSERVATIONS_008_059, Issue 7.0, Mercator Ocean International, https://catalogue.marine.copernicus.eu/documents/PUM/CMEMS-SL-PUM-008-032-068.pdf (last access: 14 April 2023), 2022.

Pujol, M.-I., Taburet, G., and SL-TAC Team: EU Copernicus Marine Service Quality Information Document for the European Seas Along Track L3 Sea Level Anomalies Nrt Tailored For Data Assimilation, SEALEVEL_EUR_PHY_L3_NRT_OBSERVATIONS_008_059, Issue 8.2, Mercator Ocean International, https://catalogue.marine.copernicus.eu/documents/QUID/CMEMS-SL-QUID-008-032-068.pdf (last access: 14 April 2023), 2023.

Rey, V., Dufresne, C., Fuda, J.-L., Mallarino, D., Missamou, T., Paugam, C., Rougier, G., and Taupier-Letage, I.: On the use of long-term observation of water level and temperature along the shore for a better understanding of the dynamics: example of Toulon area, France, Ocean Dynam., 70, 913–933, 2020.

Romero, R. and Emanuel, K.: Medicane risk in a changing climate, J. Geophys. Res.-Atmos., 118, 5992–6001, 2013.

Rossi, V., Feng, M., Pattiaratchi, C., Roughan, M., and Waite, A. M.: On the factors influencing the development of sporadic

upwelling in the Leeuwin Current system, J. Geophys. Res.-Oceans, 118, 3608–3621, 2013.

Salusti, E.: Satellite images of upwellings and cold filament dynamics as transient effects of violent air-sea interactions downstream from the island of Sardinia (western Mediterranean Sea), J. Geophys. Res.-Oceans, 103, 3013–3031, 1998.

Sarhan, T., García-Lafuente, J., Vargas, M., Vargas, J. M., and Plaza, F.: Upwelling mechanisms in the northwestern Alboran Sea, J. Marine Syst., 23, 317–331, 2000.

Shchepetkin, A. F. and McWilliams, J. C.: The regional oceanic modeling system (ROMS): a split-explicit, free-surface, topography-following-coordinate oceanic model, Ocean Model., 9, 347–404, 2005.

Sotillo, M. G., Mourre, B., Mestres, M., Lorente, P., Aznar, R., García-León, M., Liste, M., Santana, A., Espino, M., and Álvarez, E.: Evaluation of the operational CMEMS and coastal downstream ocean forecasting services during the storm Gloria (January 2020), Frontiers in Marine Science, 8, 644525, https://doi.org/10.3389/fmars.2021.644525, 2021.

Tintoré, J., Vizoso, G., Casas, B., Heslop, E., Pascual, A., Orfila, A., Ruiz, S., Martínez-Ledesma, M., Torner, M., Cusí, S., Diedrich, A., Balaguer, P., Gómez-Pujol, L., Álvarez-Ellacuria, A., Gómara, S., Sebastian, K., Lora, S., Beltrán, J. P., Renault, L., Juzà, M., Álvarez, D., March, D., Garau, B., Castilla, C., Cañellas, T., Roque, D., Lizarán, I., Pitarch, S., Carrasco, M. A., Lana, A., Mason, E., Escudier, R., Conti, D., Sayol, J. M., Barceló, B., Alemany, F., Reglero, P., Massuti, E., Vélez-Belchí, P., Ruiz, J., Oguz, T., Gómez, M., Álvarez, E., Ansorena, L., and Manriquez, M.: SOCIB: the Balearic Islands Observing and Forecasting System responding to science, technology and society needs, Mar. Technol. Soc. J., 47, 17 pp., 2013.

Verbrugge, N., Etienne, H., Corgnati, L., Mantovani, C., Reyes, E., Solabarrieta, L., Rubio, A., Carval, T., Mader, J., and Drouineau, L.: EU Copernicus Marine Service Product User Manual for the Global Ocean- in-situ Near real time observations of ocean currents, INSITU_GLO_PHY_UV_DISCRETE_NRT_013_048, Issue 2.2, Mercator Ocean International, https://catalogue.marine.copernicus.eu/documents/PUM/CMEMS-INS-PUM-013-048.pdf (last access: 14 April 2022), 2022a.

Verbrugge, N., Etienne, H., Corgnati, L., Mantovani, C., Reyes, E., Solabarrieta, L., Rubio, A., Carval, T., Mader, J., and Drouineau, L.: EU Copernicus Marine Service Quality Information Document for the Global Ocean- in-situ Near real time observations of ocean currents, INSITU_GLO_PHY_UV_DISCRETE_NRT_013_048, Issue 2.2, Mercator Ocean International, https://catalogue.marine.copernicus.eu/documents/QUID/CMEMS-INS-QUID-013-048.pdf (last access: 14 April 2023), 2022b.

Volpe, G., Colella, S., Brando, V. E., Forneris, V., La Padula, F., Di Cicco, A., Sammartino, M., Bracaglia, M., Artuso, F., and Santoleri, R.: Mediterranean ocean colour Level 3 operational multi-sensor processing, Ocean Sci., 15, 127–146, https://doi.org/10.5194/os-15-127-2019, 2019.

Wehde, H., von Schuckmann, K., Pouliquen, S., Grouazel, A., Bartolome, T., Tintore, J., De Alfonso Alonso-Munoyerro, M., Carval, T., Racapé, V., and the INSTAC team: EU Copernicus Marine Service Quality Information Document for the Mediterranean Sea- In-Situ Near Real Time Observations, INSITU_MED_PHYBGCWAV_DISCRETE_MYNRT_013_035, Issue 2.2, Mercator Ocean International, https://catalogue.marine.copernicus.eu/documents/QUID/CMEMS-INS-QUID-013-030-036.pdf (last access: 14 April 2023), 2022.

Table of contents

Copernicus Ocean State Report | OSR7 | 2023

Chapter 1: Introduction

1.1 Introduction to the 7th edition of the Copernicus Ocean State Report (OSR7). K. von Schuckmann et al.

1.2 Evaluation of operational ocean forecasting systems from the perspective of the users and the experts. S. A. Ciliberti et al.

Chapter 2: Updated and new pathways in ocean science

2.1 Comparing global trends in marine cold spells and marine heatwaves using reprocessed satellite data. R. Peal et al.

2.2 South Atlantic overturning and heat transport variations in ocean reanalyses and observation-based estimates. J. A. Baker et al.

2.3 Satellite monitoring of surface phytoplankton functional types in the Atlantic Ocean over 20 years (2002–2021). H. Xi et al.

2.4 The dynamical role of upper layer salinity in the Mediterranean Sea. A. Aydogdu et al.

2.5 Baltic Sea freshwater content. U. Raudsepp et al.

2.6 High-frequency radar-derived coastal upwelling index. P. Lorente et al.

2.7 Ocean heat content in the Iberian–Biscay–Ireland regional seas. Á. de Pascual-Collar et al.

Chapter 3: Ocean state and change for relevance to society

3.1 Dissolved oxygen as an indicator of multiple drivers of the marine ecosystem: the southern Adriatic Sea case study. V. Di Biagio et al.

3.2 Characterization of the organic vs. inorganic fraction of suspended particulate matter in coastal waters based on ocean color radiometry remote sensing. H. Loisel et al.

3.3 Recent changes in extreme wave events in the south-western South Atlantic. C. B. Gramcianinov et al.

Chapter 4: Specific events in the ocean in 2021

4.1 Unusual coccolithophore blooms in Scottish waters. R. Renshaw et al.

4.2 Recent variations in oceanic transports across the Greenland–Scotland Ridge. M. Mayer et al.

4.3 Intense wind-driven coastal upwelling in the Balearic Islands in response to Storm Blas (November 2021). B. Mourre et al.